

V. 121, NO. 2, MARCH 2024

ACI STRUCTURAL

JOURNAL



American Concrete Institute

CONTENTS

Editorial Board

Michael Kreger, Editor-in-Chief University of Alabama Catherine French University of Minnesota Mary Beth Hueste Texas A&M University **David Sanders** Iowa State University Gustavo Parra-Montesinos University of Wisconsin-Madison

Special Issue Guest Editors

Liberato Ferrara, Politecnico di Milano Eric L. Kreiger, U.S. Army Engineer Research and Development Center

Board of Direction

President

Antonio Nanni

Vice Presidents

Maria Juenger Michael J. Paul

Directors

Oscar R. Antommattei Peter Barlow Michael C. Brown Arturo Gaytan Covarrubias Anthony R. DeCarlo Jr. John W. Gajda Carol Hayek Kamal H. Khayat Robert C. Lewis Anton K. Schindler Matthew R. Sherman Lawrence L. Sutter

Past President Board Members

Jeffrey W. Coleman Cary S. Kopczynski Charles K. Nmai

Executive Vice President

Frederick H. Grubbe

Staff

Publisher John C. Glumb

Managing Director, Engineering and Professional Development Michael L. Tholen

Enaineers Will J. Gold Matthew R. Senecal Michael L. Tholen Gregory M. Zeisler

Managing Editor Lauren E. Mentz

Associate Editor Kimberly K. Olesky

Editors Erin N. Azzopardi Lauren C. Brown Kaitlyn J. Dobberteen Tiesha Elam Angela R. Noelker Kelli R. Slayden



ACI STRUCTURAL JOURNAL

March 2024, V. 121, No. 2

A JOURNAL OF THE AMERICAN CONCRETE INSTITUTE AN INTERNATIONAL TECHNICAL SOCIETY

SPECIAL ISSUE: Advances in Construction Practices for Additive Construction

- 37 Three-Dimensional-Printed Engineered, Strain-Hardening Geopolymer Composite as Permanent Formwork for Construction of Reinforced Concrete Beam, by Shin Hau Bong, Behzad Nematollahi, Viktor Mechtcherine, Victor C. Li, and Kamal H. Khayat
- 49 Approach for Production of Textile-Reinforced Beams and Slabs Using Three-Dimensional Concrete Printing, by Egor Ivaniuk and Viktor Mechtcherine
- Modeling of Concrete Printing Process with Frictional Interface, by 71 Ignasius P. A. Wijaya, Eric Kreiger, and Arif Masud

ALSO FEATURING

- 5 Development of Compressive Fracture Energy Model for Confined Normal-Strength Concrete, by Xiaoran Song
- 19 Cyclic Behavior of Reinforced Concrete Flexural Members to Changing Design Parameters, by Jessica Gitomarsono, Min-Yuan Cheng, and Marnie B. Giduquio
- 57 Prediction of Tensile Properties of Ultra-High-Performance Concrete Using Artificial Neural Network, by Amjad Y. Diab and Anca C. Ferche
- 87 Ultimate Shear Strength Prediction for Slender Reinforced Concrete Beams without Transverse Reinforcement Using Machine Learning Approach, by Ju Dong Lee and Thomas H.-K. Kang
- 99 Shear Strength of Concrete Block Masonry Using Direct Shear Test, by Muhammad Masood Rafi and Sher Khan
- 111 Shear Strength of Reinforced Concrete Columns with External Post-Tensioned Clamps, by Julian D. Rincon, Yu-Mei Chen, Santiago Pujol, Aishwarya Y. Puranam, and Shyh-Jiann Hwang
- 127 Practical Approach to Predict Web-Shear Strength of Deep Prestressed Hollow-Core Slabs, by Ernesto Hernández, Alessandro Palermo, and Ali Amin
- 143 Outrigger Action in Tall Core-Wall Buildings with Flat-Plate Framing, by Connie I. Chen and Jack P. Moehle
- 153 Effect of Bond Condition on Cyclic Behavior of Post-Tensioned Concrete Beams with Carbon Fiber-Reinforced Polymer Tendons, by Fei Peng, Weichen Xue, and Shulu Zhang

Contents continued on next page

Discussion is welcomed for all materials published in this issue and will appear ten months from this journal's date if the discussion is received within four months of the paper's print publication. Discussion of material received after specified dates will be considered individually for publication or private response. ACI Standards published in ACI Journals for public comment have discussion due dates printed with the Standard.

ACI Structural Journal
Copyright © 2024 American Concrete Institute. Printed in the United States of America.

The ACI Structural Journal (ISSN 0889-3241) is published bimonthly by the American Concrete Institute. Publication office: 38800 Country Club Drive, Farmington Hills, MI 48331. Periodicals postage paid at Farmington, MI, and at additional mailing offices. Subscription rates: \$199 per year, payable in advance. POSTMASTER: Send address changes to: ACI Structural Journal, 38800 Country Club Drive, Farmington Hills, MI 48331.

Direct correspondence to 38800 Country Club Drive, Farmington Hills, MI 48331. Telephone: +1.248.848.3700. Facsimile (FAX): +1.248.848.3701. Website: http://www.concrete.org.

CONTENTS

- 165 Response of Reinforced Concrete Shell Elements Subjected to In-Plane and Out-of-Plane Shear, by Giorgio T. Proestos, Evan C. Bentz, and Michael P. Collins
- 181 Behavior of Shear-Critical Concrete Deep Beams Monitored with Digital Image Correlation Equipment, by Dhanushka K. Palipana and Giorgio T. Proestos
- 193 2023 Reviewers List

MEETINGS

APRIL

7-12—RILEM Spring Convention 2024, Milan, Italy, https://rilem.cte-eventi.com

10-26—The Masonry Society's 2024 Spring Meeting, Virtual, https:// masonrysociety.org/event/2024-springmeeting-virtual

14-17—PTI Post-Tensioning Convention, Indianapolis, IN, www.post-tensioning.org/events/conventions.aspx

15-18—CRSI 2024 Spring Business & Technical Meeting, Anaheim, CA, www. crsi.org/event/2024-spring-business-technical-meeting

16-17—1st RILEM International Conference on Mineral Carbonation for Cement and Concrete, Aachen, Germany, www.rilem.net/agenda/1st-internationalrilem-conference-on-mineral-carbonationfor-cement-and-concrete-1569

18-19—Cementitious Materials International Technical and Trade Congress, Casablanca, Morocco, https://industrylink.eu/event/cementitious-2024

22-24—2024 ICRI Spring Convention, Boston, MA, https://www.icri.org/event/2024-icri-spring-convention-save-the-date/

ACI CONCRETE CONVENTION: FUTURE DATES

2024—March 24-28, Hyatt Regency New Orleans, New Orleans, LA
2024—November 3-7, Philadelphia Marriott Downtown, Philadelphia, PA
2025—March 30-April 3, Sheraton Centre Toronto Hotel, Toronto, ON, Canada

For additional information, contact:

Event Services, ACI 38800 Country Club Drive Farmington Hills, MI 48331 Telephone: +1.248.848.3795 email: conventions@concrete.org

ON FRONT COVER: 121-M14, Fig. 12—Examples of structures and techniques implemented by novel dry-forming technology: (a) pillar coral 3D-printed structures (left); 121-S17, Fig. 6—View on bottom surface of manufactured elements: (a) beam (center); 121-M13, Fig. 7—(e) Optical microscope image of surface of three-dimensionally printed specimen with polyvinyl alcohol fibers (right).

ON BACK COVER: 121-S19, p. 70, Fig. 1—Additive construction process: (a) machine.

Permission is granted by the American Concrete Institute for libraries and other users registered with the Copyright Clearance Center (CCC) to photocopy any article contained herein for a fee of \$3.00 per copy of the article. Payments should be sent directly to the Copyright Clearance Center, 21 Congress Street, Salem, MA 01970. ISSN 0889-3241/98 \$3.00. Copyring done for other than personal or internal reference use without the express written permission of the American Concrete Institute is prohibited. Requests for special permission or bulk copying should be addressed to the Managing Editor, ACI Structural Journal, American Concrete Institute.

The Institute is not responsible for statements or opinions expressed in its publications. Institute publications are not able to, nor intend to, supplant individual training, responsibility, or judgment of the user, or the supplier, of the information presented.

Papers appearing in the ACI Structural Journal are reviewed according to the Institute's Publication Policy by individuals expert in the subject area of the papers.

Contributions to ACI Structural Journal

The ACI Structural Journal is an open forum on concrete technology and papers related to this field are always welcome. All material submitted for possible publication must meet the requirements of the "American Concrete Institute Publication Policy" and "Author Guidelines and Submission Procedures." Prospective authors should request a copy of the Policy and Guidelines from ACI or visit ACI's website at www.concrete.org prior to submitting contributions.

Papers reporting research must include a statement indicating the significance of the research.

The Institute reserves the right to return, without review, contributions not meeting the requirements of the Publication Policy.

All materials conforming to the Policy requirements will be reviewed for editorial quality and technical content, and every effort will be made to put all acceptable papers into the information channel. However, potentially good papers may be returned to authors when it is not possible to publish them in a reasonable time.

Discussion

All technical material appearing in the ACI Structural Journal may be discussed. If the deadline indicated on the contents page is observed, discussion can appear in the designated issue. Discussion should be complete and ready for publication, including finished, reproducible illustrations. Discussion must be confined to the scope of the paper and meet the ACI Publication Policy.

Follow the style of the current issue. Be brief-1800 words of double spaced, typewritten copy, including illustrations and tables, is maximum. Count illustrations and tables as 300 words each and submit them on individual sheets. As an approximation, 1 page of text is about 300 words. Submit one original typescript on 8-1/2 x 11 plain white paper, use 1 in. margins, and include two good quality copies of the entire discussion. References should be complete. Do not repeat references cited in original paper; cite them by original number. Closures responding to a single discussion should not exceed 1800-word equivalents in length, and to multiple discussions, approximately one half of the combined lengths of all discussions. Closures are published together with the discussions.

Discuss the paper, not some new or outside work on the same subject. Use references wherever possible instead of repeating available information.

Discussion offered for publication should offer some benefit to the general reader. Discussion which does not meet this requirement will be returned or referred to the author for private reply.

Send manuscripts to: http://mc.manuscriptcentral.com/aci

Send discussions to: Journals.Manuscripts@concrete.org

LETTER FROM THE GUEST EDITORS

Additive construction (that is, three-dimensional [3-D] construction printing) has gained significant momentum in a short time frame, with the first buildings being completed in 2014/2015 and the first major publication on materials in 2012. While there are several potential options, the field of additive construction (AC) has been dominated by mortar/ concrete materials. This method of construction places material without formwork present, resulting in a unique relationship between material and structural performance during construction that is not considered in traditional concrete construction. The popularity is a result of the potential of the technology to improve productivity and cost of construction, as well as improving structural performance through geometrical freedom, the ability to mobilize, and the ability to produce structures in dangerous or remote places. As a result, the number of high-visibility and high-risk projects being executed and proposed has become more common, while the industry is left without a general knowledge of the construction practices and structural performance or a structural code/guidance to assist designers, contractors, and inspectors. Therefore, it is imperative that the concrete industry be educated in the current state and limitations of the technology.

The intent of this joint special issue is to provide awareness to professionals in the concrete industry to the technical construction (materials and structural) aspects of the

technology. This joint special issue of the ACI Structural Journal and ACI Materials Journal contains nine manuscripts focused on construction aspects of additive construction using cement-based materials. It should be highlighted that the number of manuscripts received/accepted for this joint special issue is indicative of the difference in the amount of research or publicly shared information on structural and construction aspects of AC compared to the amount of research on materials, as showcased in the November 2021 special issue of the ACI Materials Journal. The papers in these joint special issues cover a wide range of topics including structural topics on testing reinforced beams and modeling the construction process, and materials topics on the characterizing extrusion, enhancing, and testing mechanical properties; shoreline resiliency; fracture behavior; and quality control methods. It is the hope of the editors that this brief introduction will help to provide the readers with insight to the current state of research on structural/materials performance and the construction process, the structural/ materials considerations that come into play when considering this technology, and how research in this area can benefit the concrete construction industry as a whole.

Liberato Ferrara Eric L. Kreiger

NOTES:

Title No. 121-S14

Development of Compressive Fracture Energy Model for Confined Normal-Strength Concrete

by Xiaoran Song

The damage in reinforced concrete (RC) columns under concentric compressive load conditions tends to localize within certain regions. The softening branches of the stress-strain curves for confined concrete are gauge-length-dependent. The sizedependent confined model, when applied to numerical simulations, will bring in mesh-dependency problems. This paper develops a compressive fracture energy model for confined normal-strength concrete to predict the strain-softening behavior of RC columns. The compressive load-deflection response data of 47 normalstrength RC columns under concentric load conditions are collected to form a database. Then, an exponential function, with the best fit to the tested post-peak softening curves, is adopted to compute the compressive fracture energy. The effect of confinement on the compressive fracture energy is studied, and an empirical expression is proposed to predict the compressive fracture energy. For validation, the proposed compressive fracture energy model is introduced into a uniaxial concrete model to simulate the softening responses of RC columns under large deformations. It is found that the predicted force-displacement response without compressive fracture energy regularization is extremely brittle, which deviates significantly from the test results. While the proposed compressive fracture model provides an objective and accurate prediction of the softening responses of RC columns, it can also be used for collapse assessment of RC structures against extreme load conditions.

Keywords: compressive fracture energy; confined concrete; crack band approach; mesh-size dependence; normal-strength concrete; strain softening.

INTRODUCTION

Owing to its extensive availability and relatively lower costs, concrete is one of the most widely used materials in civil engineering. As a brittle material, concrete exhibits significant strain-softening responses beyond the peak compressive strength (Chen and Han 1988). To improve the ductility and provide sufficient deformation capacity for concrete structures against extreme load conditions, carefully designed transverse steel hoops are set up for a better confinement of the concrete. Over the past 50 years, extensive research efforts have been carried out to develop analytical models for confined concrete for a better understanding of the confinement effect provided from the steel hoops. Among these studies, the concept of effective confinement area proposed by Sheikh and Uzumeri (1982) and further extended by Mander et al. (1988b) has received wide application and become the basis of many analytical models. Table 1 summarizes some of the stress-strain (σ - ϵ) models for confined normal-strength concrete. These confinement models (Scott et al. 1982; Mander et al. 1988b; Saatcioglu and Razvi 1992; Hoshikuma et al. 1997; Légeron and Paultre 2003) are established according to different tests. Using a regression analysis, the predicted equations of confined peak stress, peak strain, and the slope of the softening branch, with the best fit to the test data, are developed.

Based on the existing confinement models, two square reinforced concrete (RC) columns are selected as a reference, to compare their performance. Figure 1 shows the reinforcement details of the two columns, with the volumetric ratio of the steel hoop as the main difference. Figure 2 shows the predicted σ - ϵ curves for the confined concrete of the two RC columns. As shown in Fig. 2, the predicted peak stress and peak strain from different analytical models are relatively consistent with each other. However, the predicted strain-softening behavior, that is, the slope of the softening branches, deviates significantly. The inconsistent prediction of the softening branch lies in the fact that the damage in RC columns under compressive load conditions tends to localize within certain regions, which is termed as the compressive damage zone (CDZ) according to Markeset and Hillerborg (1995). If the external load applied on the specimen moves toward the softening branches, the material strains in the CDZ will continuously increase according to the σ - ϵ laws, while the region outside the CDZ unloads elastically to maintain the mechanical equilibrium. It has been experimentally observed by Jansen and Shah (1997) and van Vliet and van Mier (1996) that most of the inelastic deformation of the specimen concentrated in the CDZ. This localized deformation in the CDZ makes the measured strain gauge length-dependent. For example, Hoshikuma et al. (1997) took the whole specimen length as the gauge length. The measured deformation contains a great portion of elastic unloading deformation. Therefore, the analytical model developed gives much smaller post-peak strains because the localized deformation in the CDZ is averaged over the whole specimen. These confinement models, when applied to numerical simulations, will produce mesh-size-dependent results. The post-peak behavior of the overall structure will depend on the number of elements. Coleman and Spacone (2001) discussed the mesh-size dependence problem in force-based beam-column elements through three numerical examples. In all the cases, the force-deflection responses of the RC members lost the objectivity. Pugh et al. (2015)

ACI Structural Journal, V. 121, No. 2, March 2024.

MS No. S-2020-532.R2, doi: 10.14359/51740284, received June 25, 2021, and reviewed under Institute publication policies. Copyright © 2024, American Concrete Institute. All rights reserved, including the making of copies unless permission is obtained from the copyright proprietors. Pertinent discussion including author's closure, if any, will be published ten months from this journal's date if the discussion is received within four months of the paper's print publication.

Table 1—Summary of confinement models for normal-strength concrete

Reference	Ascending branch σ - ϵ	Descending branch σ-ε
Hoshikuma et al. (1997)	$\sigma = E_c \mathcal{E} \left[1 - \frac{1}{n} \left(\frac{\mathcal{E}}{\mathcal{E}_{cc}} \right)^{n-1} \right]$ $n = \frac{E_c \mathcal{E}_{cc}}{E_c \mathcal{E}_{cc} - f_{cc}}$	$\sigma = f_{cc} - E_{des}(\varepsilon - \varepsilon_{cc})$ $E_{des} = \frac{11.2}{\rho f_{yh} f_{co}^2}$
Mander et al. (1988b)	$\sigma = rac{f_{cc} \chi r}{r-1+\chi^r}, \chi = \epsilon/\epsilon_{cc} \ r = rac{E_c}{E_c-f_{cc}/\epsilon_{cc}}$	$\sigma = rac{f_{cc}xr}{r-1+x^r}, x = arepsilon/arepsilon_{cc} \ r = rac{E_c}{E_c-f_{cc}/arepsilon_{cc}}$
Scott et al. (1982)	$\sigma = K f_{co} \left[\frac{2\varepsilon}{0.002K} - \left(\frac{\varepsilon}{0.002K} \right)^2 \right]$ $K = 1 + \rho f_{yh} f_{co}$	$\sigma = f_{cc}[1 - Z_m(\varepsilon - 0.002K)] > 0.2f_{cc}$ $Z_m = 0.5 / \left[\left(\frac{3 + 0.29f_c}{145f_c - 1000} \right) + 0.75\rho_s \sqrt{\frac{b_s}{s}} - 0.002K \right]$
Saatcioglu and Razvi (1992)	$\sigma = f_{cc} \left[2 \left(\frac{\varepsilon}{\varepsilon_{cc}} \right) - \left(\frac{\varepsilon}{\varepsilon_{cc}} \right)^2 \right]^{1/(1+2\kappa)} \kappa = k_1 f_{le} / f_{co}$	$\sigma = f_{cc} - \frac{0.15 f_{cc}}{\varepsilon_{85} - \varepsilon_{cc}} (\varepsilon - \varepsilon_{cc})$ $\varepsilon_{85} = 260 \rho \varepsilon_1 + 0.0038$
Légeron and Paultre (2003)	$\begin{split} \sigma_c &= f_{cc} \bigg[\frac{k (\varepsilon / \varepsilon_{cc})}{k - 1 + (\varepsilon / \varepsilon_{cc})^k} \bigg] \\ k &= E_{c} / (E_c - f_{cc} / \varepsilon_{cc}) \end{split}$	$\sigma = f_{cc} \exp[k_1(\varepsilon - \varepsilon_{cc})^{k2}]$ $k_1 = \ln 0.5/(\varepsilon_{cc50} - \varepsilon_{cc})^{k2}$ $k_2 = 1 + 25(I_{c50})^2$

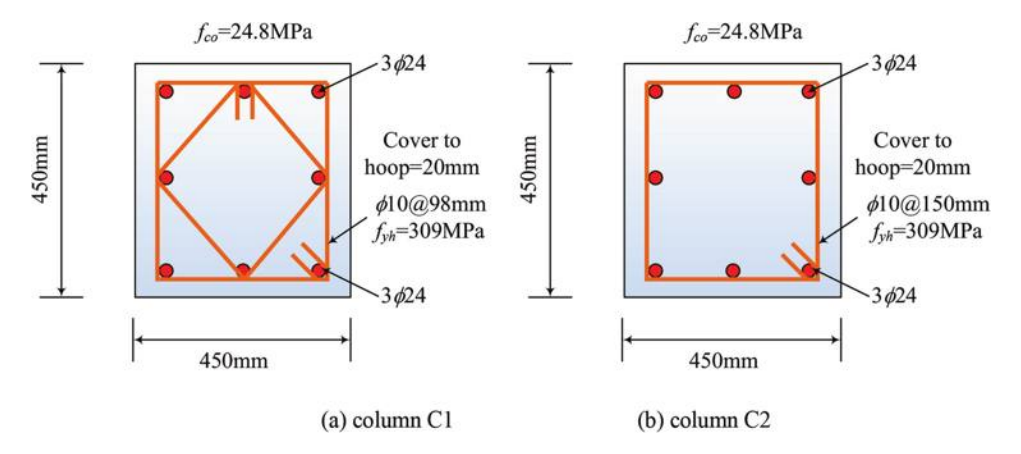


Fig. 1—Reinforcement details of RC columns.

studied the flexural response of RC shear walls and found that for compressive failure specimens, the conventional material model showed mesh-size dependency in the prediction of the drift capacity of shear walls. Li et al. (2017) found that the post-blast residual resistance of RC columns is very sensitive to the size of finite elements.

To eliminate the mesh-size dependence problem in finite element (FE) simulation, extensive regularization algorithms have been proposed. Coleman and Spacone (2001), Jirásek and Bauer (2012), and Kunnath (2018) summarize different regularization techniques to address this issue. Generally, the regularization method can be grouped as the crack band approach and nonlocal model. In the crack band approach, the σ-ε curve input into the FE simulation is adjusted according to the length of the element so that the areas enclosed under the softening branch will integrate into a constant fracture energy. In the nonlocal model, internal variables need to be weighted spatially averaged (for integral type) or incorporate a higher-order gradient (for gradient type) before updating the constitutive relations. In both integral and gradient types, the implementation of the nonlocal model is rather sophisticated. Besides, owing to the lower computational efficiency, the nonlocal model might not be applied to large-scale structures. The crack band approach, as the simplest remedy with easy implementation, has received wide application in civil engineering. The core of the crack band approach is the fracture energy, which is denoted by the area enclosed under the post-peak stress-displacement curves. The compressive fracture energy of unconfined concrete has been well studied (Jansen and Shah 1997; Lertsrisakulrat et al. 2001; Wu and Wei 2016). However, research on compressive fracture energy of confined concrete is limited. Wu and Wei (2016) proposed a compressive fracture energy model for fiberreinforced polymer (FRP)-confined concrete to predict the post-peak compressive stress-strain curve, including the localization failure. Akiyama et al. (2010) developed a compressive fracture energy model for confined highstrength concrete. Most of the test data in the Akiyama model are high-strength concrete with compressive strength greater than 100 MPa (14.5 ksi), confined by high-strength steel hoops (yield strength > 1000 MPa [145 ksi]). These models (Wu and Wei 2016; Akiyama et al. 2010) might not be applicable to confined normal-strength concrete due to the different confinement mechanism and failure modes.

Motivated by the limitations, the present paper develops a compressive fracture energy model for confined normal-strength concrete. To this end, load-deflection data of 47 normal-strength RC columns under concentric load conditions are collected to form a database. Then, an exponential function with the best fit to the tested post-peak softening

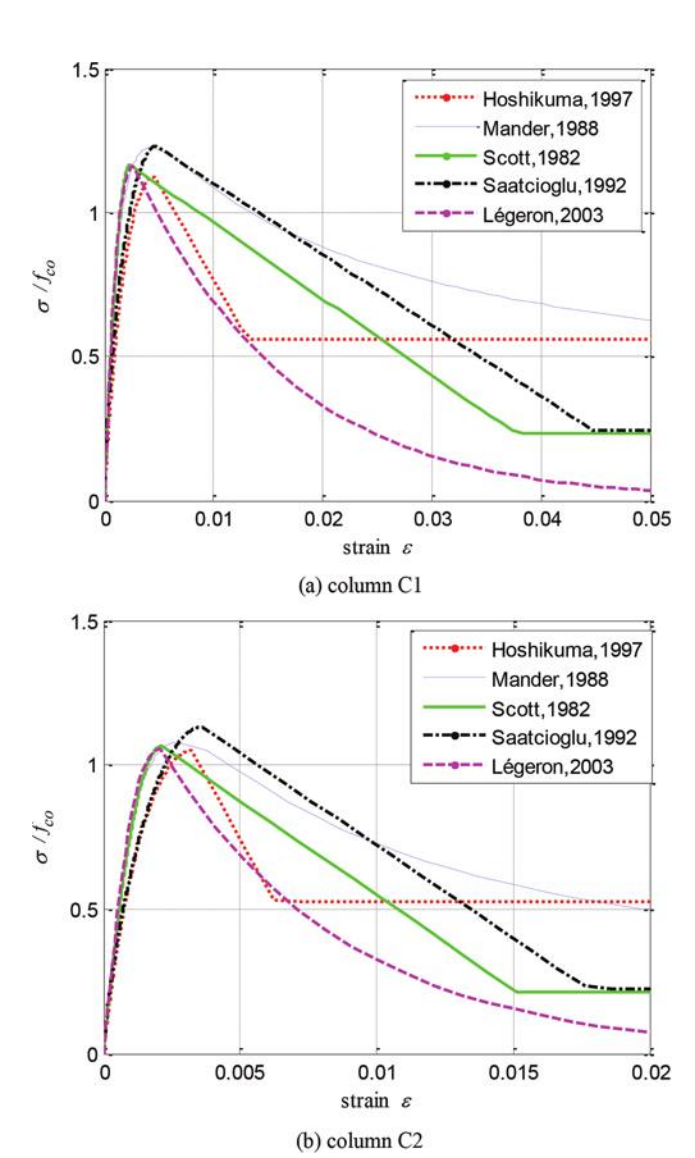


Fig. 2—Comparison of stress-strain curves calculated from different confinement models.

curves is adopted to compute the compressive fracture energy using numerical integration. The effect of confinement on the compressive fracture energy is studied, and an empirical expression is proposed to predict the compressive fracture energy. For validation purposes, the developed compressive energy model, together with a uniaxial concrete material, is introduced into a beam-column fiber element to simulate the softening responses of RC columns under combined axial load and large flexural deformation.

RESEARCH SIGNIFICANCE

The damage in RC columns under concentric compressive load conditions tends to localize within certain regions. The softening branches of the stress-strain curves for confined concrete are gauge-length-dependent. The size-dependent confinement model, when applied to numerical simulations, will bring in mesh-size dependence problems. This paper develops a fracture energy model for objective modeling of compressive strain-softening responses of RC columns. The proposed model can be used for the collapse assessment of RC structures against extreme load conditions, where

accurate modeling of the softening responses is significant. In these cases, the softening branch of the compressive σ - ϵ curve needs to be adjusted to maintain constant fracture energy.

EXPERIMENTAL DATABASE

Overall database

A database is assembled according to the tests of confined RC columns under concentric compressive load conditions in the literature. The published test data need to be carefully selected, and some of the test data need to be discarded. The database is developed according to the following three criteria. First, the main research target of the present study is to develop a compressive fracture energy model for normal-strength concrete. Therefore, the tested specimen with unconfined concrete strength $f_{co} > 50$ MPa (7.3 ksi) is not considered. It is well acknowledged that the highstrength RC column poses less-ductile behavior than the normal-strength RC column. Besides, for the high-strength specimen, additional active mixtures of superfine powder, such as silica fume, need to be used to reach the target compressive strength (Guo 2014), while for normal-strength concrete, silica fume is not required in the mixture design. The presence of additional mixtures is believed to have an impact on the compressive fracture energy. Second, the specimen with the yield strength of steel hoop $f_{vh} > 500$ MPa (72.5 ksi) is also discarded. For RC columns tied with highstrength steel hoops, it has been observed by Akiyama et al. (2010) and Cusson and Paultre (1994) that the stresses in the hoop were much lower than the yield strength at the peak resistance of the specimen. The confinement provided by the high-strength hoop is different from those tied with a normal-strength hoop. Third, the test program should report load-deflection data for both unconfined and confined specimens for better investigation of the effect of confinement on the compressive fracture energy.

Table 2 presents the experimental database of confined and unconfined RC columns, including 26 circular columns and 21 square columns. The outer perimeters of the specimens range from 400 to 500 mm (15.7 to 19.7 in.). The volumetric ratios of the transverse steel hoops range from 0.22 to 3.1%. In addition to the confined RC columns, the unconfined specimen is also included in the database.

Extraction of compressive fracture energy

The compressive fracture energy (G_{fc}) is defined as the area enclosed under post-peak stress-inelastic displacement curves, as presented in Fig. 3(b). Most of the experimental studies simply reported the stress-strain curves of the specimens. Therefore, the post-peak stress-inelastic displacement curves need to be computed based on the stress-strain curves. First, based on the reported stress-strain curves, the stress-displacement curve of the specimen is obtained by multiplying the strain with the gauge length. Second, using the stress-displacement curves developed, the post-peak inelastic displacement is obtained by subtracting the displacement at the peak stress and adding the elastic recovery owing to the reduction of stress in the post-peak region. The slope of the unloading path of the σ - ε curve

Table 2—Test results of confined and unconfined RC columns

Reference	No.	d, mm	c, mm	d_h , mm	s, mm	ρ _w , %	f _{yh} , MPa	f _{co} , MPa	k_e	fl _e , MPa	f_{le}/f_{co}	$G_{fc0},G_{fc},$ N/mm	G_{fc}/G_{fc0}	A	В
	1*	500	25	12	41	2.50	340	29	0.983	4.18	0.144	3036.52	86.03	58.64	0.80
	2	500	25	12	69	2.50	340	29	0.950	2.42	0.083	1020.15	28.90	19.25	0.79
	3	500	25	12	103	1.00	340	29	0.911	1.55	0.053	491.40	13.92	11.35	0.80
	4	500	25	10	119	0.60	320	29	0.890	0.85	0.029	283.88	8.04	8.31	1.15
	5	500	25	10	36	2.00	320	29	0.986	3.13	0.108	2279.66	64.59	45.83	0.82
	6	500	25	16	93	2.00	307	29	0.926	2.83	0.098	1330.40	37.69	29.99	1.11
Mander et al.	Plain	500	25	_	_	_	_	29	_	0.00	0.000	35.29	1.00	1.36	1.44
(1988a)	7	500	25	12	52	2.00	340	32	0.987	3.33	0.104	962.91	51.40	30.34	0.91
	8	500	25	12	52	2.00	340	30	0.987	3.33	0.111	1093.71	34.25	24.32	1.32
	9	500	25	12	52	2.00	340	32	0.987	3.33	0.104	1626.91	50.97	28.45	0.84
	10*	500	25	12	52	2.00	340	30	0.986	3.33	0.111	3329.03	104.24	69.06	0.84
	11	500	25	12	52	2.00	340	30	1.002	3.39	0.113	1089.16	34.12	19.81	0.96
	12	500	25	12	52	2.00	340	32	0.986	3.33	0.104	1445.89	45.31	27.42	0.95
	Plain	500	25	_	_	_	_	32	_	0.00	0.000	31.51	1.00	1.08	1.30
	LC1	500	0	10	300	0.21	295	28.8	0.711	0.22	0.008	147.98	5.42	1.42	1.36
	LC2	500	0	10	150	0.43	295	28.8	0.866	0.55	0.019	197.42	7.23	14.66	1.27
Hoshikuma et al.	LC3	500	0	10	100	0.64	295	28.8	0.917	0.87	0.030	423.63	15.52	13.00	1.01
(1997)	LC4	500	0	10	50	1.28	295	28.8	0.969	1.83	0.064	443.16	16.23	1.52	1.59
	LC5	500	0	13	300	0.36	295	28.8	0.713	0.38	0.013	229.11	8.39	26.65	1.11
	LC6	500	0	16	300	0.55	295	28.8	0.714	0.58	0.020	157.06	5.75	36.70	1.02
	Plain	400	13	_	_	_	_	27.3	_	0.00	0.000	35.15	1.00	1.42	1.36
	1	400	13	12	135	0.91	328	27.3	0.855	1.29	0.047	393.63	11.20	14.66	1.27
Zahn (1985)	2	400	13	10	135	0.63	466	27.3	0.853	1.28	0.047	387.94	11.04	13.00	1.01
Zaiii (1983)	Plain	400	13	_	_	_	_	27.2	_	0.00	0.000	36.96	1.00	1.52	1.59
	3	400	13	12	75	1.63	328	27.2	0.941	2.56	0.094	763.00	20.65	26.65	1.11
	4	400	13	10	75	1.13	466	27.2	0.938	2.52	0.093	829.24	22.44	36.70	1.02

is taken as the elastic modulus of the material (Markeset and Hillerborg 1995). As shown in Fig. 3(c), the inelastic displacement with respect to σ can be expressed as

$$\delta_d(\sigma) = \delta - \frac{\sigma - f_{cc}}{E_c} L_u \tag{1}$$

where δ_d is the post-peak inelastic displacement corresponding to the stress level σ ; f_{cc} is the peak strength of the confined concrete specimen; E_c is the elastic modulus of the material; and L_u is the gauge length of the specimen.

Figure 4(a) presents some of the test results of circular specimens from Mander et al. (1988a). Based on the tested σ - ε curves, σ - δ_d curves are computed correspondingly and presented in Fig. 4(b). As shown in Fig. 4, none of the test results presents complete σ - ε curves. Most of the tests were prematurely stopped with a relatively large residual strength, especially for those specimens tied with large volumetric hoop ratios. One of the reasons might be attributable to the fact that in the post-peak σ - ε curve, localized deformations are developed in the CDZ, making it difficult to measure

the deformation over that region. Another reason is that the longitudinal steel bars might be subjected to buckling failure after the fracture of the hoop. Note that the load sustained by the core concrete is computed by subtracting the contribution of longitudinal steel bars and the cover concrete from the total load. The start of bar buckling is not easily detectable during the test process, which makes it difficult to separate the contribution from the steel bars and core concrete. The incomplete σ - δ_d curve cannot be directly used to compute the compressive fracture energy, which is defined as the entire area under the σ - δ_d curve.

To establish the compressive fracture energy of confined concrete, the tested post-peak σ - δ_d curve is fitted using a nonlinear function. The fitted post-peak σ - δ_d curves are further numerically integrated to compute the compressive fracture energy. As shown in Table 1, different post-peak models have been proposed. The post-peak model should match well with the test results. In the present study, an exponential function, similar to Légeron and Paultre (2003), Akiyama et al. (2010), and Wu and Wei (2016), is selected. The function is formulated as

Table 2 (cont.)—Test results of confined and unconfined RC columns

Reference	No.	d, mm	c, mm	d_h , mm	s, mm	ρ _w ,	f _{yh} , MPa	f _{co} , MPa	k_e	fl _e , MPa	f_{le}/f_{co}	$G_{fc0},G_{fc},\ m N/mm$	G_{fc}/G_{fc0}	A	В
	1	450	20	_	_	_	_	21.76	_	0.00	0.000	26.07	1.00	1.18	0.91
	2	450	20	0	0	1.82	309	21.76	0.755	2.12	0.097	611.87	23.47	19.66	1.03
	3	450	20	10	72	1.82	309	21.76	0.755	2.12	0.097	537.08	20.60	14.06	1.04
	6	450	20	10	72	1.74	309	21.76	0.687	1.85	0.085	598.95	22.97	20.03	1.08
	7	450	20	10	72	1.74	309	21.76	0.687	1.85	0.085	497.85	19.09	13.47	1.00
	11	450	20	_	_	_	_	29.02	_	0.00	0.000	46.11	1.00	1.71	1.21
	12	450	20	10	98	1.40	309	29.02	0.703	1.52	0.052	329.85	7.15	8.70	1.04
	13	450	20	10	72	1.82	309	29.02	0.755	2.12	0.073	560.04	12.15	13.96	1.02
	14	450	20	10	88	2.24	296	29.02	0.723	2.40	0.083	470.62	10.21	12.44	1.31
	15	450	20	10	64	3.09	296	29.02	0.772	3.53	0.122	879.19	19.07	21.00	1.38
Scott et al. (1982)	17	450	20	10	98	1.34	309	29.02	0.640	1.32	0.045	321.66	6.98	9.25	1.16
()	18	450	20	10	72	1.74	309	29.02	0.687	1.85	0.064	534.46	11.59	13.76	1.05
	19	450	20	12	88	2.13	296	29.02	0.664	2.09	0.072	606.05	13.14	15.24	1.01
	20	450	20	12	64	2.93	296	29.02	0.709	3.07	0.106	1585.16	34.38	34.85	0.89
	26	450	20	_	_	_	_	30.73	_	0.00	0.000	22.53	1.00	0.67	0.63
	22	450	20	10	98	1.40	309	30.73	0.703	1.52	0.049	286.88	9.77	9.47	1.62
	23	450	20	10	72	1.82	309	30.73	0.755	2.12	0.069	929.99	31.67	24.68	0.91
	24	450	20	12	88	2.24	309	30.73	0.728	2.52	0.082	1110.10	37.81	26.20	0.79
	25*	450	20	12	64	3.09	309	30.73	0.777	3.71	0.121	2189.67	74.58	49.88	0.86
	21	450	20	_	_	_	_	23.47	_	0.00	0.000	22.79	1.00	0.79	1.19
	27	450	20	_		_	_	26.62	_	0.00	0.000	29.36	1.00	1.17	1.12

^{*}Test data deviated significantly from majority trend of data and are not incorporated into development of G_{fc} .

Note: d is cross-section dimensions; c is cover concrete to steel hoop; f_{co} is unconfined compressive strength of concrete; d_h is diameter of steel hoop; s is space between two adjacent hoops; f_{yh} is yield strength of steel hoop; p_w is volumetric ratio of steel hoops (p_w should be measured by area of core concrete, which is defined by central lines between steel hoops); k_e is confinement effectiveness coefficient; f_{le} is effective confinement pressure; G_{fc} is compressive fracture energy for unconfined concrete; A and B are parameters in fitted curve.

$$\frac{\sigma}{f_{cc}} = \exp\left[-\left(\frac{\delta_d}{A}\right)^B\right] \tag{2}$$

where A and B are the model parameters, which control the shape of the post-peak curve and can be determined according to the tested σ - δ_d results using the least-squares regression method. Based on the fitted function, the compressive fracture energy can be obtained

$$G_{fc} = \int_0^\infty \sigma d\delta_d = \int_0^\infty f_{cc} \exp\left[-\left(\frac{\delta_d}{A}\right)^B\right] d\delta_d$$
 (3)

Figure 5 shows the extracted σ - δ_d curves and the fitted exponential functions. The test results in the literature (Mander et al. 1988a; Scott et al. 1982; Zahn 1985; Hoshikuma et al. 1997) do not report σ - δ_d curves. Therefore, σ - δ_d curves are computed based on the proposed algorithm. As shown in Fig. 5, the fitted exponential function can match well the test results of the post-peak responses of the confined and unconfined specimens. The fitted σ - δ_d curves are further implemented to compute the compressive fracture energy. The results are summarized in Table 2.

DEVELOPMENT OF COMPRESSIVE FRACTURE ENERGY

Compressive fracture energy for unconfined concrete

Confined concrete will degenerate into unconfined concrete when the confinement effect is diminished. The compressive fracture energy for unconfined concrete is fundamental for confined concrete. Several research efforts have been carried out to study the compressive fracture energy for unconfined concrete. Based on the test results, Akiyama et al. (2010) proposed an equation

$$G_{fc0} = 134 - 93.3k_b \tag{4}$$

where G_{fc0} is the compressive fracture energy for unconfined concrete; k_b is a model parameter; and $k_b = \min(40/f_{co}, 1.0)$; and f_{co} is the unconfined strength of concrete, in MPa.

Wu and Wei (2016) reviewed the definition of compressive fracture energy for unconfined concrete. The proposed model from Wu and Wei (2016) is given as

$$\frac{G_{fc0}}{G_{f30}} = \left(\frac{f_{co}}{f_{30}}\right)^{0.15} \tag{5}$$

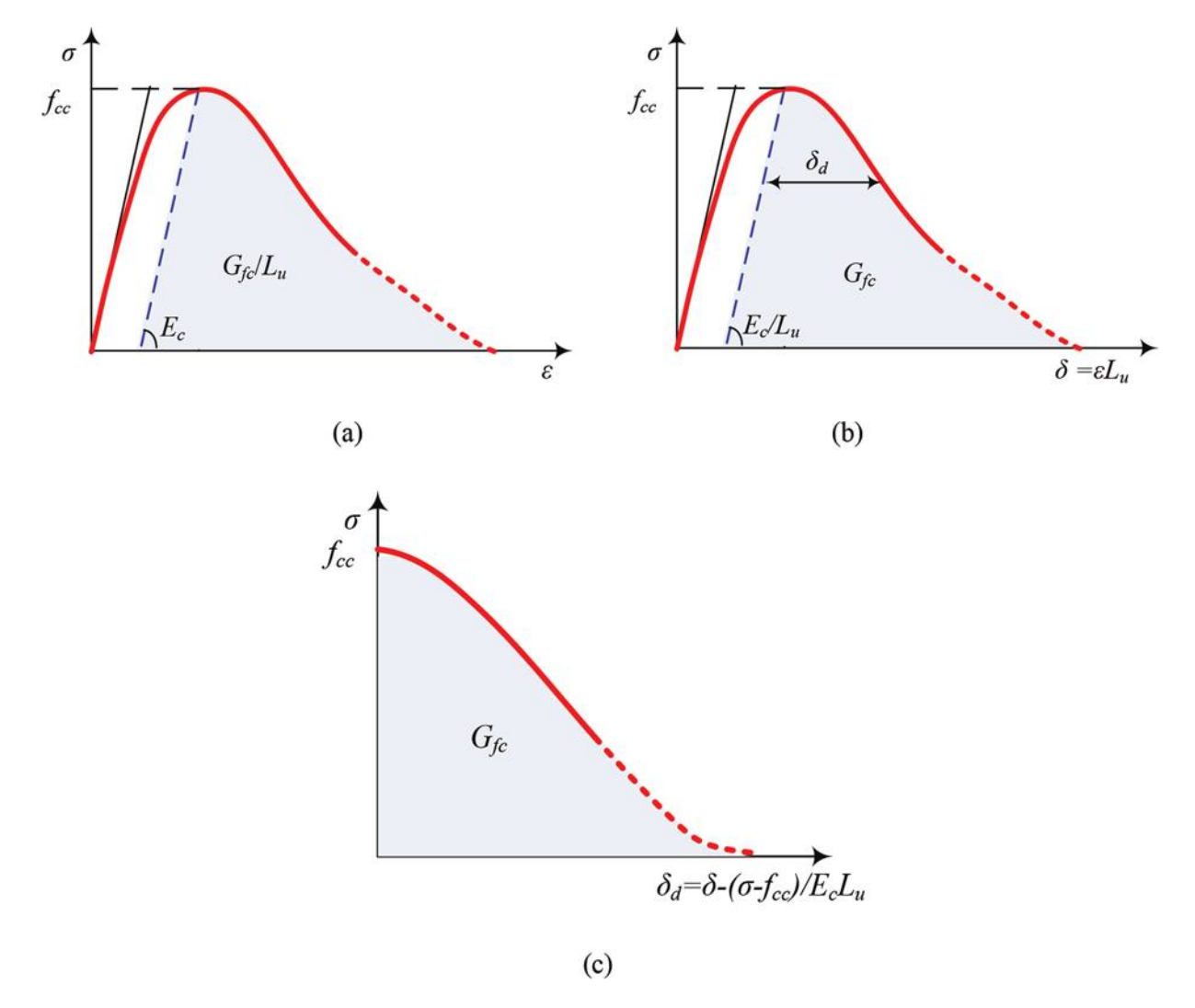


Fig. 3—Extraction of compressive fracture energy from test results: (a) stress-strain curve; (b) stress-displacement curve; and (c) post-peak stress-inelastic displacement curve.

where f_{30} is a normalized factor and $f_{30} = 30$ MPa (4.35 ksi); and G_{f30} is the compressive fracture energy of Grade 30 concrete and $G_{f30} = 27.5$ N/mm (0.157 kip/in.), according to Wu and Wei (2016).

As shown in Eq. (4) and (5), the unconfined strength f_{co} is the sole parameter considered in the proposed models. Lertsrisakulrat et al. (2001) introduced an additional factor related to the dimensions of the specimen in developing the compressive fracture energy model

$$\frac{G_{fc0}}{L_d} = 0.086 f_{co}^{1/4} \tag{6}$$

where L_d is defined as

$$L_d = \begin{cases} 1.36 & D^* < 100 \\ -3.53 \times 10^{-5} (D^*)^2 + 1.71 & 100 \le D^* \le 180 \\ 0.57 & D^* > 180 \end{cases}$$
(7)

where D^* is defined as the square root of the cross-section area, in mm. According to the equations proposed by Lertsrisakulrat et al. (2001), a large-scale specimen will have a higher G_{fc0} than a small-scale one, given the same f_{co} .

Equations (4) to (6) were based on the tests of small-scale cylinder specimens with the diameter d = 100 or 150 mm (3.9 or 5.9 in.). These models might not be applicable to large-scale specimens. Figure 6 presents the comparison results of compressive fracture energy for large unconfined RC columns. The proposed models from Akiyama et al. (2010), Wu and Wei (2016), and Lertsrisakulrat et al. (2001) are also added. As shown in Fig. 6, there is a clear increasing trend of the compressive fracture energy with the increasing of the compressive strength. While the effect of crosssection dimensions on the G_{fc0} is not evident by comparing the test results of large-scale specimens with small-scale ones, the proposed model from Akiyama et al. (2010) overestimates most of the unconfined specimens for f_{co} < 50 MPa (7.3 ksi). The increasing trend of G_{fc0} along with f_{co} is also not reasonably considered in the model. Among the existing models, the compressive fracture energy model proposed by Wu and Wei (2016) can match well with the tests of large-scale specimens. Considering the difficulty of testing the descending branches of σ - ϵ curves, the scatter between the tested results and Wu and Wei's model is acceptable. Currently, it is assumed that f_{co} is the only model parameter that affects G_{fc0} . Other factors, such as the maximum

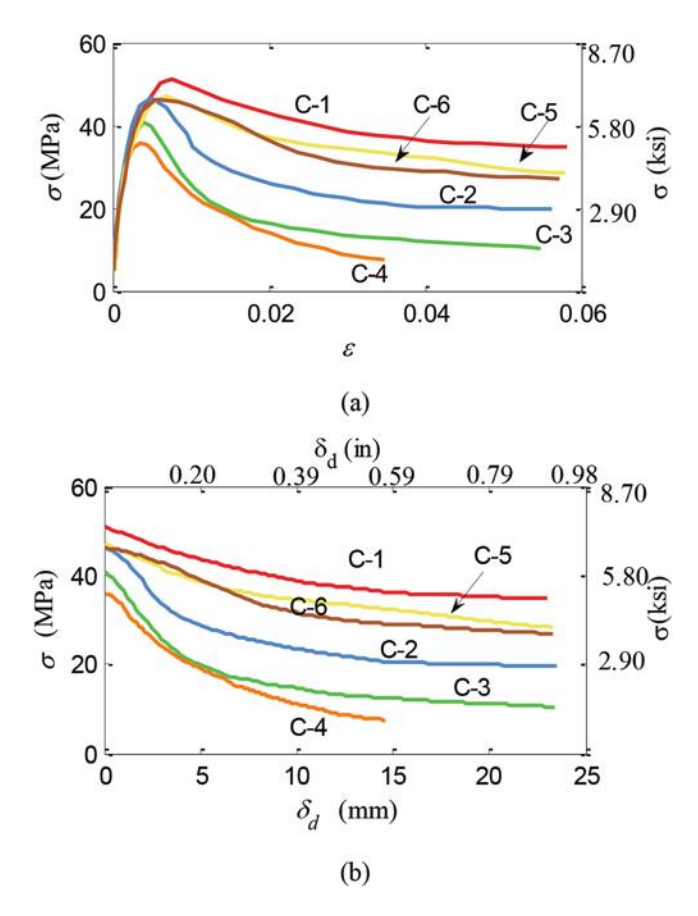


Fig. 4—Test results from Mander et al. (1988a): (a) stress-strain curves; and (b) extracted stress-inelastic displacement curves.

aggregate size and the shape of the aggregate, are not considered. If these factors are taken into consideration in developing G_{fc0} , the scatter will be further reduced.

Compressive fracture energy for confined concrete

Based on the compressive fracture energy of unconfined concrete, the effect of confinement on the G_{fc} is studied. The effect of confinement on the peak strength and peak strain of normal-strength concrete has been well studied (Mander et al. 1988b; Scott et al. 1982; Zahn 1985; Hoshikuma et al. 1997). Generally, the improvements in the peak strength and peak strain are expressed as a function of confinement pressure f_l provided by the steel hoops. Based on the equations of equilibrium, the confinement pressure applied on the core concrete should be equal to the tensile forces from the steel hoops. For uniformly reinforced circular and square columns, f_l can be formulated as

$$f_l = 0.5 \rho_w f_{sh} \tag{8}$$

where ρ_w is the volumetric ratio of the hoops; and f_{sh} is the stress of the steel hoops at the peak strain. For normal-strength concrete tied with normal-strength hoops, the steel hoop can reach its yield strength at the peak resistance of the specimen. Therefore, f_{sh} is taken as the yield strength of the steel hoops.

Owing to the arching effect, the confinement pressures are not uniformly applied onto the core concrete. The area of effectively confined concrete is less than the core area bounded by the steel hoops. The concept of effective confined area, first proposed by Sheikh and Uzumeri (1982) and further refined by Mander et al. (1988b), is used to calculate the effective confinement pressure f_{le} as

$$f_{le} = k_e f_l \tag{9}$$

where k_e is the confinement effectiveness coefficient, which is defined as the effective confined area divided by the area of the core concrete. According to Mander et al. (1988b), for spirally reinforced circular columns, k_e can be formulated as

$$k_e = \frac{(1 - 0.5s'/d_s)}{(1 - \rho_{cc})} \tag{10}$$

where s' is the net space between the two adjacent hoops; d_s is the diameter of the spiral between bar centers; and ρ_{cc} is the area ratio for the longitudinal steel bars, measured with respect to the area of the core concrete.

For square columns, k_e is given as (Mander et al. 1988b)

$$k_e = \frac{\left(1 - \sum_{i=1}^{n} \frac{(w_i)^2}{6b_c d_c}\right) \left(1 - \frac{s'}{2b_c}\right) \left(1 - \frac{s'}{2d_c}\right)}{(1 - \rho_{cc})} \tag{11}$$

where w_i is the net space between the adjacent restrained longitudinal bars; and b_c and d_c are the dimensions of the core concrete. The definition of the variables in Eq. (11) is demonstrated in Fig. 7. By introducing k_e into the definition of effective confinement pressure, the effects of cross-section type, as well as the placements of longitudinal bars, are considered.

Based on the effective confinement pressure f_{le} , Fig. 8 presents the σ - δ_d curves for specimens with different magnitudes of f_{le}/f_{co} . As clearly shows in Fig. 8, with the increasing of f_{le}/f_{co} from 0.03 to 0.10, the slope of the descending branch is gradually reduced. As a result, the compressive fracture energy, denoted by the area enclosed under the σ - δ_d curves, gradually increases with the increasing of effective confinement pressures. It is also deduced from Fig. 8(b) that the σ - δ_d curve of the square RC column tested by Scott et al. (1982) coincides well with those of circular RC columns tested by Zahn (1985). As a result, the areas enclosed under the σ - δ_d curves are almost the same, demonstrating that RC columns with a similar value of f_{le}/f_{co} will share approximately the same amount of compressive fracture energy. The comparison study indicates that the cross-section shape is not an influential factor with respect to the post-peak response of the confined concrete specimen. Therefore, the effect of cross-section shape is only implicitly considered in the proposed model by introducing k_e into the definition of f_{le} .

Finally, by comparing the σ - δ_d curves with different magnitudes of f_{le}/f_{co} , it is clearly shown that the scatter of the post-peak responses is gradually increasing. The large data scatter for higher values of f_{le}/f_{co} might be attributable to

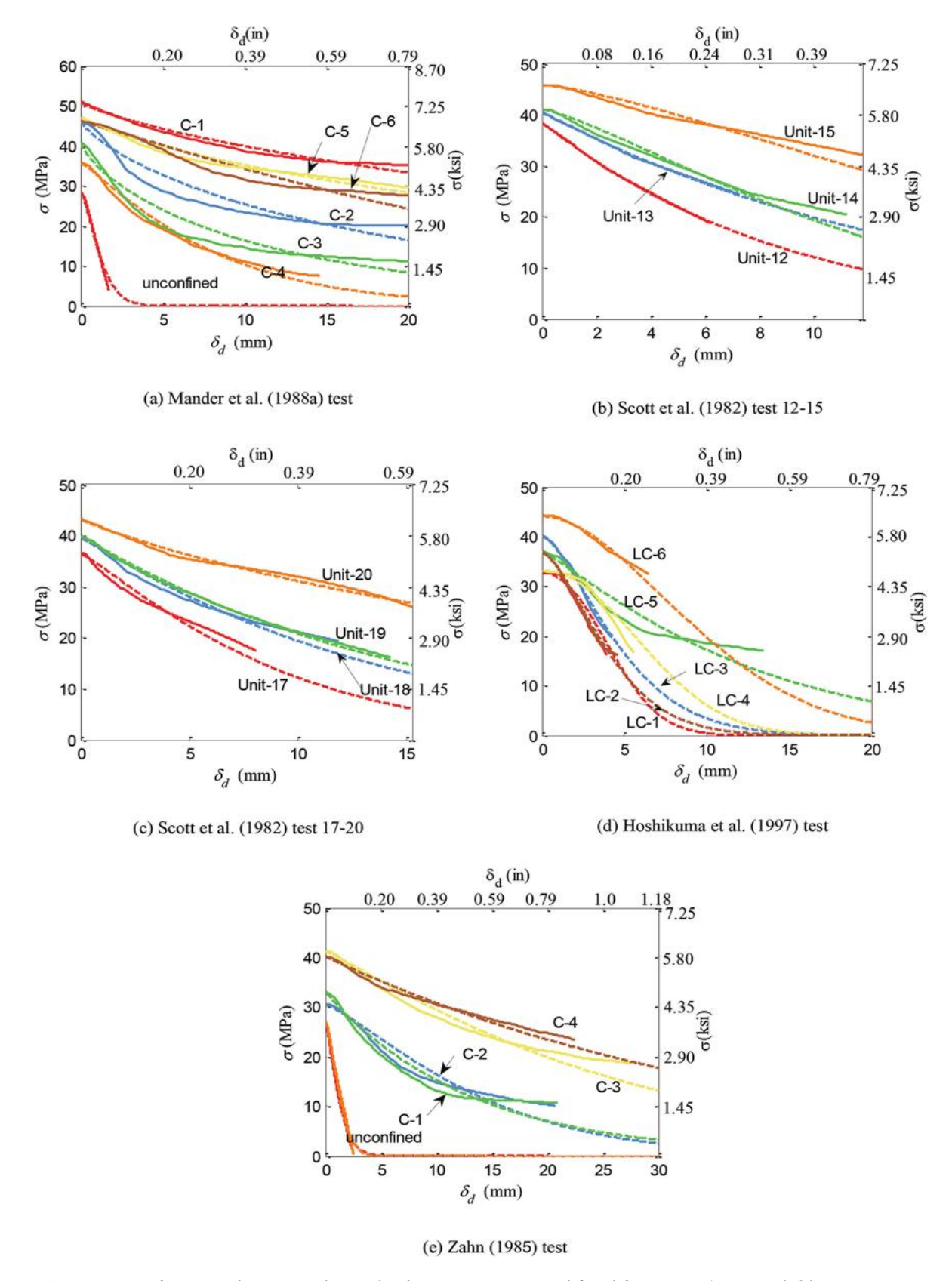


Fig. 5—Comparison of extracted stress-inelastic displacement curves and fitted functions. (Note: Solid lines are extracted test results; dashed lines are fitted functions.)

the buckling of longitudinal bars during the testing process. For RC columns with closely spaced hoops, larger axial demand needs to be applied onto the specimens, making the longitudinal bars more likely to initiate buckling failure. The

buckling failure is hard to detect, which makes it difficult to accurately evaluate the load sustained by the core concrete. The larger axial demands also cause local distortion of the

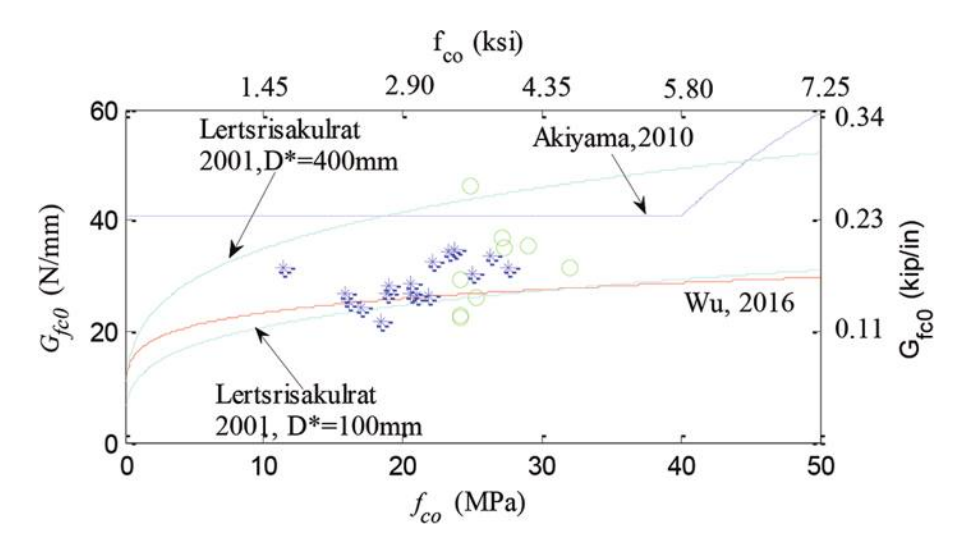


Fig. 6—Comparison of test results of compressive fracture energy for unconfined concrete with various models. (Note: Circles are test results of large-scale specimens from Table 2; asterisks are test results of small cylinder specimens from Wu and Wei [2016].)

RC section, as pointed out by Scott et al. (1982). It becomes quite difficult to accurately record the concrete strain.

Based on the foregoing discussions, the normalized effective confinement pressure f_{le}/f_{co} is taken as the sole model parameter in developing the compressive fracture energy model for confined concrete. To make the predicted equation dimensionless, the compressive fracture energy for unconfined concrete is used as a normalized factor. Table 2 presents the test results used to calibrate the model. Some of the test data, denoted by an asterisk, deviated significantly from the majority trend of the data and are not incorporated into the development of G_{fc} . Using the Bisquare regression algorithm, a robust regression analysis is carried out to study the relationship between G_{fc}/G_{fc0} and f_{le}/f_{co} . Compared with the least-squares regression method, robust regression is less sensitive to the outliers of the data points. After trial-anderror analysis, a quadratic function is selected to describe the relationship between G_{fc}/G_{fc0} and f_{le}/f_{co} . The developed formula shown in Fig. 9 is expressed as

$$G_{fc} = G_{fc0} \left\{ 1 + 157 \left(\frac{f_{le}}{f_{co}} \right) + 1204 \left(\frac{f_{le}}{f_{co}} \right)^2 \right\}$$
 (12)

The constant term 1.0 is selected so that G_{fc} degenerated into G_{fc0} when $f_{le}/f_{co} = 0$.

Comparison with existing model

Akiyama et al. (2010) proposed an equation to predict the compressive fracture energy for confined high-strength concrete. The proposed model is given as

$$G_{fc} = G_{fc0} \left\{ 1 + 157 \left(\frac{f_{le}}{f_{co}} \right) - 77.3 \left(\frac{f_{le}}{f_{co}} \right)^2 \right\}$$
 (13)

Most of the test data used to calibrate Eq. (13) are highstrength RC columns tied with high-strength steel hoops $(f_{yh} > 1000 \text{ MPa } [145 \text{ ksi}])$. For validation purposes, the

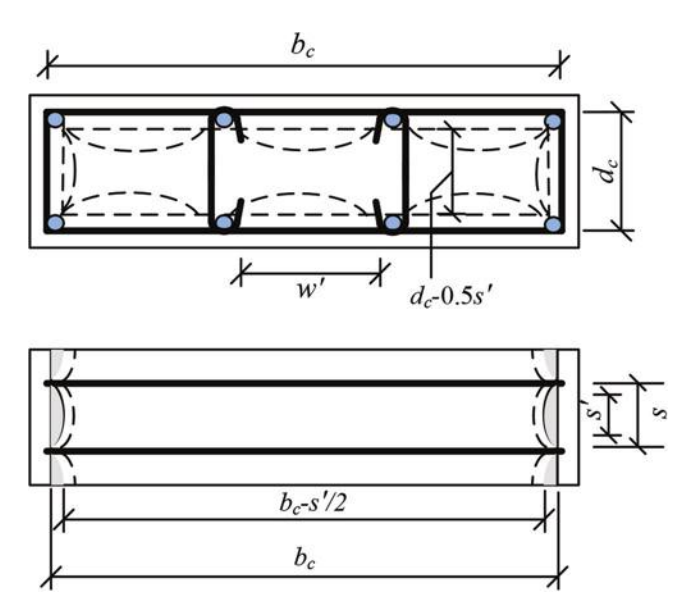


Fig. 7—Definition of effective confinement area (from Mander et al. [1988b].)

performance of the proposed model and Akiyama's model is examined by comparing the tested and predicted G_{fc}/G_{fc0} .

Figure 10 shows the comparison study results. Generally, the proposed model has a higher model accuracy—with a mean predicted-to-test ratio of 1.02 and a standard deviation of 0.39—while Akiyama's model underestimates the G_{fc} / G_{fc0} , with a mean predicted-to-test ratio of 0.72 and a standard deviation of 0.28. The unsatisfactory performance of Akiyama's model lies in the fact that most of the tested specimens are high-strength RC columns. It has been observed by several researchers that high-strength RC columns exhibit a much more brittle failure compared with normalstrength concrete. As reported by Hong et al. (2006) and Cusson and Paultre (1994), RC columns with $f_{co} > 100$ MPa (14.5 ksi) quickly lost the load-carrying capacity after the peak strength, even though the RC columns were densely reinforced. Owing to the higher elastic modulus and smaller internal cracks, the lateral expansions of the high-strength

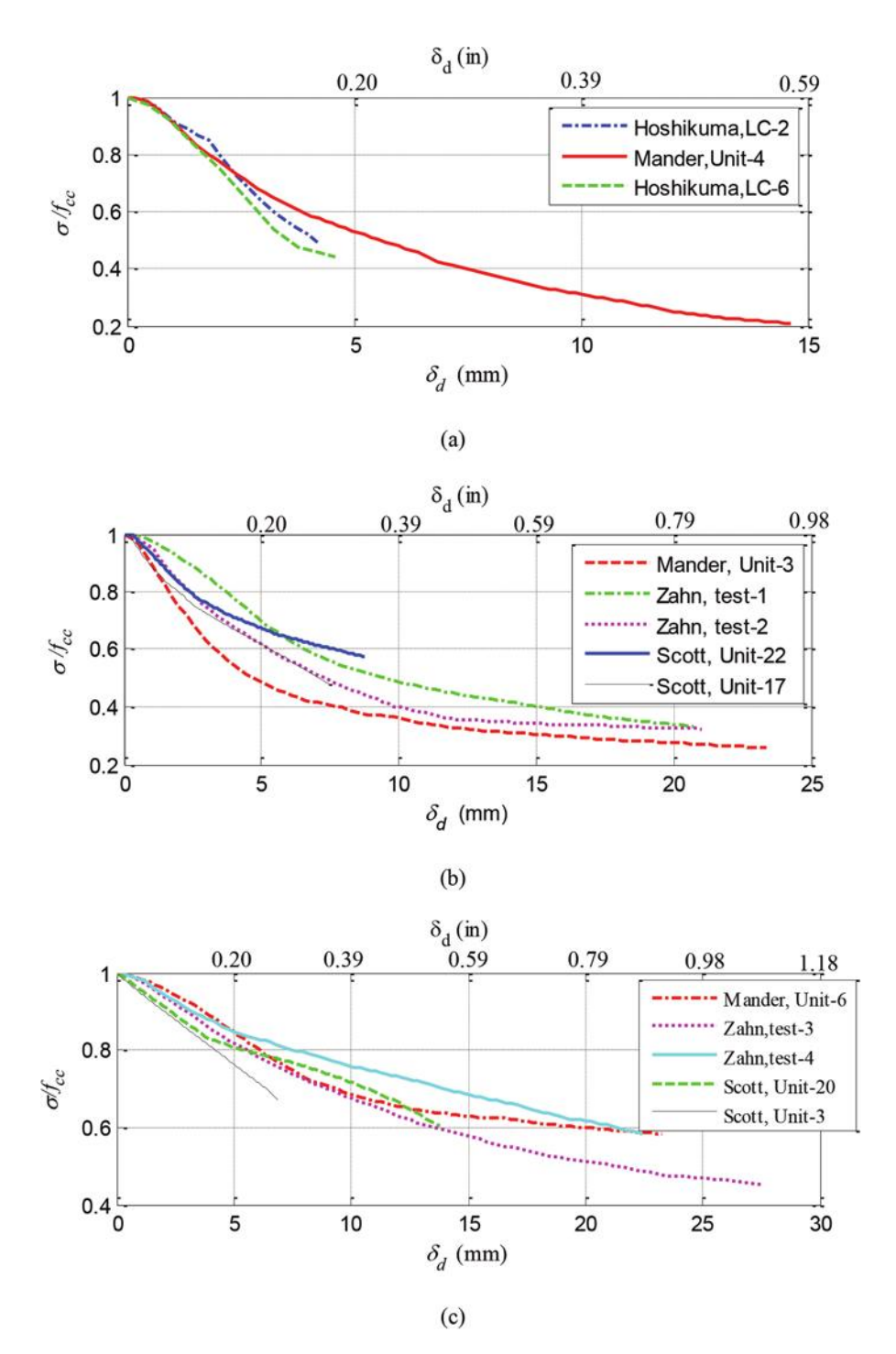


Fig. 8—Effect of confinement pressure on post-peak responses of confined concrete: (a) $f_{le}/f_{co} = 0.03$; (b) $f_{le}/f_{co} = 0.05$; and (c) $f_{le}/f_{co} = 0.10$.

concrete are not fully developed, leading to a less effective confinement pressure in the steel hoops. The transverse steel hoops might not be an effective measure to ensure a ductile post-peak behavior of high-strength RC columns.

VALIDATION AND APPLICATION

Test information

To further examine the accuracy of the proposed model, RC columns tested by Sheikh and Yeh (1990) are numerically studied with and without compressive fracture energy regularization. Figure 11(a) shows the test setup from Sheikh and Yeh (1990). The reinforcement details for the specimens with

configurations E, A, and D, shown in Fig. 11(b), are further summarized in Table 3. As shown in Fig. 11, two specially designed hinges were placed at the end of the specimens. During the test, a constant axial load *N* was applied onto the specimens using the horizontal hydraulic jack. Then, two equal vertical loads were applied using the actuator at the third points of the specimen, creating a shear force-free region. Meanwhile, the horizontal hydraulic jack needs several adjustments to keep a constant axial load condition. The test was stopped until the lateral load dropped to zero or the axial load could not maintain the predetermined axial load.

Numerical model

The RC column is modeled using a fiber-section beamcolumn element in LS-DYNA, an explicit code software. The cross section of an RC column is divided into fibers, and only uniaxial material models are required in the numerical analysis. It is well accepted that the fiber-section element is reliable in predicting the axial-bending interaction effects on RC members. For concrete under compression, the

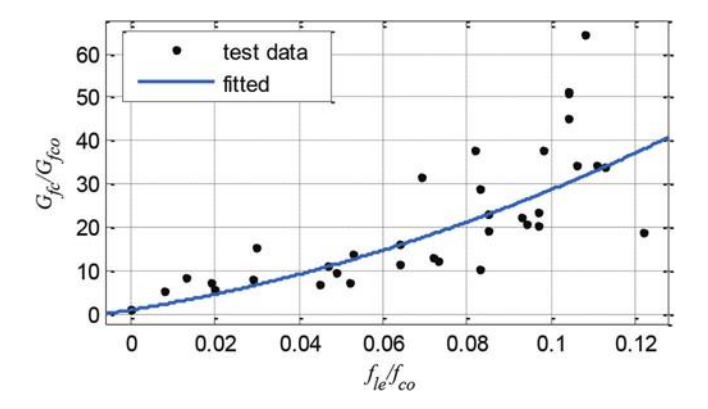


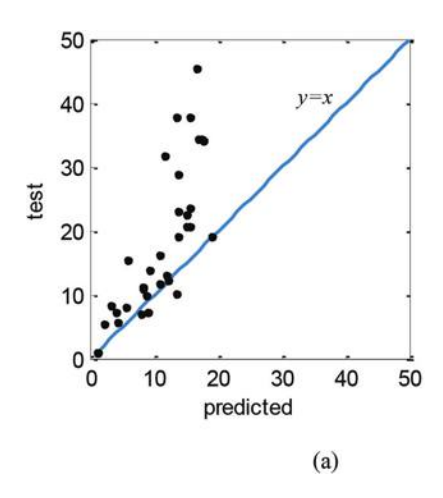
Fig. 9—Effect of confinement pressure on compressive fracture energy.

monotonic envelope curve follows the model proposed by Scott et al. (1982), with a parabolic function in the ascending branch and a linear softening branch. The unloading and reloading behavior of concrete under compression follows the hysteresis rules proposed by Yassin (1994). The details of the hysteresis rules can also be found in Spacone et al. (1996). For concrete under tension, elastic behavior is assumed until the stress reaches the ultimate tensile strength f_t . Beyond f_t , the stress reduces linearly with the increasing of the tensile strain. As shown in Fig. 12, the compressive envelope curve is controlled by the peak strength f_{cc} at peak strain ϵ_{cc} and the strain ϵ_{20} in the softening branch at which the stress drops to $20\% f_{cc}$. For f_{cc} and ϵ_{cc} , the predicted equations proposed by Scott et al. (1982) are

$$f_{cc}/f_{co} = K \tag{14a}$$

$$\varepsilon_{cc}/\varepsilon_c = K$$
 (14b)

$$K = 1 + \rho_s f_{vh} / f_{co} \tag{14c}$$



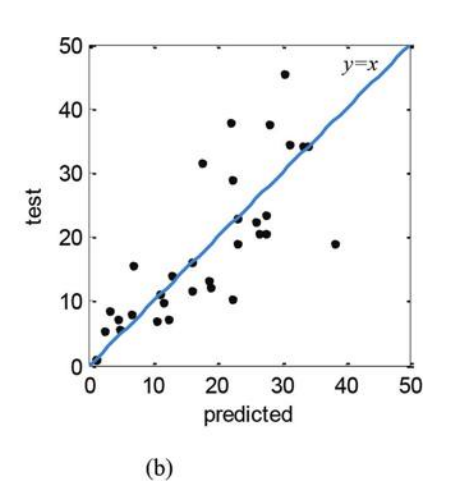


Fig. 10—Performance of compressive fracture energy model for confined concrete: (a) Akiyama et al. (2010) model; and (b) proposed model.

Table 3—Geometric and material properties of RC columns from Sheikh and Yeh (1990)

Specimen	b, mm (in.)	c, mm (in.)	f _c , MPa (ksi)	Longitudinal bar	d_h , mm (in.)	s, mm (in.)	f _{yh} , MPa (ksi)	ρ _w , %	N/f _c A
A-3	305 (12)	14 (0.55)	31.809 (4.61)	8 No. 6	10 (0.39)	107.95 (4-1/4)	489.9 (71)	1.68	0.61
A-11	305 (12)	16 (0.63)	27.945 (4.05)	8 No. 6	6 (0.24)	107.95 (4-1/4)	469.2 (68)	0.77	0.74
D-5	305 (12)	14 (0.55)	31.257 (4.53)	12 No. 5	10 (0.39)	114.3 (4-1/2)	489.9 (71)	1.68	0.46
D-7	305 (12)	16 (0.63)	26.22 (3.80)	12 No. 5	6 (0.24)	53.975 (2-1/8)	469.2 (68)	1.62	0.78
E-2	305 (12)	12.5 (0.49)	31.395 (4.55)	8 No. 6	13 (0.51)	114.3 (4-1/2)	483 (70)	1.69	0.61
E-8	305 (12)	14 (0.55)	25.944 (3.76)	8 No. 6	10 (0.39)	127 (5)	483 (70)	0.84	0.78

Note: b is cross-section dimensions; c is cover concrete to steel hoop; f_c is compressive strength of concrete using standard cylinder tests; d_h is diameter of steel hoop; g is space between two adjacent hoops; g is a said load on RC column; g is gross section area.

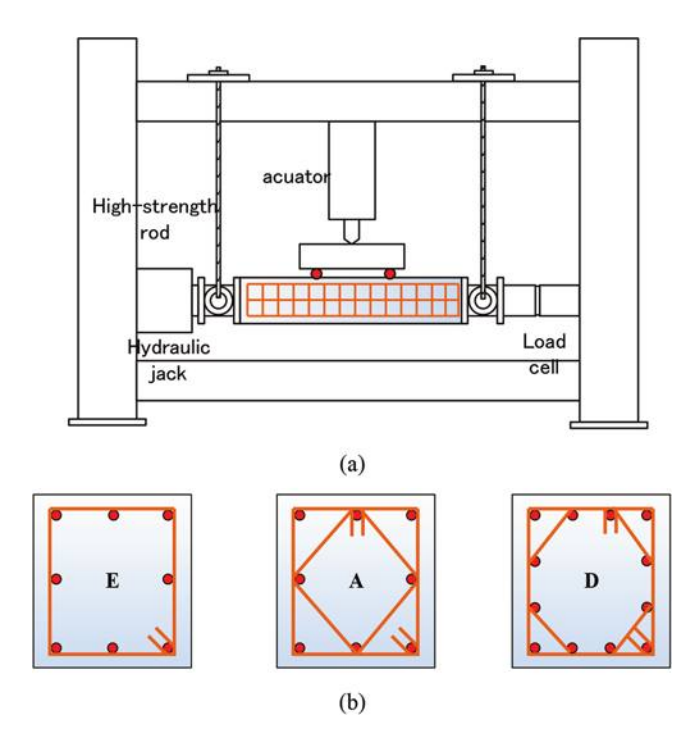


Fig. 11—Test setup and reinforcement details of specimens: (a) test setup; and (b) reinforcement details.

where K is the improvement factor of f_{cc} and ε_{cc} , due to the confinement from steel hoops; f_{co} is the unconfined concrete strength; and ρ_s is the volumetric ratio of the steel hoop with respect to the area of the core concrete, which is computed from the outside of the hoops. Scott el al. (1982) does not give an expression of ε_{20} . Instead, the slope of the post-peak curve is developed by a regression analysis, which is given as

$$Z_m = 0.5 / \left[\left(\frac{3 + 0.29 f_{co}}{145 f_{co} - 1000} \right) + 0.75 \rho_s \sqrt{\frac{b_s}{s}} - 0.002 K \right]$$
(15)

where b_s is the width of the core concrete, measured from the outside of the steel hoops. Substitute Z_m into the compressive envelope curve (Table 1), and ε_{20} according to Scott's model is obtained

$$\varepsilon_{20} = 0.8/Z_m + \varepsilon_{cc} \tag{16}$$

As shown in Eq. (15) and (16), ε_{20} is not relevant to the length of the integration point L_c . Therefore, one can expect that the areas enclosed under the post-peak σ - ε curves will not integrate into a constant compressive fracture energy when using different element sizes or different numbers of integration points.

To make the results of numerical simulation objective, ε_{20} needs to be adjusted according to L_c to reach a constant G_{fc} . Considering the definition of G_{fc} , the shaded area in Fig. 12 is equal to G_{fc}/L_c . This leads to the following expression for ε_{20R}

$$\varepsilon_{20R} = 0.8 \left(\frac{2G_{fc}}{L_{cfcc}} - \frac{f_{cc}}{E_c} \right) + \varepsilon_{cc}$$
 (17)

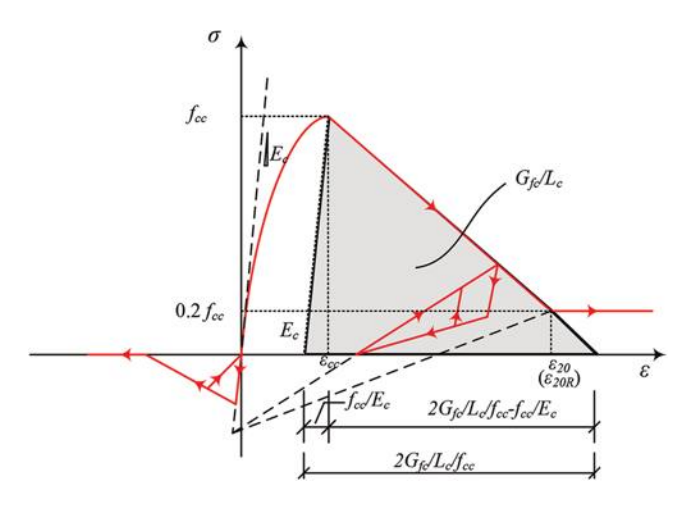


Fig. 12—Uniaxial concrete model with compressive fracture energy regularization.

where L_c is the length of the integration point. The present study adopted a single integration-point beam element. In this case, L_c degenerates into the size of the FE.

RESULTS AND DISCUSSION

Figure 13 presents the predicted force-displacement curves, together with the test results. The numerical analysis is carried out with the three different element sizes $L_c = 75$, 100, and 150 mm (3.0, 3.9, and 5.9 in.). With the increasing vertical displacement, a plastic hinge will gradually develop at the shear-free region of the specimen. As shown in Fig. 13, the analysis results based on the original Scott et al. model are extremely brittle. In nearly all the cases, the RC columns quickly lose the load-carrying capacity instantaneously beyond the peak resistance. This is because the Scott et al. model is developed based on the tests of RC columns with a 400 mm (15.7 in.) gauge length, which is not consistent with the element size in the numerical model. It is clear from the numerical simulations that the strain concentrates into one element at the midspan position. The inelastic strain in this element increases rapidly as the RC column enters the softening responses. The post-peak σ - δ curve from a smaller element size will present more brittle behavior and less dissipated energy (area under the curve) if the softening branches of the σ-ε curve are not adjusted correctly according to G_{fc} .

The predicted force-displacement responses based on the developed compressive fracture energy model are nearly the same for different element sizes. Based on the proposed compressive fracture energy model, the softening branch of the σ - ε curve is adjusted so that the elements with different sizes will dissipate the same amount of energy in the postpeak responses. Besides, the analysis results match well with the test results. For specimens with configurations A and D, the mean predicted-to-test results of ultimate displacement at which the resistance drops to zero is 1.13. If the softening branch of the σ-ε curve is not correctly adjusted, the predictedto-test ratio is 0.26. The comparison results demonstrate the accuracy of the proposed G_{fc} model for confined concrete. For specimens with configuration E, the overpredicted softening response is because of the buckling of the middle longitudinal steel bar, which is not restrained by any steel

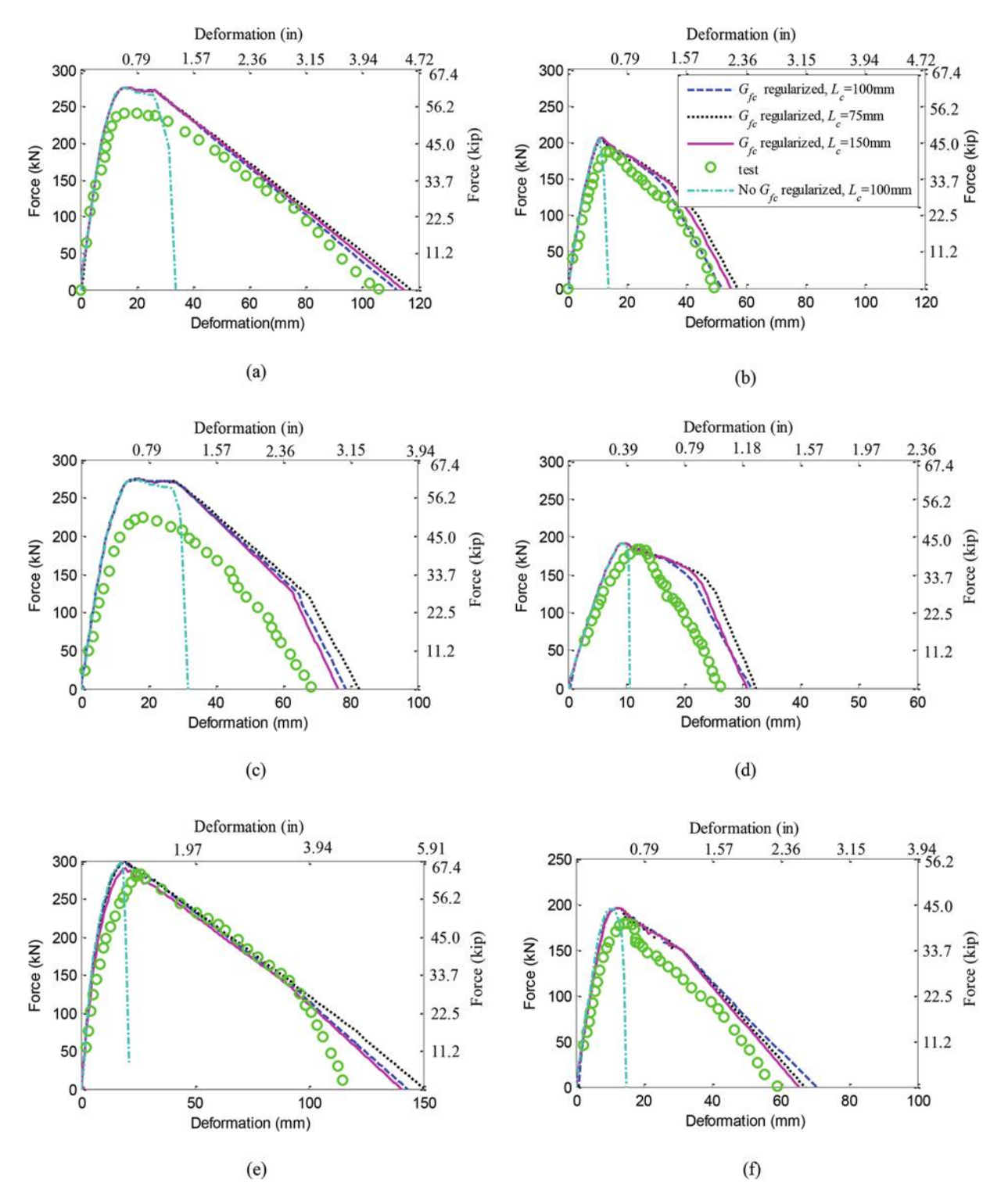


Fig. 13—Comparison of numerical and tested force-deflection responses of RC columns: (a) A3; (b) A11; (c) E2; (d) E8; (e) D5; and (f) D7. (Note: L_c is element size.)

hoop, as reported by Sheikh and Yeh (1990). The buckling of the steel bars reduces the confinement pressure, leading to the crushing failure of the core concrete, accompanied by the quick loss of resistance of the specimen. As pointed out by Welt et al. (2018), the Mander model might overestimate the effective confinement area of confined RC sections if every other longitudinal bar is restrained by the hoops. Despite the divergence in specimens with configuration E, the proposed compressive fracture energy model provides an accurate and objective prediction of the softening responses

of RC structures. The proposed model can be used for the collapse assessment of RC structures against extreme load conditions. In these cases, the collapse of the overall structure is dominated by the crushing failure of RC columns, and accurate modeling of the softening responses is significant.

CONCLUSIONS

This paper presents a systematic study of a compressive fracture energy model G_{fc} for confined normal-strength concrete. The conclusions of the present work are:

- 1. The existing confinement models for normal-strength concrete give a consistent prediction of the confined peak stress and peak strain; however, significant differences are observed in predicting the softening branches of the stress-strain curves. The post-peak strain relies on the gauge length used in the tests.
- 2. For unconfined concrete, the compressive fracture energy model developed by Wu and Wei (2016) matches well with the test results of large-scale reinforced concrete (RC) columns. The compressive fracture energy gradually increases along with the unconfined concrete strength f_{co} . For confined concrete, the compressive fracture energy increases substantially along with the effective confinement pressure f_{le} . Both circular and square RC columns with a similar value of $f_{le}f_{co}$ will share approximately the same amount of compressive fracture energy. The cross-section type and dimensions are not influential factors for the compressive fracture energy of either confined or unconfined concrete.
- 3. The proposed G_{fc} model provides an objective prediction of the softening force-displacement responses of RC columns under large deformations. Meanwhile, the analysis results match well with the test results. The mean predicted-to-test result of ultimate displacement at which the resistance drops to zero is 1.13. The analyzed force-displacement responses without compressive fracture energy regularization significantly underestimate the softening responses and the ultimate displacement of the RC column, with an average predicted-to-test ratio of 0.26.
- 4. The proposed model can be used for the collapse assessment of RC structures against extreme load conditions. In these cases, the collapse of the overall structure is dominated by the crushing failure of RC columns, and accurate modeling of the softening responses is significant.

AUTHOR BIOS

Xiaoran Song is a Lecturer at Shijiazhuang Tiedao University, Shijiazhuang, Hebei, China. He received his BS and PhD in civil engineering from Tianjin University, Tianjin, China, in 2011 and 2017, respectively. His research interests include numerical modeling and reliability evaluation of civil structures under extreme load conditions.

ACKNOWLEDGMENTS

The author would like to thank the editors and anonymous reviewers for their constructive comments. The author wishes to dedicate this paper to his parents, for their continual support and company in carrying out this study.

REFERENCES

Akiyama, M.; Suzuki, M.; and Frangopol, D. M., 2010, "Stress-Averaged Strain Model for Confined High-Strength Concrete," *ACI Structural Journal*, V. 107, No. 2, Mar.-Apr., pp. 179-188.

Chen, W.-F., and Han, D.-J., 1988, *Plasticity for Structural Engineering*, Springer, New York, 606 pp.

Coleman, J., and Spacone, E., 2001, "Localization Issues in Force-Based Frame Elements," *Journal of Structural Engineering*, ASCE, V. 127, No. 11, pp. 1257-1265. doi: 10.1061/(ASCE)0733-9445(2001)127:11(1257)

Cusson, D., and Paultre, P., 1994, "High-Strength Concrete Columns Confined by Rectangular Ties," *Journal of Structural Engineering*, ASCE, V. 120, No. 3, pp. 783-804. doi: 10.1061/(ASCE)0733-9445(1994)120:3(783)

Guo, Z., 2014, *Principles of Reinforced Concrete*, Butterworth-Heinemann, Oxford, UK, 606 pp.

Hong, K.-N.; Han, S.-H.; and Yi, S.-T., 2006, "High-Strength Concrete Columns Confined by Low-Volumetric-Ratio Lateral Ties," *Engineering Structures*, V. 28, No. 9, pp. 1346-1353. doi: 10.1016/j.engstruct.2006.01.010 Hoshikuma, J.; Kawashima, K.; Nagaya, K.; and Taylor, A. W., 1997, "Stress-Strain Model for Confined Reinforced Concrete in Bridge Piers," *Journal of Structural Engineering*, ASCE, V. 123, No. 5, pp. 624-633. doi: 10.1061/(ASCE)0733-9445(1997)123:5(624)

Jansen, D. C., and Shah, S. P., 1997, "Effect of Length on Compressive Strain Softening of Concrete," *Journal of Engineering Mechanics*, ASCE, V. 123, No. 1, pp. 25-35. doi: 10.1061/(ASCE)0733-9399(1997)123:1(25) Jirásek, M., and Bauer, M., 2012, "Numerical Aspects of the Crack Band Approach," *Computers & Structures*, V. 110-111, pp. 60-78. doi: 10.1016/j.

compstruc.2012.06.006

Kunnath, S. K., 2018, "Modeling of Reinforced Concrete Structures for Nonlinear Seismic Simulation," *Journal of Structural Integrity and Maintenance*, V. 3, No. 3, pp. 137-149. doi: 10.1080/24705314.2018.1492669

Légeron, F., and Paultre, P., 2003, "Uniaxial Confinement Model for Normal- and High-Strength Concrete Columns," *Journal of Structural Engineering*, ASCE, V. 129, No. 2, pp. 241-252. doi: 10.1061/(ASCE)0733-9445(2003)129:2(241)

Lertsrisakulrat, T.; Watanabe, K.; Matsuo, M.; and Niwa, J., 2001, "Experimental Study on Parameters in Localization of Concrete Subjected to Compression," *Doboku Gakkai Ronbunshu*, V. 2001, No. 669, pp. 309-321.

Li, Z.-X.; Zhong, B.; Shi, Y.; and Yan, J.-B., 2017, "Nonlocal Formulation for Numerical Analysis of Post-Blast Behavior of RC Columns," *International Journal of Concrete Structures and Materials*, V. 11, No. 2, pp. 403-413. doi: 10.1007/s40069-017-0201-z

Mander, J. B.; Priestley, M. J. N.; and Park, R., 1988a, "Observed Stress-Strain Behavior of Confined Concrete," *Journal of Structural Engineering*, ASCE, V. 114, No. 8, pp. 1827-1849. doi: 10.1061/(ASCE)0733-9445(1988)114:8(1827)

Mander, J. B.; Priestley, M. J. N.; and Park, R., 1988b, "Theoretical Stress-Strain Model for Confined Concrete," *Journal of Structural Engineering*, ASCE, V. 114, No. 8, pp. 1804-1826. doi: 10.1061/(ASCE)0733-9445(1988)114:8(1804)

Markeset, G., and Hillerborg, A., 1995, "Softening of Concrete in Compression—Localization and Size Effects," *Cement and Concrete Research*, V. 25, No. 4, pp. 702-708. doi: 10.1016/0008-8846(95)00059-L

Pugh, J. S.; Lowes, L. N.; and Lehman, D. E., 2015, "Nonlinear Line-Element Modeling of Flexural Reinforced Concrete Walls," *Engineering Structures*, V. 104, pp. 174-192. doi: 10.1016/j.engstruct.2015.08.037

Saatcioglu, M., and Razvi, S. R., 1992, "Strength and Ductility of Confined Concrete," *Journal of Structural Engineering*, ASCE, V. 118, No. 6, pp. 1590-1607. doi: 10.1061/(ASCE)0733-9445(1992)118:6(1590)

Scott, B. D.; Park, R.; and Priestley, M. J. N., 1982, "Stress-Strain Behavior of Concrete Confined by Overlapping Hoops at Low and High Strain Rates," *ACI Journal Proceedings*, V. 79, No. 1, Jan.-Feb., pp. 13-27. Sheikh, S. A., and Uzumeri, S. M., 1982, "Analytical Model for Concrete Confinement in Tied Columns," *Journal of the Structural Division*, ASCE,

V. 108, No. 12, pp. 2703-2722. doi: 10.1061/JSDEAG.0006100
Sheikh, S. A., and Yeh, C.-C., 1990, "Tied Concrete Columns under Axial Load and Flexure," *Journal of Structural Engineering*, ASCE, V. 116, No. 10, pp. 2780-2800. doi: 10.1061/(ASCE)0733-9445(1990)116:10(2780)

Spacone, E.; Filippou, F. C.; and Taucer, F. F., 1996, "Fibre Beam–Column Model for Non-Linear Analysis of R/C Frames: Part I. Formulation," *Earth-quake Engineering & Structural Dynamics*, V. 25, No. 7, pp. 711-725. doi: 10.1002/(SICI)1096-9845(199607)25:7<711::AID-EQE576>3.0.CO;2-9

van Vliet, M. R. A., and van Mier, J. G. M., 1996, "Experimental Investigation of Concrete Fracture under Uniaxial Compression," *Mechanics of Cohesive-Frictional Materials*, V. 1, No. 1, pp. 115-127. doi: 10.1002/(SICI)1099-1484(199601)1:1<115::AID-CFM6>3.0.CO;2-U

Welt, T.; Lehman, D.; Lowes, L.; and LaFave, J., 2018, "A Constitutive Model for Confined Concrete in Slender Rectangular RC Sections Incorporating Compressive Energy," *Construction and Building Materials*, V. 193, pp. 344-362. doi: 10.1016/j.conbuildmat.2018.10.138

Wu, Y.-F., and Wei, Y., 2016, "Stress–Strain Modeling of Concrete Columns with Localized Failure: An Analytical Study," *Journal of Composites for Construction*, ASCE, V. 20, No. 3, p. 04015071. doi: 10.1061/(ASCE)CC.1943-5614.0000634

Yassin, M. H. M., 1994, "Nonlinear Analysis of Prestressed Concrete Structures under Monotonic and Cyclic Loads," PhD thesis, University of California, Berkeley, Berkeley, CA.

Zahn, F. A., 1985, "Design of Reinforced Concrete Bridge Columns for Strength and Ductility," PhD thesis, University of Canterbury, Christchurch, New Zealand, 405 pp.

Title No. 121-S15

Cyclic Behavior of Reinforced Concrete Flexural Members to Changing Design Parameters

by Jessica Gitomarsono, Min-Yuan Cheng, and Marnie B. Giduquio

An experimental study was conducted to evaluate the cyclic behavior of reinforced concrete (RC) flexural members with different design parameters. Twenty-five large-scale beam specimens were tested under lateral displacement reversals using a test setup intended to impose single-curvature deformation. Test parameters investigated include: 1) specimen aspect ratio, a/d; 2) designated shear stress demand, $V_{Mpr}/b_w d\sqrt{f_c'}$; 3) spacing of transverse reinforcement, s; 4) diameter of longitudinal reinforcement, db; and 5) tension-to-compression reinforcement ratio. All specimens were designed in compliance with ACI 318-19 using Grade 60 $(f_v = 60 \text{ ksi } [414 \text{ MPa}])$ reinforcing steel and a specified concrete strength of 4 ksi (27.6 MPa). Test results indicated that specimen peak lateral strength, V_{peak}, can be acceptably estimated by V_{Mn}, the shear corresponding to the development of the nominal flexural strength at the beam fixed end. The V_{peak}/V_{Mn} ratio increased as the normalized peak shear stress, $V_{peak}/b_w d\sqrt{f_{cm}}$, decreased, where $b_{\mbox{\tiny W}}$ d, and $f_{\mbox{\tiny cm}}$ were the beam width, effective depth, and concrete cylinder strength, respectively. Specimen ultimate drift, du, was also found to be more sensitive to the normalized peak shear stress, $V_{peak}/b_w d\sqrt{f_{cm}}$. Specimen ultimate drift, d_w tended to increase as the $V_{peak}/b_w d\sqrt{f_{cm}}$ decreased. The average normalized energy dissipation capacity generally increased as the specimen normalized peak shear stress decreased, the aspect ratio increased, and the spacing of transverse reinforcement was reduced. Finally, specimen effective lateral stiffness increased as the shear span decreased or the reinforcement ratio on the tension side increased.

Keywords: aspect ratio; deformation; diameter of longitudinal reinforcement; energy; reinforcement ratio; shear stress; stiffness; strength; transverse reinforcement spacing.

INTRODUCTION

In high seismic regions, buildings are expected to respond nonlinearly when subjected to strong ground motions (ASCE/SEI 7-22 [ASCE 2022]). For moment-resisting frames, the design concept of strong-column/weak-beam, typically adopted by building codes such as ACI 318-19 (ACI Committee 318 2019), intends to stimulate the nonlinear response of the frame, which is primarily attributed to the formation of plastic hinges in beams. As a result, the beam force-deflection characteristics, particularly under cyclic loading, both within and beyond the elastic limit, have a great influence on the seismic performance of the moment-resisting frame. Several previous studies investigated cyclic responses of reinforced concrete (RC) flexural members, and key findings are briefly reviewed.

Brown and Jirsa (1971) tested 12 specimens to investigate the influences of loading history, amount of longitudinal reinforcement, shear span, and stirrup spacing on

the cyclic behavior of RC beams. Specimens were loaded to shear stress levels of approximately 1.6 to $5.5\sqrt{f_{cm}(\mathrm{psi})}$ (0.13 to $0.46\sqrt{f_{cm}(\mathrm{MPa})}$), where f_{cm} was the tested concrete cylinder strength. Based on test results, Brown and Jirsa (1971) concluded that specimens with closer stirrup spacing maintained load and energy absorption capacity over a larger number of cycles. Specimens that had the same amount of longitudinal reinforcement but with reduced shear span resulted in failure within fewer cycles. Specimens subjected to larger shear force (with more longitudinal reinforcement) also failed in fewer cycles than those subjected to smaller shear force.

Based on the test results of two specimens (Specimens 35 and 43), Popov et al. (1972) indicated that larger and more closely spaced stirrups in beams resulted in reduced stiffness deterioration, improved energy dissipation capacity, and increased rotational capacity. Both beam specimens had a shear span-to-effective depth ratio of 3.1 and were subjected to cyclic load with a maximum shear stress level of approximately $5.5\sqrt{f_{cm}(\text{psi})}$ ($0.46\sqrt{f_{cm}(\text{MPa})}$).

The shear decay behavior of RC flexural members was later investigated by Scribner and Wight (1978) through tests of 12 specimens. The maximum shear stress of test specimens ranged from $2.0\sqrt{f_{cm}(\mathrm{psi})}$ $(0.17\sqrt{f_{cm}(\mathrm{MPa})})$ to approximately $6.0\sqrt{f_{cm}(\mathrm{psi})}$ $(0.50\sqrt{f_{cm}(\mathrm{MPa})})$. Test results showed that maximum shear stress was the most important factor in determining a member's ability to withstand repeated inelastic loading. Specimens with higher shear stress demand exhibited a more severe loss of strength and energy dissipation capacity.

More recently, the effects of hoop spacing on the cyclic response of two large RC beam specimens were reported (Panagiotou et al. 2013). Two specimens had identical geometry and longitudinal reinforcement design but with different transverse reinforcement ratios due to different hoop spacing. The shear stress demand for the two specimens was around $1.7\sqrt{f_{cm}(\mathrm{psi})}$ (0.14 $\sqrt{f_{cm}(\mathrm{MPa})}$). Test results showed that damage initiation and damage progression in both specimens were dominated by the buckling of longitudinal reinforcement. Reducing the s/d_b ratio from 7.8 to 4.3 resulted in an increase in specimen drift capacity from 2.7 to

ACI Structural Journal, V. 121, No. 2, March 2024.

MS No. S-2022-153.R1, doi: 10.14359/51740244, received August 24, 2022, and reviewed under Institute publication policies. Copyright © 2024, American Concrete Institute. All rights reserved, including the making of copies unless permission is obtained from the copyright proprietors. Pertinent discussion including author's closure, if any, will be published ten months from this journal's date if the discussion is received within four months of the paper's print publication.

5.3%, where s was the hoop reinforcement spacing, and d_b was the longitudinal reinforcement diameter.

These past researchers identified key design parameters affecting the cyclic behavior of RC flexural members. However, conflicts were observed regarding the influences of some design parameters. For example, although the majority of the research results indicated that providing more and closely spaced transverse reinforcement improved the seismic performance of the specimens, the shear slippage along the cracks that developed perpendicularly to the longitudinal axis raised questions about the effectiveness of transverse reinforcement at closer spacing (Jirsa 1973; Scribner and Wight 1978; Wibowo et al. 2017). There is still some room for research to further understand the cyclic behavior of RC flexural members.

A systematic test program consisting of 25 large-scale RC beam specimens tested under lateral displacement reversals was developed for this study. Primary test parameters included: 1) shear span-to-effective depth ratio; 2) shear stress demand; 3) amount/spacing of transverse reinforcement; 4) diameter of longitudinal reinforcement; and 5) tension-to-compression reinforcement ratio. Mechanisms that limited the peak strength and initiated the force loss are identified first. The influences of these parameters on the specimen peak strength, deformation capacity, and energy dissipation capacity are then discussed.

RESEARCH SIGNIFICANCE

Previous tests on the cyclic response of RC flexural members typically involved multiple design parameters that presented difficulties in identifying the influence of individual parameters on a certain response. Through a systematic test program, the influences of the selected design parameters on the cyclic behavior of RC flexural members were investigated in this research. The test program was deliberately designed such that the effects of each selected design parameter can be examined as independently as possible. Findings from this study are expected to be useful for the design and modeling of RC flexural members.

EXPERIMENTAL PROGRAM

Test specimens

Specimens were constructed and tested in an upright position. Each specimen consisted of a top concrete block, a beam segment, and a concrete base block. Lateral displacement reversals were applied at the top concrete block, while a fixed boundary condition was provided by the concrete base block. This test setup (with more details described later) imposed single-curvature deformation to the test specimens, where moment increased linearly from the center of the load application to the fixed end of the beam, and shear was constant along the beam span.

An identical beam cross section of 18.9×29.5 in. $(480 \times 750 \text{ mm})$ was used for all specimens. The span of the specimen was determined based on the shear span-to-effective depth ratio, a/d, where a was the shear span measured from the center of the load application to the fixed end of the beam, and d was the beam effective depth. Three a/d ratios of approximately 2.0, 3.5, and 5.0 were investigated.

Please note that a/d of 2.0 represents the smallest dimension permitted by ACI 318-19, while a/d of 5.0 represents a beam having a clear span of approximately 22 ft (6740 mm) if the inflection point is assumed at midspan. Specimen nominal dimensions and section reinforcement layout with respect to the loading direction are illustrated in Fig. 1. The key design parameters of all specimens are summarized in Table 1.

All specimens were designed using the specified concrete strength, f_c , of 4000 psi (27.6 MPa) and Grade 60 (f_v = 60 ksi [414 MPa]) reinforcing steel. Longitudinal reinforcement was provided based on the designated shear stress demand, $V_{Mpr}/b_w d\sqrt{f_c'}$, where V_{Mpr} was defined as the probable flexural strength, M_{pr} , divided by the shear span, a; b_w was the beam width; d was the beam effective depth; and f_c' was the specified concrete strength. This $V_{Mpr}/b_w d\sqrt{f_c'}$ represented the shear corresponding to the development of M_{pr} at the beam fixed end. The probable flexural strength, M_{pr} , was determined using the ACI 318-19 equivalent rectangular concrete stress distribution and steel stress of $1.25f_v$. For specimens with a/d of approximately 2.0, longitudinal reinforcement was provided to induce low, medium, and high $V_{Mpr}/b_w d$ of approximately $2\sqrt{f_c'(\text{psi})}$ (0.17 $\sqrt{f_c'(\text{MPa})}$), 5 $\sqrt{f_c'(\text{psi})}$ (0.42 $\sqrt{f_c'(\text{MPa})}$), and $8\sqrt{f_c'(\text{psi})}$ (0.67 $\sqrt{f_c'(\text{MPa})}$), respectively. The smallest tensile longitudinal reinforcement in these specimens, $V_{Mpr}/b_w d$ of approximately 2 $\sqrt{f_c'(\text{psi})}$ (0.17 $\sqrt{f_c'(\text{MPa})}$), was approximately 40% higher than the minimum required by ACI 318-19 as the larger of 3 $\sqrt{f_c'(\text{psi})}/f_v(0.25\sqrt{f_c'(\text{MPa})}/f_v)$ and $200/f_v(\text{psi})(1.4/f_v(\text{MPa}))$. To satisfy the maximum longitudinal reinforcement ratio of 2.5% per ACI 318-19, specimens with a/d of approximately 3.5 were designed with $V_{Mpr}/b_w d$ of approximately 2 or 5 $\sqrt{f_c'(\text{psi})}$ (0.17 or 0.42 $\sqrt{f_c'(\text{MPa})}$), while specimens with a/d of 5.0 were designed with $V_{Mpp}/b_w d$ of approximately 2 $\sqrt{f_c'(\text{psi})}$ (0.17 $\sqrt{f_c'(\text{MPa})}$) only.

Symmetric longitudinal reinforcement was typically provided at the top and bottom of the cross section, except for six specimens where the area of the top reinforcement was two times the area of the bottom reinforcement to investigate the effect of the tension-to-compression reinforcement ratio. Top longitudinal reinforcement was subjected to tension when the specimen was loaded in the positive direction (W side), as shown in Fig. 1 and 2.

No. 8 (D25) longitudinal reinforcement was typically used, except for four specimens. Compared to specimens L6 3.5 and M6 3.5, where No. 8 (D25) longitudinal reinforcement was used, specimens L6 3.5D and M6 3.5D using No. 10 (D32) longitudinal reinforcement were meant to investigate the effects of s/d_b , a ratio of the spacing of the transverse reinforcement, s, to the diameter of the longitudinal reinforcement, d_b . For specimens L5 5.0D and L6 5.0D with a/d of 5.0, using No. 10 (D32) longitudinal reinforcement was meant to have the same configuration of transverse reinforcement (two legs per set) as those in specimens with the same shear stress but with different a/d, as shown in Fig. 1. Please note that using No. 8 (D25) longitudinal reinforcement to achieve that designed shear stress of $2\sqrt{f_c'(\text{psi})}$ (0.17 $\sqrt{f_c'(\text{MPa})}$) in these two specimens resulted in more than three longitudinal bars in each row; therefore,

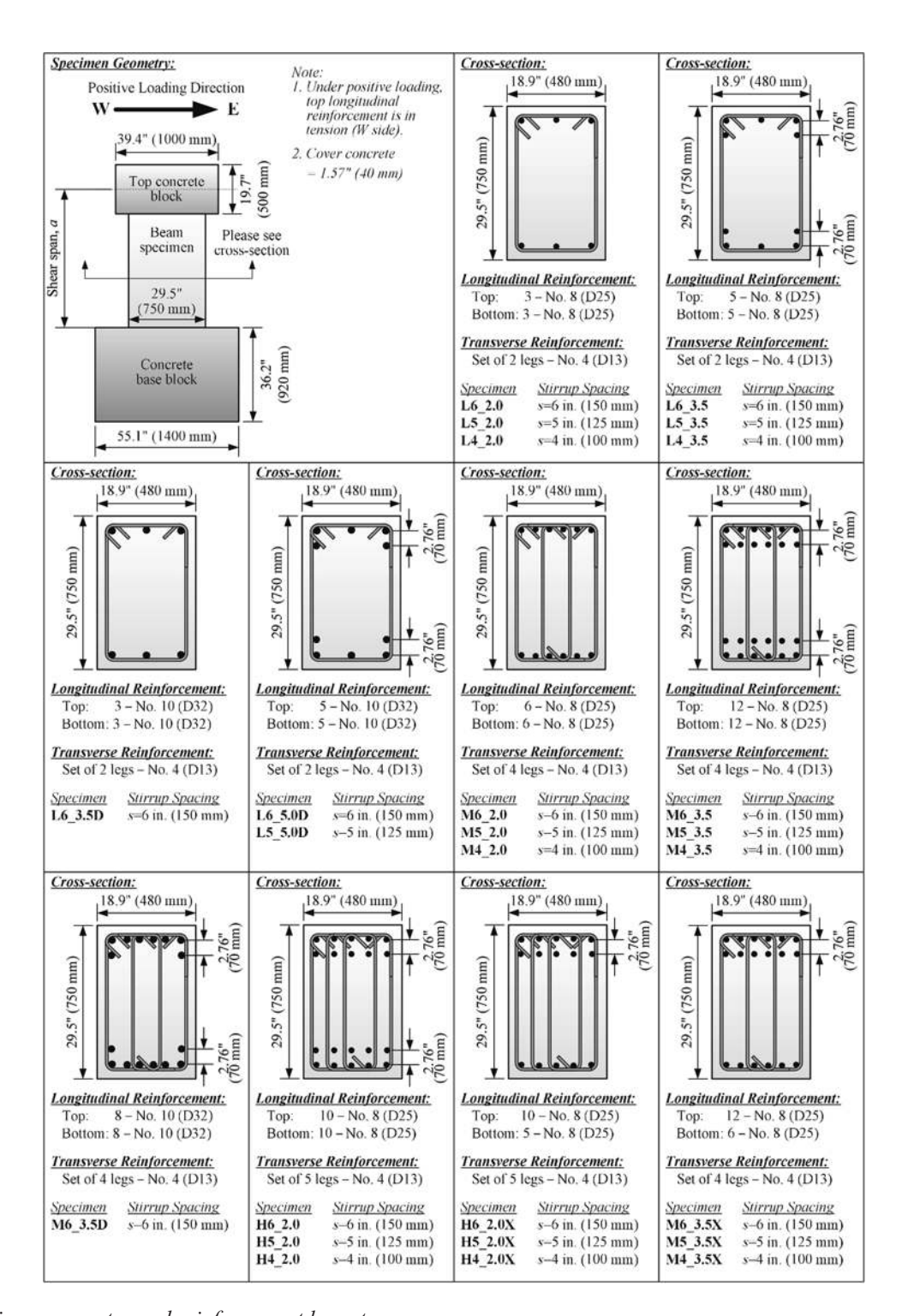


Fig. 1—Specimen geometry and reinforcement layout.

crossties would be required to provide lateral support on alternate bars in accordance with ACI 318-19.

Transverse reinforcement was first determined using a spacing, s, of 6 in. (150 mm) in the longitudinal direction to ensure V_s per Eq. (1) was greater than V_{Mpr} , assuming specimen shear capacity was contributed by transverse reinforcement only, as suggested by ACI 318-19 for beams in high seismic regions. In Eq. (1), A_v is the total leg area per set of transverse reinforcement; f_{yt} is the nominal yield stress of transverse reinforcement; d is the effective depth; and s is the spacing of transverse reinforcement in the longitudinal

direction. The larger V_{Mpr} was considered for the V_s provided in specimens with an asymmetric longitudinal reinforcement layout. The 6 in. (150 mm) spacing resulted from the smallest value of d/4 (~6.4 in. [162 mm]), six times the longitudinal bar diameter, d_b (6 in. [150 mm] for No. 8 bar), and 6 in. (150 mm) required by ACI 318-19. To investigate the effects of the amount/spacing of transverse reinforcement, the same set of transverse reinforcement was then provided in another two specimens having the same longitudinal reinforcement (same V_{Mpr}) but with reduced spacings at 5 and 4 in. (125 and 100 mm). These two specimens, consequently, had reduced

Table 1—Specimen design parameters

	f_c' , ksi		-		V _{Mpr} † (MPa)	Longitudinal (Grad	reinforcement le 60)	Transverse reinforcement		
Specimen	(MPa)	a, in. (mm)	d, in. (mm)	a/d	$\frac{b_w d\sqrt{f_c'(\text{psi})}^{\dagger}}{b_w d\sqrt{f_c'(\text{psi})}}^{\dagger} \text{ (MPa)}$	Тор	Bottom	(Grade 60)	s/d_b	V_s/V_{Mpr}^{\dagger}
L6_2.0	4 (27.6)	53.2 (1350)	27.0 (685)	2.0	±2.7 (±0.22)	3 No. 8 (D25)	3 No. 8 (D25)	2 legs No. 4 (D13) @ 6 in. (150 mm)	5.9	±1.3
L5_2.0	4 (27.6)	53.2 (1350)	27.0 (685)	2.0	±2.7 (±0.22)	3 No. 8 (D25)	3 No. 8 (D25)	2 legs No. 4 (D13) @ 5 in. (125 mm)	4.9	±1.5
L4_2.0	4 (27.6)	53.2 (1350)	27.0 (685)	2.0	±2.7 (±0.22)	3 No. 8 (D25)	3 No. 8 (D25)	2 legs No. 4 (D13) @ 4 in. (100 mm)	3.9	±1.9
L6_3.5	4 (27.6)	92.9 (2360)	25.9 (657)	3.6	±2.5 (±0.21)	5 No. 8 (D25)	5 No. 8 (D25)	2 legs No. 4 (D13) @ 6 in. (150 mm)	5.9	±1.4
L5_3.5	4 (27.6)	92.9 (2360)	25.9 (657)	3.6	±2.5 (±0.21)	5 No. 8 (D25)	5 No. 8 (D25)	2 legs No. 4 (D13) @ 5 in. (125 mm)	4.9	±1.6
L4_3.5	4 (27.6)	92.9 (2360)	25.9 (657)	3.6	±2.5 (±0.21)	5 No. 8 (D25)	5 No. 8 (D25)	2 legs No. 4 (D13) @ 4 in. (100 mm)	3.9	±2.1
L6_3.5D	4 (27.6)	92.9 (2360)	26.8 (681)	3.5	±2.4 (±0.20)	3 No. 10 (D32)	3 No. 10 (D32)	2 legs No. 4 (D13) @ 6 in. (150 mm)	4.6	±1.4
L6_5.0D	4 (27.6)	132.7 (3370)	25.7 (653)	5.2	±2.7 (±0.22)	5 No. 10 (D32)	5 No. 10 (D32)	2 legs No. 4 (D13) @ 6 in. (150 mm)	4.6	±1.3
L5_5.0D	4 (27.6)	132.7 (3370)	25.7 (653)	5.2	±2.7 (±0.22)	5 No. 10 (D32)	5 No. 10 (D32)	2 legs No. 4 (D13) @ 5 in. (125 mm)	3.9	±1.5
M6_2.0	4 (27.6)	53.2 (1350)	27.0 (685)	2.0	±5.2 (±0.43)	6 No. 8 (D25)	6 No. 8 (D25)	4 legs No. 4 (D13) @ 6 in. (150 mm)	5.9	±1.3
M5_2.0	4 (27.6)	53.2 (1350)	27.0 (685)	2.0	±5.2 (±0.43)	6 No. 8 (D25)	6 No. 8 (D25)	4 legs No. 4 (D13) @ 5 in. (125 mm)	4.9	±1.6
M4_2.0	4 (27.6)	53.2 (1350)	27.0 (685)	2.0	±5.2 (±0.43)	6 No. 8 (D25)	6 No. 8 (D25)	4 legs No. 4 (D13) @ 4 in. (100 mm)	3.9	±2.0
M6_3.5	4 (27.6)	92.9 (2360)	25.6 (650)	3.6	±5.6 (±0.47)	12 No. 8 (D25)	12 No. 8 (D25)	4 legs No. 4 (D13) @ 6 in. (150 mm)	5.9	±1.2
M5_3.5	4 (27.6)	92.9 (2360)	25.6 (650)	3.6	±5.6 (±0.47)	12 No. 8 (D25)	12 No. 8 (D25)	4 legs No. 4 (D13) @ 5 in. (125 mm)	4.9	±1.5
M4_3.5	4 (27.6)	92.9 (2360)	25.6 (650)	3.6	±5.6 (±0.47)	12 No. 8 (D25)	12 No. 8 (D25)	4 legs No. 4 (D13) @ 4 in. (100 mm)	3.9	±1.8
M6_3.5D	4 (27.6)	92.9 (2360)	26.1 (665)	3.6	±6.1 (±0.51)	8 No. 10 (D32)	8 No. 10 (D32)	4 legs No. 4 (D13) @ 6 in. (150 mm)	4.6	±1.1
H6_2.0	4 (27.6)	53.2 (1350)	25.6 (650)	2.1	±8.3 (±0.69)	10 No. 8 (D25)	10 No. 8 (D25)	5 legs No. 4 (D13) @ 6 in. (150 mm)	5.9	±1.0
H5_2.0	4 (27.6)	53.2 (1350)	25.6 (650)	2.1	±8.3 (±0.69)	10 No. 8 (D25)	10 No. 8 (D25)	5 legs No. 4 (D13) @ 5 in. (125 mm)	4.9	±1.2
H4_2.0	4 (27.6)	53.2 (1350)	25.6 (650)	2.1	±8.3 (±0.69)	10 No. 8 (D25)	10 No. 8 (D25)	5 legs No. 4 (D13) @ 4 in. (100 mm)	3.9	±1.5
H6 2.0X	4 (27.6)	53.2 (1350)	25.6 (650)	2.1	+8.3 (+0.69)	10 No. 8 (D25)	5 No. 8 (D25)	5 legs No. 4 (D13)	5.9	+1.0
	4 (27.0)	33.2 (1330)	27.0 (685)*	2.0*	-4.4 (-0.37)	10 140. 6 (D25)	3 110. 0 (B23)	@ 6 in. (150 mm)	3.7	-1.9
H5 2.0X	4 (27.6)	53.2 (1350)	25.6 (650)	2.1	+8.3 (+0.69)	10 No. 8 (D25)	5 No. 8 (D25)	5 legs No. 4 (D13)	4.9	+1.2
113_2.UA	7 (27.0)	JJ.2 (1JJU)	27.0 (685)*	2.0*	-4.4 (-0.37)	10 140. 0 (D23)	J 110. 0 (D23)	@ 5 in. (125 mm)	7.7	-2.3
H4 2.0X	4 (27.6)	53.2 (1350)	25.6 (650)	2.1	+8.3 (+0.69)	10 No. 8 (D25)	5 No. 8 (D25)	5 legs No. 4 (D13)	3.9	+1.5
117_2.UA	7 (27.0)	33.2 (1330)	27.0 (685)*	2.0* -4.4 (-0.37)		10 110. 0 (D23)	J 110. 0 (D23)	@ 4 in. (100 mm)	3.9	-2.9
M6 3.5X	4 (27.6)	92.9 (2360)	25.6 (650)	3.6	+5.6 (+0.47)	12 No. 8 (D25)	6 No. 8 (D25)	4 legs No. 4 (D13)	5.9	+1.2
1410_3.3A	7 (27.0)	72.9 (2300)	27.0 (685)*			12 110. 0 (D23)	0 110. 0 (D23)	@ 6 in. (150 mm)	5.9	-2.3
M5 3.5X	4 (27.6)	92.9 (2360)	25.6 (650)	3.6	+5.6 (+0.47)	12 No. 8 (D25)	6 No. 8 (D25)	4 legs No. 4 (D13)	4 9	+1.5
1V13_3.3A	7 (27.0)	72.7 (2300)	27.0 (685)*	3.4*	-3.0 (-0.25)	12 110. 0 (D23)	0 110. 0 (D23)	@ 5 in. (125 mm)	4.9	-2.7
M4 3.5X	4 (27.6)	92.9 (2360)	25.6 (650)	3.6	+5.6 (+0.47)	12 No. 8 (D25)	6 No. 8 (D25)	4 legs No. 4 (D13)	3.9	+1.8
111 T_3.3A	1 (27.0)	72.7 (2300)	27.0 (685)*	3.4*	-3.0 (-0.25)	12 110. 0 (D23)	0 110. 0 (D23)	@ 4 in. (100 mm)	3.9	-3.4

^{*}Negative loading direction wherein side with lower flexural reinforcement is in tension.

 $^{^{\}dagger}\text{The}$ "+" and "-" signs refer to positive and negative loading directions, respectively.

 s/d_b and increased V_s/V_{Mpr} compared to the counterpart specimen with 6 in. (150 mm) transverse reinforcement spacing. In all of the test specimens, the first hoop was placed at 2 in. (50 mm) distance away from the fixed end of the beam segment. The closed transverse reinforcement consisted of a stirrup having seismic hooks at both ends and a crosstie with a 90-degree hook at one end and a 135-degree hook at another end. The crosstie was placed consistently on the W side of the test specimens (refer to Fig. 1).

$$V_s = \frac{A_{\nu} f_{yt} d}{s} \tag{1}$$

Experimental setup and instrumentation

The experimental setup for all test specimens is schematically presented in Fig. 2. The concrete base block was fixed to the strong floor using four 2.7 in. (69 mm) diameter high-strength threaded rods. Lateral displacement reversals were applied at the top concrete block through two 220 kip (100 tonf) actuators. This test setup was intended to impose single-curvature deformation to the test specimen with negligible axial force.

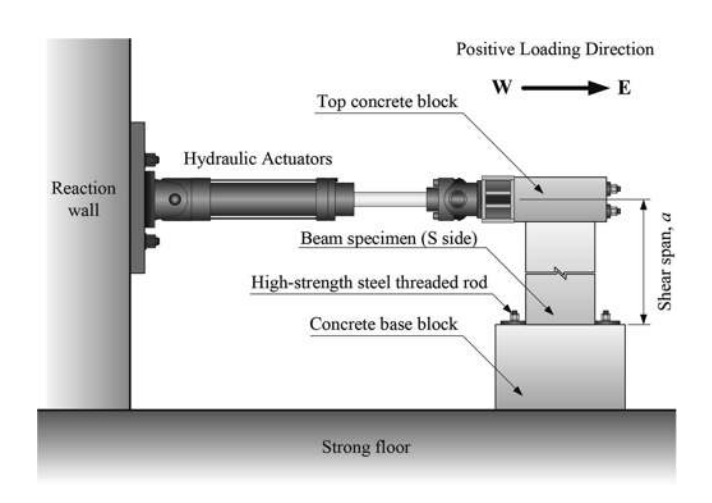


Fig. 2—Experimental setup.

Actuators were deformation-controlled during the test. The loading history is presented in Fig. 3, where drift ratio is defined as the lateral deformation measured at the load application divided by the specimen shear span, *a*. The positive drift corresponds to the actuator pushing toward the east direction.

A total of five linear variable differential transformers (LVDTs) were used to measure exterior movement of the specimen. One LVDT was placed at the center of the load application. Two LVDTs were installed at midheight of the concrete base block and the other two LVDTs were installed 1.0 in. (25 mm) below the top face of the concrete base block to measure the lateral movement, in-plane rotation, and out-of-plane rotation (twist) of the concrete base block. An optical infrared-based system was used to monitor the exterior deformation of the beam segment. This system tracked the movements of multiple points, referred to as "markers," which were attached on the N face of the specimens in a 6 in. (150 mm) grid pattern. Typical marker and LVDT layouts for all specimens are shown in Fig. 4. In addition, strain gauges were attached to the reinforcing bars at several locations.

EXPERIMENTAL RESULTS

Materials

Concrete materials were supplied by a local ready mixed concrete company. The requested maximum coarse aggregate size for all concrete materials was 0.5 in. (13 mm). Specimens were constructed in an upright position. The concrete base block was cast first, followed by the beam segment and the top concrete block. Concrete compressive strength for the beam segment of each specimen is shown in Table 2. Concrete strength, f_{cm} , was determined based on the average of the compressive strengths of four 4 x 8 in. (100 x 200 mm) cylinders, which were tested within 24 hours after the test of the corresponding beam specimen.

The direct tensile test, in accordance with ASTM A370 (2020), was conducted to determine the mechanical properties of the reinforcing steel. A set of three steel coupons with a length of at least 24 in. (610 mm) was prepared for each

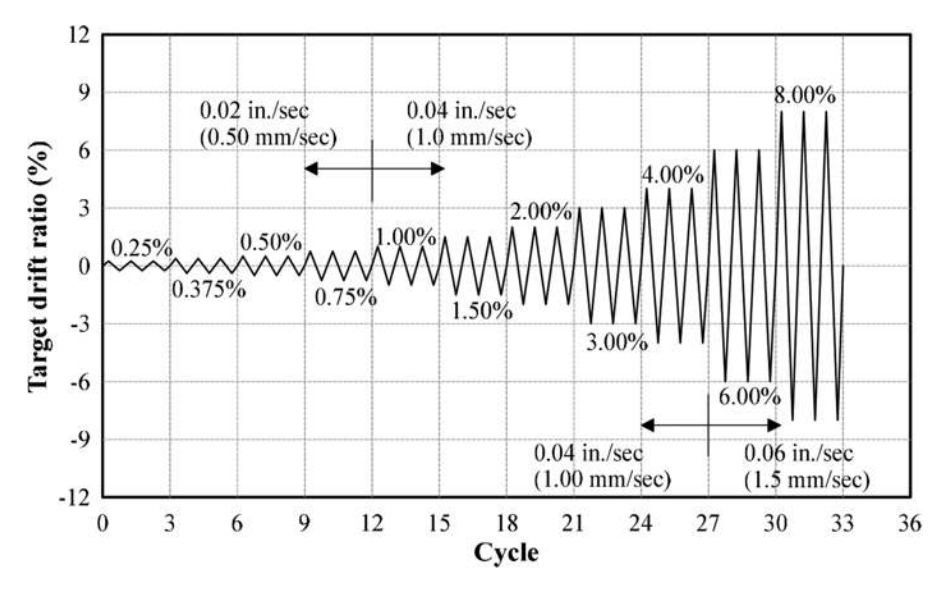


Fig. 3—Loading history.

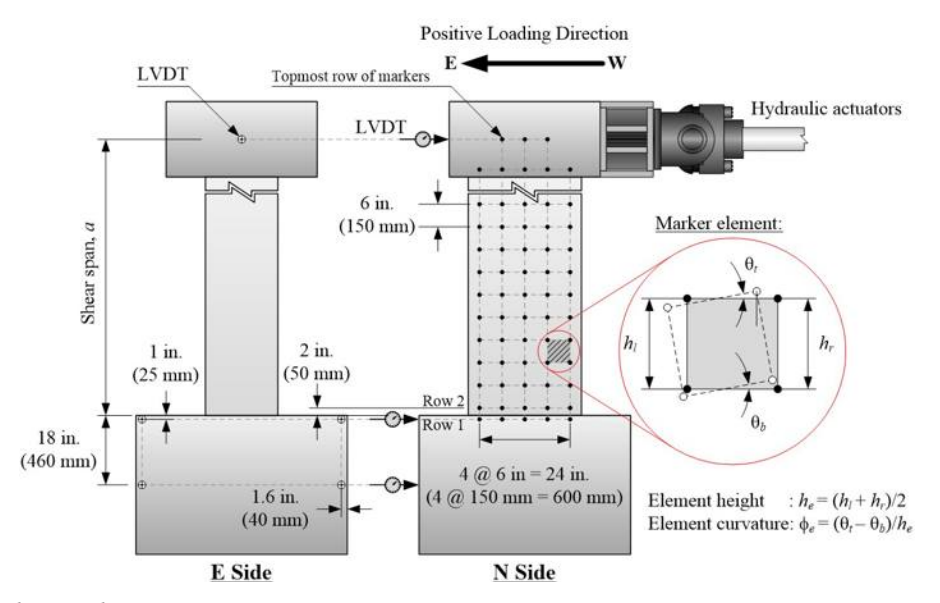


Fig. 4—Markers and LVDT locations.

Table 2—Tested material properties

	Longit	udinal reinforcemen	nt	Tra	insverse reinforceme	nt	
Specimen	Size	f _{ym} , ksi (MPa)	f _{um} , ksi (MPa)	Size	f _{ytm} , ksi (MPa)	f _{utm} , ksi (MPa)	f _{cm} , ksi (MPa)
L6_2.0	No. 8 (D25)	65.7 (453)	85.5 (589)	No. 4 (D13)	67.2 (463)	85.2 (587)	5.5 (38)
L5_2.0	No. 8 (D25)	65.7 (453)	85.5 (589)	No. 4 (D13)	67.2 (463)	85.2 (587)	6.0 (42)
L4_2.0	No. 8 (D25)	65.7 (453)	85.5 (589)	No. 4 (D13)	67.2 (463)	85.2 (587)	6.1 (42)
L6_3.5	No. 8 (D25)	65.7 (453)	85.5 (589)	No. 4 (D13)	67.2 (463)	85.2 (587)	4.3 (30)
L5_3.5	No. 8 (D25)	65.7 (453)	85.5 (589)	No. 4 (D13)	67.2 (463)	85.2 (587)	5.2 (36)
L4_3.5	No. 8 (D25)	65.7 (453)	85.5 (589)	No. 4 (D13)	67.2 (463)	85.2 (587)	5.1 (35)
L6_3.5D	No. 10 (D32)	68.5 (472)	80.7 (557)	No. 4 (D13)	67.2 (463)	85.2 (587)	5.0 (35)
L6_5.0D	No. 10 (D32)	68.5 (472)	80.7 (557)	No. 4 (D13)	67.2 (463)	85.2 (587)	5.8 (40)
L5_5.0D	No. 10 (D32)	68.5 (472)	80.7 (557)	No. 4 (D13)	67.2 (463)	85.2 (587)	5.5 (38)
M6_2.0	No. 8 (D25)	66.0 (455)	86.0 (593)	No. 4 (D13)	67.2 (463)	85.2 (587)	5.3 (36)
M5_2.0	No. 8 (D25)	65.7 (453)	85.5 (589)	No. 4 (D13)	67.2 (463)	85.2 (587)	5.1 (35)
M4_2.0	No. 8 (D25)	69.8 (481)	89.2 (615)	No. 4 (D13)	67.2 (463)	85.2 (587)	5.7 (39)
M6_3.5	No. 8 (D25)	65.7 (453)	85.5 (589)	No. 4 (D13)	67.2 (463)	85.2 (587)	5.3 (36)
M5_3.5	No. 8 (D25)	65.7 (453)	85.5 (589)	No. 4 (D13)	67.2 (463)	85.2 (587)	5.0 (35)
M4_3.5	No. 8 (D25)	65.7 (453)	85.5 (589)	No. 4 (D13)	67.2 (463)	85.2 (587)	4.5 (31)
M6_3.5D	No. 10 (D32)	68.5 (472)	80.7 (557)	No. 4 (D13)	67.2 (463)	85.2 (587)	5.6 (39)
H6_2.0	No. 8 (D25)	65.7 (453)	85.5 (589)	No. 4 (D13)	67.2 (463)	85.2 (587)	3.8 (26)
H5_2.0	No. 8 (D25)	65.7 (453)	85.5 (589)	No. 4 (D13)	67.2 (463)	85.2 (587)	4.5 (31)
H4_2.0	No. 8 (D25)	65.7 (453)	85.5 (589)	No. 4 (D13)	67.2 (463)	85.2 (587)	4.2 (29)
H6_2.0X	No. 8 (D25)	65.7 (453)	85.5 (589)	No. 4 (D13)	67.2 (463)	85.2 (587)	4.4 (30)
H5_2.0X	No. 8 (D25)	65.7 (453)	85.5 (589)	No. 4 (D13)	67.2 (463)	85.2 (587)	4.3 (29)
H4_2.0X	No. 8 (D25)	65.7 (453)	85.5 (589)	No. 4 (D13)	67.2 (463)	85.2 (587)	4.4 (30)
M6_3.5X	No. 8 (D25)	65.7 (453)	85.5 (589)	No. 4 (D13)	67.2 (463)	85.2 (587)	5.4 (37)
M5_3.5X	No. 8 (D25)	65.7 (453)	85.5 (589)	No. 4 (D13)	67.2 (463)	85.2 (587)	5.7 (39)
M4_3.5X	No. 8 (D25)	65.7 (453)	85.5 (589)	No. 4 (D13)	67.2 (463)	85.2 (587)	5.6 (39)

bar size per delivery of reinforcement, and steel strain was determined using an optical infrared-based system where markers were installed with a gauge length of 8 in. (203

mm). The measured yield stress (f_{ym} or f_{ytm}) and peak stress (f_{um} or f_{utm}), obtained from the average of the three coupons, are summarized in Table 2.

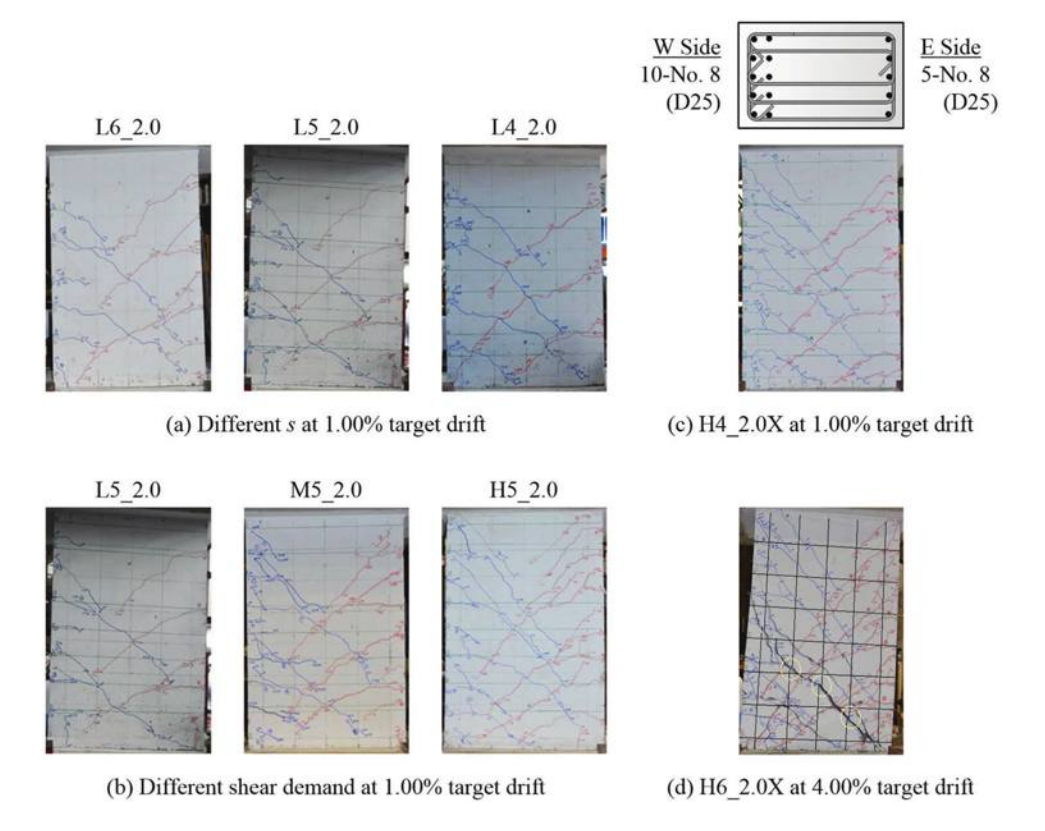


Fig. 5—Specimen damage progression.

Progression of damage

Both horizontal and inclined cracks were observed on the S side of all test specimens during the first loading cycle to 0.25% target drift. During 1.00% target drift cycles, new cracks developed. The number of cracks was similar for specimens reinforced with the same longitudinal reinforcement regardless of transverse reinforcement spacing (refer to Fig. 5(a)). With the same aspect ratio, however, specimens with higher shear demand appeared to have a larger number of horizontal cracks (Fig. 5(b)). This pattern was also observed in specimens with asymmetric longitudinal reinforcement. As shown in Fig. 5(c), more horizontal cracks developed on the W side, where more longitudinal reinforcement was provided.

During 1.0% target drift cycles, sliding along the interface between the beam fixed end and the concrete base block was observed in specimens with less longitudinal reinforcement, as in specimen L6_2.0. For comparison, sliding was not obvious in specimen L5_5.0D until the 4.0% target drift cycles. Peak forces were achieved in most of the specimens between 3.0 and 4.0% target drift cycles. The major inclined crack(s), defined as the one(s) with a relatively larger crack width among the observed cracks, became obvious during the 3.0 to 4.0% target drift cycles. Abrasion along inclined cracks was typically observed during the 3.0% target drift cycles and became obvious during the 4.0% target drift cycles, as shown in Fig. 5(d). This abrasive action deteriorated the concrete in the web region.

After reaching peak lateral strength, V_{peak} , corner concrete at the fixed end spalled off. The continuous loosening of concrete cover caused the longitudinal reinforcement to be exposed in some specimens. Loud "bang" sounds were

heard, each accompanied by a kinking response on the load-deflection curve, in most of the test specimens during the 6.0 to 8.0% target drift cycles. The "bang" sound appeared to be associated with the debonding of the transverse reinforcement.

At the final state, buckling of longitudinal reinforcement was observed in all test specimens. Buckling of longitudinal reinforcement was more severe in the longitudinal reinforcement on the W side, where crossties were provided to form the closed transverse reinforcement. Except for specimens M6_2.0, M4_2.0, H6_2.0, H5_2.0, M6_3.5X, M5_3.5X, and M4_3.5X, the 135-degree hook of either the crosstie (parallel to the shear direction) or the U-shaped stirrup was pushed out from the core. After the removal of loose concrete, the integrity of the core concrete (concrete within the closed transverse reinforcement) appeared to be better in specimens with a low aspect ratio and low shear demand. The final states of all test specimens are presented in Fig. 6.

Specimen hysteretic responses, expressed in terms of lateral load versus drift, are presented in Fig. 7. The drift presented in Fig. 7 has been adjusted from the target values to account for the lateral movements and rotations of the concrete base block. The key test results for all test specimens are summarized in Table 3.

DISCUSSION

Mechanisms

In this section, a quantitative way to determine the mechanisms that limit the force and initiate the force loss are presented. To achieve that, four deformation components, including: 1) flexural deformation; 2) shear deformation; 3) deformation due to fixed-end rotation; and 4) fixed-end

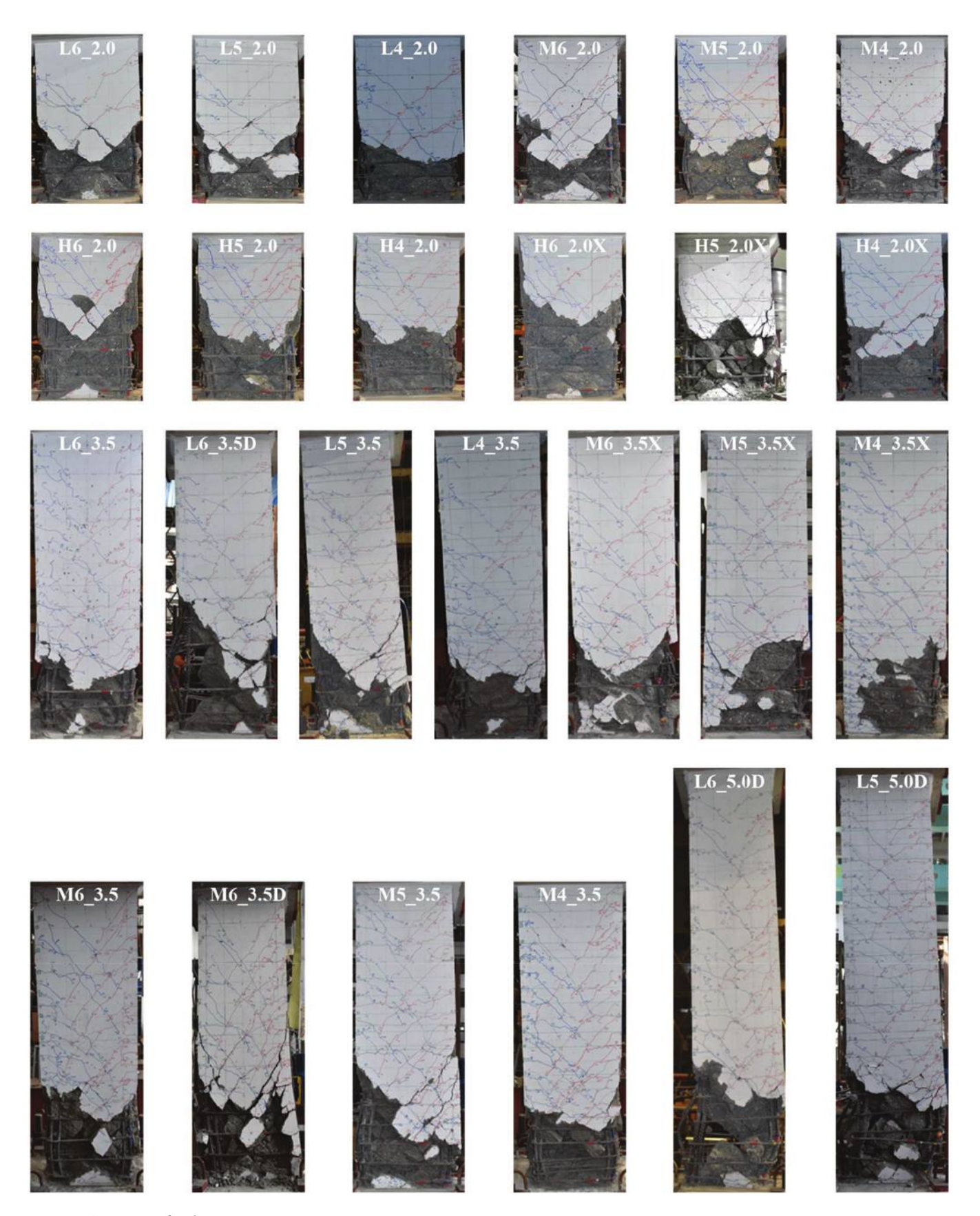


Fig. 6—Specimen final state.

sliding were determined first using data from the optical tracking system. Each deformation component represented a mechanism through which the force was transferred. Flexural deformation, evaluated using markers between Row 2 and

the topmost row of markers (center of load application), as shown in Fig. 4, represented the deformation due to the rotation of the beam. Flexural deformation was obtained based on the moment-area theorem, where curvature was assumed

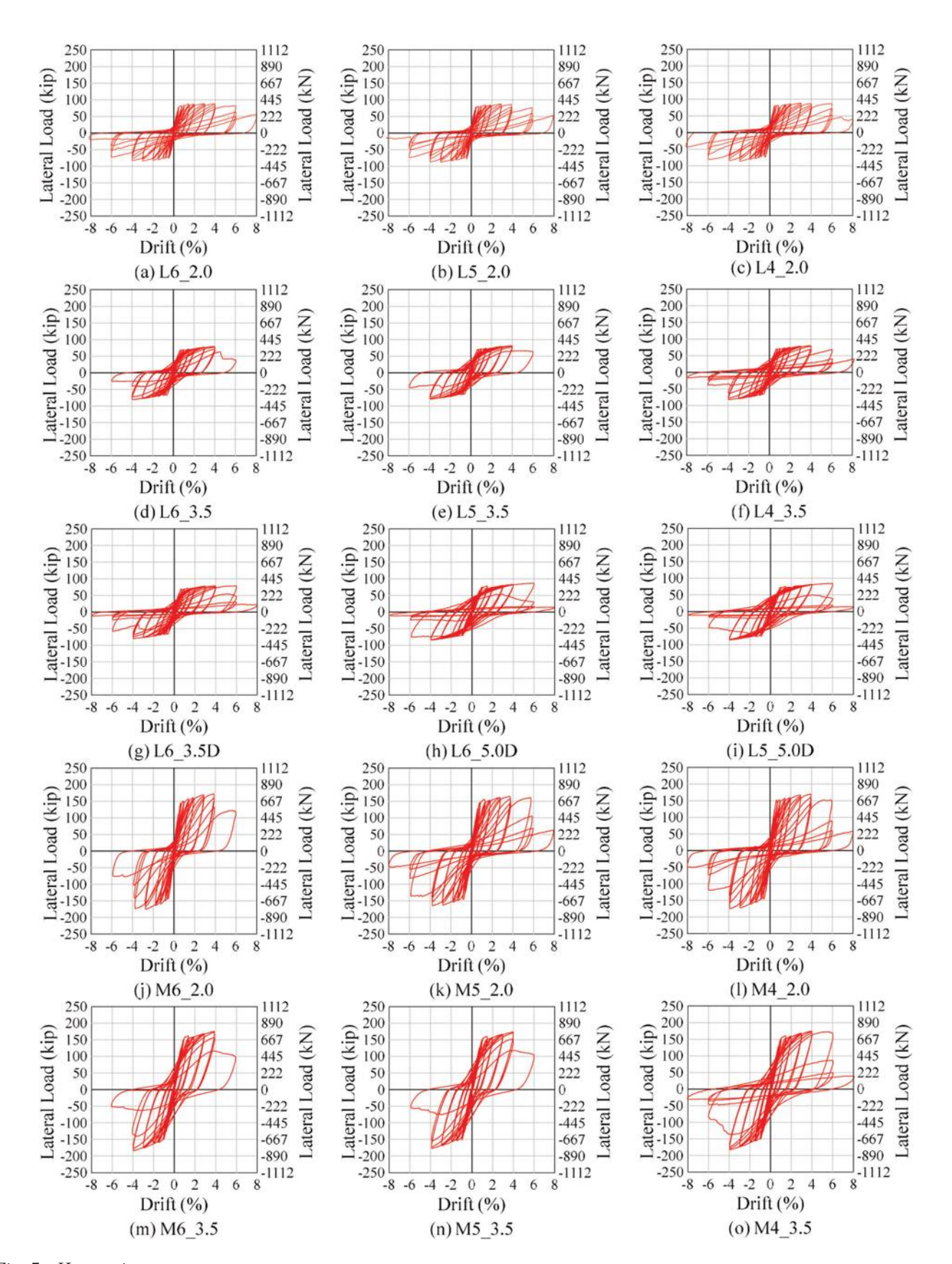


Fig. 7—Hysteretic response.

to be uniformly distributed between two consecutive rows of markers. This uniformly distributed curvature was the average of the curvature values of all marker elements in the same row, and the element curvature was determined using the data from the four markers at the corners of a marker element, as shown schematically in Fig. 4. Shear deformation referred to the rest of the deformation between Row 2 and the topmost row of markers. Deformation due

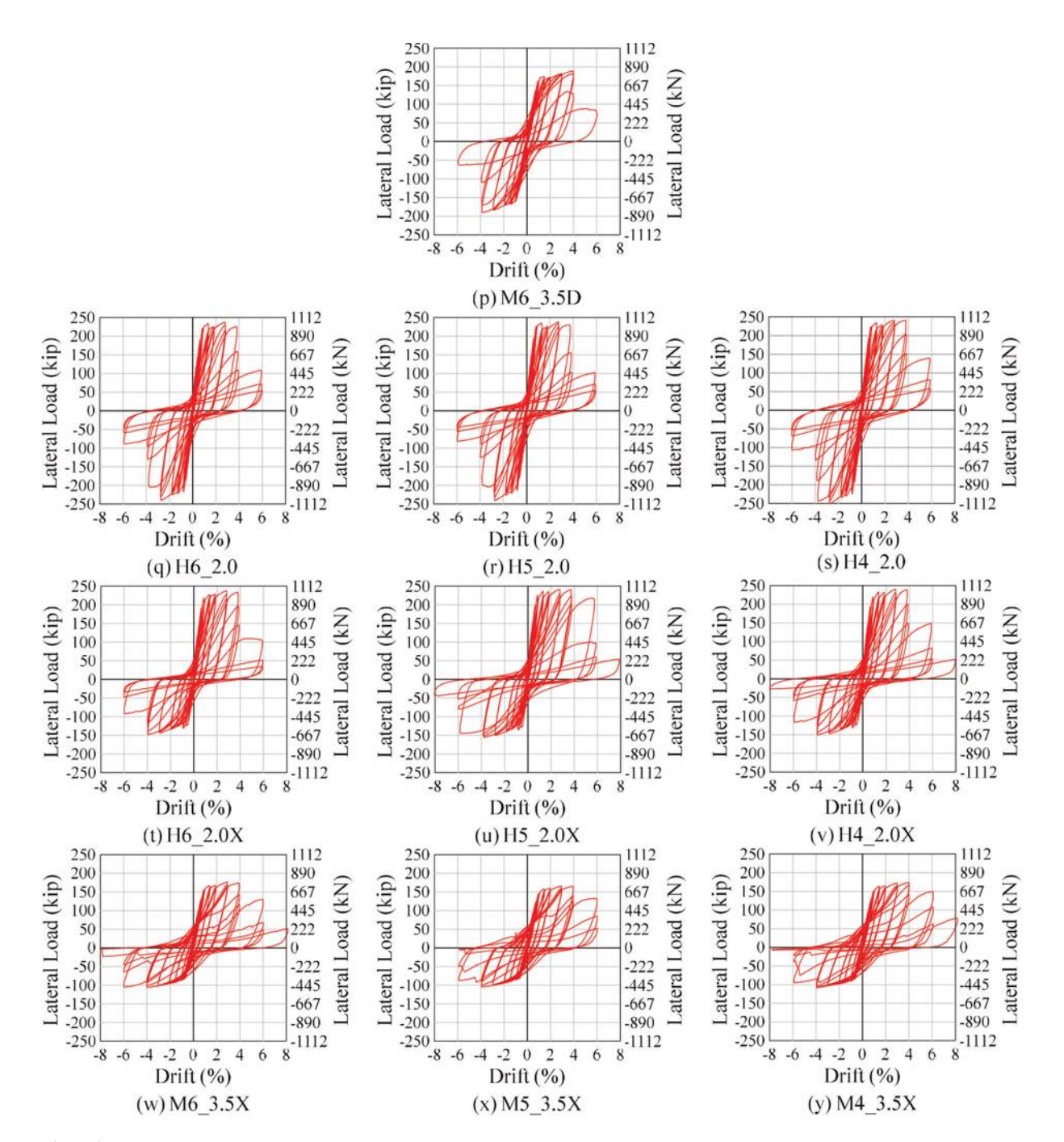


Fig. 7 (cont.)—Hysteretic response.

to fixed-end rotation and fixed-end sliding were determined using the rows of markers immediately above and below the interface between the wall and concrete base block, that is, Row 1 and Row 2 markers in Fig. 4. Due to damaged concrete cover, marker results were typically available only up to the drift level when the specimen achieved the peak lateral force.

Specimens were subjected to three loading cycles at each target drift level. Using the results of specimen L4_3.5 in the positive loading direction as a typical example, the force-displacement envelopes of the three loading cycles for each deformation component are shown in Fig. 8. Comparing first-cycle envelopes of the four deformation components in Fig. 8, the deformation due to fixed-end rotation exhibits an apparent change in stiffness from 0.5 to 1.0% target drift

(symbol "◇" → symbol "o"), while the other three deformation components exhibited a limited increase in displacement between these two drift levels. The apparent change of stiffness (slope) in the load-deformation hysteretic response of specimen L4_3.5 was primarily attributed to the inelastic response of the deformation due to fixed-end rotation. Given that, it should be acceptable to conclude that the mechanism that limited the force was associated with the deformation due to fixed-end rotation.

It can also be observed in Fig. 8 that as the force drops in the repeated cycles, corresponding displacements in the four deformation components either increase or decrease. A drop in force accompanied by a decrease in displacement indicates a "recovery" response where force is likely to be restored once the displacement increases again. However, a

Table 3—Summary of test results

Specimen	Loading direction	V _{peak} , kip (kN)	$\frac{V_{peak}}{b_w d \sqrt{f_{cm}(psi)}} (MPa)$	V_{Mn}^* , kip (kN)	V_{peak} / V_{Mn}	V_{s}/V_{peak}^{*}	d _{peak} , %	d_u , %	Force loss initiation†	Peak force limit mechanism [†]
1.6.20	East (+)	88.5 (393.7)	2.34 (0.19)	76.5 (340.5)	1.16	1.39	2.95	6.64	SH	FR
L6_2.0	West (-)	-83.9 (-373.4)	-2.22 (-0.18)	-76.5 (-340.5)	1.10	1.46	-2.96	-6.05	SH, FS	FR
15.20	East (+)	87.7 (390.2)	2.22 (0.18)	76.9 (341.9)	1.14	1.68	2.86	6.28	SH, FS, SR	FR
L5_2.0	West (-)	-87.5 (-389.1)	-2.22 (-0.18)	-76.9 (-341.9)	1.14	1.68	-2.93	-5.99	FR, SH, FS	FR
T. 4. 2. 0	East (+)	88.9 (395.4)	2.23 (0.19)	76.9 (342.2)	1.16	2.07	2.96	6.00	SH, FS, FR	FR
L4_2.0	West (-)	-86.2 (-383.5)	-2.17 (-0.18)	-76.9 (-342.2)	1.12	2.14	-2.89	-5.96	SH, FS	FR
1625	East (+)	79.2 (352.1)	2.47 (0.21)	68.5 (304.6)	1.16	1.49	4.01	4.72	SH, FS	FR
L6_3.5	West (-)	-80.7 (-359.2)	-2.52 (-0.21)	-68.5 (-304.6)	1.18	1.46	-3.95	-3.97	FR, SH, FS	FR
	East (+)	81.7 (363.6)	2.32 (0.19)	69.5 (309.0)	1.18	1.73	3.91	5.39	SH, FS	FR
L5_3.5	West (-)	-79.4 (-353.1)	-2.25 (-0.19)	-69.5 (-309.0)	1.14	1.78	-3.89	-4.69	SH, FR, FS	FR
	East (+)	80.5 (357.9)	2.31 (0.19)	69.4 (308.5)	1.16	2.19	3.98	6.21	SH, FS	FR
L4_3.5	West (-)	-82.0 (-364.6)	-2.35 (-0.19)	-69.4 (-308.5)	1.18	2.15	-3.93	-4.56	SH, FL	FR
7 (2 50	East (+)	78.9 (350.8)	2.20 (0.18)	70.9 (315.3)	1.11	1.55	5.93	6.00	SH, FS	FR
L6_3.5D	West (-)	-79.9 (-355.3)	-2.23 (-0.19)	-70.9 (-315.3)	1.13	1.53	-3.95	-5.05	SH, FR, FS	FR
7.6.500	East (+)	86.8 (386.3)	2.35 (0.19)	78.3 (348.4)	1.11	1.35	5.95	6.01	SH, FS, FR	FR
L6_5.0D	West (-)	-84.4 (-375.5)	-2.28 (-0.19)	-78.3 (-348.4)	1.08	1.39	-3.91	-5.85	SH, FR, FS	FR
7.5.500	East (+)	84.7 (376.7)	2.35 (0.20)	78.1 (347.2)	1.09	1.66	5.84	6.00	FR, SH, FS	FR
L5_5.0D	West (-)	-85.6 (-380.5)	-2.37 (-0.20)	-78.1 (-347.2)	1.10	1.64	-3.90	-4.71	SH, FR, FS	FR
	East (+)	172.1 (765.3)	4.64 (0.39)	148.8 (661.8)	1.16	1.43	3.83	3.86	SH, SL	FR
M6_2.0	West (-)	-174.9 (-778.0)	-4.71 (-0.39)	-148.8 (-661.8)	1.18	1.40	-2.72	-3.77	SH, SR	FR
145.20	East (+)	164.2 (730.2)	4.51 (0.37)	147.9 (658.0)	1.11	1.79	3.67	5.75	SH	FR
M5_2.0	West (-)	-164.3 (-730.8)	-4.51 (-0.37)	-147.9 (-658.0)	1.11	1.79	-3.73	-5.87	SH	FR
M4 20	East (+)	170.2 (757.1)	4.42 (0.37)	157.5 (700.4)	1.08	2.16	3.89	5.96	SH, FS	FR
M4_2.0	West (-)	-175.2 (-779.3)	-4.55 (-0.38)	-157.5 (-700.4)	1.11	2.10	-3.87	-3.90	SH, FS	FR
MC 2.5	East (+)	175.3 (779.6)	4.98 (0.41)	154.6 (687.5)	1.13	1.33	3.86	4.54	SH, FS	FR
M6_3.5	West (-)	-183.5 (-816.3)	-5.21 (-0.43)	-154.6 (-687.5)	1.19	1.27	-3.93	-3.96	SH, FR, FS	FR
M5 2.5	East (+)	173.6 (772.4)	5.08 (0.42)	154.1 (685.2)	1.13	1.61	3.95	4.73	SH, FR, FS	FR
M5_3.5	West (-)	-177.2 (-788.1)	-5.18 (-0.43)	-154.1 (-685.2)	1.15	1.58	-3.87	-4.36	SH, FR, FS	FR
M4 2.5	East (+)	174.5 (776.4)	5.38 (0.45)	153.2 (681.3)	1.14	2.00	3.96	6.02	SH, FR, FS	FR
M4_3.5	West (-)	-182.8 (-813.0)	-5.63 (-0.47)	-153.2 (-681.3)	1.19	1.91	-3.91	-4.61	SH, FR, FS	FR
M6 25D	East (+)	189.0 (840.9)	5.11 (0.42)	177.6 (790.1)	1.06	1.26	3.94	3.99	SH, FS	FR
M6_3.5D	West (-)	-190.2 (-846.2)	-5.14 (-0.43)	-177.6 (-790.1)	1.07	1.25	-3.85	-3.88	SH, FR, FS	FR
ц6 2 0	East (+)	237.2 (1055.3)	7.96 (0.66)	223.3 (993.4)	1.06	1.23	2.77	4.17	SH, FS	FR
H6_2.0	West (-)	-239.9 (-1067.0)	-8.05 (-0.67)	-223.3 (-993.4)	1.07	1.21	-2.71	-3.51	SH, FS	FR
115 2.0	East (+)	238.1 (1059.1)	7.34 (0.61)	225.5 (1003.0)	1.06	1.47	2.72	4.04	SH, FS, FR	FR
H5_2.0	West (-)	-240.6 (-1070.4)	-7.42 (-0.62)	-225.5 (-1003.0)	1.07	1.45	-2.72	-3.48	SH, FS	FR
H4 2.0	East (+)	241.1 (1072.3)	7.69 (0.64)	224.6 (998.9)	1.07	1.81	3.75	3.81	SH, FS, FR	FR
П4_2.0	West (-)	-250.6 (-1114.6)	-8.00 (-0.66)	-224.6 (-998.9)	1.12	1.74	-2.74	-3.79	SH, FS	FR
H6 20V	East (+)	237.6 (1056.8)	7.41 (0.61)	225.6 (1003.6)	1.05	1.23	2.78	3.82	SH, FS	FR
H6_2.0X	West (-)	-147.7 (-657.1)	-4.37 (-0.36)	-128.1 (-569.6)	1.15	2.08	-3.91	-3.96	SH, FS	FR
H5 2.0X	East (+)	241.5 (1074.1)	7.61 (0.63)	225.3 (1002.3)	1.07	1.45	2.74	5.74	SH, FS	FR
113_2.UA	West (-)	-155.6 (-692.4)	-4.66 (-0.39)	-127.8 (-568.6)	1.22	2.37	-3.76	-5.84	SH, FS	FR

Table 3 (cont.)—Summary of test results

114 2 OV	East (+)	240.3 (1068.8)	7.49 (0.62)	225.6 (1003.6)	1.06	1.82	2.79	3.82	SH, FS, FR	FR
H4_2.0X	West (-)	-150.7 (-670.3)	-4.46 (-0.37)	-128.1 (-569.6)	1.18	3.05	-3.89	-5.43	SH, FS	FR
M6 25V	East (+)	176.8 (786.3)	4.97 (0.41)	155.2 (690.2)	1.14	1.32	2.91	4.99	SH, FS	FR
M6_3.5X	West (-)	-105.4 (-468.7)	-2.81 (-0.23)	-87.9 (-390.8)	1.20	2.33	-3.91	-5.99	FR, SH, FS	FR
M5 25V	East (+)	165.7 (737.0)	4.54 (0.38)	155.6 (692.1)	1.06	1.69	2.91	5.42	SH, FS	FR
M5_3.5X	West (-)	-104.7 (-465.8)	-2.72 (-0.23)	-88.2 (-392.3)	1.19	2.81	-3.82	-5.53	SH	FR
M4 3.5X	East (+)	173.9 (773.6)	4.81 (0.40)	155.4 (691.5)	1.12	2.01	3.97	6.10	SH, FS	FR
1V14_3.3A	West (-)	-108.1 (-480.7)	-2.83 (-0.24)	-88.1 (-391.8)	1.23	3.41	-3.93	-5.91	SH, FS	FR

^{*}Using tested material properties.

 $^{^{\}dagger}FL$ is flexure; SH is shear; FR is fixed-end rotation; FS is fixed-end sliding.

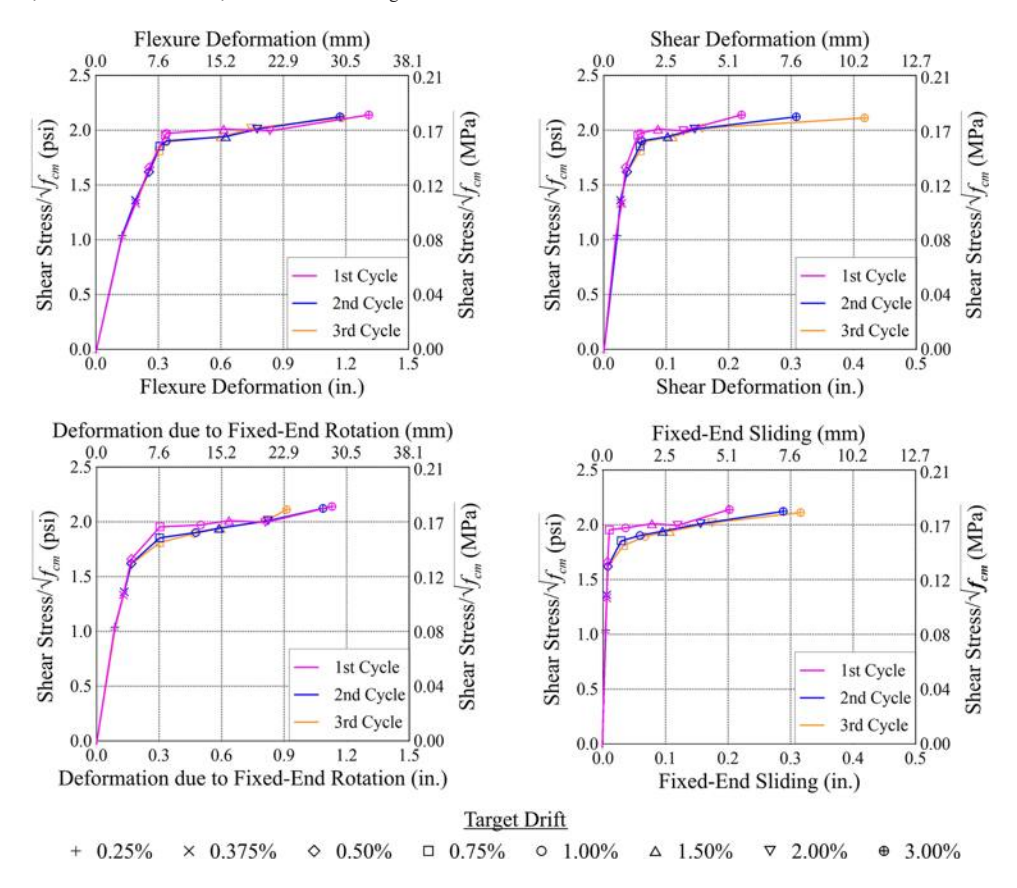


Fig. 8—Loss of force mechanism for L4_3.5.

drop in force accompanied by an increase in displacement indicates a "softening" response, which contributes to the loss of the force in the repeated cycles. As shown in Fig. 8, the softening response was first observed in fixed-end sliding at 0.75% target drift (symbol "□") and became more apparent thereafter. The softening response was also first observed in shear deformation at 1.5% target drift (symbol " \triangle ") and became more apparent afterward. Flexural deformation and deformation due to fixed-end rotation did not show apparent softening responses up to 3.0% target drift. As a result, it should be acceptable to conclude that the mechanisms associated with shear deformation and fixed-end sliding were responsible for the loss of force in pecimen L4 3.5. Using the described approaches, mechanisms that limit the peak force and initiate the force loss for all test specimens are summarized in Table 3. Available data indicated that shear was responsible for the initiation of force loss in all test specimens.

Component deformation percentage

The influences of the transverse reinforcement spacing/amount on the drift contribution of the four deformation components were investigated first. As shown in Fig. 9(a), for example, drift contribution of each deformation component is determined at the peak of the first cycle of every drift for a specimen trio (M6_3.5, M5_3.5, and M4_3.5) with the same longitudinal reinforcement layout but different spacing/amount of transverse reinforcement. Results from Fig. 9(a) suggest that the influence of transverse reinforcement spacing/amount on drift contribution of each deformation component appears to be limited and inconsistent, even in shear deformation. The overall trend at different

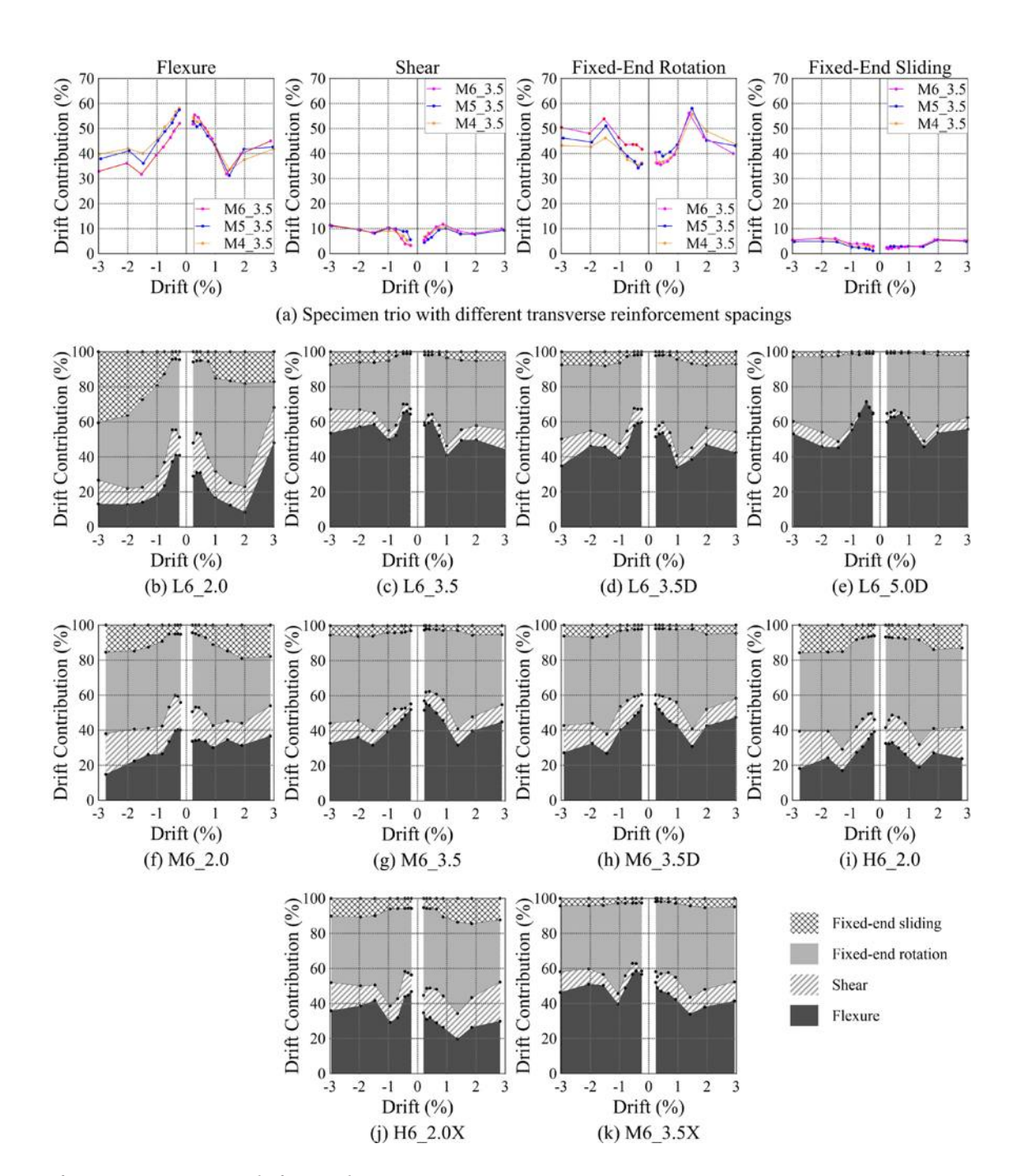


Fig. 9—Deformation component drift contribution.

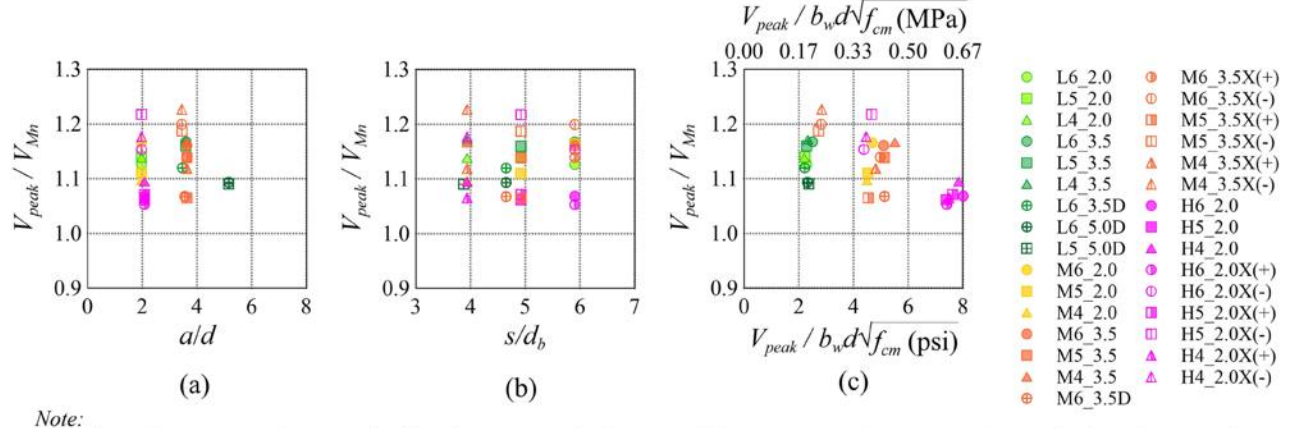
drift levels appears to be similar in all three specimens. Due to length limitation, only the results from specimens with transverse reinforcement spaced at 6 in. (150 mm) are shown in Fig. 9(b) to (k) to explore the effects of other design parameters.

For specimens with an aspect ratio of 2.0, based on test results among specimens L6_2.0, M6_2.0, and H6_2.0, it appeared that specimens with larger shear stress demands resulted in a smaller percentage of fixed-end sliding after approximately 0.75% target drift, which was more apparent between specimens L6_2.0 and M6_2.0. This trend, however, was not obvious for specimens with an aspect ratio of 3.5. The increased fixed-end sliding from approximately 0.5 to 1.0% drift was believed to be associated with the yielding of the longitudinal reinforcement, and this increment was more

obvious in specimens with low longitudinal reinforcement ratios.

Comparing test results among specimen trio L6_2.0, L6_3.5, and L6_5.0D and specimen pair M6_2.0 and M6_3.5, it may be concluded that specimen aspect ratio had the most significant impact on the drift contribution percentages at all drift levels. As the aspect ratio increases, with a similar shear stress demand, the drift contributions from fixed-end sliding and shear deformation decrease and drift contribution from flexural deformation increases, while drift contribution from the deformation due to fixed-end rotation is similar.

For specimens with an asymmetric longitudinal reinforcement layout, the overall trend of specimens H6_2.0X and M6_3.5X in the positive loading direction, where the tension



Results in the positive and negative loading directions are both presented for specimens with asymmetric longitudinal reinforcement layout.

Average results are presented for specimens with symmetric longitudinal reinforcement layout.

Fig. 10—Design parameters on V_{peak}/V_{Mn}.

side had more longitudinal reinforcement, was similar to that of specimens H6_2.0 and M6_3.5, respectively. In the negative loading direction, however, the drift contributions from fixed-end sliding were slightly lower at a drift ratio greater than 0.75% in specimens H6_2.0X and M6_3.5X when compared to those in specimens M6_2.0 and L6_3.5, respectively.

Strength

From Table 3, it appears that specimen peak lateral force, V_{peak} , was limited by the mechanism associated with the deformation due to fixed-end rotation. As a result, an attempt was made to estimate the peak strength using V_{Mn} . The V_{Mn} , representing the shear corresponding to the development of nominal flexural strength at the base of the specimen, was determined as M_n/a , where M_n was the nominal flexural strength per ACI 318-19 using tested material properties, and a was the shear span. As reported in Table 3, the V_{peak}/V_{Mn} exceeded 1.0 for all test specimens, which ranged between 1.05 and 1.18 in the positive loading direction, and 1.07 and 1.23 in the negative loading direction. As a result, using V_{Mn} to predict specimen peak strength, V_{peak} , was a good approximation.

The influences of a/d, s/d_b , and $V_{peak}/b_w d\sqrt{f_{cm}}$ on V_{peak}/V_{Mn} were investigated through the plots presented in Fig. 10. All presented values were calculated based on tested material properties. From Fig. 10, it appears that V_{peak}/V_{Mn} was highly influenced by the normalized peak shear stress, $V_{peak}/b_w d\sqrt{f_{cm}}$. The trend in Fig. 10 suggests that V_{peak}/V_{Mn} increases approximately linearly as $V_{peak}/b_w d\sqrt{f_{cm}}$ decreases. Another possible design parameter that influenced the V_{peak}/V_{Mn} , although only based on the two pairs of specimens in this study, appeared to be the bar size. As can be seen in Table 3 and Fig. 10, specimens L6_3.5D and M6_3.5D using No. 10 longitudinal bars showed relatively lower V_{peak}/V_{Mn} compared to specimens L6_3.5 and M6_3.5 using No. 8 longitudinal bars and with other design parameters almost identical.

The aforementioned observations may be explained as follows: under proper conditions, tensile reinforcement can

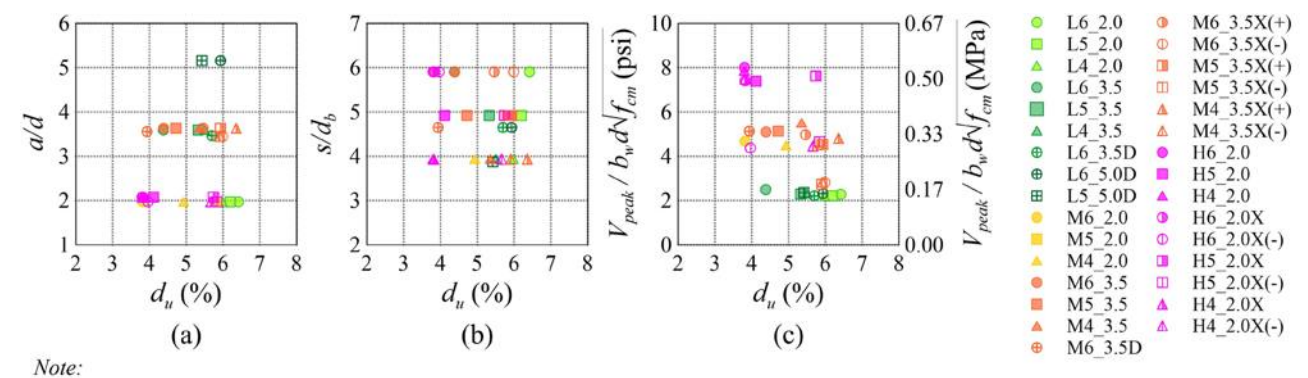
be stressed into the strain-hardening range, which is believed to be the primary contributor to the flexural overstrength. The degree of strain hardening in the longitudinal reinforcement in tension positively correlates with the degree of V_{peak}/V_{Mn} . When subjected to large inelastic deformation, as in the cases of all specimens tested in this study, factors that may affect the degree of strain hardening in the tensile longitudinal reinforcement include at least the: 1) bond properties; and 2) stability of compression force.

Bond demand increased as the shear stress or bar size increased. Increasing concrete strength could improve bond properties. Concrete strength in the concrete base block and the beam segment did not vary significantly among the test specimens. Providing more and closer transverse reinforcement, on the other hand, was expected to improve not only the bond properties but also the stability of compression force. However, test results showed that the change in the amount/spacing of transverse reinforcement for specimens having the same longitudinal reinforcement layout had a negligible influence on V_{peak}/V_{Mn} . On the other hand, the confinement term for the development length of straight reinforcement, $(c_b + K_{tr})/d_b$, as per ACI 318-19, ranged from 1.34 to 3.23 in the tested specimens. It suggested that bond properties within the beam segment appeared to be similar when this confinement term was greater than 1.34.

The V_{peak}/V_{Mn} for specimens with an asymmetric longitudinal reinforcement layout was consistently higher in the negative loading direction when the less-reinforced side was subjected to tension, as can be seen in Table 3 and Fig. 10. Furthermore, the V_{peak}/V_{Mn} of those specimens, on average, were even higher than the rest of the specimens in the negative loading direction. This trend was likely attributed to the lower shear stress demand and more stable compression force when the less-reinforced side was subjected to tension.

Deformation

The ultimate drift, d_u , reported in Table 3, was determined based on the following two scenarios, whichever was met first: 1) when force dropped by 20% between the first and third loading cycles within the same target drift level, and the peak force in the first loading cycle of the next target



Results in the positive and negative loading directions are both presented for specimens with asymmetric longitudinal reinforcement layout. Average results are presented for specimens with symmetric longitudinal reinforcement layout.

Fig. 11—Design parameters on d_u.

drift level was lower than the peak force in the third loading cycle of the drift of concern; or 2) when force dropped by 20% from the peak force on the envelope of hysteretic response. Using the minimum corresponding drifts of these two scenarios would avoid overestimation of d_u when the specimen failed to sustain the load in the repeated cycles at the same target drift level. Test results in Table 3 indicate that a minimum drift capacity of 3.5% can be achieved for all specimens designed with a wide range of parameters and in compliance with ACI 318-19.

The influences of a/d, s/d_b , and $V_{peak}/b_w d\sqrt{f_{cm}}$ on d_u were investigated through the plots presented in Fig. 11. The scatter of results suggested that it was not possible to predict specimen d_u with good accuracy using the parameters investigated. Despite that, specimen peak shear stress, $V_{peak}/b_w d\sqrt{f_{cm}}$, appeared to have relatively more influence on specimen d_u . Results from Fig. 11(c), on average, indicate that specimen d_u tends to decrease from 6 to 4% as the peak shear stress increases from 2 to $8\sqrt{f_{cm}(\text{psi})}$ (0.17 to 0.67 $\sqrt{f_{cm}(\text{MPa})}$). This trend supports the previous discussion that the mechanism that initiated the loss of force in all specimens was associated with shear. The trend that d_u increased as the specimen shear stress demand decreased has been reported before from tests of RC squat walls (Cheng et al. 2021).

Reducing a/d has been reported to result in smaller drift capacity of RC members in some existing research. Test results from this study, however, showed that the influence of a/d on specimen d_u was not apparent when specimens had similar normalized peak shear stress, $V_{peak}/b_w d\sqrt{f_{cm}}$ (refer to Fig. 11(a)). A typical experimental program in previous studies used specimens with the same longitudinal reinforcement layout but with different a/d, wherein specimen peak shear stress increased as the a/d decreased, thus leading to the decrease in specimen d_u .

There was no consistent trend to identify the effects of the amount/spacing of transverse reinforcement on d_u . Among all specimens tested in this study, only specimen trio M6_3.5, M5_3.5, and M4_3.5 showed that d_u consistently increased as the s/d_b of transverse reinforcement reduced in both loading directions. Based on the experimental observation, the d_u not being improved by the reduced spacing or increased amount of transverse reinforcement in several

specimens was likely due to two reasons. First, the major inclined cracks in specimens with larger amount of, and more closely spaced, transverse reinforcement developed at a shallower angle with respect to the transverse direction, as can be observed in specimen trio L6_2.0, L5_2.0, and L4_2.0, presented in Fig. 12. Thus, transverse reinforcement became less effective in this case. Second, specimens typically lost the concrete cover severely after 4.0% target drift, and the anchorage of transverse reinforcement deteriorated, which made the transverse reinforcement less effective at a similar drift level.

For specimens with asymmetric longitudinal reinforcement, test results showed that d_u was typically smaller in the positive loading direction where the less-reinforced side was subjected to compression. As can be seen in Fig. 11(b), the obtained d_u in the positive and negative loading directions from specimens with asymmetric longitudinal reinforcement layouts was within the range of other symmetrically reinforced specimens with a similar shear stress demand.

ENERGY DISSIPATION

In this study, the normalized energy dissipation capacity in each loading cycle was determine based on Fig. 13(a), where A_{loop} was the area enclosed by the hysteresis loop, and A_T^+ and A_T^- were the elastic strain energies in the positive and negative loading directions, respectively. The average of the normalized energy dissipation capacities in the three loading cycles at each drift level is presented in Fig. 13(b) to (i), where the horizontal axis is the average drift level in the positive and negative loading directions.

The average normalized energy dissipation capacity generally increased as the normalized peak shear stress decreased, the aspect ratio increased, and the spacing of transverse reinforcement was reduced (amount increased). The amount and spacing of transverse reinforcement appeared to have more influence on energy dissipation capacities in specimens with an aspect ratio of approximately 2.0. The influence of the aspect ratio on the energy dissipation capacity was not obvious before 3.0% drift. In specimens with the same aspect ratio, the average normalized energy dissipation capacity consistently increased as the normalized peak shear stress decreased. The results in specimens with an asymmetric longitudinal reinforcement layout appeared to be

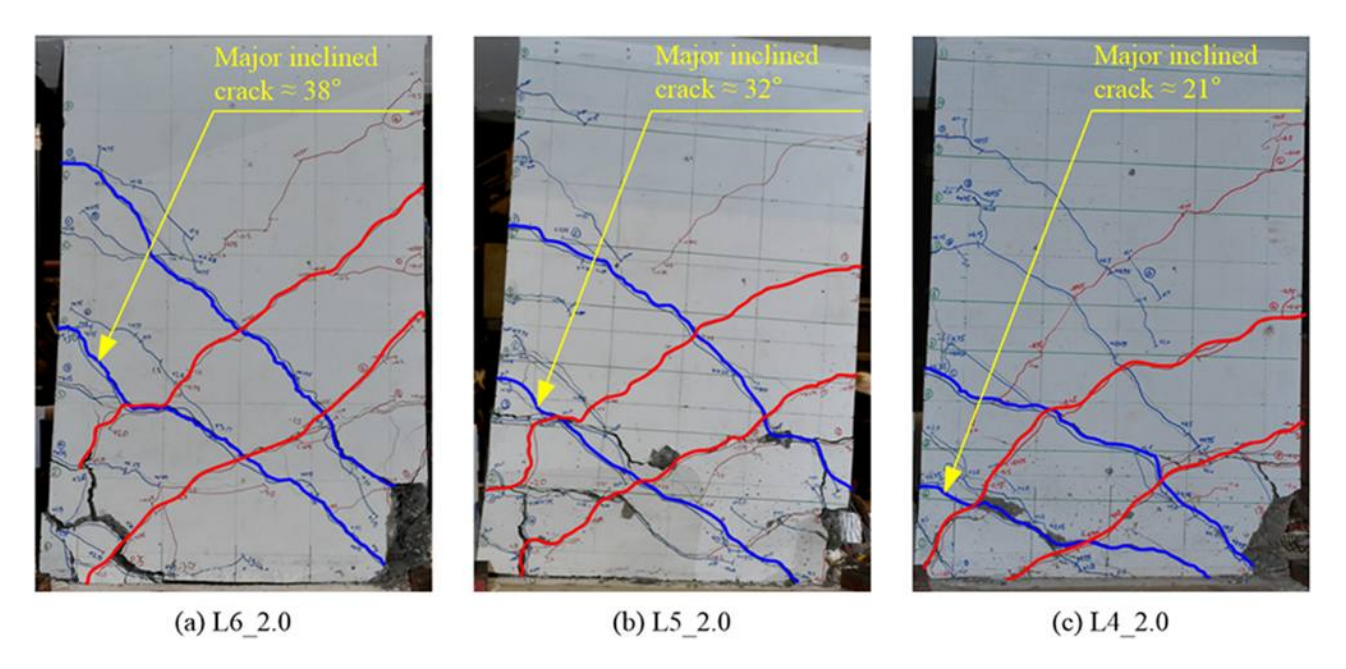


Fig. 12—Inclined crack angle at 4.0% target drift.

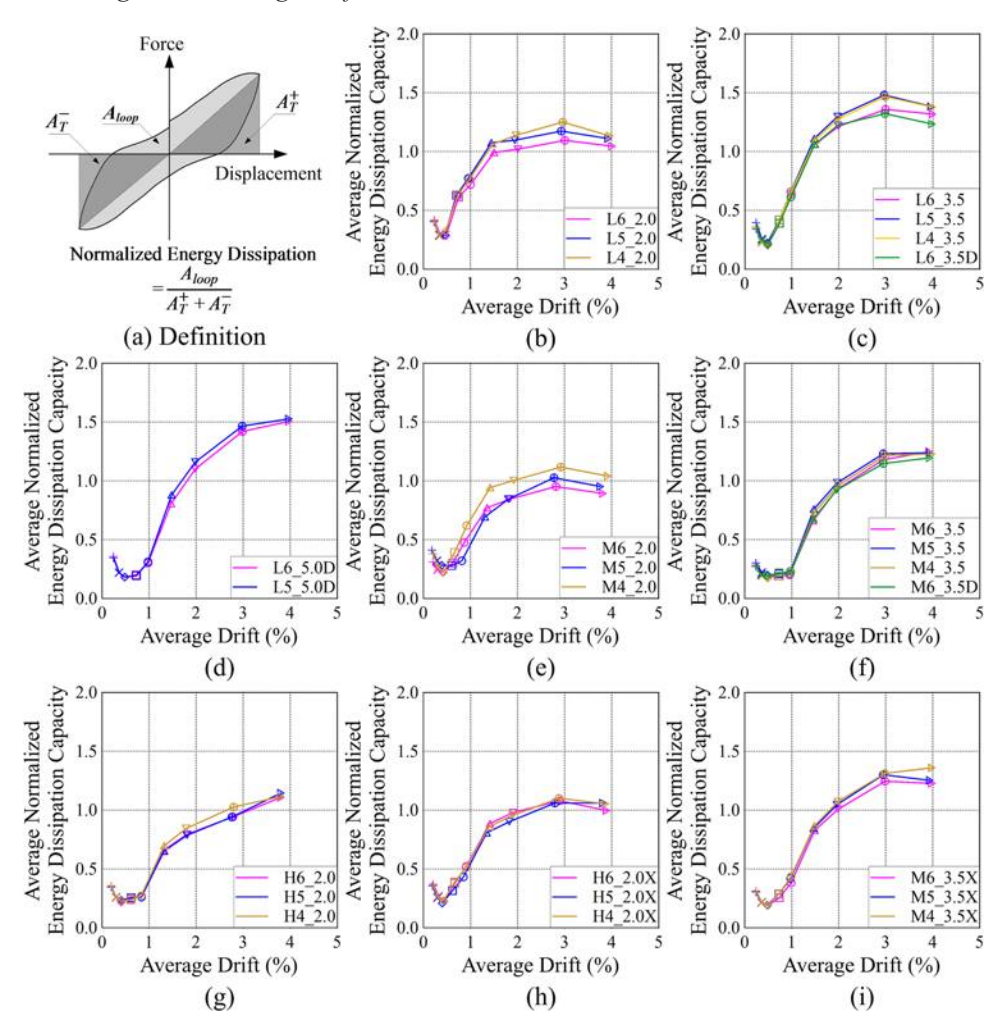
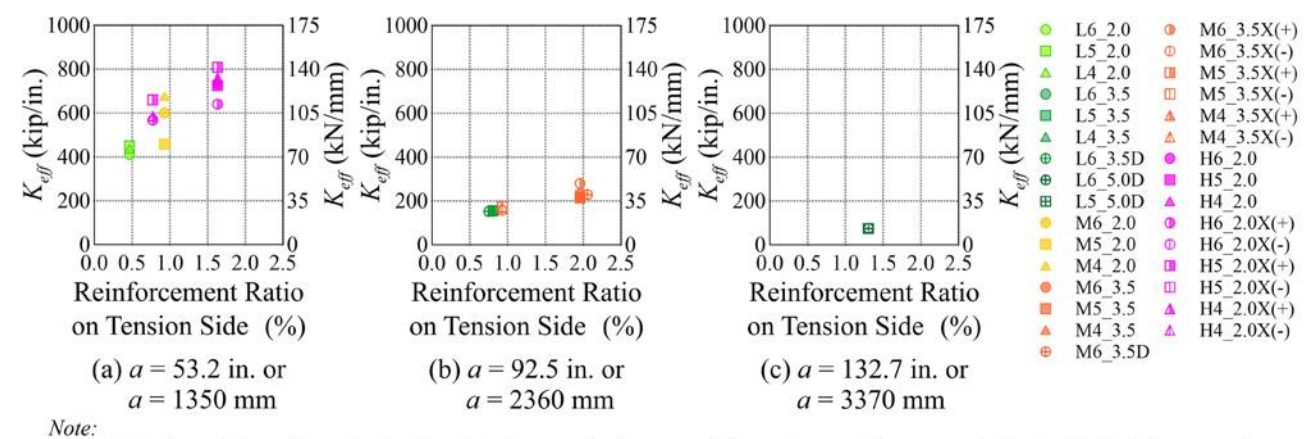


Fig. 13—Normalized energy dissipation capacity.

close to the specimens with a symmetric longitudinal reinforcement layout, and the amount of longitudinal reinforcement on each side was identical to the more-reinforced side. The normalized energy dissipation capacities of specimens

using larger diameters of longitudinal reinforcement were consistently lower than their counterpart specimens with smaller diameters of longitudinal reinforcement.



Results in the positive and negative loading directions are both presented for specimens with asymmetric longitudinal reinforcement layout.

Average results are presented for specimens with symmetric longitudinal reinforcement layout.

Fig. 14—Effective lateral stiffness.

EFFECTIVE LATERAL STIFFNESS

Specimen effective lateral stiffness, K_{eff} , was determined based on the idealized bilinear load-deformation response as per ASCE/SEI 41-17 (ASCE 2017). The effective lateral stiffness of all specimens versus the reinforcement ratio on the tension side, determined as the area of longitudinal reinforcement on the tension side divided by the width of the beam, b_w , and effective depth, d, is presented in Fig. 14. Results suggest that K_{eff} increased as the shear span decreased or the reinforcement ratio on the tension side increased. The influence of transverse reinforcement spacing/amount on K_{eff} was not apparent.

CONCLUSIONS

Twenty-five reinforced concrete (RC) beam specimens subjected to lateral displacement reversals were tested. The key test parameters were specimen aspect ratio, shear stress demand, transverse reinforcement spacing, diameter of longitudinal reinforcement, and tension-to-compression reinforcement ratio. Based on limited test results, the following conclusions are drawn:

- 1. Analytical results indicated that the mechanism limiting the force in the test specimens was associated with the rotational deformation at the beam fixed end, while the mechanism that initiated the loss of force was generally associated with shear deformation and/or fixed-end sliding.
- 2. The amount/spacing of transverse reinforcement considered in this study appeared to have a negligible effect on the strength and deformation capacity of the beam specimens.
- 3. Peak shear strength, V_{peak} , of all test specimens can be reasonably predicted by V_{Mn} , the shear associated with the development of nominal flexural strength at the beam fixed end.
- 4. The V_{peak}/V_{Mn} appeared to increase linearly as the normalized peak shear stress, $V_{peak}/b_w d\sqrt{f_{cm}}$, decreased.
- 5. A minimum drift capacity of 3.5% was achieved for all specimens designed with a wide range of parameters and in compliance with ACI 318-19. Among the test parameters investigated, specimen drift capacity, d_u , appeared to be more sensitive to the normalized peak shear stress, $V_{peak}/b_w d\sqrt{f_{cm}}$.

- 6. The average normalized energy dissipation capacity generally increased as the specimen normalized peak shear stress decreased, the aspect ratio increased, and the spacing of transverse reinforcement was reduced.
- 7. Specimen effective lateral stiffness increased as the shear span decreased or the reinforcement ratio on the tension side increased.

AUTHOR BIOS

Jessica Gitomarsono is a Structural Engineer at Suharno and Partners, Semarang, Indonesia. She received her BS in civil and environmental engineering from Bandung Institute of Technology, Bandung, Indonesia, and her MS and PhD in civil and construction engineering from the National Taiwan University of Science and Technology, Taipei, Taiwan.

ACI member Min-Yuan Cheng is a Professor in the Department of Civil and Construction Engineering at the National Taiwan University of Science and Technology. He is a member of ACI Subcommittee 318-J, Joints and Connections (Structural Concrete Building Code), and Joint ACI-ASCE Committee 352, Joints and Connections in Monolithic Concrete Structures.

ACI member Marnie B. Giduquio is a Project Assistant Professor in the Department of Civil and Construction Engineering at the National Taiwan University of Science and Technology. He received his BS in civil engineering from the University of San Carlos, Cebu City, Philippines, and his MS and PhD in civil and construction engineering from the National Taiwan University of Science and Technology.

NOTATION

$A_{loop} =$	area enclosed by each hysteresis loop; refer to Fig. 13
--------------	---

 A_T^+ = elastic strain energy in positive loading direction; refer to Fig. 13

 $A_T^-=$ elastic strain energy in negative loading direction; refer to Fig. 13

 A_{ν} = total leg area per set of transverse reinforcement

a = beam shear span, defined as distance between center of loading application and beam fixed end

 b_w = beam width

c_b = lesser of: a) distance from center of bar to nearest concrete surface; and b) one-half center-to-center spacing of bars being developed

d = beam effective depth

 I_b = diameter of longitudinal reinforcement

 d_{peak} = corresponding drift at specimen peak shear strength, V_{peak}

 d_u = specimen ultimate drift

 f_c' = specified concrete compressive strength

 f_{cm} = average measured concrete compressive strength

 f_{um} = average measured peak stress of longitudinal reinforcement

 f_{utm} = average measured peak stress of transverse reinforcement

 f_y = nominal yield stress of longitudinal reinforcement

 \hat{f}_{ym} = average measured yield stress of longitudinal reinforcement \hat{f}_{yt} = nominal yield stress of transverse reinforcement

 f_{ytm} = average measured yield stress of transverse reinforcement

average height of marker element; refer to Fig. 4 height of left side of marker element; refer to Fig. 4

 h_r height of right side of marker element; refer to Fig. 4

specimen effective lateral stiffness transverse reinforcement index

 M_n nominal flexural strength probable flexural strength

spacing of transverse reinforcement

shear associated with development of M_n at beam fixed end,

shear associated with development of M_{pr} at beam fixed end, $V_{Mpr} = M_{pr}/a$

specimen peak shear strength

specimen shear capacity contributed by transverse reinforcement only

curvature of marker element; refer to Fig. 4

rotation of bottom row of markers in marker element; refer to θ_b Fig. 4

rotation of top row of markers in marker element; refer to Fig. 4

REFERENCES

ACI Committee 318, 2019, "Building Code Requirements for Structural Concrete (ACI 318-19) and Commentary (ACI 318R-19) (Reapproved 2022)," American Concrete Institute, Farmington Hills, MI, 624 pp.

ASCE/SEI 7-22, 2022, "Minimum Design Loads and Associated Criteria for Buildings and Other Structures," American Society of Civil Engineers, Reston, VA, 975 pp.

ASCE/SEI 41-17, 2017, "Seismic Evaluation and Retrofit of Existing Buildings," American Society of Civil Engineers, Reston, VA, 576 pp.

ASTM A370-20, 2020, "Standard Test Methods and Definitions for Mechanical Testing of Steel Products," ASTM International, West Conshohocken, PA, 50 pp.

Brown, R. H., and Jirsa, J. O., 1971, "Reinforced Concrete Beams under Load Reversals," ACI Journal Proceedings, V. 68, No. 5, May, pp. 380-390.

Cheng, M.-Y.; Wibowo, L. S. B.; Giduquio, M. B.; and Lequesne, R. D., 2021, "Strength and Deformation of Reinforced Concrete Squat Walls with High-Strength Materials," ACI Structural Journal, V. 118, No. 1, Jan., pp. 125-137.

Jirsa, J. O., 1973, "Factors Influencing the Hinging Behavior of Reinforced Concrete Members under Cyclic Overloads," Paper No. 147, Session 3D, Proceedings of the Fifth World Conference on Earthquake Engineering (5WCEE), V. 1, Rome, Italy, pp. 1198-1204.

Panagiotou, M.; Visnjic, T.; Antonellis, G.; Galanis, P.; and Moehle, J. P., 2013, "Effect of Hoop Reinforcement Spacing on the Cyclic Response of Large Reinforced Concrete Special Moment Frame Beams," PEER Report 2013/16, Pacific Earthquake Engineering Research Center, University of California, Berkeley, Berkeley, CA, 117 pp.

Popov, E. P.; Bertero, V. V.; and Krawinkler, H., 1972, "Cyclic Behavior of Three R.C. Flexural Members with High Shear," Report No. EERC 72-5, Earthquake Engineering Research Center, University of California, Berkeley, Berkeley, CA, 91 pp.

Scribner, C. F., and Wight, J. K., 1978, "Delaying Shear Strength Decay in Reinforced Concrete Flexural Members under Large Load Reversals,' Report No. UMEE 78R2, University of Michigan, Ann Arbor, MI, 246 pp.

Wibowo, L. S. B.; Cheng, M.-Y.; Huang, F.-C.; and Tai, T.-Y., 2017, "Effectiveness of High-Strength Hoops in High-Strength Flexural Members," ACI Structural Journal, V. 114, No. 4, July-Aug., pp. 887-897. doi: 10.14359/51689620

Title No. 121-S16

Three-Dimensional-Printed Engineered, Strain-Hardening Geopolymer Composite as Permanent Formwork for Construction of Reinforced Concrete Beam

by Shin Hau Bong, Behzad Nematollahi, Viktor Mechtcherine, Victor C. Li, and Kamal H. Khayat

Extrusion-based concrete printing technology allows the fabrication of permanent formwork with intricate shapes, into which fresh concrete is cast to build structural members with complex geometries. This significantly enhances the geometric freedom of concrete structures without the use of expensive temporary formwork. In addition, with proper material choice for the permanent formwork, the load-bearing capacity and durability of the resulting structure can be improved. This paper investigates the concrete printing of permanent formwork for reinforced concrete (RC) beam construction. A three-dimensional (3-D)-printable engineered geopolymer composite or strain-hardening geopolymer composite (3DP-EGC or 3DP-SHGC), recently developed by the authors, was used to fabricate the permanent formwork. The 3DP-EGC exhibits strainhardening behavior under direct tension. Two different printing patterns were used for the soffit of the permanent formwork to investigate the effect of this parameter on the flexural performance of RC beams. A conventionally mold-cast RC beam was also prepared as the control beam for comparison purposes. The results showed that the RC beams constructed using the 3DP-EGC permanent formwork exhibited superior flexural performance to the control beam. Such beams yielded significantly higher cracking load (up to 43%), deflection at ultimate load (up to 60%), ductility index (50%), and absorbed energy (up to 107%) than those of the control beam. The ultimate load was comparable with or slightly higher than that of the control beam. Furthermore, the printing pattern at the soffit of the permanent formwork was found to significantly influence the flexural performance of the RC beams.

Keywords: engineered geopolymer composite (EGC); permanent formwork; reinforced concrete beam; strain hardening; three-dimensional (3-D) concrete printing.

INTRODUCTION

The use of temporary formwork for concrete construction has a significant impact on construction speed, cost, and wastage. The cost of temporary formwork, which is commonly made of timber or metal, is estimated to be approximately 35 to 60% of the overall cost of concrete construction. The cost of a temporary formwork system generally includes, but is not limited to, the material cost; the labor cost for fabricating, assembling, and stripping the formwork; the equipment cost for handling the formwork; and the cost of the releasing agent applied on the formwork system. Temporary timber formwork is a major source of wastage in construction as it would be eventually discarded after several times of use. Moreover, the geometric freedom of concrete structures is considerably limited by the formwork shape, unless a high cost is paid for the manufacture of

bespoke formwork with complex geometry. Using concrete printing technology to manufacture permanent formwork can be a potential solution to tackle the aforementioned issues. Unlike conventional temporary formwork, threedimensional (3-D)-printed concrete (3DPC) permanent formwork serves to mold the fresh concrete to the required shape and dimensions. The 3DPC permanent formwork also becomes part of the concrete member, contributing to the final structural capacity of the member throughout the service life of the concrete structure.⁴ In addition, 3DPC permanent formwork with complex geometry can be easily manufactured, which significantly enhances the geometric freedom of the concrete structure. With the proper material choice for the fabrication of the 3DPC permanent formwork, the durability of the resulting structure can also be enhanced when the formwork serves as a protective coating. It is important to point out that no additional cost is associated with increasing the complexity of 3DPC permanent formwork.⁵ A comprehensive review of the potential economic impact of concrete printing technology on the current construction industry can be found in De Schutter et al.⁶

Over the past few years, several studies have been conducted on the construction of reinforced concrete (RC) column or beam specimens using engineered cementitious composites (ECC), strain-hardening cement-based composites (SHCC), or other types of high-performance fiberreinforced cementitious composites (HPFRCC) as precast permanent formwork.7-13 For instance, Pan et al.7 investigated the seismic behavior of the RC columns produced using precast steel-reinforced ECC permanent formwork. The results showed that such RC columns exhibited higher energy dissipation capacity, shear capacity, and ductility than those of the conventionally mold-cast RC column under seismic loading conditions. Tian et al.⁸ investigated the axial behavior of the RC column constructed using grid-reinforced ultra-high-performance concrete (UHPC) as the precast permanent formwork. Carbon fiber-reinforced polymer (CFRP) grid and stainless-steel grid were used as the reinforcement. The results showed that such RC columns exhibited higher axial load-carrying capacity and stiffness

ACI Structural Journal, V. 121, No. 2, March 2024.

MS No. S-2022-159.R2, doi: 10.14359/51739159, received December 15, 2022, and reviewed under Institute publication policies. Copyright © 2024, American Concrete Institute. All rights reserved, including the making of copies unless permission is obtained from the copyright proprietors. Pertinent discussion including author's closure, if any, will be published ten months from this journal's date if the discussion is received within four months of the paper's print publication.

than those of the conventionally mold-cast RC column. However, the ductility and crack resistance of the RC columns decreased due to the brittle nature of UHPC. The authors reported that the use of CFRP grids could improve the ductility and toughness of the RC columns as compared to the stainless-steel grid.

The effects of surface treatment of permanent formwork on the mechanical performance of structural elements have also been studied. Leung and Cao10 investigated the flexural performance of concrete beams constructed using ECC as the precast permanent formwork with different surface treatments. The results showed that the beams constructed using the ECC permanent formwork with transverse grooves along the surface exhibited significantly higher flexural capacity than that of the beam with a smooth surface. Zhang et al. 11 studied the shear behavior of the RC beams without shear reinforcement constructed using precast ECC permanent formwork. Three different surface conditions—namely smooth interface, anchored interface, and rugged interface were prepared to investigate the interface bond strength between the ECC permanent formwork and concrete core. The RC beam constructed using ECC permanent formwork significantly improved the shear and deformation capacities compared to those of the conventionally mold-cast RC beams without shear reinforcement. The ECC permanent formwork with a rugged interface exhibited the highest interface bond strength compared to that with a smooth or anchored interface. The interface bond strength between the ECC permanent formwork and concrete core was found to have a limited correlation to the shear capacity of the RC beams.

Recently, some studies have been conducted to build RC structures using 3DPC permanent formwork. 14-16 Vantyghem et al.14 manufactured and tested a 4 m long topologyoptimized post-tensioned concrete girder constructed using 3-D-printed hollow girder segments. The girder segments were produced using a 3-D-printable ordinary portland cement (OPC)-based mortar. The printed girder segments and post-tensioning cables were assembled, and a shrinkagecompensating high-strength OPC mortar was then used to fill the hollow interior of the post-tensioning cables. Finally, a post-tensioning force of 50 kN was applied. The topologyoptimized beam made of 3-D-printed girder segments saved nearly 20% volume of concrete when compared to the conventional beam constructed with a T-section girder with the same dimensions and total deflection. Anton et al. 15 manufactured nine 2.7 m high columns with complex geometry and surface texture. The hollow permanent formwork was 3-D-printed using an OPC mortar. Subsequently, a conventional steel reinforcement cage was placed in the printed permanent formwork, followed by the casting of fresh concrete. In another study, Zhu et al. 16 investigated the structural performance of the RC columns under compression. The 3DPC permanent formwork for the columns was made using a 3-D-printable OPC mortar. The printable mortar contained 6 mm long polyethylene fibers and calcium carbonate whisker to reduce shrinkage and enhance the micromechanical performance of the printing material. Subsequently, the conventional steel reinforcement cages with three different longitudinal steel reinforcement ratios (0.0, 1.9, and 2.5%) were placed inside the 3DPC permanent formwork, and fresh concrete was cast into it. Conventional mold-cast RC columns with the same reinforcement ratios were also manufactured for comparison. The results showed that the load-bearing capacity and stiffness of the RC column made with the 3DPC permanent formwork were higher than those of the control RC columns. This was due to the higher strength of the printable mortar used for manufacturing the 3DPC permanent formwork as compared to the cast-in-place concrete (40 MPa as compared to 30 MPa), as well as the higher confinement effect from the 3DPC permanent formwork. Furthermore, good bonding was observed at the interface of the concrete core and the 3DPC permanent formwork.

It should be noted that the aforementioned 3DPC permanent formwork systems were manufactured using 3-D-printed OPC mortars, which have very limited or no contribution to the final load-bearing capacity and crack control of the concrete structure. In addition, OPC was used as the main binder in the mixture compositions, which compromises the sustainability credentials of concrete printing due to the high carbon emissions and embodied energy associated with OPC production.^{17,18} Therefore, the study at hand aims to investigate the performance of RC beams constructed using permanent formwork made of a 3-D-printable engineered geopolymer composite (3DP-EGC) or strain-hardening geopolymer composite (3DP-SHGC). The authors recently developed a 3DP-EGC. Similar to 3-D-printable ECC (3DP-ECC), the 3DP-EGC shows strain-hardening behavior under uniaxial tension. 19 However, the environmental footprint of the 3DP-EGC is significantly lower than that of the 3DP-ECC, as the 3DP-EGC is made of geopolymer. Geopolymer uses industrial waste materials such as fly ash and slag and does not contain any OPC, thereby reducing carbon emissions by as much as 80%.²⁰ In addition, EGC exhibits superior sulfuric acid resistance to ECC.²¹ Two permanent formwork systems with different printing patterns were manufactured using the 3DP-EGC. The flexural performance of the RC beams constructed with the permanent formwork was evaluated by conducting four-point bending tests. The results were also compared with those of the conventionally moldcast RC beam.

RESEARCH SIGNIFICANCE

Using temporary formwork for concrete construction often leads to high material, labor, and machinery costs, as well as noticeable time delays, negative environmental footprints, and limited geometrical freedom. To tackle this, concrete printing technology can be used to produce 3DPC permanent formwork with complex shapes, into which fresh concrete can be cast to build concrete structures with complex geometries. In addition, when a suitable type of concrete is used to produce 3DPC permanent formwork, the durability and load-bearing capacity of the resulting concrete structure can be enhanced. This study investigates the use of a recently developed 3DP-EGC, exhibiting strain-hardening behavior in direct tension, to produce 3DPC permanent formwork for the construction of RC beams.

PROPERTIES OF 3DP-EGC AND CONCRETE FOR CASTING RC BEAMS

The 3DP-EGC mixture developed in the authors' previous study¹⁹ was used to print the permanent formwork in this investigation. The details of the 3DP-EGC mixture, including the mixture proportions, printing performances, and rheological and mechanical properties, were presented and discussed in the authors' previous study.¹⁹ The key mechanical properties of the 3DP-EGC and its counterpart mold-cast EGC at 28 days are given in Table 1. The typical tensile stress-strain curves of the 3DP-EGC are shown in Fig. 1. It should be noted that the repeatability of the key performance characteristics and robustness of the 3DP-EGC have been investigated in the authors' previous study.¹⁹ The current paper only deals with the application of the developed 3DP-EGC for the production of 3DPC permanent formwork for RC beam construction.

Table 1—Mechanical properties of 3DP-EGC and its counterpart mold-cast EGC at 28 days (adopted from authors' previous study¹⁹)

Mechanical properties	Mold-cast EGC	3DP-EGC		
Average compressive strength	62.1 MPa	58.2, 53.6, and 47.4 MPa*		
Average density	1921 kg/m ³	1874 kg/m ³		
Average modulus of rupture	6.9 MPa	8.0 MPa [†]		
Average uniaxial tensile strength	3.4 MPa	3.8 MPa [‡]		
Average tensile strain capacity	2.1%	1.8%‡		

^{*}Measured in longitudinal, lateral, and perpendicular directions, respectively.

^{*}Measured in longitudinal direction.

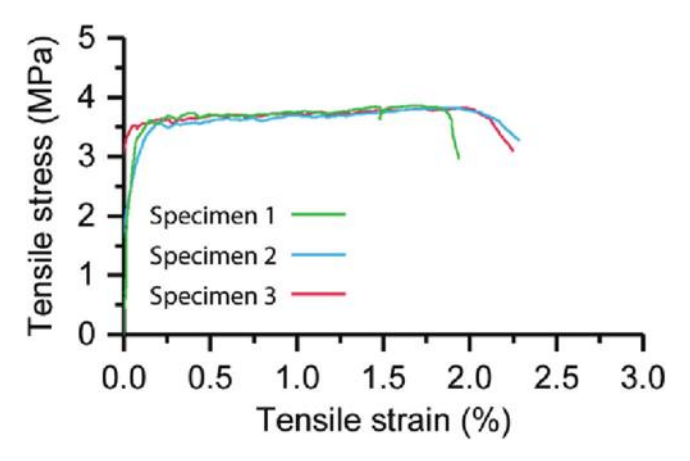


Fig. 1—Typical tensile stress-strain curves of 3DP-EGC; reproduced from authors' previous study. 19

The concrete used in this study for casting the RC beam specimens was a conventional OPC concrete with a target characteristic compressive strength exceeding 40 MPa at 28 days and had a maximum nominal aggregate size of 14 mm. The slump test performed before casting the RC beam specimens yielded a value of approximately 130 mm. To determine the compressive strength of the concrete, 12 concrete cylinders (100 mm diameter x 200 mm height) were produced during casting of the RC beam specimens. The compression test on the concrete cylinders was conducted on the same day as the bending tests. The density of the concrete cylinders was determined by weighing the air-dried specimens before the compression test. The average compressive strength (f_{cm}) and density (ρ) of the concrete were measured to be 44.6 \pm 2.2 MPa and 2395 \pm 16 kg/m³, respectively. According to AS 1379-2007,²² the characteristic compressive strength of the concrete (f_c) at 28 days was calculated to be 41.5 MPa.

EXPERIMENTAL PROCEDURES Details of beam specimens

As shown in Fig. 2, all beam specimens had a 200 x 300 mm ($W \times D$) rectangular cross section and a length of 1800 mm. The tensile reinforcements were 2N20 (that is, two 20 mm ribbed steel bars with yield stress f_{sy} of 500 MPa). The compressive reinforcements were 2N10 (that is, two 10 mm ribbed steel bars with f_{sy} of 500 MPa). To avoid shear failure prior to flexural failure, stirrups made of 12 mm ribbed steel bars (with f_{sy} of 500 MPa) were placed 100 mm center-to-center with a cover of 25 mm.

The flexural load-bearing capacity and shear capacity of the conventionally mold-cast RC beam with the aforementioned reinforcement were determined in accordance with AS 3600:2018,²³ as shown in Appendix A.* Using the calculated ultimate shear capacity (V_u) value (refer to Appendix A) as the applied shear force, the applied bending moment was calculated to be 259.0 kN·m, which was much higher than the ultimate moment capacity (M_u) of the RC beam (71.9 kN·m). Therefore, the RC beam would fail in flexural mode rather than in shear mode. In addition, the cracking moment (M_{cr}) of the mold-cast RC beam was calculated to be 12.9 kN·m.

3-D printing process and testing of specimens

A gantry-type concrete printing machine was used in this study. A detailed description of the printer can be found in

^{*}The Appendix is available at www.concrete.org/publications in PDF format, appended to the online version of the published paper. It is also available in hard copy from ACI headquarters for a fee equal to the cost of reproduction plus handling at the time of the request.

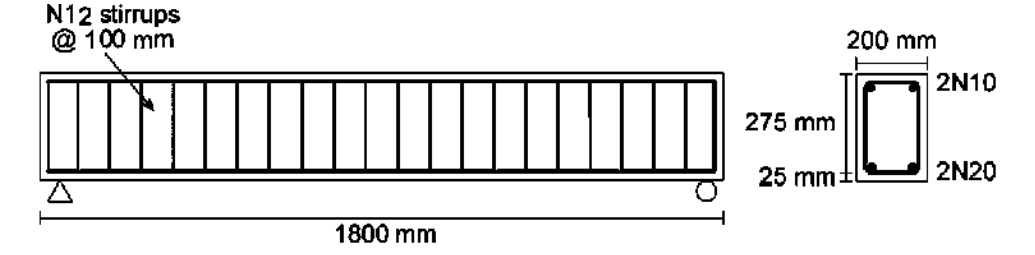


Fig. 2—Dimensions and reinforcement detailing of RC beam specimens.

[†]Measured in perpendicular direction.

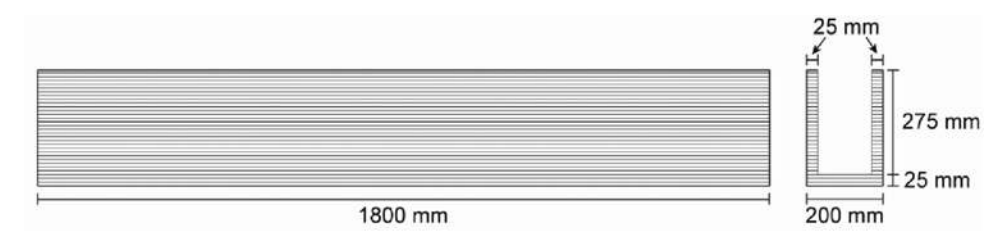


Fig. 3—Dimensions of 3DP-EGC permanent formwork.

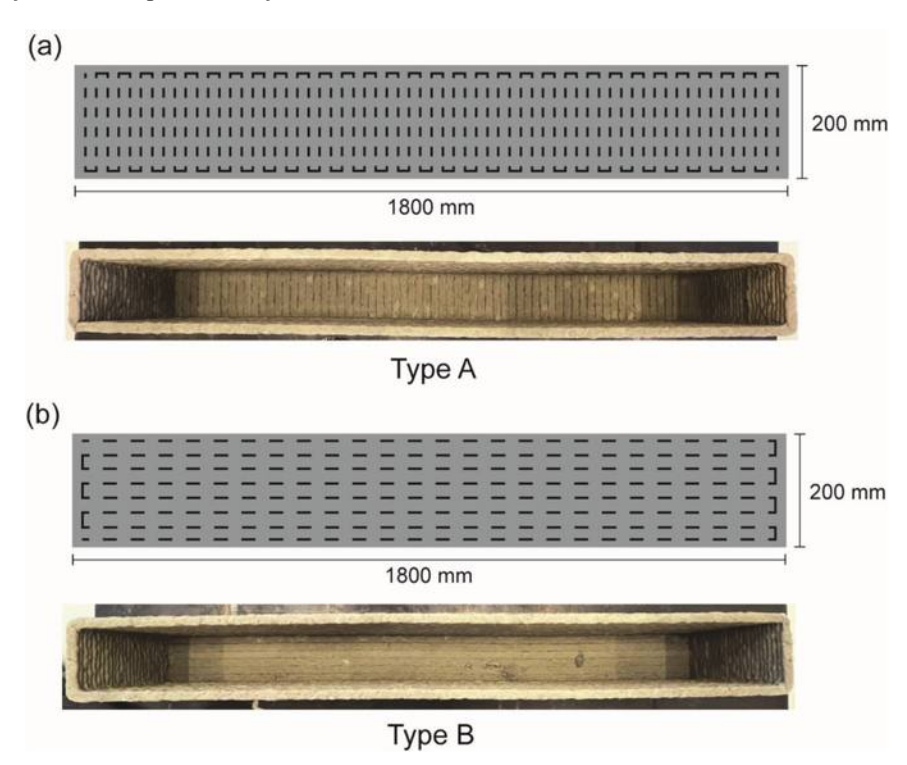


Fig. 4—Printing patterns at soffit of 3DP-EGC permanent formwork. Dotted line represents moving path of printhead.

Bong et al.²⁴ A 20 mm circular nozzle was used for printing the permanent formwork. The dimensions of the formwork are schematically illustrated in Fig. 3. Two different printing patterns (Fig. 4) for the soffit (that is, tension region) of the permanent formwork were designed and used to investigate the effect of this parameter on the flexural performance of the RC beam. The RC beam made using the 3DP-EGC permanent formwork with a Type A printing pattern was denoted as the Type A beam. Similarly, the beam made using the 3DP-EGC permanent formwork with a Type B printing pattern was denoted as the Type B beam. The printing speed and extrusion rate were 25 mm/s and ~0.75 L/min, respectively. After printing, the 3DP-EGC permanent formwork systems were covered with a plastic sheet and left in the laboratory environment at room temperature (23 ± 3°C).

After 21 days of ambient temperature curing, the reinforcement cages were placed inside the printed formwork, and the OPC concrete was cast (Fig. 5). The conventionally mold-cast RC beam (that is, the control cast-in-place beam) with the same dimensions was also prepared using temporary formwork for comparison purposes. Subsequently, all RC beam specimens were covered with a plastic sheet and left in the laboratory environment at room temperature until testing. All specimens were tested after 28 days of age.

The flexural performance of the RC beam specimens was evaluated by conducting four-point bending tests; Fig. 6 shows the test setup schematically. All specimens were tested with the midspan measuring 400 mm under displacement control at the rate of 0.5 mm/min. A linear variable differential transformer (LVDT) was used to determine the midspan deflection, and two more LVDTs were used to monitor the vertical displacement at the supports. The resulting force versus midspan deflection curves are presented in the "Results and Discussion" section.

Flexural capacity of RC beam made with 3DP-EGC permanent formwork

Similar to the calculation of M_{cr} of the conventionally mold-cast RC beam presented in Appendix A, the M_{cr} of the RC beam specimens produced using the 3DP-EGC permanent formwork was calculated by transforming the 3DP-EGC permanent formwork sections to an equivalent area of concrete, as schematically illustrated in Fig. 7. It should be noted that the anisotropic behavior due to the 3D-printing process was ignored in the calculations. In other words, only for the purpose of this calculation, the 3DP-EGC permanent formwork was assumed to be a mold-cast EGC permanent formwork. In addition, it was assumed that the

steel reinforcement in the compressive region has a negligible effect on the M_{cr} . Table 2 presents the material characteristics of the concrete, the EGC, and steel reinforcement used for the calculation of the M_{cr} of the cross section. The calculation procedure to determine the M_{cr} of the RC beam specimens made using the 3DP-EGC permanent formwork is summarized in Appendix B. Based on the calculations presented in Appendix B, the M_{cr} of the RC beam specimens made using the 3DP-EGC permanent formwork was calculated to be 16.9 kN·m.

The M_u of the RC beam specimens made using the 3DP-EGC permanent formwork can be calculated using the equilibrium equations. The corresponding stress and strain diagrams for the cross section are presented in Fig. 8. It is assumed that the steel is in yield condition, while the steel reinforcement in the compressive region has a negligible effect on the M_u . The anisotropic behavior due to the 3D-printing process was also ignored. Table 3 presents the material characteristics of the EGC used for the calculation





Fig. 5—(a) Reinforcement cages placed inside 3DP-EGC permanent formwork and temporary formwork; and (b) OPC concrete cast inside 3DP-EGC permanent formwork and temporary formwork.

of the M_u of the cross section. The calculation procedure to determine the M_u of RC beam specimens made using the 3DP-EGC permanent formwork is presented in Appendix B. Based on the calculations presented in Appendix B, the M_u of the RC beam specimens constructed using the 3DP-EGC permanent formwork was calculated to be 78.8 kN·m.

RESULTS AND DISCUSSION

Figure 9 presents the force versus midspan deflection curves of all RC beam specimens. As shown in Fig. 9(b), after reaching the yielding force, both Type A and Type B beams exhibited deflection-hardening behavior, while the control beam showed typical deflection-softening behavior. Table 4 summarizes the cracking force (P_{cr}) , yielding force (P_v) , ultimate force (P_{ult}) , and the corresponding deflection values of all RC beam specimens. In both Type A and Type B beams, the P_{cr} values and their corresponding deflection values (δ_{cr}) were higher than those of the control beam. The P_{cr} and δ_{cr} of the Type A beam were 11% and 20% higher than those of the control beam, respectively. The corresponding values for the Type B beam were 43% and 40%, respectively. When comparing the results obtained for Type A and Type B beams, the P_{cr} and δ_{cr} of the Type B beam were 29% and 17% higher than those of the Type A beam, respectively. This is because, in the Type B beam, the tensile stresses are parallel to the printing direction, where the tensile ductility of EGC contributes to a greater extent to the cracking resistance of the beam. However, in the Type A beam, the tensile stresses are perpendicular to the printing direction of the filaments at the soffit of the formwork. Therefore, the resistance of the Type A beam to cracking is mainly governed by the bond strength

Table 2—Material characteristics used to calculate M_{cr}

Concrete modulus of elasticity *E_c , MPa	31,887
EGC modulus of elasticity † E_E , MPa	17,835
Mean value of flexural tensile strength [‡] MOR, MPa	6.9
Characteristic flexural tensile strength $f_{ct,f'}$, MPa	6.2
Steel modulus of elasticity E_s , MPa	200,000

^{*}Derived in accordance with Clause 3.1.2 of AS 3600.23

 $^{^{\$}}$ Adopted from authors' previous study¹⁹ for ambient temperature-cured mold-cast EGC. $^{\$}$ fcr_t $' = MOR - 1.645 \times$ (standard deviation), in accordance with Section 3.2.2 of JSCE.²⁵

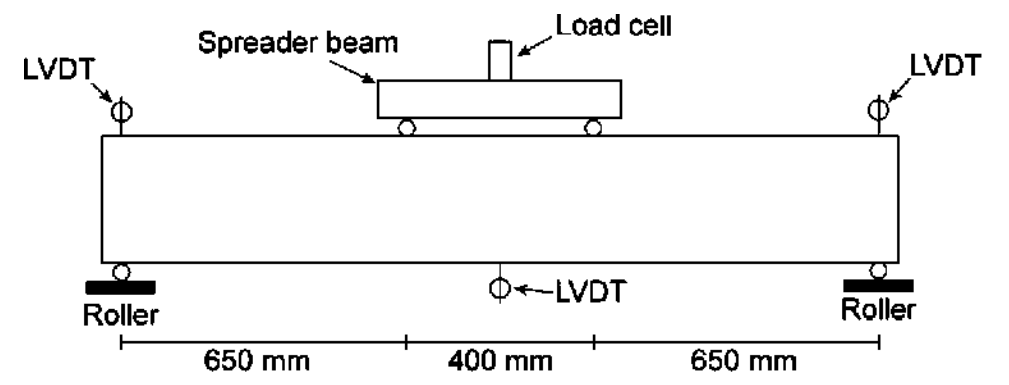


Fig. 6—Four-point bending test setup.

[†]Derived in accordance with Section 3.4 of JSCE.²⁵

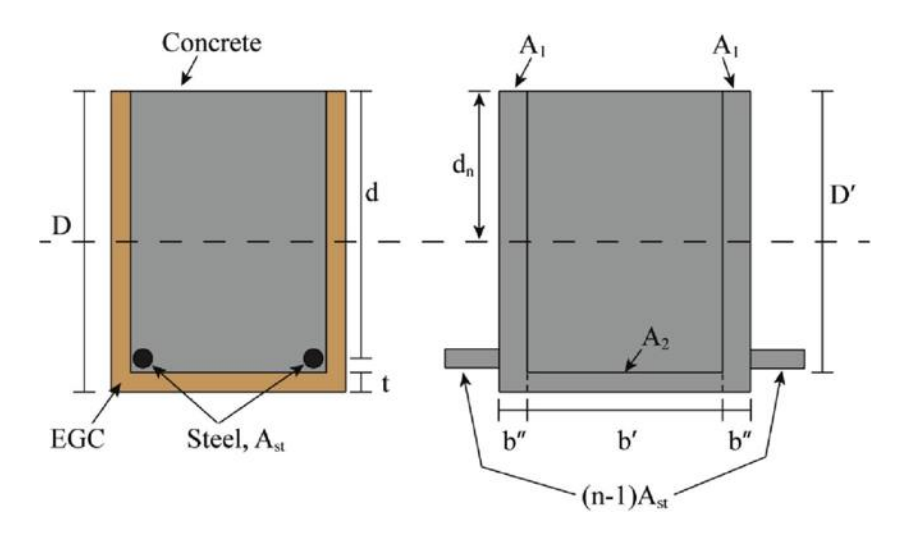


Fig. 7—Transformed sections of steel and 3DP-EGC permanent formwork to equivalent concrete area.

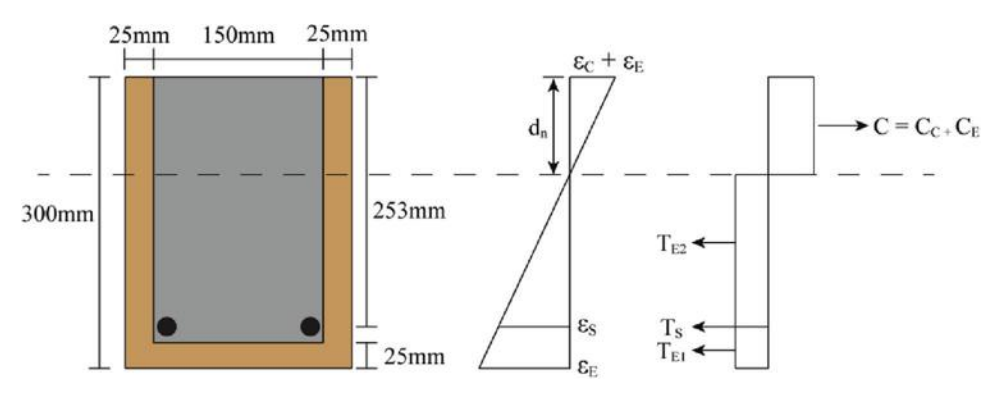


Fig. 8—Stress and strain diagrams of cross section of RC beams made using 3DP-EGC permanent formwork.

Table 3—Material characteristics of EGC used to derive M_u

-	
Mean value of compressive strength* f_{CE} , MPa	62.1
Characteristic compressive strength $^{\dagger}f_{CEk}'$, MPa	55.4
Mean value of ultimate tensile strength* σ_{ult} , MPa	3.4
Characteristic ultimate tensile strength $^{\ddagger}f_{ultk}$, MPa	3.2
Material factor γ_c^{\S}	1.3

*Adopted from authors' previous study¹⁹ for ambient temperature-cured mold-cast EGC. $^{\dagger}f_{CEk}' = f_{CE}' - 1.645 \times (\text{standard deviation})$, in accordance with Section 3.1 of JSCE. 25 $^{\dagger}f_{ultk} = \sigma_{ult} - 1.645 \times (\text{standard deviation})$, in accordance with Section 3.2.4 of JSCE. 25 According to Section 3.2.1 of JSCE. 25

of the adjacent printed filaments, which is generally weaker compared to the strength of the printed filaments.

The P_y and its corresponding deflection (δ_y) of the RC beam specimens were well comparable as identical steel reinforcement was used in all RC beams. As shown in Table 4, the P_{ult} of the Type A beam was comparable with that of the control beam. However, the deflection at the ultimate load (δ_{ult}) was 59% higher than that of the control beam. The P_{ult} and δ_{ult} of the Type B beam were 5% and 60%, respectively, higher than those of the control beam. The significantly higher δ_{ult} of Type A and Type B beams is attributed to the strain hardening of the 3DP-EGC layers at the soffit of the permanent formwork. It should be noted that the P_{ult} of the Type B beam was slightly higher (5%) than that of the Type A beam. This

Table 4—Flexural test results of RC beam specimens

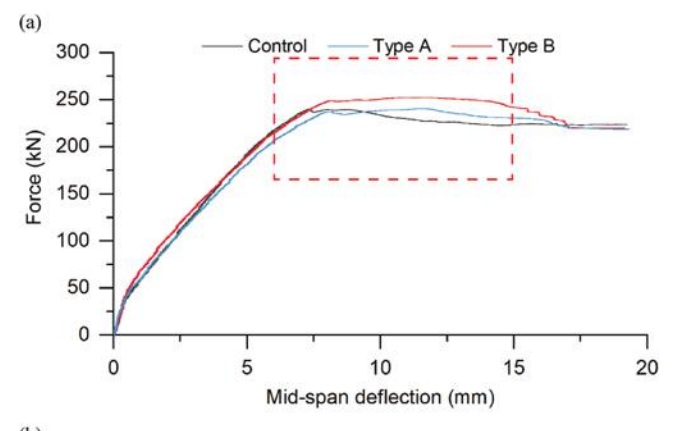
Properties	Control	Type A	Type B		
Cracking force P _{cr} , kN	38.2	42.2	54.5		
Deflection at cracking force δ_{cr} , mm	0.5	0.6	0.7		
Yielding force P _y , kN	203.4	198.7	206.6		
Deflection at yielding force δ_y , mm	5.4	5.6	5.6		
Ultimate force P _{ult} , kN	239.9	240.4	252.4		
Deflection at ultimate force δ_{ult} , mm	7.3	11.6	11.7		

is due to the higher fiber-bridging efficiency of 3DP-EGC in the Type B beam as the tensile stresses are parallel to the printing direction in this beam.

Using the M_{cr} and M_u values calculated in the previous sections, the calculated cracking force ($P_{cr,cal}$) and the calculated ultimate force ($P_{ult,cal}$) of all RC beam specimens are summarized and compared with the test results in Table 5. It should be noted that the $P_{cr,cal}$ and $P_{ult,cal}$ values are based on theoretical calculations for comparison purposes only, and not aimed to be used for prediction. The P_{cr} and $P_{cr,cal}$ values of the control beam were comparable ($P_{cr}/P_{cr,cal} = 0.96$). Similar to the control beam, the P_{cr} and $P_{cr,cal}$ values of the Type B beam were also comparable ($P_{cr}/P_{cr,cal} = 1.05$). However, the P_{cr} value of the Type A beam was lower than its $P_{cr,cal}$ value ($P_{cr}/P_{cr,cal} = 0.81$). This is because the 3DP-EGC permanent formwork was assumed to be a quasimold-cast EGC permanent formwork in the calculations. In

Table 5—Comparison of measured and calculated cracking and ultimate forces of RC beam specimens

RC beam ID	Measured cracking force P_{cr} , kN	Calculated cracking force $P_{cr.cal}$, kN	$P_{cr}/P_{cr.cal}$	Measured ultimate force P_{ult} , kN	Calculated ultimate force $P_{ult,cal}$, kN	$P_{ult}/P_{ult.cal}$
Control	38.2	39.8	0.96	239.9	221.3	1.08
Type A	42.2	52.0	0.81	240.4	242.4	0.99
Type B	54.5	52.0	1.05	252.4	242.4	1.04



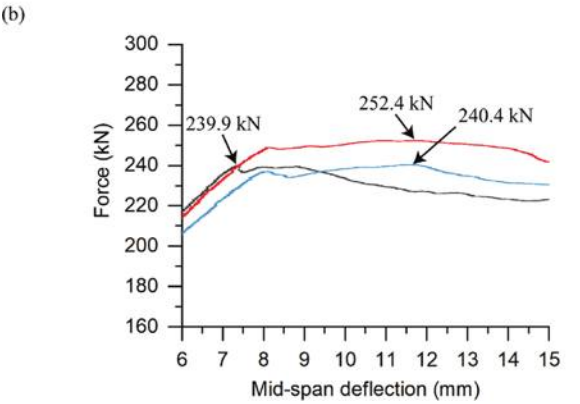


Fig. 9—(a) Force-versus-midspan deflection curves of RC beam specimens; and (b) enlargement of area shown in rectangle in (a) showing ultimate forces of RC beam specimens.

addition, in the Type A beam, cracking was initiated at the interfaces between printed filaments, which are generally weaker compared to the strength of the printed filaments. The cracking patterns of the RC beams are discussed in the following paragraphs. As shown in Table 5, the P_{ult} values of all RC beam specimens were comparable with their corresponding $P_{ult,cal}$ values. The ratios of $P_{ult}/P_{ult,cal}$ of the control beam, Type A beam, and Type B beam were equal to 1.08, 0.99, and 1.04, respectively.

Table 6 presents the ductility index and absorbed energy of all RC beams. This index gives δ_{ult}/δ_y —that is, the ratio of deflection at ultimate force to deflection at yielding force. The absorbed energy of the RC beam specimens was calculated from the area under the load versus midspan deflection curves (refer to Fig. 9(a)) up to the midspan deflection corresponding to P_{ult} . As shown in Table 6, the ductility indexes of both Type A and Type B beams were identical and 50% higher than that of the control beam. This is due to the significantly higher δ_{ult} of Type A and Type B beams. Similar to the ductility index, the absorbed energy values of Type A and Type B beams were 94% and 107% higher than that of

Table 6—Ductility index and absorbed energy of RC beam specimens

RC beam ID	Ductility index	Absorbed energy, kJ/m ²
Control	1.4	1046
Type A	2.1	2026
Type B	2.1	2162

the control beam, respectively. The absorbed energy of the Type B beam was approximately 7% higher than that of the Type A beam, which is due to the higher ultimate force of the Type B beam (refer to Table 4). The significantly higher ductility index and absorbed energy of Type A and Type B beams (constructed using the 3DP-EGC permanent formwork) clearly show their superior flexural performance to the conventionally mold-cast RC beam specimen.

Figures 10 to 12 show the cracking patterns of the control, Type A, and Type B beams at the ultimate loads, respectively. It should be noted that white paint was sprayed on the specimens before conducting the four-point bending tests to obtain clear visible cracks. Figure 10(a) shows a typical cracking pattern of flexural failure of the conventionally mold-cast RC beam. The flexural cracks initiated from the bottom (tension region) of the beam and propagated toward the two loading points (refer to Fig. 10(b) and (c)) as the load increased. In addition, several inclined cracks were observed along the shear span; refer to Fig. 10(d) and (e).

For the Type A beam, a single large crack accompanied by multiple fine cracks was observed at the bottom of the beam; refer to Fig. 11(d). It should be pointed out that these cracks developed at the interfaces between printed filaments; refer to Fig. 11(c) and (d). This can be traced back to the fact that the bond strength between the adjacent printed filaments is weak compared to the strength of the printed filaments. As the load increased, the existing large crack propagated toward the two loading points. However, the crack did not propagate as far from the bottom of the beam as in the control beam, and multiple fine cracks developed in the 3DP-EGC permanent formwork; refer to Fig. 11(b) to (e). In contrast, in the Type B beam, a significant number of fine cracks were observed in the tension region at the ultimate load; refer to Fig. 12(b) to (e). The cracking behavior observed in the Type B beam is very beneficial for improving the cracking resistance and durability of the RC beam. This is because multiple microcracks (with widths typically below 100 μm) can significantly delay the transport of aggressive agents (for example, chlorides) to steel bars.²⁶

Figures 13 to 15 show the cracking pattern of the control, Type A, and Type B beams at 16 mm midspan deflection, respectively. It should be noted that all RC beam specimens exhibited deflection softening at a midspan deflection of

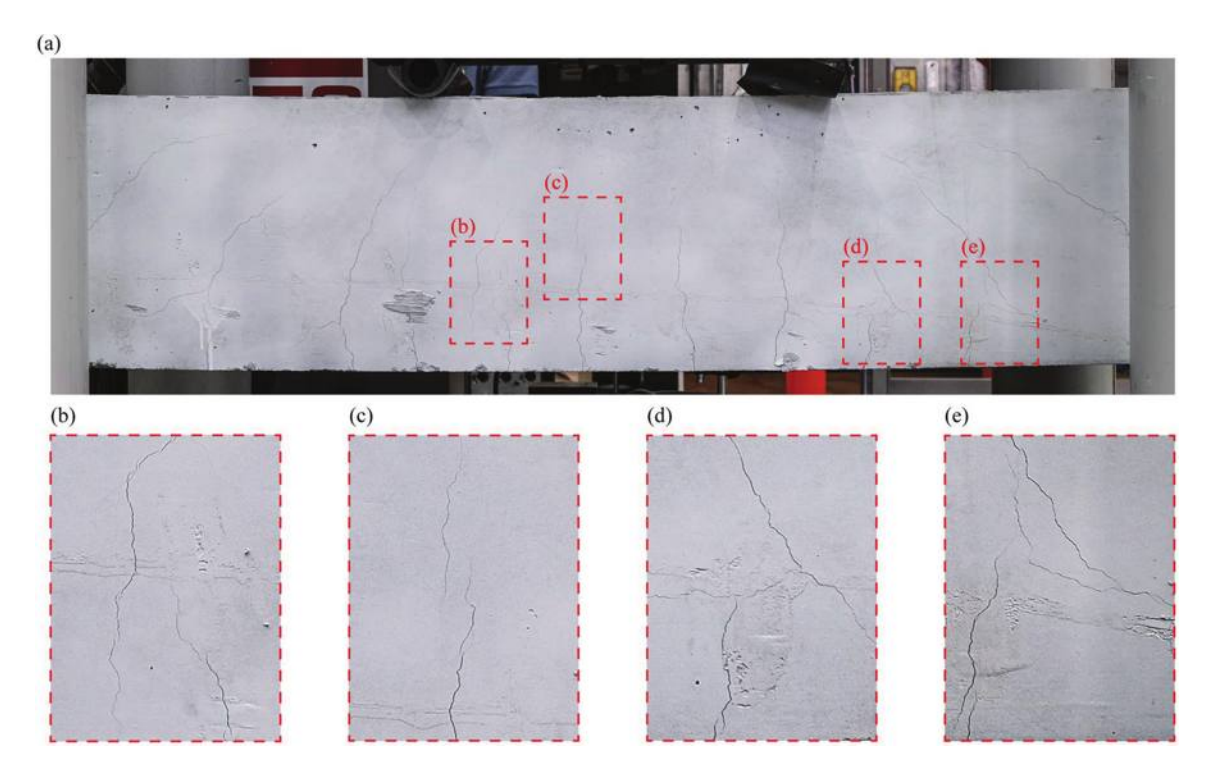


Fig. 10—(a) Cracking pattern of control beam at ultimate load; and (b), (c), (d), and (e) 300% enlargement of areas shown in rectangles in (a).

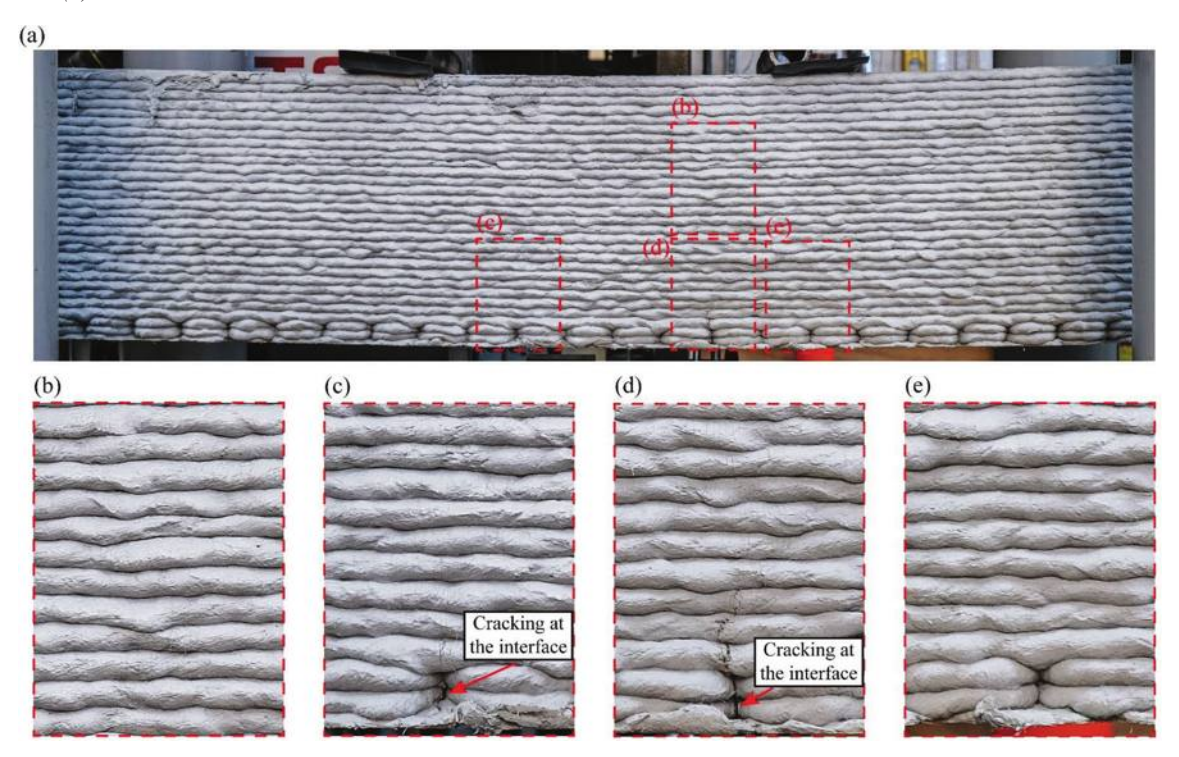


Fig. 11—(a) Cracking pattern of Type A RC beam at ultimate load; and (b), (c), (d), and (e) 300% enlargement of areas shown in rectangles in (a) showing multiple fine cracks.

16 mm. Figure 12(a) shows that in the control beam, the cracks at the midspan significantly widened as the deflection increased. In addition, the concrete crushing in the compression zone (that is, between two loading points) of the control beam was observed; refer to Fig. 13(a). In the Type A beam, the large crack shown in Fig. 14(d) was widely opened and propagated toward the compressive region as the deflection

increased. However, in the Type B beam, the existing fine cracks shown in Fig. 15(d) developed into a larger crack that propagated toward the compressive region as the deflection increased.

Figure 16 shows the cracking pattern of the bottom side of all RC beams after unloading. Multiple fine cracks were observed on the bottom side of the control and Type A

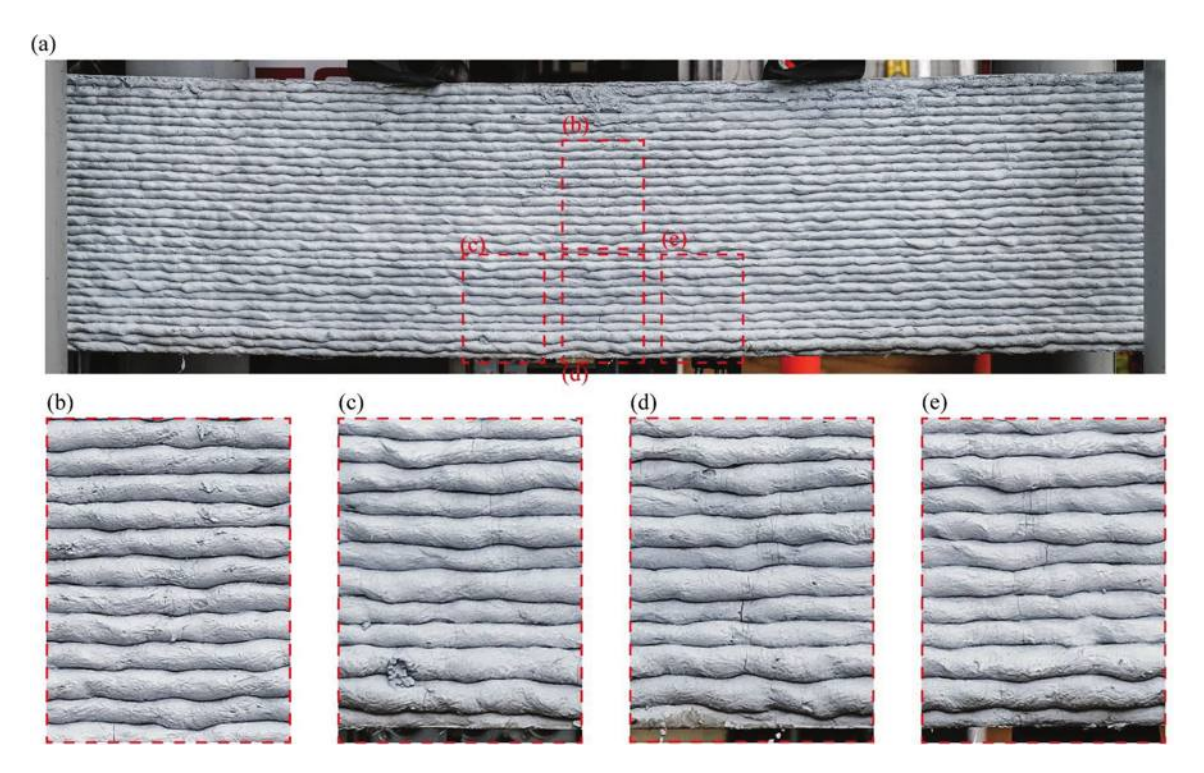


Fig. 12—(a) Cracking pattern of Type B RC beam at ultimate load; and (b), (c), (d), and (e) 300% enlargement of areas shown in rectangles in (a) showing multiple fine cracks.

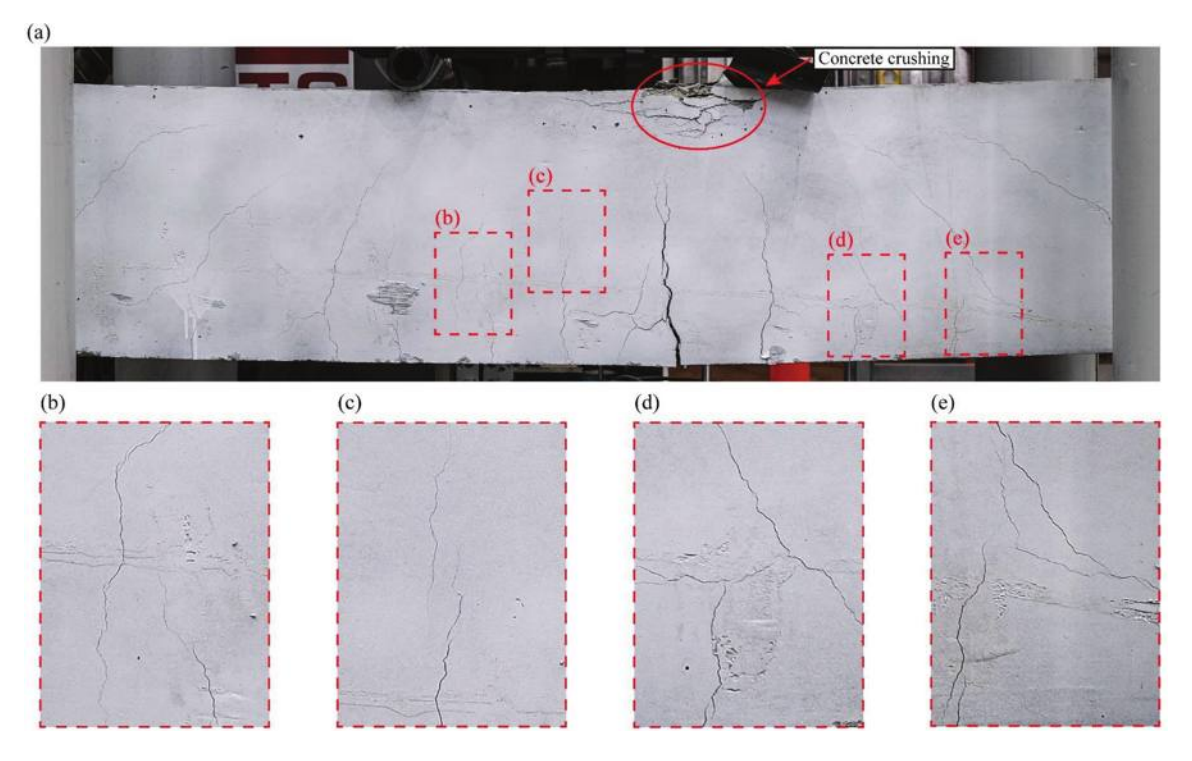


Fig. 13—(a) Cracking pattern of control beam at midspan deflection of 16 mm; and (b), (c), (d), and (e) 300% enlargement of areas shown in rectangles in (a).

beams. However, only a single large crack was observed on the bottom side of the Type B beam. These observations demonstrated that the printing pattern of the formwork base has a significant influence on the cracking pattern of the RC beam constructed using the 3DP-EGC permanent formwork.

Similar to the control beam, concrete crushing in the compression zone of both Type A and Type B beams was

observed (Fig. 16). It is interesting to note that in the Type A and Type B beams, concrete crushing in the compression zone was not observed on the 3DP-EGC permanent formwork; compare Fig. 13(a) with Fig. 14(a) and 15(a). It was also noted that in the compression zone, the 3DP-EGC permanent formwork was debonded from the cast concrete at the midspan of the beams (Fig. 17).

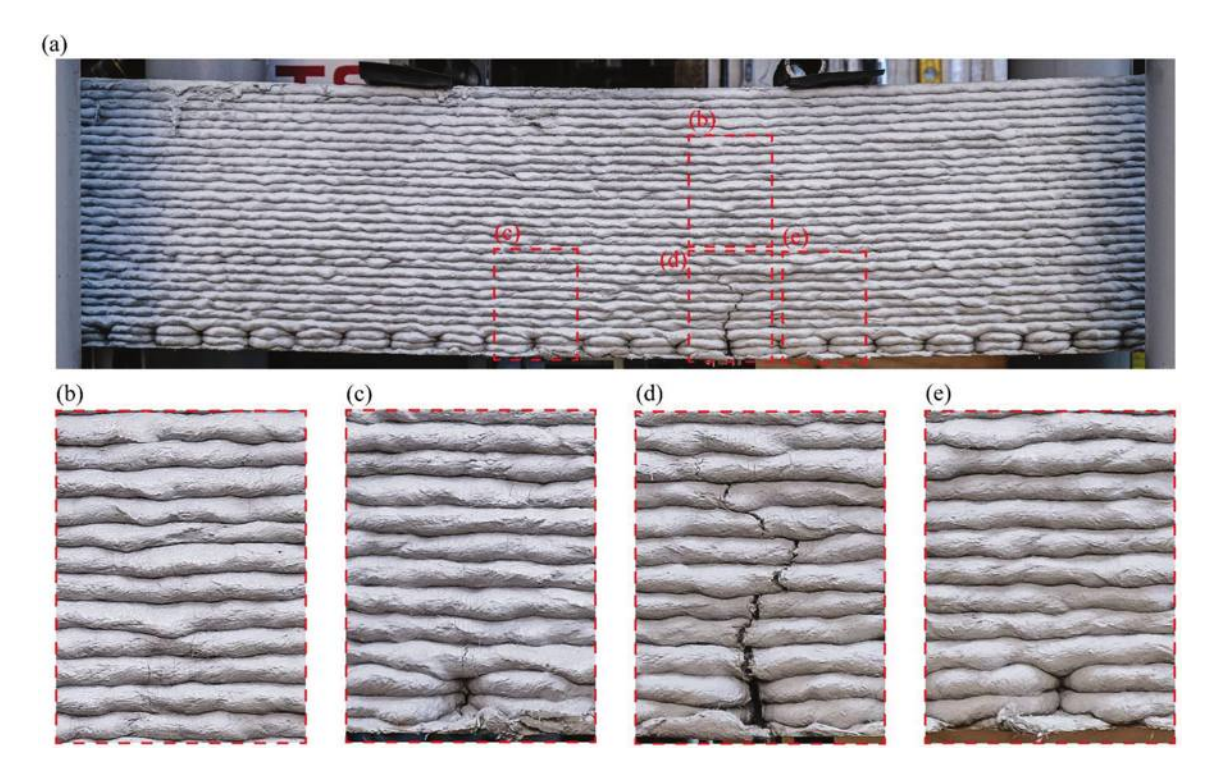


Fig. 14—(a) Cracking pattern of Type A RC beam at midspan deflection of 16 mm; and (b), (c), (d), and (e) 300% enlargement of areas shown in rectangles in (a) showing multiple fine cracks.

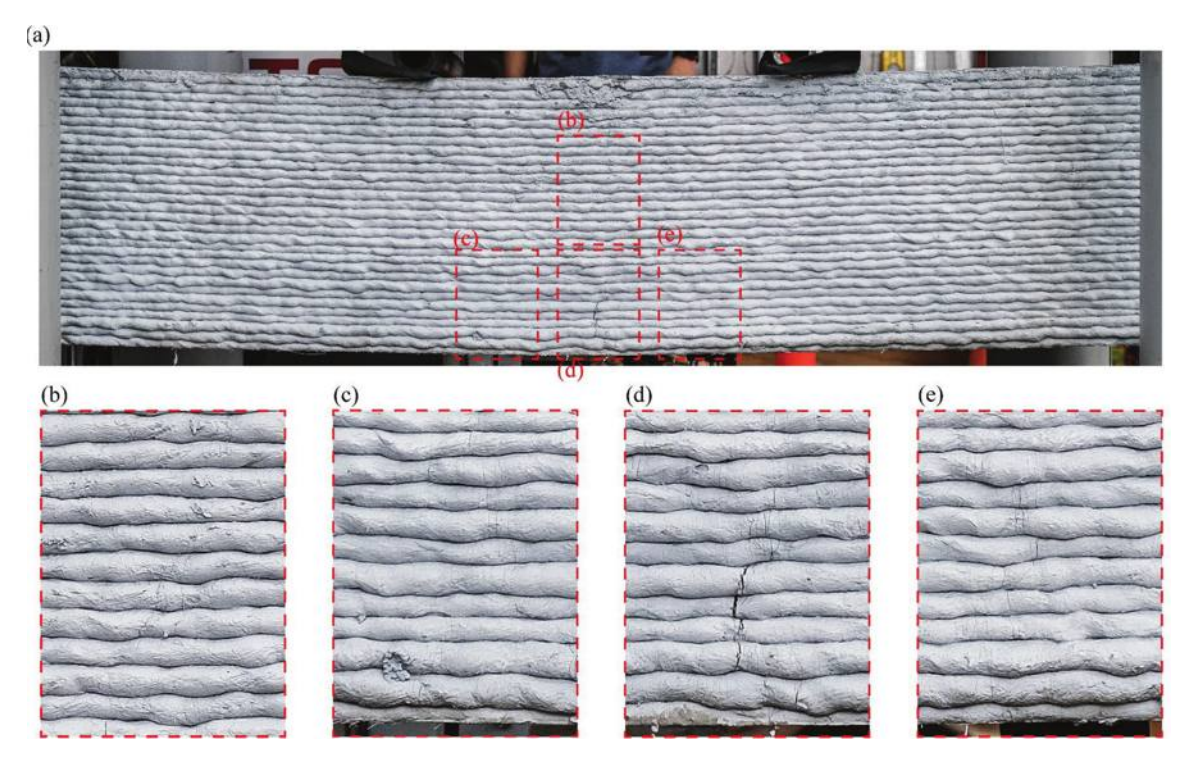


Fig. 15—(a) Cracking pattern of Type B RC beam at midspan deflection of 16 mm; and (b), (c), (d), and (e) 300% enlargement of areas shown in rectangles in (a) showing multiple fine cracks.

CONCLUSIONS

This paper evaluates the behavior and performance of three-dimensional (3-D)-printable engineered geopolymer composite (3DP-EGC) permanent formwork for the construction of reinforced concrete (RC) beams. Two different printing patterns were used at the soffit of the permanent formwork to investigate the effect of printing direction on the flexural

performance of RC beams. The results were compared with those obtained for a conventionally mold-cast RC beam (that is, the control beam). Based on the experimental results, the following conclusions are drawn:

1. The RC beams made using the 3DP-EGC permanent formwork exhibited superior flexural performance in comparison to the control beam. In addition, the experimental

results indicated that the interface between the 3DP-EGC permanent formwork and concrete core did not initiate any premature failure.

2. The RC beams produced using the 3DP-EGC permanent formwork exhibited significantly higher cracking load (up to 43%), deflection at the ultimate load (up to 60%), ductility index (50%), and absorbed energy (up to 107%) than those



Control beam



Type A beam



Type B beam

Fig. 16—Cracking pattern of bottom side (tension region) of RC beam specimens; photos were taken after unloading.

of the control beam. However, the ultimate flexural load capacity for the RC beams made using the 3DP-EGC permanent formwork was not significantly higher than that of the control beam.

3. After steel yielding, both Type A and Type B beams with the 3DP-EGC permanent formwork exhibited deflection-hardening behavior, while the control beam showed typical deflection-softening behavior. Type A and Type B beams had printed filaments perpendicular and parallel, respectively, to the principal tensile stress on the bottom of the beams. The ability of the ductile EGC in the permanent formwork to continue sharing the load with steel beyond yielding contributes to the superior performance of the beams with the 3DP-EGC permanent formwork. In contrast, the cracked concrete in the control beam gave up carrying tensile forces at this stage of loading.

4. The printing pattern at the soffit of the permanent formwork was found to have a significant influence on the flexural performance of the RC beams. For the Type A beam, the cracking initiated at the interfaces between printed filaments and was accompanied by multiple fine cracks as the load increased. In the case of the Type B beam, a significant number of fine cracks were observed in the tension region and ultimately developed into a larger crack that propagated toward the compression zone as the deflection increased. The formation of multiple fine cracks with tight crack widths is very beneficial for improving the durability of the RC beam, as they can significantly delay the transport of aggressive agents (for example, chlorides) to steel bars.

The work presented in this paper proves the effectiveness of using the 3DP-EGC permanent formwork system for the construction of RC beams. The following can be explored in future studies: a) the interface bond between the permanent formwork and concrete core in relation to different

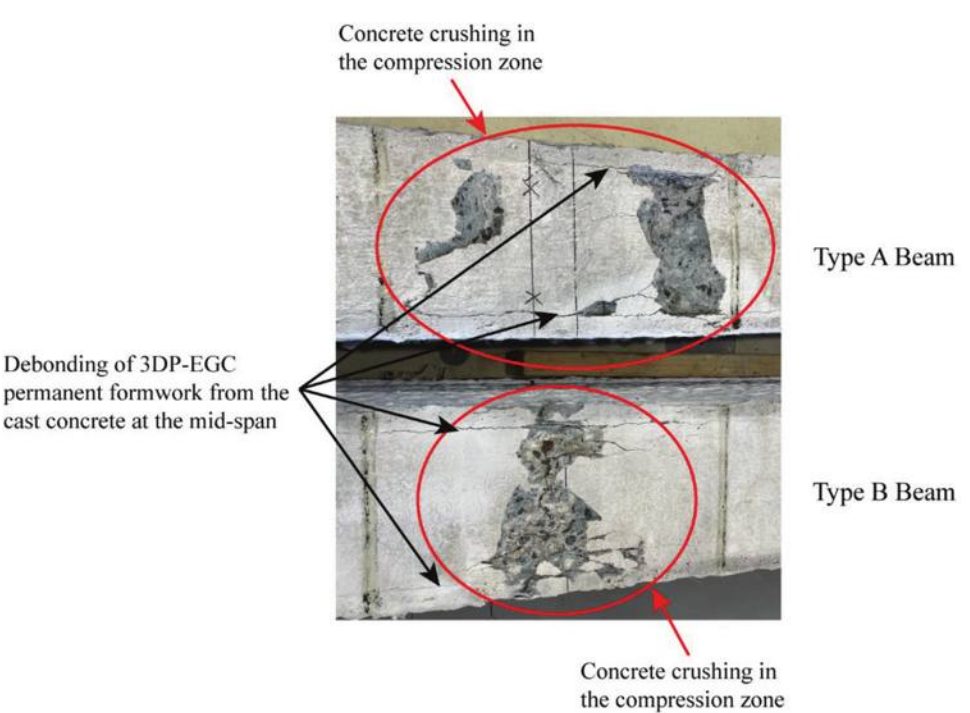


Fig. 17—Debonding of 3DP-EGC permanent formwork from cast concrete in compression zone at midspan; photos of top views of beam specimens were taken after unloading.

printing patterns; b) the durability of RC beams built by the 3DP-EGC permanent formwork; c) the shear behavior of RC beams without stirrups made by using the 3DP-EGC permanent formwork; and d) the topology optimization of the RC beams built by the 3DP-EGC permanent formwork.

AUTHOR BIOS

Shin Hau Bong is a Postdoctoral Research Fellow at the National University of Singapore, Singapore. He received his BSc and PhD from Swinburne University of Technology, Melbourne, VIC, Australia. His research interests include low-carbon concrete and fiber-reinforced cementitious materials for three-dimensional (3-D) concrete printing applications.

Behzad Nematollahi is an Assistant Professor at the University of Sheffield, Sheffield, UK. Previously, he was an Assistant Professor and Australian Research Council Discovery Early Career Researcher Award (DECRA) Fellow at Swinburne University of Technology. His research interests include 3-D concrete printing, geopolymer concrete, low-carbon concrete, and high-performance fiberreinforced cementitious composites.

ACI member Viktor Mechtcherine is a Professor at the Technische Universität Dresden in Dresden, Saxony, Germany.

Victor C. Li, FACI, is the E.B. Wylie Collegiate Chair Professor in the Department of Civil and Environmental Engineering at the University of Michigan, Ann Arbor, MI. His research interests include the micromechanics and design of ultra-ductile and green cementitious composites, their application to innovative and sustainable infrastructure systems, and the integration of materials and structural design.

Kamal H. Khayat, FACI, is a Professor at Missouri University of Science and Technology, Rolla, MO.

ACKNOWLEDGMENTS

This project was supported by the Australian Research Council Discovery Project DP210101680, Discovery Early Career Researcher Award DE180101587, and Linkage Infrastructure, Equipment and Facilities Grant LE170100168, as well as the funding received under the 2018 Australia-Germany Joint Research Cooperation Scheme funded by Universities Australia and German Academic Exchange Service. The first two authors also acknowledge the comments from Professor J. Sanjayan at the Swinburne University of Technology on designing the cast reinforced concrete beam and for reviewing the initial draft of the manuscript.

REFERENCES

- 1. Johnston, D. W., "Design and Construction of Concrete Formwork," *Concrete Construction Engineering Handbook*, E. G. Nawy, ed., CRC Press, Boca Raton, FL, 2008, pp. 7.1-7.48.
- 2. Jha, K. N., Formwork for Concrete Structures, Tata McGraw Hill Education Private Limited, New Delhi, India, 2012, 573 pp.
- 3. Arumsari, P., and Xavier, C., "Cost and Time Analysis on the Selection of Formwork Installation Method," *IOP Conference Series: Earth and Environmental Science*, V. 426, 2020, Article No. 012042. doi: 10.1088/1755-1315/426/1/012042
- 4. Wringley, R. G., "Permanent Formwork in Construction (CIRIA C558)," CIRIA/The Concrete Society, London, UK, 2001, pp. 13-16.
- 5. García de Soto, B.; Agustí-Juan, I.; Hunhevicz, J.; Joss, S.; Graser, K.; Habert, G.; and Adey, B. T., "Productivity of Digital Fabrication in Construction: Cost and Time Analysis of a Robotically Built Wall," *Automation in Construction*, V. 92, 2018, pp. 297-311. doi: 10.1016/j.autcon.2018.04.004
- 6. De Schutter, G.; Lesage, K.; Mechtcherine, V.; Nerella, V. N.; Habert, G.; and Agusti-Juan, I., "Vision of 3D Printing with Concrete—Technical, Economic and Environmental Potentials," *Cement and Concrete Research*, V. 112, 2018, pp. 25-36. doi: 10.1016/j.cemconres.2018.06.001
- 7. Pan, Z.; Zhu, Y.; Qiao, Z.; and Meng, S., "Seismic Behavior of Composite Columns with Steel Reinforced ECC Permanent Formwork and Infilled Concrete," *Engineering Structures*, V. 212, 2020, Article No. 110541. doi: 10.1016/j.engstruct.2020.110541

- 8. Tian, H.; Zhou, Z.; Zhang, Y.; and Wei, Y., "Axial Behavior of Reinforced Concrete Column with Ultra-High Performance Concrete Stay-In-Place Formwork," *Engineering Structures*, V. 210, 2020, Article No. 110403. doi: 10.1016/j.engstruct.2020.110403
- 9. Huang, B.-T.; Li, Q.-H.; Xu, S.-L.; and Li, C.-F., "Development of Reinforced Ultra-High Toughness Cementitious Composite Permanent Formwork: Experimental Study and Digital Image Correlation Analysis," *Composite Structures*, V. 180, 2017, pp. 892-903. doi: 10.1016/j.compstruct.2017.08.016
- 10. Leung, C. K. Y., and Cao, Q., "Development of Pseudo-Ductile Permanent Formwork for Durable Concrete Structures," *Materials and Structures*, V. 43, No. 7, 2010, pp. 993-1007. doi: 10.1617/s11527-009-9561-4
- 11. Zhang, R.; Hu, P.; Zheng, X.; Cai, L.; Guo, R.; and Wei, D., "Shear Behavior of RC Slender Beams without Stirrups by Using Precast U-Shaped ECC Permanent Formwork," *Construction and Building Materials*, V. 260, 2020, Article No. 120430. doi: 10.1016/j.conbuildmat.2020.120430
- 12. Li, H.; Leung, C. K. Y.; Xu, S.; and Cao, Q., "Potential Use of Strain Hardening ECC in Permanent Formwork with Small Scale Flexural Beams," *Journal of Wuhan University of Technology-Materials Science Edition*, V. 24, No. 3, 2009, pp. 482-487. doi: 10.1007/s11595-009-3482-5
- 13. Qiao, Z.; Pan, Z.; Xue, W.; and Meng, S., "Experimental Study on Flexural Behavior of ECC/RC Composite Beams with U-Shaped ECC Permanent Formwork," *Frontiers of Structural and Civil Engineering*, V. 13, No. 5, 2019, pp. 1271-1287. doi: 10.1007/s11709-019-0556-0
- 14. Vantyghem, G.; De Corte, W.; Shakour, E.; and Amir, O., "3D Printing of a Post-Tensioned Concrete Girder Designed by Topology Optimization," *Automation in Construction*, V. 112, 2020, Article No. 103084. doi: 10.1016/j.autcon.2020.103084
- 15. Anton, A.; Bedarf, P.; Yoo, A.; Dillenburger, B.; Reiter, L.; Wangler, T.; and Flatt, R. J., "Concrete Choreography: Prefabrication of 3D-Printed Columns," *Fabricate 2020: Making Resilient Architecture*, J. Burry, J. Sabin, B. Sheil, and M. Skavara, eds., UCL Press, London, UK, 2020, pp. 286-293.
- 16. Zhu, B.; Nematollahi, B.; Pan, J.; Zhang, Y.; Zhou, Z.; and Zhang, Y., "3D Concrete Printing of Permanent Formwork for Concrete Column Construction," *Cement and Concrete Composites*, V. 121, 2021, Article No. 104039. doi: 10.1016/j.cemconcomp.2021.104039
- 17. Huntzinger, D. N., and Eatmon, T. D., "A Life-Cycle Assessment of Portland Cement Manufacturing: Comparing the Traditional Process with Alternative Technologies," *Journal of Cleaner Production*, V. 17, No. 7, 2009, pp. 668-675. doi: 10.1016/j.jclepro.2008.04.007
- 18. Taylor, M.; Tam, C.; and Gielen, D., "Energy Efficiency and CO₂ Emissions from the Global Cement Industry," *Energy Efficiency and CO₂ Emission Reduction Potentials and Policies in the Cement Industry*, International Energy Agency (IEA), Paris, France, 2006, pp. 61-67.
- 19. Bong, S. H.; Nematollahi, B.; Nerella, V. N.; and Mechtcherine, V., "Method of Formulating 3D-Printable Strain-Hardening Alkali-Activated Composites for Additive Construction," *Cement and Concrete Composites*, V. 134, 2022, Article No. 104780. doi: 10.1016/j.cemconcomp.2022.104780
- 20. Duxson, P.; Provis, J. L.; Lukey, G. C.; and van Deventer, J. S. J., "The Role of Inorganic Polymer Technology in the Development of 'Green Concrete'," *Cement and Concrete Research*, V. 37, No. 12, 2007, pp. 1590-1597. doi: 10.1016/j.cemconres.2007.08.018
- 21. Ohno, M., and Li, V. C., "Sulfuric Acid Resistance of Strain Hardening Fiber Reinforced Geopolymer Composite," *The Indian Concrete Journal*, V. 93, No. 12, 2019, pp. 47-53.
- 22. AS 1379-2007, "Specification and Supply of Concrete," Standards Australia, Sydney, NSW, Australia, 2007, 42 pp.
- 23. AS 3600:2018, "Concrete Structures," Standards Australia, Sydney, NSW, Australia, 2018, 256 pp.
- 24. Bong, S. H.; Xia, M.; Nematollahi, B.; and Shi, C., "Ambient Temperature Cured 'Just-Add-Water' Geopolymer for 3D Concrete Printing Applications," *Cement and Concrete Composites*, V. 121, 2021, Article No. 104060. doi: 10.1016/j.cemconcomp.2021.104060
- 25. JSCE, "Recommendations for Design and Construction of High Performance Fiber Reinforced Cement Composites with Multiple Fine Cracks (HPFRCC)," Concrete Engineering Series No. 82, Japan Society of Civil Engineers, Tokyo, Japan, 2008.
- 26. Li, V. C., "Durability of Engineered Cementitious Composites (ECC) and Reinforced ECC (R/ECC) Structural Members," *Engineered Cementitious Composites (ECC): Bendable Concrete for Sustainable and Resilient Infrastructure*, Springer-Verlag GmbH, Berlin, Germany, 2019, pp. 225-260.

Title No. 121-S17

Approach for Production of Textile-Reinforced Beams and Slabs Using Three-Dimensional Concrete Printing

by Egor Ivaniuk and Viktor Mechtcherine

Despite all the recent advances in the development of threedimensional (3-D) concrete printing (3DCP), this technology still has many unresolved problems. In most of the completed projects with the application of 3DCP, the focus was mainly on mastering the printing of vertical walls, while horizontal structural elements were produced with conventional methods—that is, using formwork, which reduces the level of technology automation, or using prefabricated elements, which makes the construction dependent on their availability and supply.

In this contribution, the authors propose new methods of manufacturing slabs and beams directly on site by extruding concrete onto a textile reinforcement mesh laid on a flat surface. Specimens obtained from a slab produced following this method were used for mechanical testing and investigation of the concrete-reinforcement interface zone. Finally, as proof of the feasibility of the proposed approach, a demonstrator representing a full-scale door lintel was manufactured.

Keywords: additive manufacturing (AM); concrete extrusion; digital concrete; digital construction; textile reinforcement; three-dimensional (3-D) concrete printing (3DCP).

INTRODUCTION

In the past few years, large-scale additive manufacturing (AM) technologies have become increasingly widespread in the construction industry. Of all of the available AM technologies, extrusion-based three-dimensional (3-D) concrete printing (3DCP) seems to be the most suitable for large-scale applications and is surely the most commonly applied in the practice of construction. However, some aspects of construction using 3DCP by layered extrusion still need to be developed. One of these aspects is the creation of horizontal and inclined structural elements, such as floors and roofs, as well as window and door lintels.

In most of the completed projects, the slabs were produced by conventional methods—that is, using formwork or prefabricated elements. While such traditional methods are highly reliable, they have their drawbacks when applied in the context of 3DCP. Formwork and supports need to be assembled manually, which reduces the level of technology automation and the speed of construction. The use of prefabricated elements, in contrast, offers high construction speeds but also makes the construction dependent on the availability and supply of these elements (refer to Fig. 1(a)).

An alternative approach was demonstrated at ETH Zurich. In the Fast Complexity project, a modular soffit was assembled from prefabricated modules produced using 3-D printing.⁵ These modules can be created directly in-place, thereby making the process independent of external

supplies; however, creating the slab in this way can be very time-consuming.

In addition to the methods used in conventional construction, the roof can be built directly on the construction site by 3-D printing arches and domes. With this approach, full automation can be achieved, but very fast-setting concrete must be used to ensure adequate printing speed. The use of fast-setting concrete can have a negative impact on the strength characteristics of the printed structure, especially when printing large structures, because the long time intervals between printing the layers reduce the strength of the interlayer bond. This method is also less reliable as there is a risk of collapse when cantilevers are printed, especially in poorly controlled construction site conditions. A company presented a vision of how arch printing can be used to create flat slabs, but so far, no examples of the implementation of this approach have been presented (refer to Fig. 1(b)).

The creation of openings in printed walls can also be realized by methods similar to those presented previously for the creation of slabs and roofs, with similar advantages and disadvantages. The first possible solution is the manual erection of the formwork (refer to Fig. 2(a)). The second option is the use of prefabricated beams or frames (refer to Fig. 2(b)). Beams can be made of different materials, including wood, steel, and reinforced concrete. In this case, the size of the openings is limited by the length of the available elements. The third approach to creating openings is printing arches (refer to Fig. 2(c)).

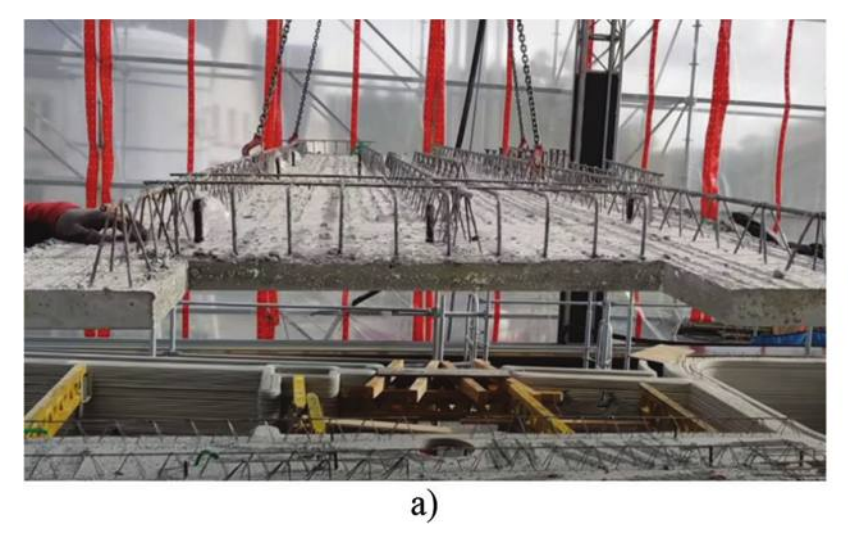
It can be concluded that all available technologies for creating horizontal and inclined structural elements have their disadvantages. The use of formwork slows down construction and makes it difficult to automate it, the use of prefabricated elements limits the self-sufficiency of 3DCP, and printing arches does not yet have sufficient reliability.

RESEARCH SIGNIFICANCE

3DCP technology has the potential to revolutionize the construction industry, enabling faster, cheaper, and safer construction. However, at the current stage, all existing methods for creating non-vertical elements have certain disadvantages. In this paper, a new approach for creating reinforced beams and slabs directly at the

ACI Structural Journal, V. 121, No. 2, March 2024.

MS No. S-2022-179.R2, doi: 10.14359/51739158, received December 2, 2022, and reviewed under Institute publication policies. Copyright © 2024, American Concrete Institute. All rights reserved, including the making of copies unless permission is obtained from the copyright proprietors. Pertinent discussion including author's closure, if any, will be published ten months from this journal's date if the discussion is received within four months of the paper's print publication.



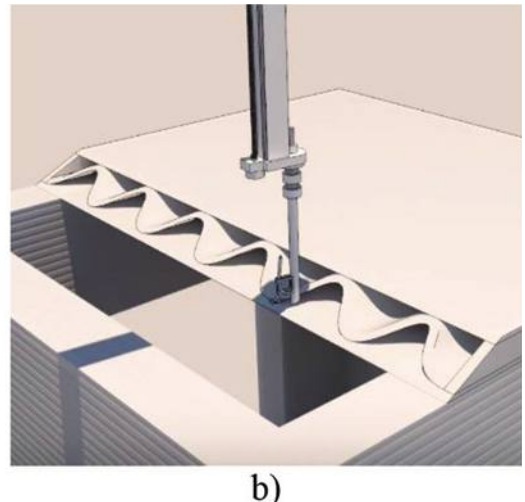


Fig. 1—Approaches to fabrication of slabs: (a) using precast concrete forms³; and (b) 3-D printing arches using fast-setting concrete.⁴







Fig. 2—Existing approaches to create 3D-printed wall openings: (a) using supporting structures⁴; (b) using frames or lintels⁷; and (c) printing arches with fast-setting concrete.⁸

construction site is proposed. It uses 3-D printing and overcomes the disadvantages of the other approaches. The proposed methodology simultaneously enables rapid construction with high geometrical freedom in fabrication, is reliable, and makes construction using 3-D printing independent of the availability of prefabricated elements.

PROPOSED APPROACH

With the proposed approach, beams and slabs are produced on site using a 3-D printer. This requires a flat horizontal surface of sufficient size within the reach of the 3-D printer to serve as a printing bed. Such a surface could be, for example, a foundation slab covered with a polyethylene film to prevent adhesion between the slab and the freshly printed concrete.

Fabrication of beams

Within the framework of the proposed approach, three different methods can be used. In the first method, the entire volume of a reinforced beam is created using full-width printing (FWP) (refer to Fig. 3(a)). FWP implies that the width of the extruded layer is equal to the width of the wall. 10 The second method uses filament printing (FP), in which the nozzle width is smaller than the printed wall, and the beam is created by extruding several concrete filaments parallel to each other (refer to Fig. 3(b)). In the third proposed method, only the contour of the beam is printed to serve as integrated formwork, and its interior is filled with flowable concrete (refer to Fig. 3(c)). Self-consolidating concrete can be used for the filling, or alternatively, concrete used for 3-D printing, but with an increased dose of high-range waterreducing admixture (HRWRA). In the second case, however, additional compaction may be required, including the use

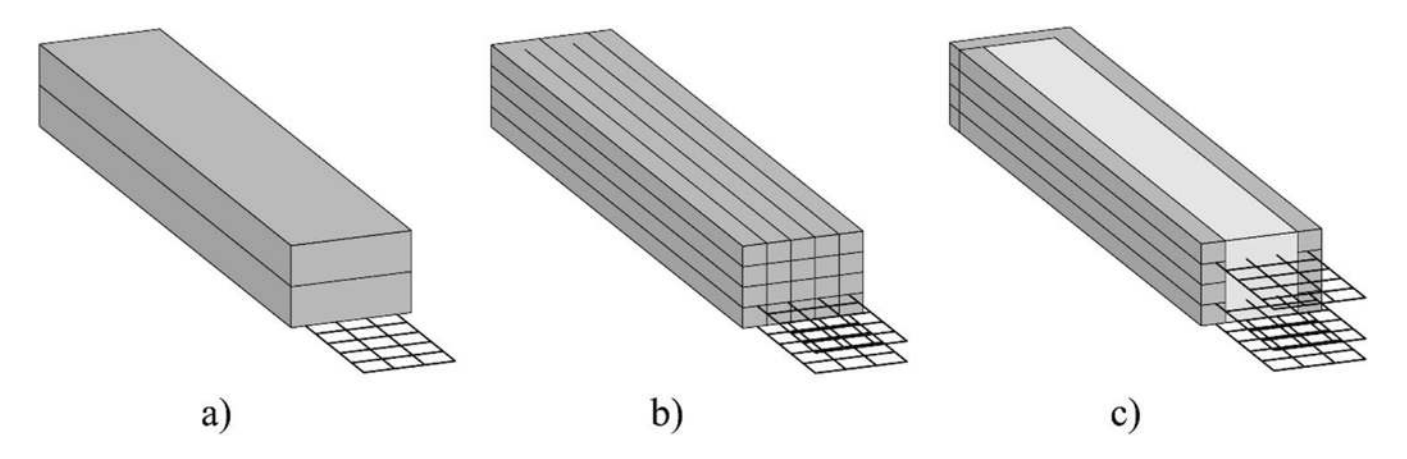


Fig. 3—Schemes for production of beams according to proposed methods: (a) with full-width printing; (b) with filament printing; and (c) with printing of integrated formwork.

of vibrators. In this case, special attention should be paid to whether the printed contour of the element is sufficiently hardened.

Reinforcement strategies are similar for all three methods, and they all use a reinforcement mesh precut to the dimensions of the beam being fabricated. In addition to reinforcement in the longitudinal direction of the beam, textile meshes also increase tensile strength in the perpendicular direction, which is especially important for beams fabricated using FP.

The reinforcement of the lower surface of the beam can be performed by laying textile mesh directly on the printing bed and then depositing concrete layers on top of it. This is possible because the textile reinforcement, which is usually made of carbon, alkali-resistant (AR) glass, or basalt fibers, is resistant to corrosion and does not require full coverage with concrete. It is also lighter and has a higher tensile strength in comparison to conventional steel reinforcement. 11 The advantages of this method of reinforcement are the high production speed of beams and that the entire cross section of the beam works in compression. However, a (too) small concrete cover potentially can lead to a lack of bonding between the reinforcement and the concrete and poor protection of the reinforcement against high temperatures in case of fire, but both these disadvantages can be compensated by subsequent shotcreting the bottom of the beam. 12 The use of this approach can be justified when shotcrete is already planned in construction—for example, to level internal walls. Another approach to increase the concrete cover is to use a special textile mesh, which has pins in the direction perpendicular to the plane of the mesh. 13 In this case, the printed concrete must be flowable enough to penetrate through the mesh.

Alternatively, reinforcement meshes can be placed between the layers during printing. To avoid the formation of cold joints, the time interval between the printing of the layer on which the mesh is placed and the subsequent layer should be as short as possible. In this case, steel mesh can also be used because a sufficient concrete cover is provided to protect it against corrosion. The minimum possible concrete cover is equal to the height of one printed layer. If needed, reinforcement mesh can be placed at various heights of the beam. Figure 3 shows examples of different reinforcement

options: a) reinforcement mesh placed only at the bottom; b) two reinforcement meshes at the bottom; and c) bottom and top reinforcement of the beam. It should be noted that the beams produced by the proposed method do not have shear reinforcement, so they can only be used in cases where the expected shear loads do not exceed the shear resistance of the concrete used.

Fabrication of slabs

The proposed slab fabrication methods are similar to those previously presented for beam production. In the first method, the entire volume of the slab is created by extrusion, similar to the manufacturing of a beam in Fig. 3(b). This method requires no additional flowable concrete or equipment beyond the 3-D printer itself, but it also has several drawbacks. First, creating a slab in this manner is associated with a long printing path, which can be time-consuming, especially when printing large slabs by depositing filaments with a small-nozzle cross section. Second, there is a risk of cavities forming inside the slab in case of extrusion difficulties.

In contrast, the use of the second method, in which a contour is printed and then filled with flowable concrete, has a number of advantages. Slabs can be created quickly due to much shorter printing paths, and the risk of void formation is minimal. The contour of a slab can be printed in any shape, including nonlinear ones, allowing the geometrical freedom provided by 3-D printing technology to be used to a high extent. Obviously, the fabrication of curved slabs using traditional casting methods is more expensive and time-consuming.

Another advantage is the possibility of placing the necessary utilities inside the printed contour of the slab. In addition, while the printed contour of the slab is not yet hardened, the necessary holes can easily be cut into it and utilities can be routed through them. Furthermore, before the contour of the slab is filled, steel wire loops can be tied to the reinforcement and later used to attach the slab to the crane slings. The possibility of using a 3-D printer as a construction crane will increase the degree of automation and avoid the need for additional machinery at the construction site.¹⁴

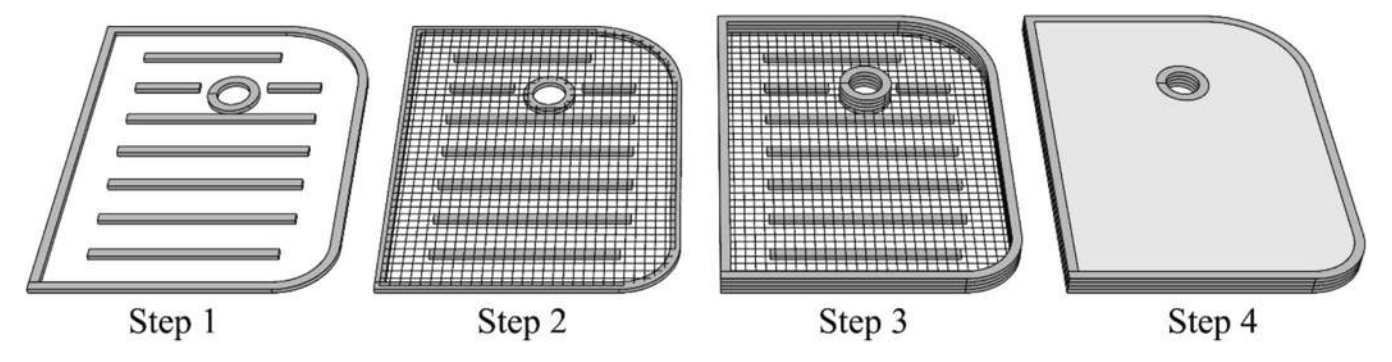


Fig. 4—Step-by-step scheme for manufacturing reinforced slab with circular opening according to proposed method.

In the proposed methods, the slabs are reinforced with meshes, and, as for the beams, it is possible to reinforce the bottom surface of the slab with a textile mesh by placing it on the printing bed and creating the slab on top of it. A textile or steel reinforcement mesh can also be installed between the printed layers, but it must be ensured that there is no excessive sagging of the mesh, otherwise the uniform width of concrete cover will not be provided. This can be achieved by printing additional supports inside the contour, on which the reinforcement mesh will lie.

Figure 4 shows an example of the fabrication process of a slab with a circular opening. The slab is reinforced with a mesh placed between the first and second layers only. In the first step, the first layer of the slab contour and the opening contour, as well as additional supports for the reinforcement mesh, are printed. In the second step, the reinforcement mesh is installed. Then, the contours of the slab and the opening are printed until the required slab height is reached. Finally, the space between the slab contour and the opening contour is filled with flowable, preferably self-consolidating, concrete. If it is necessary to install utilities inside the slab, it is possible to place only part of the concrete, just above the level of the reinforcement. After the fill concrete has sufficiently stiffened, the utilities can be installed on its surface, and then the remaining concrete can be placed.

EXPERIMENTAL PROCEDURE

The main objective of the experiments carried out in this study was to evaluate the feasibility of the proposed methods for fabricating beams and slabs. The possibility of integrating reinforcement meshes between printed layers has been proven previously. ¹⁵ In the research at hand, particular attention was paid to integrating reinforcement by 3-D concrete printing on top of a textile mesh laid on the printing base surface.

Materials

The composition of the fine-grained concrete used for 3-D printing in this study is similar to that presented earlier in the research by Nerella et al., ¹⁶ denoted there as Mixture A. However, several changes have been made. In this investigation, the cement was replaced by CEM I 52.5R and the dosage of HRWRA was reduced to 1.0% by mass of binder (bmob) (refer to Table 1). A similar mixture composition, but with a higher dosage of HRWRA equal to 1.5% bmob,

Table 1—Mixture compositions

	I .			
Density	3-D printing	Casting		
kg/m ³	Weight per unit	volume, kg/m ³		
3100	391	391		
2271	213	213		
1400	213	213		
2650	252	252		
2650	252	252		
2650	756	756		
1000	138	138		
1010	7	11		
	3100 2271 1400 2650 2650 2650 1000	Density, kg/m ³ Weight per unit 3100 391 2271 213 1400 213 2650 252 2650 252 2650 756 1000 138		

^{*}Aqueous suspension of microsilica with dry mass content of $50 \pm 2\%$.

Note: PCE is polycarboxylate ether.

was used to fill the slab. The compressive strength of both mixtures after 1 day was 26 MPa and slightly exceeded 100 MPa at a concrete age of 28 days.

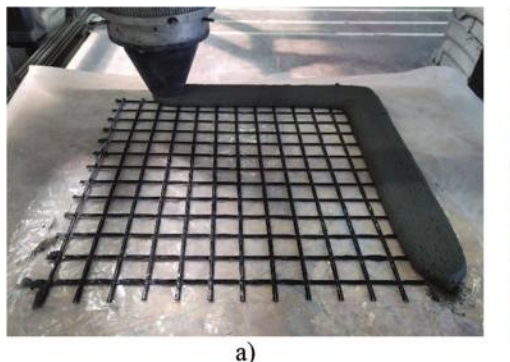
Carbon textile mesh impregnated with epoxy resin was used to reinforce the fabricated elements. The strands of the mesh were perpendicular to each other, and the distances between the axes of adjacent strands were 38 mm in both directions.

Fabrication of structural elements

To validate the approach of manufacturing structural elements using the proposed methods, a scaled-down model of the slab and a full-size beam were produced. In both cases, 3-D printing was performed by means of a gantry concrete printer developed at Technische Universität Dresden. ¹⁰

A 1 m long single-layer beam was produced by printing over a textile mesh laid on the printing bed. The printing was performed using a horizontally oriented nozzle with a rectangular outlet of 150×50 mm.

A slab with dimensions of 600 x 600 mm was produced by printing its contour on the surface of a textile mesh and then filling it with flowable concrete (refer to Fig. 5). Because the concrete used to fill the slab was not self-consolidating concrete, but the same concrete used for 3-D printing with an increased dose of HRWRA, a trowel was used to facilitate its distribution. The contour consisted of two layers, each approximately 20 mm high. The printing was carried out with a vertically oriented circular nozzle with a diameter of 60 mm. The day after the slab was created, it was cut to



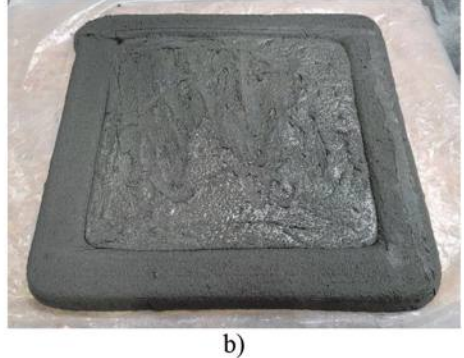


Fig. 5—Demonstration of process of creating a slab: (a) 3-D printing of slab contour; and (b) contour filled with concrete.

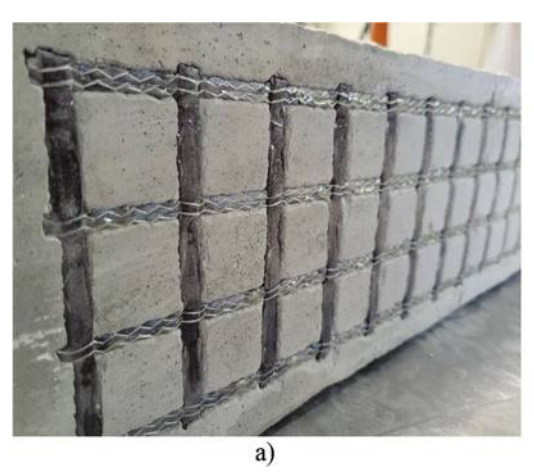




Fig. 6—View of bottom surface of manufactured elements: (a) beam; and (b) slab.

produce specimens for the bending test and for microscopic examination.

Bending test

The prisms cut from the slab were made in such a way that in each of them, the textile strand was parallel to the longitudinal axis and passed through the center of the bottom surface. The length of the samples was 140 mm. The width of all the samples was 38 mm, which is equal to the spacing between the axes of the neighboring threads in the textile mesh used. The height of the samples was 34 mm and was obtained after leveling the top surface of the plate with a saw.

Six samples produced in this manner were tested in a three-point bending test the day after the slab was produced. The time of testing was chosen based on the fact that the proposed technology implies the mounting and loading of the elements the very next day after their manufacturing. The test was performed using a testing machine with a distance between supports equal to 120 mm and under a constant loading rate of 2 mm/min.

EXPERIMENTAL RESULTS AND DISCUSSION Concrete cover

Inspection of the fabricated elements showed that the concrete used for the 3-D printing did not penetrate under the reinforcement mesh, but tightly enveloped it from the other sides (refer to Fig. 6(a)). Concrete used for filling/

casting was more flowable and thus able to penetrate under the textile mesh and cover it from all sides, although there were still places, mostly at the intersections of the strands, where the reinforcement was not completely covered (refer to Fig. 6(b)).

Samples cut from the slab were examined with a digital microscope. Inspection of the samples showed that the width of the concrete cover reached approximately 1.8 mm in the central part of the slab (refer to Fig. 7). In addition, no cavities or cracks were found along the perimeter of the reinforcing strands, which may indicate good bond between the reinforcement and the concrete used to fill the slab.

Bending test results

The results of the bending test are shown in Fig. 8(a). All specimens yielded two peaks in the recorded force-displacement diagrams. The first, smaller peak occurred at beam deformations between 0.12 and 0.17 mm in conjunction with the opening of a vertical crack in the concrete originating from the tension zone (refer to Fig. 8(b)). The average value of maximum force at the smaller peak among all specimens F_{cr} was 1004 N, with a relative standard deviation (RSD) value of 5.3%.

After the first peak, the force decreased slightly, but then increased again until the specimen failed. The average value of the ultimate force F_u was 2563 N, with an RSD value of 16.9%. In all experiments, the failure occurred due to the destruction of concrete in the zone of its contact with

the reinforcement, while the reinforcement itself remained intact. The relatively low strength of the concrete on the first day and the small width of the concrete cover are among the possible reasons for such behavior.

Beam calculation

Because the specimens in the bending test exhibited flexural failure, the maximum moment of resistance of the cross

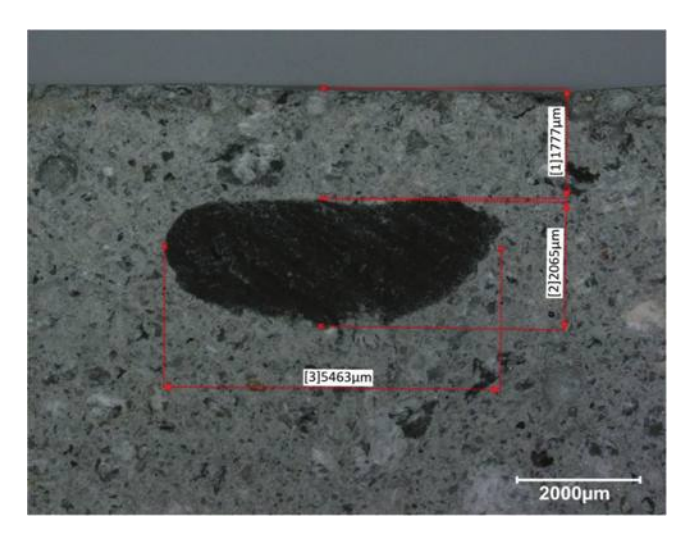


Fig. 7—Concrete cover formed in central part of slab after filling with flowable concrete.

section before cracking M_{cr} can be calculated based on the test results using Eq. (1)

$$M_{cr} = \frac{F_{cr} \cdot l_s}{4} = 30.1 \text{ N} \cdot \text{m}$$
 (1)

where F_{cr} is the maximum value of the applied force required to initiate concrete cracking, obtained during experiments; and l_s is the span of a specimen in the bending test equal to 0.12 m (refer to Fig. 9, left).

The width w of the specimens in the bending test was 38 mm, which is also the spacing between adjacent strands of the reinforcement mesh used. Therefore, it can be assumed that the wider beam, which has the same height h_s of 34 mm and is made using the same reinforcement mesh as the samples in the bending test, consists of several segments—beams with cross sections equal to those of the specimens tested in the bending test (refer to Fig. 9, right). In this case, the maximum moment that can act on each of these segments before cracking will be equal to the value of M_{cr} obtained previously.

Assuming that this beam is used as a lintel, in which case the fresh concrete laid on top of the beam would exert a uniformly distributed load, M_{cr} can be represented as follows

$$M_{cr} = \frac{q_{cr} \cdot l_b^2}{8} \tag{2}$$

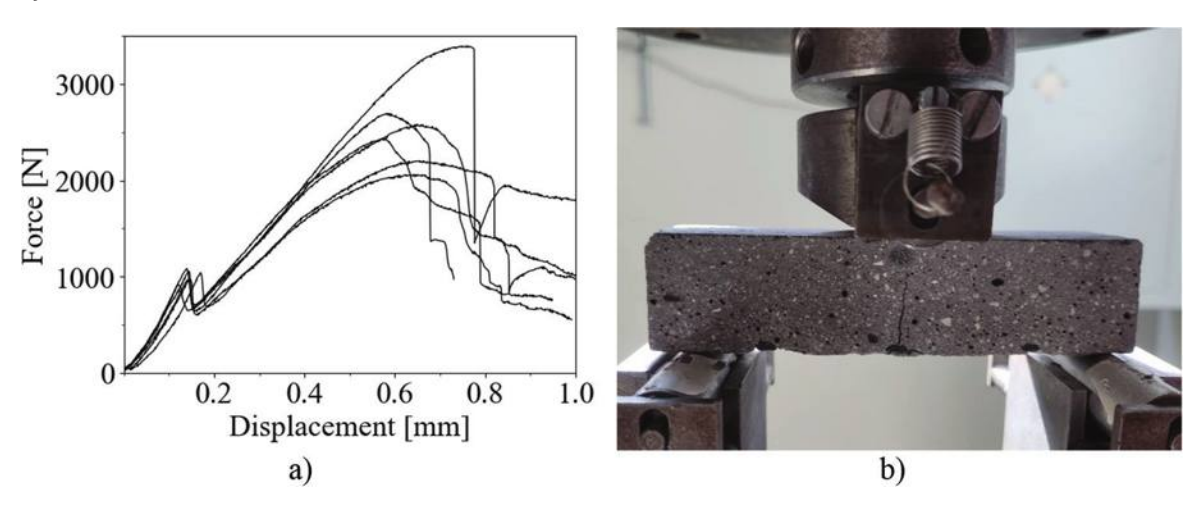


Fig. 8—(a) Results of bending test; and (b) crack formation in tensile zone of specimen during test.

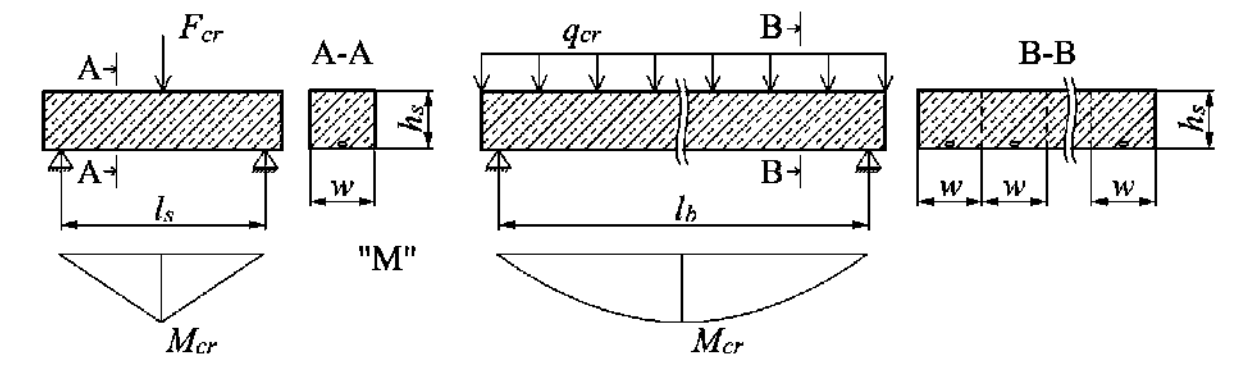


Fig. 9—Schemes of bending test (left); and lintel loaded with fresh printed concrete (right), with corresponding moment diagrams.

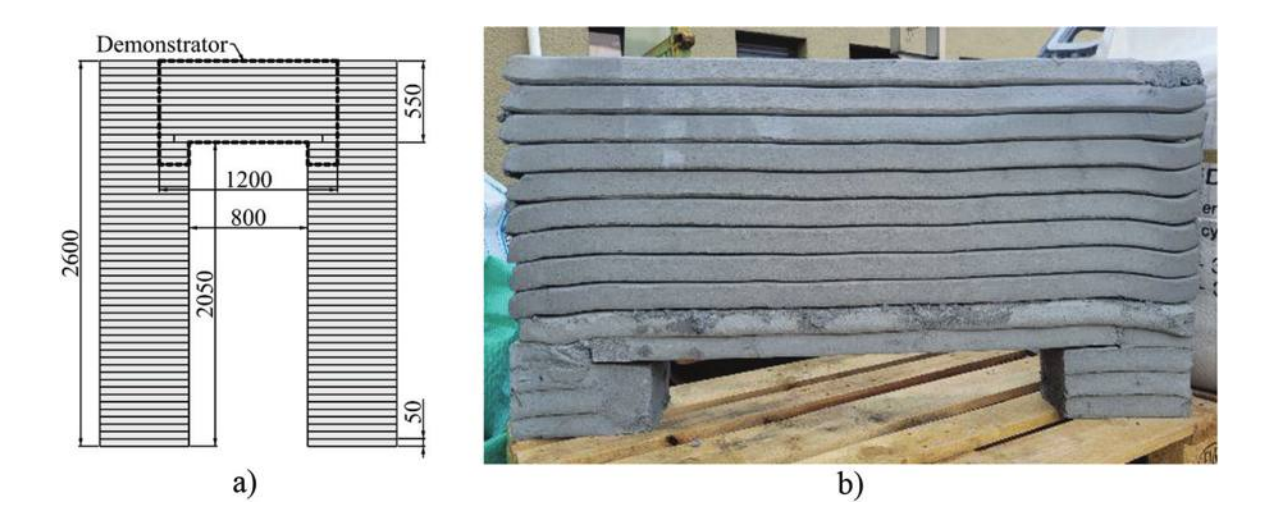


Fig. 10—(a) Scheme of doorway; and (b) manufactured demonstrator. (Note: Units in mm.)

where l_b is the span of the beam; and q_{cr} is the maximum value of a uniformly distributed load on a segment of the lintel with a width w required to initiate cracking.

Assuming the span l_b equal to 0.8 m, which is a typical width of a window or a door, it is possible to find q_{cr} , which will be equal to 376 N/m. This value also can be expressed using Eq. (3)

$$q_{cr} = \rho \cdot g \cdot w \cdot h_{cr} \tag{3}$$

where ρ is the concrete density, which is 2108 kg/m³ for the concrete used; g is the gravitational acceleration equal to 9.81 m/s²; and h_{cr} is the maximum height of concrete that can be deposited above the lintel without the formation of cracks in it. Using Eq. (3), the h_{cr} can be obtained equal to 0.48 m.

Similarly, the ultimate height of concrete h_u required for failure of a lintel can be calculated. To do this, in Eq. (1), the ultimate force F_u required for the beam fracture should be used instead of F_{cr} . In this case, the maximum moment of resistance of the section M_u will be 76.9 N·m and the maximum allowable height of the fresh concrete h_u will be 1.22 m.

It can be concluded that a reinforced lintel, fabricated using the proposed method and having a height of 34 mm, can only withstand a load from 0.48 m of fresh concrete placed above it without cracking 1 day after its production. This may be sufficient for buildings with relatively low ceiling heights, but the presented calculation is a very conservative one. With the continuing stiffening and hardening of concrete printed over the lintel, its weight will be increasingly redistributed to the walls next to the opening, thereby considerably reducing the load on the lintel. Hardened layers of concrete printed above the lintel will also redistribute the loads from the next floor or roof.

Demonstration of application

To demonstrate the feasibility of the proposed method of creating load-bearing horizontal elements for and with 3DCP technology, a full-size demonstrator was created, representing a lintel over a doorway (refer to Fig. 10).

A beam with a length of 1 m and a cross section of 150 x 50 mm was fabricated by 3DCP on a textile mesh laid on the printing bed and used as a lintel. It was placed on two printed concrete supports so that the resulting span was 800 mm. Ten layers of concrete were printed on top of this beam, each layer 50 mm high. No deformations or damages to the lintel were observed during or after the printing of layers above it.

SUMMARY AND CONCLUSIONS

This paper proposes new methods for fabricating reinforced beams and slabs for three-dimensional (3-D)-printed concrete structures. These methods are outperforming all existing approaches because they enable the production of load-bearing horizontal elements of free geometry quickly and directly at the construction site. According to the technology proposed, the elements can be reinforced either by placing a reinforcement mesh between the layers, or by depositing concrete directly on a textile mesh laid on the printed surface. The paper at hand focused on the second approach, which had not been investigated as of yet.

For this purpose, a beam and a slab were produced using the proposed method. The examination of the produced slab showed that the depth of the concrete cover obtained after placing a flowable concrete in top of the mesh reached approximately 1.8 mm. While the results of tests on specimens made from the slab indicated the possibility that the protective layer of concrete created was insufficient to make full use of the reinforcement's mechanical properties, the performance of the slab has been proved fully satisfactory for the purpose of creating horizontal supports such as lintels. The calculations based on the bending test results showed that the bending strength of a beam produced using the proposed technology and having a height of 34 mm only is absolutely sufficient for some applications on the first day after its fabrication.

To demonstrate the feasibility of the proposed technology, a full-size demonstrator, representing a lintel over an 800 mm wide doorway, was successfully fabricated and tested by printing concrete layers upon it.

AUTHOR BIOS

Egor Ivaniuk is a Doctoral Researcher at Technische Universität Dresden, Dresden, Germany, where he received his MS in the advanced computational and civil engineering structural studies (ACCESS) program. His research interests include three-dimensional (3-D) printing of concrete, strain-hardening cementitious composites, and textile reinforcement.

ACI member Viktor Mechtcherine has served as a Professor and Director of the Institute of Construction Materials, Faculty of Civil Engineering at Technische Universität Dresden, since 2006. He received ACI's Wason Medal for Materials Research in 2017.

ACKNOWLEDGMENTS

This paper is a part of the first author's PhD dissertation. The authors would like to thank the German Research Foundation (Deutsche Forschungsgemeinschaft – [DFG]) for the funding of the project "Adaptive Concrete Diamond Construction (ACDC)," project number 424057211, within the Priority Program "Adaptive Modularized Constructions Made in Flux: Precise and Rapid Building" (SPP 2187).

REFERENCES

- 1. Buswell, R. A.; da Silva, W. R. L.; Bos, F. P.; Schipper, H. R.; Lowke, D.; Hack, N.; Kloft, H.; Mechtcherine, V.; Wangler, T.; and Roussel, N., "A Process Classification Framework for Defining and Describing Digital Fabrication with Concrete," *Cement and Concrete Research*, V. 134, No. 8, Aug. 2020, p. 106068. doi: 10.1016/j.cemconres.2020.106068
- 2. Mechtcherine, V.; Bos, F. P.; Perrot, A.; Leal da Silva, W. R.; Nerella, V. N.; Fataei, S.; Wolfs, R. J. M.; Sonebi, M.; and Roussel, N., "Extrusion-Based Additive Manufacturing with Cement-Based Materials Production Steps, Processes, and their Underlying Physics: A Review," *Cement and Concrete Research*, V. 132, June 2020, p. 106037. doi: 10.1016/j.cemconres.2020.106037
- 3. PERI 3D Construction GmbH, "3D Printing Solutions," Weißenhorn, Germany, https://www.peri3dconstruction.com/en. (last accessed Jan. 26, 2024)
- 4. Apis Cor, Melbourne, FL, https://www.apis-cor.com/. (last accessed Jan. 26, 2024)

- 5. Anton, A.; Jipa, A.; Reiter, L.; and Dillenburger, B., "Fast Complexity: Additive Manufacturing for Prefabricated Concrete Slabs," *Second RILEM International Conference on Concrete and Digital Fabrication: Digital Concrete 2020*, 2020, pp. 1067-1077.
- 6. Carneau, P.; Mesnil, R.; Roussel, N.; and Baverel, O., "An Exploration of 3D Printing Design Space Inspired by Masonry," *Proceedings of the IASS Annual Symposium 2019 Structural Membranes 2019: Form and Force*, Oct. 2019, Barcelona, Spain, pp. 1-10.
- 7. SQ4D, Patchogue, NY, https://www.sq4d.com/. (last accessed Jan. 26, 2024)
- 8. Twente Additive Manufacturing, Nelson, BC, Canada, https://www.twente-am.com/. (last accessed Jan. 26, 2024)
- 9. Wangler, T.; Lloret, E.; Reiter, L.; Hack, N.; Gramazio, F.; Kohler, M.; Bernhard, M.; Dillenburger, B.; Buchli, J.; Roussel, N.; and Flatt, R., "Digital Concrete: Opportunities and Challenges," *RILEM Technical Letters*, V. 1, 2016, pp. 67-75. doi: 10.21809/rilemtechlett.2016.16
- 10. Mechtcherine, V.; Nerella, V. N.; Will, F.; Näther, M.; Otto, J.; and Krause, M., "Large-Scale Digital Concrete Construction CONPrint3D Concept for On-Site, Monolithic 3D-Printing," *Automation in Construction*, V. 107, Apr. 2019, p. 102933. doi: 10.1016/j.autcon.2019.102933
- 11. Alrshoudi, F., "Textile-Reinforced Concrete Versus Steel-Reinforced Concrete in Flexural Performance of Full-Scale Concrete Beams," *Crystals*, V. 11, No. 11, 2021, p. 1272. doi: 10.3390/cryst11111272
- 12. TUDALIT e.V, "Reinforcement with Textile Concrete According to the General Building Supervisory Approval (abZ) Z-31.10-182," 2018.
- 13. Mechtcherine, V., and Nerella, V. N., "Integration der Bewehrung beim 3D-Druck mit Beton," *Beton- und Stahlbetonbau*, V. 113, No. 7, 2018, pp. 496-504. doi: 10.1002/best.201800003
- 14. Khoshnevis, B., "Automated Construction by Contour Crafting Related Robotics and Information Technologies," *Automation in Construction*, V. 13, No. 1, 2004, pp. 5-19. doi: 10.1016/j.autcon.2003.08.012
- 15. Wang, W.; Konstantinidis, N.; Austin, S.; Cavalaro, S.; and Cecinia, D., "Flexural Behaviour of AR-Glass Textile Reinforced 3D Printed Concrete Beams," Second RILEM International Conference on Concrete and Digital Fabrication, 2020, pp. 728-737.
- 16. Nerella, V. N., Näther, M., Iqbal, A.; Butler, M.; and Mechtcherine, V., "Inline Quantification of Extrudability of Cementitious Materials for Digital Construction," *Cement and Concrete Composites*, V. 95, Mar. 2019, pp. 260-270. doi: 10.1016/j.cemconcomp.2018.09.015

Title No. 121-S18

Prediction of Tensile Properties of Ultra-High-Performance Concrete Using Artificial Neural Network

by Amjad Y. Diab and Anca C. Ferche

A multilayer perceptron artificial neural network (MLP-ANN) was developed to calculate the cracking stress, tensile strength, and strain at tensile strength of ultra-high-performance concrete (UHPC), using the mixture design parameters and strain rate during testing as inputs. This tool is envisioned to provide reference values for direct tension test results performed on UHPC specimens, or to be employed as a framework to determine the tension response characteristics of UHPC in the absence of experimental testing, with minimal computational effort to determine the tensile characteristics. A database of 470 data points was compiled from 19 different experimental programs with the direct tensile strength, cracking stress, and strain at tensile strength corresponding to different UHPC mixtures. The model was trained, and its accuracy was tested using this database. A reasonably good performance was achieved with the coefficients of determination, R², of 0.91, 0.81, and 0.92 for the tensile strength, cracking stress, and strain at tensile strength, respectively. The results showed an increase in the cracking tensile stress and tensile strength for higher strain rates, whereas the strain at tensile strength was unaffected by the strain

Keywords: artificial neural network (ANN); cracking stress; machine learning; multilayer perceptron (MLP); tensile strength; ultra-high-performance concrete (UHPC).

INTRODUCTION

Ultra-high-performance concrete (UHPC) is widely recognized as a cementitious composite with a discontinuous pore structure, incorporating steel fiber reinforcement.¹ UHPC is attracting increased use due to its outstanding material properties, such as high compressive strength, high tensile strength, excellent crack control properties, selfconsolidating workability, and exceptional durability in aggressive environments.^{2,3} These characteristics make it possible, in some cases, to significantly reduce or eliminate conventional reinforcement and allow the use of thinner concrete sections in practical applications.⁴ As a result, UHPC becomes an advantageous choice in highperformance applications, such as long-span precast pretensioned elements, bridge decks, offshore platforms, nuclear power plant buildings, and blast- and impact-resistant structures.5

UHPC was introduced for the first time in 1994, 6,7 and it differs from ordinary concrete in various aspects, including low water-cement ratio (w/c), the incorporation of silica fume with optimized quantities of portland cement, fine aggregates, and the absence of coarse aggregates. Recent efforts have concentrated on the formulation of UHPC mixtures that are more economical and have enhanced sustainability characteristics, $^{9-17}$ resulting in the incorporation of

additional supplementary cementitious materials (SCMs) within the UHPC mixture, such as fly ash (FA), granulated blast-furnace slag (GBFS), metakaolin, and the use of limestone powder. ¹³⁻¹⁶

The incorporation of fiber reinforcement in the UHPC mixture, such as steel or propylene fibers, results in postcracking ductility and enhanced energy absorption capacities that are not superior to conventional concrete. As a result, UHPC provides a reliable solution for cases when high strain rates are generated by impact loads, blast, and seismic loading.¹⁸ While the strain-rate sensitivity of conventional concrete is known to be strongly dependent on the quality of the concrete mixture, 19,20 for fiber-reinforced concrete, the strain-rate sensitivity is highly influenced by additional factors, such as fiber volume percentage, fiber type, and fiber bond strength.^{21,22} Several studies examined the tensile behavior of various UHPC mixtures at varying strain rates²¹⁻²⁶ and shed light on its influence on mechanical properties such as the cracking stress, tensile strength, and the strain at tensile strength. The findings demonstrate that UHPC has a complex behavior, depending on the strain rate, and the mixture composition in terms of SCMs, fiber reinforcement type, and the overall mixture design.

Numerous empirical models were developed to estimate the dynamic increase factor for UHPC, 27,28 all indicating that the response of UHPC is even more sensitive to the strain rate than conventional concrete due to the presence of the fiber reinforcement. 29 In addition, the low w/c and inclusion of SCMs promote the formation of a denser structure, 30,31 which in turn increases strain-rate sensitivity according to the Stefan effect. 32

The direct tension tests, splitting tensile tests, and flexural tests are the three most commonly used testing procedures for characterizing the behavior of UHPC in tension. 32-34 The experimentally measured tensile strength values vary depending on the tensile stress distribution and boundary conditions corresponding to these different tests. 35 Among them, the direct tension test presents the advantage of a uniform stress condition and the ability to record the complete stress-strain response before and after cracking. As such, in terms of insight for material characterization, the authors view the direct tension test as superior compared to

ACI Structural Journal, V. 121, No. 2, March 2024.

MS No. S-2022-248.N1, doi: 10.14359/51740245, received June 29, 2023, and reviewed under Institute publication policies. Copyright © 2024, American Concrete Institute. All rights reserved, including the making of copies unless permission is obtained from the copyright proprietors. Pertinent discussion including author's closure, if any, will be published ten months from this journal's date if the discussion is received within four months of the paper's print publication.

the splitting tensile and flexural tests. Nevertheless, it presents well-known challenges pertaining to the execution of the test, especially, ensuring a uniform uniaxial stress condition before and after cracking.

Typically, UHPC mixtures are classified according to their post-cracking stress-strain response into strain-softening or strain-hardening materials. Figure 1 displays typical strain-softening and strain-hardening behavior. The cracking stress (f_{cr}) is defined as the stress at which the first crack occurs, the tensile strength (f_t') is defined as the maximum tensile stress, and the strain at tensile strength (ε_t), refers to the strain corresponding to f_t' . The work presented herein was performed to provide values for the cracking stress, tensile strength, and the strain at peak stress of UHPC mixtures tested under different strain rates, based on information related to the mixture design.

Overall, the tensile response of UHPC is highly influenced by numerous factors, including the w/c, SCMs-to-cement ratio, high-range water-reducing admixture-to-cement ratio, and fiber volume and type, in addition to the tensile strain rate. These factors were observed from previous experimental programs to have a higher impact on the tensile strength than the compressive strength of UHPC; consequently, the empirical approaches commonly used to estimate the tensile strength of conventional concrete as a function of the compressive strength only would not be adequate for UHPC.37 For example, the fiber volume of a mixture was shown to have a higher degree of influence on the tensile strength than the compressive strength.²⁵⁻²⁷ At the same time, in the design of structural elements cast with UHPC, the tensile strength of the UHPC material is usually considered as a contributing factor to the strength of the element. Therefore, there is an urgent need for a reliable approach to determine the tensile strength of UHPC. The work presented herein is an effort toward this endeavor. Previously, multilayer perceptron artificial neural network (MLP-ANN) models have been effectively used in a variety of UHPC applications, including the prediction of the mechanical properties of UHPC mixtures, such as their compressive strength, modulus of elasticity, flowability, and porosity.³⁸⁻⁴² The goal of this research was to develop an MLP-ANN framework for calculating the cracking stress, tensile strength, and the strain at tensile strength of UHPC, using as inputs the parameters found to be influential, as previously mentioned. This tool is envisioned to provide reference values for direct tension test results performed on UHPC, or to be employed as a framework to determine the tension response characteristics of UHPC in the absence of experimental testing.

RESEARCH SIGNIFICANCE

In contrast to structural elements cast with conventional concrete, the tensile strength of UHPC is typically a design factor contributing to the strength of UHPC members. Determining the tensile strength of UHPC, however, poses several challenges and introduces a degree of uncertainty that is not yet well understood. An MLP-ANN model was developed for calculating the cracking stress, tensile strength, and the strain at the tensile strength of UHPC using as input information pertaining to the mixture design. To the

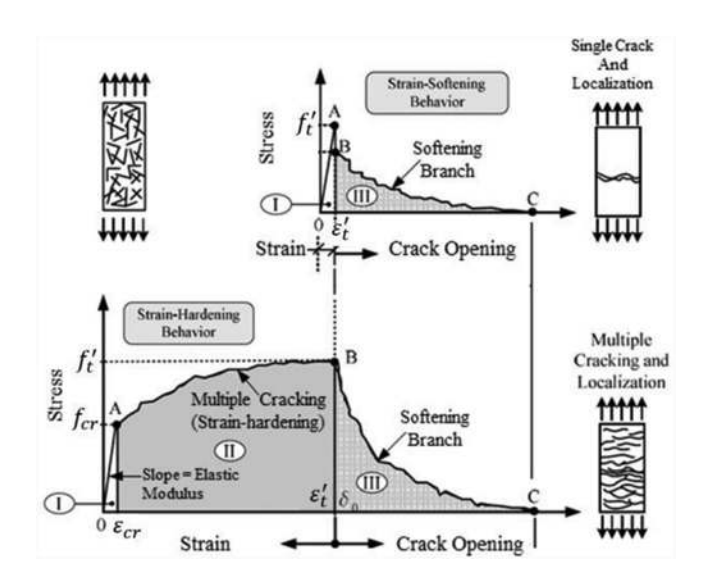


Fig. 1—Typical UHPC stress-strain response in tension: (a) strain-softening behavior; and (b) strain-hardening behavior.³⁶

authors' best knowledge, no previous studies address the prediction of the aforementioned tensile properties of UHPC using MLP-ANN. The authors believe that the procedures proposed in this study will be of general interest to the practicing engineers and standards committees, with the goal of accelerating the widespread adoption of UHPC components in structural applications. The MLP-ANN presented herein was developed based on a database of 470 data points, and it is hoped to be used to provide a baseline for the experimentally determined tensile properties in an effort to reduce the inherent uncertainty associated with tensile testing, or to be employed as a framework to establish the tension response characteristics of UHPC in the absence of experimental testing.

ARTIFICIAL NEURAL NETWORKS

Overview

An artificial neural network (ANN) is a data processing paradigm inspired by the biological neural system. This paradigm is reliant on the shape of the information processing system. ANNs have a mechanism for extracting interconnections from complex data and can be used to discover patterns and identify trends that would typically be obscured. ANN is a type of nonlinear function approximator that creates mapping between the input and output parameters. The network uses learning capabilities derived from the given inputs, Making this approach ideal for predicting the UHPC tensile properties due to the relatively large number of input parameters controlling these properties and the nonlinear relationship between the given inputs and outputs. A flowchart representing the general design and development procedure for an ANN is shown in Fig. 2.

The perceptron is the most basic type of neural network architecture and is being used in numerous advanced neural network applications. It is composed of multiple weighted connections and an activation function that connects the input and output layers. 45,46 The activation function decides whether to activate the neuron based on the input values and their weights, as explained in the following section. The

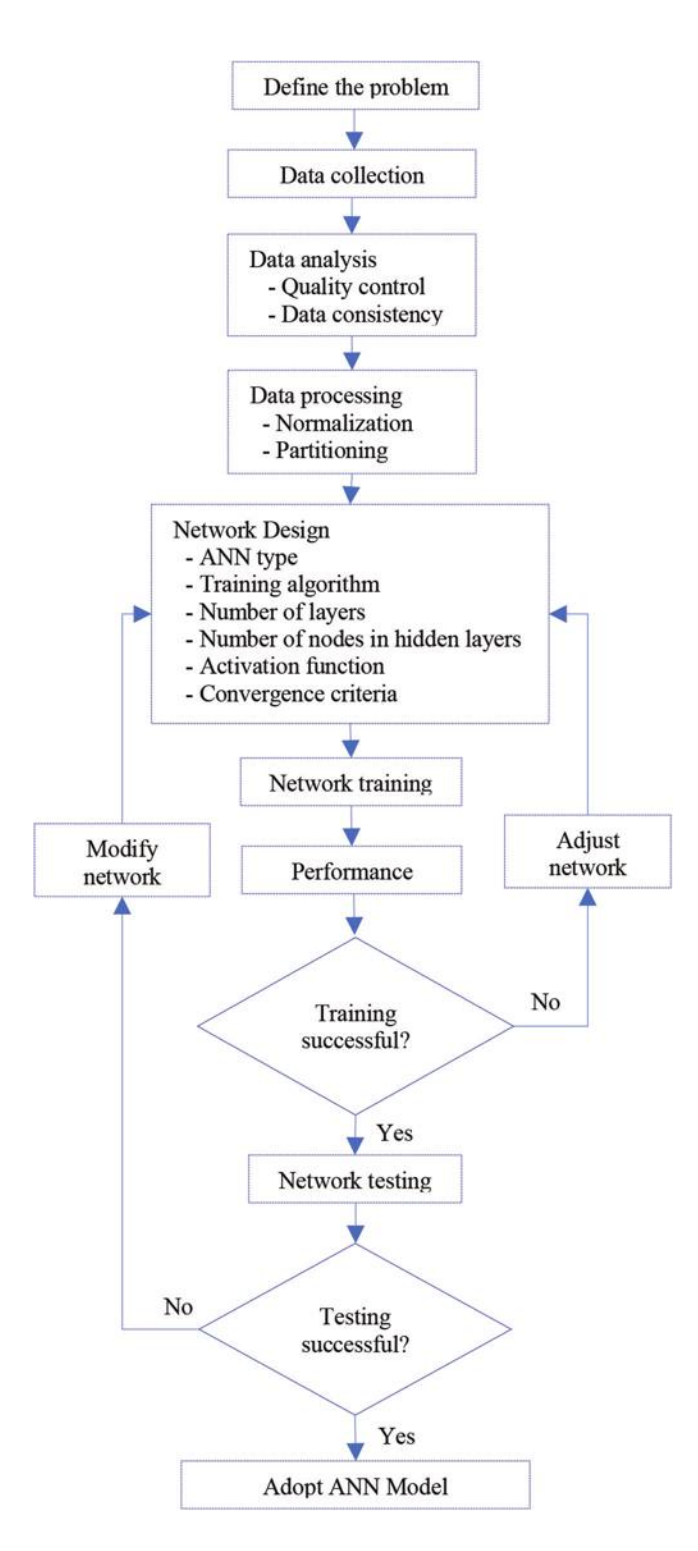


Fig. 2—ANN design and development procedure flowchart.

basic mechanism of the artificial neuron used in ANNs is shown in Fig. 3.

Feed-forward networks and recurrent networks are the two main types of ANNs. The MLP-ANN is one of the most widely used feed-forward ANNs, ⁴⁷ and it represents a modification of Rosenblatt's perceptron model that includes hidden layers between the input and output layers. The goal of the architecture is to optimize the number of layers and neurons in each layer so that the network can solve the regression or classification problem with the given parameters. ⁴⁸ Figure 4 shows the input layer variables, hidden layers, and output

layer variables in a schematic diagram of the preliminary layout of the MLP-ANN structure used in this study. The algorithm was developed using the Python programming language.

Activation functions

The challenge with employing neural network architectures consists of the difficulty in designing algorithms that successfully learn patterns in data sets. Numerous strategies were explored to increase the effectiveness of these learning algorithms, such as normalizing the data points and optimizing the activation functions used in the ANN. An activation function determines whether to activate the given neuron, providing an output depending on the input values multiplied by their corresponding weights.

The hyperbolic tangent, sigmoid functions, and the rectified linear unit function (ReLU) are some of the most commonly used activation functions. The ReLU has been shown to be the most effective activation function for both regression and classification purposes.⁴⁹ The graphical representation of the ReLU activation function is depicted in Fig. 5; the function receives modified inputs, multiplying by their respective weights and adding the bias values. Finally, the neuron outputs a value depending on the weighted values of the inputs. The benefit of using the ReLU consists of its capacity to discard neurons with negative weights and biases in the learning process, allowing for a faster and more precise learning process. The ReLU function was employed as the activation function for the hidden layers in this study, whereas a linear activation function was used for the output layer.

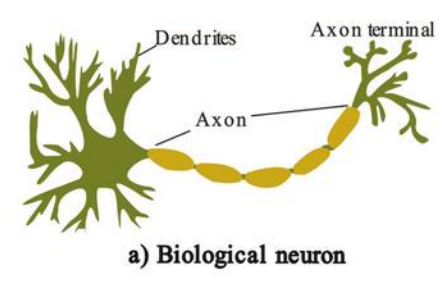
Training model

The ANN's training phase is critical, and it represents a function minimization problem in which an error function is minimized, assisting in the selection of the optimal weights. Rumelhart et al.⁵⁰ developed one of the most widely used training algorithms, the backpropagation method for neural networks, in which the neural network procedure repeatedly customizes the weights of the connections in the network to minimize the difference between the actual output vector (experimentally measured tensile properties) and the predicted output vector (predicted tensile properties).

The backpropagation technique analyzes the information in two steps: initially, in the forward pass, it calculates the outputs and the error at the output layer. This is followed by the backward pass, as it updates the weights of the same units using the error at the output layer. This technique is repeated until the error converges to a minimum value, at which point the cost function is specified. For convergence, several optimization techniques are generally applied, including the schematic gradient descent ⁵¹⁻⁵³ and the Adam optimizer. ⁵⁴ In this work, the Adam optimizer was used as the optimization algorithm.

Model performance evaluation

After the training phase, the accuracy of the model was verified with respect to calculating the cracking stress, the tensile strength, and the strain at the tensile strength. The root-mean-square error (RMSE) and coefficient of determination (R^2) were used as statistical parameters to determine the accuracy of the predictions of the model, calculated as shown in Eq. (1) and (2)



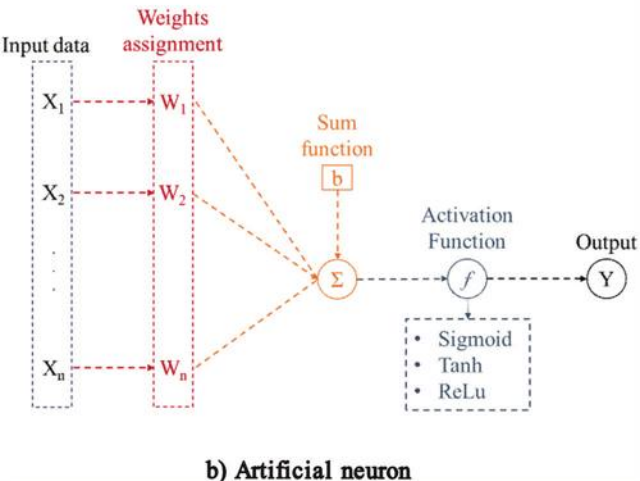


Fig. 3—Mechanism of artificial neuron depicting biological neuron.

RMSE =
$$\sqrt{\frac{\sum_{i=1}^{n} (Y_{pred} - Y_{ref})^2}{n}}$$
 (1)

$$R^{2} = 1 - \frac{\sum_{i=1}^{n} (Y_{pred} - Y_{ref})^{2}}{\sum_{i=1}^{n} (Y_{ref})^{2}}$$
 (2)

where n is the total number of data points; Y_{pred} is the calculated value; and Y_{ref} is the experimental value.

The RMSE is one of the most frequently used error-index statistics.55 RMSE compares experimental and predicted values and evaluates the square root of the mean residual error, indicating the error in units of the constituent of interest. The optimum RMSE value is zero, indicating a perfect match. The coefficient of determination (R^2) compares the accuracy of the model to that of a basic benchmark model, where the prediction is the mean of all samples.⁵⁶ The R^2 statistics are based on linear relationships between experimental and predicted values and may produce biased findings when the relationship is not linear or when the database contains numerous outliers. The value of R^2 is unity when there is equality between the observed and predicted values. A combination of the performance indicators described previously can provide an impartial estimate of the neural network models' prediction ability.

DATABASE

Whereas recently, the focus in the literature has been primarily on the prediction algorithms in machine learning applications and the optimization of these algorithms, the importance of a dependable, representative, and sufficient database is oftentimes neglected, even though the database characteristics have a crucial role in developing a successful model. Sufficient data size is regarded as data that cover

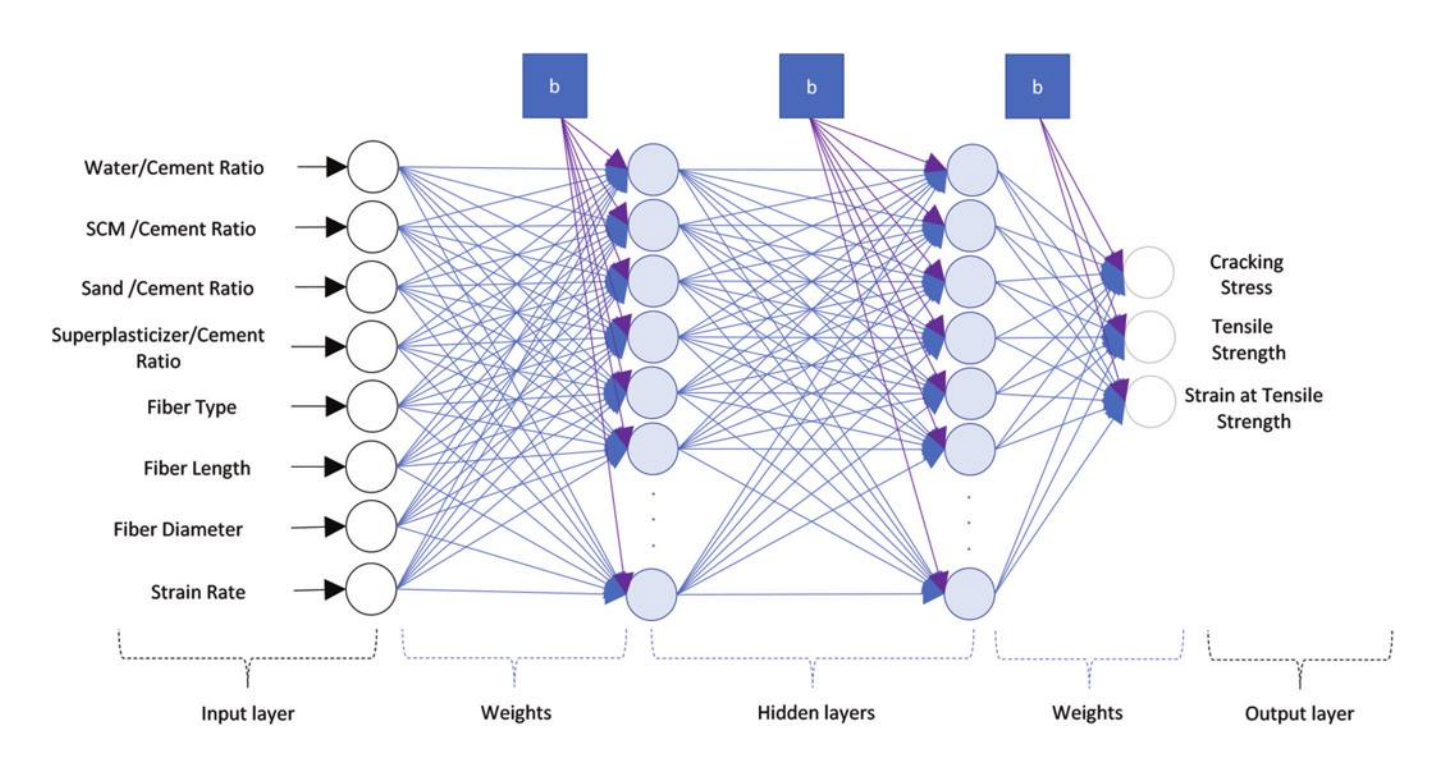


Fig. 4—Schematic representation of MLP-ANN.

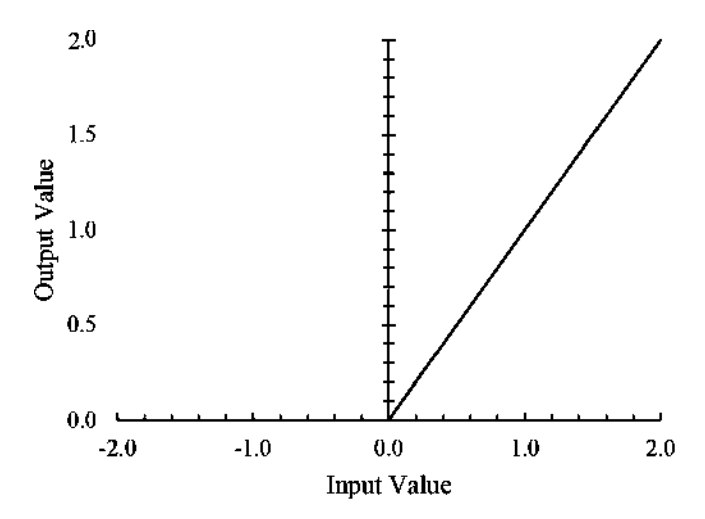


Fig. 5—Graphical representation of ReLU activation function.

all possible parameter combinations that determine the outputs the model is to predict, allowing the entire problem to be effectively simulated. A reliable database is especially important in the case of experimental databases, which frequently exhibit a considerable variance between results due to both unforeseen errors that were not accounted for while planning the experiment and inherent biases while implementing the experiment.

A database of 470 data points was compiled from 19 different experimental programs with the direct tensile strength, ^{18,25,26,57-72} cracking stress, and strain at the tensile strength of UHPC mixtures. These values were obtained from tests conducted on UHPC specimens that were tested under uniaxial tension at different strain rates. Table A1 in the Appendix summarizes the specimens compiled from the literature. Using this database, each input training vector was assigned 16 parameters, summarized in Table 1. The output vector includes the value of the tensile strength, cracking stress, and the strain at the tensile strength. The range, mean, and standard deviation values of the parameters included in the database are listed in Table 1.

Anonlinear relationship was found between the fiber aspect ratio (fiber length/fiber diameter) and the UHPC mechanical properties characterizing the tensile response. This is primarily due to the fact that the fiber diameter has a more pronounced influence compared to the fiber length. ^{29,66,72} For example, Park et al. ⁷⁰ tested UHPC specimens cast with fibers having the same aspect ratio but different lengths and diameters and observed different tensile responses. As such, in this study, the fiber aspect ratio was disaggregated to capture the fact that the length and diameter of the fibers influence the tensile response differently and, therefore, need to be assigned different weights in the MLP-ANN model.

For the mixtures that contained fibers of the same type but with different lengths or diameters, a weighted average length or diameter was set as representative for the sample. The number of threads of the twisted fibers, the number of bends on hooked fibers, and the ultimate tensile strength of the fibers were not considered as parameters in the prediction model, as observations from experimental testing in the literature indicate they have negligible effects on the tensile strength properties. ^{66,72} Following similar reasoning, the influence of the curing regime and duration were also neglected in the formulation of the model, as were the constituents of the fine aggregate component, such as silica flour and glass sand.

The reliability of this database stems from the fact that its data points are based on experimental results reported in the literature rather than simulated values, which can often be subjective based on the models selected. A frequency assessment conducted on the database showed that the input parameters captured a reasonably acceptable range for the model to be accurate in predicting the dependent variables. This is illustrated in Fig. 6, which shows a pairplot distribution graph, constructed using Python's seaborn module. 73,74 Figure 6 allows the visualization of the given data such that the interrelationships between the different input and output parameters are illustrated. In addition, the range of the collected data is also displayed. For example, for the collected database, the average tensile strength of the UHPC mixtures is approximately 10 MPa and the w/c is approximately 0.2. These ranges can also help identify the limitations of the current database—for instance, more data are needed to fully analyze the effect of FA on the tensile properties of UHPC. This is illustrated by the frequency distribution plot for FA, with the majority of the data points having no FA in the mixture design. Only a minor portion of the data points have FA, with a percentage of up to 25% replacement. Overall, Fig. 6 illustrates that the constructed database covers a wide range of parameters that are used in UHPC mixtures. The relationships between the input and output parameters can also be visualized from Fig. 6. For example, for the tensile strength, analyzing the plot including the w/cand tensile strength, an inverse correlation can be observed. On the other hand, a positive correlation is revealed between the strain rate and tensile strength.

It should be noted that some of the concrete variables can be dependent on each other. Hence, the correlation coefficients between all possible variables have been derived and are presented in Fig. 7. Positive unity indicates a perfect positive correlation, negative unity shows a perfect negative correlation, and zero shows no correlation between the parameters. As expected, there is a strong positive correlation, with values higher than 0.75 between the strain rate and the cracking stress and tensile strength, whereas there is no clear correlation between the strain rate and the strain at tensile strength. In addition, the preliminary analysis indicates that the polyethylene fibers have a more pronounced influence on the strain at tensile strength of UHPC, compared to the steel fibers.

As part of data processing, outliers were identified and removed from the database. For the experimental studies that performed tests on multiple specimens of the same mixture design, the standard deviation and the mean values were calculated for the tensile properties. The experimental data with values that were higher or lower than twice the standard deviation difference from the mean value were considered outliers and were removed accordingly.

Table 1—Descriptive statistics of input and output variables in database

Parameter	Symbol	Units	Category	Min.	Mean	Max.	Standard deviation
Water-cement ratio	w/c	_	Input	190	22.2	35	4.25
Fly ash-cement ratio	FA/C	_	Input	0.0	1.5	25	5.4
Sand-cement ratio	Sa/C	_	Input	12.5	134	164	22.2
Silica fume-cement ratio	SF/C	_	Input	0.0	23.6	39	8.0
GGBFS-cement ratio	BFS/C	_	Input	0.0	5.0	107	19.5
High-range water-reducing admixture	S/B	_	Input	0.5	3.6	6.7	2.6
Straight fiber, %*	SF	_	Input	0.0	1.0	3	0.9
Straight fibers length	SFL	mm	Input	0.0	11.3	30	9.2
Straight fibers diameter	SFD	mm	Input	0.0	0.1	0.40	0.1
Hooked fiber, %*	HF	_	Input	0.0	0.26	3.6	0.6
Hooked fibers length	HFL	mm	Input	0.0	7.1	62.0	14.3
Hooked fibers diameter	HFD	mm	Input	0.0	0.1	0.9	0.2
Twisted fiber, %*	TF	_	Input	0.0	0.4	3.0	0.8
Twisted fibers length	TFL	mm	Input	0.0	4.9	30.0	9.6
Twisted fibers diameter	TFD	mm	Input	0.0	0.06	0.3	0.1
Polyethylene fibers, %*	PE	_	Input	0.0	0.2	2.1	0.6
Tensile strain rate	SR	s^{-1}	Input	0.00006	18.5	161	39.4
Tensile strength	TS	MPa	Output	3.8	17.3	68.1	9.6
Cracking stress	CTS	MPa	Output	4.8	11.3	32.7	4.8
Strain at tensile strength	STS	×10 ⁻³	Output	0.2	11.8	80	13.2

^{*}Fibers are provided by percentage of fiber volume to entire mixture volume.

Note: C is percentage relative to cement weight; B is percentage relative to total binder weight; 1 mm = 0.039 in.; 1 MPa = 145 psi.

Data normalization

Following the removal of outliers from the database, the next stage was data normalization. In general, the input and output data have different identities with no or minimal similarities. Data normalization removes the risk of neural network bias toward various identities. To prevent difficulties connected with the learning rate of the MLP-ANN, the min-max normalization method was used in this work⁷³; data scaling between 0 and 1 was performed.

Data leakage

Data leakage is one of the main challenges facing machine learning applications⁷⁵; it occurs when the data used to train a machine learning algorithm contains the information about the validation model that might not be available in the practical applications of the model. Data leakage can cause the machine learning algorithm to show good prediction results in both the test and training data sets but perform poorly in practical prediction applications.

There are mainly two types of data leakage ⁷⁶: feature and train-test leakage. Feature leakage is common in classification problems and occurs when one of the parameters used includes data that will not be available in the practical applications. Train-test leakage is more common in regression problems and occurs when training data has leaked information of the test data; this can be avoided by removing the randomization in sectioning the test and train ing sets to ensure that the algorithm is not trained on data similar to

the one the algorithm is to be tested on. Train-test leakage was avoided by using different experimental programs in the training and testing phases.

Data fitting

Figure 8 depicts the three possible outcomes for data fitting. Underfitting occurs when the learning algorithm is unable to find a solution that fits the training examples well, while overfitting occurs when the learning algorithm finds an excellent solution for the training data but predicts unusual results in terms of new data other than the data for which it was trained. Overfitting can be a major issue in the machine learning process as it hinders the ability to generalize models. This can be caused due to a variety of reasons, such as presence of noise in the data set, insufficient data used for the training phase, or overly complex prediction algorithms. 77,78

To avoid overfitting in the developed MLP-ANN model, the data was partitioned into two sets: training and test data sets. The training data set included 80% of the total data points and was used to aid the model in learning the prediction patterns, while the test data set comprised 20% of the total data. Underfitting would show the model having low accuracies in both the training and test data sets, while overfitting would show the model having high accuracy in the training phase with low accuracy in the test phase. Neither issue is observed for the model developed in this study.

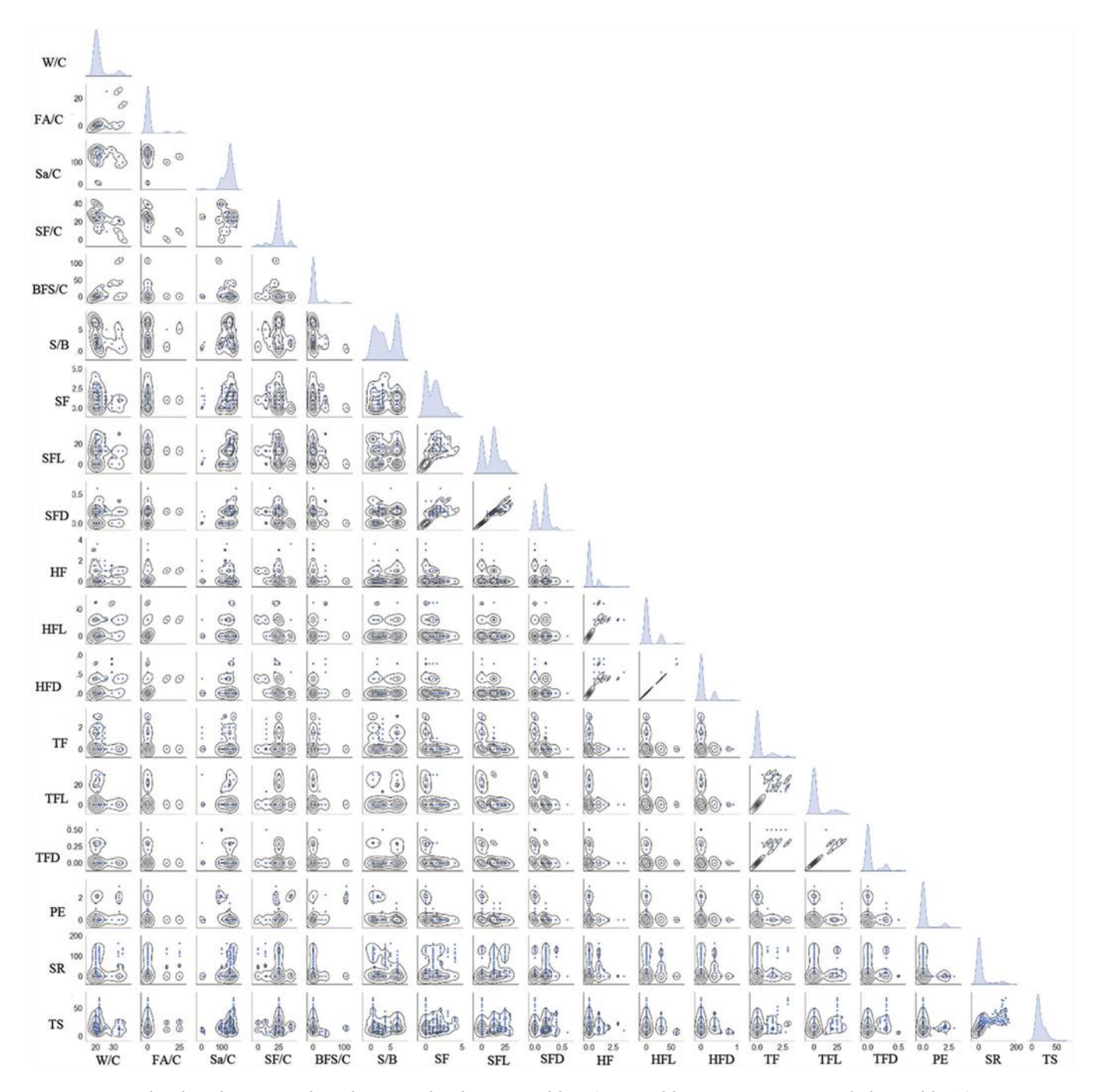


Fig. 6—Pairplot distribution analysis between database variables. (Note: Abbreviations are provided in Table 1.)

DISCUSSION OF RESULTS

The architecture of the MLP-ANN was developed to achieve the lowest mean squared error (MSE) in the development phase and the corresponding R^2 and RMSE when comparing the experimental and predicted results. Table 2 shows the corresponding MSE with the different number of neurons for the MLP-ANN model predicting the cracking stress, tensile strength, and the strain at tensile strength. Using a trial-and-error approach, testing neuron configurations with numbers ranging from five to 40 neurons, the optimum number of neurons converged to 25 neurons in each hidden layer, reaching the minimum MSE of 6.8, as shown in Table 2.

The results of the performance evaluation of the selected models are presented in Table 3; similar values were obtained in terms of the performance measures for the training and test sets discussed previously, indicating a proper performance of the MLP-ANN model developed. Figure 9 shows the comparison between the experimental and predicted results for the cracking stress, tensile strength, and the strain at tensile strength. The model shows accurate results in predicting the tensile strength characteristics based on the mentioned input parameters. In addition, the similarity of the R^2 and RMSE values between the training and test data sets indicates overfitting was not an issue in the prediction process, with no need for compensating techniques such as regularization.

Shown in Fig. 9 is the comparison between experimental and predicted values of the tensile properties, differentiating based on the strain rate employed during testing

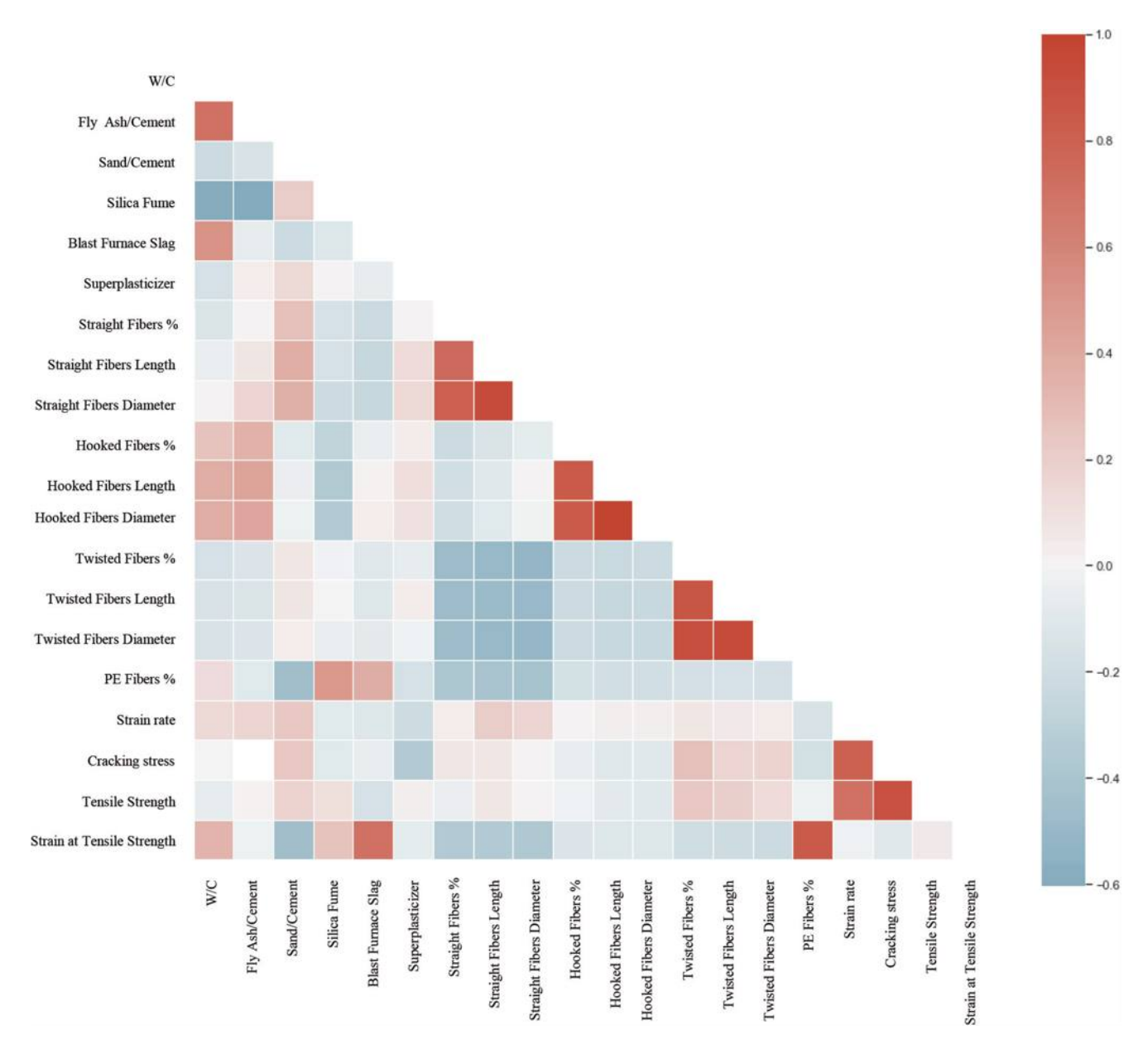


Fig. 7—Correlation analysis between database variables.

Table 2—Corresponding MSE relative to number of neurons in first and second hidden layer

				Number of	neurons in first la	iyer			
	_	5	10	15	20	25	30	35	40
	5	22	10.5	11.3	11.5	9	8.2	8.4	7.6
	10	14.3	10.8	9.5	10.2	7.9	7.8	7.8	7.8
Number	15	12.4	12.5	8.9	9.2	7.7	8.7	7.4	7.5
of neurons in second	20	17.2	10.4	8.5	7.8	7.5	7.5	7.2	9
layer	25	16.5	12.3	8.2	7.6	6.8	8.6	7.1	8.4
	30	16.2	12	9.2	7.1	7.2	7	8.3	7.8
	35	10.7	11	8.5	7.5	8.6	7.5	7	7.3
	40	11	9.1	7.7	9.3	7	6.9	7.3	7

and identifying the values obtained at strain rates below or above $0.1~\rm s^{-1}$. A strain rate of $0.1~\rm s^{-1}$ was shown to be the threshold beyond which the strain rate effects become significantly more pronounced for UHPC materials. ^{79,80} The

overall accuracy for predicting the cracking stresses and the tensile strength decreases for UHPC specimens tested under higher strain rates (over 0.1 s⁻¹), illustrated in Fig. 9. The prediction of the strain at the tensile strength, however,

Table 3—MLP-ANN model performance evaluation for predicting UHPC tensile properties

Data set	Tensile	strength	Crack	ing stress	Strain at tensile strength			
	R^2	R ² RMSE		RMSE	R^2	RMSE		
Train	0.92	2.5	0.92	1.4	0.92	2.4		
Test	0.91	2.4	0.81	1.8	0.92	2.7		

does not appear to be impacted by the higher strain rates. As shown in Fig. 9 and reported in previous studies, ^{56-59,64} increased tensile strengths are obtained for higher strain rates. This is likely due to UHPC's dense structure and the increased bond strength between the cement matrix and the fiber reinforcement at elevated tensile strain rates. ⁸⁰

The model successfully differentiates between strainhardening and strain-softening behavior based on the calculated values for the cracking stress and the tensile strength. Strain-softening mixtures result in equal values between the cracking stress and the tensile strength, whereas strainhardening mixtures display a lower cracking stress compared to the tensile strength, as expected.

As shown in Fig. 9, the accuracy of the prediction algorithm was not significantly impacted by the assumptions made to characterize the database, including the use of the weighted average approach for UHPC mixtures containing fibers of the same type (straight, hooked, or twisted) but with different lengths and diameters. In addition, assumptions such as neglecting the number of bends in hooked fibers and threads in twisted fibers, not including the curing regime and duration, also had a minor effect on the accuracy of the predicted tensile properties.

The limitations of the proposed algorithm are largely related to the range of parameters covered in the database compiled. This model should not be expected to perform adequately for UHPC mixture designs that differ significantly from the ones analyzed herein. For example, there was insufficient data in the literature on the response of mixture designs that include basalt or cellulose fibers or metakaolin as SCMs. As such, the authors recommend against using the proposed model for these types of mixtures. However, should more data be available, the model could be expanded to include a broader range of mixture designs.

CONCLUSIONS

A multilayer perceptron artificial neural network (MLP-ANN) was developed for the prediction of cracking stress, tensile strength, and strain at tensile strength of various ultra-high-performance concrete (UHPC) mixtures. The following can be concluded:

- 1. The proposed MLP-ANN model proved to be an effective tool in predicting the tensile behavior of UHPC mixtures. An indication of the accuracy of the model consists of the coefficient of determination. The results of the predictions for the MLP-ANN algorithm showed R^2 values of 0.91, 0.81, and 0.92 for the tensile strength, cracking stress, and strain at tensile strength, respectively.
- 2. This procedure has the potential to decrease the effort, costs, and time to design a UHPC mixture without

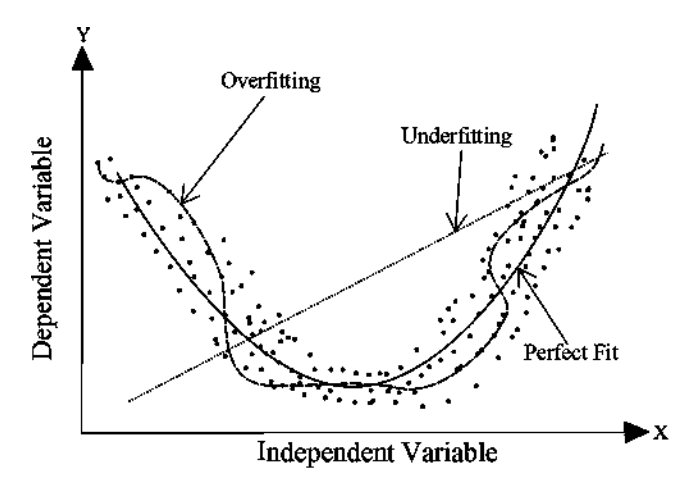


Fig. 8—Data fitting cases.

performing multiple mixture trials. This method should also be useful in the preliminary design and analysis of structural members by providing an initial estimate of the tensile strength based on the used UHPC mixture design.

- 3. The model was developed to achieve the lowest mean squared error (MSE) in the development phase and the corresponding R^2 and root-mean-square error (RMSE) when comparing the experimental and predicted results. Employing a trial-and-error approach and testing various configurations of neurons ranging from 5 to 40 neurons, the optimum number of neurons converged to 25 neurons in each hidden layer, reaching the minimum MSE of 6.8.
- 4. The similarity of the R^2 and RMSE values between the training and test data sets indicates overfitting was not an issue in the prediction process, with no need for correction techniques such as regularization.
- 5. The correlation analysis and the test results displayed the strain rate's pronounced influence on the cracking stress and the tensile strength of UHPC mixtures. In contrast, the strain rate has minimal effect on the strain at tensile strength of the mixtures investigated in this study.
- 6. A nonlinear relationship was found between the fiber aspect ratio (fiber length/fiber diameter) and the UHPC tensile properties. As such, in this study, the fiber aspect ratio was disaggregated to capture the fact that the length and diameter of the fibers influence the tensile response differently and, therefore, were assigned different weights in the MLP-ANN model.
- 7. The mixture design constituents, including the water-cement ratio (w/c), high-range water-reducing admixture ratio, supplementary cementitious materials (SCMs) ratio, sand ratio, and fiber reinforcement characteristics, in addition to the tensile strain rate, proved to be sufficient in accurately predicting the tensile behavior of UHPC mixtures.

DATABASE AND ALGORITHM AVAILABILITY

The database, MLP-ANN algorithm, and user instructions are available for sharing upon request from the corresponding author.

AUTHOR BIOS

Amjad Y. Diab is a PhD Student at The University of Texas at Austin, Austin, TX. His research interests include performance assessment and

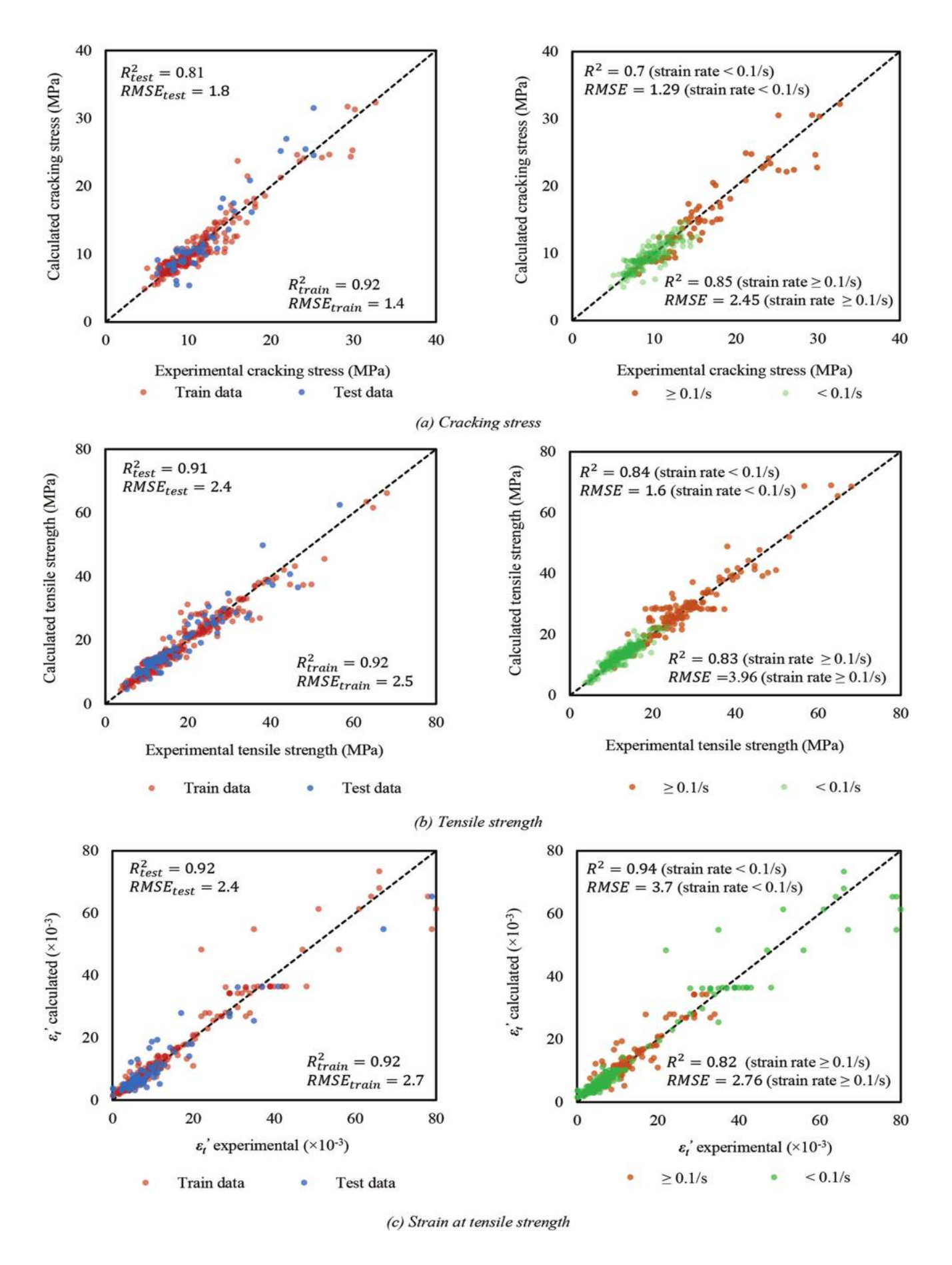


Fig. 9—Comparison between experimental and calculated values of UHPC in terms of train-test and strain rates. (Note: 1.0 MPa = 145 psi.)

analysis of concrete structures, structural implications of deterioration mechanisms, and sustainability of concrete structures.

Anca C. Ferche is an Assistant Professor in the Department of Civil, Architectural, and Environmental Engineering at The University of Texas at Austin. She received her PhD from the University of Toronto, Toronto, ON, Canada, in 2020. Her research interests include performance assessment and analysis of reinforced concrete structures, concrete deterioration mechanisms, and rehabilitation of structures.

ACKNOWLEDGMENTS

The presented work was a part of a research project on UHPC sponsored by the Precast/Prestressed Concrete Institute (PCI). The authors would like to acknowledge the sponsorship from PCI for their funding and support for this project.

REFERENCES

- 1. AASHTO T 397-22, "Standard Method of Test for Uniaxial Tensile Response of Ultra-High Performance Concrete," American Association of State Highway and Transportation Officials, Washington, DC, 2022.
- 2. Toutlemonde, F.; Kretz, T.; Généreux, G.; Resplendino, J.; Pillard, W.; Guérinet, M.; and Rougeau, P., "French Standards for Ultra-High Performance Fiber-Reinforced Concrete (UHPFRC)," *High Tech Concrete: Where Technology and Engineering Meet*, D. A. Hordijk and M. Luković, eds., Springer, Cham, Switzerland, 2018, pp. 1601-1609.
- 3. Voo, Y. L.; Foster, S. J.; and Voo, C. C., "Ultra High-Performance Concrete Segmental Bridge Technology: Toward Sustainable Bridge Construction," *Journal of Bridge Engineering*, ASCE, V. 20, No. 8, 2015, pp. 1-12.
- 4. Azmee, N. M., and Shafiq, N., "Ultra-High Performance Concrete: From Fundamental to Applications," *Case Studies in Construction Materials*, V. 9, No. 197, 2018, pp. 1-15.
- 5. Haber, Z. B.; De la Varga, I.; Graybeal, B. A.; Nakashoji, B.; and El-Helou, R., "Properties and Behavior of UHPC-Class Materials," Report No. FHWA-HRT-18-036, Federal Highway Administration, Office of Infrastructure Research and Development, McLean, VA, 2018, 170 pp.
- 6. Richard, P., and Cheyrezy, M. H., "Reactive Powder Concretes With High Ductility and 200-800 MPa Compressive Strength," *Concrete Technology: Past, Present, and Future*, SP-144, P. K. Mehta, ed., American Concrete Institute, Farmington Hills, MI, 1994, pp. 507-518.
- 7. de Larrard, F., and Sedran, T., "Optimization of Ultra-High-Performance Concrete by the Use of a Packing Model," *Cement and Concrete Research*, V. 24, No. 6, 1994, pp. 997-1009.
- 8. Reiterman, P., "Influence of Metakaolin Additive and Nanoparticle Surface Treatment on the Durability of White Cement Based Concrete," *European Journal of Environmental and Civil Engineering*, V. 24, No. 13, 2020, pp. 2270-2283.
- 9. Cuenca, E.; Postolachi, V.; and Ferrara, L., "Cellulose Nanofibers to Improve the Mechanical and Durability Performance of Self-Healing Ultra-High-Performance Concretes Exposed to Aggressive Waters," *Construction and Building Materials*, V. 374, No. 4, Apr. 2023, Article No. 130785.
- 10. Kannikachalam, N. P.; di Summa, D.; Borg, R. P.; Cuenca, E.; Parpanesi, M.; De Belie, N.; and Ferrara, L., "Assessment of Sustainability and Self-Healing Performances of Recycled Ultra-High-Performance Concrete," *ACI Materials Journal*, V. 120, No. 1, Jan. 2023, pp. 117-132.
- 11. Cuenca, E.; Criado, M.; Giménez, M.; Alonso, M. C.; and Ferrara, L., "Effects of Alumina Nanofibers and Cellulose Nanocrystals on Durability and Self-Healing Capacity of Ultrahigh-Performance Fiber-Reinforced Concretes," *Journal of Materials in Civil Engineering*, ASCE, V. 34, No. 8, 2022, p. 04022154.
- 12. Cuenca, E.; Lo Monte, F.; Moro, M.; Schiona, A.; and Ferrara, L., "Effects of Autogenous and Stimulated Self-Healing on Durability and Mechanical Performance of UHPFRC: Validation of Tailored Test Method through Multi-Performance Healing-Induced Recovery Indices," *Sustainability*, V. 13, No. 20, 2021, p. 11386.
- 13. Cuenca, E., and Serna, P., "Autogenous Self-Healing Capacity of Early-Age Ultra-High-Performance Fiber-Reinforced Concrete," *Sustainability*, V. 13, No. 6, 2021, p. 3061.
- 14. Bonetti, R.; Bayrak, O.; Folliard, K.; and Drimalas, T., "A Framework for Determining Direct Tensile Properties of Ultra-High-Performance Concrete," *ACI Materials Journal*, V. 120, No. 2, Mar. 2023, pp. 87-95.
- 15. Park, S.; Wu, S.; Liu, Z.; and Pyo, S., "The Role of Supplementary Cementitious Materials (SCMs) in Ultra High Performance Concrete (UHPC): A Review," *Materials*, V. 14, No. 6, 2021, p. 1472.
- 16. Bharadwaj, K., "Supplementary Cementitious Materials in Portland-Limestone Cements," *ACI Materials Journal*, V. 119, No. 2, Mar. 2022, pp. 141-154.

- 17. Tadros, M.; Lawler, J.; El-Khier, M. A.; Gee, D.; and Kurt, A., "Implementation of Ultra-High Performance Concrete in Long-Span Precast Pretensioned Elements for Concrete Buildings and Bridges," *Precast/Prestressed Concrete Institute*, V. 10, No. 1, Jan. 2021.
- 18. Wille, K., and Naaman, A. E., "Fracture Energy of UHP-FRC Under Direct Tensile Loading," *Proceedings of the Seventh International Conference on Fracture Mechanics of Concrete and Concrete Structures (FraMCoS-7)*, B. H. Oh, ed., Jeju, South Korea, 2010, pp. 65-72.
- 19. Abrams, D. A., "Effect of Rate of Application of Load on the Compressive Strength of Concrete," *ASTM Proceedings*, V. 17, No. 1, 1917, pp. 364-377.
- 20. Bischoff, P. H., and Perry, S. H., "Compressive Behaviour of Concrete at High Strain Rates," *Materials and Structures*, V. 24, No. 6, 1991, pp. 425-450.
- 21. Suaris, W., and Shah, S. P., "Strain-Rate Effects in Fibre-Reinforced Concrete Subjected to Impact and Impulsive Loading," *Composites*, V. 13, No. 2, 1982, pp. 153-159.
- 22. Gopalaratnam, V. S., and Shah, S. P., "Properties of Steel Fiber Reinforced Concrete Subjected to Impact Loading," *ACI Journal Proceedings*, V. 83, No. 1, Jan.-Feb. 1986, pp. 117-126.
- 23. Wang, Z.-L.; Liu, Y.-S.; and Shen, R. F., "Stress-Strain Relationship of Steel Fiber-Reinforced Concrete Under Dynamic Compression," *Construction and Building Materials*, V. 22, No. 5, 2008, pp. 811-819.
- 24. Bindiganavile, V., and Banthia, N., "Impact Response of the Fiber-Matrix Bond in Concrete," *Canadian Journal of Civil Engineering*, V. 32, No. 5, 2005, pp. 924-933.
- 25. Pyo, S.; Wille, K.; and El-Tawil, S., "Strain Rate Dependent Properties of Ultra High Performance Fiber Reinforced Concrete (UHP-FRC) Under Tension," *Cement and Concrete Composites*, V. 56, 2015, pp. 15-24.
- 26. Wille, K.; Xu, M.; and El-Tawil, S., "Dynamic Impact Factors of Strain Hardening UHP-FRC Under Direct Tensile Loading at Low Strain Rates," *Materials and Structures*, V. 49, No. 4, 2016, pp. 1351-1365.
- 27. Park, S. H.; Kim, D. J.; and Kim, S. W., "Investigating the Impact Resistance of Ultra-High-Performance Fiber-Reinforced Concrete Using an Improved Strain Energy Impact Test Machine," *Construction and Building Materials*, V. 125, No. 1, 2016, pp. 145-159.
- 28. Malvar, L. J., and Ross, C. A., "Review of Strain Rate Effects for Concrete in Tension," *ACI Materials Journal*, V. 95, No. 6, Nov.-Dec. 1998, pp. 735-739.
- 29. Cadoni, E.; Meda, A.; and Plizzari, G. A., "Tensile Behaviour of FRC under High Strain-Rate," *Materials and Structures*, V. 42, No. 9, 2009, pp. 1283-1294.
- 30. Rossi, P., "A Physical Phenomenon Which Can Explain the Mechanical Behaviour of Concrete under High Strain Rates," *Materials and Structures*, V. 24, No. 6, 1991, pp. 422-424.
- 31. Rossi, P.; van Mier, J. G. M.; and Boulay, C., "The Dynamic Behaviour of Concrete: Influence of Free Water," *Materials and Structures*, V. 25, No. 9, 1992, pp. 509-514.
- 32. ASTM C496/C496M-17, "Standard Test Method for Splitting Tensile Strength of Cylindrical Concrete Specimens," ASTM International, West Conshohocken, PA, 2017, 5 pp.
- 33. ASTM C1609/C1609M-19a, "Test Method for Flexural Performance of Fiber-Reinforced Concrete (Using Beam With Third-Point Loading)," ASTM International, West Conshohocken, PA, 2019, 9 pp.
- 34. Kim, J. J., and Taha, R., "M. "Experimental and Numerical Evaluation of Direct Tension Test for Cylindrical Concrete Specimens," *Advances in Civil Engineering*, V. 2014, No. 1, 2014, pp. 1-8.
- 35. Maalej, M., and Li, V. C., "Flexural/Tensile-Strength Ratio in Engineered Cementitious Composites," *Journal of Materials in Civil Engineering*, ASCE, V. 6, No. 4, 1994, pp. 513-528.
- 36. Naaman, A. E., and Reinhardt, H. W., "Proposed Classification of HPFRC Composites Based on Their Tensile Response," *Materials and Structures*, ASCE, V. 39, No. 5, 2007, pp. 547-555.
- 37. Abellán-García, J., "Four-Layer Perceptron Approach for Strength Prediction of UHPC," *Construction and Building Materials*, V. 256, No. 1, 2020, p. 119465.
- 38. Abellán-García, J., "Artificial Neural Network Model for Strength Prediction of Ultra-High-Performance Concrete," *ACI Materials Journal*, V. 118, No. 4, July 2021, pp. 3-14.
- 39. Ghafari, E.; Bandarabadi, M.; Costa, H.; and Júlio, E., "Design of UHPC Using Artificial Neural Networks," *Brittle Matrix Composites*, A. M. Brandt, J. Olek, M. A. Glinicki, and C. K. Y. Leung, eds., Woodhead Publishing, Sawston, UK, 2012, pp. 61-69.
- 40. Abellán García, J.; Fernandez Gomez, J.; and Torres Castellanos, N., "Properties Prediction of Environmentally Friendly Ultra-High-Performance Concrete Using Artificial Neural Networks," *European Journal of Environmental and Civil Engineering*, V. 26, No. 6, 2022, pp. 2319-2343.
- 41. Mostafa, S. A.; Ahmed, N.; Almeshal, I.; Tayeh, B. A.; and Elgamal, M. S., "Experimental Study and Theoretical Prediction of Mechanical

- Properties of Ultra-High-Performance Concrete Incorporated With Nanorice Husk Ash Burning at Different Temperature Treatments," *Environmental Science and Pollution Research International*, V. 29, 2022, pp. 75380-75401.
- 42. Mahjoubi, S.; Meng, W.; and Bao, Y., "Auto-Tune Learning Framework for Prediction of Flowability, Mechanical Properties, and Porosity of Ultra-High-Performance Concrete (UHPC)," *Applied Soft Computing*, V. 115, 2022, p. 108182.
- 43. Zakaria, M.; Shebany, M.; and Sarhan, S., "Artificial Neural Network: A Brief Overview," *International Journal of Engineering Research and Applications*, V. 4, No. 2, 2014, pp. 7-12.
- 44. Gunasekara, C.; Atzarakis, P.; Lokuge, W.; Law, D. W; and Setunge, S., "Novel Analytical Method for Mix Design and Performance Prediction of High Calcium Fly Ash Geopolymer Concrete," *Polymers*, V. 13, No. 6, 2021, pp. 1-21.
- 45. Rosenblatt, F., "The Perceptron: A Probabilistic Model for Information Storage and Organization in the Brain," *Psychological Review*, V. 65, No. 6, 1958, pp. 386-408.
- 46. Estebon, M. D., "Perceptrons: An Associative Learning Network," Virgina Tech, Blacksburg, VA, 1997.
- 47. Asteris, P. G.; Skentou, A. D.; and Bardhan, A., "Predicting Concrete Compressive Strength Using Hybrid Ensembling of Surrogate Machine Learning Models," *Cement and Concrete Research*, V. 145, No. 1, 2021, pp. 1-23.
- 48. Ramchoun, H.; Amine, M.; and Idrissi, J., "Multilayer Perceptron: Architecture Optimization and Training," *International Journal of Interactive Multimedia and Artificial Intelligence*, V. 4, No. 1, 2016, pp. 1-26.
- 49. Bircanoğlu, C., and Arıca, N. "A Comparison of Activation Functions in Artificial Neural Networks," 2018 26th Signal Processing and Communications Applications Conference (SIU), İzmir, Turkey, 2018, pp. 1-4.
- 50. Rumelhart, D. E.; Hinton, G. E.; and Williams, R. J., "Learning Representations by Back-Propagating Errors," *Nature*, V. 323, No. 6088, 1986, pp. 533-536.
- 51. Hoang, N.-D.; Nguyen, Q.-L.; and Tran, X.-L., "Automatic Detection of Concrete Spalling Using Piecewise Linear Stochastic Gradient Descent Logistic Regression and Image Texture Analysis," *Complexity*, V. 2019, No. 1, 2019, pp. 1-14.
- 52. Awolusi, T. F.; Oke, O. L.; and Akinkurolere, O. O., "Performance Comparison of Neural Network Training Algorithms in the Modeling Properties of Steel Fiber Reinforced Concrete," *Heliyon*, V. 5, No. 1, 2019, pp. 1-27.
- 53. Su, C., and Wang, W., "Concrete Cracks Detection Using Convolutional Neural Network Based on Transfer Learning," *Mathematical Problems in Engineering*, V. 2020, No. 1, 2020, pp. 1-10.
- 54. Collier, M., and Urdiales, H. "Scalable Deep Unsupervised Clustering with Concrete GMVAEs," arXiv, 2019, pp. 1-5.
- 55. Moriasi, D. N.; Arnold, J. G.; Van Liew, M. W.; Bingner, R. L.; Hamel, R. D.; and Veith, T. L., "Model Evaluation Guidelines for Systematic Quantification of Accuracy in Watershed Simulations," *Transactions of the ASABE*, V. 50, No. 3, 2007, pp. 885-900.
- 56. Gupta, P.; Seetharaman, A.; and Raj, J. R., "The Usage and Adoption of Cloud Computing by Small and Medium Businesses," *International Journal of Information Management*, V. 33, No. 5, 2013, pp. 861-874.
- 57. Park, J. K.; Kim, S.-W.; and Kim, D. J., "Matrix-Strength-Dependent Strain-Rate Sensitivity of Strain-Hardening Fiber-Reinforced Cementitious Composites under Tensile Impact," *Composite Structures*, V. 162, No. 1, 2017, pp. 313-324.
- 58. Ranade, R.; Li, V. C.; and Heard, W. F., "Tensile Rate Effects in High Strength-High Ductility Concrete," *Cement and Concrete Research*, V. 68, No. 1, 2015, pp. 94-104.
- 59. Tran, N. T., and Kim, D. J., "Synergistic Response of Blending Fibers in Ultra-High-Performance Concrete under High Rate Tensile Loads," *Cement and Concrete Composites*, V. 78, No. 1, 2017, pp. 132-145.
- 60. Tran, N. T.; Tran, T. K.; and Kim, D. J., "High Rate Response of Ultra-High-Performance Fiber-Reinforced Concretes under Direct Tension," *Cement and Concrete Research*, V. 69, No. 1, 2015, pp. 72-87.

- 61. Chun, B., and Yoo, D.-Y., "Hybrid Effect of Macro and Micro Steel Fibers on the Pullout and Tensile Behaviors of Ultra-High-Performance Concrete," *Composites Part B: Engineering*, V. 162, No. 1, 2019, pp. 344-360.
- 62. Bian, C., and Wang, J.-Y., "Mechanical and Damage Mechanisms of Reinforced Ultra-High-Performance Concrete Under Tensile Loading," *Construction and Building Materials*, V. 226, 2019, pp. 259-279.
- 63. Wang, J.-Y., and Guo, J.-Y., "Damage Investigation of Ultra High-Performance Concrete under Direct Tensile Test Using Acoustic Emission Techniques," *Cement and Concrete Composites*, V. 88, No. 1, 2018, pp. 17-28.
- 64. Yoo, D.-Y., and Kim, M.-J., "High Energy Absorbent Ultra-High-Performance Concrete with Hybrid Steel and Polyethylene Fibers," *Construction and Building Materials*, V. 209, No. 1, 2019, pp. 354-363.
- 65. Pyo, S.; El-Tawil, S.; and Naaman, A. E., "Direct Tensile Behavior of Ultra-High Performance Fiber Reinforced Concrete (UHP-FRC) at High Strain Rates," *Cement and Concrete Research*, V. 88, No. 1, 2016, pp. 144-156.
- 66. Le Hoang, A., and Fehling, E., "Influence of Steel Fiber Content and Aspect Ratio on the Uniaxial Tensile and Compressive Behavior of Ultra-High-Performance Concrete," *Construction and Building Materials*, V. 153, No. 1, 2017, pp. 790-806.
- 67. Kamal, A.; Kunieda, M.; and Ueda, N., "Evaluation of Crack Opening Performance of a Repair Material with Strain Hardening Behavior," *Cement and Concrete Composites*, V. 30, No. 10, 2008, pp. 863-871.
- 68. Ranade, R.; Li, V. C.; Stults, M. D.; Heard, W. F.; and Rushing, T. S., "Composite Properties of High-Strength, High-Ductility Concrete," *ACI Materials Journal*, V. 110, No. 4, July-Aug. 2013, pp. 413-422.
- 69. Yu, K.-Q.; Lu, Z.-D.; and Dai, J.-G., "Direct Tensile Properties and Stress-Strain Model of UHP-ECC," *Journal of Materials in Civil Engineering*, ASCE, V. 32, No. 1, 2020, pp. 1-13.
- 70. Park, S. H.; Kim, D. J.; and Ryu, G. S., "Tensile Behavior of Ultra High Performance Hybrid Fiber Reinforced Concrete," *Cement and Concrete Composites*, V. 34, No. 2, 2012, pp. 172-184.
- 71. Yavaş, A.; Hasgul, U.; and Turker, K., "Effective Fiber Type Investigation on the Shear Behavior of Ultrahigh-Performance Fiber-Reinforced Concrete Beams," *Advances in Structural Engineering*, V. 22, No. 7, 2019, pp. 1591-1605.
- 72. Voss, M. S.; Riding, K. A.; and Alrashidi, R. S., "Comparison between Direct Tension, Four-Point Flexure, and Simplified Double-Punch Tests for UHPC Tensile Behavior," *Journal of Materials in Civil Engineering*, ASCE, V. 34, No. 9, 2022, pp. 1-12.
- 73. Delen, D.; Sharda, R.; and Bessonov, M., "Identifying Significant Predictors of Injury Severity in Traffic Accidents Using a Series of Artificial Neural Networks," *Accident Analysis & Prevention*, V. 38, No. 3, 2006, pp. 434-444.
- 74. Rajagopalan, G., A Python Data Analysi's Toolkit: Learn Python and Python-Based Libraries with Applications in Data Analysis and Statistics, Apress, Berkeley, CA, 2014.
- 75. Nayak, S. K., and Ojha, A. C., "Data Leakage Detection and Prevention: Review and Research Directions," *Machine Learning and Information Processing: Proceedings of ICMLIP*, 2019.
- 76. Shabtai, A.; Elovici, Y.; and Rokach, L., *A Survey of Data Leakage Detection and Prevention Solutions*, Springer Science & Business Media, New York, 2012.
- 77. Bilbao, I., and Bilbao, J., "Overfitting Problem and the Over-Training in the Era of Data: Particularly for Artificial Neural Networks," 2017 Eighth International Conference on Intelligent Computing and Information Systems (ICICIS), Cairo, Egypt, V. 1, 2017, pp. 173-177.
- 78. Ying, X., "An Overview of Overfitting and its Solutions," *Journal of Physics: Conference Series*, V. 1168, No. 2, 2019, pp. 1-6.
- 79. Hentz, S.; Donzé, F. V.; and Daudeville, L., "Discrete Element Modelling of Concrete Submitted to Dynamic Loading at High Strain Rates," *Computers & Structures*, V. 82, No. 29-30, 2004, pp. 2509-2524. 80. Thomas, R. J., and Sorensen, A. D., "Review of Strain Rate Effects
- 80. Thomas, R. J., and Sorensen, A. D., "Review of Strain Rate Effects for UHPC in Tension," *Construction and Building Materials*, V. 153, 2017, pp. 846-856.

Table A1—Database description

			oc ac	,5011	P	•															
Ref.	Speci- mens	w/c	FA/C	Sa/C	SF/C	GGBFS /C	S/B	SF	SFL	SFD	HF	HFL	HFD	TF	TFL	TFD	PE	SR	DTS	CTS	SC
Unit	N/A	%	%	%	%	%	%	%	mm	mm	%	mm	mm	%	mm	mm	%	S-1 (×10 ⁻³)	MPa	MPa	με
Park et al. ⁵⁷	53	20 to 35	0 to 25	100 to 125	0 to 25	0	0.9 to 6.7	1	13	0.2	1	30	0.375	0	0	0	0	0.3 to 161,000	10.4 to 43.2	N/A	4 to 2.1
Pyo et al. ²⁵	36	22	0	134	25	0	0.5	0 to 3	0 to 25	0 to 0.4	0	0	0	0 to 3	18 to 25	0.3	0	0.1 to 100	8.11 to 24.1	6.22 to 14.6	1.7 to 48
Reanade et al. ⁵⁸	36	20.8	0	70	39	0	1.8	0	0	0	0	0	0	0	0	0	2.14	0.1 to 10,000	14.5 to 22.8	6.6 to 14.6	22 to 48
Tran and Kim ⁵⁹	46	20	0	110	25	0	6.7	0 to 1.5	0 to 30	0 to 0.3	0 to 1.5	30	0.375	0 to 1.5	24.3 to 30	0.27 to 0.3	0	0.167 to 37,000	9.2 to 39.4	N/A	2.3 to 20
Tran et al. ⁶⁰	72	20	0	110	25	0	6.7	0 to 1.5	0 to 19	0 to 0.2	0	0	0	0 to 1.5	20	0.2	0	0.167 to 23,700	10.1 to 37.4	N/A	44,606
Wille et al. ²⁶	36	19	0	92	25	0	6.7	0 to 3	0 to 13	0 to 0.2	0 to 3	30	0.38	0 to 3	18	0.3	0	0.1 to 100	11.1 to 24.9	7.3 to 17.1	44,659
Chun and Yoo ⁶¹	12	25	0	110	25	0	2	0 to 2	13 to 30	0.2 to 0.3	0 to 2	30	0.38	0 to 2	30	0.3	0	0.083	12.25 to 17.68	5.91 to 11.35	44,720
Bian and Wang ⁶²	6	20	0	164	30	0	1.3	1 to 2	16	0.2	0	0	0	0	0	0	0	0.2	9.3 to 10.6	10.1 to 12	0.2 to 4.5
Wang and Guo ⁶³	9	20	0	134	30	0	0.5	1.5 to 2.5	13	0.2	0	0	0	0	0	0	0	0.2	7.7 to 10.8	7.7 to 13	0.2 to 4
Yoo and Kim ⁶⁴	12	20	0	110	25	0	6.5	0 to 2	0 to 19.5	0 to 0.2	0	0	0	0 to 2	30	0.3	0 to 1.5	0.3	12 to 20.3	4.76 to 9.98	44,671
Pyo et al. ⁶⁵	38	22	0	134	25	0	0.5	0 to 3	0 to 25	0 to 0.4	0	0	0	0 to 3	25	0.3	0	66,000 to 146,000	19.9 to 68.1	13.2 to 32.7	44,640
Le Hoang and Fehling ⁶⁶	36	20	0	147	21	0	3	1.5 to 3	9 to 20	0.15 to 0.25	0	0	0	0	0	0	0	0.067	7.71 to 14.4	5.05 to 15.3	N/A
Wille and Naaman ¹⁸	7	22	0	129	25	0	0.54	0 to 2.5	0 to	0 to 0.2	0 to 2	30	0.38	0 to 2	0 to 30	0 to 0.3	0	0.33	8 to 15.5	N/A	1.7 to 6.1
Kamal et al. ⁶⁷	3	20	0	12.5	25	0	2	0.5 to 1.5	6	0.012	0	0	0	0	0	0	0	2	3.8 to 10	N/A	28 to 58
Ranade et al. ⁶⁸	6	21	0	60 to 97	39	0	0.009 to 0.024	0	0	0	0 to 3.6	0 to 30	0 to 0.55	0	0	0	0 to 2	0.03	10.4 to 14.5	N/A	1.8 to 35
Yu et al. ⁶⁹	14	33	0	71	21.4	107	0.005	0	0	0	0	0	0	0	0	0	1.5 to 3	0.2	10.29 to 17.89	8.15 to 12.09	22 to 80
Park et al. ⁷⁰	16	20	0	110	25	0	0.067	0 to 2	13 to 24	0.2 to 0.3	0 to	0 to 62	0 to 0.775	0 to 1	0 to 30	0 to 0.3	0	0.04	8.08 to 18.56	7.09 to 11.35	0.9 to 6.4
Yavaş et al. ⁷¹	16	29	0	157	20	40	0.016	0 to 1.5	0 to 13	0 to 0.16	0 to 1.5	0 to 60	0 to 0.9	0	0	0	0	0.07	4.2 to 9.4	N/A	N/A
Voss et al. ⁷²	10	21	0	97.5	9.7	19.3	0.03	0 to 2.78	0 to 13	0 to 0.2	0	0	0	0 to 2.78	0 to 13	0 to 0.5	0	0.3	4.9 to 7.0	N/A	N/A

Note: Abbreviations are provided in Table 1.

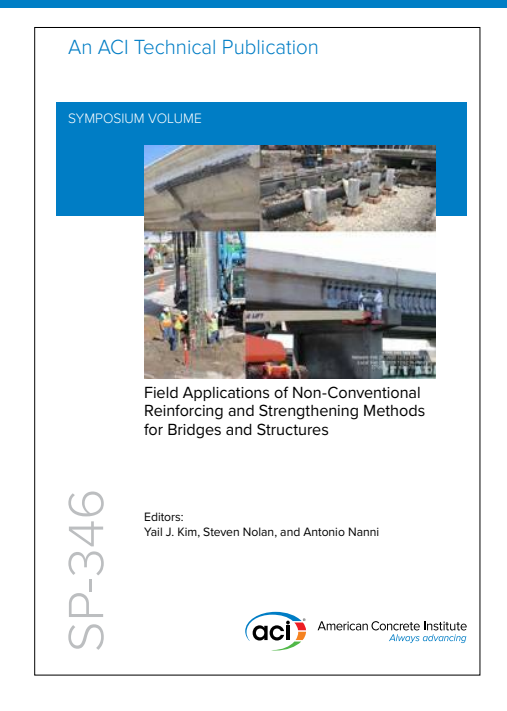
Symposium Publications from ACI



SP-345: Materials, Analysis, Structural Design and Applications of Textile Reinforced Concrete/Fabric Reinforced Cementitious Matrix

Several state-of-the-art sessions on textile-reinforced concrete/fabric-reinforced cementitious matrix (TRC/FRCM) were organized by ACI Committee 549 in collaboration with RILEM TC MCC during the ACI Fall 2019 Convention in Cincinnati, OH, and the ACI Virtual Technical Presentations in June 2020. The forum provided a unique opportunity to collect information and present knowledge in the field of TRC and FRCM as sustainable construction materials.

Available in PDF format: \$69.50 (FREE to ACI members)



SP-346: Field Applications of Non-Conventional Reinforcing and Strengthening Methods for Bridges and Structures

A sustainable built environment requires a comprehensive process from material selection through to reliable management. Although traditional materials and methods still dominate the design and construction of our civil infrastructure, nonconventional reinforcing and strengthening methods for concrete bridges and structures can address the functional and economic challenges facing modern society.

Available in PDF format: \$69.50 (FREE to ACI members)













Title No. 121-S19

Modeling of Concrete Printing Process with Frictional Interface

by Ignasius P. A. Wijaya, Eric Kreiger, and Arif Masud

Three-dimensional (3-D) concrete printing is invariably accompanied by slippage between the printed structure and the platform, which affects the shape of the printed object. This study employs a physics-based friction model in a finite-deformation interfacial kinematic framework to model relative slipping between the bottom layer and the supporting surface. The constitutive model that is specialized for cementitious materials is based on an extension of the Drucker-Prager plasticity model. The evolution of material parameters due to thixotropy and hydration reaction results in increased stiffness that gives rise to the non-physical bounce-back phenomenon. A bounce-back control algorithm is presented and used in conjunction with the plasticity model as well as the interfacial frictional model. The printing process is simulated through an algorithm that controls the kinematics of the nozzle and links the material timescales of curing with the timescales of layered printing. The model and method are validated against experimental data, and several interesting test cases are presented.

Keywords: concrete printing; geometric instability; material instability; printing-induced deformation; structural failure.

INTRODUCTION

The growing interest in additive construction (AC) technologies for the placement of cementitious materials (for example, mortars and concrete) is creating new opportunities for the construction industry (Khan et al. 2020). This formwork-free method, shown in Fig. 1, delivers a cementitious material by pumping it through a nozzle (Fig. 1(a)) and placing materials in consecutive layers using an AC platform (Fig. 1(b)), commonly referred to as a three-dimensional (3-D) printer. This technology allows for the construction of complex geometries and a higher degree of automation than other construction methods. Without geometric constraints from formwork, designers have greater flexibility in selecting the shape of structures, thereby allowing topologically optimized designs that have the potential to reduce the volume of material used, optimize the geometry, lower costs, and increase the speed of construction (Jagoda 2020; Kreiger et al. 2019, 2020; Wangler et al. 2019). Therefore, considerable efforts have been devoted to the development of concrete printing technology (Ngo et al. 2018; Paolini et al. 2019), including modeling the AC process (Roussel et al. 2020; Suiker 2018), where the rheological properties of early-age cementitious materials play an important role (Le et al. 2012a; Roussel 2018).

To ensure safety, quality, and economy, engineers design formwork for concrete to resist the lateral pressure of fresh concrete (ACI Committee 347 2004). Similarly, structures that use AC must meet specific strength and stability requirements.

Specifically, designs should consider the evaluation of the structure's geometry to resist two modes of failure: elastoplastic buckling and plastic collapse (Wolfs and Suiker 2019), as shown in Fig. 2. It is important to note that the assumption of elastic buckling—that is, buckling that occurs when the structure is completely elastic—has been used extensively in the literature (Suiker et al. 2020). In general, buckling may occur when part of the structure has been plasticized. In the present paper, the assumption of elastic buckling, which may in fact be an approximation of the in-place experimental observation reported in the literature, is not used. This results in a method that gives a more accurate prediction of buckling when part of the structure has plasticized.

While failure is inherently design a structural the design of mainproblem, components tain stability and withstand construction loads 1) an understanding of the age (0 to 120 minutes) development of material properties (elastic modulus and compressive strength) (Harbouz et al. 2023; Reiter et al. 2018; Kupwade-Patil et al. 2016); and 2) possible small-scale misalignments during the layering process. At this stage, constitutive models are necessary to describe the mechanical properties of very-early-age cementitious materials that exhibit thixotropy (Roussel 2006) and evolve through the flocculation and hydration processes (Gawin et al. 2006; de Miranda et al. 2023; Perrot et al. 2016). Because the layering of cementitious materials induces deformations as the material is extruded from the printer nozzle, the material evolution intimately links material property evolution (material timescales) with the geometric shape evolution of the structure (construction timescales) (Diggs-McGee and Kreiger 2021; Perrot et al. 2016). The evolution of material properties at very early ages for specific materials can be evaluated by determining the compressive stress-strain behavior through uniaxial compression tests at different time increments. Work has shown that the early-age behavior of cementitious materials follows a bilinear elastoplastic model (Tripathi et al. 2022). Accounting for the evolution of mechanical properties is important as a high rate of construction (high build rate) can trigger instabilities as the material may not have gained enough strength or stiffness to carry the load of the

ACI Structural Journal, V. 121, No. 2, March 2024.

MS No. S-2022-309.R2, doi: 10.14359/51740243, received May 24, 2023, and reviewed under Institute publication policies. Copyright © 2024, American Concrete Institute. All rights reserved, including the making of copies unless permission is obtained from the copyright proprietors. Pertinent discussion including author's closure, if any, will be published ten months from this journal's date if the discussion is received within four months of the paper's print publication.



Fig. 1—AC process: (a) material extrusion; and (b) printing machine. (Note: U.S. Army Corps of Engineers images by J. Eastman.)

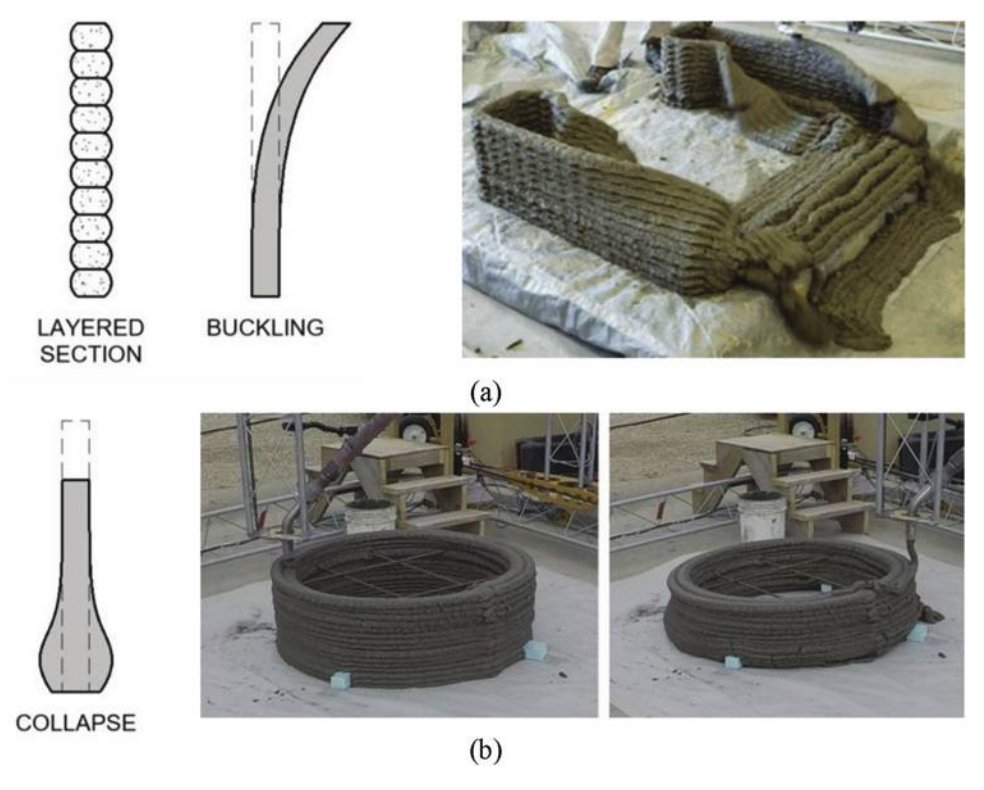


Fig. 2—Failure modes: (a) elastic buckling; and (b) plastic collapse. (Note: U.S. Army Corps of Engineers images by M. Kreiger.)

subsequent layers (Wolfs et al. 2018). On the other hand, a lower build rate can result in reduced interfacial strength between layers due to differential curing (Le et al. 2012b). Another consideration is the deformation that occurs during the construction process. Because very-early-age concrete has a relatively low stiffness, the local deformation induced during the construction process may lead to significant deviation from the intended design specifications. These considerations motivate the development of models that accommodate material timescales and build rates, while featuring a variational framework that can account for the large deformations that invariably occur prior to failure. Such a model can then be used to optimize the printing rate and predict the onset of failure that may be triggered by material or

geometric instabilities. In the reported literature, this has been done experimentally by evaluating the buildability, or the stable height before failure, of specific geometries that are designed to promote failures (Suiker et al. 2020; Tripathi et al. 2022; Wolfs and Suiker 2019).

While some have presented the use of design equations that can be employed for evaluating simple structures (for example, square or circular shell structures) (Roussel 2018; Suiker 2018), more complicated structures require sophisticated numerical modeling methods to evaluate the component stability during construction. Numerical modeling has been used to evaluate the placement process by material extrusion (Comminal et al. 2020; Reinold et al. 2022; Roussel et al. 2020; Spangenberg et al. 2021) and to evaluate

the construction process after the material has been placed (Nedjar 2022; Wijaya et al. 2022). By employing numerical modeling methods to optimize the build rate, component geometry, and material properties, it will be possible to evaluate larger structures and structurally optimized non-rectilinear components.

Modeling the layered deposition process in AC is a nonclassical problem as it involves material evolution. Therefore, the mechanical material coefficients that are needed in the constitutive equations change during the initial phase of the problem. These evolving coefficients can also have consequences on the validity of the constitutive equations. For example, satisfaction of the Legendre-Hadamard or ellipticity conditions can be compromised. Furthermore, material evolution can also lead to the violation of the second law of thermodynamics when standard constitutive models are employed. In addition, the geometric evolution leads to a mathematical problem because the free surface of the previously layered material becomes the domain interior contact surface when a subsequent layer of material is deposited. The continuously evolving domain and Neumann boundaries changing into domain interior interlayer surfaces lead to a nonclassical variational problem that can trigger numerical instability in the computational framework.

A previous publication by the authors developed a model that accounts for the expected elastoplastic behavior of the fresh layered material (Wijaya et al. 2022). The model employs a finite-deformation framework so that it can simulate the mechanism of structural failure without using restrictive assumptions such as elastic buckling. It also accounts for the evolution of material properties using an elastoplastic model with evolving constitutive parameters. Modeling the evolving mechanical properties of materials through time-dependent constitutive parameters was previously evaluated and was determined to lead to stiffening effects that violate the second law of thermodynamics (Bažant 1979, 1988; Wijaya et al. 2022). In addition, it also produces a non-physical behavior: deformation reduction, termed as "bounce-back." These issues were addressed in Wijaya et al. (2022) through a bounce-back control (BBC) algorithm, which can be invoked alongside the return-mapping algorithm employed in the plasticity model. It is important to note that the inelastic constitutive relation implies the dependence of the model on the loading history. In the context of printing concrete, the loading history is a function of the printing rate and trajectory. This effect is captured by simulating the printing process through an algorithm that is based on the notion of the ghost-mesh method. Because a finite-deformation elastoplastic constitutive relation is used, the model can capture the two modes of failure commonly observed during the cementitious material AC process: elastoplastic buckling and plastic collapse.

Another important consideration is the potential slip between the printed structure and substrate that is induced during the material placement process that has been shown experimentally (Wolfs et al. 2018). The magnitude of the slip depends on the tribology of the structure-substrate interface and the contact area. Depending on its magnitude,

the slip may contribute significantly to the deviation of the printed structure from the intended design specification. More importantly, the slip can also contribute to the onset of component failure. This aspect, which was not modeled in Wijaya et al. (2022), will be explored in this paper. The slip will be modeled through the contact-friction model (Laursen and Simo 1993; Masud et al. 2012), which is integrated into the method proposed in Wijaya et al. (2022). The objectives of this paper are to present a penalty-based contact-friction formulation that can model this interfacial slip and to demonstrate how the proposed method can account for more realistic scenarios encountered in 3-D printing.

RESEARCH SIGNIFICANCE

This paper addresses an important issue of structure-substrate slipping in 3-D layered printing of materials. A physics-based contact-friction model is embedded in a finite-deformation framework together with a modified form of the Drucker-Prager plasticity model. The effect of evolving material properties alongside the printing rate and the print trajectory are accounted for in the proposed method. The method can simulate both material and geometric failure during the process of printing the structure. It is tested on problems for which experimental data exists and then applied to the printing of a complex engineered structure to show the range of applicability of the method to problems of practical interest.

CONTINUUM FORMULATION OF CONTACT-FRICTION PROBLEM

This paper explores the effect of slip between the printed structure and the substrate. The slip contributes to the deviation from the intended design specifications. It may also significantly alter the stress distribution and the onset of failure. To model the slip, a formulation for the contactfriction problem was employed based on the framework presented in Laursen and Simo (1993). In this formulation, a deformable solid Ω with boundary Γ that undergoes finite deformation given by the deformation map φ_t was considered. The impenetrability constraint and contact friction are imposed between $\varphi_t(\Gamma)$ and the contact plane Γ_P . The constraint is imposed by applying contact traction t_c on Γ_P , where t_c can be resolved into normal $(t_N \mathbf{v})$ and tangential components (t_T) , as shown in Fig. 3. For the sake of computational efficiency, the constraint is imposed only on the part of the boundary $\varphi_t(\Gamma_C)$ that comes in contact with Γ_P . The gap function $g(x) = g(\varphi_t(X))$ is defined as the shortest distance between $x \in \varphi_t(\Gamma_C)$ and Γ_P . The normal traction t_N is defined as follows

$$t_N = \varepsilon_N \langle g \rangle$$
 (1)

where ε_N is the penalty parameters for the impenetrability constraint; and $<\cdot>$ is the Macaulay bracket, which returns the positive part of the operand as follows

$$\langle g \rangle = \frac{g + |g|}{2} \tag{2}$$

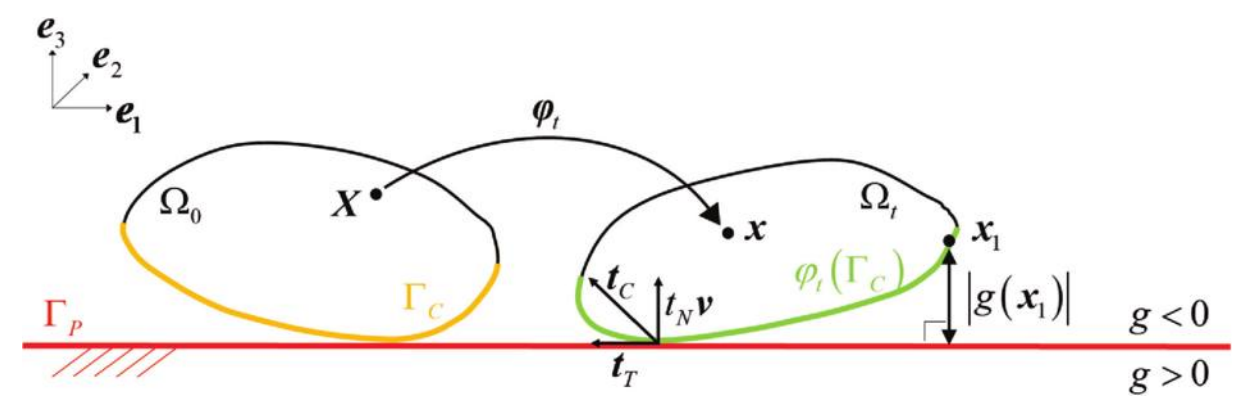


Fig. 3—Contact-friction problem in finite deformation.

The frictional response is modeled through the regularized Coulomb friction model. First, the yield function ϕ is defined, which puts an inequality constraint to the tangential traction t_T

$$\phi = ||\mathbf{t}_T|| - \mu \mathbf{t}_N \le 0 \tag{3}$$

where μ_f is the frictional coefficient. Then, the flow rule for the tangential slip is defined as follows

$$\dot{\mathbf{\phi}}_T - \zeta \frac{\mathbf{t}_T}{\|\mathbf{t}_T\|} = \frac{1}{\varepsilon_T} \mathcal{L}_v \mathbf{t}_T \tag{4}$$

$$\zeta \ge 0, \, \phi \zeta = 0 \tag{5}$$

where ε_T is the tangential penalty parameter; and ζ is the consistency parameter. The boundary value problem is solved through an incremental solution procedure. Quantities at time t_n are denoted by variables with subscript n, while variables without the subscript refer to quantities at time t_{n+1} . In this work, the backward Euler method was employed. However, any other appropriate time integrator can also be used. To integrate in time from a known state t_n , first, a trial state is computed. If the constraint condition (Eq. (3)) is violated, then a return map is applied that enforces the constraint for the tangential slip such that Eq. (3) to (5) are satisfied. The resulting scheme is a return-mapping algorithm, which is commonly used in elastoplastic problems (Simo and Hughes 1998). To make the discussion precise, the return-mapping algorithm for the regularized Coulomb friction is as follows

$$\boldsymbol{t}_{T}^{trial} = \boldsymbol{t}_{Tn} + \varepsilon_{T} [\boldsymbol{\varphi} - \boldsymbol{\varphi}_{n}] \tag{6}$$

$$\phi^{trial} = \|\mathbf{t}_{T}^{trial}\| - \mu_{f}t_{N} \leq 0 \tag{7}$$

$$t_{T} = \begin{cases} t_{T}^{trial} & \text{if } \phi^{trial} \leq 0 \text{ (stick)} \\ \mu t_{N} \frac{t_{T}^{trial}}{\|t_{T}^{trial}\|} & \text{otherwise (slip)} \end{cases}$$
(8)

The contact traction is included in the balance equation presented in Appendix A.*

MODELING CEMENTITIOUS MATERIAL FOR AC

Early-age concrete belongs to the family of yield-stress fluids. In the fresh state, it behaves like a solid when the applied stress is below a critical stress and behaves like a fluid otherwise. Because the interest is in the structural behavior before and up to the onset of failure, printed concrete is modeled as an elastoplastic solid. To be able to capture the two dominant modes of failure in the concrete printing process—namely, elastoplastic buckling and plastic collapse, a finite-deformation elastoplastic constitutive relation is needed. Following Wijaya et al. (2022), the Drucker-Prager plasticity model is employed to capture the plastic behavior of cementitious materials. To keep the discussion self-contained, the model is summarized in this section. For a more detailed discussion, the reader is referred to Wijaya et al. (2022).

It should be noted that the properties of cementitious materials change during the printing process. This evolution is often modeled by the dependence of constitutive parameters on time. However, the evolution of parameters associated with the stiffening of materials, when employed in standard constitutive models, results in bounce-back. It was shown in Wijaya et al. (2022) that for the constitutive model in Eq. (12), this phenomenon indicates the violation of the second law of thermodynamics. The bounce-back issue was addressed in Wijaya et al. (2022) with a newly proposed BBC algorithm. This section presents a concise discussion on bounce-back and the numerical implementation of the BBC algorithm.

Elastoplastic constitutive model for cementitious materials

To begin the discussion, consider a multiplicative decomposition (Kröner 1959; Lee 1969) of the deformation gradient F into the elastic F^e and plastic F^p parts.

$$\mathbf{F} = \mathbf{F}^e \mathbf{F}^p \tag{9}$$

^{*}The Appendix is available at www.concrete.org/publications in PDF format, appended to the online version of the published paper. It is also available in hard copy from ACI headquarters for a fee equal to the cost of reproduction plus handling at the time of the request.

The elastic left Cauchy-Green tensor b^e and its spectral decomposition are given as follows

$$\boldsymbol{b}^{e} = \boldsymbol{F}^{e} \boldsymbol{F}^{e,T} \tag{10}$$

$$\boldsymbol{b}^{e} = \sum_{A=1}^{3} (\lambda_{A}^{e})^{2} \boldsymbol{n}^{A} \otimes \boldsymbol{n}^{A}$$
 (11)

where $F^{e,T}$ is the transpose of the elastic deformation gradient; λ^e are the principal stresses; and n^A are the eigenvectors. The following hyperelastic model is used to represent the elastic part of the material behavior

$$\psi = \frac{1}{2} \kappa \log[J^e]^2 + \mu \sum_{A=1}^{3} \log[\overline{\lambda}_A^e]^2$$
 (12)

$$J^e = \lambda_1^e \lambda_2^e \lambda_3^e \tag{13}$$

$$\overline{\lambda}_A^e = (J^e)^{-1/3} \lambda_A^e \tag{14}$$

where κ is the bulk modulus; μ is the elastic modulus; and $\bar{\lambda}^e$ represents the stretch from the volume-preserving part of the deformation. The yield function for the Drucker-Prager model $\Pi(\sigma)$ is defined in term of Cauchy stress σ as follows

$$\Pi(\mathbf{\sigma}) = \Pi(I_1, J_2) = [2J_2]^{1/2} + \frac{\alpha}{3}I_1 - \sigma_y \le 0$$
 (15)

$$I_1 = \sigma_1 + \sigma_2 + \sigma_3 \tag{16}$$

$$J_2 = \frac{1}{2} (s_1^2 + s_2^2 + s_3^2) \tag{17}$$

$$s_A = \sigma_A - \frac{1}{3}I_1 \tag{18}$$

where σ_A is the eigenvalue of σ ; and A ranges from 1 to 3. α and σ_{ν} are the material parameters. Let \mathcal{L}_{ν} be the Lie derivative operator and $\dot{\gamma}$ be the plastic consistency parameter. The associative flow rule is defined in terms of the normal to the yield function N as follows.

$$\mathcal{L}_{\nu}\boldsymbol{b}^{e} = -2\dot{\gamma}J^{-1}N\boldsymbol{b}^{e} \tag{19}$$

$$n = \frac{\partial \Pi}{\partial \mathbf{\sigma}} \tag{20}$$

The implementation of the proposed constitutive model is presented in Box A in Wijaya et al. (2022).

Modeling material evolution: BBC algorithm

One way to model evolving material properties in cementitious materials during the printing process is through the evolution of the material parameters in the hyperelastic model. The time dependence of the material parameters can be described directly, as a function of time, or indirectly, through differential equations, such as in the curing models. In either case, the time dependency of parameters results in the dependence of the constitutive models on time. To understand the implication of this stiffening effect when

used in conventional constitutive models, consider the case of constant traction loading (constant Neumann boundary conditions) on a block of material. Assuming that the direct form of constitutive equations is used, the increase in stiffness results in the reduction in the deformation even though the traction is held constant. This is a non-physical behavior that is manifested by the model and is termed as bounce-back. It has been shown in Wijaya et al. (2022) that for a class of constitutive models, such as presented in Eq. (12), bounceback indicates a violation of the second law of thermodynamics. In the present work, the BBC algorithm is employed (Wijaya et al. 2022), which was designed to prevent the bounce-back effect in the constitutive models when the evolving material parameters result in the stiffening of the material. Furthermore, for the constitutive model presented in Eq. (12), it has been shown that the algorithm ensures the satisfaction of the second law of thermodynamics (Wijaya et al. 2022).

The BBC algorithm for the constitutive model (Eq. (12)) is presented in Box 1. Note that the material parameters κ and μ are a function of time, and therefore the value should be computed with respect to the current time. The output of the bounce-back algorithm presented in Box 1 is the corrected value of the elastic left Cauchy-Green tensor b^e emanating from the last converged step, which then becomes an input to the return-mapping algorithm for the plasticity model. For a more detailed discussion, the reader is referred to Wijaya et al. (2022).

Box 1—BBC algorithm (Wijaya et al. 2022)

- Step 1: Retrieve data at the integration point: $\{F_n, \sigma_n\}$
- Step 2: Spectral decomposition: $\sigma_n = \sum_{A=1}^{3} \sigma_{A,n} n_n^A \otimes n_n^A$, $\tau_{A,n} = \det(F_n)\sigma_{A,n}$ Step 3: Compute elastic strain:

a)
$$\tilde{\epsilon}^{\it e}_{{\it A},n} \, = \, \frac{1}{2\mu} \tau_{{\it A},n} + \frac{1}{3} (\tau_{1,n} + \tau_{2,n} + \tau_{3,n}) \Big(\frac{1}{3\kappa} - \frac{1}{2\mu} \Big)$$

b)
$$\tilde{\lambda}_{An}^{e} = \exp[\tilde{\epsilon}_{An}^{e}]$$

c)
$$\boldsymbol{b}_{n}^{e} = \sum_{A=1}^{3} (\tilde{\lambda}_{A,n}^{e})^{2} \boldsymbol{n}_{n}^{A} \otimes \boldsymbol{n}_{n}^{A}$$

MODELING AC PROCESS WITH CEMENTITIOUS MATERIALS

Because the Drucker-Prager model and BBC algorithm bring inelastic processes into the constitutive model, the solution of the governing equation (Eq. (A4) in the Appendix) is dependent on the loading history. In the context of additive manufacturing, the loading comes from the self-weight of the printed object. Therefore, it is necessary to also model the process of printing to be able to properly capture the inelastic effects induced during the layering process.

The algorithm proposed in Wijaya et al. (2022) is adopted in the present work. The governing equation (Eq. (A4)) is numerically solved through the finite element method, where the Gaussian quadrature rule is used for numerical integration. The geometry to be printed is associated with domain Ω_0 , which is then discretized into a finite element mesh. The printing process is modeled through the assignment of material parameters at integration points $g \in \Omega_0$,



Experiments

Fig. 4—Modeling AC process.

which keeps track of the time of deposition of the material and, therefore, its curing, as the time evolves. Let $\Omega_{PR} \subset$ Ω_0 be part of the domain that has been printed and $\Omega_{NPR} \subset$ Ω_0 be part of the domain that is yet to be printed. If an integration point is in $\mathbf{g} \in \Omega_{PR}$, then the material parameters of the cementitious material are used. Otherwise, scaled-down material parameters are used such that the material point has negligible stiffness and zero density, thereby constituting what is termed as the ghost element. An internal variable Θ assigned to the integration point is used to mark whether the integration point is in Ω_{PR} or Ω_{NPR} . The value of $\Theta = 1$ denotes that the integration point belongs to Ω_{PR} , while the value $\Theta = 0$ denotes that the integration point belongs to Ω_{NPR} . This notion is similar to that in the level-set method, which is commonly used to implicitly represent the geometry of an object.

The printed domain Ω_{PR} can be monitored by controlling the value of Θ . At time t=0, all integration points are assigned the value $\Theta=0$. Then, a moving point p(t) and an associated printing region $R_{PR} \subset \Omega$ around p(t) are defined to represent the kinematics of the printing nozzle and a region around the nozzle where the material is being printed. As the nozzle moves, the integration point in the printing region, $g \in R_{PR}$, is assigned a value of $\Theta=1$. Consequently, with time, the size of Ω_{PR} increases, and the printing process ends when $\Omega_{PR}=\Omega$.

The time when an integration point is printed is recorded by assigning the current time t_{n+1} to an internal variable t_g when $\mathbf{g} \in R_{PR}$ for the first time. This variable represents the deposition time needed to compute the evolving material parameters. The summary of the printing algorithm is presented in Box 2, where ε_E is the scale factor for the integration points in Ω_{NPR} . At this point, all the ingredients to model the AC process are present, as illustrated in Fig. 4.

Remark—Sensor-based information on the evolving field variables at select points in the printed structure can be incorporated in forward simulations in the 3-D print process (Masud and Goraya 2022).

Box 2—Algorithm for simulation of printing process

- Step 1: Retrieve data: $\{t_{n+1}, \Theta_n, t_g, g\}$
- Step 2: Compute current location of the moving point: $p(t_{n+1}) = (x_p(t_{n+1}), y_p(t_{n+1}), z_p(t_{n+1}))$

Model

- Step 3: Determine whether the current integration point is in $\mathbf{g} \in R_{PR}$ and update Θ : If $\mathbf{g} \in R_{PR}$ then $\Theta_{n+1} = 1$ else $\Theta_{n+1} = \Theta_n$
- Step 4: Use the appropriate material parameters. If $\Theta_n = 1$ then $t_g = t_{g,n}$, $E = E(t_{n+1} t_g)$, $\rho = \rho(t_{n+1} t_g)$ else $t_g = t_{n+1}$, $E = \varepsilon_E E(0)$, $\rho = 0$

Elastoplastic material model

NUMERICAL RESULTS

All numerical test cases presented in this paper are contact problem in \mathbb{R}^3 , where the contact plane Γ_P is represented by the plane z = 0. For this choice of contact plane

$$\mathbf{v} = (0,0,1) \tag{21}$$

$$\mathbf{\tau}^{\alpha} = \mathbf{e}^{\alpha} \tag{22}$$

where \mathbf{v} is the unit normal frictional surface; and e^{α} is the standard basis function for \mathbb{R}^3 . None of the test cases impose Dirichlet boundary conditions. A standard eight-node linear hexahedral element is used to discretize the domain in all the cases. Because the model presented in Eq. (12) gives close to a linear response before yielding, the elastic material parameters are approximated in terms of elastic modulus E and Poisson's ratio \mathbf{v} using the following relations.

$$\kappa = \frac{E}{3(1-2\nu)}, \ \mu = \frac{E}{2(1+\nu)}$$
(23)

For all printing simulations, the scale factor $\varepsilon_E = 10^{-4}$ is used.

Sliding of elastic block

To validate the formulation and the numerical implementation of the frictional contact model, an elastic block that slides against a rough rigid floor was considered, as presented by Simo and Laursen (1992). The block has 4 x 1 x 2 dimensions and is discretized into 20 x 1 x 10 elements. The boundary conditions are shown in Fig. 5(a). The material has elastic modulus E = 1000 and Poisson's ratio v = 0.3. A Coulomb friction law is imposed at the contact plane between the block and the rigid surface with frictional constant $\mu_f = 0.5$, $\varepsilon_N = 10^8$, and $\varepsilon_T = 10^5$. No frictional traction is allowed in the thickness direction by imposing $[t_T]_2 = 0$. Frictional traction is also not allowed at the first and last nodes of the contact surface Γ_C to conform with the problem

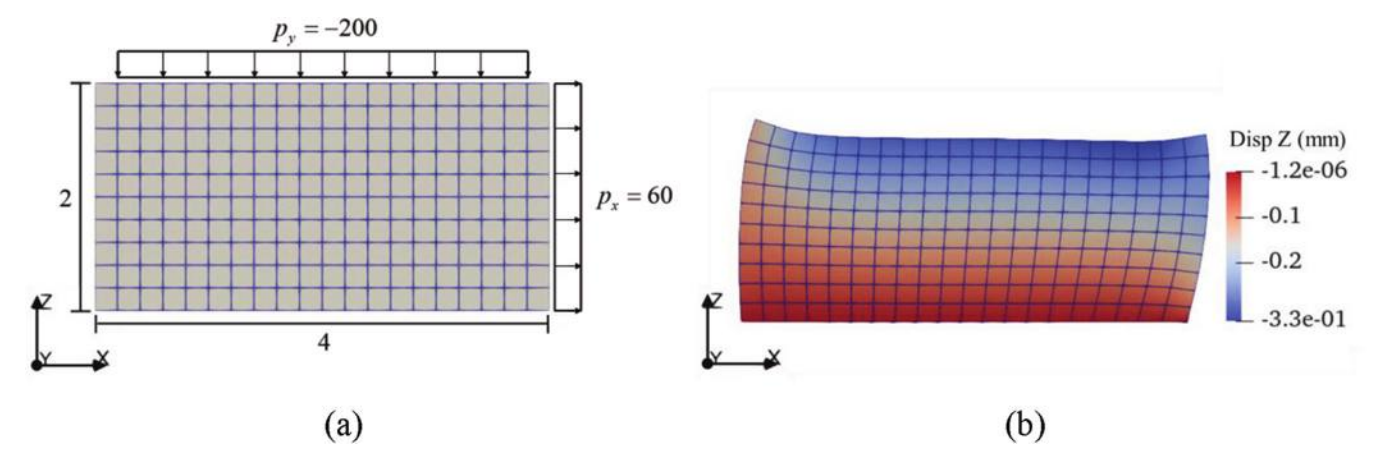


Fig. 5—Sliding block problem: (a) boundary conditions; and (b) deformation.

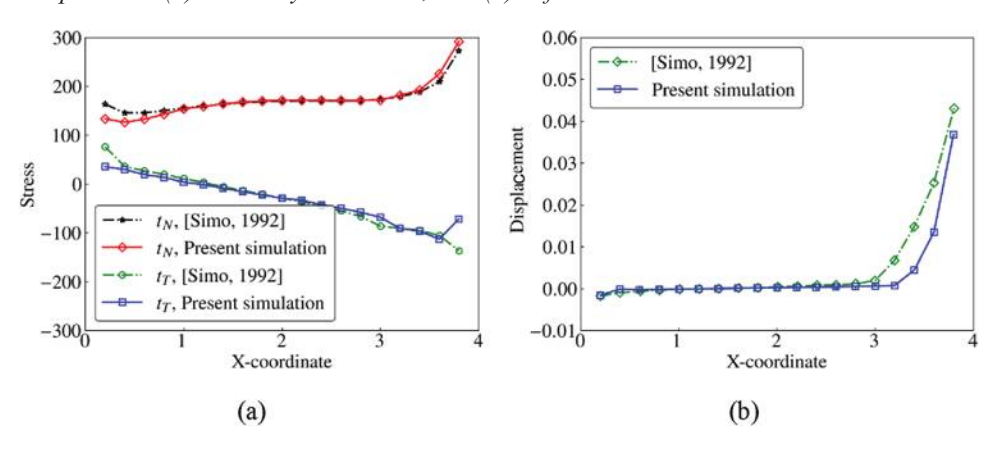


Fig. 6—Comparison with Simo and Laursen (1992): (a) contact traction; and (b) slip displacement.

described in Simo and Laursen (1992). This zero-friction at the first and last node is imposed by setting $\mu_f = 0$ for the closest integration points to the edge of the block (x = 1 and x = 4). For surface integration on the hexahedral element, the 10 x 10 integration rule is used to integrate the frictional term in Eq. (4). The resulting deformation is shown in Fig. 5(b).

The results are compared with the no-augmentation case presented by Simo and Laursen (1992). The comparison of contact traction is presented in Fig. 6(a), where a good match with the reference data can clearly be seen. The only significant deviation is in the tangential traction at x = 0.2 and x = 3.8. In the present simulation, the tangential traction at these two nodes is smaller in magnitude compared to the neighbor nodes. This is because the tangential traction was set to be zero at x = 1 and x = 4. The interface slip displacement is compared in Fig. 6(b). In the present simulation, the slip occurs at x > 3.2, while the data from Simo and Laursen (1992) show that the slip occurs at x > 3. The discrepancy may be attributed to the difference in how zero tangential traction at the first and last nodes is imposed. Nevertheless, the general behavior of the overall slip is comparable between the two methods.

Printing of hollow cylinder

This section presents simulations of the printing process of a hollow cylinder. The cylinder has a centerline radius of 250 mm. The width and height of each layer is 40 and

10 mm, respectively. Linear hexahedral elements are used to discretize the domain. Each layer is discretized into 8 x 2 elements in the cross section, and 40 elements are used along the circumference. The algorithm in Box 2 is used to simulate the printing process. The description of nozzle trajectory and the print region are given in Wijaya et al. (2022). The simulation was performed with time-step size $\Delta t = 0.9425$ seconds. Two cases are considered: in the first case, the base of the cylinder is held fixed; in the second case, instead of applying Dirichlet boundary conditions, the contact-friction model is used at the base of the cylinder with $\varepsilon_N = \varepsilon_T = 0.1$ and $\mu_f = 0.045$. The frictional coefficient is chosen such that the displacement of the base of the cylinder matches well with the experiments in Wolfs et al. (2018). Furthermore, simulations are carried out with and without BBC, and the response is compared.

Material parameters for the constitutive model are obtained through the uniaxial compression and direct shear tests in Wolfs et al. (2018). The procedure for the extraction of material parameters and conversion between Mohr-Coulomb and Drucker-Prager parameters can be found in Wijaya et al. (2022). Because the material is evolving during the printing process, it is necessary to conduct the tests at several time points. It is also important to note that in Wolfs et al. (2018), it is reported that to be able to conduct the uniaxial compression and direct shear tests, material that is extracted from the 3-D printer needs to be compacted to obtain a homogeneous sample. This results in material parameters that give stiffer

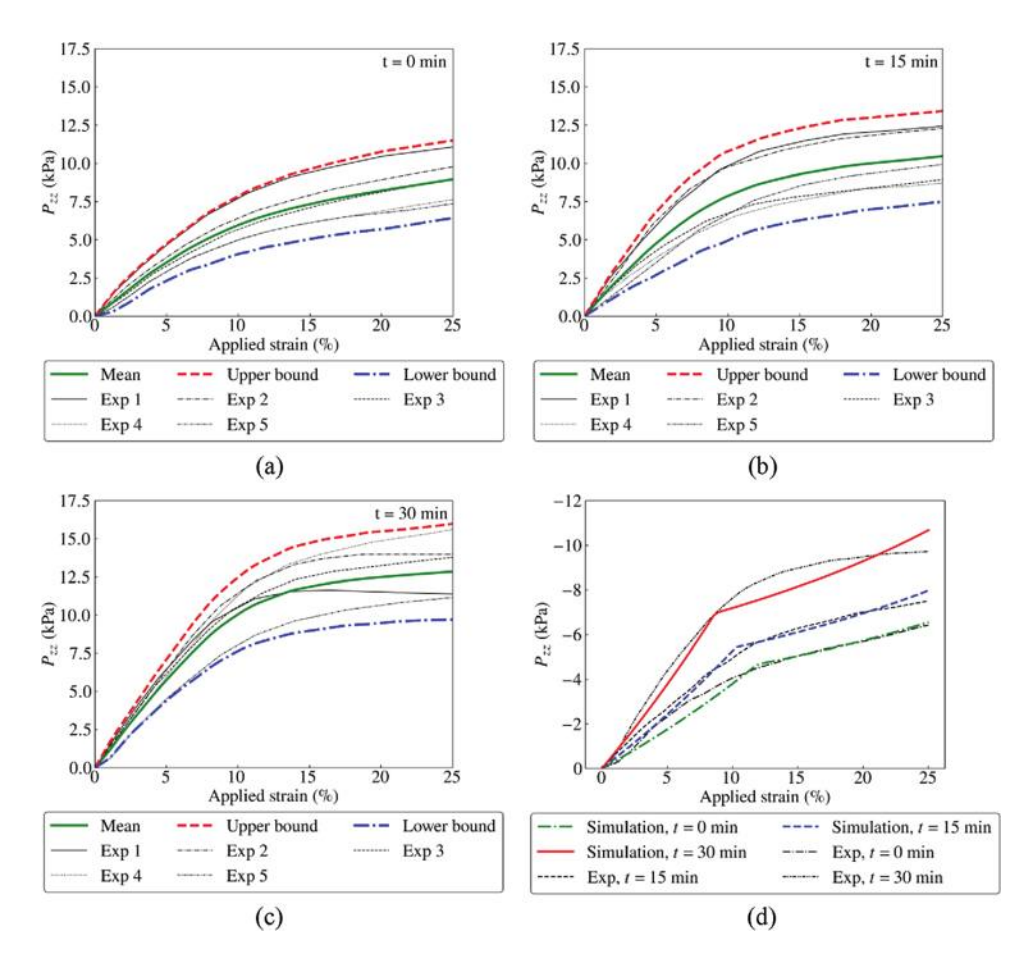


Fig. 7—Uniaxial compression test results at: (a) 0 minutes; (b) 15 minutes; (c) 30 minutes; and (d) comparison between simulation and lower bound.

and stronger modeled responses than the actual printed concrete that is not compacted during the actual printing process. Therefore, the material parameters used in this section are adjusted to match the lower bound of the uniaxial compression test results. The lower bound is chosen as 1.75 standard deviation below the mean. Figures 7(a) to (c) show the mean, upper bound, and lower bound for three different time points, respectively. Material parameters are obtained by fitting the material parameters to the lower-bound curve. Figure 7(d) shows the comparison between simulations using the material parameters given in Table 1 and the lower bound of the uniaxial compression test results. Linear interpolation is used to calculate the material parameters between the time points reported in Table 1.

The temporal and spatial evolution of the elastic modulus is shown in Fig. 8. Figures 9 and 10 include the experimentally obtained data (Wolfs et al. 2018) on the vertical alignment of five cylinders, which are used as reference data for comparison with the current numerical simulations. Figure 9 compares simulations with and without BBC. At the completion of layer 23, there is a small difference between simulations with and without BBC. However, this small difference becomes more significant as the subsequent layers are placed and the structure gets closer to the point of buckling failure. Halfway through the printing of layer 26 (denoted by layer 25.5), the difference between simulations with and without BBC becomes noticeable. This is expected because BBC contributes to the plastic deformation. The structure

Table 1—Material parameters

	E, kPa	ν	σ _y , kPa	α	ρ, kg/m ³
0 minutes	32.5	0.3	3	0.47453	2070
15 minutes	45	0.3	3.5	0.47453	2070
30 minutes	70	0.3	4.5	0.47453	2070

simulated with BBC collapsed before the completion of layer 26. Figure 10 shows the comparison between the case with a fixed cylinder base and the case where the friction model is used on the cylinder base. Failure also occurs earlier when the base of the cylinder is allowed to move. The case with the friction model and BBC reaches failure before the completion of layer 26. The rest of the cases reach failure at approximately the start of the printing of layer 27. These simulation-based failures match well with the experiments presented in Wolfs et al. (2018), where the five printed cylinders collapsed after the printing of layers 25, 27, 30, 31, and 31, respectively.

Printing structural system with crosslinking infill pattern

This section presents the simulation of a structure with the embedded structural mechanics concept of crosslinking of components to show the applicability of the method to large-scale systems. The objective of this test problem is to show that the digital twin can be used to simulate the AC process,

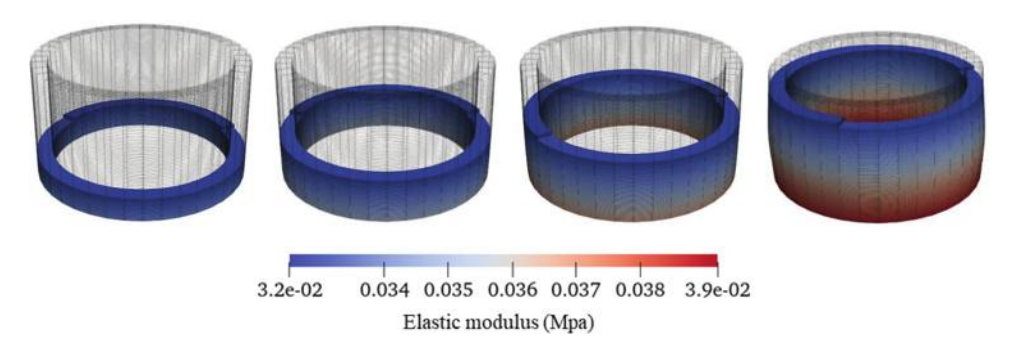


Fig. 8—Evolution of elastic modulus during printing process.

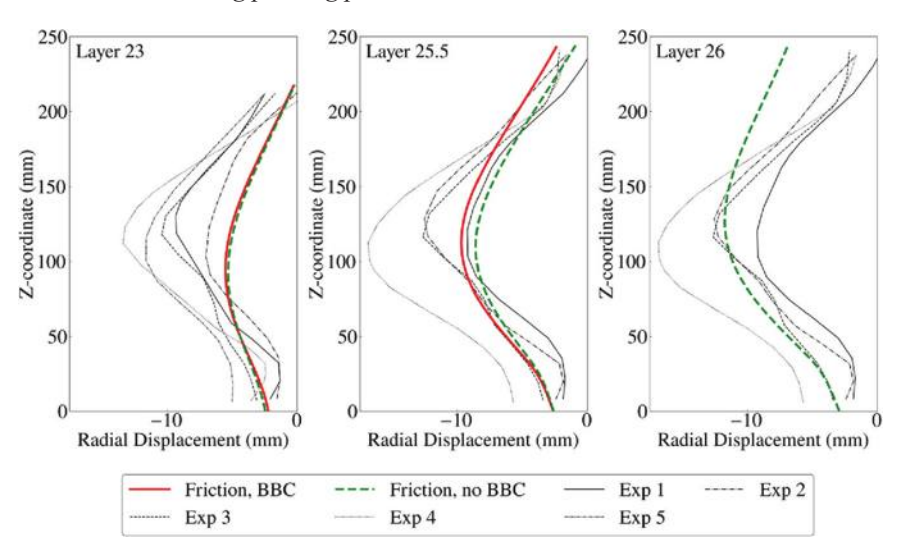


Fig. 9—Effect of BBC: maximum radial deformation compared with experimental data in Wolfs et al. (2018).

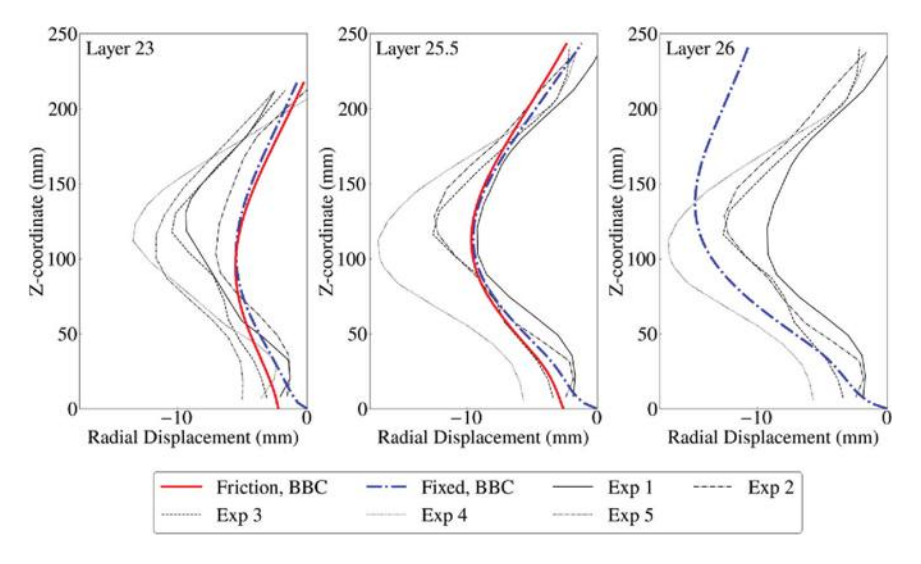


Fig. 10—Effect of slippage: maximum radial deformation compared with experimental data in Wolfs et al. (2018).

and also show that by changing the process parameters, failure can be induced. As such, this methodology can be implemented to optimize the various variables that can affect successful printing of the structure and result in a stable and buildable structure.

The structure comprises two straight walls with two half-cylinders at the two ends. The cross-sectional dimensions of the structure are given in Fig. 11, and the height of the structure is 2 m. Figures 12 and 13 show the infill patterns for the straight and curved sections of the wall, respectively.

The layer width and height are 5 and 2.5 cm, respectively. In this simulation, the base of the structure is held fixed. The printing speed and nozzle trajectory are selected such that one layer of the structure can be printed in 24 minutes, which results in good bond strength between successive layers, according to the study presented in Le et al. (2012b). First, the inside shell is printed, which takes 6 minutes. Next, the outer shell is printed, also taking 6 minutes. Lastly, the zigzag infill pattern is printed, which takes 12 minutes. The details of the print trajectory along with the corresponding

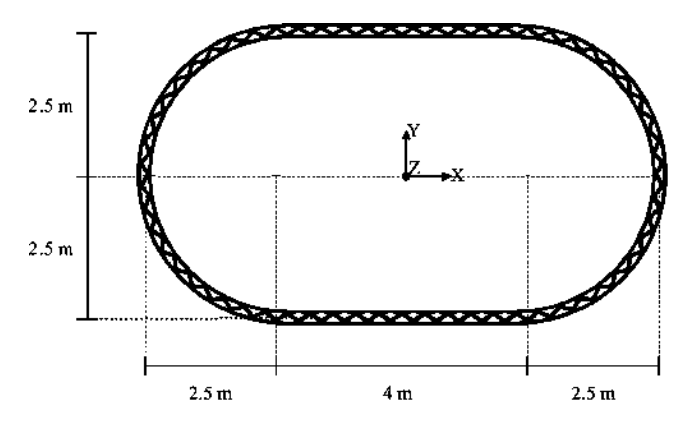


Fig. 11—Maximum radial deformation compared with experimental data.

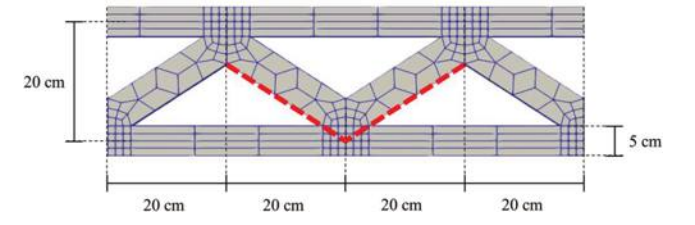


Fig. 12—Straight wall infill pattern.

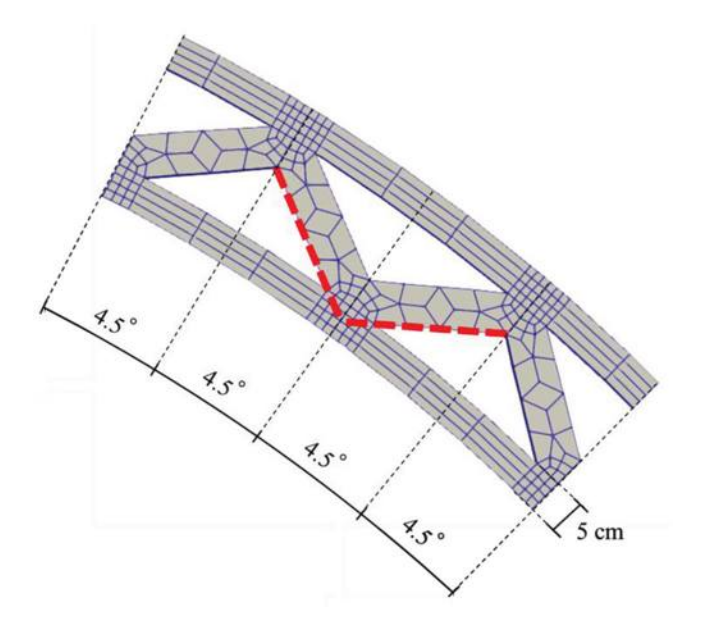


Fig. 13—Circular wall infill pattern.

timeline are shown in Fig. 14. The simulation is conducted with a time-step increment $\Delta t = 60$ seconds.

The evolution of material parameters is taken as follows

$$E = \begin{cases} 0.015 \text{ MPa} + 0.0002t \text{ MPa/min} & \text{if } t \le 240 \text{ min} \\ 0.063 \text{ MPa} + 5.5t \text{ MPa/min} & \text{if } t > 240 \text{ min} \end{cases}$$
(24)

$$v = 0.3 \tag{25}$$

$$\sigma_y = \begin{cases} 0.015 \text{ MPa} + 0.0002t \text{ MPa/min} & \text{if } t \le 240 \text{ min} \\ 0.0055t \text{ MPa/min} & \text{if } t > 240 \text{ min} \end{cases}$$
(26)

$$\alpha = 0.47453 \tag{27}$$

The elastic modulus and yield stress rapidly increase after 240 minutes because it is assumed that curing due to the hydration process starts at this point. The spatial distribution of the evolving elastic modulus in the first layer at the 24th minute is shown in Fig. 15. This layout follows the printing trajectory shown in Fig. 14.

This numerical example demonstrates the capability of the method to simulate and analyze the effect of material evolution, print speed, and nozzle trajectory on the printed structure. Fresh concrete typically has low stiffness, and there is a risk that the printed parts can significantly deform and therefore deviate from the intended geometric shape. Figure 16 shows the print-induced displacement, which indicates how much the print has deviated away from the intended design geometry. A significant part of the displacement magnitude shown in Fig. 16(d) comprises the vertical component of the displacement shown in Fig. 16(c). The two semicircular sections deform outward, causing the straight segments to lean inwards, thereby leading to a global mode of deformation. This global mode has an effect on the local stress distribution in the inner and outer walls. The line plots of the deformed shape along the height in the z-direction and stress induced due to self-weight of the inner and outer walls at two different locations are shown in Fig. 17 and 18. The deviation from the vertical alignment of the printed geometry is the result of the inelastic behavior of the material and the incremental deposition of the material in the AC process. Figure 19 shows the zoom view of the in-plane connectivity of the inner and outer walls of the topmost layer. The purpose of the infill is to tie the two walls, thereby providing lateral stability to the structure. The points where infill connects the inner and outer walls are relatively stiff and, therefore, result in higher local stresses. The deformation and stress along one of the semicircles at different heights are shown in Fig. 20 to 22. The displacement line plots represent the outer surface of the outer wall and the inner surface of the inner wall. In Fig. 20, it can be clearly seen that the radius of the outer wall fluctuates by 0.7 cm about the mean radius. This pattern may be a combined effect of the lateral restraint provided by the infill that couples the inner and outer walls to stabilize the structure and the local deformation in the outer wall due to the hoop stresses.

One of the main concerns in 3-D printing with concrete is the potential failure during the printing process. The proposed method is able to capture both modes of failure that are encountered in 3-D concrete printing. To demonstrate this, the same structure was printed with the same material parameters, but with five times the printing speed as compared to the case shown in Fig. 14. A faster rate of printing results in less time for the printer to come around and place the next layer of material. However, the material may not have had enough time to gain strength and stiffness to carry the load. Figure 23 shows the simulation at five times the printing speed, where the outer shell displays local buckling of the wall. The structure fails before it reaches 0.5 m in height, and the mode of failure is buckling of the outer shell, which triggers geometric failure of the structure. This ability to

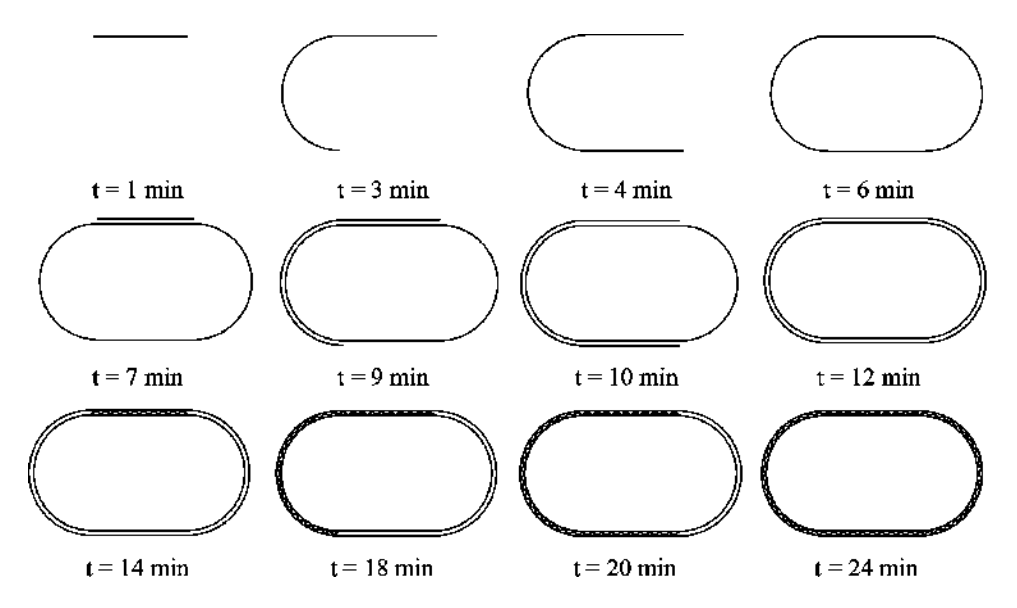


Fig. 14—Printing trajectory and corresponding time point.

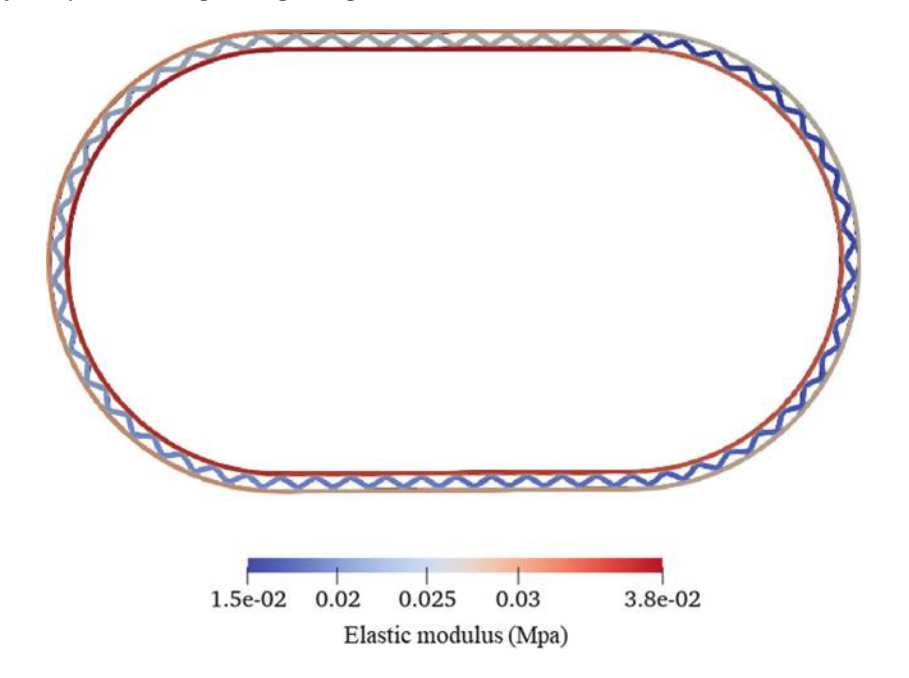


Fig. 15—Spatial variation of evolving elastic modulus during printing process.

computationally verify the buildability of the structure is a significant contribution of the method presented in this paper and can be employed to check whether the structure is buildable and that the printing-induced deformations are acceptable.

CONCLUSIONS

Modeling the process of layered deposition of material is a nonclassical problem from the perspective of material and structural modeling. Unlike the standard modeling and analysis problems in solid and structural mechanics, it involves materials that evolve. Therefore, the mechanical material parameters that are needed in the constitutive equations change during the simulation of the construction process, which can lead to the violation of the second law of thermodynamics when standard constitutive models are employed. Secondly, additive construction (AC) involves a systematic process

through which the material is deposited, thereby leading to the evolving shape of the structure.

These two evolving processes—material property evolution and geometric shape change—are both intricately coupled in the computational framework. The buildability of the structure in the physical manufacturing process and the stability of the digital twin in the virtual environment are a function of the intricate interplay of timescales that come from intrinsic material properties and physical timescales of the printing process.

This paper presents a numerical method wherein both issues are addressed such that a stable numerical method emerges. The method accounts for slippage between the first printed layer and the supporting surface through a penalty-based contact-friction model. It also employs an algorithm that is based on a novel ghost-mesh method to account for the printing path and speed. This algorithm, together

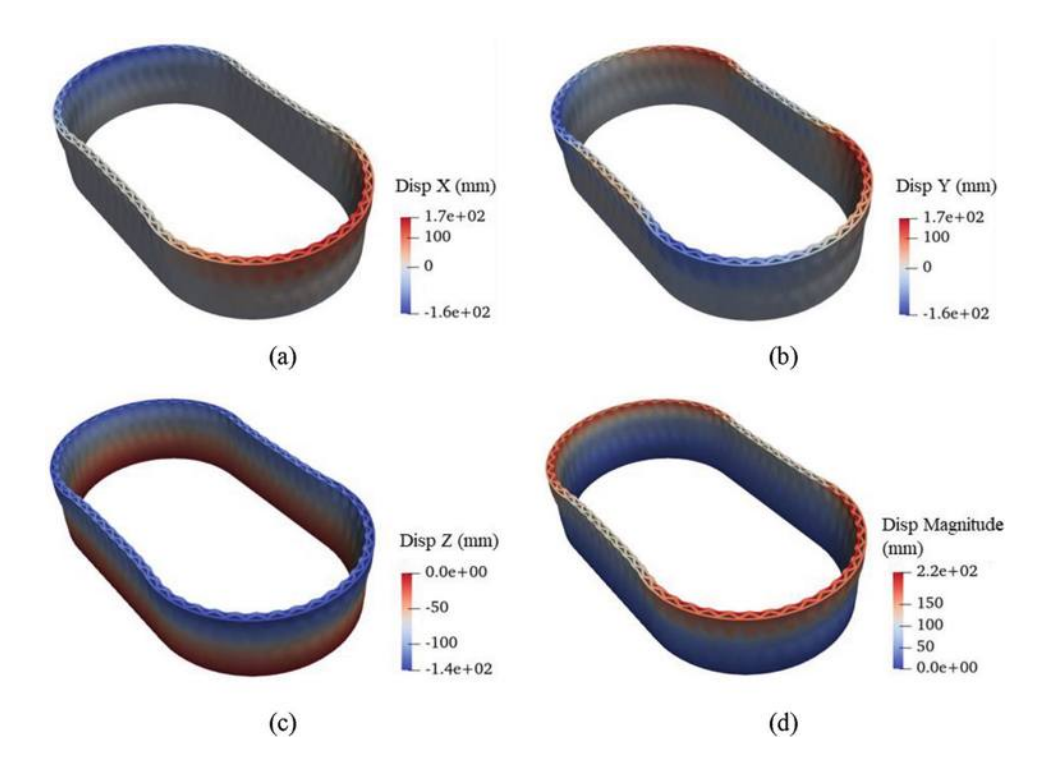


Fig. 16—Displacement of printed structure: (a) disp-X; (b) disp-Y; (c) disp-Z; and (d) magnitude.

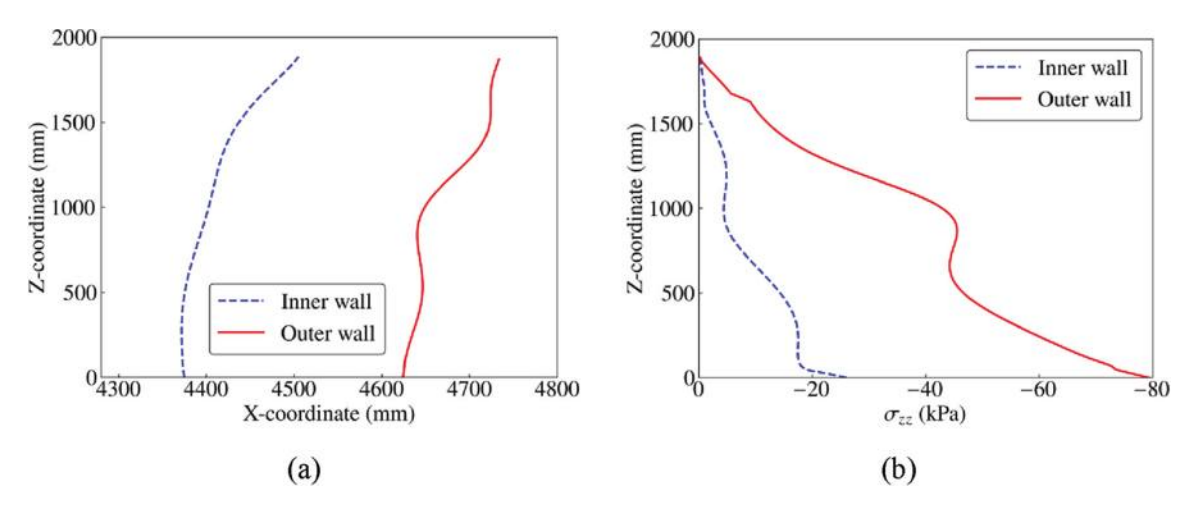


Fig. 17—Cross section y = 0, wall at x = 4.5 m: (a) y-z-coordinate of inner and outer walls; and (b) σ_{zz} in inner and outer walls.

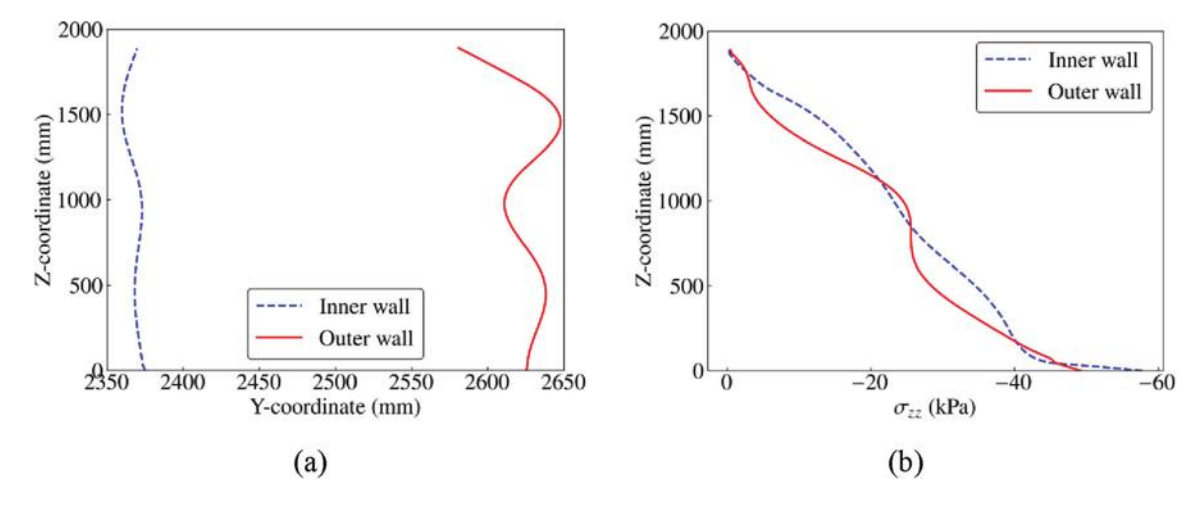


Fig. 18—Cross section x = 0, wall at y = 2.5 m: (a) x-z-coordinate of inner and outer walls; and (b) σ_{zz} in inner and outer walls.

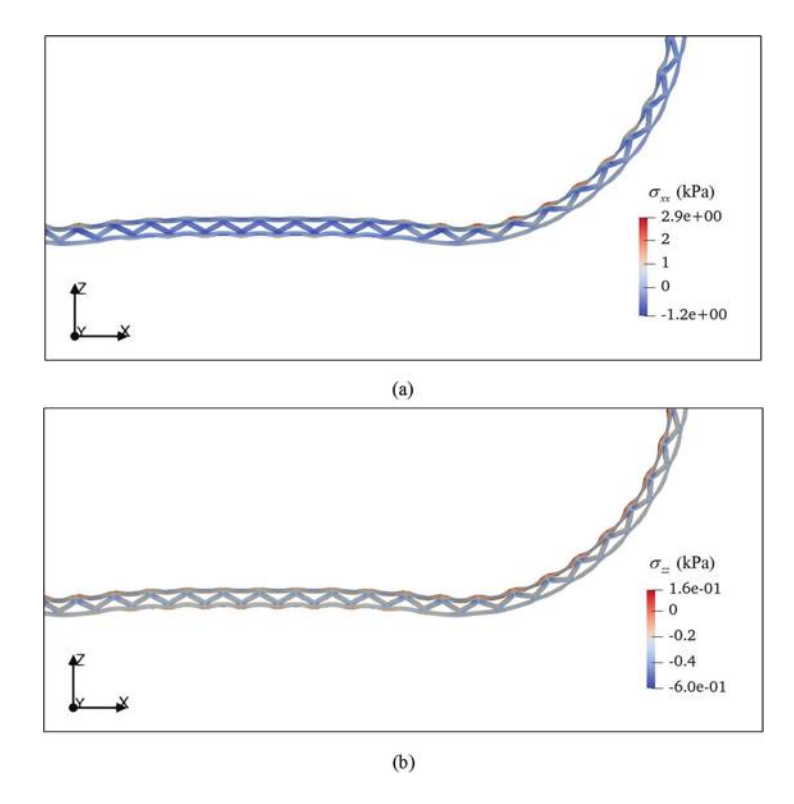


Fig. 19—Segment of straight and curved portion of wall with infill: (a) σ_{xx} ; and (b) σ_{zz} .

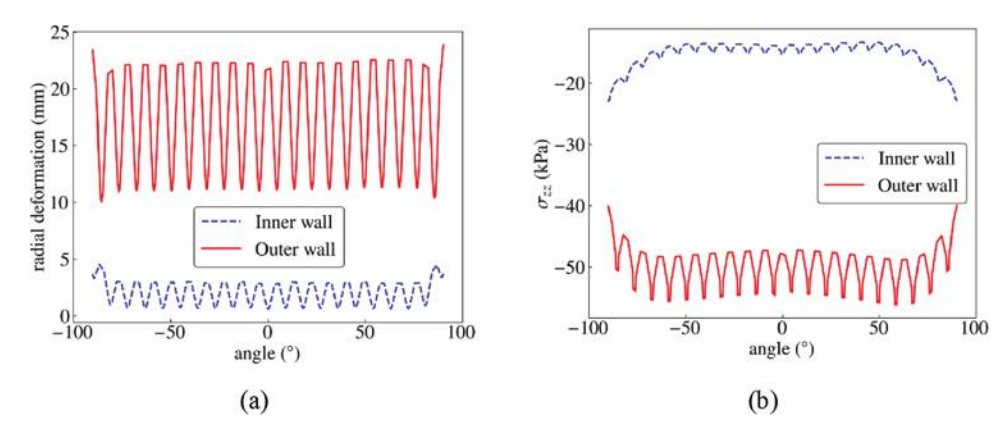


Fig. 20—Cross section z = 500, wall at x > 2 m: (a) radial displacement of inner and outer walls; and (b) σ_{zz} in inner and outer walls.

with the inelastic constitutive relations, tightly couples the timescales of material evolution with the timescales of the layering of the material. The method is tested on carefully designed problems for which experimentally obtained data are available, and it is then applied to a complex geometric structure to highlight its range of application.

A numerical three-dimensional (3-D) printing simulation of a hollow cylinder is presented. The cases where the base of the cylinder is held fixed and where frictional slip is permitted are simulated and compared. It is shown that the simulated structure experienced earlier failure when slippage is accounted for in the simulation. In addition, constitutive models with and without bounce-back control (BBC) are also compared. To establish the scalability of the proposed method, the last test case presents printing of a structure comprising two straight walls and two half-cylinders at either end, along with an infill for structural stability. To highlight the advantages of numerical modeling,

the rate of printing is increased, which shows that the structure reaches failure much earlier when the material has not gained enough strength to be able to carry the load of subsequent layers, thereby triggering material instability. These examples demonstrate the capability of the method to analyze the effects of material evolution, printing speed, and trajectory on the buildability of the printed structure. They also highlight that simulation-based design of the printing process can not only help optimize the printing rate but can also predict the onset of failure that may get triggered by material or geometric instability. These simulations can also provide insights into the stability of a structure and help in setting limits on acceptable tolerances for manufacturing-induced deformations in printed structures.

AUTHOR BIOS

Ignasius P. A. Wijaya is a PhD Student in the Department of Civil and Environmental Engineering at the University of Illinois Urbana-

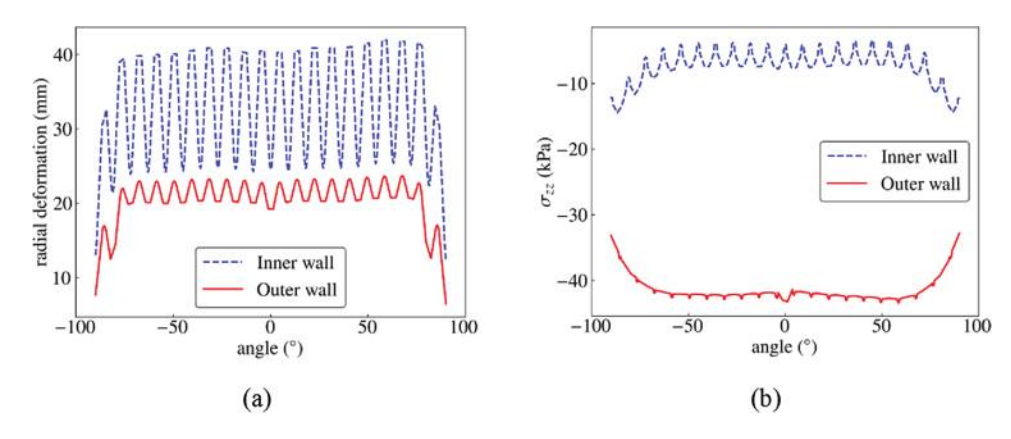


Fig. 21—Cross section z = 1000, wall at x > 2 m: (a) radial displacement of inner and outer walls; and (b) σ_{zz} in inner and outer walls.

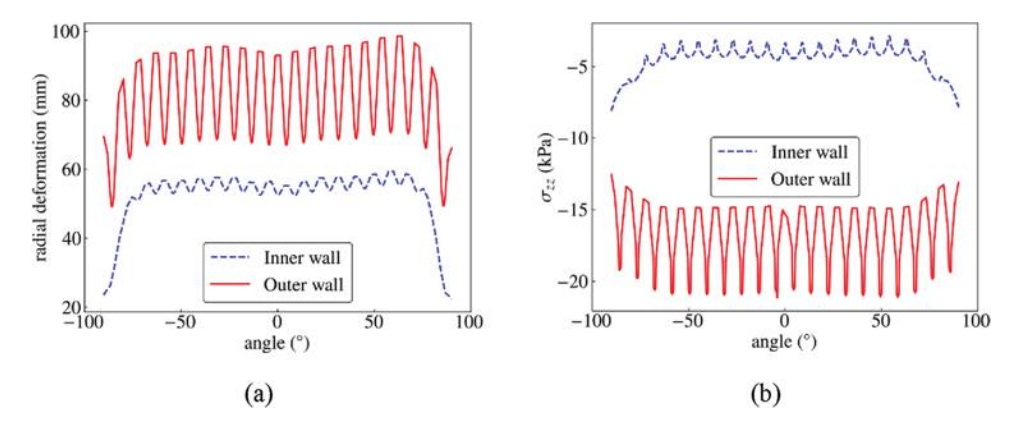


Fig. 22—Cross section z = 1500, wall at x > 2 m: (a) radial displacement of inner and outer walls; and (b) σ_{zz} in inner and outer walls.

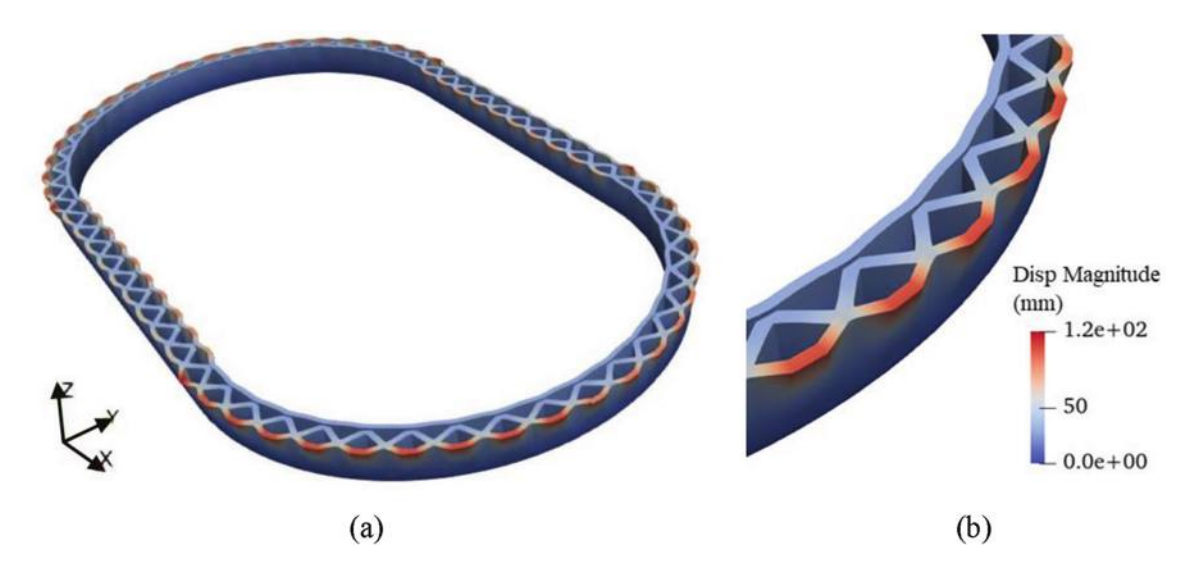


Fig. 23—Buckling of outer shell.

Champaign (UIUC), Urbana, IL. He received his BS from Parahyangan Catholic University, Bandung, West Java, Indonesia, and his MS from UIUC. His research interests include material and process modeling in three-dimensional (3-D) printing, numerical methods for viscoelastic materials, and stabilized finite element methods.

ACI member Eric Kreiger is a Research Civil Engineer at the U.S. Army Corps of Engineers Engineer Research and Development Center (ERDC) Construction Engineering Research Laboratory (CERL) in Champaign, IL. He is the Structural Engineering and Materials Lead for ERDC's Additive Construction (construction-scale 3-D printing) program located at CERL. He is Chair of ACI Subcommittee 564-B, Structural Design and Testing. He received his BS and MS from Michigan Technological University,

Houghton, MI. His research interests include full-scale structural testing of large-scale additively constructed components, engineering design and decision analysis using remote data, material degradation, structural assessment using sensors and nondestructive testing techniques, and hazard risk assessment.

Arif Masud is the John and Eileen Blumenschein Professor of Mechanics and Computations in the Department of Civil and Environmental Engineering and the Department of Aerospace Engineering at UIUC. He has made fundamental and pioneering contributions to the development of variational multiscale (VMS) methods for fluid and solid mechanics, which are ideally suited for the modeling of coupled multiphysics phenomena in science and engineering.

ACKNOWLEDGMENTS

This material is based upon work supported by the U.S. Army Corps of Engineers (USACE) Engineer Research and Development Center (ERDC) - Construction Engineering Research Laboratory (CERL) under contract W9132T22C0020.

REFERENCES

ACI Committee 347, 2004, "Guide to Formwork for Concrete (ACI 347-04)," American Concrete Institute, Farmington Hills, MI, 32 pp.

Bažant, Z. P., 1979, "Thermodynamics of Solidifying or Melting Viscoelastic Material," *Journal of the Engineering Mechanics Division*, ASCE, V. 105, No. 6, pp. 933-952. doi: 10.1061/JMCEA3.0002555

Bažant, Z. P., ed., 1988, Mathematical Modeling of Creep and Shrinkage of Concrete, John Wiley & Sons, Inc., New York.

Comminal, R.; Leal da Silva, W. R.; Andersen, T. J.; Stang, H.; and Spangenberg, J., 2020, "Modelling of 3D Concrete Printing Based on Computational Fluid Dynamics," *Cement and Concrete Research*, V. 138, Article No. 106256. doi: 10.1016/j.cemconres.2020.106256

de Miranda, L. R. M.; Marchesini, F. H.; Lesage, K.; and De Schutter, G., 2023, "The Evolution of the Rheological Behavior of Hydrating Cement Systems: Combining Constitutive Modeling with Rheometry, Calorimetry and Mechanical Analyses," *Cement and Concrete Research*, V. 164, Article No. 107046. doi: 10.1016/j.cemconres.2022.107046

Diggs-McGee, B. N., and Kreiger, E. L., 2021, "Using Isolated Temporal Analysis to Aid in the Assessment of Structural Element Quality for Additive Construction," *Standards Development for Cement and Concrete for Use in Additive Construction*, S. Z. Jones and E. L. Kreiger, eds., ASTM International, West Conshohocken, PA, pp. 117-143. doi: 10.1520/STP163620200105

Gawin, D.; Pesavento, F.; and Schrefler, B. A., 2006, "Hygro-Thermo-Chemo-Mechanical Modelling of Concrete at Early Ages and Beyond. Part I: Hydration and Hygro-Thermal Phenomena," *International Journal for Numerical Methods in Engineering*, V. 67, No. 3, pp. 299-331. doi: 10.1002/nme.1615

Harbouz, I.; Yahia, A.; Roziere, E.; and Loukili, A., 2023, "Printing Quality Control of Cement-Based Materials under Flow and Rest Conditions," *Cement and Concrete Composites*, V. 138, Article No. 104965. doi: 10.1016/j.cemconcomp.2023.104965

Jagoda, J. A., 2020, "An Analysis of the Viability of 3D-Printed Construction as an Alternative to Conventional Construction Methods in the Expeditionary Environment," master's thesis, Air Force Institute of Technology, Wright-Patterson AFB, OH, 121 pp.

Khan, M. S.; Sanchez, F.; and Zhou, H., 2020, "3-D Printing of Concrete: Beyond Horizons," *Cement and Concrete Research*, V. 133, Article No. 106070. doi: 10.1016/j.cemconres.2020.106070

Kreiger, E.; Diggs-McGee, B.; Wood, T.; MacAllister, B.; and Kreiger, M., 2020, "Field Considerations for Deploying Additive Construction," *Second RILEM International Conference on Concrete and Digital Fabrication: Digital Concrete 2020*, F. P. Bos, S. S. Lucas, R. J. M. Wolfs, and T. A. M. Salet, eds., Springer International Publishing, Cham, Switzerland, pp. 1147-1163. doi: 10.1007/978-3-030-49916-7_109

Kreiger, E. L.; Kreiger, M. A.; and Case, M. P., 2019, "Development of the Construction Processes for Reinforced Additively Constructed Concrete," *Additive Manufacturing*, V. 28, pp. 39-49. doi: 10.1016/j. addma.2019.02.015

Kröner, E., 1959, "Allgemeine Kontinuumstheorie der Versetzungen und Eigenspannungen," *Archive for Rational Mechanics and Analysis*, V. 4, No. 1, pp. 273-334. (in German) doi: 10.1007/BF00281393

Kupwade-Patil, K.; Tyagi, M.; Brown, C. M.; and Büyüköztürk, O., 2016, "Water Dynamics in Cement Paste at Early Age Prepared with Pozzolanic Volcanic Ash and Ordinary Portland Cement Using Quasielastic Neutron Scattering," *Cement and Concrete Research*, V. 86, pp. 55-62. doi: 10.1016/j.cemconres.2016.04.011

Laursen, T. A., and Simo, J. C., 1993, "A Continuum-Based Finite Element Formulation for the Implicit Solution of Multibody, Large Deformation-Frictional Contact Problems," *International Journal for Numerical Methods in Engineering*, V. 36, No. 20, pp. 3451-3485. doi: 10.1002/nme.1620362005

Le, T. T.; Austin, S. A.; Lim, S.; Buswell, R. A.; Gibb, A. G. F.; and Thorpe, T., 2012a, "Mix Design and Fresh Properties for High-Performance Printing Concrete," *Materials and Structures*, V. 45, No. 8, pp. 1221-1232. doi: 10.1617/s11527-012-9828-z

Le, T. T.; Austin, S. A.; Lim, S.; Buswell, R. A.; Law, R.; Gibb, A. G. F.; and Thorpe, T., 2012b, "Hardened Properties of High-Performance Printing Concrete," *Cement and Concrete Research*, V. 42, No. 3, pp. 558-566. doi: 10.1016/j.cemconres.2011.12.003

Lee, E. H., 1969, "Elastic-Plastic Deformation at Finite Strains," *Journal of Applied Mechanics*, V. 36, No. 1, pp. 1-6. doi: 10.1115/1.3564580

Masud, A., and Goraya, S., 2022, "Variational Embedding of Measured Data in Physics-Constrained Data-Driven Modeling," *Journal of Applied Mechanics*, V. 89, No. 11, Article No. 111001. doi: 10.1115/1.4055256

Masud, A.; Truster, T. J.; and Bergman, L. A., 2012, "A Unified Formulation for Interface Coupling and Frictional Contact Modeling with Embedded Error Estimation," *International Journal for Numerical Methods in Engineering*, V. 92, No. 2, pp. 141-177. doi: 10.1002/nme.4326

Nedjar, B., 2022, "Incremental Viscoelasticity at Finite Strains for the Modelling of 3D Concrete Printing," *Computational Mechanics*, V. 69, No. 1, pp. 233-243. doi: 10.1007/s00466-021-02091-5

Ngo, T. D.; Kashani, A.; Imbalzano, G.; Nguyen, K. T. Q.; and Hui, D., 2018, "Additive Manufacturing (3D Printing): A Review of Materials, Methods, Applications and Challenges," *Composites Part B: Engineering*, V. 143, pp. 172-196. doi: 10.1016/j.compositesb.2018.02.012

Paolini, A.; Kollmannsberger, S.; and Rank, E., 2019, "Additive Manufacturing in Construction: A Review on Processes, Applications, and Digital Planning Methods," *Additive Manufacturing*, V. 30, Article No. 100894. doi: 10.1016/j.addma.2019.100894

Perrot, A.; Rangeard, D.; and Pierre, A., 2016, "Structural Built-Up of Cement-Based Materials Used for 3D-Printing Extrusion Techniques," *Materials and Structures*, V. 49, No. 4, pp. 1213-1220. doi: 10.1617/s11527-015-0571-0

Reinold, J.; Nerella, V. N.; Mechtcherine, V.; and Meschke, G., 2022, "Extrusion Process Simulation and Layer Shape Prediction during 3D-Concrete-Printing Using the Particle Finite Element Method," *Automation in Construction*, V. 136, Article No. 104173. doi: 10.1016/j. autcon.2022.104173

Reiter, L.; Wangler, T.; Roussel, N.; and Flatt, R. J., 2018, "The Role of Early Age Structural Build-Up in Digital Fabrication with Concrete," *Cement and Concrete Research*, V. 112, pp. 86-95. doi: 10.1016/j.cemconres.2018.05.011

Roussel, N., 2006, "A Thixotropy Model for Fresh Fluid Concretes: Theory, Validation and Applications," *Cement and Concrete Research*, V. 36, No. 10, pp. 1797-1806. doi: 10.1016/j.cemconres.2006.05.025

Roussel, N., 2018, "Rheological Requirements for Printable Concretes," *Cement and Concrete Research*, V. 112, pp. 76-85. doi: 10.1016/j.cemconres.2018.04.005

Roussel, N.; Spangenberg, J.; Wallevik, J.; and Wolfs, R., 2020, "Numerical Simulations of Concrete Processing: From Standard Formative Casting to Additive Manufacturing," *Cement and Concrete Research*, V. 135, Article No. 106075. doi: 10.1016/j.cemconres.2020.106075

Simo, J. C., and Hughes, T. J. R., 1998, *Computational Inelasticity*, Springer-Verlag New York, Inc., New York.

Simo, J. C., and Laursen, T. A., 1992, "An Augmented Lagrangian Treatment of Contact Problems Involving Friction," *Computers & Structures*, V. 42, No. 1, pp. 97-116. doi: 10.1016/0045-7949(92)90540-G

Spangenberg, J.; Leal da Silva, W. R.; Comminal, R.; Mollah, M. T.; Andersen, T. J.; and Stang, H., 2021, "Numerical Simulation of Multi-Layer 3D Concrete Printing," *RILEM Technical Letters*, V. 6, pp. 119-123. doi: 10.21809/rilemtechlett.2021.142

Suiker, A. S. J., 2018, "Mechanical Performance of Wall Structures in 3D Printing Processes: Theory, Design Tools and Experiments," *International Journal of Mechanical Sciences*, V. 137, pp. 145-170. doi: 10.1016/j.ijmecsci.2018.01.010

Suiker, A. S. J.; Wolfs, R. J. M.; Lucas, S. M.; and Salet, T. A. M., 2020, "Elastic Buckling and Plastic Collapse during 3D Concrete Printing," *Cement and Concrete Research*, V. 135, Article No. 106016. doi: 10.1016/j.cemconres.2020.106016

Tripathi, A.; Nair, S. A. O.; and Neithalath, N., 2022, "A Comprehensive Analysis of Buildability of 3D-Printed Concrete and the Use of Bi-Linear Stress-Strain Criterion-Based Failure Curves towards Their Prediction," *Cement and Concrete Composites*, V. 128, Article No. 104424. doi: 10.1016/j.cemconcomp.2022.104424

Wangler, T.; Roussel, N.; Bos, F. P.; Salet, T. A. M.; and Flatt, R. J., 2019, "Digital Concrete: A Review," *Cement and Concrete Research*, V. 123, Article No. 105780. doi: 10.1016/j.cemconres.2019.105780

Wijaya, I. P. A.; Kreiger, E.; and Masud, A., 2022, "An Elastic-Inelastic Model and Embedded Bounce-Back Control for Layered Printing with Cementitious Materials," *International Journal for Numerical Methods in Engineering*, V. 123, No. 21, pp. 5098-5125. doi: 10.1002/nme.7044

Wolfs, R. J. M., and Suiker, A. S. J., 2019, "Structural Failure during Extrusion-Based 3D Printing Processes," *International Journal of Advanced Manufacturing Technology*, V. 104, No. 1-4, pp. 565-584. doi: 10.1007/s00170-019-03844-6

Wolfs, R. J. M.; Bos, F. P.; and Salet, T. A. M., 2018, "Early Age Mechanical Behaviour of 3D Printed Concrete: Numerical Modelling and Experimental Testing," *Cement and Concrete Research*, V. 106, pp. 103-116. doi: 10.1016/j.cemconres.2018.02.001

ACI Chapter!

The American Concrete Institute has Chapters and Student Chapters located throughout the world. Participation in a local chapter can be extremely rewarding in terms of gaining greater technical knowledge and networking with leaders in the concrete community.

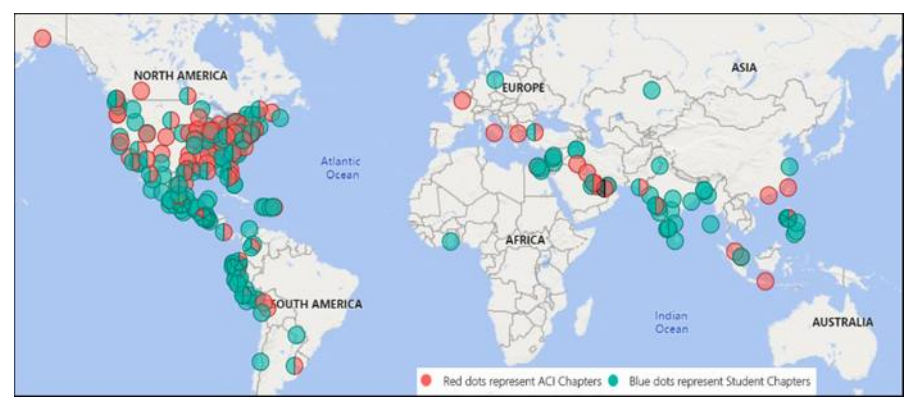
Because chapters are distinct and independent legal entities, membership includes both ACI members and non-ACI members and is made up of a diverse blend of architects, engineers, consultants, contractors, educators, material suppliers, equipment suppliers, owners, and students—basically anyone interested in concrete. Many active ACI members initially became involved in ACI through their local chapter. In addition to technical programs and publications, many chapters sponsor ACI Certification programs, ACI educational seminars, project award recognition programs, and social events with the goal of advancing concrete knowledge.

Check out the Chapters Special Section from the November 2020 *Concrete International*: www.concrete.org/publications/concreteinternational.aspx

Student Chapters

Join or form an ACI Student Chapter to maximize your influence, knowledge sharing, and camaraderie! ACI has 240+ student chapters located throughout the world, each providing opportunities for students to:

- Connect with their peers and participate in concrete-related activities such as: student competitions, ACI Conventions, ACI Certification Programs, ACI Educational Seminars, local chapter meetings, social events, and community service projects;
- Network with members of local chapters, many of whom have been in the industry for decades and can help to develop professional relationships and offer career advice;
- Win recognition for their universities through the University Award; and
- Learn about the many scholarships and fellowships offered by the ACI Foundation and by ACI's local chapters.













Title No. 121-S20

Ultimate Shear Strength Prediction for Slender Reinforced Concrete Beams without Transverse Reinforcement Using Machine Learning Approach

by Ju Dong Lee and Thomas H.-K. Kang

A great deal of attention has been applied recently to machine learning (ML) algorithms to solve difficult engineering problems in the field of structural engineering. Using borrowed features of ML algorithms (implemented), a solution to one of the most troublesome problems in concrete structures—namely, shear—is proposed. The understanding of shear failure in reinforced concrete (RC) structures has led to numerous laboratory investigations and analytical studies over the last century. Due to decades of efforts afforded by researchers, significant experimental shear test results have been created and archived. This data provides an opportune environment to implement ML techniques and evaluate model efficiency and accuracy. The focus of this paper is on ML modeling of the shear-transfer mechanism for slender RC beams without transverse reinforcement. Test results for 1149 RC beams were incorporated in the ML analysis for training (80%) and testing (20%) purposes. Prior to the ML analysis, a correlation coefficient analysis was conducted to determine if given design parameters affected shear strength. When compared to the data used, code-based shear equations provided with large safety margins gave reasonable predictions. Exponential-based Gaussian process regression (GPR) ML models yielded comparable predictions. Of the 19 ML models employed, most were considered as an effective strength predictive tools. These ML model predictions were compared to each other and with design provision shear equations.

Keywords: machine learning (ML); prediction; reinforced concrete (RC) slender beams; shear database; shear strength.

INTRODUCTION

Traditionally, structural conundrums bound by parameter effects and interdependency have been verified through experimental testing and numerical modeling. This definitive approach, however, requires significant expenditure, time, and effort. Modeling is also difficult in addressing variability and complex parameter interdependency. Current provisions in concrete design rely on empirical equations derived from limited experimental testing results. Conservatively, safety margin excess is inevitable to prevent unexpected failure. As an alternative to traditional applied empirical equations, machine learning (ML) techniques—a subfield of artificial intelligence (AI)-based approaches—have gained attention in the field of structural engineering over the past decade due to their accuracy in spite of large variability and parameter interdependency. Software applications and ML techniques ascertain trends and patterns amidst massive data without explicit programming.

Among uses in structural engineering, ML algorithms have been employed to monitor structure health, evaluate

performance, and predict behavior (Feng et al. 2021). The application of ML algorithms (for example, risk and resilience analysis) has thrived, given the enormity of data present. Examples of ML applications in monitoring health and evaluating performance are available in Butcher et al. (2014), Gui et al. (2017), Vitola et al. (2017), Yan et al. (2013), Chou et al. (2014), and Omran et al. (2016). Previously conducted structural and mechanical experimental test data may also be used in the ML approach to predict behavioral characteristics of structures, such as material properties, component capacities, and seismic resistance. The field is promising in that it affords the ability to replace (or supplement) difficult and/or costly experimental tests. However, application is in its infancy due to limited available data. Thoughts pertaining to recent studies using the ML approach for reinforced concrete (RC) structures to predict capacities are introduced as follows.

Zhang et al. (2022) applied the random forest (RF) ML model to account for variables in evaluating ultimate shear capacity of RC beams, whose hyperparameters were tuned using the beetle antennae search algorithm. In this study, two sets of databases consisting of 194 RC beams with stirrups and 1849 RC beams without stirrups were used to edify the ML model. The ML models developed performed well in predicting shear capacities with correlation coefficients at 0.94. However, the study failed to consider shear span-to-effective depth ratios (a/d) governing shear mechanisms between deep and slender beams (Lee and Mander 2022, 2023). By separating input data for deep and slender beams based on a/d = 2.5, predictions using the ML model would have significantly improved.

Alotaibi et al. (2021) predicted punching shear capacity of fiber-reinforced concrete (FRC) slabs using 20 ML algorithms, including: regression learner; tree ensemble; support vector machine (SVM); regression decision tree; Gaussian process regression (GPR); and artificial neural networks (ANNs). The ML models were prepared, tested, and validated using 148 experimental test results. The authors found highest accuracy in the ANN models. To render ease of accessibility to the structural practitioner, the authors developed a

ACI Structural Journal, V. 121, No. 2, March 2024.

MS No. S-2022-327.R1, doi: 10.14359/51740246, received July 20, 2023, and reviewed under Institute publication policies. Copyright © 2024, American Concrete Institute. All rights reserved, including the making of copies unless permission is obtained from the copyright proprietors. Pertinent discussion including author's closure, if any, will be published ten months from this journal's date if the discussion is received within four months of the paper's print publication.

neuro-nomograph technique based on ANN model results. Predictions using the neuro-nomograph approach showed remarkable accuracy with mean and coefficient of variation values between tested versus predicted of 1.00 and 0.05, respectively.

Feng et al. (2021) implemented ensemble ML methods, including: RF; adaptive boosting; gradient boosting regression tree, and extreme gradient boosting (XGBoost) to create predictive models for reinforced RC deep beams with and without transverse reinforcement. In this study, the authors used 271 test results, which were split into training and testing sets through tenfold cross-validation. The hyperparameters were determined by the grid search method with feature importance and partial dependence analysis conducted. When compared to mechanic-driven models in design provisions, such as the Chinese code (GB 50010-2010), U.S. code (ACI 318), Canadian code (CAN/CSA A23.3-04), and European code (Eurocode 2), the predictive models based on ensemble ML showed a significantly superior outcome.

Given current design provisions' limitations regarding ultra-high-performance concrete (UHPC) hinder its use in concrete structures, Solhmirzaei et al. (2022) presented an ML-based flexural design approach for UHPC beams. The authors applied support vector machine regression (SVMR) to predict flexural capacity and multi-gene genetic programming (MGGP) to derive an equation through data-driven analysis. A parametric study conducted regarding the flexural capacity of UHPC beams demonstrated the merit of the proposed ML data-driven equation and application in design of concrete structures.

To overcome the low accuracy and dissemination generally found in existing design equations for prediction of punching shear capacity in fiber-reinforced polymer (FRP)-RC slabs having no transverse reinforcement, Truong et al. (2022) investigated ML algorithms. In their study, three ML techniques, including support vector regression (SVR), RF, and XGBoost, were considered with a grid search method and a fivefold cross-validation. Against an experimental database consisting of 104 specimens, all three ML showed better agreement than code-based design methods and existing models. In particular, the XGBoost-based ML model showed superior outcomes.

The aforementioned studies show promising potential in ML algorithms based on previously conducted test results and that various types of structural performance can be evaluated with reasonable accuracy. Among them, application of ML in predicting the shear strengths of RC beams may have the greatest potential as significant efforts have already been made in the past decades to combine and archive broad shear testing results. Several large shear databases have been developed (Reineck et al. 2013, 2014; Reineck and Todisco 2014; Todisco et al. 2015) and used to verify various shear theories and equations (Collins et al. 1996; Lee and Watanabe 2000; Tureyen and Frosch 2003; Bentz et al. 2006; Brown and Bayrak 2008; Hsu et al. 2010; Choi et al. 2016). However, ML applications using these shear databases have been limited or inappropriately used. For example, Feng et al. (2021) focused only on deep beams, and Zhang et al. (2022) did not account for differing shear mechanisms. To address these shortcomings, the focus of this study is on the application of ML methods to slender non-shear-reinforced beams whose a/d are greater than 2.5. To lessen ML method implementation barriers, models available in MATLAB Toolbox were used. A total of 19 ML models were exercised and verified using experimental results from 1149 beam tests. Their outcomes were compared with each other and with those derived from shear equations found in design codes

RESEARCH SIGNIFICANCE

The behavior and mechanism of shear failure are some of the most complicated problems in RC structures. To date, no rational or prevailing model explains this phenomenon due to the number of parameters and their interdependency associated with the shear failure as well as uncertainties tied to concrete embedment. Therefore, shear design provisions, including AASHTO LRFD and ACI building codes, use empirical equations, indued with complications and limitations. This study aims to provide an alternative to solve the issue using an ML approach. Expensive and time-consuming testing can be partially replaced with ML methods.

MACHINE LEARNING MODELS

A description of several ML algorithms implemented in this study is provided in the following discussion.

Linear regression model

Regression represents the method of finding the relation between input parameters and output variables. Among regression methods, linear regression captures the relationship between independent variables (parameters) and dependent variables (outcomes) by fitting a straight line. Linear regression models are applied and extensively used in practical applications because statistical properties are easily determined (Yan and Su 2009). The study presented herein considers normal, interaction, robust, and stepwise linear models. Linear models include an intercept and linear terms for each predictor, whereas an interaction model contains all products of pairs of distinct predictors in addition to intercept and linear terms. Robust and stepwise methods refer to the means with which the model is fit to the data. The robust fit creates a model whereby outliers have little effect and the manual process of discarding them is not required, whereas the stepwise fit starts from a simple model such as a constant and adds or subtracts terms one at a time, choosing the optimal term each time until no further improvement is achieved.

Regression decision tree

As a supervised learning technique, regression decision trees have been widely used in ML to derive a strategy to reach a particular goal in data mining (Rokach and Maimon 2014). Decision trees employ an order of simple rules to predict outcomes through the iterative segmentation process. The decision tree is comprised of roots, leaves, and branches. In general, data sets are arranged at the root and their paths along the tree branches are determined based on the conditional criteria at every node in the tree. MATLAB Toolbox

provides three decision tree algorithms, including: 1) coarse tree; 2) medium tree; and 3) fine tree. All three tree algorithms have fast prediction speeds, small memory use, and easy interpretability. The difference that distinguishes one from the other is the flexibility of the model, which is low in the coarse tree and high in the fine tree. The maximum number of splits (leaves) to make coarse, medium, and fine distinctions between classes is 4, 20, and 100, respectively.

Support vector machines (SVMs)

Another supervised learning model based on statistical learning frameworks is known as SVM. It is often considered one of the most robust prediction methods. Grounded on finding an optimal hyperplane, an SVM training algorithm constructs a model that assigns data into two categories with the largest margin. Along with performing linear classification, SVMs can conduct nonlinear classifications using various kernel functions that allow mapping input data into high-dimensional feature spaces. The detailed training algorithm of SVMs is available in Deng et al. (2012). Five different SVM models available in the MATLAB Toolbox were implemented in this study: 1) linear; 2) quadratic; 3) fine Gaussian; 4) medium Gaussian; and 5) coarse Gaussian.

Tree ensemble

Tree ensembles create multiple learning models and combine them to improve result accuracy. Because the decision-making process is based on various models, increased accuracy is expected when the models have more significant diversity. Tree ensembles are suitable for regression and classification. Two popular ensemble methods used in the present study are bagging and boosting, which use different approaches to produce weak learners. Using bootstrap sampling, bagging generates weak learners in parallel. Boosting creates weak learners in sequential so that the previous weak learner affects the sequent learners. Bagging increases the accuracy of models by reducing variance and eliminating overfitting, whereas boosting generates better predictions through studying errors from previous predictions.

Gaussian process regression

As a generic supervised ML tool, the Gaussian process is commonly used to solve regression and probabilistic classification problems. GPR is a nonparametric regression method that implements Gaussian processes for regression purposes based on Bayesian principles. GPR provides uncertainty estimates for its prediction, which is widely applied in the field and in practice. Rather than determining specific relations of parameters with outcome, GPR attempts to represent probability distributions over admissible functions that fit the data. Thus, training data are implemented through different learning processes compared to other supervised learning tools, which calculate the probability distribution of parameters of a specific model (Wang 2022). Squared exponential GPR, Matern 5/2 GPR, exponential GPR, and rational quadratic GPR are taken into account in the present

study. Details regarding differences among those GPRs are available in Sanders (2019).

CHARACTERISTICS OF DATABASE Experimental shear database

Test results of non-shear-reinforced RC beams assembled by Collins et al. (2008) were used in the present study. Similarly, Zhang et al. (2022) conducted ML analysis using 1848 RC beams from the same database. However, the authors considered the data set as a single case for RC beams with no transverse reinforcement, whereas the data set should have been divided to address deep and slender beams. As a result, ML analysis showed unsatisfactory outcomes. Reported root-mean-square error (RMSE) and coefficient of determination (R^2) for the testing data set were 53.91 and 0.88, respectively. Other studies using ML algorithms as strength predictive tools showed better performance with less data. For example, Feng et al. (2021) showed RMSE = 50.34 and $R^2 = 0.93$ for 271 RC deep beams, Olalusi and Awoyera (2021) had RMSE = 32.68 and R^2 = 0.94 for 326 steel FRC (SFRC) slender beams, and Alotaibi et al. (2021) showed RMSE = 18.48 and R^2 = 0.98 for 148 FRC slabs. Given that differing shear-transfer mechanisms take place depending on the a/d, such as arch action governing in deep beams at a/d < 2.5 and truss action in slender beams at a/d > 2.5, the analysis must be conducted separately for the two cases (Lee 2020).

To address the shortcomings of Zhang et al. (2022), the present study divided the original shear database of Collins et al. (2008) into two categories based on *a/d* and focused only on slender beams. In addition, members with section heights less than 100 mm (4.3 in.) were filtered out, due to non-representation of actual RC beam shear behavior. Experimental test results of 1149 slender RC beams were used in the ML analysis. Characteristics of the shear database considered several types of loading (simply supported beam versus continuous beams and point load versus uniform load). The majority of these tests involved simply supported beams subjected to point loads (84%). Effect of loading type was not taken into account and deemed not within the scope of this paper.

Distribution of design parameters in the shear database is presented in Fig. 1. Parameters known to affect the shear strength of RC beams include both dependent and independent variables, and are identified as: 1) effective depth (d) from 80 to 3000 mm (3.15 to 118 in.); 2) effective section width (b_w) from 71 to 3000 mm (2.8 to 118 in.) (note: web width was used for T-sections); 3) concrete compressive strength (f_c) from 6.1 to 127.5 MPa (870 to 13,200 psi); 4) yield strength of flexural reinforcement (f_v) from 276 to 1779 MPa (39 to 254 ksi); 5) amount of flexural reinforcement (A_s) from 35.7 to 18,450 mm² (0.055 to 28.6 in.²); 6) aggregate size (a_g) from 1 to 50 mm (0.039 to 2 in.); 7) steel ratio ($\rho_f = A_s/b_w d$) from 0.001 to 0.066; and 8) a/d from 2.5 to 15. Due to variable ranges in design parameters, ultimate shear strengths (outcomes) varied widely from 12.6 to 1575 kN (2.8 to 354 kip), with those having few data points not shown in the distributions.

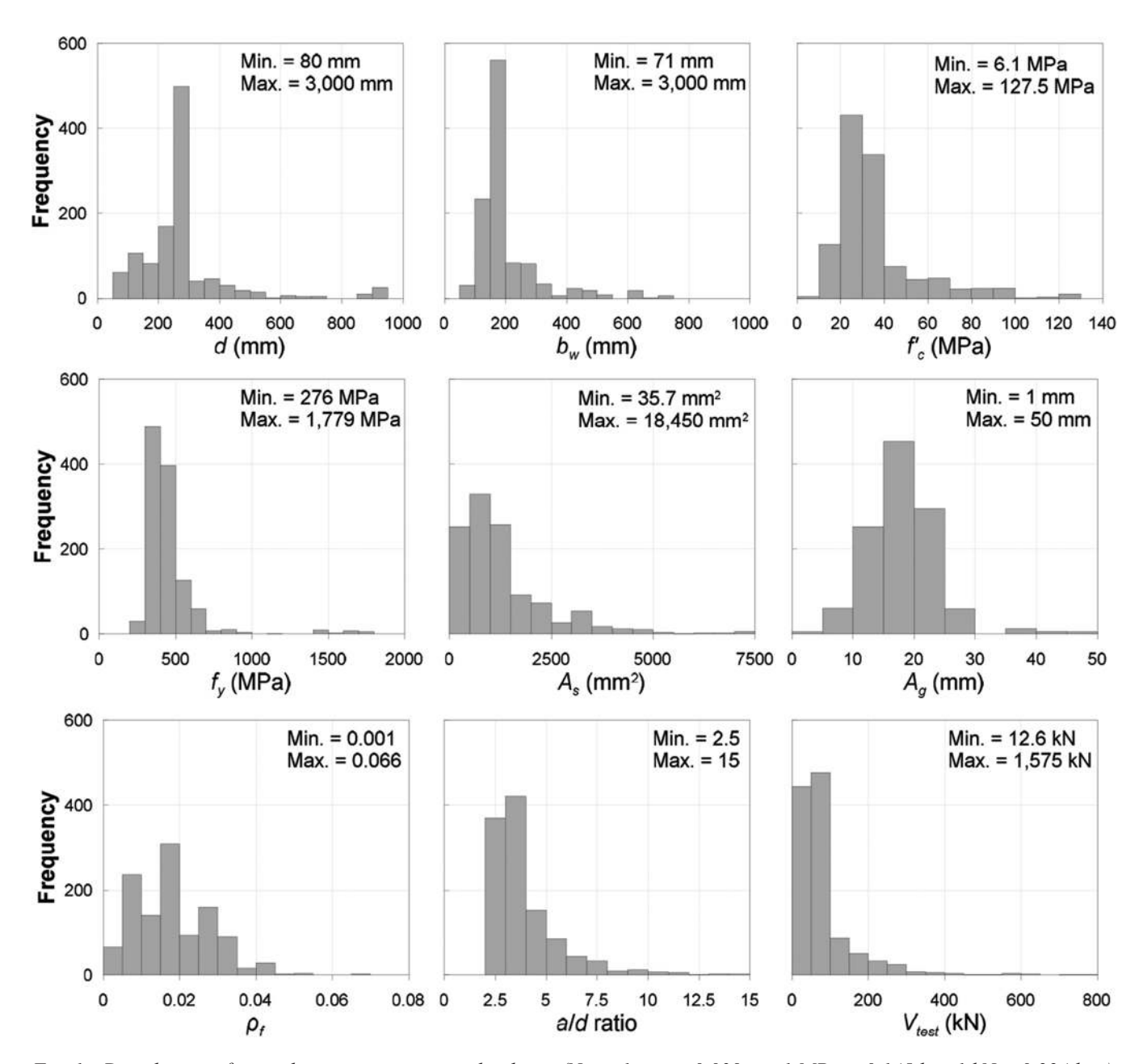


Fig. 1—Distribution of main design parameters in database. (Note: 1 mm = 0.039 in.; 1 MPa = 0.145 ksi; 1 kN = 0.224 kip.)

Correlation of design parameters

Prior to running ML analysis, it is important to consider design parameters (input data) investigated among the factors considered in the analysis to improve accuracy and running speed. To determine related parameters and relative contribution to shear capacity, the correlation coefficient between input parameters (f_c ', b_w , d, A_s , ρ_f , a_g , f_y , and a/d) and output (V_{test}) was obtained using Pearson's approach as

$$r_{xy} = \frac{\sum_{i=1}^{n} (x_i - \overline{x})(y_i - \overline{y})}{\sqrt{\sum_{i=1}^{n} (x_i - \overline{x})^2} \sqrt{\sum_{i=1}^{n} (y_i - \overline{y})^2}}$$
(1)

where r_{xy} is correlation coefficient; n is sample size; x_i and y_i are individual sample points for input and output variables indexed with i, respectively; and \overline{x} and \overline{y} are average values for input and output variables, respectively.

The correlation between parameters and tested ultimate shear strength V_{test} is depicted in Fig. 2. Considered design

parameters include b_w , d, f_c' , f_y , A_s , a_g , ρ_f , and a/d. Given few data points exist over 400 kN (90 kip) (less than 1%), measured shear capacities exceeding 400 kN (90 kip) are not shown for clarity. Linear regression lines and calculated correlation coefficients r_{xy} are provided along the data points to evaluate the magnitude of each parameter's effect on shear strength. Three sectional properties, b_w , d, and A_s , presented the strongest correlation with shear strengths for RC beams (r_{xy} is 0.752, 0.634, and 0.858, respectively). Effects of f_c' , ρ_f , and a/d also revealed strong correlation coefficients: 0.122, -0.093, -0.146, respectively, whereas, a_g (r_{xy} = 0.005) and f_y (r_{xy} = 0.031) had almost no influence, and their effect may be negligible. Based on correlation, design parameters of b_w , d, f_c' , A_s , ρ_f , and a/d were considered in the ML analysis.

Noted is that the decreasing trend with the increase in ρ_f contrasts with findings from several experimental studies (Angelakos et al. 2001; Lubell et al. 2004; Brown et al. 2006). Discrepancy is attributed to potential data bias, because ρ_f

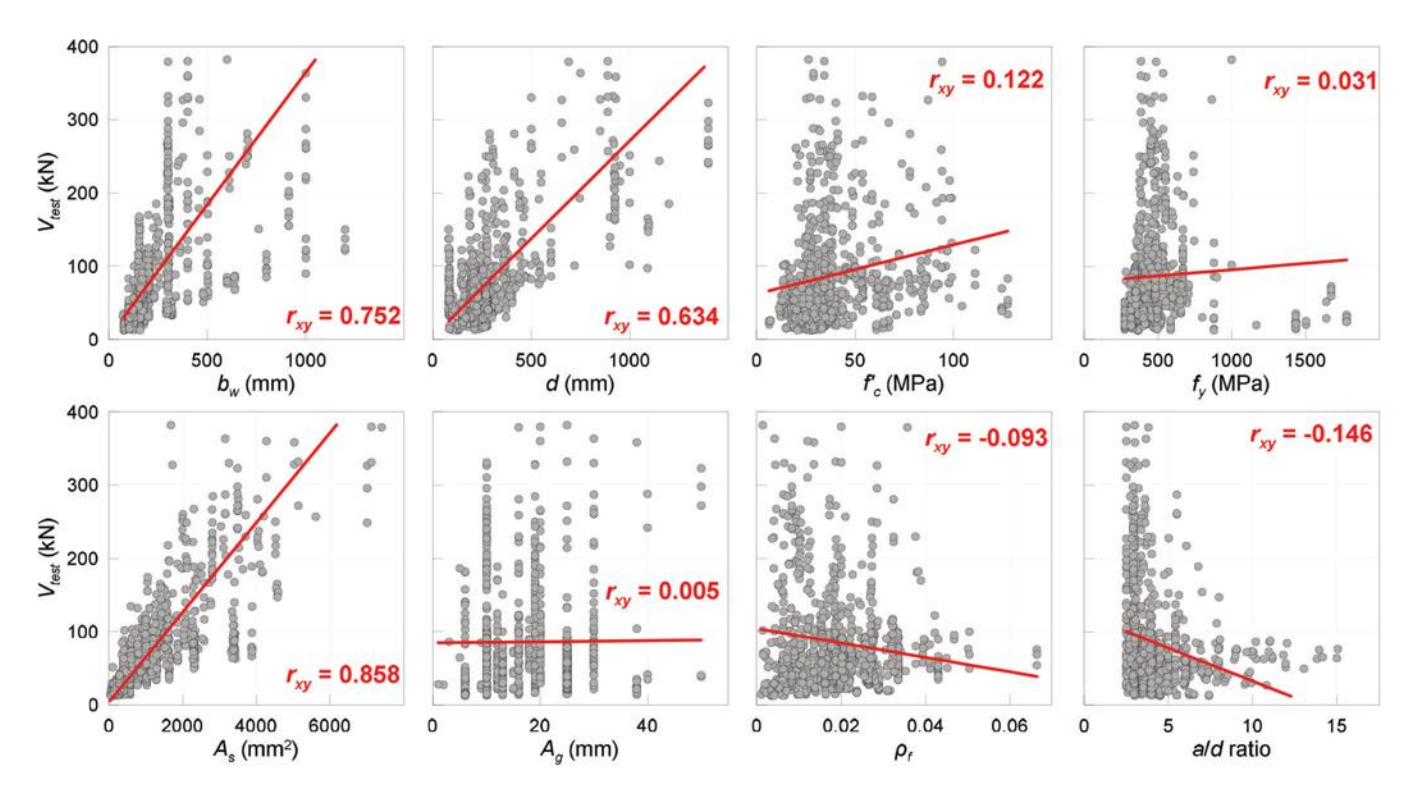


Fig. 2—Correlation between shear strength and design parameters. (Note: 1 mm = 0.039 in.; 1 MPa = 0.145 ksi; 1 kN = 0.224 kip.)

shown is primarily less than 0.04. Should ρ_f increase, the correlation of coefficient based on ρ_f may differ.

IMPLEMENTATION OF MACHINE LEARNING ALGORITHMS

Overview

Using the regression learner toolbox of MATLAB R2020a, a total of 19 ML algorithms considering six design variables $(b_w, d, f_c', A_s, \rho_f, \text{ and } a/d)$ were employed to predict ultimate shear strength of RC slender beams without transverse reinforcement. Variables identified were determined based on correlation analysis results. The database of the experimental test results was randomly divided into two data sets: training and testing. Of the 1149 experimental beam shear tests, 80% of the test results were allocated to training (920 beams) and 20% were assigned to testing (229 beams). This 80:20 allocation ratio was based on previous studies (Feng et al. 2021; Truong et al. 2022). In guiding the ML algorithms, the fivefold cross-validation was used, meaning the training data set was divided into five folds. Among the five folds, four folds were used to direct the ML algorithms, with a single fold held in reserve to validate the data model for each iteration. Said cross-validation is repeated five times until each of the five folds is used to validate the data once. After preparing the ML models using data from the 920 tested beams, the performance of each model was assessed in view of the testing set consisting of 229 beams. The ML models were run using the default setting of the regression learner toolbox, where hyperparameter options are disabled.

Evaluation criteria of ML algorithms

To evaluate performance of the ML methods, several statistical parameters including RMSE, mean absolute error

(MAE), mean absolute percent error (MAPE), and R^2 , were used. RMSE and MAPE are two of the most common statistical measures to gauge the accuracy of predicted values with actual values. R^2 is a statistical measure representing the proportion of the variation between tested and predicted values. Its range lies between 0 and 1, where an ideal model fit occurs at $R^2 = 1$. Statistical parameters denoted were calculated by

RMSE =
$$\sqrt{\frac{\sum_{i=1}^{n} (y_{test,i} - y_{pred,i})^2}{n}}$$
 (kN) (2)

MAPE =
$$\left(\frac{100}{n}\right) \sum_{i=1}^{n} \left(\frac{|\mathcal{Y}_{test,i} - \mathcal{Y}_{pred,i}|}{\mathcal{Y}_{test,i}}\right) (\%)$$
 (3)

$$R^{2} = \frac{\left[\sum_{i=1}^{n} (y_{test,i} - \overline{y}_{test})(y_{pred,i} - \overline{y}_{pred})\right]^{2}}{\sum_{i=1}^{n} (y_{test,i} - \overline{y}_{test})^{2} \sum_{i=1}^{n} (y_{pred,i} - \overline{y}_{pred})^{2}} (kN/kN)$$
(4)

where n is sample size; $y_{test,i}$ and $y_{pred,i}$ are individually tested and predicted values indexed with i, respectively; and \overline{y}_{test} and \overline{y}_{pred} are average of tested and predicted values, respectively.

Assessment of ML algorithms

Training and testing data sets—The comprehensive results of 19 ML techniques for the given shear data set are summarized in Table 1. Statistical metrics for the two data sets (training and testing) are provided. The top five ML approaches exhibiting preeminent values in terms of each metric are marked in bold, except for R^2 , whose range (0.88 and 0.96) did not significantly differ. Comparisons between

Table 1—Analysis results from 19 machine learning models

	Performance evaluation parameters												
	RMSE, kN			MAE, kN			MAPE, %			R^2 , kN/kN			
ML models	Train	Test	Test/train	Train	Test	Test/train	Train	Test	Test/train	Train	Test	Test/train	Time(s)
					Lir	ear regression	on						
Normal	6.99	6.32	0.90	3.82	3.88	1.02	25.3	25.5	1.01	0.92	0.88	0.96	0.30
Interaction	3.39	3.92	1.16	2.18	2.36	1.08	13.4	14.9	1.11	0.96	0.91	0.95	0.35
Robust	9.48	6.85	0.72	3.51	3.17	0.90	17.2	19.4	1.13	0.95	0.90	0.95	0.44
Stepwise	3.40	3.93	1.16	2.20	2.36	1.07	13.8	15.2	1.10	0.96	0.92	0.96	11.7
						Tree							
Fine	6.60	3.64	0.55	1.93	1.42	0.74	8.1	7.3	0.90	0.95	0.92	0.97	0.17
Medium	9.67	4.17	0.43	3.04	2.37	0.78	13.6	14.0	1.03	0.94	0.93	0.99	0.15
Coarse	15.48	10.40	0.67	4.79	4.24	0.89	20.4	20.3	1.00	0.92	0.88	0.96	0.16
						SVM							
Linear	8.36	6.40	0.77	3.39	3.21	0.95	17.9	19.9	1.11	0.92	0.88	0.96	1.00
Quadratic	3.38	3.68	1.09	2.01	2.04	1.01	12.1	12.7	1.05	0.93	0.89	0.96	2.95
Cubic	2.44	2.77	1.14	1.56	1.53	0.98	10.3	9.8	0.95	0.94	0.90	0.96	17.2
Fine Gaussian	20.47	11.38	0.56	4.27	2.78	0.65	11.1	10.5	0.95	0.94	0.90	0.96	0.41
Medium Gaussian	17.84	8.60	0.48	3.45	2.45	0.71	12.4	12.8	1.03	0.93	0.89	0.96	0.32
Coarse Gaussian	13.84	6.71	0.48	3.64	2.99	0.82	15.9	17.6	1.11	0.93	0.89	0.96	0.27
					Tr	ee ensemble	s						
Boosted	7.08	3.43	0.48	2.55	2.13	0.84	14.3	14.6	1.02	0.93	0.90	0.97	1.92
Bagged	7.88	3.63	0.46	2.37	1.74	0.73	10.7	9.6	0.90	0.93	0.90	0.97	1.61
						GPR							
Squared exponential	2.04	2.07	1.01	1.40	1.33	0.95	9.5	8.8	0.93	0.93	0.91	0.98	10.6
Matern 5/2	1.82	1.84	1.01	1.23	1.15	0.93	8.2	7.4	0.90	0.94	0.92	0.98	12.7
Exponential	0.97	1.23	1.27	0.55	0.58	1.05	3.3	3.3	1.00	0.94	0.92	0.98	12.3
Rational quadratic	1.84	1.85	1.01	1.25	1.16	0.93	8.4	7.5	0.89	0.95	0.93	0.98	29.9

Note: Top five ML approaches with most ideal values in terms of each metric are marked in bold.

training and testing values are provided in the third column for each evaluation criterion. Consumed time to run each model is presented in the rightmost column.

In Fig. 3, ML analysis results are graphically depicted. Results significantly differed based on ML algorithm and regression model used. Overall performance is discussed as follows.

- Linear regression algorithm—Interaction and stepwise models displayed finer predictions in terms of metrics when compared to normal and robust models.
- Tree algorithm—A better outcome was obtained for more sophisticated regression, with the best performance found in the fine model, followed by medium and coarse models.
- SVM—Among the six, cubic and quadratic models showed relatively precise predictions. Cubic SVM had small RMSE (train: 2.44; test: 2.77) and MAPE (train: 10.3%; test: 9.8%) values with reasonable test/train ratios (RMSE: 1.14 and MAPE: 0.95). All three SVM Gaussian models generally showed less appealing performance with relatively high RMSE and MAPE when compared to the other ML models. Also, training

and testing sets showed quite large differences, especially in RMSE, where the test/train ratio was 0.48.

- Tree ensemble algorithms—Both boosted and bagged trees showed similar trends for all four metrics, with reasonable but not outstanding performance observed.
- GPR-based algorithms—Showed good overall performance in all metrics. Four of the top five smallest RMSE and MAPE for both training and testing data sets are found in the GPR algorithm categories. Additionally, only minor differences existed between training and testing sets. Test/train ratios were within 1.01 to 1.27 for RMSE, 0.89 to 1.00 for MAPE, and 0.98 for R^2 . Among them, the GPR exponential model produced predictions surprisingly close to the test results, with four metrics near ideal values with only minor differences between training and testing (RMSE = 0.97 to 1.23, MAPE = 3.3%, and R^2 = 0.92 to 0.94). This is significantly improved performance when compared to the previous study by Zhang et al. (2022), which used the modified beetle antennae search-random forest (MBAS-RF) algorithm for the same database and had an RMSE = 37.53 and $R^2 = 0.93$ for the training set

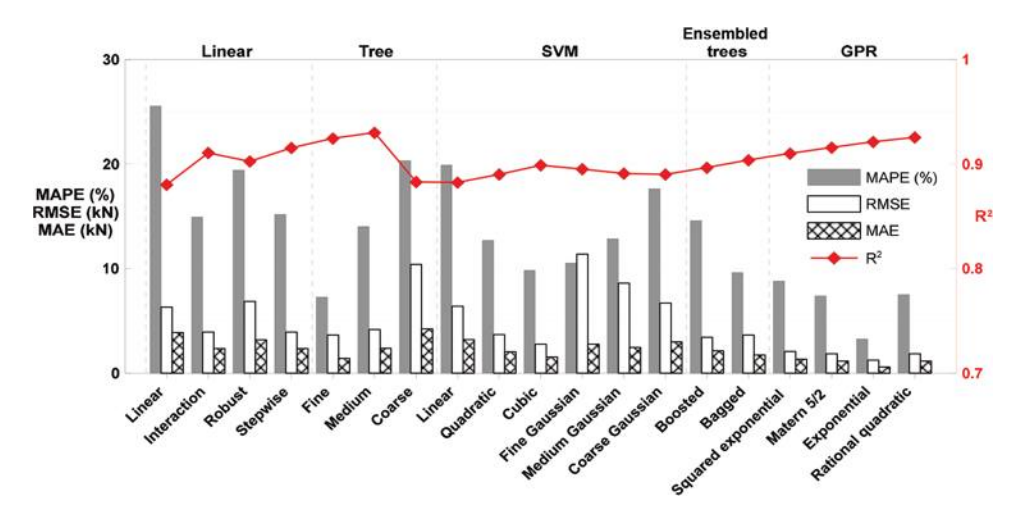


Fig. 3—Graphical comparison of ML analysis results for testing data set.

(70% of the entire data) and RMSE = 53.91 and R^2 = 0.88 for the testing set (30% of the entire data). Result difference can be ascribed to the fact that the present study divided the data set into slender and deep beams based on a/d. The conclusion is that separate ML-based analyses need to be conducted for deep and slender beams to obtain an accurate prediction of the shear strength for RC beams.

Entire data—Figure 4 illustrates the comparison of tested and ML-predicted shear strengths against the entire data set (red circle symbol for training set and blue square symbol for testing set [Note: full-color PDF can be accessed at www.concrete.org.]). Log scale was used for both x- and y-axes to effectively capture widely spread data points.

In assessing each ML model, the shear strength ratio, tested shear strength divided by predicted strength (V_{test}/V_{pred}) , was used to make a comprehensive evaluation. Statistical parameters of shear strength ratios are summarized along with the scatter plot in the figure. Overall, most ML approaches predicted shear strengths well, with data points gathered in general near the red solid line, which is indicative of $V_{test} = V_{pred}$. However, some ML models, especially linear normal regression, linear robust regression, and boosted tree ensemble models, created unreasonably high or low predictions, with data points significantly far from the $V_{test} = V_{pred}$ line. Additionally, although not shown due to implemented log scale, several cases had negative strength values, which are physically precluded. Statistical parameters used to measure results for the 19 ML models placed against the entire data are presented in Table 2. The nine parameters used include mean, standard deviation (STD), coefficient of variation (COV) for shear strength ratios. maximum, minimum, RMSE, MAPE, and R^2 . Values close to 1.0 are ideal for mean, maximum, minimum, and R^2 , whereas smaller values are preferred for STD, COV, RMSE, and MAPE. Ranking scores from 1 to 19 were awarded to each of the ML approaches according to closeness of its ideal value. Overall rank based on total score is provided in the rightmost column in the table.

Overall, the GPR exponential model showed greater performance and is ranked first in six of the nine statistical parameters (STD, COV, maximum, minimum, RMSE, and MAPE), followed by the GPR Matern 5/2 model, fine tree model, GPR rational quadratic model, and GPR squared exponential model. The accuracy of these top five models may be viewed in Fig. 4, with most data points closely scattered near the line of $V_{test} = V_{pred}$. Linear normal regression, linear robust regression, SVM linear, and all three SVM Gaussian models are not recommended for this analysis given their predictions were inaccurate and scattered in many cases. For example, the linear normal regression model showed maximum and minimum shear strength ratios as high as 155.7 and as low as -432, respectively. The implication is that some ML models can be used with great accuracy as a powerful shear predictive tool. However, selection should be based on purpose, with results double-checked with other ML, theoretical, or empirical models.

Comparison with current design provisions

Shear strengths of RC beams in the database may be predicted using shear equations found in design codes such as ACI 318-19 (ACI Committee 318 2019) and AASHTO LRFD Bridge Design Specifications (2022). In determining the shear strength of RC beams with no shear reinforcement, a single equation for one-way shear strength is used in ACI 318-19, whereas three different methods can be used in AASHTO. The three AASHTO methods are herein referred to as AASHTO simplified procedure, AASHTO general procedure with equations, and AASHTO general procedure with tables. ACI and AASHTO equations used to calculate shear strength of concrete V_c for slender beams whose shear transferring action is governed by truss action, without the consideration or contribution of shear reinforcement V_s , are summarized in Table 3. Full descriptions and detailed information about said shear equations are denoted in Collins et al. (1996), Bentz et al. (2006), and Kuchma et al. (2019).

When AASHTO general procedures with equations or tables are used for problem analysis, several trial/error iterations are necessary to determine shear strength. Based on Lee (2023), the iterative processes may be replaced with a V-M (shear versus moment) interaction approach. In the V-M interaction approach, shear and moment strengths of a given section at several strain values ($\varepsilon_x = 0$ to 0.001) are obtained. By connecting shear and moment strength results

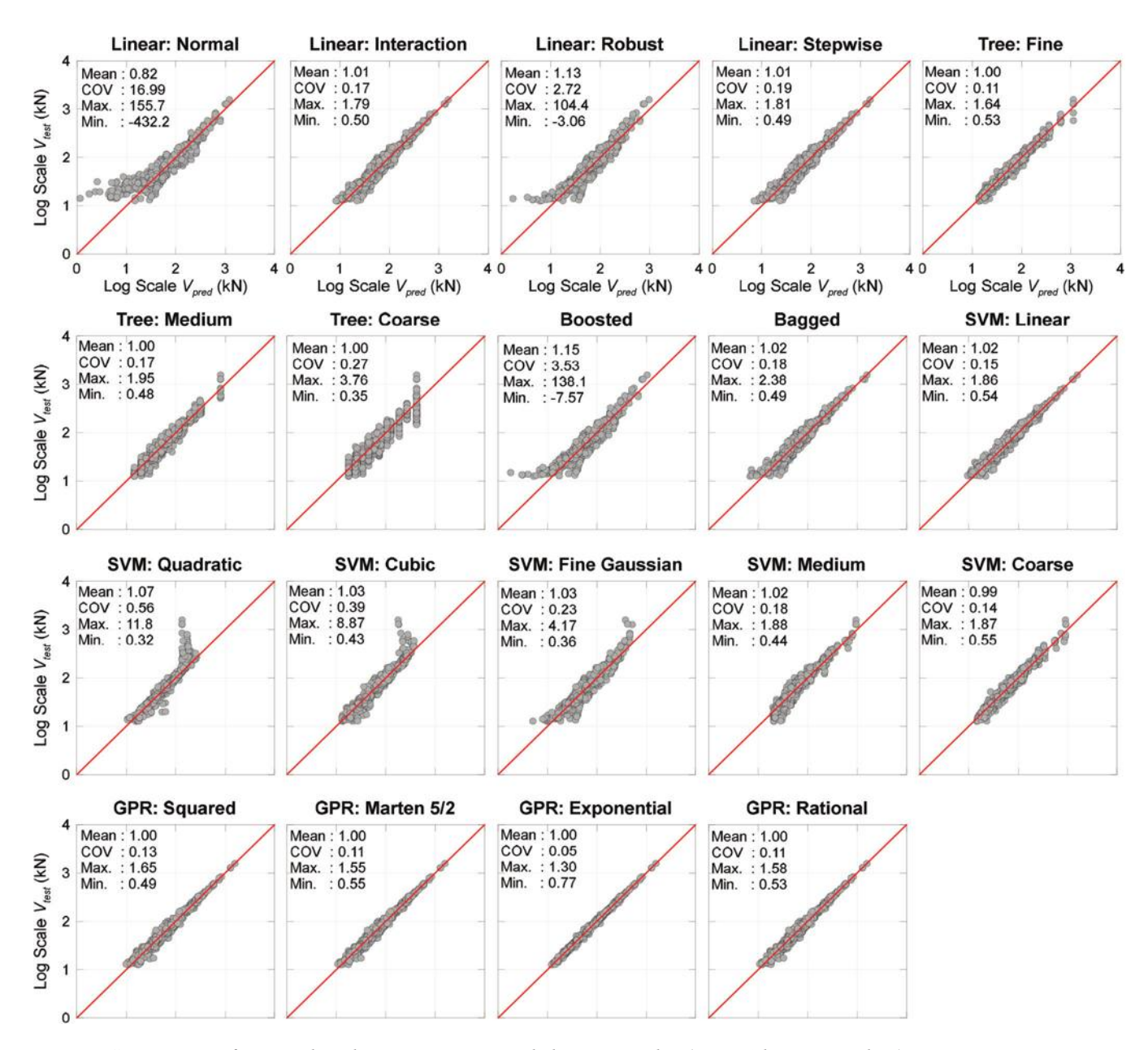


Fig. 4—Comparison of ML predicted versus experimental shear strengths. (Note: 1 kN = 0.224 kip.)

of the V-M interaction envelope, shear strength may be obtained by finding the interaction point between the V-M envelope and a loading line representing the ratio of shear and moment demands. Details regarding the V-M interaction approach are available in Lee (2023). Previous work by the author presented analysis results using AASHTO equations with the same database, but considered rectangular beams only. In the present study, T-beams are also included in the analysis by assuming the compressive zone exists within the flange depth when calculating nominal flexural capacity M_n .

Figure 5 presents scatter plots of tested strengths V_{test} versus shear strength ratio V_{test}/V_{pred} for code design equations and the two representative ML models, GPR exponential and Matern 5/2 models. Reduction factors were not taken into account to provide a direct comparison, and a log scale was used for tested strengths V_{test} on the x-axis for legibility. Shear strength ratios varied from 0.48 to 4.60, 0.37 to 4.36, 0.67 to 2.85, and 0.58 to 2.50 for ACI, simplified AASHTO,

AASHTO equation, and AASHTO table methods, respectively. These ranges are significantly wider than that denoted in the ML approach (0.77 to 1.30 for GPR exponential model and 0.55 to 1.55 for GPR Matern 5/2 model). All design equations provided reasonable predictions; degree of conservatism given ranges of average and COV of shear strength ratios were 1.20 to 1.47 and 20.1 to 35.5%, respectively. Statistical parameters used to measure the accuracy of each model are summarized in Table 4. In general, AASHTO with table had the most accurate outcomes, with ideal values of statistical parameters among design equations, followed by AASHTO with equations, ACI, and simplified AASHTO. Ideal metrics included smallest COV (=20.1%), RMSE (=5.68), MAPE (=18.56%), and R^2 (0.90) near 1.0. The implication is that enhanced sophisticated equations tend to generate more accurate predictions. The percentage of conservative predictions $V_{test}/V_{pred} < 1.0$ due to overestimated strengths was 13.3%, 16.5%, 6.8%, and 18.0%,

Table 2—ML performance measures results for entire data

					Statistica	ıl parametei	·s				
ML models	Mean	STD	COV	Max.	Min.	RMSE	MAPE	MAE	R^2	Rank	
	'			Li	near regressi	on				•	
Normal	0.82	13.93	16.99	155.74	-432.21	6.86	3.83	25.38	0.92	19	
Interaction	1.01	0.18	0.18	1.79	0.50	3.50	2.22	13.73	0.95	7	
Robust	1.13	3.07	2.72	104.37	-3.06	9.02	3.45	17.62	0.95	16	
Stepwise	1.01	0.19	0.19	1.81	0.49	3.51	2.23	14.06	0.96	9	
Tree											
Fine	1.00	0.11	0.11	1.64	0.53	6.12	1.83	7.94	0.95	3	
Medium	1.00	0.17	0.17	1.95	0.48	8.85	2.90	13.65	0.94	10	
Coarse	1.00	0.27	0.27	3.76	0.35	14.61	4.68	20.41	0.91	14	
					SVM						
Linear	1.15	4.07	3.53	138.14	-7.57	8.01	3.36	18.32	0.91	18	
Quadratic	1.02	0.18	0.18	2.38	0.49	3.44	2.02	12.25	0.92	11	
Cubic	1.02	0.15	0.15	1.86	0.54	2.51	1.56	10.21	0.93	6	
Fine Gaussian	1.07	0.60	0.56	11.75	0.32	19.01	3.98	10.99	0.93	17	
Medium Gaussian	1.03	0.41	0.39	8.87	0.43	16.42	3.25	12.52	0.92	13	
Coarse Gaussian	1.03	0.24	0.23	4.17	0.36	12.74	3.51	16.22	0.92	15	
	·			Т	ree ensemble	es					
Boosted	1.02	0.18	0.18	1.88	0.44	6.52	2.47	14.37	0.92	12	
Bagged	0.99	0.13	0.14	1.87	0.55	7.23	2.24	10.46	0.92	8	
GPR											
Squared exponential	1.00	0.13	0.13	1.65	0.49	2.05	1.38	9.40	0.93	5	
Matern 5/2	1.00	0.11	0.11	1.55	0.55	1.83	1.21	8.01	0.93	2	
Exponential	1.00	0.05	0.05	1.30	0.77	1.03	0.55	3.26	0.94	1	
Rational quadratic	1.00	0.11	0.11	1.58	0.53	1.84	1.23	8.21	0.94	4	

Note: Top five ML approaches with most ideal values in terms of each metric are marked in bold.

Table 3—Shear design equations in ACI 318-19 and AASHTO LRFD

ACI 318-19*	AASHTO
$V_c = \left[8 \lambda_s \lambda_s (\rho_w)^{1/3} \sqrt{f_c'} \right] b_w d$ $\rho_w \text{ is reinforcement steel ratio}$ $\lambda \text{ is light concrete factor}$ $\lambda_s \text{ is size effect factor} \left(\sqrt{\frac{2}{1 + d/10}} \le 1 \right)$	$V_c = 0.0316\beta\lambda\sqrt{f_c'}b_wd$ $\beta = 2.0^{\dagger}$ $\beta = \frac{4.8}{(1+750\varepsilon_s)} \frac{51^{\ddagger}}{(39+s_{xe})}$ $\beta \text{ determined from Table B5.2-1}^{\S}$

^{*}ACI shear equation for $A_v \le A_{v,min}$ with elimination of terms related to axial load (ACI 318-19, Section 22.5.5).

respectively, which implies that existing shear equations will likely provide safe design solutions. Furthermore, conservative predictions by AASHTO versus ACI shear equations are anticipated to diminish with application of strength reduction factors (for example, ϕ for shear are 0.9 and 0.75 for AASHTO LRFD and ACI 318-19, respectively).

Although shear design equations, especially AASHTO equations with tables, display good performance in assessing shear strengths with reasonable safety, too conservative of a design was found in many cases ($V_{test}/V_{pred} > 2.0$). To avoid

waste of materials due to oversizing members, adjustment in over-conservative design is needed. Given that ML showed remarkably superior performance to design equations in predicting shear strengths (average shear strength ratio of ML over 1149 RC beams was 1.00, which is ideal, with COV as small as 4.7%), ML can be used as a supplementary method to mitigate over-conservative aspects.

Thus, it is concluded that while ACI and AASHTO shear equations generally provide reasonable estimations of shear strength for non-shear-reinforced RC beams with a safety

[†]AASHTO simplified procedure for nonprestressed sections based on AASHTO, Section 5.7.3.4.1.

^{*}AASHTO general procedure (AASHTO, Section 5.7.3.4.2).

[§]AASHTO general procedure with tables (AASHTO, Appendix B5).

Table 4—Summary of statistical parameters from shear equations and ML models

	Average	COV	R^2	RMSE	MAE	MAPE	<1.0
ACI 318-19	1.46	0.341	0.90	10.95	5.55	29.79	13.3%
AASHTO*	1.47	0.355	0.90	21.29	7.46	35.16	16.5%
$AASHTO^{\dagger}$	1.39	0.208	0.90	6.72	4.56	26.44	6.8%
AASHTO‡	1.20	0.201	0.90	5.68	3.41	18.56	18.0%
GPR Matern 5/2	1.00	0.107	0.93	1.83	1.21	8.01	51.6%
GPR exponential	1.00	0.047	0.94	1.03	0.55	3.26	51.7%

^{*}AASHTO simplified procedure for nonprestressed sections based on AASHTO, Section 5.7.3.4.1.

[‡]AASHTO general procedure with tables (AASHTO, Appendix B5).

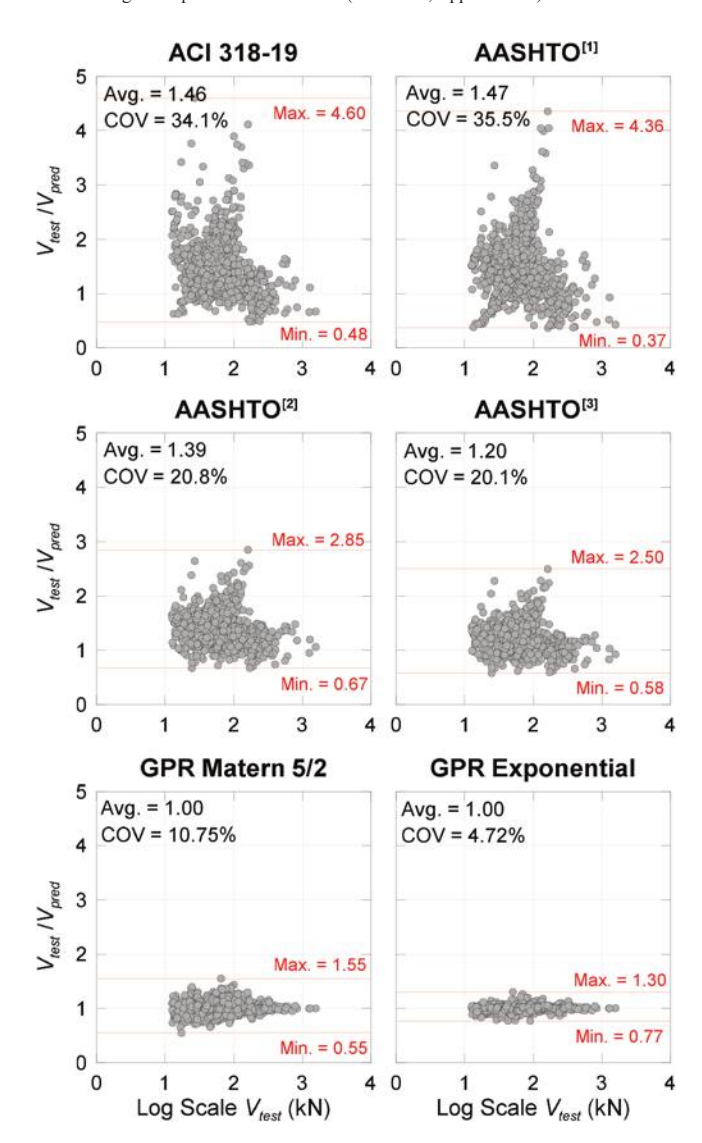


Fig. 5—Comparison of shear equations in design codes versus ML model. (Note: AASHTO^[1] is AASHTO simplified procedure; AASHTO^[2] is AASHTO general procedure with equations; and AASHTO^[3] is AASHTO general procedure with tables. 1 kN = 0.224 kip.)

margin, the ML approach can be used as an alternative tool to avoid overly excessive designs by accurately predicting shear capacities. Because both approaches possess different

scopes and purposes, it is not appropriate to conclude that the ML approach outperforms code-based shear equations.

CONCLUSIONS

In this study, the possibility of assessing shear strengths using machine learning (ML) algorithms was explored. To bridge gaps in previous studies and determine accurate performance, this study focused on shear test data of non-shear-reinforced slender reinforced concrete (RC) beams. By filtering previously published shear database data, test results of 1149 beams were obtained and used for training (80%) and testing (20%) purposes. Results from 19 different ML models were compared with each other and results from shear equations found in design codes. Key conclusions based on this study can be drawn as follows:

- Prior to applying ML approaches, the correlation coefficient between influencing parameters and the shear strength needs to be investigated. Correlation analysis illustrated the strongest influencers being b_w, d, and A_s with intermediate influencers of f_c', ρ_f, and a/d. No influence on shear strength was exhibited by a_g and f_y. An increasing trend in the shear strength was found based on the expansion of d, b_w, and f_c', and the decrease of a/d and ρ_f.
- A total of 19 ML models were employed to create shear strength predictions. It was found that accuracy and effectiveness of ML mechanisms in predicting shear strength of RC beams can vary depending on ML model used. The Gaussian process regression (GPR) exponential ML model showed surprisingly accurate predictions, whereas inferior performance was prominent in several other ML models, such as linear normal regression and support vector machine (SVM) linear models. The outcome is that the selection of the ML model used for shear prediction must be chosen carefully.
- Design-provision shear equations were used to predict shear strength. All shear equations generally provided reasonable predictions with a somewhat high conservative aspect. However, over-conservative and unconservative predictions were also obtained even after strength reduction factors were taken into consideration. Two ML models, which displayed greatest accuracy among the 19 ML models, identified better outcomes than code-based shear equations.

[†]AASHTO general procedure (AASHTO, Section 5.7.3.4.2).

- Based on this study, current shear design equations supplemented with the use of ML algorithms can help provide more reasonable predictions by eliminating unsafe or too conservative estimations. Selection of an appropriate ML model(s) should consider review of several models.
- Some limitations are present in this study, as only commonly known influential factors on shear were considered. To improve the accuracy of predictions, it would be beneficial to incorporate additional factors that were not accounted for, such as loading type and variations in material properties, into the ML model. Additionally, the analysis in this study excluded overly small RC beams that do not exhibit typical shear behaviors. Therefore, the findings of this study may not be applicable to such beams.

The present study focused on slender RC beams without shear reinforcement. Future studies may be conducted to verify effectiveness of ML algorithms for slender RC beams with shear reinforcement, and deep RC beams with/without shear reinforcement.

AUTHOR BIOS

ACI member Ju Dong Lee is a Postdoctoral Research Associate at Texas A&M Transportation Institute. He received his BS from Sungkyunkwan University, Seoul, South Korea; his MS from Seoul National University, Seoul, South Korea; and his PhD from Texas A&M University, College Station, TX. His research interests include the development of rational shear design specifications for reinforced and prestressed concrete structures.

Thomas H.-K. Kang, FACI, is a Professor of structural engineering and interdisciplinary artificial intelligence at Seoul National University. He is a member of ACI Subcommittee 318-T, Post-Tensioned Concrete; Joint ACI-PTI Committee 320, Post-Tensioned Structural Concrete Code; Joint ACI-ASCE Committees 352, Joints and Connections in Monolithic Concrete Structures, and 423, Prestressed Concrete; and Joint ACI-ASME Committee 359, Concrete Containments for Nuclear Reactors. He received the ACI Wason Medal for Most Meritorious Paper in 2009. His research interests include the design and behavior of reinforced, prestressed, and post-tensioned concrete structures.

ACKNOWLEDGMENTS

This work was supported by the National Research Foundation of Korea (NRF) grant (NRF-2021R1A1A5A1032433), and by the Institute of Information & Communications Technology Planning & Evaluation (IITP) grant funded by the Korean government (MSIT) [No. 2021-0-01343]. The authors also acknowledge partial supports by the Institute of Construction and Environmental Engineering at Seoul National University. The views expressed are those of authors, and do not necessarily represent those of the sponsors.

REFERENCES

AASHTO, 2022, "AASHTO LRFD Bridge Design Specifications," ninth edition, American Association of State Highway and Transportation Officials, Washington, DC.

ACI Committee 318, 2019, "Building Code Requirements for Structural Concrete (ACI 318-19)," and Commentary (ACI 318R-19) (Reapproved 2022)," American Concrete Institute, Farmington Hills, MI, 624 pp.

Alotaibi, E.; Mostafa, O.; Nassif, N.; Omar, M.; and Arab, M. G., 2021, "Prediction of Punching Shear Capacity for Fiber-Reinforced Concrete Slabs Using Neuro-Nomographs Constructed by Machine Learning," *Journal of Structural Engineering*, ASCE, V. 147, No. 6, p. 04021075. doi: 10.1061/(ASCE)ST.1943-541X.0003041

Angelakos, D.; Bentz, E. C.; and Collins, M. P., 2001, "Effect of Concrete Strength and Minimum Stirrups on Shear Strength of Large Members," *ACI Structural Journal*, V. 98, No. 3, Mar.-Apr., pp. 290-300.

Bentz, E. C.; Vecchio, F. J.; and Collins, M. P., 2006, "Simplified Modified Compression Field Theory for Calculating Shear Strength of Reinforced Concrete Elements," *ACI Structural Journal*, V. 103, No. 4, July-Aug., pp. 614-624.

Brown, M. D., and Bayrak, O., 2008, "Design of Deep Beams Using Strut-and-Tie Models—Part I: Evaluating U.S. Provisions," *ACI Structural Journal*, V. 105, No. 4, July-Aug., pp. 395-404.

Brown, M. D.; Bayrak, O.; and Jirsa, J. O., 2006, "Design for Shear Based on Loading Condition," *ACI Structural Journal*, V. 103, No. 4, July-Aug., pp. 541-550.

Butcher, J. B.; Day, C.; Austin, J.; Haycock, P.; Verstraeten, D.; and Schrauwen, B., 2014, "Defect Detection in Reinforced Concrete Using Random Neural Architectures," *Computer-Aided Civil and Infrastructure Engineering*, V. 29, No. 3, pp. 191-207. doi: 10.1111/mice.12039

Choi, K.-K.; Kim, J.-C.; and Park, H.-G., 2016, "Shear Strength Model of Concrete Beams Based on Compression Zone Failure Mechanism," *ACI Structural Journal*, V. 113, No. 5, Sept.-Oct., pp. 1095-1106. doi: 10.14359/51689032

Chou, J.-S.; Tsai, C.-F.; Pham, A.-D.; and Lu, Y.-H., 2014, "Machine Learning in Concrete Strength Simulations: Multi-Nation Data Analytics," *Construction and Building Materials*, V. 73, pp. 771-780. doi: 10.1016/j.conbuildmat.2014.09.054

Collins, M. P.; Bentz, E. C.; and Sherwood, E. G., 2008, "Where is Shear Reinforcement Required? Review of Research Results and Design Procedures," *ACI Structural Journal*, V. 105, No. 5, Sept.-Oct., pp. 590-600.

Collins, M. P.; Mitchell, D.; Adebar, P.; and Vecchio, F. J., 1996, "A General Shear Design Method," *ACI Structural Journal*, V. 93, No. 1, Jan.-Feb., pp. 36-45.

Deng, N.; Tian, Y.; and Zhang, C., 2012, Support Vector Machines: Optimization-Based Theory, Algorithms, and Extensions, CRC Press, Boca Raton, FL, 345 pp.

Feng, D.-C.; Wang, W.-J.; Mangalathu, S.; Hu, G.; and Wu, T., 2021, "Implementing Ensemble Learning Methods to Predict the Shear Strength of RC Deep Beams with/without Web Reinforcements," *Engineering Structures*, V. 235, p. 111979. doi: 10.1016/j.engstruct.2021.111979

Gui, G.; Pan, H.; Lin, Z.; Li, Y.; and Yuan, Z., 2017, "Data-Driven Support Vector Machine with Optimization Techniques for Structural Health Monitoring and Damage Detection," *KSCE Journal of Civil Engineering*, V. 21, No. 2, pp. 523-534. doi: 10.1007/s12205-017-1518-5

Hsu, T. T. C.; Laskar, A.; and Mo, Y.-L., 2010, "Shear Strengths of Prestressed Concrete Beams, Part 2: Comparisons with ACI and AASHTO Provisions," *ACI Structural Journal*, V. 107, No. 3, May-June, pp. 340-345.

Kuchma, D.; Wei, S.; Sanders, D.; Belarbi, A.; and Novak, L., 2019, "The Development of the One-Way Shear Design Provisions of ACI 318-19," *ACI Structural Journal*, V. 116, No. 4, July, pp. 185-295. doi: 10.14359/51716739

Lee, J. D., 2020, "Development of a Truss-Arch Model Unified for Flexure and Shear-Critical Interaction of Structural Concrete Members," PhD dissertation, Department of Civil and Environmental Engineering, Texas A&M University, College Station, TX.

Lee, J. D., 2023, "Assessment of AASHTO Shear Design Based on the Modified Compression Field Theory Using V-M Interaction Diagram," *ACI Structural Journal*, V. 120, No. 1, Jan., pp. 241-251.

Lee, J. D., and Mander, J. B., 2022, "Unified Truss-Arch Model for the Analysis of Bending-Shear Interaction in Reinforced Concrete Members," *Journal of Structural Engineering*, ASCE, V. 148, No. 7, p. 04022074. doi: 10.1061/(ASCE)ST.1943-541X.0003380

Lee, J. D., and Mander, J. B., 2023, "Verification of Truss-Arch Model Unified for RC Beams with Stirrups Using Shear Database," *Engineering Structures*, V. 287, p. 116180. doi: 10.1016/j.engstruct.2023.116180

Lee, J.-Y., and Watanabe, F., 2000, "Shear Design of Reinforced Concrete Beams with Shear Reinforcement Considering Failure Modes," *ACI Structural Journal*, V. 97, No. 3, May-June, pp. 477-484.

Lubell, A.; Sherwood, T.; and Collins, M., 2004, "Safe Shear Design of Large Wide Beams," *Concrete International*, V. 26, No. 1, Jan., pp. 66-78.

Olalusi, O. B., and Awoyera, P. O., 2021, "Shear Capacity Prediction of Slender Reinforced Concrete Structures with Steel Fibers Using Machine Learning," *Engineering Structures*, V. 227, p. 111470. doi: 10.1016/j. engstruct.2020.111470

Omran, B. A.; Chen, Q.; and Jin, R., 2016, "Comparison of Data Mining Techniques for Predicting Compressive Strength of Environmentally Friendly Concrete," *Journal of Computing in Civil Engineering*, ASCE, V. 30, No. 6, p. 04016029. doi: 10.1061/(ASCE)CP.1943-5487.0000596

Reineck, K.-H.; Bentz, E.; Fitik, B.; Kuchma, D. A.; and Bayrak, O., 2014, "ACI-DAfStb Databases for Shear Tests on Slender Reinforced Concrete Beams with Stirrups," *ACI Structural Journal*, V. 111, No. 5, Sept.-Oct., pp. 1147-1156. doi: 10.14359/51686819

Reineck, K.-H.; Bentz, E. C.; Fitik, B.; Kuchma, D. A.; and Bayrak, O., 2013, "ACI-DAfStb Databases of Shear Tests on Slender Reinforced Concrete Beams Without Stirrups," *ACI Structural Journal*, V. 110, No. 6, Nov.-Dec., pp. 867-875.

Reineck, K.-H., and Todisco, L., 2014, "Database of Shear Tests for Non-Slender Reinforced Concrete Beams Without Stirrups," *ACI Structural Journal*, V. 111, No. 6, Nov.-Dec., pp. 1363-1372. doi: 10.14359/51686820 Rokach, L., and Maimon, O., 2014, *Data Mining with Decision Trees:*

Theory and Applications, World Scientific Publishing, Singapore.

Sanders, B., 2019, "Breast Cancer with Machine Learning in MATLAB," MS thesis, Department of Mathematics, Texas Technical University, Lubbock, TX.

Solhmirzaei, R.; Salehi, H.; and Kodur, V., 2022, "Predicting Flexural Capacity of Ultrahigh-Performance Concrete Beams: Machine Learning-Based Approach," *Journal of Structural Engineering*, ASCE, V. 148, No. 5, p. 04022031. doi: 10.1061/(ASCE)ST.1943-541X.0003320

Todisco, L.; Reineck, K. H.; and Bayrak, O., 2015, "Database with Shear Tests on Non-Slender Reinforced Concrete Beams with Vertical Stirrups," *ACI Structural Journal*, V. 112, No. 6, Nov.-Dec., pp. 761-769. doi: 10.14359/51688055

Truong, G. T.; Hwang, H.-J.; and Kim, C.-S., 2022, "Assessment of Punching Shear Strength of FRP-RC Slab-Column Connections Using Machine Learning Algorithms," *Engineering Structures*, V. 255, p. 113898. doi: 10.1016/j.engstruct.2022.113898

Tureyen, A. K., and Frosch, R. J., 2003, "Concrete Shear Strength: Another Perspective," *ACI Structural Journal*, V. 100, No. 5, Sept.-Oct., pp. 609-615.

Vitola, J.; Pozo, F.; Tibaduiza, D.; and Anaya, M., 2017, "A Sensor Data Fusion System Based on k-Nearest Neighbor Pattern Classification for Structural Health Monitoring Applications," *Sensors*, V. 17, No. 2, p. 417. doi: 10.3390/s17020417

Wang, J., 2022, "An Intuitive Tutorial to Gaussian Processes Regression," arXiv:2009.10862, 17 pp. doi: 10.48550/ARXIV.2009.10862

Yan, K.; Xu, H.; Shen, G.; and Liu, P., 2013, "Prediction of Splitting Tensile Strength from Cylinder Compressive Strength of Concrete by Support Vector Machine," *Advances in Materials Science and Engineering*, V. 2013, pp. 1-13. doi: 10.1155/2013/597257

Yan, X., and Su, X., 2009, *Linear Regression Analysis: Theory and Computing*, World Scientific Publishing, Singapore.

Zhang, J.; Sun, Y.; Li, G.; Wang, Y.; Sun, J.; and Li, J., 2022, "Machine-Learning-Assisted Shear Strength Prediction of Reinforced Concrete Beams with and without Stirrups," *Engineering with Computers*, V. 38, No. 2, pp. 1293-1307. doi: 10.1007/s00366-020-01076-x

Title No. 121-S21

Shear Strength of Concrete Block Masonry Using Direct Shear Test

by Muhammad Masood Rafi and Sher Khan

This paper presents the details of experimental testing of block masonry triplets using the direct shear test to investigate the shear behaviors of block unit-mortar interfaces. Hollow blocks of 100 and 150 mm (4 and 6 in.) thickness and solid blocks of 100 mm (4 in.) thickness were included in the testing program. These were combined with mortars of three grades to cast a total of 84 triplets. In addition to testing the triplets in an unconfined state, three increasing levels of precompression stresses were used separately to test the confined specimens. The shear behaviors of the tested triplets were not influenced by block strength, while shear strength increased (almost) linearly with mortar strength. The mean peak shear stress for the unconfined triplets was 0.4 MPa (58 psi), whereas the average shear modulus of the joint for these triplets was 6.20 times the mortar compressive strength. The Mode II fracture energy of the masonry joints increased at higher precompression levels. The methods of determining shear strength, shear modulus, and shear strength parameters for the mortar joint in block masonry are proposed using the observed data.

Keywords: block masonry triplets; fracture energy; mortar grade; precompression stress; shear modulus; shear strength.

INTRODUCTION

Unreinforced masonry (URM) structures are common building types in different parts of the world. The walls in URM structures are made of masonry units that are joined together by mortar. A variety of masonry units and mortar types are employed in the construction of URM buildings. The masonry unit types include sun-dried adobe bricks, fire-clay bricks, cement concrete blocks, and stone units, 1,2 while the mortar types are cement mortar, mud mortar, and cement-lime mortar. Despite variations in the construction practices and quality, this particular building typology is witnessed in both developed and developing countries, 3-5 which is the result of several advantages associated with URM buildings, such as rapid construction, low construction and maintenance costs, ease of availability of materials, inexpensive labor, 6,7 and lesser technological demands for construction.

The walls in URM structures act as the main load-resisting elements that support the gravity load and resist the lateral load applied due to earthquakes or wind. These walls generally provide satisfactory resistance to compressive forces but are weak in tension and shear. Because masonry is also a brittle material, these weaknesses often result in the catastrophic failures of URM structures during earthquakes, which have been documented by different researchers in the existing literature.⁸⁻²³ The most common failure mode observed during these instances was sliding shear failure of

the URM in-plane walls. This failure is influenced by the shear strength of the unit-mortar bed joint.^{8,11} Therefore, shear strength is an important parameter for the seismic design of masonry structures.²⁴

Although masonry is a composite material, the bond between masonry units and mortar allows the composite structure to behave monolithically, 25,26 and the mechanical properties of masonry structures are controlled by masonry units, mortar, and their bond. 27,28 The bond strength in shear sliding at the unit-mortar interface depends on interface cohesion and friction. The quantification of these parameters is vital for conducting the nonlinear numerical analysis of masonry structures.

Block masonry URM buildings are constructed using both solid and hollow concrete blocks in the parts of Pakistan where clay bricks are not available. These, however, are non-engineered structures (in most cases), as they are constructed without any engineering design due to the absence of a design code. Because Pakistan is a seismically active region, the presence of these non-engineered structures creates a vulnerable built environment. This vulnerability has been illustrated during several past earthquakes in different parts of the country. The damage to property and loss of life during these incidents cause tremendous direct and indirect economic losses. There is an urgent need to conduct research to formulate the necessary design guidelines for block masonry URM structures in the country. This paper addresses this gap in knowledge in part. The results of an experimental study to investigate the relationship between the block and mortar compressive strength and joint shear strength have been reported in this paper. This investigation was carried out by conducting shear-compression testing on block masonry triplets. This test method is used to characterize the nonlinear shear-sliding behavior of masonry along the unit-mortar interface without the need to make complex testing arrangements.^{29,30} The connecting planes between the unit and mortar are subjected to pure shear stresses in this test method. The present study is unique in that this is the first effort (to the best of the authors' knowledge) to study this aspect of seismic behavior of block masonry URM structures locally in Pakistan. However, the models suggested in this paper are general in nature and may

ACI Structural Journal, V. 121, No. 2, March 2024.

MS No. S-2022-343.R3, doi: 10.14359/51740247, received June 9, 2023, and reviewed under Institute publication policies. Copyright © 2024, American Concrete Institute. All rights reserved, including the making of copies unless permission is obtained from the copyright proprietors. Pertinent discussion including author's closure, if any, will be published ten months from this journal's date if the discussion is received within four months of the paper's print publication.

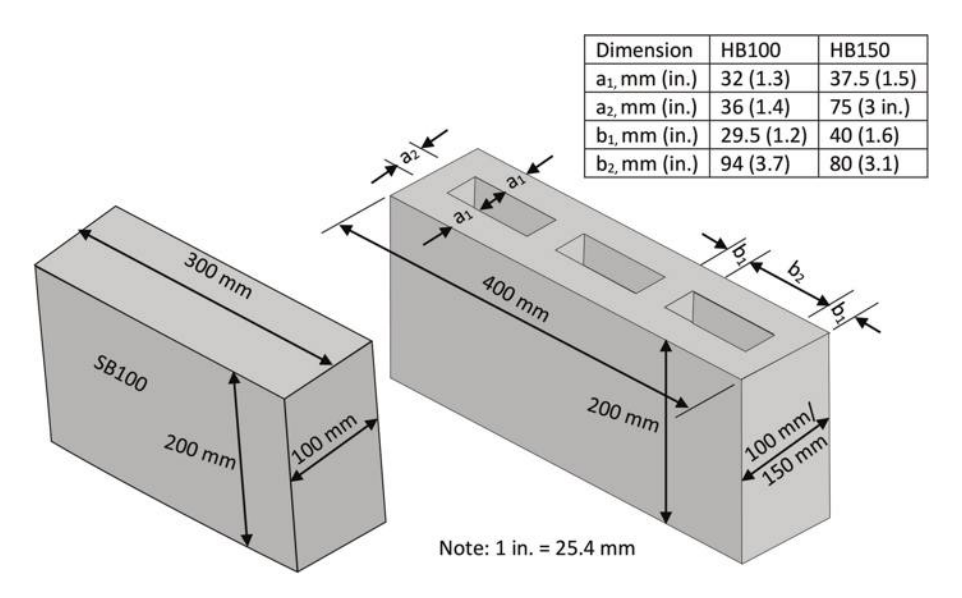


Fig. 1—Schematic of solid and hollow blocks.

be applicable in other regions of the world where similar construction practices exist.

RESEARCH SIGNIFICANCE

Adequate shear capacity must be provided in structural members, as shear failure causes rapid strength degradation and substantial loss of energy dissipation capacity.³¹ Presently, guidelines for designing masonry structures are unavailable in Pakistan. Given the geographical position of the country in a seismically active zone, these guidelines must be made available to reduce earthquake losses. This paper addresses a significant gap in the existing knowledge to understand and quantify the shear behavior of block masonry URM structures. The proposed models for the estimation of shear strength and shear modulus may apply to block masonry structures elsewhere owing to their general nature.

TESTING PROGRAM

Materials

Three types of cement concrete blocks were employed in the testing program described in this paper, which included 100 and 150 mm (4 and 6 in.) thick hollow blocks and 100 mm (4 in.) thick solid blocks. These blocks were purchased from a local supplier. The typical details of both types of blocks are illustrated in Fig. 1. Solid blocks are designated as SB100 (100 mm [4 in.] thick blocks). Similarly, 100 and 150 mm (4 and 6 in.) thick hollow blocks are designated as HB100 and HB150, respectively. The net areas of the HB100 and HB150 blocks were 29,848 and 41,640 mm² (46 and 64.5 in.²), respectively. The compressive strengths of blocks of each type (average of three blocks) are as follows: HB100 = 5.07 MPa (735 psi), HB150 = 4.72 MPa (685 psi), and SB100 = 8.40 MPa (1218 psi).

Three grades of cement-sand mortars were used for the casting of specimens. The ratio of cement to sand in these mortars was 1:2 (designated as M2), 1:3 (designated as M3), and 1:6 (designated as M6) by weight. The employed mortar grades cover the full range of typical mortars to

simulate modern masonry construction.³² The strengths obtained from testing different batches of these mortar grades covered a wide range representing strong, intermediate, and weak mortars, as discussed later. Natural sand was used in the mortar mixtures, which had a fineness modulus of 1.95. The water-cement ratio (w/c) for mortars was kept at 0.7, and potable tap water was used to prepare the mortar mixture. The cement was ordinary portland cement, which complied with ASTM C150-04.³³ The unit mass of cement was 1075 kg/m³ (67 lb/ft³).

Specimens and testing program

Masonry triplets were employed to determine the shear strength along the block-mortar interface. A total of 84 triplets were cast and tested by combining the aforementioned block and mortar types. These were based on a comparative analysis approach of the experimental data to characterize the shear behaviors of the tested specimens, which is discussed in the forthcoming sections.

Each masonry triplet was made using three block units with full mortar bed joints. The thickness of the mortar joints was kept constant at 12 mm (0.47 in.) (Fig. 2). These triplets were cast on a level surface as vertical prisms by an expert mason in the Material Testing Laboratory of NED University of Engineering and Technology in Pakistan. Each block unit was leveled appropriately, and the plumb of the prism was also checked. The completed specimens were closed in plastic bags, which were opened after 24 hours of casting to spray water on the mortar joints before the bags were closed again. This process was repeated continuously for 7 days. The bags were then closed until the 26th day after casting. The triplets of each type were cast using a single batch of mortar. The mortar strength in compression was determined for each batch by testing respective 100 x 200 mm (4 x 8 in.) cylinders on the 28th day after casting. The details of the triplets and corresponding mortar strength (f_m) are given in Table 1. The triplets are designated using a nomenclature based on the combination of block and mortar types. For

Table 1-Mortar strength, shear strength, and shear modulus of joints of triplets

			Unconfined		Con	fined I	Confi	ned II	Confined III	
S. No	Triplet	Mortar strength, MPa	τ_{max} , MPa	G_m , MPa	τ _{max} , MPa	G_m , MPa	τ_{max} , MPa	G_m , MPa	τ _{max} , MPa	G_m , MPa
1.	HB100M2	16.62	0.314	573.74	0.962	487.07	1.288	314.97	1.298	296.24
2.	HB150M2	19.37	0.342	582.86	0.922	523.64	1.10	262.15	1.355	344.61
3.	HB100M3	19.40	0.30	583.60	0.848	542.12	1.288	232.31	1.47	326.69
4.	HB150M3	20.58	0.350	629.72	0.855	537.01	1.159	329.00	1.337	325.72
5.	HB100M6	6.53	0.206	199.29	0.657	813.66	0.867	304.08	0.988	362.71
6.	SB100M2	25.34	0.422	833.10	1.130	196.85	1.417	104.42	1.686	198.05
7.	SB100M6	8.14	0.249	269.36	0.803	265.091	1.006	116.00	1.168	172.83

Note: 1 MPa = 145 psi.



Fig. 2—Testing arrangement for confined triplet.

example, HB150M3 represents the triplets made of HB150 blocks and Grade M3 mortar.

The test setup for the triplets and instrumentation are shown in Fig. 2. The testing of the triplets was carried out in displacement-controlled mode using a 500 kN (112 kip) universal testing machine (UTM). The loading rate of the specimen corresponded to a constant machine-head movement of 0.5 mm/min (0.02 in./min). It is seen in Fig. 2 that the blocks on both sides of the central block were supported on thick rectangular steel plates, which were placed on the bottom plate of the UTM.

The triplets were tested with (confined) and without (unconfined) applying precompression. Unconfined triplets were tested to obtain the initial shear strength of the mortar joint. Three specimens of each type (with and without precompression) were tested to determine an average of interface shear strength properties. Three levels³⁰ of precompression (axial) stresses of 0.265, 0.536, and 0.79 MPa (38.44, 77.74, and 114.58 psi) were applied normally to the bed joint for the confined triplets. These were based on estimated vertical loads for two-, four-, and six-story high walls made of the same type of block units. The aforementioned precompression levels will be referred to as Confined I, Confined II, and Confined III, respectively, in the forthcoming discussion. Garcia-Ramonda et al.³⁴ suggested a precompression stress of 0.3 MPa (43.5 psi) for a two-story masonry

building, which is similar to the value used in this paper. Similarly, Cavalheiro and Pedroso³⁵ employed precompression stresses of 0.57 and 1.14 MPa (82.67 and 165.34 psi), corresponding to vertical loads applied by four- and eightstory buildings, respectively. Therefore, the precompression stresses corresponding to a four-story building are similar in the present study and the study conducted by Cavalheiro and Pedroso.³⁵ Precompression load was applied by manually tightening the nuts of four horizontal steel rods, as shown in Fig. 2. This load was monitored with the help of a load cell. The failure of the triplet in shear was caused by the separation of the end block for the unconfined triplets. Conversely, the failure was arbitrarily taken for the confined triplets at a point where considerable slip has taken place and the postpeak load has stabilized to a residual load level (zero cohesion). The ultimate displacement for triplets can be taken at a point where the post-peak load has reached 50% of the peak load.11 The data of central block displacement/slip were measured with the help of two linear variable differential transducers (LVDTs), which were mounted on end blocks to record the relative displacement of the central block (Fig. 3). An average of data recorded by both LVDTs was taken as block displacement. The data of load and slip were analyzed to determine the shear strength, shear modulus, cohesion, friction coefficient, and fracture energy of the mortar joints.

RESULTS AND DISCUSSION

Failure mode

Typical failure modes were observed in the unconfined triplets, which were not influenced by either mortar or block unit types. The failure in these triplets occurred on the block-mortar interface (pure shear bond failure) without any damage to the block units. As a result, the shear strength of unconfined triplets was governed by the block-mortar interface bond strength. These specimens failed immediately as sliding/slip started at one of the two mortar joints at the maximum load due to the formation of a shear-sliding crack, and the end block detached from the rest of the specimen (Fig. 3). This signifies that failure was brittle for unconfined triplets.

The confined triplets exhibited behaviors that differed from the unconfined triplets in a few respects. First, the failure of these specimens was not brittle, and the central block slipped gradually with a decrease in the post-peak shear load. The failure in these triplets started with the

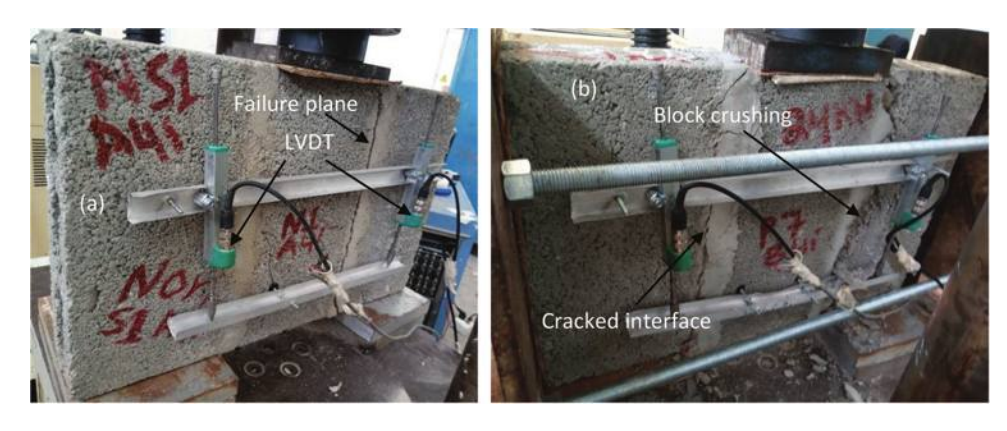


Fig. 3—Failure mode of triplet: (a) unconfined triplet; and (b) confined triplet.

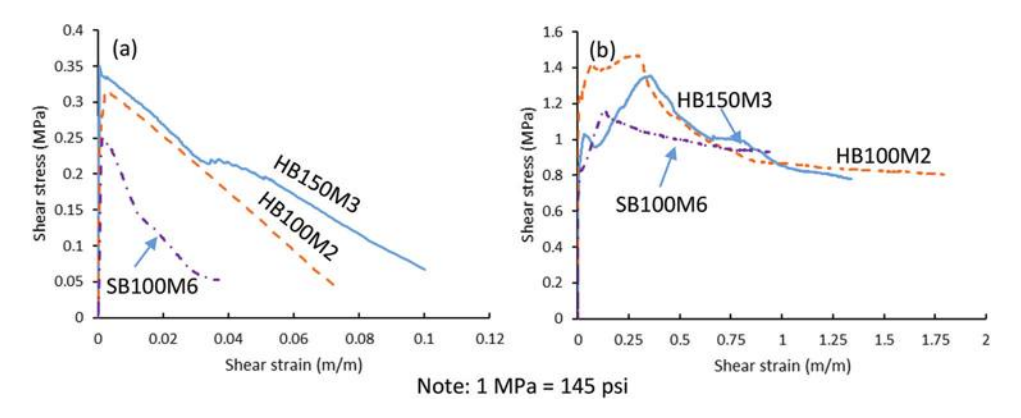


Fig. 4—Comparison of stress-strain curves of triplets made with different block strengths: (a) unconfined triplets; and (b) Confined III level triplets.

formation of a shear-sliding crack at one of the two interfaces at a load level less than the peak load. The confinement provided by the axial load (precompression) locked the central block without any decrease in the applied shear load. The mortar at the second interface cracked in shear at the maximum load for the confined triplets, which initiated the shear sliding of the central block.

A few exceptions, however, apply for the triplets made of M2 and M3 mortars and subjected to Confined II (0.536 MPa [77.74 psi]) and Confined III (0.79 MPa [114.58 psi]) levels of precompression. Some cracking and crushing of the central block at the second interface in the direction of the applied shear load were observed in these triplets, resulting from a slight increase in the applied precompression caused by the dilatancy effects of the cracked joint. As a result, the fracture passed through both the block unit and mortar in these triplets at the second interface. The crushing of the block was more pronounced in the triplets made of M2 mortar tested at the Confined III level of precompression. In particular, it was so severe for the 150HBM2-type triplets at the Confined III level that hardly any slip occurred in these specimens, and the failure of the triplet resulted from the block crushing at the interface. It can be inferred from this that the failure in these specimens was not pure shear-sliding failure. Nevertheless, the influence of unit deformation on the triplet failure behavior can be neglected owing to higher block stiffness as compared to the mortar.²⁸ In addition, the British standard BS EN 1052-3:200230 has suggested that the data of triplets failing by crushing and splitting of the units can be used as a lower bound to the shear strength.

Shear stress-strain behavior

Figure 4 illustrates shear stress-strain curves for a few triplet types to investigate the effects of block strength on the shear behavior of the mortar joints. The results of triplets made of HB150, HB100, and SB100 blocks are shown in Fig. 4 for the triplet tested in the unconfined state and at the Confined III (0.79 MPa [114.58 psi]) precompression level. Shear stress was obtained by dividing the shear load by twice the area of the central block, whereas the strain was calculated by dividing the slip by the joint thickness (12 mm [0.47 in.]). As noted earlier, the compressive strength of HB150, HB100, and SB100 was 4.72, 5.07, and 8.40 MPa (685, 735, and 1218 psi), respectively. It is seen in Fig. 4 that the peak shear stress (τ_{max}) of the triplets made with SB100 block was the lowest, even though the compressive strength of this block was the highest. The results for triplets made with other mortar grades and block types and tested at other precompression levels are similar. It can be inferred that the shear behavior of the block-mortar interface was not influenced by the block type (hollow or solid block), thickness, or strength. These findings are similar to those reported by Tomaževič²⁴ for hollow blocks made of various geometrical proportions. Given this, triplets were not tested using all three block types at each mortar grade.

It is seen in Fig. 4 that the shear stress-strain curve for an unconfined triplet can be idealized as a bilinear curve

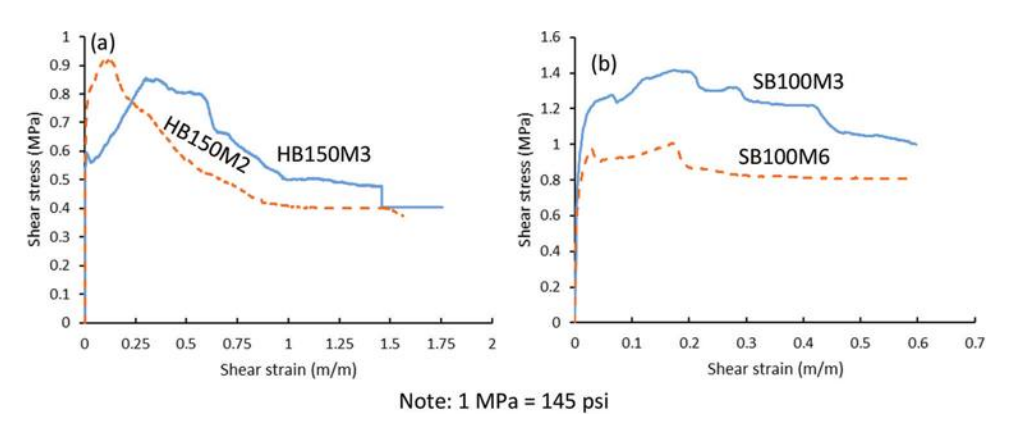


Fig. 5—Effects of mortar strength on shear stress-strain curves of triplets: (a) Confined I level triplets; and (b) Confined II level triplets.

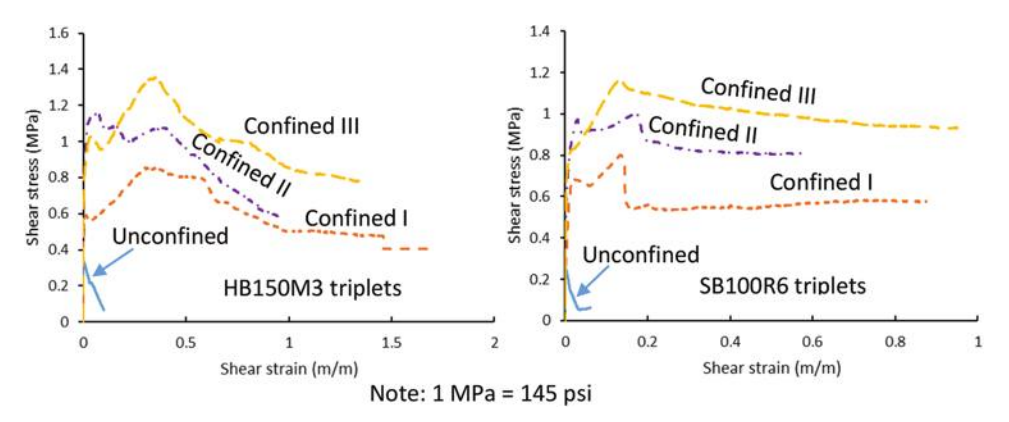


Fig. 6—Effects of precompression on shear stress-strain curves of triplets.

comprising an ascending branch up to the peak shear stress and a following descending branch, which is formed due to decreasing joint friction. Conversely, the stress-strain curve for a confined triplet is quadrilinear. The first part of the ascending branch is formed by the elastic deformation of the joint, where shear stress increases rapidly and remains proportional to the strain. The second part of the curve has a lesser slope and is a result of decreased friction and cohesion of the joint. This is followed by a third branch, which is formed at the beginning of the slip at the first cracked interface. This cracking causes a further decrease in the slope of the curve. This branch is extended up to τ_{max} . The fourth and final branch is the descending part of the curve, where the behavior of the joint is similar to the unconfined triplet and is controlled by decreasing friction.

The data of shear stress-strain curves plotted in Fig. 4 indicate the influence of mortar strength on τ_{max} . This aspect is further investigated in Fig. 5 by comparing typical shear stress-strain curves for a few triplet types that were cast with different mortar grades using the same block type. The results at two precompression levels are shown in Fig. 5 due to the similarity of behaviors with the unconfined triplets and triplets tested at the Confined III level of precompression. It is seen in Fig. 5 that the shear resistance of the interface is influenced by mortar compressive strength, and the triplets cast with higher mortar strength provided higher shear strength for the joint. Although Tomaževič²⁴ reported that shear strength was not dependent on the mortar strength, the behaviors of triplets observed in this study are different.

Figure 6 illustrates typical plots that can be used to study the effects of levels of confinement on the shear stress-strain behaviors of the tested specimens. It is seen in Fig. 6 that the shear resistance of the interface increased at higher precompression. This is because higher precompression provides larger confinement to the interface against shear failure. The post-peak softening branches of the confined triplets are considerably longer than those of the unconfined triplets, which confirms the earlier observation related to the brittle response of the latter triplet types. A summary of τ_{max} of all the tested triplet types is given in Table 1. It is noted that τ_{max} for the unconfined triplets varied from 0.21 to 0.422 MPa (30.46 to 61.21 psi), which is referred to as initial shear strength. These values correspond to $0.032f_m$ and $0.017f_m$, respectively, with an average of $0.021f_m$. Paulay and Priestley³⁶ suggested $0.03f_m$ as the initial shear strength for masonry, which is slightly higher than the average value observed in this study.

Figure 7 illustrates a correlation between τ_{max} and f_m for unconfined and confined triplets. A linear regression analysis of the data in each plot in Fig. 7 provided a correlation coefficient, which is also shown in each plot. A reasonably good fitting of the experimental data is seen in Fig. 7 with the regression line, which is indicated by $R^2 > 0.75$.

The obtained relationships from the regression analyses in Fig. 7 are described by Eq. (1) to (4), which can be used to obtain, respectively, initial shear strength (unconfined) and shear strength at the Confined I, II, and III levels of precompression for f_m varying from 6.5 to 25 MPa (943 to 3626 psi).

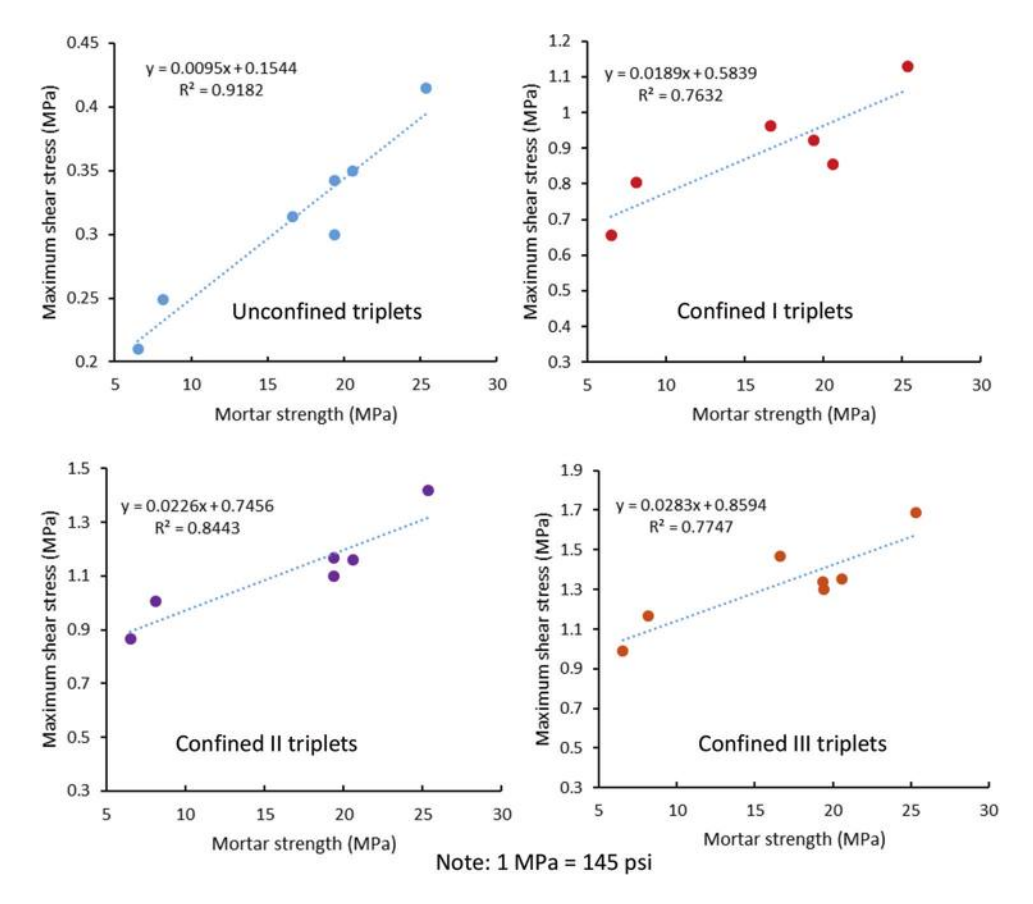


Fig. 7—Correlation between peak shear stress and mortar strength.

Linear interpolation between the employed precompression levels can provide shear strength at an intermediate precompression level.

$$\tau_{max} = \frac{1}{104} f_m + 0.15 \tag{1}$$

$$\tau_{max} = \frac{1}{53} f_m + 0.58 \tag{2}$$

$$\tau_{max} = \frac{1}{42} f_m + 0.77 \tag{3}$$

$$\tau_{max} = \frac{1}{35} f_m + 0.86 \tag{4}$$

The values of the chord shear modulus of the mortar joint (G_m) are provided in Table 1, which were determined using Eq. $(5)^{37}$ by employing the shear stress-strain curves of the triplets

$$G_m = \frac{v_2 - v_1}{\gamma_2 - 0.000050} \tag{5}$$

where v_2 is the shear stress corresponding to 33% of τ_{max} ; v_1 is the shear stress corresponding to a shear strain of 50 millionths; and γ_2 is the shear strain caused by stress v_2 . It is noted in Table 1 that G_m values for the unconfined triplets are in the range of 199 to 833 MPa (28,863 to 120,816 psi). These increased with f_m and varied between 30.1 f_m and 34.52 f_m , with an average of 31.68 f_m . The average values for the Confined I, II, and III triplets as a function

of f_m are $29.40f_m$, $14.60f_m$, and $15f_m$, respectively. This indicates that the highest G_m values were obtained for the unconfined triples, which decreased with increasing precompression. In particular, the decrease was considerable between the Confined I and II levels of precompression. Further, G_m values were similar at the Confined II and III levels of precompression.

Figure 8 illustrates variations of G_m with f_m for the unconfined and confined triplets. Regression analyses provided the relations between these parameters, which are given by Eq. (6) to (9), respectively, for the unconfined, Confined I, Confined II, and Confined III triplets. The regression lines shown in each plot in Fig. 8 indicate high correlation coefficients with the experimental data, as the lowest R^2 value was 0.85.

$$G_m = 31.91 f_m - 0.88 \tag{6}$$

$$G_m = 28.28f_m + 12.25 \tag{7}$$

$$G_m = 12.53 f_m + 29.90 \tag{8}$$

$$G_m = 10.29f_m + 119.12 \tag{9}$$

Joint shear strength parameters

The shear failure behaviors of masonry joints are represented by the Coulomb shear failure criterion (Eq. (10)), which relates shear and normal stresses linearly.

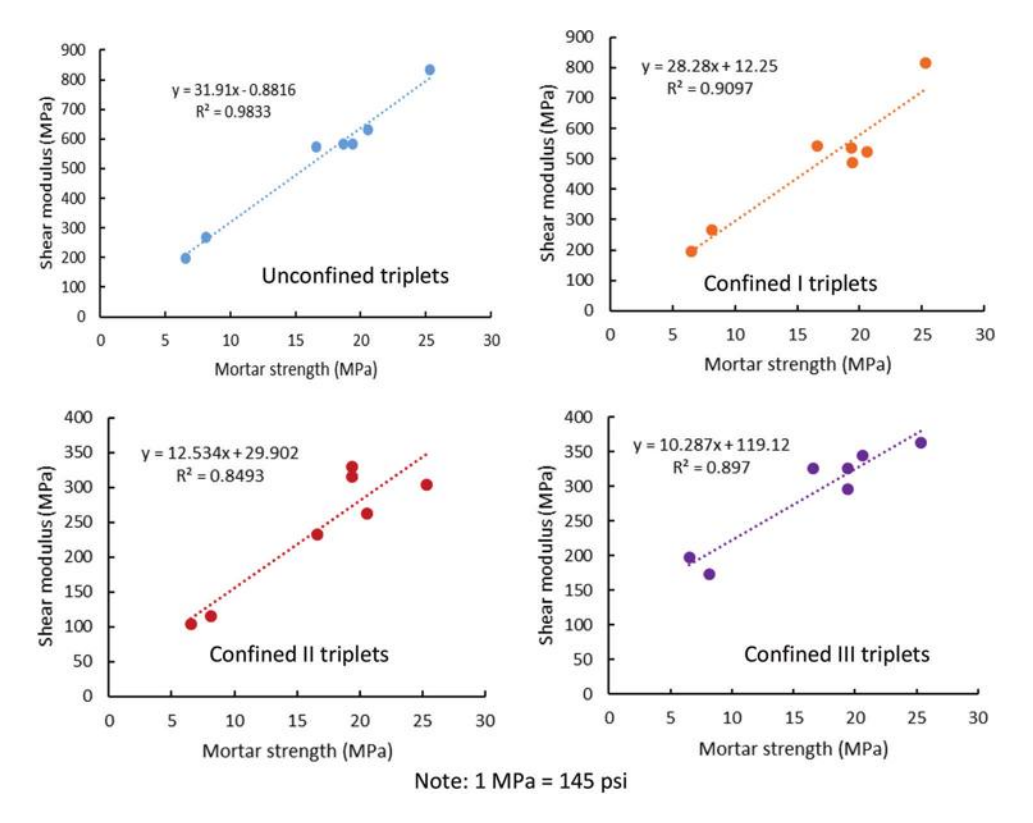


Fig. 8—Shear modulus of joint versus mortar strength.

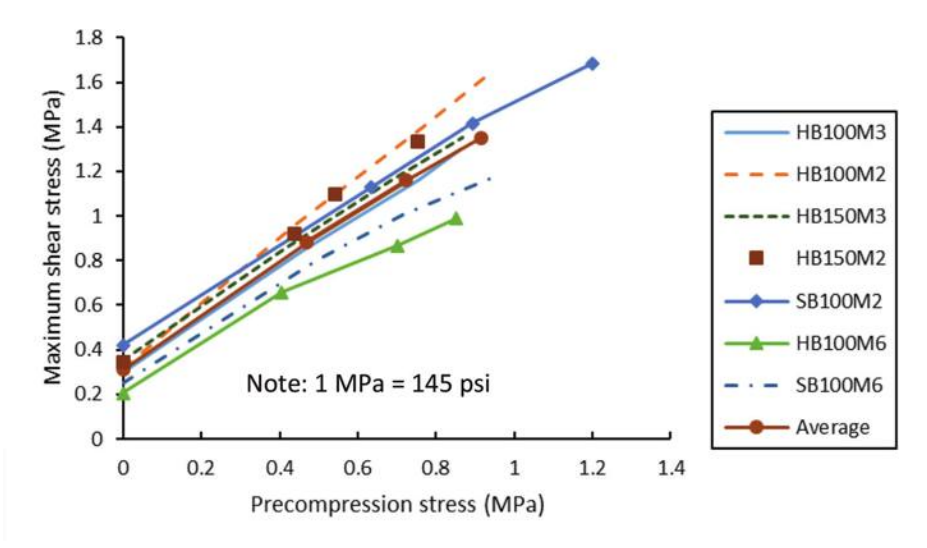


Fig. 9—Relation between shear strengths.

$$\tau_{max} = c + \mu f_p \tag{10}$$

where c is the cohesion between the masonry unit and mortar, which is taken as τ_{max} at zero precompression (unconfined shear strength); μ is the coefficient of friction between the unit and mortar at the joint, which is taken as $\tan \phi$; f_p is the axial stress (precompression stress); and ϕ is the angle of internal friction.

Figure 9 illustrates the plots of τ_{max} versus f_p for all the tested triplet types. It is seen that the shear behaviors of the triplets made with different types of mortar changed marginally at a particular level of precompression. In particular, the differences in τ_{max} for the triplets made of M2 and M3 mortars are small at each level of precompression stress. Further, the

triplets cast with M2 and M6 mortars provide upper and lower bounds for τ_{max} , respectively, at each precompression level. Given this, an average curve was used to propose a generalized relationship between τ_{max} and f_p . The average curve is also shown in Fig. 9. Note that Barattucci et al.³² reported τ_{max} for the unconfined clay brick masonry triplet as 0.93 and 0.80 MPa (135 and 116 psi) by using 1:3 and 1:6 mortars, which also supports the finding in this paper related to small changes in τ_{max} with mortar strength for the unconfined triplets.

The observed average curve (Fig. 9) was used to obtain the relationship between τ_{max} and f_p by conducting a linear regression analysis. The resulting expression is given by Eq. (11)

Table 2—Shear strength parameters available in literature

Author	Masonry unit type	c, MPa	μ	φ, rad
Incerti et al. ¹⁰	Clay brick	0.27	0.36	0.34
Pavan and Nanjunda Rao ¹¹	Clay brick	0.43	0.43	0.40
Barattucci et al. ³²	Clay brick with 1:3 mortar	0.93	1.0	0.78
Barattucci et al. ³²	Clay brick with 1:6 mortar	0.80	1.0	0.78
Barattucci et al. ³²	Clay brick with 1:9 mortar	0.36	1.0	0.78
Lourenço et al. ³⁸	Clay brick	1.39	1.03	0.79
Almeida et al. ³⁹	Clay brick	_	1.15	0.855
Abdou et al. ⁴⁰	Clay brick	1.27	1.05	0.81
Lizárraga and Pérez-Gavilán ⁴¹	Concrete block	0.55	1.05	0.81
Lizárraga and Pérez-Gavilán ⁴¹	Concrete block	0.46	1.21	0.88
Bolhassani et al. ⁴²	Concrete block	_	0.99	0.78
Pasquantonio et al. ⁴³	Concrete block	0.37	0.61	0.552
Singhal and Rai ⁴⁴	Clay brick	0.43	1.2	0.88
Abdelmoneim Elamin Mohamad and Chen ⁴⁵	Self-insulating concrete	0.54	0.67	0.60
Ferretti et al. ⁴⁶	Calcium silicate brick masonry	0.13	0.50	0.463

Note: 1 MPa = 145 psi.

$$\tau_{max} = 0.32 + 1.14 f_p \tag{11}$$

The average values of c, μ , and ϕ from Eq. (11) came out to be 0.32 MPa (58 psi), 1.14, and 49 degrees (0.785 rad), respectively. The correlation coefficient for Eq. (11) was nearly 1.0, which indicates an excellent correlation of experimental data with the regression line. Therefore, Eq. (11) can be used for estimating shear strength parameters of the block unit-mortar interface over a range of f_m employed in this study. Alternatively, Eq. (1) to (4) may be employed for determining τ_{max} at different levels of f_p for a particular f_m value, which can be used to estimate c and ϕ values more accurately by carrying out a regression analysis. Further, although 150 mm (6 in.) thick solid blocks were not used in the testing program, it can be inferred that the presented results in Eq. (1) to (4), (6) to (8), and (11) apply to these blocks as well.

Table 2 provides c, μ , and ϕ values reported by different researchers in the available literature. It is noted in Table 2 that large variations exist in the shear strength parameters reported by authors from different regions. This signifies their dependence on the variability of materials from place to place. Further, the c values reported by Barattucci et al.³² for the 1:3 and 1:6 mortars are considerably higher compared to the value of 0.32 determined in this study and some of the other studies 10,11,41,43-45 included in Table 2. This is despite the smaller μ value in the study conducted by Barattucci et al.32 compared to the present study. Further, a considerably small value of c for the clay brick masonry has been reported by Incerti et al. 10 Finally, Eurocode 647 recommended c and μ of 0.2 MPa (29 psi) and 0.4, respectively, for concrete masonry with mortar grades ranging from M10 to M20. It is noted that both of these are considerably low as compared to those obtained from Eq. (11).

Fracture energy

The amount of energy required to form a shear crack along the unit-mortar interface is called Mode II fracture energy (G_t^{II}) . This energy is calculated as the area under the shear stress-slip curve for the region of the curve corresponding to zero cohesion. 48,49 Figure 10 illustrates a plot of G_f^{II} versus f_p for all the triplet types tested in this study. It is seen that fracture energy for the triplet types made of the same mortar grade is similar and is uninfluenced by the block type. An exception to this is the triplets made of M2 mortar. Of the three triplet types made of this mortar grade, a considerably higher energy dissipation at all three levels of confinement is seen in Fig. 10 for the HB100M2-type triplets. Further, although the fracture energy increased at higher applied precompression for all triplet types, HB150M2-type triplets showed a decrease in fracture energy at the Confined II and III levels of precompression, which could be the result of the mixed failure of shear sliding and block crushing for these triplet types, as mentioned earlier. This resulted in a very small amount of energy for these triplets at the Confined III level of precompression. Although Jafari et al. 28 reported decreased fracture energy with an increase in the applied precompression stress, this type of behavior was not found for the triplets tested in this study. Small variations in fracture energy, however, were observed at the Confined III level of precompression for similar triplet types made of either Grade M3 or M6 mortar.

CONCLUSIONS

This paper describes the details of the experimental testing of triplets made of concrete blocks. Hollow blocks of 100 and 150 mm (4 and 6 in.) thickness and solid blocks of 100 mm (4 in.) thickness of each type were used and were combined with three mortar grades. The mortar grades were described by mortars made of 1:2 (Grade M2), 1:3 (Grade M3), and 1:6 (Grade M6) ratios of cement and sand by weight.

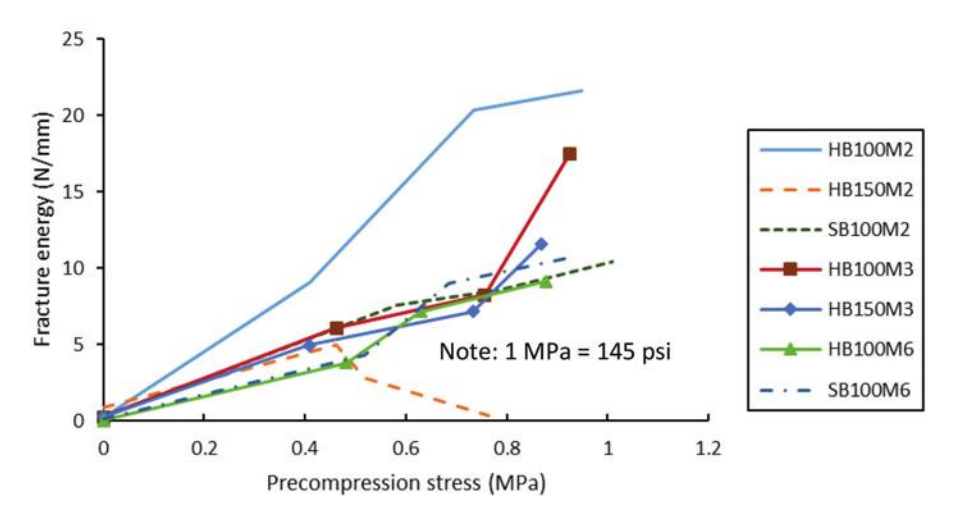


Fig. 10—Variations in fracture energy versus precompression stress.

A total of 84 specimens were tested using three levels of precompression stress. The applied stresses in these levels were 0.265 MPa (38.44 psi) (designated as Confined I), 0.536 MPa (77.74 psi) (designated as Confined II), and 0.79 MPa (114.58 psi) (designated as Confined III). Triplets in unconfined states were also tested to determine initial shear strength. The following conclusions can be drawn from the study presented in this paper:

- 1. Although the confinement of the mortar joint provided by the precompression stress increased its shear capacity, higher levels of confinement caused the splitting of the block unit at the interface when the mortar strength was significantly greater than the block strength.
- 2. No influence of block thickness, type, or strength was found on the shear strength of the block unit-mortar interface. This, however, increased (almost) linearly with the mortar strength.
- 3. The shear modulus of the mortar joint varied linearly with the mortar strength. The average shear modulus for the unconfined triplets was 31.7 times the mortar strength. The shear modulus increased at the Confined I level of precompression. The shear modulus decreased with increased levels of applied precompression although it was nearly the same at higher levels of applied precompression (Confined II and III)
- 4. Triplets made of M2 and M6 mortars provided upper and lower bounds for shear strength, respectively, at each level of confinement. Owing to small differences in shear strength at the unconfined state and each confinement level, an average curve of shear stress versus precompression stress was employed to determine shear strength parameters.
- 5. Relationships were proposed for determining shear modulus, shear strength, and shear strength parameters of block masonry joints as a function of the mortar strength.
- 6. Shear fracture (Mode II fracture) energy increased with the level of confinement. It was similar for the triplet types made of M3 and M6 mortar up to the Confined II level of precompression and was not influenced by the block type. Nevertheless, changes in fracture energy of triplets made of different block types using M2 mortar at different levels of confinement were inconsistent.

7. It is understood that the findings reported in this paper apply to the type of concrete blocks and mortar grades employed and may not apply to other types of blocks and mortars used in construction.

AUTHOR BIOS

Muhammad Masood Rafi is a Professor and Chair in the Department of Earthquake Engineering at NED University of Engineering and Technology, Karachi, Sindh, Pakistan. His research interests include seismic analysis and retrofitting of reinforced concrete (RC) and masonry structures, durability of concrete, finite element analysis, fire resistance of concrete structures, post-earthquake fire, fiber-reinforced polymer (FRP)-reinforced structures, deflection of concrete structures, recycling of concrete, and disaster management and risk reduction.

Sher Khan is a PhD Student in the Department of Earthquake Engineering at NED University of Engineering and Technology, where he received his master's degree in 2021. He received his bachelor's degree from the Balochistan University of Information Technology, Engineering and Management Sciences (BUITEMS), Quetta, Balochistan, Pakistan, in 2018. His research interests include the seismic behavior of masonry structures, earthquake engineering, and durability of concrete.

ACKNOWLEDGMENTS

The authors wish to acknowledge the financial support provided by the Higher Education Commission for this project under the National Research Program for Universities (NRPU). Help from all the laboratory technical staff members is also acknowledged. The author(s) declare(s) that there is no conflict of interest.

REFERENCES

- 1. Murmu, A. L., and Patel, A., "Towards Sustainable Bricks Production: An Overview," *Construction and Building Materials*, V. 165, Mar. 2018, pp. 112-125. doi: 10.1016/j.conbuildmat.2018.01.038
- 2. Zhang, L., "Production of Bricks from Waste Materials A Review," *Construction and Building Materials*, V. 47, Oct. 2013, pp. 643-655. doi: 10.1016/j.conbuildmat.2013.05.043
- 3. Bhattacharya, S.; Nayak, S.; and Dutta, S. C., "A Critical Review of Retrofitting Methods for Unreinforced Masonry Structures," *International Journal of Disaster Risk Reduction*, V. 7, Mar. 2014, pp. 51-67. doi: 10.1016/j.ijdrr.2013.12.004
- 4. Dehghan, S. M.; Najafgholipour, M. A.; Baneshi, V.; and Rowshanzamir, M., "Mechanical and Bond Properties of Solid Clay Brick Masonry with Different Sand Grading," *Construction and Building Materials*, V. 174, June 2018, pp. 1-10. doi: 10.1016/j.conbuildmat.2018.04.042
- 5. Resketi, N. A., and Toufigh, V., "Enhancement of Brick-Mortar Shear Bond Strength Using Environmental Friendly Mortars," *Construction and Building Materials*, V. 195, Jan. 2019, pp. 28-40. doi: 10.1016/j.conbuildmat.2018.10.118
- 6. ElGawady, M.; Lestuzzi, P.; and Badoux, M., "A Review of Conventional Seismic Retrofitting Techniques for URM," *Proceedings of the 13th*

- *International Brick/Block Masonry Conference*, D. R. W. Martens and A. T. Vermeltfoort, eds., Amsterdam, the Netherlands, July 2004, p. 1-10.
- 7. Bovo, M.; Mazzotti, C.; and Savoia, M., "Analysis of Structural Behaviour of Historical Stone Arches and Vaults: Experimental Tests and Numerical Analyses," *Structural Analysis of Historical Constructions: Proceedings of the International Conference on Structural Analysis of Historical Constructions (SAHC 2012)*, J. Jasieńko, ed., Wrocław, Poland, Oct. 2012, pp. 635-643.
- 8. Yang, X.; Wu, H.; Zhang, J.; and Wang, H., "Shear Behavior of Hollow Concrete Block Masonry with Precast Concrete Anti-Shear Blocks," *Advances in Materials Science and Engineering*, V. 2019, 2019, Article No. 9657617, 10 pp. doi. 10.1155/2019/9657617
- 9. Fiorentino, G.; Forte, A.; Pagano, E.; Sabetta, F.; Baggio, C.; Lavorato, D.; Nuti, C.; and Santini, S., "Damage Patterns in the Town of Amatrice after August 24th, 2016, Central Italy Earthquakes," *Bulletin of Earthquake Engineering*, V. 16, No. 3, Mar. 2018, pp. 1399-1423. doi: 10.1007/s10518-017-0254-z
- 10. Incerti, A.; Rinaldini, V.; and Mazzotti, C., "The Evaluation of Masonry Shear Strength by Means of Different Experimental Techniques: A Comparison between Full-Scale and Laboratory Tests," *Brick and Block Masonry Trends, Innovations and Challenges: Proceedings of the 16th International Brick and Block Masonry Conference (IBMAC 2016), Padova, Italy, 26-30 June 2016*, C. Modena, F. da Porto, and M. R. Valluzzi, eds., CRC Press, London, UK, 2016, pp. 1645-1652.
- 11. Pavan, G. S., and Nanjunda Rao, K. S., "Behavior of Brick-Mortar Interfaces in FRP-Strengthened Masonry Assemblages under Normal Loading and Shear Loading," *Journal of Materials in Civil Engineering*, ASCE, V. 28, No. 2, Feb. 2016, p. 04015120. doi: 10.1061/(ASCE) MT.1943-5533.0001388
- 12. Sherafati, M. A., and Sohrabi, M. R., "Performance of Masonry Walls during Kaki, Iran, Earthquake of April 9, 2013," *Journal of Performance of Constructed Facilities*, ASCE, V. 30, No. 3, June 2016, p. 04015040. doi: 10.1061/(ASCE)CF.1943-5509.0000788
- 13. Basset-Salom, L., and Guardiola-Villora, A., "Seismic Performance of Masonry Residential Buildings in Lorca's City Centre, after the 11th May 2011 Earthquake," *Bulletin of Earthquake Engineering*, V. 12, No. 5, Oct. 2014, pp. 2027-2048, doi: 10.1007/s10518-013-9559-8
- 14. Sayın, E.; Yön, B.; Calayır, Y.; and Karaton, M., "Failures of Masonry and Adobe Buildings during the June 23, 2011 Maden-(Elazığ) Earthquake in Turkey," *Engineering Failure Analysis*, V. 34, Dec. 2013, pp. 779-791. doi: 10.1016/j.engfailanal.2012.10.016
- 15. Lourenço, P. B.; Avila, L.; Vasconcelos, G.; Alves, J. P. P.; Mendes, N.; and Costa, A. C., "Experimental Investigation on the Seismic Performance of Masonry Buildings Using Shaking Table Testing," *Bulletin of Earthquake Engineering*, V. 11, No. 4, Aug. 2013, pp. 1157-1190. doi: 10.1007/s10518-012-9410-7
- 16. Parisi, F., and Augenti, N., "Seismic Capacity of Irregular Unreinforced Masonry Walls with Openings," *Earthquake Engineering & Structural Dynamics*, V. 42, No. 1, Jan. 2013, pp. 101-121. doi: 10.1002/eqe.2195
- 17. Oyguc, R., and Oyguc, E., "2011 Van Earthquakes: Lessons from Damaged Masonry Structures," *Journal of Performance of Constructed Facilities*, ASCE, V. 31, No. 5, Oct. 2017, p. 04017062. doi: 10.1061/(ASCE)CF.1943-5509.0001057
- 18. Ingham, J., and Griffith, M., "Performance of Unreinforced Masonry Buildings during the 2010 Darfield (Christchurch, NZ) Earthquake," *Australian Journal of Structural Engineering*, V. 11, No. 3, 2010, pp. 207-224.
- 19. Brzev, S.; Astroza, M.; and Moroni Yadlin, M. O., "Performance of Confined Masonry Buildings in the February 27, 2010 Chile Earthquake," EERI Report, Earthquake Engineering Research Institute, Oakland, CA, 2010, 15 pp.
- 20. Zhao, B.; Taucer, F.; and Rossetto, T., "Field Investigation on the Performance of Building Structures during the 12 May 2008 Wenchuan Earthquake in China," *Engineering Structures*, V. 31, No. 8, Aug. 2009, pp. 1707-1723. doi: 10.1016/j.engstruct.2009.02.039
- 21. Zhang, M., and Jin, Y., "Building Damage in Dujiangyan during Wenchuan Earthquake," *Earthquake Engineering and Engineering Vibration*, V. 7, No. 3, Sept. 2008, pp. 263-269. doi: 10.1007/s11803-008-0870-3
- 22. Dowling, D. M.; Diaz, J.; and Samali, B., "Horizontal Shear Testing of Mudbrick Masonry Mortar Joints," *Proceedings of the 7th Australasian Masonry Conference*, M. Masia, ed., Newcastle, NSW, Australia, 2004, pp. 378-387.
- 23. FEMA 306, "Evaluation of Earthquake Damaged Concrete and Masonry Wall Buildings: Basic Procedures Manual," prepared by Applied Technology Council, Federal Emergency Management Agency, Washington, DC, 1998, 270 pp.
- 24. Tomaževič, M., "Shear Resistance of Masonry Walls and Eurocode 6: Shear versus Tensile Strength of Masonry," *Materials and Structures*, V. 42, No. 7, Aug. 2009, pp. 889-907. doi: 10.1617/s11527-008-9430-6

- 25. Pekmezci, B. Y., and Pekmezci, I. P., "Development of Shear Strength Index Test Probe: Its Application on Historic Structures," *International Journal of Building Pathology and Adaptation*, V. 40, No. 5, Dec. 2022, pp. 693-711. doi: 10.1108/IJBPA-10-2020-0089
- 26. Meli, R.; Brzev, S.; Astroza, M.; Boen, T.; Crisafulli, F.; Dai, J.; Farsi, M.; Hart, T.; Mebarki, A.; Moghadam, A. S.; Quiun, D.; Tomazevic, M.; and Yamin, L., "Seismic Design Guide for Low-Rise Confined Masonry Buildings," Earthquake Engineering Research Institute, Oakland, CA, Aug. 2011, 91 pp.
- 27. Venkatarama Reddy, B. V., and Vyas, C. V. U., "Influence of Shear Bond Strength on Compressive Strength and Stress–Strain Characteristics of Masonry," *Materials and Structures*, V. 41, No. 10, Dec. 2008, pp. 1697-1712. doi: 10.1617/s11527-008-9358-x
- 28. Jafari, S.; Rots, J. G.; and Esposito, R., "Core Testing Method to Assess Nonlinear Shear-Sliding Behaviour of Brick-Mortar Interfaces: A Comparative Experimental Study," *Construction and Building Materials*, V. 244, May 2020, Article No. 118236. doi: 10.1016/j.conbuildmat.2020.118236
- 29. Jukes, P., and Riddington, J. R., "A Review of Masonry Joint Shear Test Methods," *Masonry International*, V. 11, No. 2, 1997, pp. 37-43.
- 30. BS EN 1052-3:2002, "Methods of Test for Masonry Part 3: Determination of Initial Shear Strength," British Standards Institution, London, UK, 2002, 18 pp.
- 31. Mwafy, A., and Elnashai, A., "Importance of Shear Assessment of Concrete Structures Detailed to Different Capacity Design Requirements," *Engineering Structures*, V. 30, No. 6, June 2008, pp. 1590-1604. doi: 10.1016/j.engstruct.2007.10.015
- 32. Barattucci, S.; Sarhosis, V.; Bruno, A. W.; D'Altri, A. M.; de Miranda, S.; and Castellazzi, G., "An Experimental and Numerical Study on Masonry Triplets Subjected to Monotonic and Cyclic Shear Loadings," *Construction and Building Materials*, V. 254, Sept. 2020, Article No. 119313. doi: 10.1016/j.conbuildmat.2020.119313
- 33. ASTM C150-04, "Standard Specification for Portland Cement," ASTM International, West Conshohocken, PA, 2004, 8 pp.
- 34. Garcia-Ramonda, L.; Pelà, L.; Roca, P.; and Camata, G., "Cyclic Shear-Compression Testing of Brick Masonry Walls Repaired and Retrofitted with Basalt Textile Reinforced Mortar," *Composite Structures*, V. 283, Mar. 2022, Article No. 115068. doi: 10.1016/j.compstruct.2021.115068
- 35. Cavalheiro, O. P., and Pedroso, G. M., "Experimental Data on Hollow Block Prisms Using Direct Shear Test," *Proceedings of the 12th International Brick/Block Masonry Conference (12th IB2MaC)*, J. M. Adell, ed., Madrid, Spain, 2000, pp. 433-440.
- 36. Paulay, T., and Priestley, M. J. N., *Seismic Design of Reinforced Concrete and Masonry Buildings*, John Wiley & Sons, Inc., New York, 1992, 768 pp.
- 37. ASTM C469/C469M-14, "Standard Test Method for Static Modulus of Elasticity and Poisson's Ratio of Concrete in Compression," ASTM International, West Conshohocken, PA, 2014, 5 pp.
- 38. Lourenço, P. B.; Barros, J. O.; and Oliveira, J. T., "Shear Testing of Stack Bonded Masonry," *Construction and Building Materials*, V. 18, No. 2, Mar. 2004, pp. 125-132. doi: 10.1016/j.conbuildmat.2003.08.018
- 39. Almeida, J. A. P. P.; Bordigoni, D.; Pereira, E. B.; Barros, J. A. O.; and Aprile, A., "Assessment of the Properties to Characterise the Interface between Clay Brick Substrate and Strengthening Mortar," *Construction and Building Materials*, V. 103, Jan. 2016, pp. 47-66. doi: 10.1016/j.conbuildmat.2015.11.036
- 40. Abdou, L.; Ami Saada, R.; Meftah, F.; and Mebarki, A., "Experimental Investigations of the Joint-Mortar Behaviour," *Mechanics Research Communications*, V. 33, No. 3, May-June 2006, pp. 370-384. doi: 10.1016/j. mechrescom.2005.02.026
- 41. Lizárraga, J. F., and Pérez-Gavilán, J. J., "Parameter Estimation for Nonlinear Analysis of Multi-Perforated Concrete Masonry Walls," *Construction and Building Materials*, V. 141, June 2017, pp. 353-365. doi: 10.1016/j.conbuildmat.2017.03.008
- 42. Bolhassani, M.; Hamid, A. A.; Lau, A. C. W.; and Moon, F., "Simplified Micro Modeling of Partially Grouted Masonry Assemblages," *Construction and Building Materials*, V. 83, May 2015, pp. 159-173. doi: 10.1016/j.conbuildmat.2015.03.021
- 43. Pasquantonio, R. D.; Parsekian, G. A.; Fonseca, F. S.; and Shrive, N. G., "Experimental and Numerical Characterization of the Interface between Concrete Masonry Block and Mortar," *Revista IBRACON de Estruturas e Materiais*, V. 13, No. 3, May-June 2020, pp. 578-592. doi: 10.1590/s1983-41952020000300008
- 44. Singhal, V., and Rai, D. C., "Suitability of Half-Scale Burnt Clay Bricks for Shake Table Tests on Masonry Walls," *Journal of Materials in Civil Engineering*, ASCE, V. 26, No. 4, Apr. 2014, pp. 644-657. doi: 10.1061/(ASCE)MT.1943-5533.0000861
- 45. Abdelmoneim Elamin Mohamad, A.-B., and Chen, Z., "Experimental and Numerical Analysis of the Compressive and Shear Behavior for a New

- Type of Self-Insulating Concrete Masonry System," Applied Sciences, V. 6, No. 9, Sept. 2016, Article No. 245. doi: 10.3390/app6090245
- 46. Ferretti, F.; Mazzotti, C.; Esposito, R.; and Rots, J. G., "Shear-Sliding Behavior of Masonry: Numerical Micro-Modeling of Triplet Tests," *Computational Modelling of Concrete Structures*, G. Meschke, B. Pichler, and J. Rots, eds., CRC Press, London, UK, 2018, pp. 941-951.

 47. EN 1996-1-1:2005, "Eurocode 6 - Design of Masonry Structures
- Part 1-1: General Rules for Reinforced and Unreinforced Masonry
- Structures," European Committee for Standardization, Brussels, Belgium, 2005, 125 pp.
- 48. Stockl, S.; Hofmann, P.; and Mainz, J., "A Comparative Finite Element Evaluation of Mortar Joint Shear Tests," *Masonry International*, V. 3, No. 3, 1990, pp. 101-104.
- 49. Rots, J. G., Structural Masonry: An Experimental/Numerical Basis for Practical Design Rules (CUR Report 171), CRC Press, Boca Raton, FL, 1997, 166 pp.



OUR MISSION

We make strategic investments in ideas, research, and people to create the future of the concrete industry.

Through its councils and programs, the ACI Foundation helps to keep the concrete industry at the forefront of advances in material composition, design, and construction.





OUR FOCUS



Identifying technologies and innovations which provide needed solutions for the concrete industry



Seeking concrete research projects that further the knowledge and sustainability of concrete materials, construction, and structures



Supporting our future concrete innovators and leaders by administering fellowships and scholarships



Helping honorably discharged veterans with our Veterans Rebate for ACI Certification program

Title No. 121-S22

Shear Strength of Reinforced Concrete Columns with External Post-Tensioned Clamps

by Julian D. Rincon, Yu-Mei Chen, Santiago Pujol, Aishwarya Y. Puranam, and Shyh-Jiann Hwang

An alternative method to retrofit reinforced concrete (RC) columns with insufficient shear reinforcement is investigated. The retrofit involves external prestressing of the columns in the transverse direction to increase both shear strength and drift capacity. External post-tensioned clamps, consisting of high-strength steel rods connecting a set of steel angles, were applied around the columns at different spacings and initial post-tensioning stresses. The tension induced in the steel rods exerts lateral confining pressure on the column by bearing of the angles against the corners of the column. Ten RC columns furnished with external post-tensioned clamps were tested under cyclic loads and approximately constant axial loads. In addition, six RC beams with clamps were tested under monotonically increasing loads. Both the column and beam specimens were fabricated with no transverse reinforcement in the form of conventional steel ties. Therefore, the external clamps were the only source of reinforcement resisting shear. The lateral prestress provided by the clamps was observed to increase the shear stress at the formation of the first inclined crack and at failure. As a result, the mode of failure of columns vulnerable in shear changed from shear failure to a more ductile failure dominated by flexure. The observed increase in shear strength is dependent on the lateral prestress and the tensile strength of the concrete. A simple equation, based on the mechanics of materials, is presented to calculate the shear strength of RC columns with external prestressing.

Keywords: external post-tensioned clamps; lateral prestress; reinforced concrete (RC) columns; retrofit; shear strength.

INTRODUCTION

The work presented in this paper was undertaken to investigate the effects of external prestressing with clamps on the shear strength of reinforced concrete (RC) columns. This report focuses on the ability of clamps to prevent shear failure before flexural yielding of the longitudinal reinforcement. That is one of the most brittle and dangerous modes of failure in RC. It not only affects the ability of the structure to resist strong shaking but also the capacity of the structure to resist its own weight.¹⁻³ To prevent brittle shear failure, the shear strength of RC members must be designed to exceed the shear demand associated with the flexural strength. Nevertheless, the building stock in seismic regions is heavily populated by buildings that do not meet that demand. Reports of RC building collapses during past earthquakes have identified column failures as one of the primary causes. 4-9 What is more, shear failure of RC columns due to inadequate transverse reinforcement is a recurring observation.

A considerable amount of work on the topic of shear strength of RC for cyclic demands has been done. Yet, the subject is not well understood. Wight and Sozen¹⁰ observed that displacement reversals beyond the yield displacement decrease the shear strength and/or stiffness of RC columns. Loss of shear strength and/or stiffness was related to the formation of inclined cracks, spalling of the concrete cover, expansion of the ties, and loss of interlock resistance of the concrete along inclined cracks. Nonetheless, RC columns with light transverse reinforcement can fail in shear at low drift ratios before yielding of the longitudinal reinforcement.

Recent work by Joint ACI-ASCE Subcommittee 445-B^{11,12} suggests that resistance to shear is not affected in a critical fashion by cycles in the linear range of response. That observation reduces the problem of shear failure before flexural yielding to that studied early on by Mörsch¹³ and Richart.¹⁴ The literature on the subject of shear failure before flexural yielding is abundant and spans from simple solutions (for example, Richart) to highly elaborate ones (for example, the Modified Compression Field Theory [MCFT]¹⁵). A review of the state of the art was produced by Belarbi et al.¹⁶

Nevertheless, the scope of these studies has mostly been limited to specimens with conventional ties. Studies of the shear strength of RC columns with post-tensioning transverse reinforcement have been scarce. Two relevant investigations into the topic were carried out by Yamakawa et al.¹⁷ and Skillen.¹⁸ Yamakawa et al.¹⁷ tested 31 small-scale RC columns with widely spaced conventional ties. Of the 31 specimens, 22 were strengthened with post-tensioned external clamps, and the remaining nine had no external clamps. Yamakawa et al.'s test results showed that the post-tensioned clamps were effective in preventing shear failure in the retrofitted columns. Skillen¹⁸ tested two largescale RC columns to study the effect of lateral pressure by means of external clamps. His proposed clamps were simpler to fabricate and easier to install in comparison with the clamps used by Yamakawa et al. Skillen's test results suggested again that the shear strength of columns with light transverse reinforcement can be increased by applying post-tensioning transverse reinforcement. Still, a number of questions remain. In relation to the work of Yamakawa et al., there are questions about how to extrapolate their results from small-scale columns to full-scale columns with

ACI Structural Journal, V. 121, No. 2, March 2024.

MS No. S-2022-384.R2, doi: 10.14359/51740248, received September 10, 2023, and reviewed under Institute publication policies. Copyright © 2024, American Concrete Institute. All rights reserved, including the making of copies unless permission is obtained from the copyright proprietors. Pertinent discussion including author's closure, if any, will be published ten months from this journal's date if the discussion is received within four months of the paper's print publication.

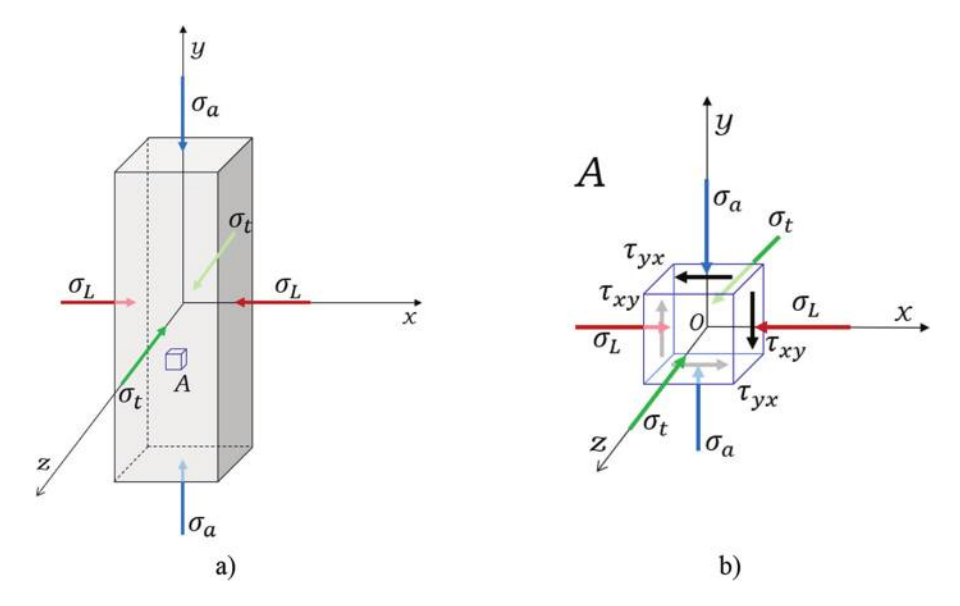


Fig. 1—(a) RC column under axial and lateral stresses; and (b) infinitesimal three-dimensional element oriented to x-y-z-axes. (Note: σ_a is normal longitudinal stress, σ_L is normal transverse stress in parallel direction to x-axis, σ_t is normal transverse stress in parallel direction to z-axis, τ_{xy} is shear stress acting on x-face in direction of y-axis, and τ_{yx} is shear stress acting on y-face in direction of x-axis.)

sizes more representative of what is common in the field. The specimens studied by Skillen were larger, but he tested only two columns, and that is not enough in a problem with as much uncertainty as shear has.

Olesen et al.'s¹⁹ work on the shear of RC beams is of critical relevance to this investigation because it provides a method to consider the effects of lateral prestress on shear strength. Prestressing of concrete structures is generally performed to control flexural cracks and deflections with tendons in the axial direction of a given member. In an attempt to delay the onset and development of shear cracking, tests on columns and beams with post-tensioned transverse reinforcement were conducted at the University of Canterbury (UC) in New Zealand and the National Center for Research on Earthquake Engineering (NCREE) in Taiwan. Lateral prestress was observed to increase the shear stress at the first diagonal cracking and to preclude the formation of large crisscrossing inclined cracks caused by cyclic demands.

RESEARCH SIGNIFICANCE

A method consisting of applying external lateral prestress to retrofit RC columns vulnerable in shear is investigated. The proposed method is easy to design and implement and lends itself as a practical solution for retrofitting large inventories of structures, or in developing countries. Experimental tests conducted on large-scale RC columns showed the effectiveness of external lateral prestress in increasing column shear strength and drift capacity. A simple equation, based on mechanics, for calculating the shear strength of RC columns with lateral prestress is presented.

TECHNICAL FRAMEWORK

The shear strength, denoted as v_c , can be approximated as the shear at the point of first inclined cracking.¹⁴ An expression for the load causing shear cracking in a concrete element

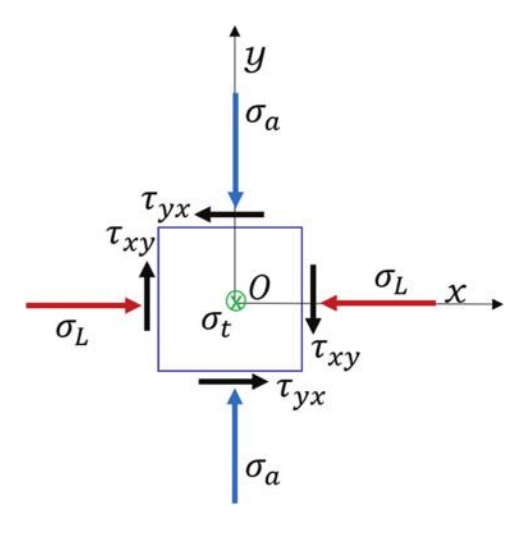


Fig. 2—Two-dimensional view of same element shown in Fig. 1(b).

subjected to lateral prestress is derived using the procedure outlined by Olesen et al. 19

In Fig. 1(a), an RC column is depicted under axial compressive stress and lateral confinement in two directions perpendicular to its longitudinal axis. In this figure, σ_a is the normal longitudinal stress, σ_L is the normal transverse stress in the x-direction, and σ_t is the normal transverse stress in the z-direction. An infinitesimal element within the column is labeled as "A" and illustrated in Fig. 1(b). A two-dimensional view of element A is presented in Fig. 2. Equilibrium of this element requires the shear stresses τ_{xy} and τ_{yx} to be equal in magnitude and opposite in direction ($\tau_{xy} = \tau_{yx}$). The Mohr's circle in Fig. 3 illustrates the relationship among σ_L , σ_a , and τ_{xy} required for equilibrium.

In Fig. 3, σ_1 and σ_2 represent the maximum and minimum principal stresses, respectively, acting on inclined planes free of shear, as shown in Fig. 4. Compressive stresses are

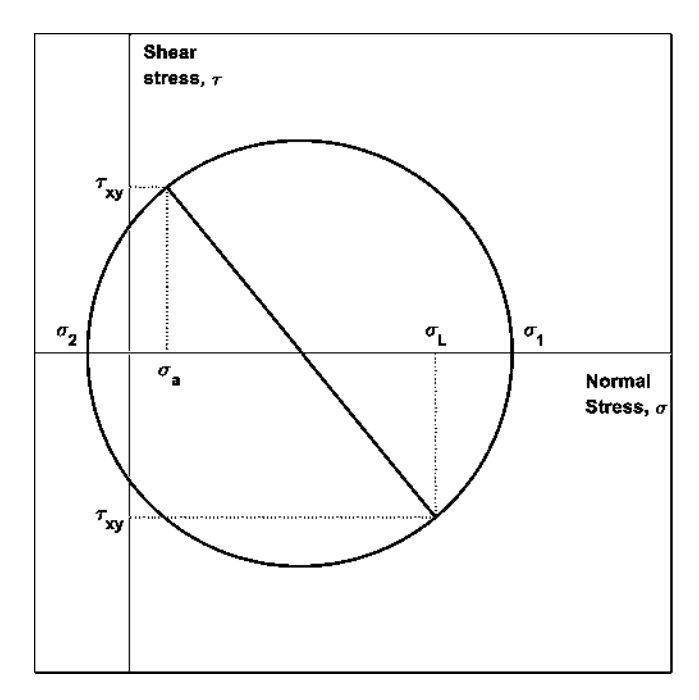


Fig. 3—Mohr's circle corresponding to stresses acting on element shown in Fig. 2.

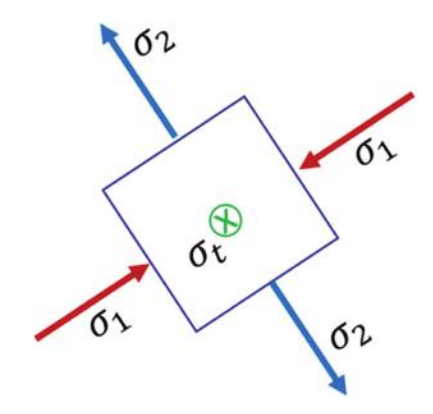


Fig. 4—Principal stresses. (Note: σ_1 is algebraically larger principal stress [compressive stress], σ_2 is algebraically smaller principal stress [tensile stress], and σ_t is normal transverse stress in parallel direction to z-axis.)

drawn as positive, while tensile stresses are drawn as negative. Stress σ_2 is expected to be tensile at inclined cracking.

The principal stresses σ_1 and σ_2 can be calculated using Eq. (1)

$$\sigma_{1,2} = \frac{\sigma_a + \sigma_L}{2} \pm \sqrt{\left(\frac{\sigma_a - \sigma_L}{2}\right)^2 + \tau^2} \tag{1}$$

where σ_1 is the algebraically larger principal stress (compressive stress); σ_2 is the algebraically smaller principal stress (tensile stress); σ_a is the normal longitudinal stress; σ_L is the normal transverse stress in the parallel direction to the x-axis; and τ is shear stress.

In Fig. 5(a), element A is shown on a plane constructed parallel to the directions of stresses σ_1 and σ_t , while Fig. 5(b) illustrates element A on a plane parallel to the directions of stresses σ_2 and σ_t . Notice that the directions parallel to stresses σ_1 , σ_2 , and σ_t represent the principal stress directions.

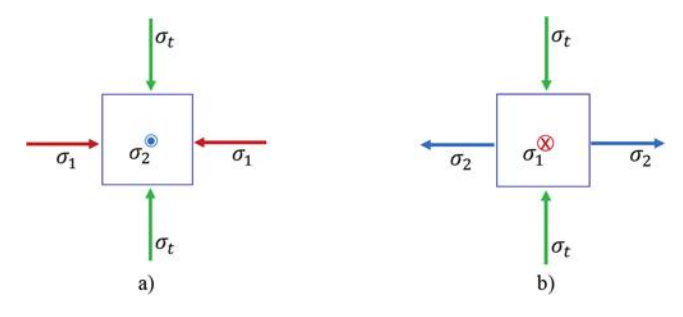


Fig. 5—(a) Stresses seen on plane $\sigma_1 - \sigma_t$; and (b) stresses seen on plane $\sigma_2 - \sigma_t$.

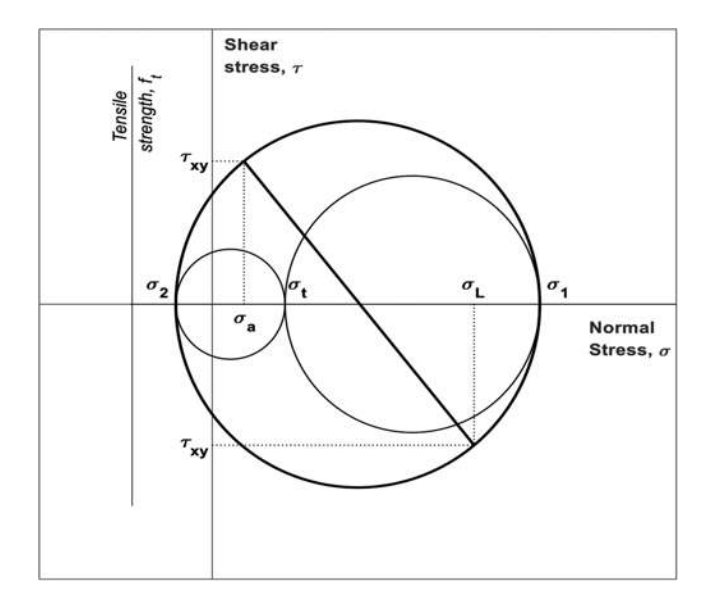


Fig. 6—Mohr's circles for three-dimensional element A shown in Fig. 1.

The corresponding Mohr's circles for these stresses are presented in Fig. 6.

Note that the circles depicted in Fig. 6 are drawn for the case where $\sigma_L > \sigma_t$, with both being compressive stresses. The vertical line on the left represents the tensile strength of the concrete, denoted as f_t . An inclined shear crack is assumed to occur when the principal stress σ_2 exceeds the tensile strength of the concrete f_t . Equating the principal stress σ_2 to the tensile strength f_t gives the following equations for the shear stress in the concrete at inclined cracking.

$$-f_t = \frac{\sigma_a + \sigma_L}{2} - \sqrt{\left(\frac{\sigma_a - \sigma_L}{2}\right)^2 + \tau^2}$$
 (2)

Solving for τ

$$\tau = f_t \cdot \sqrt{\left(1 + \frac{\sigma_a}{f_t}\right) \left(1 + \frac{\sigma_L}{f_t}\right)}$$
 (3)

Equation (3) can be rewritten as follows

$$v_c = v_{c_o} \cdot \sqrt{1 + \frac{\sigma_L}{f_t}} \tag{4}$$

where v_c is the shear strength attributable to the concrete in the presence of lateral confining stress σ_L ; v_{c_o} is the

Table 1—Specimen details

Specimen	Type of test	Application of P.T.	A.L.R.	a/d	f_c' , MPa	$f_t/\sqrt{f_c'}$, MPa	E_c , GPa
C3		2			30	0.49	21
C5		2			36	0.37	20
C6	C	2	0.15	3.6	24	0.46	29
C7		2	0.13	3.0	26	0.48	32
C8		2			31	0.40	29
С9		2			23	0.49 0.37 0.46 0.48	29
SC1		2			21	_	_
SC2	C	2	0.3	2.2	23	_	_
SC3		2		2.2	25	_	_
SC4		2	0.4		25	_	_
B1A		N.A.	0				
B1B		N.A.	0				
B2A		2	0				
B2B		2	0				
B3A		2	0				
ВЗВ	M	2	0	2.2	41	0.53	27
B4A	IVI	1	0	2.2	41	0.55	21
B4B		1	0				
B5A		1	0				
B5B		1	0				
B6A		2	0			0.49 0.37 0.46 0.48 0.40 0.40	
B6B		1	0				

Note: C is cylic; M is monotonic; P.T. is prestress applied in one or two directions; A.L.R. is axial load ratio $P/f_c'A_g$; a/d is shear span-to-effective depth ratio; f_c' is concrete cylinder compressive strength; f_i is concrete tensile strength determined as splitting strength of 100 x 200 mm cylinders; E_c is modulus of concrete.

resistance to shear attributable to concrete in the absence of lateral prestress; σ_L is the lateral confining stress; and f_t is the tensile strength of concrete, and it is assumed to be close to $1/3\sqrt{f_t'}$ MPa.

The primary conclusion drawn from Eq. (4) is that the shear strength attributable to the concrete is proportional to $\sqrt{1 + \frac{\sigma_L}{f_t}}$, and this dependence hinges on both the lateral confining stress σ_L and the tensile strength of the concrete f_t .

EXPERIMENTAL DATA

Column tests

Specimen description—Ten RC columns furnished with clamps were tested under displacement reversals and approximately constant axial loads (Tables 1 and 2). Of these 10 columns, six were tested at the Structures Laboratory of UC, and four were tested at NCREE. The UC columns were tested as single-curvature cantilevers, and the NCREE columns were tested in double curvature. Following the nomenclature by Skillen, ¹⁸ the UC columns were labeled C3, C5, C6, C7, C8, and C9, and the NCREE columns were labeled SC1, SC2, SC3, and SC4. The test columns at UC were part of a larger project that also included the testing of columns with post-tensioned clamps as a repair measure. ²⁰ Figures 7 to 9 provide details of the columns tested at UC and NCREE. The UC columns had cross-sectional dimensions

of 500 x 500 mm, a clear height of 1530 mm, and eight 32 mm diameter longitudinal reinforcing bars. The NCREE columns had cross-sectional dimensions of 750 x 750 mm, a clear height of 3000 mm, and twelve 32 mm diameter longitudinal reinforcing bars. The shear span-to-effective depth ratio (*a/d*) was 3.6 for UC columns and 2.2 for NCREE columns. The longitudinal reinforcement ratio was approximately 2.6% for UC columns and 1.7% for NCREE columns. All the columns were fabricated with no internal ties. This was done for two reasons: 1) to represent an extreme case of an older RC column with wide tie spacing; and 2) to simplify the estimation of the shear that is resisted by the external transverse reinforcement (clamps). Table 2 summarizes the measured properties of the longitudinal reinforcement and the post-tensioning transverse reinforcement.

At UC, specimens were cast lying on their sides in a single lift and cured for 7 days under plastic, with water dousing occurring during at least the first 3 days. The concrete mixture was supplied by a ready mixed concrete supplier. The cement used was ASTM Type I portland, and the coarse aggregate was a blend of 60% crushed stone (maximum size of 13 mm) and 40% natural alluvial "Greywacke" aggregate (maximum size of 19 mm). The cylinder compressive strength ranged from 21 to 36 MPa.

The specimens at NCREE were also cast on their sides and cured with water dousing three times a day for 7 days. The

Table 2—Longitudinal reinforcement and post-tensioning rods properties

	Lon	gitudinal re	inforcement		Post-tensioning reinforcement						
Specimen	A_s , mm ²	ρ _l , %	f _y , MPa	f _u , MPa	A_{pt} , mm ²	s _{pt} , mm	r _{pt} , %	f_{pty} , MPa	f_{ptu} , MPa		
СЗ						300	0.21				
C5	6434				314	200	0.32				
С6		2.6	555	698		200	0.32	820*	922		
C7		2.0				300	0.21	820	922		
C8	(8 \phi 32 mm)				(2 \phi 16 mm)	200	0.32				
С9			518	647		300	0.21				
SC1	9651				408	200	0.27		1600		
SC2	9031	1.7	166	(00	408	200	0.27	1245			
SC3	(12 † 22)	1.7	466 690	(2 ± 10)	300	0.18	1243	1000			
SC4	(12 \phi 32 mm)				(2 \phi 18 mm)	200	0.27				
B1A						_	0	_	_		
B1B						_	0	_	_		
B2A	982					95	0.3	260			
B2B	982				57	95	0.3		369		
B3A						143	0.2		309		
ВЗВ		2.0	550	680		143	0.2				
B4A		2.0	330	080		143	0.2	290	452		
B4B	1					143	0.2	290	452		
B5A	(2.1.25				(2.1.6)	95	0.3	289	468		
B5B	(2 \phi 25 mm)	n)			(2 \phi 6 mm)	95	0.3	290	452		
B6A	1					190	0.15	200	468		
B6B	1					190	0.15	290			

^{*}For clamps with no welds (as in C3), nominal resistance to shear provided by clamps is inferred to be close to $v_s = r_{pt} \cdot 0.6 f_{pty}$ instead of $v_s = r_{pt} \cdot f_{pty}$.

Note: A_s is total area of longitudinal reinforcement; ρ_l is longitudinal reinforcement ratio; f_y is longitudinal reinforcement yield stress; f_u is longitudinal reinforcement ultimate stress; A_{pt} is area of post-tensioning transverse reinforcement (one clamp, two legs); s_{pt} is spacing of clamps; r_{pt} is reinforcement ratio of post-tensioning transverse reinforcement; f_{pty} is post-tensioning transverse reinforcement yield stress; f_{ptu} is post-tensioning transverse reinforcement ultimate stress.

concrete mixture was supplied by a ready mixed concrete supplier. The cement used was ASTM Type I portland. The nominal coarse aggregate size was 19 mm. The cylinder compressive strength ranged from 21 to 25 MPa.

External post-tensioned clamps on columns

The clamps studied are similar to those used by Skillen. ¹⁸ They consisted of four corner brackets, each made with pairs of steel angles, and high-strength threaded rods connecting the brackets (Fig. 10). A key difference from the clamps used by Skillen ¹⁸ is that the clamps used in this study were welded. Welding was applied to prevent the concentration of shear force in rods. Welding can be avoided if the clamps are sized assuming their strength is controlled by the rod sections working in shear. That is, $v_s = r_{pt} \cdot 0.6 f_{pty}$ instead of $v_s = r_{pt} \cdot f_{pty}$.

For the tests at UC, clamps were fabricated with 16 mm thick angles and 16 mm diameter threaded rods with a measured yield stress of 820 MPa. The spacing between clamps s_{pt} was either 200 or 300 mm (Table 3). The post-tensioned transverse reinforcement area ratio r_{pt} , calculated using Eq. (5), was 0.21 or 0.32%. The initial prestress in the threaded rods f_{pti} ranged from 0.1 f_{pty} (low prestress) to 0.7 f_{pty}

(high prestress), where f_{pty} is the yield stress of the threaded rods. The equivalent lateral confining stress caused by the clamps on the column σ_L is expressed as the transverse reinforcement ratio times the initial prestress in the clamps, and it is calculated using Eq. (6). This stress ranged from 0.2 to 1.7 MPa.

For the tests at NCREE, clamps were fabricated with 25 mm thick angles and 18 mm diameter threaded rods with a mean measured yield stress of 1250 MPa. The spacing between clamps s_{pt} was 200 or 300 mm (Table 3). The post-tensioned transverse reinforcement area ratio r_{pt} was 0.18 or 0.27%. The initial prestress in the threaded rods ranged from 0.1 f_{pty} to 0.55 f_{pty} . The equivalent lateral confining stress caused by the clamps on the column σ_L ranged from 0.3 to 1.8 MPa

$$r_{pt} = \frac{A_{pt}}{b \cdot s_{pt}} \tag{5}$$

$$\sigma_L = r_{pt} \cdot f_{pti} \tag{6}$$

where r_{pt} is the post-tensioned transverse reinforcement area ratio; A_{pt} is the total area of post-tensioned transverse reinforcement within spacing s_{pt} ; b is the width of

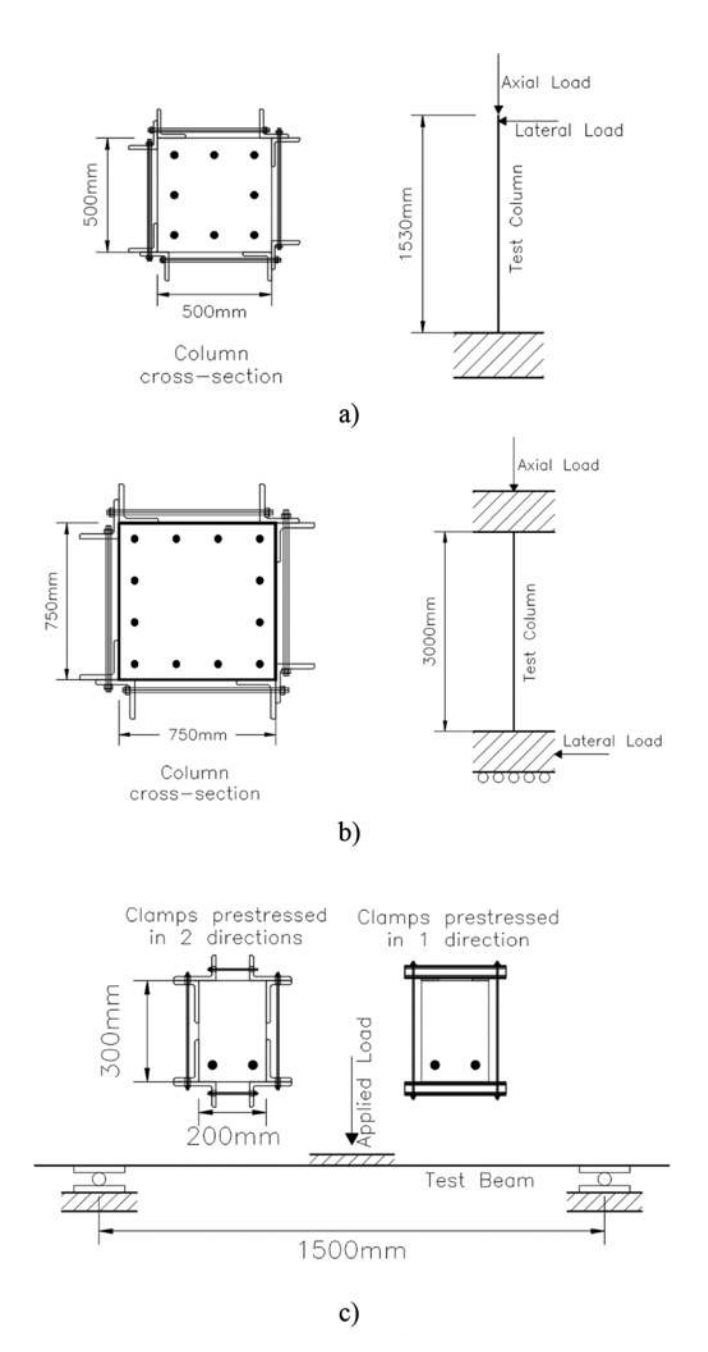


Fig. 7—Typical dimensions: (a) columns at UC; (b) columns at NCREE; and (c) beams.

the compression face of the column; s_{pl} is the spacing of post-tensioned transverse reinforcement; σ_L is the lateral confining stress caused by the clamps; and f_{pli} is the initial prestress in the clamps.

Application of clamps—Pairs of steel angles were positioned at the four corners of the concrete column and connected to each other with steel threaded rods. All rods were equipped with load cells, placed between the steel angle and a 12 mm thick washer (Fig. 11). Clamps with low initial prestress were snug-tightened using a spanner. In contrast, for clamps with intermediate or high prestress $(f_{pti} > 0.4f_{pty})$, additional force was applied using a hydraulic bolt tensioner. Gradual increments in force, following a crisscross tightening sequence, ensured even forces in the rods and prevented rotation of the clamps.

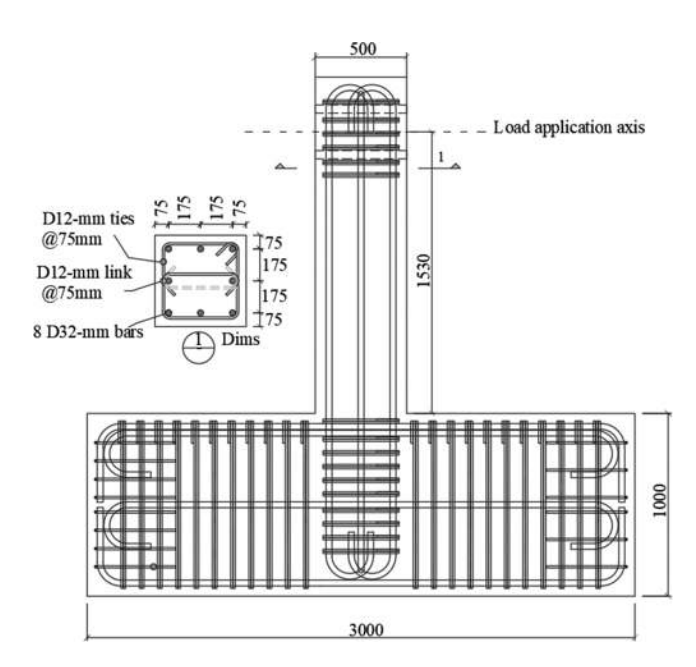


Fig. 8—Details of columns tested at UC.

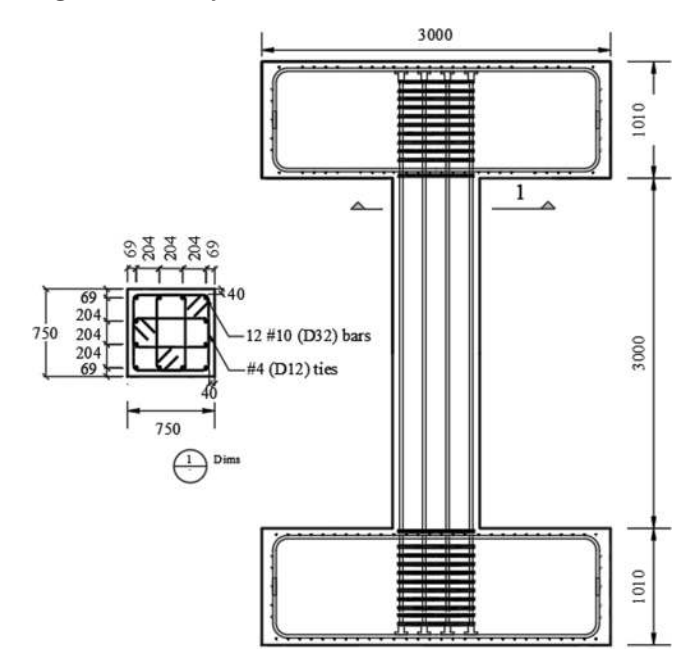


Fig. 9—Details of columns tested at NCREE.

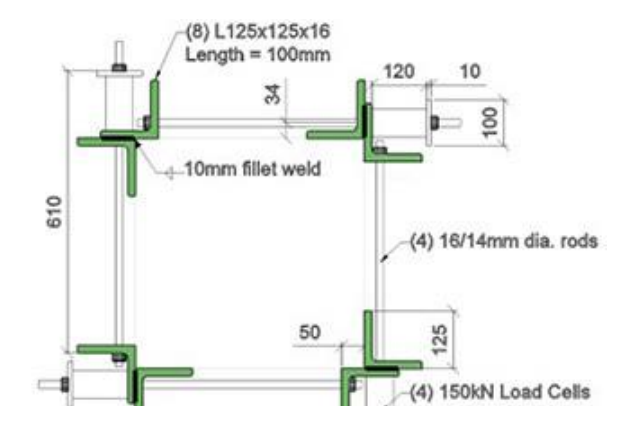


Fig. 10—Post-tensioned clamps applied on column.

Table 3—Summary of test results

Specimen	f_c' , MPa	A.L.R.	P.T.	S _{pt} , mm	s _{pt} /d	r _{pt} , %	σ_L , MPa	v _c , MPa	$v_c/\sqrt{f_c'},$ MPa	v _{max} , MPa	v _s , MPa	$(v_{max} - v_s),$ MPa	$(v_{max}-v_s)/\sqrt{f_c'}$, MPa
C3	30		2	300	0.71	0.21	0.2	1.5	0.27	2.3	_	_	_
C5	36		2	200	0.47	0.32	0.3	1.9	0.32	2.7	_	_	_
C6	24	0.15	2	200	0.47	0.32	1.7	2.2	0.45	2.5	_	_	_
C7	26		0.15	2	300	0.71	0.21	0.7	1.9	0.37	2.5	_	_
C8	31		2	200	0.47	0.32	1.0	2.2	0.39	2.5	_	_	_
C9	23		2	300	0.71	0.21	1.1	2.0	0.42	2.5	_	_	_
SC1	21		2	200	0.29	0.27	0.3	2.0	0.44	2.9	_	_	_
SC2	23	0.3	2	200	0.29	0.27	1.8	2.9	0.62	3.2	_	_	_
SC3	25		2	300	0.44	0.18	1.2	2.5	0.51	3.1	_	_	_
SC4	25	0.4	2	200	0.29	0.27	1.8	3.1	0.64	3.5	_	_	_
B1A		0	_	_	_	0	0.0	1.8	0.30	2.0	0	2.0	0.30
B1B		0	_	_	_	0	0.0	1.8	0.27	2.1	0	2.1	0.27
B2A		0	2	95	0.38	0.3	0.0	1.7	0.27	2.9	1.11	1.8	0.28
B2B		0	2	95	0.38	0.3	0.6	2.0	0.31	3.6	1.11	2.5	0.55
B3A		0	2	143	0.57	0.2	0.0	1.8	0.28	2.5	0.74	1.8	0.39
ВЗВ	41	0	2	143	0.57	0.2	0.4	2.3	0.37	3.2	0.74	2.5	0.50
B4A	41	0	1	143	0.57	0.2	0.0	1.8	0.28	2.8	0.90	1.9	0.30
B4B		0	1	143	0.57	0.2	0.5	_	0.34	3.8	0.90	2.9	0.59
B5A		0	1	95	0.38	0.3	0.8	2.1	0.31	3.4	1.40	2.0	0.34
B5B			1	95	0.38	0.3	0.0	2.0	0.33	3.6	1.36	2.2	0.32
B6A		0	2	190	0.76	0.15	0.4	2.0	0.31	2.7	0.70	2.0	0.31
B6B		0	1	190	0.76	0.15	0.4	2.1	0.33	2.8	0.70	2.1	0.33

Note: f_c' is concrete cylinder compressive strength; A.L.R. is axial load ratio $P/f_c'A_g$; P.T. is prestress applied in one or two directions; s_{pt} is spacing of clamps; d is effective depth, distance from centroid of exterior layer of longitudinal steel to outermost fiber in compression; r_{pt} is reinforcement ratio of post-tensioning transverse reinforcement; σ_L is lateral confining stress caused by clamps on column; v_c is shear stress at inclined cracking; v_{max} is maximum measured shear stress; v_s is shear strength contribution of transverse reinforcement, calculated as $v_s = r_{pt} \cdot f_{ptu}$ (applicable to beams only).

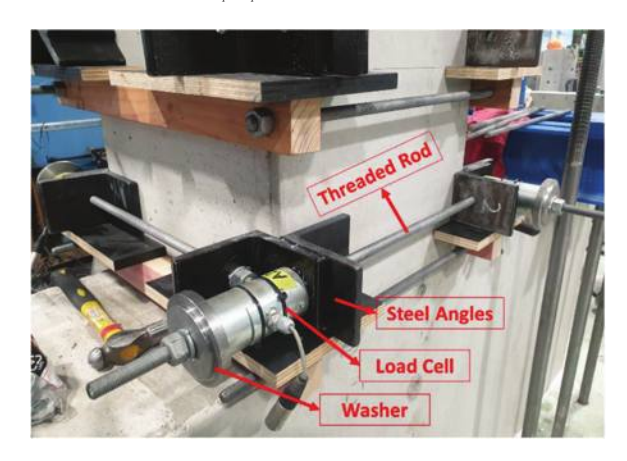


Fig. 11—Application of clamps.

Procedure for column tests

Figures 12(a) and (b) show the test setup at UC and NCREE, respectively. The axial load ratio (A.L.R. = $P/A_g f_c$ ') was 0.15 for columns tested at UC and 0.3 (SC1, SC2, and SC3) or 0.4 (SC4) for columns tested at NCREE. The loading protocol is shown in Fig. 13. Three cycles were applied at each drift ratio. Testing was paused at points of peak displacement and zero lateral load to record data. Cracks were marked at each

peak displacement. Testing concluded when the peak lateral load in a given cycle was less than 50% of the maximum.

Beam tests

Specimen description—Six simply supported RC beams furnished with clamps were tested under monotonic loads applied at midspan (Tables 1 and 2). Figures 7 and 14 show typical details of the beam specimens. The test beams had cross-sectional dimensions of 200 x 300 mm, with a distance between support centerlines of 1500 mm. The clear distance between support faces was 550 mm. Longitudinal reinforcement consisted of two 25 mm diameter steel bars with a measured yield stress of 550 MPa (averaging results from three coupons). The longitudinal reinforcement ratio was 2%. The effective depth, defined as the distance from the centroid of the exterior layer of longitudinal steel to the outermost fiber in compression, was 250 mm. The a/d was 2.2.

All six beams were cast from a single batch of concrete. After the concrete set, wet hessian cloth (burlap) and plastic were placed over the beams. Curing lasted for 7 days, with water dousing occurring once a day. The formwork was stripped after 3 days of casting. At 28 days, the measured compressive cylinder strength was 41 MPa on average. The





Fig. 12—Test setup at: (a) UC; and (b) NCREE.

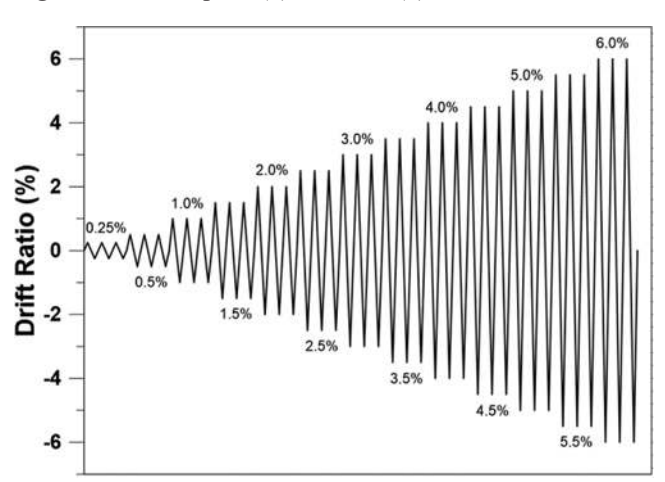


Fig. 13—Loading protocol for columns.

concrete cylinders were kept under the same curing conditions as the beams and were also cured for 7 days, with water dousing occurring simultaneously with the beams.

Similar to the columns, the test beams were fabricated with no conventional stirrups, with post-tensioning being the only source of steel resisting shear. The nominal resistance to shear v_n was calculated using Eq. (7), which is based on observations made by Richart. Equation (7) expresses the nominal resistance to shear v_n as the sum of contributions to shear attributed to the concrete v_c and the transverse reinforcement v_s .

$$v_n = v_c + v_s \tag{7}$$

The test beams were designed to fail in shear. In all cases, the nominal resistance to shear v_n was smaller than the calculated unit plastic shear stress v_p . The unit plastic shear stress is associated with the shear force at flexural yielding V_p . This force is obtained from a sectional moment analysis (Eq. (8)

to (10)). The calculated shear plastic stress v_p for measured properties was 3.8 MPa.

To obtain the contribution to the shear resistance of the concrete v_c , in the absence of lateral prestress, one beam without clamps was tested (B1). The concrete resistance to shear v_c averaged 1.8 MPa from tests of each beam span B1A and B1B. The remaining five beams were furnished with clamps at different spacings s_{pt} and, by varying the initial prestress in the clamps, different lateral confining pressures. The nominal shear resistance provided by the clamps ranged from 0.7 MPa (for beams B6A and B6B) to 1.4 MPa (for beam B5A)

$$M_p = A_s \cdot f_v \cdot j \cdot d \tag{8}$$

$$V_p = \frac{M_p}{a^*} \tag{9}$$

$$v_p = \frac{V_p}{b \cdot d} \tag{10}$$

where M_p is the moment at flexural yielding at the critical section; A_s is the cross-sectional area of the reinforcing bars; f_y is the measured yield stress of the longitudinal reinforcement; j is the ratio of the internal lever arm to the effective depth (assumed as 0.9); d is the effective depth; V_p is the shear force associated with M_p ; a^* is the distance from center of roller supports to face of midspan loading plate (in beams); v_p is the unit shear stress associated with V_p ; and b is the column width.

External post-tensioned clamps on beams

Two types of clamps were used for the RC beam tests: clamps applying prestress in one or two directions (Fig. 14). Table 1 provides information on the beams tested with prestress applied in one or two directions. Clamps applying

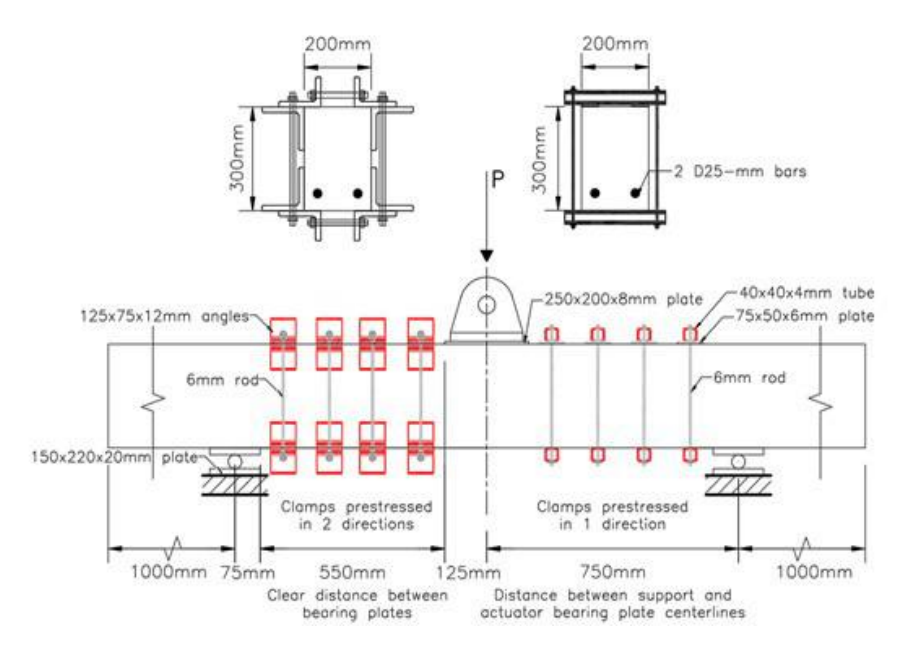


Fig. 14—Details of beams.

prestress in one direction, parallel to the applied force, were fabricated from 40 x 40 x 4.0 mm rectangular hollow tubes, 6 mm diameter threaded rods, and 75 mm wide bearing steel plates. The plates were placed on the face of the beam in compression, and their width matched the size of the two-directional clamps. Clamps applying prestress in two directions were similar to the clamps used for columns. They consisted of 12 mm thick angles and 6 mm diameter threaded rods. The measured ultimate stress of the threaded rods ranged from 368 to 468 MPa. The spacing of the clamps s_{pt} ranged from 95 to 143 mm (0.38 < s_{pt}/d < 0.76). The post-tensioned transverse reinforcement area ratio r_{pt} , calculated using Eq. (5), ranged from 0.15 to 0.3%. The lateral confining stress caused by the clamps on the beam σ_L , calculated using Eq. (6), ranged from 0 to 0.8 MPa.

Procedure for beam tests

Each beam underwent two tests (tests A and B), resulting in a total of 12 tests. Heavy-size clamps were applied to one side of the beam, aiming to induce failure on the opposite side. The shear strength contribution of the heavy clamps was 4.5 MPa, which was approximately 1.2 times the calculated shear stress v_p at yielding of the longitudinal reinforcement. On the opposite side of the beam, either no clamps, as in the case of the bare beam (tests B1A and B1B), or smaller clamps were installed. Figure 15 illustrates the beam specimen with heavy clamps on one side and smaller clamps on the other side. The applied load was increased in steps of approximately 10 kN. After each load increment, cracks were marked and measured. This process continued until shear failure occurred on one side of the beam. Subsequently, the heavy clamps were relocated to the failed side, and the beam underwent testing again.



Fig. 15—Test setup for beams.

EXPERIMENTAL RESULTS AND DISCUSSIONResults from columns

Hysteretic response—Table 3 provides a summary of the test results. The hysteretic responses for all the columns are shown in Fig. 16 and 17. Figure 16 focuses on the columns tested at UC. In this figure, the top three plots correspond to columns with a transverse reinforcement area ratio of 0.21% (clamps spaced at 300 mm) but with different initial post-tensioning stresses. Column C3 had clamps with low initial prestress ($f_{pti} = 0.1 f_{pty}$), C7 had intermediate initial prestress ($f_{pti} = 0.4 f_{pty}$), and C9 had high initial prestress ($f_{pti} = 0.7 f_{pty}$), resulting in equivalent σ_L values of 0.2, 0.7, and 1.1 MPa, respectively.

Moving to the bottom three plots in Fig. 16, these show the response of columns with a transverse reinforcement area ratio of 0.32% (clamps spaced at 200 mm). Columns C5, C8, and C6 had clamps with low, intermediate, and high initial prestress, respectively, resulting in equivalent σ_L values of 0.3, 1.0, and 1.7 MPa.

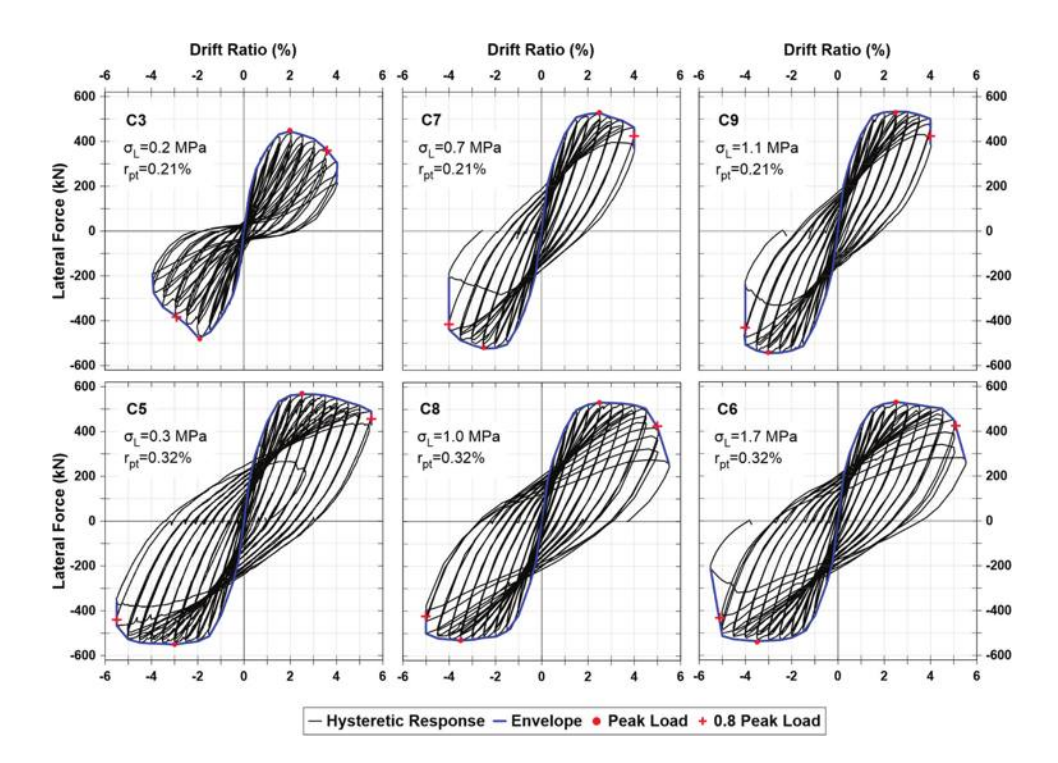


Fig. 16—Hysteretic response of columns tested at UC.

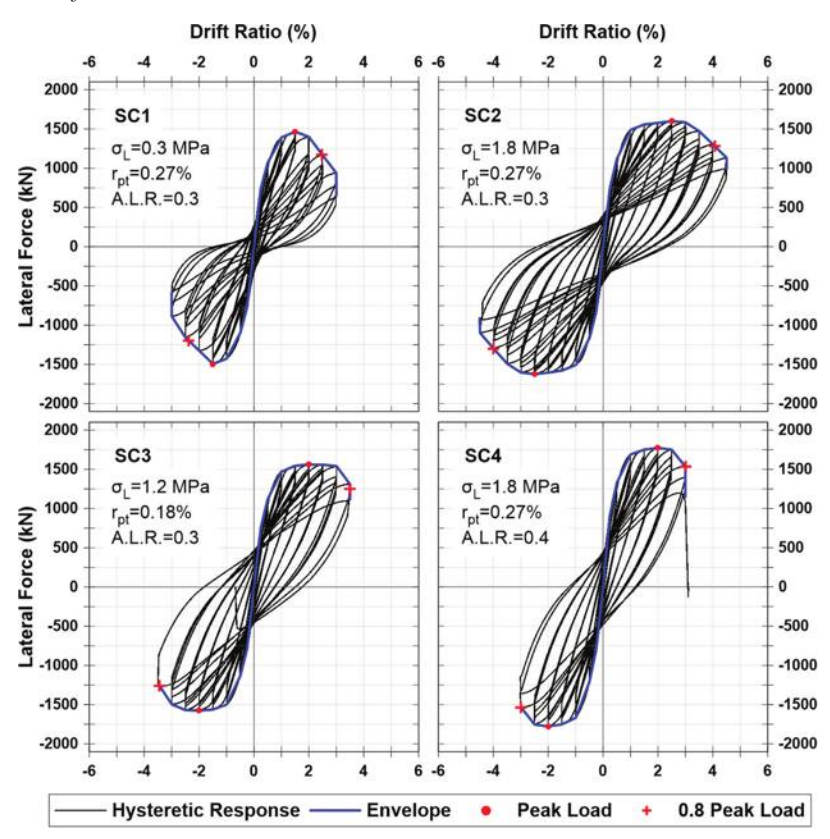


Fig. 17—Hysteretic response of columns tested at NCREE.

These data suggest that an increase in initial prestress led to a more ductile column response. For instance, Column C3 exhibited shear disintegration of the concrete core, while the response of C9 was dominated by flexure with a larger drift capacity.

All the columns but C3 reached flexural yielding. Having no welds in clamps, C3 did not yield in flexure because its nominal shear strength was close to $v_c + r_{pt} \cdot 0.6 f_{pty}$ (instead of $v_c + r_{pty} \cdot f_y$), which is smaller than the unit shear associated with flexural yielding. For all other columns, yielding occurred at a drift ratio of approximately 1.5%. The peak measured load was 525 kN on average, and the associated shear stress was 2.5 MPa. Table 4 lists the measured peak loads and drift capacities for all 10 columns. The peak

loads reported in Table 4 represent the maximum shear forces applied in both pushing and pulling directions. Drift capacity is defined as the drift that the column reaches before its lateral load resistance drops to 80% of the maximum measured load. Testing concluded when the peak lateral load in a given cycle was less than 50% of the maximum.

Figure 17 shows the response from columns tested at NCREE. Column SC1 had clamps with low initial prestress ($f_{pti} = 0.1 f_{pty}$), while SC2, SC3, and SC4 had clamps with intermediate initial prestress ($f_{pti} = 0.55 f_{pty}$). The transverse reinforcement area ratio was 0.18% for SC3 and 0.27% for

Table 4—Peak loads and drift capacities

				Peak	loads	
Specimen	f _c ', MPa	r _{pt} , %	σ_L , MPa	Pushing direction, kN	Pulling direction, kN	D.C.,
СЗ	30	0.21	0.2	450	480	3.0
C5	30	0.32	0.3	570	550	5.5
С6	24	0.32	1.7	530	540	5.0
C7	26	0.21	0.7	530	520	4.0
C8	31	0.32	1.0	530	530	5.0
С9	23	0.21	1.1	530	540	4.0
SC1	21	0.27	0.3	1465	1495	2.5
SC2	23	0.27	1.8	1600	1625	4.0
SC3	25	0.18	1.2	1560	1575	3.5
SC4	25	0.27	1.8	1770	1780	3.0

Note: f_c' is concrete cylinder compressive strength; r_{pt} is reinforcement ratio of post-tensioning transverse reinforcement; σ_L is lateral confining stress caused by clamps; D.C. is drift capacity, defined as drift ratio associated with 20% decrease in lateral load resistance of column. It is calculated with help of envelope of load-displacement loops. Two values of drift capacities are obtained (pulling and pushing directions), but only smaller value is reported.

the other columns. The lateral confining stress σ_L , calculated using Eq. (6), was 0.3, 1.8, 1.2, and 1.8 MPa for SC1, SC2, SC3, and SC4, respectively.

All the columns reached yielding of the longitudinal reinforcement at a drift ratio of approximately 1.2%. The measured peak loads ranged from 1465 to 1780 kN. Differences in peak loads were likely due to the applied lateral prestress, ranging from 0.3 to 1.8 MPa, and the higher axial load $(0.4A_gf_c')$ in SC4. Table 4 shows the peak loads and drift capacities.

Clamp stress—Forces in the clamps were measured at one end of each threaded rod using load cells. Clamp stresses were calculated as the measured force divided by the net rod cross-sectional area (approximately 80% of the gross area; refer to Table 2). Figure 18 presents a graphical representation of clamp stresses measured in the test of SC1. The figure includes data for the first three clamps positioned at the ends of the column. Each curve in the figure shows the change in the stress in threaded rods parallel to the applied lateral force. The markers on the curves represent measurements taken at peak displacements during the first cycle at each displacement target. Note that each curve has a different origin on the horizontal axis, and the spacing between vertical gridlines corresponds to 100 MPa. The vertical axis represents the applied unit shear stress V/bd divided by $\sqrt{f_c}$, where V is the applied lateral force, b is the width of the column or dimension perpendicular to the direction of the applied force, d is the effective depth of the column, and f_c' is the concrete cylinder compressive strength on the day of testing in MPa.

All the curves in Fig. 19 show no change in clamp stress before the applied shear stress exceeded a threshold. This threshold indicates the formation of inclined cracks and has been assumed to be a reasonable approximation of the contribution to shear strength attributable to the concrete v_c . Changes in clamp stress after inclined cracking were more noticeable in columns with low initial prestress. These

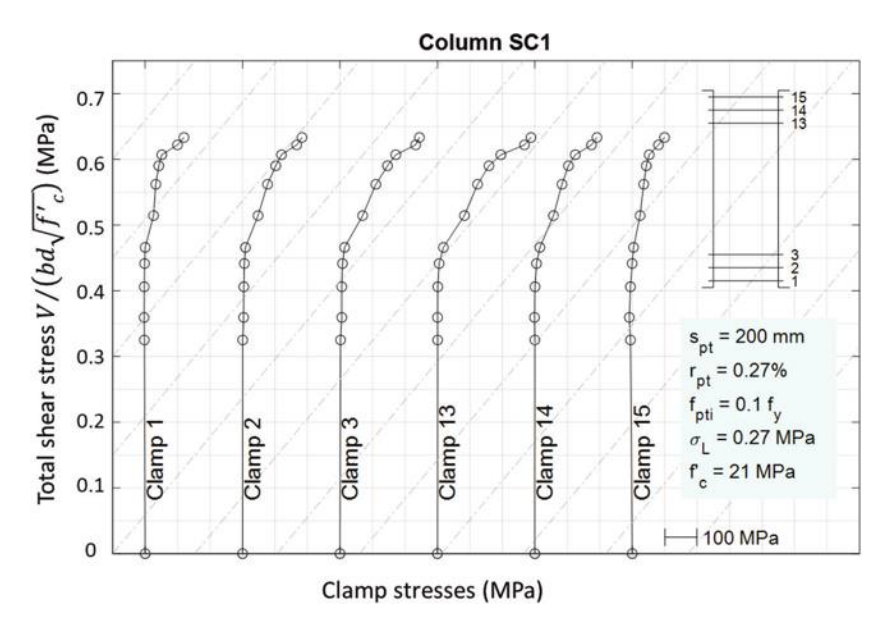


Fig. 18—Total shear stress versus stress in key clamps, Column SC1. (Note: s_{pt} is spacing between clamps, r_{pt} is post-tensioned transverse reinforcement area ratio, f_{pti} is initial prestress in clamps [as fraction of yield stress of high-strength rods f_{pty}], σ_L is lateral prestress caused by clamps on column, and f_c ' is measured concrete cylinder strength at test day.)

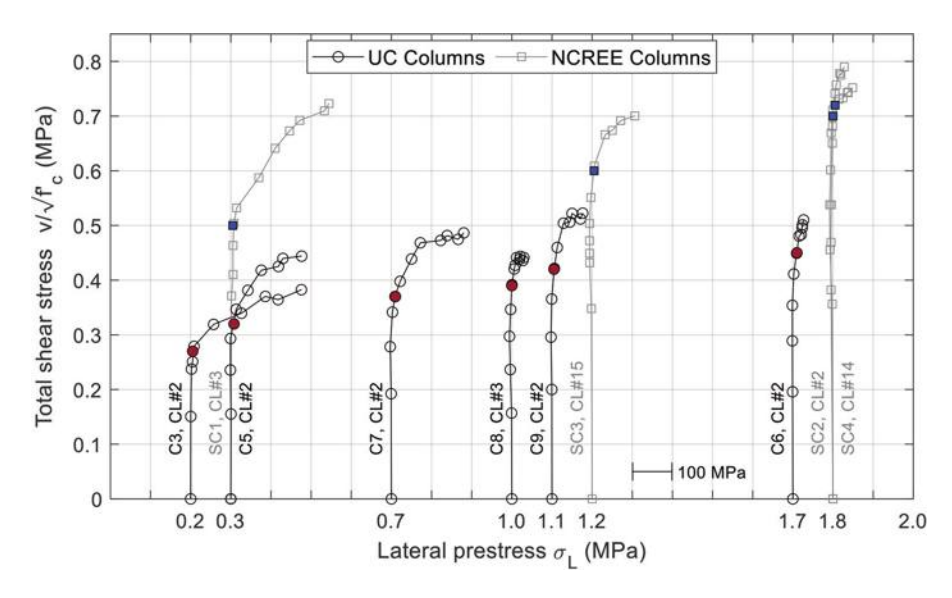


Fig. 19—Shear stress versus clamp stresses (selected clamps).

Table 5—Applied shear stress and clamp stresses, in MPa

	23	C	25	(C6	(C 7	C	C8	C	9	S	C1	S	C2	S	C3	S	C4
$v/\sqrt{f_c'}$	Clamp No. 2	$v/\sqrt{f_c'}$	Clamp No. 2	$v/\sqrt{f_c'}$	Clamp No. 2	$v/\sqrt{f_c'}$	Clamp No. 2	$v/\sqrt{f_c'}$	Clamp No. 3	$v/\sqrt{f_c'}$	Clamp No. 2	$v/\sqrt{f_c'}$	Clamp No. 3	$v/\sqrt{f_c'}$	Clamp No. 2	$v/\sqrt{f_c'}$	Clamp No. 15	$v/\sqrt{f_c'}$	Clamp No. 14
0.00	0	0.00	0	0.00	0	0.00	0	0.00	0	0.00	0	0.00	0	0.00	0	0.00	0	0.00	0
0.15	0	0.16	0	0.20	-1	0.19	-1	0.16	-1	0.20	-1	0.33	2	0.34	-5	0.31	-2	0.31	-2
0.24	2	0.24	-1	0.29	-1	0.28	-3	0.24	-4	0.30	-3	0.36	6	0.41	-5	0.38	-6	0.40	-7
0.25	5	0.29	-1	0.35	-1	0.34	3	0.30	-6	0.37	-1	0.41	5	0.47	-4	0.40	-6	0.47	-8
0.28	8	0.35	13	0.41	2	0.37	9	0.35	-3	0.42	6	0.44	8	0.57	-2	0.42	-6	0.53	-6
0.32	57	0.38	42	0.45	9	0.40	22	0.39	0	0.46	13	0.47	14	0.60	-1	0.44	-6	0.59	-4
0.34	126	0.42	76	0.48	15	0.44	50	0.42	6	0.50	29	0.52	70	0.62	-1	0.49	-3	0.63	-1
0.37	186	0.43	119	0.48	20	0.47	72	0.43	8	0.51	44	0.56	111	0.64	15	0.54	5	0.65	5
0.36	218	0.44	130	0.50	24	0.47	123	0.44	12	0.52	50	0.59	146	0.65	25	0.59	33	0.67	8
0.38	276	0.44	176	0.50	23	0.48	139	0.44	19	0.51	71	0.61	172	0.66	36	0.59	50	0.69	17
		_	_	0.51	27	0.47	166	0.44	21	0.5225	76	0.63	233	0.65	37	0.61	71	0.68	20
_	_		_	_	_	0.49	180	0.44	28		_	0.64	245	0.66	49	0.62	106	0.70	28
_	_	_	_	_	_	_	_	0.44	30	_	_	_	_	_	_	_	_	_	_

Note: v is shear stress, calculated as V/b_d ; V is applied shear force; b is width of column; d is effective depth, distance from centroid of exterior layer of longitudinal steel to outermost fiber in compression; f_c is concrete cylinder compressive strength.

changes accelerated as applied shear stress increased. The slope of the curves relating applied shear stress and clamp stress approached r_{pt} , as observed by Richart. ¹⁴ For columns with clamps with initial prestress $f_{pti} > 0.4 f_{pty}$, the applied shear stress causing the first variation in clamp stress was less clear. Larger lateral prestress σ_{L} not only caused an increase in the shear at inclined cracking but also a reduction in the width and length of inclined cracks. Inclined cracks not forming as extensions of flexural cracks were not observed in columns with $\sigma_L > 1.7$ MPa $(0.3\sqrt{f_c'})$. As a consequence, estimating v_c from clamp-stress measurements was more difficult for specimens C6, SC2, and SC4 (where σ_L was at least 1.7 MPa). Approximate estimates of the shear stress at inclined cracking (assumed to represent v_c) were obtained from Fig. 19. Each curve in this figure represents the variation of clamp stress with increases in applied shear stress for the most critical clamp in each of the 10 test columns. The distance between vertical gridlines (100 MPa) represents the increase in clamp stress. The horizontal distance between the origin of each curve and the y-axis represents the initial lateral prestress σ_L . Curve labels indicate the specimen ID and clamp number. Colored markers indicate points chosen to represent the formation of inclined cracks, with y-coordinates representing estimates of v_c . These points were chosen considering these criteria:

- Focus on clamps between d/2 and d from column ends;
- Consider rods parallel to the applied shear force;
- Identify a noticeable increase in clamp stress;
- Compare the slope of the shear stress-clamp stress curve with the transverse reinforcement area ratio r_{pt} ; and
- Corroborate the presence of inclined cracks in photos taken when the mentioned stresses were measured.

All stresses illustrated in Fig. 19 are listed in Table 5 to allow the reader to plot the data and select different estimates for v_c if deemed necessary.

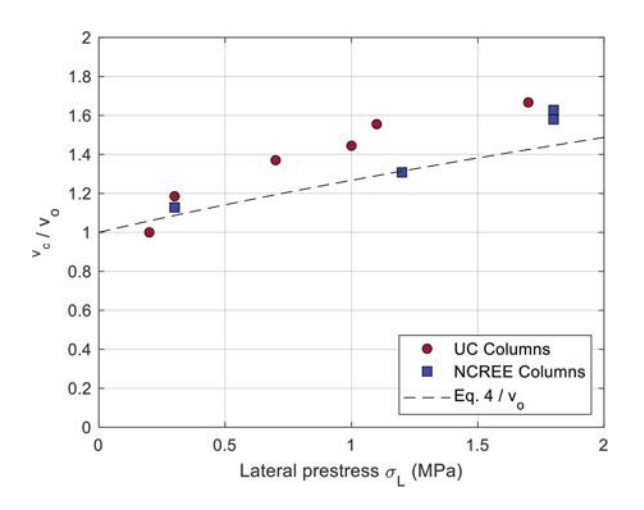


Fig. 20—Concrete shear stress versus lateral prestress.

The estimates of v_c obtained from Fig. 19 are plotted again versus the initial lateral prestress σ_L in Fig. 20, with shear stress normalized relative to a reference shear stress v_o . This reference stress is meant to represent the shear strength of a column without lateral prestress and without ties. Because shear strength is expected to be sensitive to differences in axial load and reinforcement ratio, two values of v_o were used: $0.4\sqrt{f_c'}$ MPa for the columns tested at NCREE (with $0.3 < P/A_g f_c' < 0.4$), and $0.27 \sqrt{f_c'}$ MPa for the columns tested at UC $(P/A_e f_c' = 0.15)$. For each column set, the reference value v_o was obtained as the intercept with the y-axis of a regression line fitted through the colored markers in Fig. 19. Figure 20 shows that v_c , as defined here, increased with increasing initial lateral prestress σ_L . Equation (4) produced a lower-bound estimate for this increase. The largest deviations from Eq. (4) occurred for columns with large initial lateral prestress in which detecting the formation of inclined cracks was more difficult.

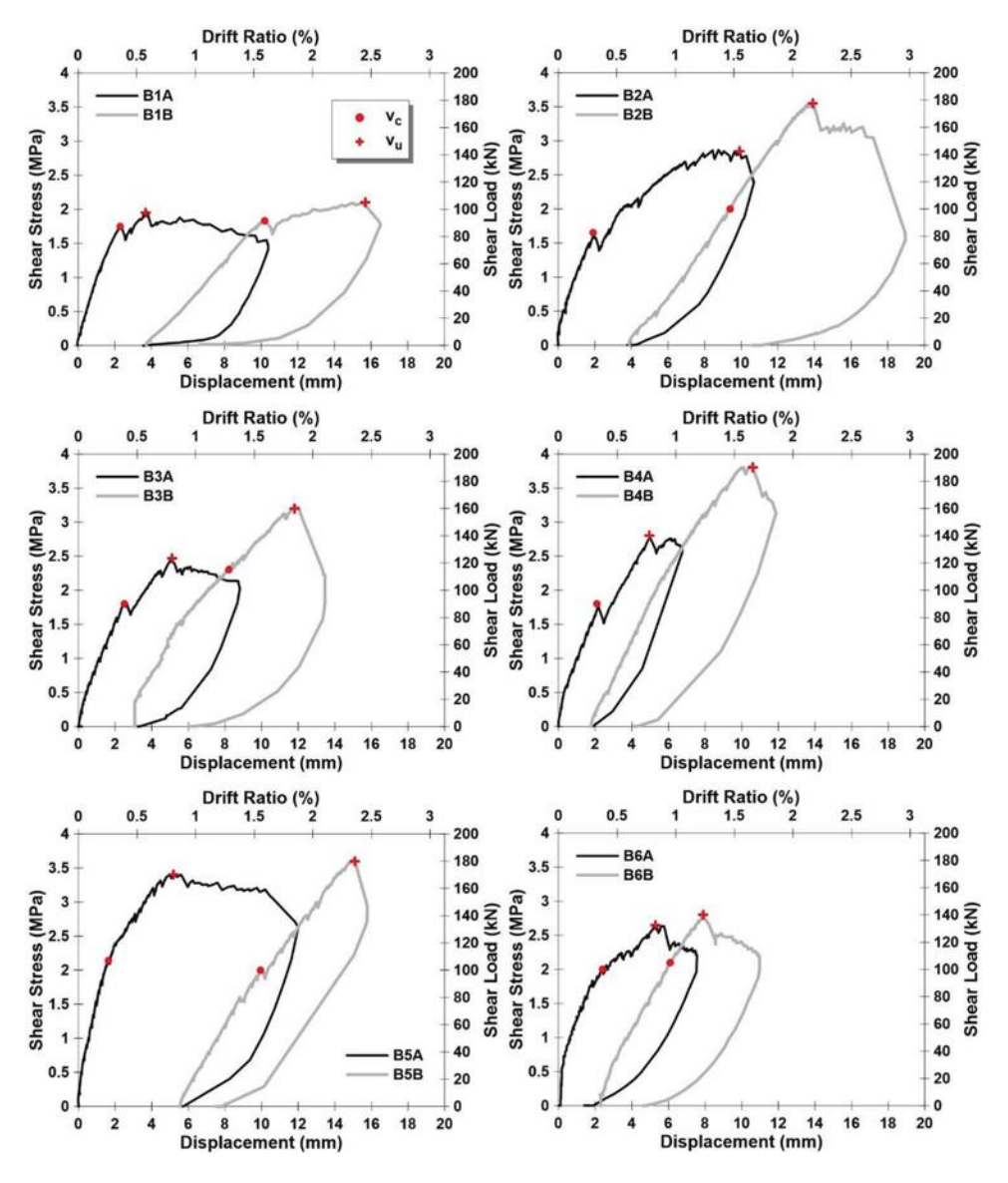


Fig. 21—Load versus deflection curves of beams.

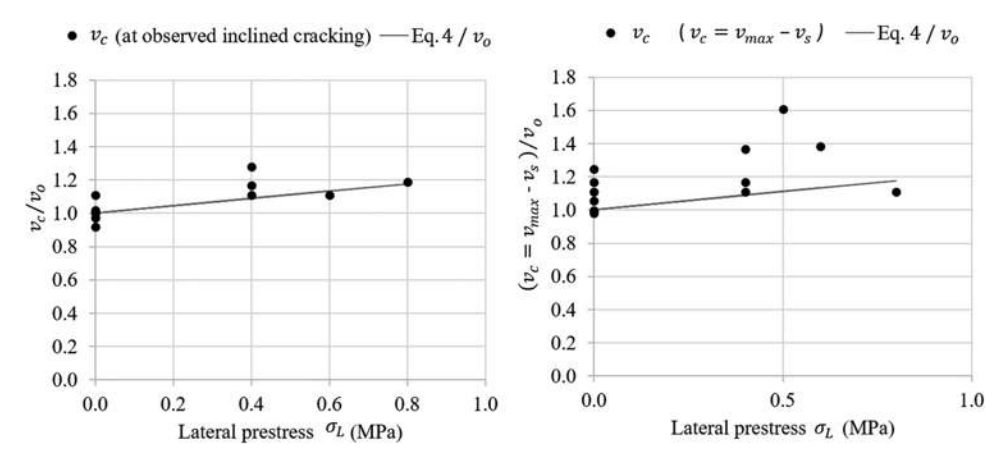


Fig. 22—Variations in v_c: (a) at observed inclined cracking; and (b) calculated as v_{max} – v_s.

Results from beams

Table 3 summarizes the test results. The load-deflection curves for all the beams are shown in Fig. 21. The objective of the beam tests was to study whether the increase in shear stress at inclined cracking observed in the column tests leads to a similar increase in monotonic shear strength. For this purpose, the test beams were proportioned to fail in shear before yielding in flexure. In all beams with clamps, shear failure occurred by fracture of the threaded rods after the formation of a large inclined crack in the beam.

Clamps installed on the beams were not instrumented. Therefore, the estimation of the load at inclined cracking relied purely on visual observation. Except for test 4B, in which a clear observation was not obtained, the load at inclined cracking was clearly identified—to the best judgment of the writers—during each beam test. Assuming that the shear at inclined cracking and the contribution to shear strength attributable to the concrete are similar to one another, the former was compared with the difference between the total shear measured at failure v_{max} and the contribution to shear strength attributed to the clamps v_s . Table 3 shows: a) the shear stresses at inclined cracking; b) the total shear stress at failure v_{max} ; and c) v_s obtained as the reinforcement ratio times the measured rod strength f_{ptu} . Figure 22(a) illustrates variations in shear stress at observed inclined cracking with increasing values of σ_L . Figure 22(b) illustrates variations in $v_{max} - v_s$ with increasing values of σ_L . The similarities between these two figures suggest that increases in shear stress at inclined cracking caused by increases in initial lateral prestress translated into similar increases in shear strength (for monotonically increased shear). In addition, Fig. 23 shows that increases in shear stress at inclined cracking observed in beams were comparable to those observed in columns even in beams with initial lateral prestress in a single direction (parallel to the applied force), supporting Eq. (4) and the aforementioned theoretical framework.

CONCLUSIONS

• Observations made by Richart¹⁴ on reinforced concrete (RC) beams with conventional ties led him to propose Eq. (7) (that is, $v_n = v_c + v_s$). Equation (7) expresses the nominal resistance to shear v_n as the contribution

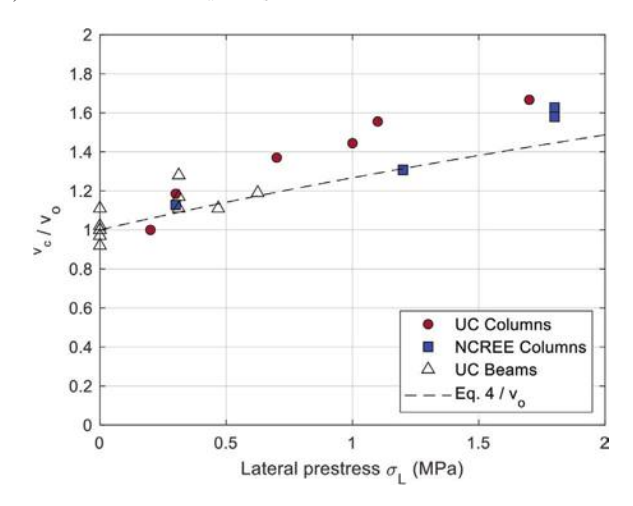


Fig. 23—Concrete shear stress versus lateral prestress (including beams).

to shear resistance attributable to the concrete v_c and the contribution attributable to the transverse reinforcement v_s . Although Eq. (7) was originally derived for RC beams with conventional ties, acceptable results were obtained assuming that post-tensioned clamps resist shear in a similar fashion to conventional ties.

- The shear strength attributable to the concrete v_c , interpreted as the shear at the formation of the first inclined crack, was observed to be nearly proportional to $\sqrt{1 + \frac{\sigma_L}{f_t}}$, where σ_L represents the lateral prestress, and f_t stands for the tensile strength of the concrete, assumed to be close to $1/3\sqrt{f_c}$ in MPa. It follows that a high value of σ_L can delay the formation of shear inclined cracks. The beam tests showed an increase in v_c at both inclined cracking and failure.
- The increase in the concrete resistance to shear v_c in the beams was observed to be unaffected by whether prestress was applied solely in the loading direction or in both the loading and transverse directions. This observation is in agreement with the Mohr's circle shown in Fig. 6. Confining stresses transverse to the loading direction (σ_t) are not expected to provide an additional benefit to the shear strength attributable to the concrete v_c .

The proposed post-tensioned clamps can be used as an
effective method to retrofit non-ductile RC columns
with insufficient transverse reinforcement. The introduction of post-tensioned clamps prevented non-ductile
columns from shear failure before flexural yielding.

ACKNOWLEDGMENTS

This study was supported by QuakeCoRE (New Zealand Centre for Earthquake Resilience) at the University of Canterbury and NCREE (National Center for Research on Earthquake Engineering) at the National Taiwan University. The first writer is thankful to the Resilience to Nature's Challenges Project for the 3-year postgraduate scholarship awarded. The writers also acknowledge the support received from the laboratory technicians: G. Keats, T. O'Connell, T. Perigo, J. Maley, D. Carney, and M. Weavers; as well as from the undergraduate students: B. Bassett-Foss, A. Meneghini, J. Wight, J. Carlielle, J. Redfern, and E. Osborn as part of their end-year project for the BE(Hons) degree in civil engineering.

AUTHOR BIOS

ACI member Julian D. Rincon is a PhD Candidate in earthquake engineering at the University of Canterbury, Christchurch, New Zealand. He received his BS from the University of Valle, Cali, Colombia. His research interests include the seismic performance of structures and the repair and retrofit of reinforced concrete structures.

ACI member **Yu-Mei Chen** is a Graduate Student in the Department of Civil Engineering at National Taiwan University, Taipei, Taiwan.

Santiago Pujol, FACI, is a Professor of civil engineering at the University of Canterbury. He is Chair of ACI Committee 133, Disaster Reconnaissance; Vice Chair of ACI Subcommittee 445-B, Shear & Torsion-Seismic Shear; and a member of ACI Committee 314, Simplified Design of Concrete Buildings; ACI Subcommittees 318-F, Foundations, and 318-IW, Wind Provisions; and Joint ACI-ASCE Committee 445, Shear and Torsion. He received his BS from the National University of Colombia, Bogotá, Colombia, and his MS and PhD from Purdue University, West Lafayette, IN. His research interests include displacement-based design of earthquakeresistant structures, instrumentation, monitoring, repair and strengthening of structures, and engineering data management.

ACI member Aishwarya Y. Puranam is an Assistant Professor in the Department of Civil Engineering at National Taiwan University. She received her BSCE, MSCE, and PhD from Purdue University in 2013, 2016, and 2018, respectively. She is a member of ACI Committee 133, Disaster Reconnaissance. Her research interests include the behavior of reinforced concrete structures subjected to seismic demands, large-scale experiments, and data preservation.

ACI member Shyh-Jiann Hwang is a Professor in the Department of Civil Engineering at National Taiwan University. He received his PhD from the University of California, Berkeley, Berkeley, CA. He is a member of Joint ACI-ASCE Committee 352, Joints and Connections in Monolithic Concrete Structures. His research interests include the shear behavior of reinforced concrete members and seismic design and retrofitting of reinforced concrete structures.

REFERENCES

- 1. Elwood, K. J., and Moehle, J. P., "Axial Capacity Model for Shear-Damaged Columns," *ACI Structural Journal*, V. 102, No. 4, July-Aug. 2005, pp. 578-587.
- 2. Henkhaus, K. W., "Axial Failure of Vulnerable Reinforced Concrete Columns Damaged by Shear Reversals," PhD dissertation, Purdue University, West Lafayette, IN, 2010.

- 3. Li, Y.-A.; Weng, P.-W.; and Hwang, S.-J., "Seismic Performance of Reinforced Concrete Intermediate Short Columns Failed in Shear," *ACI Structural Journal*, V. 116, No. 3, May 2019, pp. 195-206. doi: 10.14359/51713309
- 4. Hanson, R. D., and Degenkolb, H. J., *The Venezuela Earthquake, July 29, 1967*, American Iron and Steel Institute, Washington, DC, 1969, 176 pp.
- 5. Muguruma, H.; Nishiyama, M.; and Watanabe, F., "Lessons Learned from the Kobe Earthquake—A Japanese Perspective," *PCI Journal*, V. 40, No. 4, July-Aug. 1995, pp. 28-42.
- 6. Lew, H. S.; Leyendecker, E. V.; and Dikkers, R. D., "Engineering Aspects of the 1971 San Fernando Earthquake," Building Science Series No. 40, National Bureau of Standards, Washington, DC, 1971, 412 pp.
- 7. Yurdakul, Ö.; Duran, B.; Tunaboyu, O.; and Avşar, Ö., "Field Reconnaissance on Seismic Performance of RC Buildings after the January 24, 2020 Elazığ-Sivrice Earthquake," *Natural Hazards*, V. 105, No. 1, Jan. 2021, pp. 859-887. doi: 10.1007/s11069-020-04340-x
- 8. Milićević, I.; Marinković, M.; Blagojević, N.; and Nikolić-Brzev, S., "Performance of RC Frames in 26.11.2019. Albania Earthquake: Effects of Irregularities and Detailing," *Građevinski Materijali i Konstrukcije*, V. 64, No. 3, Aug. 2021, pp. 207-213.
- 9. Gautam, D.; Rodrigues, H.; Bhetwal, K. K.; Neupane, P.; and Sanada, Y., "Common Structural and Construction Deficiencies of Nepalese Buildings," *Innovative Infrastructure Solutions*, V. 1, No. 1, 2016, Article No. 1, 18 pp. doi: 10.1007/s41062-016-0001-3
- 10. Wight, J. K., and Sozen, M. A., "Shear Strength Decay in Reinforced Concrete Columns Subjected to Large Deflection Reversals," Engineering Experiment Station, University of Illinois Urbana-Champaign, Urbana, IL, Aug. 1973, 312 pp.
- 11. Usta, M.; Alhmood, A.; Carrillo, J.; Cladera, A.; Laughery, L.; Pujol, S.; Puranam, A.; Rautenberg, J.; Sezen, H.; Sneed, L. H.; and To, D. V., "Shear Strength of Structural Walls Subjected to Load Cycles," *Concrete International*, V. 41, No. 5, May 2019, pp. 42-48.
- 12. Shrestha, S.; Carrillo, J.; Sezen, H.; and Pujol, S., "Shear Strength of Shear-Controlled Columns under Cyclic Loading," *ACI Structural Journal*, V. 119, No. 3, May 2022, pp. 129-140.
- 13. Mörsch, E., "Der Eisenbetonbau seine Theorie und Anwendung," Konrad Wittwer GmbH & Co., Stuttgart, Germany, 1908, 376 pp. (in German)
- 14. Richart, F. E., "An Investigation of Web Stresses in Reinforced Concrete Beams," Bulletin No. 166, Engineering Experiment Station, University of Illinois Urbana-Champaign, Urbana, IL, June 1927, 106 pp. 15. Vecchio, F. J., and Collins, M. P., "The Modified Compression-Field
- Theory for Reinforced Concrete Elements Subjected to Shear," *ACI Journal Proceedings*, V. 83, No. 2, Mar.-Apr. 1986, pp. 219-231.
- 16. Belarbi, A.; Kuchma, D. A.; and Sanders, D. H., "Proposals for New One-Way Shear Equations for the 318 Building Code," *Concrete International*, V. 39, No. 9, Sept. 2017, pp. 29-32.
- 17. Yamakawa, T.; Kamogawa, S.; and Kurashige, M., "Seismic Performance and Design of RC Columns Retrofitted by PC Bar Prestressing as External Hoops," *Journal of Structural and Construction Engineering (Transactions of AIJ)*, V. 65, No. 537, 2000, pp. 107-113.
- 18. Skillen, K. C., "The Effects of Transverse Reinforcement on the Strength and Deformability of Reinforced Concrete Elements," PhD dissertation, Purdue University, West Lafayette, IN, 2020, 368 pp.
- 19. Olesen, S. E.; Sozen, M. A.; and Siess, C. P., "Investigation of Prestressed Reinforced Concrete for Highway Bridges: Part IV: Strength in Shear of Beams with Web Reinforcement," Structural Research Series No. 295, Engineering Experiment Station, University of Illinois Urbana-Champaign, Urbana, IL, Aug. 1965, 162 pp.
- 20. Rincón, J., and Pujol, S., "Retrofit and Repair of Reinforced Concrete Columns with Active Confinement," *Proceedings of the 2023 New Zealand Society for Earthquake Engineering Annual Technical, Conference*, Auckland, New Zealand, 2023, Paper No. 34, 10 pp.

REGISTER TODAY



MAY 14-16, 2024, SANTA FE, NM, USA

Hilton Santa Fe - Historic Plaza, 100 Sandoval Street

The **Technology Forum** is an innovation-focused educational and networking event for concrete professionals **powered by the ACI Foundation's Concrete Innovation Council**.

Whether you are an emerging professional or a seasoned veteran, the ACI Foundation Technology Forum is the place to learn about **current trends**, **emerging technologies**, and **discoveries within the concrete industry**.

Join us for an exciting and insightful event featuring thought leaders and technology innovators to discuss the future of the concrete industry.





Title No. 121-S23

Practical Approach to Predict Web-Shear Strength of Deep Prestressed Hollow-Core Slabs

by Ernesto Hernández, Alessandro Palermo, and Ali Amin

This study proposes a practical design approach to estimate the web-shear strength of deep prestressed hollow-core slabs (PHCS). It explores the effects of critical factors such as the shear stress distribution, biaxial tensile strength, and the reduction in effective compressive stress in concrete, quantifying their impact on web-shear strength. A data set of 85 entries is used to undertake a comparative assessment, demonstrating the improved safety and accuracy of the proposed methodology against current design provisions and previous proposals. Moreover, it is shown that neglecting the beneficial effect of the prestressing force in the transfer region leads to a conservative estimation of the web-shear strength. Furthermore, the study introduces three modified design expressions based on ACI 318-19, fib Model Code 2010, and CSA A23.3-14 standards. The proposed methodology has practical implications for enhancing the safe and cost-effective use of deep PHCS in construction practice.

Keywords: biaxial tensile strength; deep members; prestressed hollow core slabs; shear stress distribution; web-shear strength.

INTRODUCTION

Pioneering experimental research¹⁻³ on the shear behavior of prestressed hollow-core slabs (PHCS) demonstrated that the design methods used in prestressed concrete beams were suitable for estimating the shear strength of shallow PHCS (h < 315 mm). This is despite the fact that PHCS frequently lack the recommended minimum amount of shear reinforcement. However, manufacturers and design practitioners have shown interest in applications requiring greater thicknesses to enhance the system's efficiency.

As a result, over the last 25 years, several researchers⁴⁻¹⁵ have investigated the web-shear strength V_{cw} of PHCS with thicknesses ranging from 300 to 500 mm. In Europe and the United States, respectively, Pajari⁴ and Hawkins and Ghosh⁵ carried out seminal experimental programs on shear tests of deep PHCS (h > 315 mm). The authors reported that many predictions using traditional design methodologies were unconservative. The most concerning results were presented by Hawkins and Ghosh,⁵ where a measured-to-predicted ratio V_{test}/V_{pred} of as low as 0.53 was computed. Reflecting on these findings, ACI Committee 318 (in ACI 318-19) established a reduction factor (RF) of 0.5 for estimating the web-shear strength of deep PHCS not satisfying the minimum amount of shear reinforcement required by the code. ¹⁶

Subsequent experimental investigations, however, have shown that this reduction factor may be overly conservative, penalizing the system's structural efficiency.^{6,8,11,13} Furthermore, given the widespread global use of PHCS and

ACI 318's broad adoption as a reference code in design practice, there is a growing need to comprehend and quantify the factors that affect the web-shear of deep PHCS.

Hawkins and Ghosh⁵ identified several potential factors for the decay in web-shear strength, such as section width distribution, section geometry, bond strength, and prestressing force shear lag. Palmer and Schultz⁶ conducted comprehensive experiments and observed that decreases in web-shear strength were significantly associated with an increase in the initial end slip of the prestressing strands. This was attributed to the PHCS's greater thickness, which may affect the compaction level induced by the hollow core equipment, leading to lower bond strength and longer transfer length (l_w). Additionally, Palmer and Schultz¹⁷ evaluated the web-shear strength of 198 PHCS ranging from 200 to 500 mm thickness, concluding that there was no clear correlation between the size-effect phenomenon and the reduction in shear strength of deep PHCS.

Given the importance of the problem, several design expressions have been proposed in recent years (Table 1). For example, El Sayed et al. 11 and Park et al. 13 linked the overestimation of web-shear strength to the method used for computing the maximum shear stress in the cross section, proposing a strength modification factor to account for the parabolic shear stress distribution in the ACI 318 design approach. Brunesi and Nascimbene¹⁸ suggested an alternative design strategy based on PHCS void geometry. They calibrated a correction factor C_s to modify the web-shear strength estimated from Eurocode 2 (EC2).¹⁹ More recently, Fan et al.20 proposed an analytical solution using strutand-tie models (STMs), providing a simplified approach to calculate the shear strength using an approximate value of the inner lever arm (z) and avoiding the iterative process in the generation of the STM.

Despite considerable efforts to improve current design provisions, further development is necessary to enhance the safety and accuracy of design expressions. This paper introduces a practical design approach for estimating the web-shear strength of deep PHCS, extending previous concepts.^{3,17,21} Furthermore, the study identifies and quantifies factors that modify the web-shear strength, integrating them into design provisions such as ACI 318-19, ¹⁶ fib Model

ACI Structural Journal, V. 121, No. 2, March 2024.

MS No. S-2023-013.R3, doi: 10.14359/51740249, received June 14, 2023, and reviewed under Institute publication policies. Copyright © 2024, American Concrete Institute. All rights reserved, including the making of copies unless permission is obtained from the copyright proprietors. Pertinent discussion including author's closure, if any, will be published ten months from this journal's date if the discussion is received within four months of the paper's print publication.

Code (MC) 2010,²² and CSA A23.3-14.²³ Finally, based on a data set of available test results in the literature, it is demonstrated that the proposed design approach improves on existing design provisions and previous proposals in the literature.

RESEARCH SIGNIFICANCE

Experimental evidence has revealed substantial limitations in conventional design provisions for estimating the web-shear strength of deep PHCS. Furthermore, it has been demonstrated that incorporating an RF, as proposed

Table 1—Summary of web-shear design method's proposal for deep PHCS

Authors	Reference code	Modification factor
Park et al. ¹³	ACI 318-19	$\eta = \begin{cases} 0.76 \text{ for } h < 500\\ 0.50 \text{ for } h \ge 500 \end{cases}$
El Sayed et al. ¹¹	ACI 318-19	$k = \frac{750}{450 + h} \le 1$
Brunesi and Nascimbene ¹⁸	Eurocode 2	$C_{s} = C_{1} \frac{b_{1}}{r} C_{2} \frac{b_{3}}{r} C_{3} \frac{b_{2}}{b_{1} r}$ where $\begin{cases} C_{1} \frac{b_{1}}{r} = 1, & \text{if } \frac{b_{1}}{r} = 0 \\ C_{3} \frac{b_{2}}{b_{1}} = 1, & \text{if } \frac{b_{2}}{b_{1}} = 0 \\ & \text{and } 1.1 \le C_{s} \le 2 \end{cases}$

by ACI 318, can often be excessively conservative. Consequently, it is essential to develop a more reliable design method that can fully exploit the cost-effectiveness of deep PHCS. This study aims to contribute to this goal by quantifying and evaluating the critical factors that impact the web-shear strength of these members. Lastly, based on North American and European practice, three design expressions are proposed and assessed using a compiled data set.

DATA SET

To assess the goodness of fit of code provisions and proposed modifications, a data set containing 85 entries was compiled (refer to Appendix A*). This data set extends the one compiled by Tawadrous and Marcous, which contains 51 entries, with 34 entries from shear tests undertaken by references. A visual representation of the main variables in the compiled data set is illustrated in Fig. 1. These variables include the ultimate shear stress v_{ult} , compressive strength of the concrete f_c , the level of prestressing $f_{se} \times A_{ps}/A_c$, the shear span-depth ratio a_v/d_p , the thickness of the

[&]quot;The Appendix is available at www.concrete.org/publications in PDF format, appended to the online version of the published paper. It is also available in hard copy from ACI headquarters for a fee equal to the cost of reproduction plus handling at the time of the request.

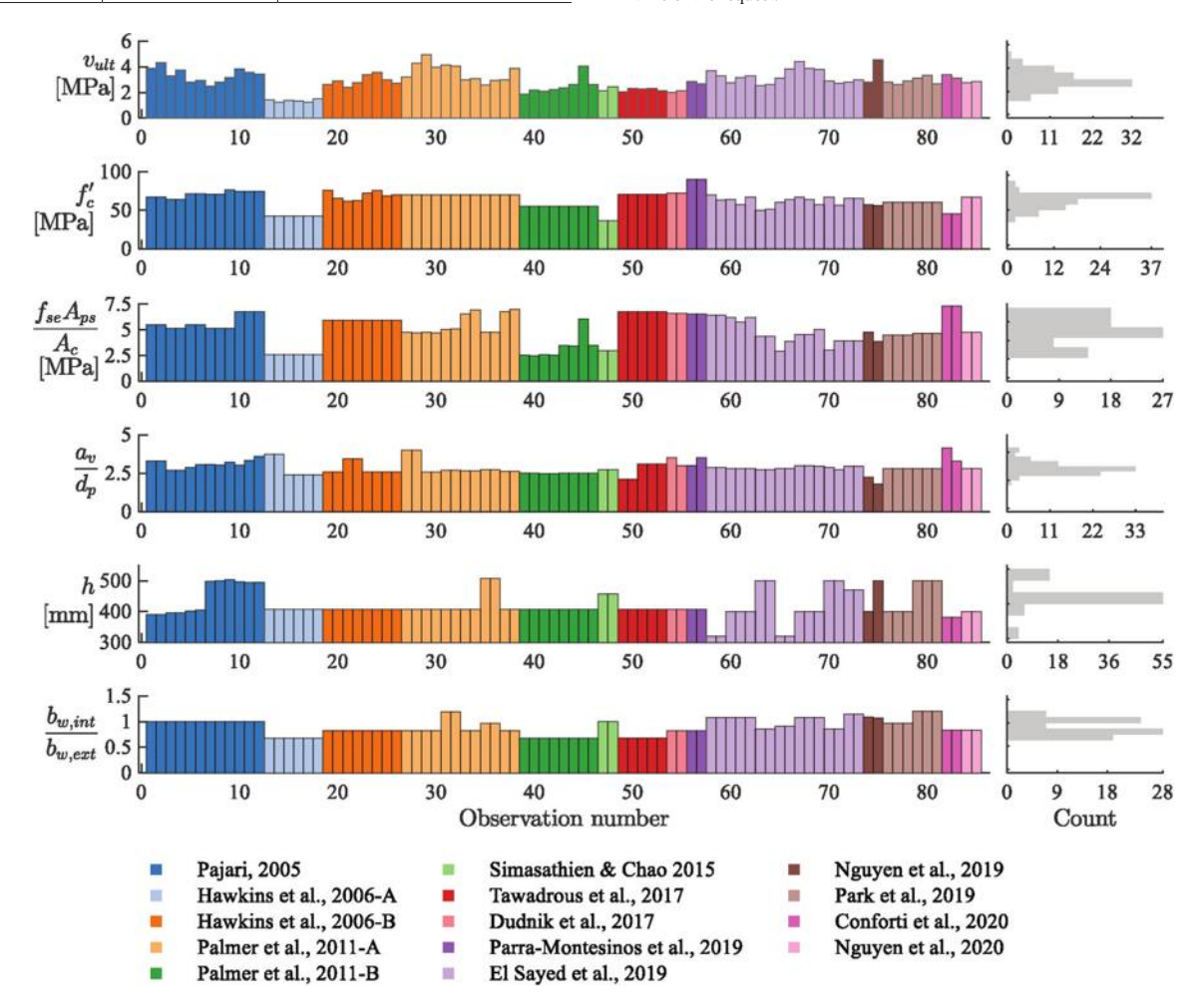


Fig. 1—Data set distribution: (a) ultimate shear stress v_{ult} ; (b) concrete compressive strength f_c '; (c) axial stress in concrete outside transfer length $f_{se} \times A_{ps}/A_c$; (d) shear span-depth ratio a_v/d_p ; (e) height of PHCS h; and (f) ratio of inner-to-outer web width $b_{w,int}/b_{w,ext}$.

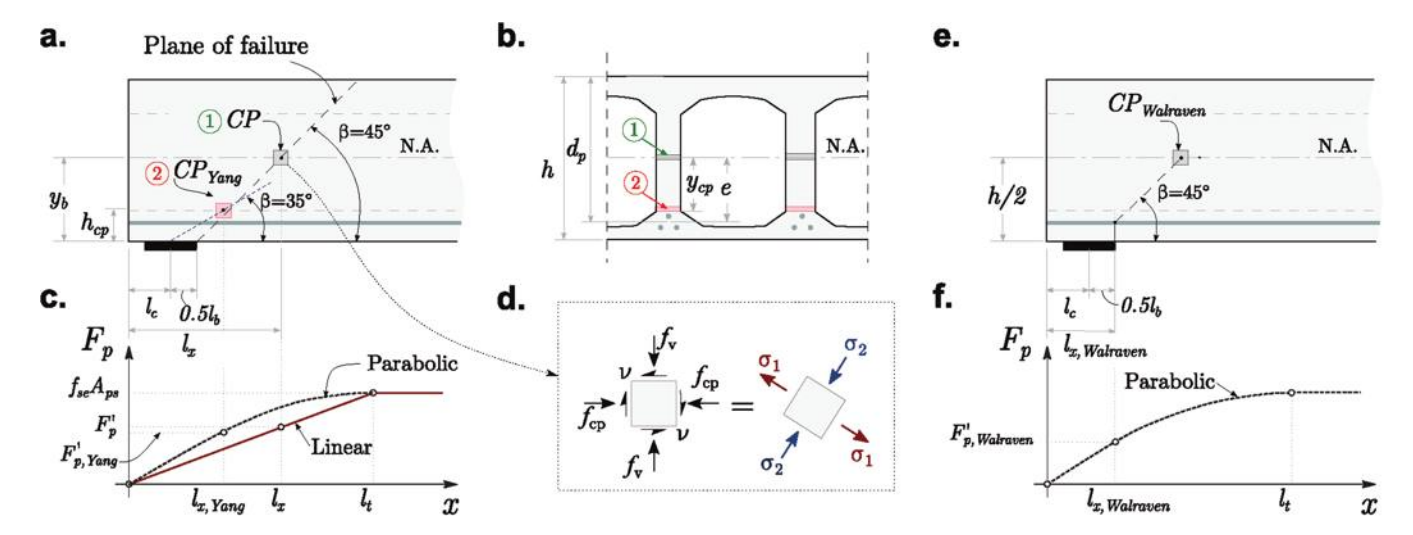


Fig. 2—Location of critical point in: (a) elevation view, and (b) section view; (c) effective prestressing force applied by strands F_p ; (d) stress at CP; (e) location of CP according to Walraven and Mercx³; and (f) effective prestressing force at CP considering shear lag.

member h, and the ratio of the internal and external web widths $b_{w,int}/b_{w,ext}$.

FACTORS AFFECTING WEB-SHEAR STRENGTH OF DEEP PHCS

Several studies^{3,5,17,21,24,25} including experimental and numerical investigations have identified various factors that impact the web-shear strength of PHCS, aside from tensile strength and prestress level. These factors include member thickness, void geometry, shear span-depth ratio, shear slag of the prestressing force, prestressing strand bond strength, and shear stress distribution along the section width. While it may be impractical to incorporate all these strength modification factors into a design expression for daily engineering practice, the authors suggest grouping and summarizing their effects through three categories: a) reduction of effective compressive stress in concrete; b) biaxial stress state at the critical point; and c) shear stress distribution along the section width. Each of these factors is discussed in the following sections.

Reduction of effective compressive stress in concrete

It is typically assumed that the effective compressive stress in concrete f_{pc} depends only on the location of the critical point (CP) and distribution of the prestressing force along the transfer length. However, this assumption may not hold true for all scenarios due to factors such as void shape, bond strength, and shear lag, which can significantly impact f_{pc} and ultimately affect the PHCS web-shear strength.^{3,17,24}

For example, the CP location is traditionally defined at the intersection of a 45-degree failure plane and the neutral axis of the section ($\sim h/2$) (point 1 in Fig. 2). However, studies using finite element analysis^{12,18,24} and refined analytical techniques⁴ have demonstrated that this assumption is not suitable for PHCS with non-circular voids. In such cases, the CP location is closer to the flange-to-web junction (point 2 in Fig. 2). This change in CP location reduces F_p and generates an additional normal and shear stresses. To account for

this new CP location when calculating f_{pc} , Yang²⁴ proposed an advanced web-shear design methodology, which is evaluated in this study.

Moreover, significantly increases in the initial end slip of prestressing strands in deep PHCS have been reported by Palmer and Schutlz⁶ and Dudnik et al.⁹ Increases in initial end slip suggest decreases in bond strength, and therefore longer transfer lengths, leading to decreases in f_{pc} .²⁶ It is important to note that El Sayed et al.¹¹ indicated the absence of any definitive correlation between the thickness of the member and the initial end slip of the strands.

Walraven and Mercx³ investigated the impact of shear lag of the prestressing force on f_{pc} along the transfer length. Their analytical investigations suggested that the compressive stress induced by the presstressing strands in this region should be distributed at a 45-degree angle to the axis of the strands. As a result, a lower f_{pc} at the CP should be considered when predicting the web-shear strength of PHCS. To facilitate practical implementation, the authors recommended computing f_{pc} using the prestressing force F_p at the inner face of the support and assuming a parabolic prestressing force distribution, as shown in Fig. 2(e) and (f).

To account for the aforementioned uncertainty in estimating f_{pc} , a sensitivity analysis is carried out assessing factors such as: 1) location of the critical point (point 1 versus point 2 in Fig. 2(a)); 2) the reduction in f_{pc} due to the larger anticipated initial end slip in deep members; and 3) the shear lag of the compressive stress as suggested in Walraven and Mercx.³ Factors 2 and 3 were assessed by applying a factor φ_{pc} to f_{pc} . The outcomes of the sensitivity analysis are outlined as follows.

Biaxial stress state at critical point

The stress analysis of simply supported PHCS shows that the CP is subjected to a biaxial tension-compression stress state, as shown in Fig. 2(d), in which the principal stresses are given by Eq. (1) and (2)

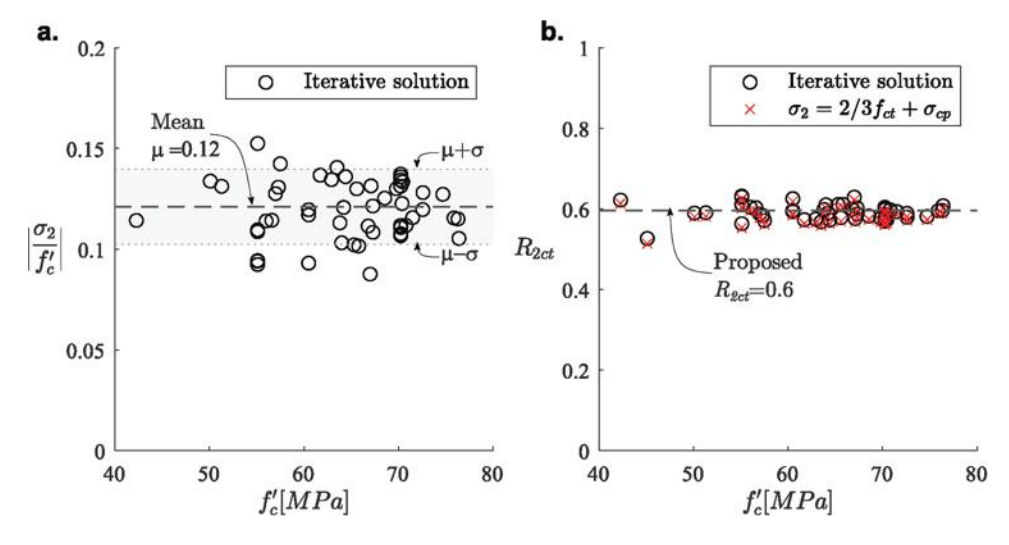


Fig. 3—Predictions of: (a) principal stress in compression σ_2 ; and (b) biaxial tensile strength reduction factor R_{2ct} for compiled data set using Hampel et al.'s failure envelope.

$$\sigma_1 = + \left[\sqrt{v^2 + \left(\frac{f_{cp}}{2}\right)^2} - \left(\frac{f_{cp}}{2}\right) \right] \tag{1}$$

$$\sigma_2 = -\left[\sqrt{v^2 + \left(\frac{f_{cp}}{2}\right)^2} + \left(\frac{f_{cp}}{2}\right)\right] \tag{2}$$

where σ_1 and σ_2 are the principal stresses in tension (+) and compression (–), respectively; and ν is the shear stress. The correlation between the principal stresses is determined by adding Eq. (1) and (2), which reduces to

$$\sigma_2 = -(\sigma_1 + f_{cp}) \tag{3}$$

It is well known that this biaxial tension-compression stress condition can significantly reduce the uniaxial tensile strength of concrete. To account for this, the biaxial tension-compression failure envelope proposed by Kupfer and Gerstle is commonly used in literature. For instance, Marí et al. Teported reduction factors in tensile strength ranging from 0.77 to 0.95 for prestressed concrete beams. Kupfer and Gerstle's failure envelope is expressed as follows

$$\frac{\sigma_1}{|f_{ct}|} = 1 + 0.8 \frac{\sigma_2}{|f_{c'}|} \tag{4}$$

where f_{ct} is the uniaxial concrete tensile strength; and f_c' is the uniaxial compressive strength of concrete. Equation (4) quantifies the effect of the normalized compressive stress in the normalized uniaxial tensile strength in the range $|\sigma_2|/|f_c'| \le 0.8$. The expression proposed by Kupfer and Gerstle³⁰ for values $|\sigma_2|/|f_c'| > 0.8$ is irrelevant to this work.

The biaxial tensile strength of concrete f_{2ct} is given by Eq. (5)

$$f_{2ct} = R_{2ct} f_{ct} \tag{5}$$

The factor $R_{2ct} = \sigma_1/f_{ct}$ is a tensile strength reduction factor accounting for the biaxial stress state. Based on Kupfer and Gerstle's expression, the reduction factor can be determined by substituting Eq. (3) in (4) and solving for σ_1/f_{ct} .

$$R_{2ct} = \left(\frac{f_c' - 0.8 f_{cp}}{f_c' + 0.8 f_{ct}}\right) \tag{6}$$

Values of R_{2ct} ranging from 0.88 to 0.94 are determined by applying Eq. (6) to the compiled data set. However, it is essential to note that Kupfer and Gerstle's expression was calibrated for concrete with uniaxial compressive strength in the range of 18 to 58 MPa, which is not in the typical range for PHCS. Additionally, recent investigations in high-strength concrete, ranging from 60 to 90 MPa, have reported a more detrimental tensile strength decay due to the biaxial stress state than for normal-strength concrete.^{27,32} Hence, to estimate the tensile strength reduction, a biaxial failure envelope for high-strength concrete derived by Hampel et al.²⁷ and recommended by the *fib* bulletin 42^{33} is used in this work. Hampel et al.'s tension-compression failure envelope is given by Eq. (7)

$$\frac{\sigma_1}{f_{ct}} = \left(a \sqrt[3]{\frac{\sigma_2}{|f_c'|} + b} + c \frac{\sigma_2}{|f_c'|} + d \right) \frac{f_c'}{f_{ct}}$$
 (7)

where
$$a = -1.3 \times 10^4 |f_c'| + 4.5 \times 10^{-2}$$
; $b = -4.5 \times 10^{-4} |f_c'| + 4.0 \times 10^{-2}$; $c = a^3 \sqrt{b-1} + d$; and $d = (f_{ct}/|f_c'|) - a^3 \sqrt{b}$.

The implementation of Hampel et al.'s failure envelope requires an iterative approach. Figure 3(a) shows the iterative solution for the normalized stress $|\sigma_2|/|f_c'|$ for each entry in the compiled data set. For consistency reasons with Hampel et al.'s formulation, the values of f_{cp} employed in Eq. (3) were calculated using the *fib* MC 2010²² approach. Results indicated a mean $|\sigma_2|/|f_c'| = 0.12$ with and a standard deviation of ± 0.02 for the compiled data set (Fig. 3(a)). Using these results, a simplified expression for calculating σ_2 , assuming $\sigma_1 \approx 2/3f_{ct}$, is given by Eq. (8)

$$\sigma_2 \approx -(2/3f_{ct} + f_{cp}) \tag{8}$$

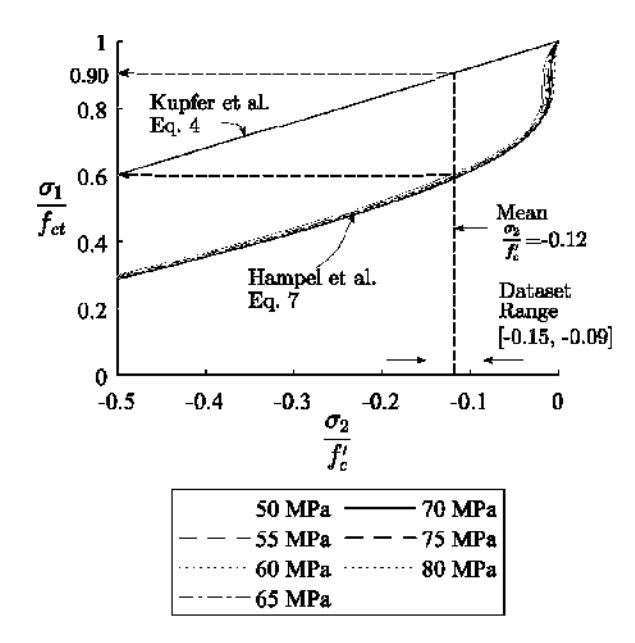


Fig. 4—Effect of biaxial tension-compression in tensile concrete strength according to Kupfer et al.'s and Hampel et al.'s failure envelopes.

Hence, the approximation of σ_2 presented in Eq. (8) can be employed in Eq. (7) to determine σ_1/f_{ct} , with a mean error less than 1%. Figure 3(b) presents the calculated values $R_{2ct} = \sigma_1/f_{ct}$ using the interactive and simplified approach. Based on these results, it was concluded that for the analyzed data set, a simpler approximation of the biaxial tensile strength reduction factor could be obtained by taking the mean value $R_{2ct} = 0.60$.

Figure 4 compares the normalized biaxial tensile strength σ_1/f_{ct} predicted by Kupfer and Gerstle's and Hampel et al.'s failure envelopes, revealing substantial discrepancies between the two methods when applied to the compiled data set. Normalized biaxial tensile strength for the mean compressive stress value $\sigma_2/|f_c'|=0.12$ were estimated at 0.90 and 0.60 for Kupfer and Gerstle's and Hampel et al.'s expressions, respectively. Furthermore, even for the member with the lowest $|\sigma_2|/|f_c'|=0.09$, Hampel et al.'s expressions computed a significant tensile strength reduction $\sigma_1/f_{ct}=0.63$.

Because PHCS are usually manufactured using high-strength concrete, it is considered that Hampel et al.'s tension-compression failure envelope is better suited for this application. It is worth remarking that more than 72% of the entries of the compiled data set have compressive strengths greater than 60 MPa (Fig. 1(b)). Moreover, Hampel et al.'s expression is consistent with the current reduction factor implicitly adopted by ACI 318-19, ¹⁶ approximated as 0.29 $\sqrt{f_c'}/0.5\sqrt{f_c'} = 0.58$. As a result, proposed modifications to the ACI 318 provision preserve the current tensile strength reduction factor.

The effect of the biaxial stress state is not explicitly included in the *fib* MC 2010 design approach for PHCS. Moreover, *fib* MC 2010 uses the characteristic value of the tensile strength f_{ctk} for determining the design tensile strength, in contrast to Eurocode 2,¹⁹ which uses the 5% fractile tensile strength of concrete $f_{ctk,min} = 0.7 f_{ctk}$. As a result, the reduction factor

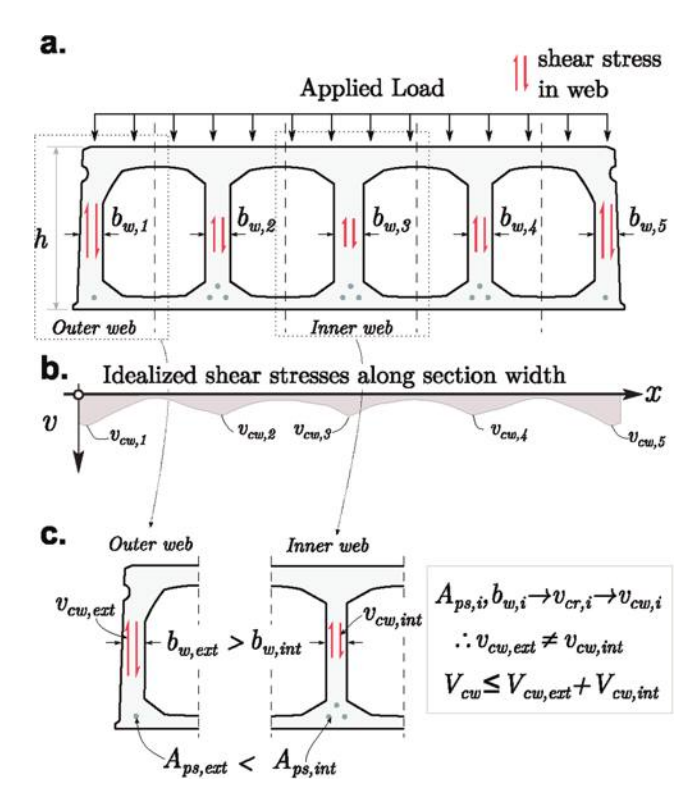


Fig. 5—Schematic illustration of shear stress distribution along section width: (a) cross section; (b) shear stress distribution; and (c) exterior and interior webs.

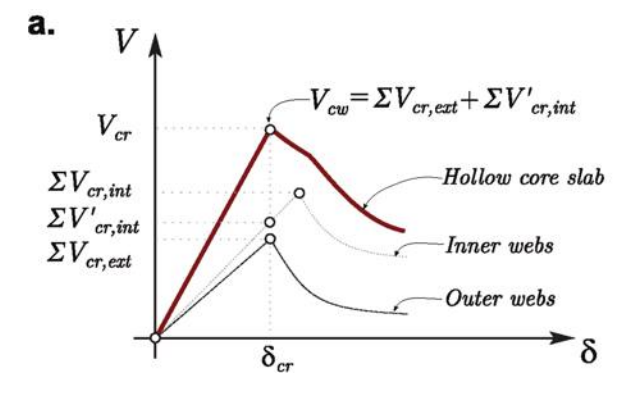
 $R_{2ct} = 0.6$ is proposed to be adopted in the *fib* MC 2010 design approach. The factor is based on an analysis of the compiled data set using Hampel et al.'s model (Fig. 3(b)).

Shear stress distribution along section width

In his research, Jonsson²¹ investigated how shear stresses are distributed across the width of PHCS (Fig. 5). He suggested that the web-shear capacity of a PHCS should be determined by the weakest or most stressed web. Webs with lower web-shear strength, including those without prestressing steel, should be excluded when calculating total web-shear strength. To account for shear stress distribution in design, Jonsson proposed using the second moment of area *I* to determine the shear stress acting on each web using its relative flexural stiffness. As a result, in a PHCS with equal web width and similar inner and outer voids, the outer webs would experience approximately 50% of the shear stress of the inner webs.

Building on Jonsson's concept, Palmer and Schultz¹⁷ proposed an alternative method for distributing the shear stress. The authors suggested using the relative web's width to distribute the shear stress and named this approach the axial stiffness method. To validate this proposal, linear finite element analyses were conducted to assess both methodologies, concluding that neither the flexural stiffness nor the axial stiffness method accurately predicts the stress distribution across the section. However, results indicated that the axial stiffness method better approximates the shear stress distribution for practical purposes.

A comprehensive understanding of the impact of shear stress distribution on the web-shear strength can be achieved



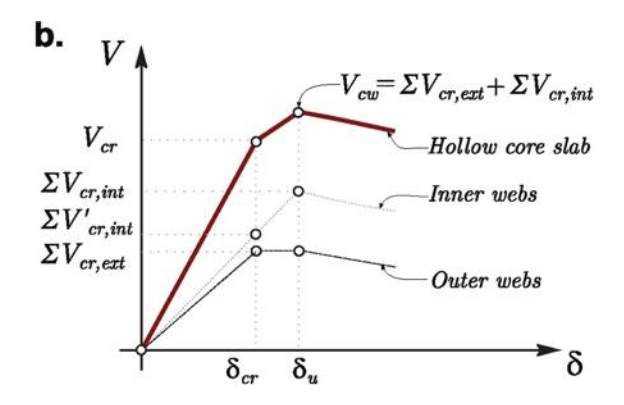


Fig. 6—Schematic force versus displacement response of deep PHCS failing in web-shear: (a) poor post-cracking shear strength; and (b) enhanced post-cracking shear strength.

by considering the cracking shear strength (V_{cr}). This parameter represents the shear force at which initial cracking occurs in either the outer or inner webs of the slab. To illustrate this concept, the PHCS section displayed in Fig. 5(a) will be examined, where different web thicknesses and prestressing steel are employed for the inner and outer webs.

Figure 6 provides two distinct force-displacement responses that can be expected from the PHCS. In Fig. 6(a), the member exhibits a poor post-cracking shear response, leading to a significant loss of strength and stiffness in the outer webs once they reach the cracking shear strength ($\Sigma V_{cr,ext}$). Consequently, the shear force initially resisted by the outer webs is redistributed to the uncracked inner webs. If the cracking shear strength of the inner webs ($\Sigma V_{cr,int}$) is unable to withstand the total shear force acting on the member, immediate failure of the PHCS occurs. This analysis reveals that the presence of weaker outer webs diminishes the web-shear strength of the inner webs from $\Sigma V_{cr,int}$ to $\Sigma V_{cr,int}$. Therefore, the total shear strength is approximated as $V_{cw} \approx \Sigma V_{cr,int}' + \Sigma V_{cr,ext}$.

Conversely, if the exterior webs exhibit a stable postcracking shear response, possibly due to the presence of transverse reinforcement or fibers, the deep PHCS may reach its theoretical web-shear strength, as illustrated in Fig. 6(b).

To incorporate and assess the shear stress distribution along the section width in current design expressions—that is, ACI 318-19, *fib* MC 2010, and CSA A23.3-14—a general design procedure is proposed as follows

Step 1: Neglect the web-shear strength of webs without prestressing strands such that $b_{w,unr}^* = 0$.

Step 2: Assume that the cracking stress equals the web-shear stress $v_{cw,i}$ computed using the selected standards. For typical PHCS, only two types of webs are needed to be considered—that is, $i = \{exterior, interior\}$.

Step 3: Estimate the shear stress factor $\varphi_{w,i}$ based on the web widths (Eq. (9)).

$$\varphi_{w,i} = \frac{b_{w,i}}{\max(b_{w,i})} \tag{9}$$

Step 4: Determine the effective web-shear stress using Eq. (10), which serves to identify the stress level at which the initial cracking will take place.

$$v_{cw} = \min\left(\frac{v_{cw,i}'}{\varphi_{w,i}}\right) \tag{10}$$

Step 5: Estimate the total web-shear strength of V_{cw} , accounting for the stress distribution according to the chosen design standards. For instance, for the ACI methodology, the web-shear strength is determined using

$$V_{cw} = v_{cw} \sum_{i=1}^{n} \varphi_{w,i} b_{w,i} d_{p,i}$$
 (11)

Step 6 (optional): In members with significant differences between the web-shear strength of the inner and outer webs, the stronger webs may have enough resistance to carry the redistributed shear force after the first cracking. In those instances, the maximum shear force that can be carried out for web type is given by

$$V^* = \max(v_{cr.int}' \cdot b_{w.int} \cdot d_n \cdot N_{int}, v_{cr.ext}' \cdot b_{w.ext} \cdot d_n \cdot N_{ext}) \quad (12)$$

where N_{int} and N_{ext} are the number of inner and outer webs, respectively. Then, the total web-shear strength is taken as the maximum of Eq. (11) and (12). A visual representation of the design procedure is shown in Fig. 7.

ASSESSMENT OF FACTORS AFFECTING WEB-SHEAR STRENGTH

The study evaluated the impact of different factors on various design expressions using the general design procedure presented in Fig. 7. Size effect and other strength reduction factors were also compared among the methodologies. Observations 29, 45, and 75 were excluded from the analysis due to unusual test conditions. Figure 8 summarizes the factors assessed in each design expression. Statistical parameters including mean value, standard deviation, coefficient of variation (COV), minimum, and maximum values were used to compare the accuracy and safety of each analysis based on the measured-to-predicted ratios V_{test}/V_{pred} . Normalized mean absolute error (NMAE) and root mean square error (RSME)³⁴ were also evaluated for comparison purposes. The NMAE is calculated using Eq. (13)

NMAE =
$$\frac{\frac{1}{n} \sum_{i=1}^{n} |y_i - \hat{y}_i|}{y_H - y_L}$$
 (13)

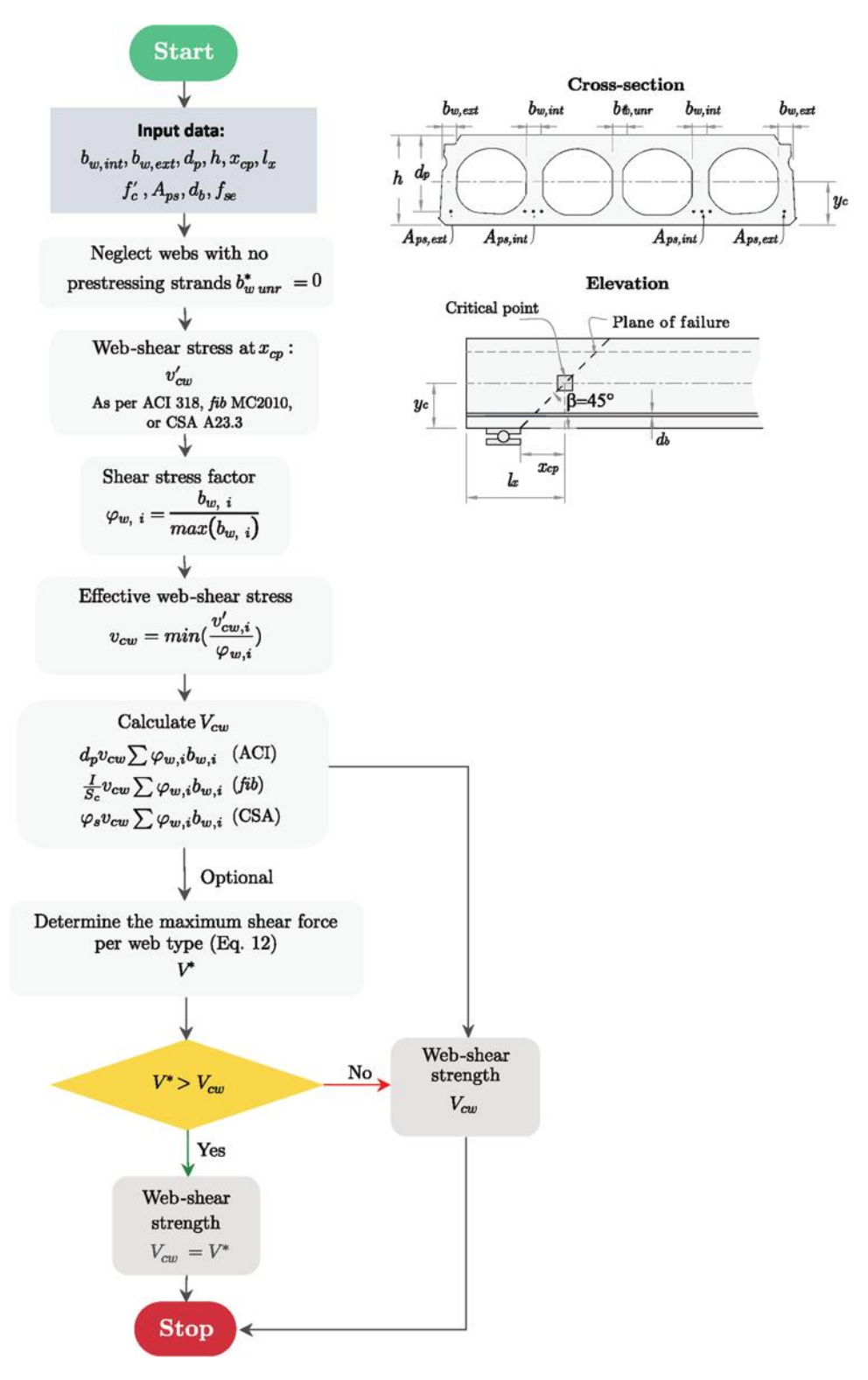


Fig. 7—Flowchart for estimation of web-shear strength.

where y_i and \hat{y}_i are the actual and predicted value for entry i; y_H is the highest actual value; y_L is the lowest actual value; and n corresponds to the number of entries in the data set. The RMSE is normalized similarly, as shown in Eq. (14)

NRMSE =
$$\frac{\sqrt{\frac{1}{n} \sum_{i=1}^{n} (y_i - \hat{y}_i)^2}}{y_H - y_L}$$
 (14)

Analyses were assessed using modified demerit point classification criteria proposed in References 35 and 36, which assign a penalty (PEN) to each tier based on the measured-to-predicted shear strength ratio (Table 2). The total number of penalty points determined the safety performance of each analysis. The demerit point classification penalizes the overestimation of strength and rewards accuracy.

The influence of each factor and a combination of factors in the ACI 318 provisions was assessed using a decision tree

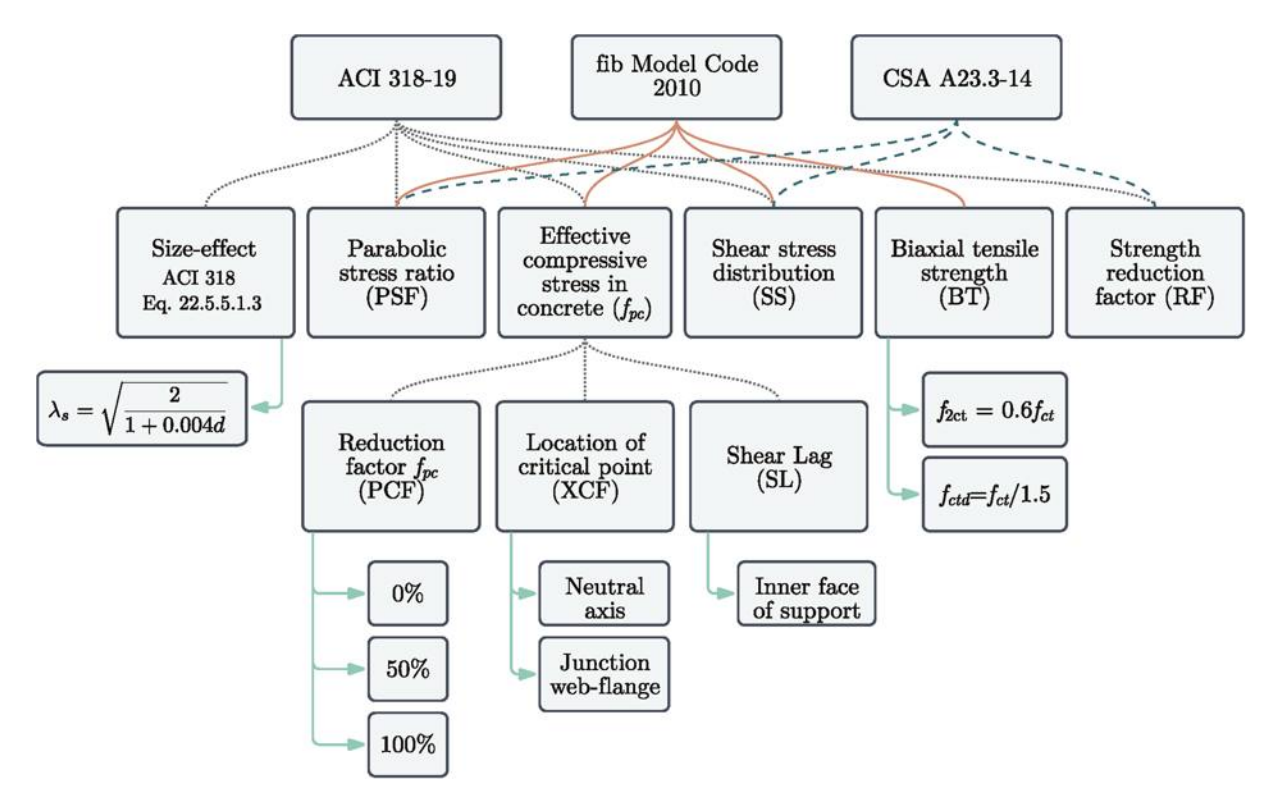


Fig. 8—Overview of factors investigated in each design methodology.

Table 2—Modified version of Demerit Points Classification (DPC)³⁶

$V_{\it test}/V_{\it pred}$	Classification	Penalty
< 0.5	Extremely dangerous	10
0.5 to 0.84	Dangerous	5
0.85 to 1.14	Appropriate safety	0
1.15 to 1.99	Conservative	1
≥2	Extremely conservative	2

analysis (Fig. 9). Similar analyses were conducted for the *fib* MC 2010 and CSA A23.3-14 provisions. A maximum combination of three factors were considered for simplicity. Table 3 presents the results for each analysis. The statistical parameters and demerit point classification were optimized to evaluate the performance of each analysis.

Current design provisions and previous proposals were also evaluated, as shown in Table 4. In addition to the previously mentioned design provisions, the analyses included the design expressions proposed by the *fib* MC 2010 level of approximation 2, Yang,²⁴ Park et al.,¹³ El Sayed et al.,¹¹ and Brunesi and Nascimbene.¹⁸

Based on the results presented in Table 3, the modified expressions assessed in analyses 15, 32, and 35 are selected for estimating the web shear strength according to the ACI 318-19, *fib* MC 2010, and CSA A23.3-14 standards, respectively. In addition, two simplified and more conservative design expressions are proposed by assuming $\varphi_{pc} = 0$ for the ACI 318-19 and *fib* MC 2010 provisions—that is, analyses 16 and 30, respectively. Similarly, a reduction factor of 0.8 is applied to the CSA A23.3-14 provision to obtain a more conservative approach. Modifications to existing design

methodologies are presented in detail in the following sections.

PROPOSED MODIFICATIONS TO CURRENT DESIGN PROVISIONS

The purpose of the proposed modifications is to improve the current design provisions without being overly conservative or changing their underlying philosophy. To this end, two design expressions for determining the web-shear stress, detailed and simplified, are provided per design code. The detailed approach incorporates the reduction of f_{pc} and the distribution of shear stresses, while the simplified approach applies only the stress distribution, ignoring the contribution of f_{pc} to shear. This simplification results in more straightforward calculations. Nevertheless, it is important to note that the simplified methods, while conservative, exhibited greater accuracy than the current design provisions.

Modifications to ACI 318-19

The modified ACI 318-19 provision for the web-shear stress using the detailed and simplified methods are given by Eq. (15) and Eq. (15b), respectively

$$v_{cwi}' = 0.29 \sqrt{f_c'} + 0.3 \varphi_{pc} \alpha_l f_{pc,i}$$
 (15)

$$v_{cwi}' = 0.29 \sqrt{f_c'}$$
 (15b)

where $\varphi_{pc} = 0.5$ is a reduction factor accounting for decreases in f_{pc} to accommodate for the shear lag, increases in end slip of prestressing, and variations in the critical point location. The factor $\alpha_l = l_x/l_t$ adjusts the effective prestress at the critical section. The transfer length is taken as $l_{tr} = 50d_b$, where d_b is the largest diameter of prestressing strand, and l_x is the

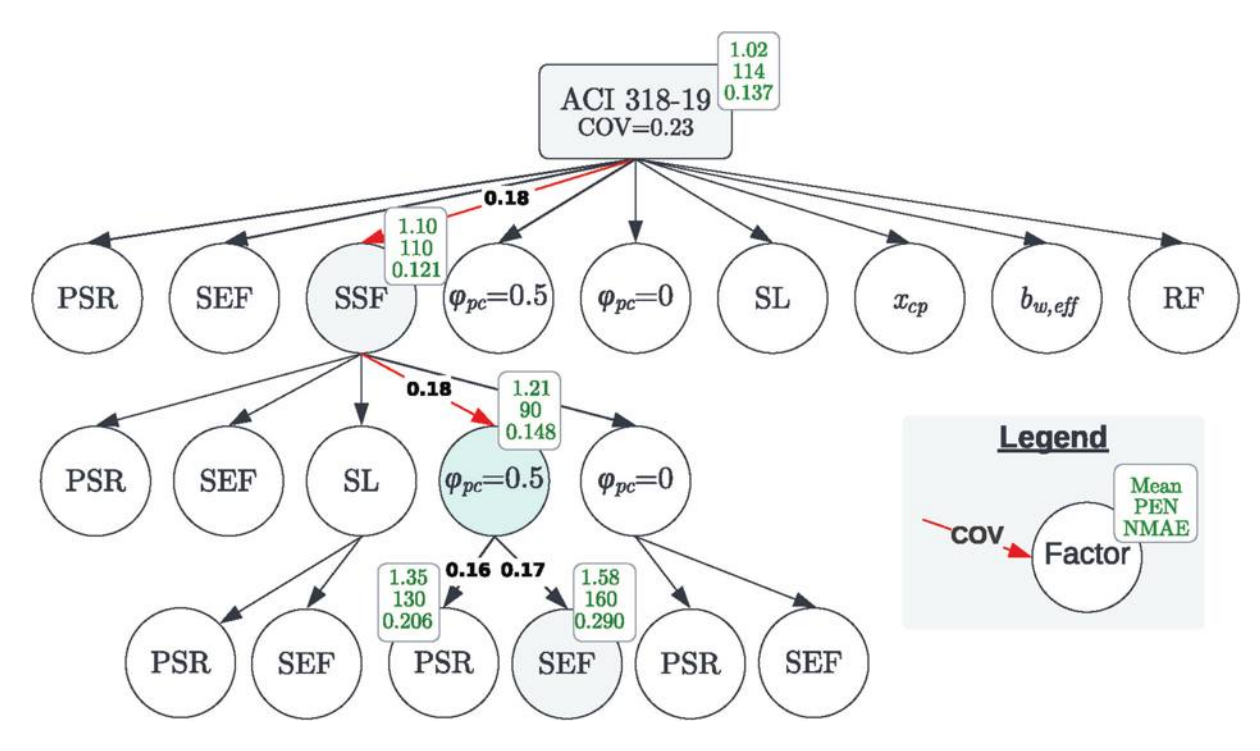


Fig. 9—Set of analysis for ACI 318 web-shear formulation. (Note: PSR is parabolic stress ratio; SEF is size-effect factor; and SSF is shear stress distribution factor along section width.)

distance from the edge of the member to the critical point located at h/2 from the inner support face. The compressive strength in concrete per web is given by Eq. (16)

$$f_{pc,i} = \frac{A_{ps}f_{se}}{b_{w,i}h} \tag{16}$$

where A_{ps} is the area of prestressing steel; f_{se} is the effective stress in prestressing steel (after allowance for all losses); and i is the web type, for typical cases {outer, inner}. The effective web shear stress v_{cw} is computed using Eq. (10). Finally, the web-shear strength is computed using Eq. (17) as follows

$$V_{cw} = d_p v_{cw} \sum_{i=1}^{n} \varphi_{w,i} b_{w,i}$$
 (17)

Modifications to fib MC 2010

The modified *fib* MC 2010 provision for the web-shear stress is given by Eq. (18) and Eq. (18b), respectively

$$v_{cwi}' = \varphi_s \sqrt{f_{2ct}^2 + \alpha_l \varphi_{pc} f_{pc} f_{2ct}}$$
 (18)

$$v_{cwi}' = f_{2ct} \tag{18b}$$

where $\varphi_{pc} = 0.9$ is a strength reduction factor determined from the statistical analysis; and $\varphi_{pc} = 0.5$ is a reduction factor accounting for decreases in f_{pc} . The biaxial tensile strength of concrete is taken as $f_{2ct} = 0.6f_{ct}$. The factor $\alpha_l = l_x/l_{bpt,95\%}$ adjusts the effective prestress at the critical section, in which the transfer length is taken as per the fib MC 2010

$$l_{bpt,95\%} = \frac{0.1\varphi_s f_{pi}}{f_{ctd.re}} \tag{19}$$

where f_{pi} is the initial prestress; $f_{ctd,re} = (f_{ctk,min}/1.5)$ is the lower design concrete tensile strength for the transmission length the strength at the time of release; $f_{ctk,min}$ is the minimum characteristic tensile strength as per fib MC 2010, Section 5.1.5; φ_s is the diameter of the prestressing strand; and l_x is the distance from the edge of the member to the critical point located at y_b from the inner support face. The compressive strength in concrete per web type is given by Eq. (16).

The web shear stress v_{cw} is determined using Eq. (10). Finally, the web-shear strength is calculated as

$$V_{cw} = \frac{I}{S_c} v_{cw} \sum_{i=1}^{n} \varphi_{w,i} b_{w,i}$$
 (20)

Modifications to CSA A23.3-14

The design provision presented in CSA A23.3 considers the effect of compressive stress due to the prestressing force in the longitudinal strain parameter at the mid height of the section ε_x . However, in this paper, the longitudinal strain at midheight is taken as $\varepsilon_x = 0$, noting that the section is prestressed. Therefore, the shear web-shear stress is determined as follows using the detailed and simplified methods are given by Eq. (21a) and Eq. (21b), respectively

$$v_{cw,i}' = \beta \sqrt{f_c'} \tag{21a}$$

$$v_{cwi}' = 0.8\beta \sqrt{f_c'} \tag{21b}$$

where β is a factor to account for the interlocking of aggregates in concrete members and given by

$$\beta = \frac{520}{1000 + S_{-}} \tag{22}$$

Table 3—Statistical parameters for modified design provisions

		Analysis			S	tatistical p	arameters			Total
Reference	No.	Description	Mean	STD	COV	Min	Max	NMAE	NRSME	PEN
	1	No factor	1.02	0.24	0.23	0.57	1.61	0.137	0.179	114
	2	RF = 0.5 as per code	2.05	0.47	0.23	1.14	3.23	0.397	0.436	162
	3	PSR	1.19	0.25	0.212	0.74	1.79	0.162	0.201	137
	4	SEF	1.14	0.25	0.222	0.64	1.75	0.158	0.197	142
	5	SSF	1.01	0.20	0.196	0.68	1.63	0.128	0.156	142
	6	$\varphi_{pc} = 0.5$	1.12	0.26	0.229	0.61	1.73	0.153	0.191	132
	7	$\varphi_{pc} = 0$	1.24	0.29	0.230	0.65	1.86	0.188	0.228	150
	8	SL	1.12	0.26	0.230	0.61	1.71	0.156	0.194	132
	9	χ_{cp}	1.28	0.41	0.321	0.59	2.67	0.213	0.258	153
	10	$b_{w,eff}$	1.03	0.22	0.215	0.64	1.65	0.128	0.166	132
Modifications to	11	RF = 0.8	1.28	0.29	0.230	0.71	2.02	0.199	0.238	151
ACI 318-19 ¹⁶	12	SSF+PSR	1.28	0.23	0.18	0.91	1.99	0.175	0.22	112
	13	SSF+SEF	1.23	0.22	0.18	0.87	1.90	0.158	0.20	100
	14	SSF+SL	1.25	0.22	0.18	0.88	1.87	0.165	0.21	100
	15	$SSF+(\varphi_{pc}=0.5)$	1.21	0.21	0.18	0.86	1.83	0.148	0.19	90
	16	$SSF+(\varphi_{pc}=0)$	1.36	0.25	0.18	0.92	1.96	0.210	0.25	128
	17	SSF+SL+PSR	1.45	0.24	0.16	1.01	2.15	0.246	0.28	148
	18	SSF+SL+SEF	1.39	0.24	0.17	0.99	2.06	0.225	0.27	138
	19	$SSF+(\varphi_{pc}=0.5)+PSR$	1.41	0.23	0.16	0.98	2.11	0.227	0.26	148
	20	$SSF+(\varphi_{pc}=0.5)+SEF$	1.35	0.23	0.17	0.96	2.02	0.206	0.25	130
	21	$SSF+(\varphi_{pc}=0)+PSR$	1.58	0.26	0.16	1.03	2.24	0.290	0.32	160
	22	$SSF+(\varphi_{pc}=0)+SEF$	1.52	0.27	0.18	1.01	2.15	0.270	0.31	156
	23	LoA-I with no factor*	1.01	0.21	0.21	0.64	1.57	0.125	0.162	121
	24	SSF^\dagger	1.30	0.24	0.18	0.87	2.08	0.182	0.23	116
	25	BT = 0.6	1.12	0.24	0.21	0.70	1.75	0.143	0.18	122
	26	$\varphi_{cp} = 0.5^*$	1.16	0.24	0.21	0.72	1.76	0.155	0.19	133
	27	$\varphi_{cp} = 0^*$	1.42	0.30	0.21	0.82	2.05	0.237	0.28	142
Modifications to <i>fib</i> MC 2010 ²² LoA-I	28	SL [†]	1.23	0.26	0.21	0.74	1.82	0.179	0.22	142
WC 2010 LOA-1	29	$SSF+BF+(\varphi_{pc}=0.5^{\dagger})$	1.20	0.20	0.17	0.86	1.84	0.143	0.18	88
	30	$SSF+BF+(\varphi_{pc}=0^{\dagger})$	1.43	0.23	0.16	0.94	2.04	0.238	0.28	150
	31	SSF+BF+SL [†]	1.62	0.30	0.18	1.09	2.60	0.299	0.33	160
	32	SSF+BF+($\varphi_{pc} = 0.5$)+(RF = 0.9)	1.33	0.22	0.17	0.96	2.05	0.197	0.24	126
	33	SSF+BF+($\phi_{pc} = 0$)+(RF = 0.9)	1.59	0.26	0.16	1.05	2.26	0.292	0.33	160
	34	No factor	1.06	0.24	0.22	0.54	1.54	0.144	0.187	134
Modifications to	35	SSF	1.16	0.20	0.18	0.80	1.67	0.135	0.179	98
CSA A23	36	SSF+PSR	1.21	0.19	0.16	0.81	1.73	0.151	0.197	91
	37	SSF+(RF=0.8)	1.45	0.25	0.18	1.00	2.09	0.246	0.288	146

Note: PSR is parabolic stress factor; SEF is size-effect factor; SSF is shear distribution factor; STD is standard deviation; φ_{pc} is reduction factor multiplying f_{pc} ; SL is shear lag as in ref; x_{cp} is location of critical point at junction flange-to-web; $b_{w,eff}$ is effective width neglecting width without reinforcement; BT is biaxial tensile strength factor multiplying f_{cm} ; RF is reduction factor multiplying web-shear strength.

^{*}Expression using the design tensile concrete strength f_{ctd} .

 $^{^\}dagger Expression$ without reduction factor of 0.8.

Table 4—Statistical parameters for design provisions and previous proposals

		Analysis			Sta	atistical p	arameters			Total
Reference	No.	Description	Mean	STD	COV	Min.	Max.	NMAE	NRSME	PEN
A CT 210 1016	1*	No RF	1.02	0.24	0.23	0.57	1.61	0.137	0.179	114
ACI 318-19 ¹⁶	2*	RF = 0.5 per code	2.05	0.47	0.23	1.14	3.23		162	
	38	LoA-I with f_{ctm}	0.74	0.15	0.21	0.46	1.13	0.296	0.341	355
CL MC 2010??	23*	LoA-I with f_{ctd}	1.01	0.21	0.21	0.64	1.57	0.125	0.162	121
fib MC 2010 ²²	38	LoA-II with f_{ctm}	0.67	0.15	0.23	0.33	1.06	0.429	0.498	420
	39	LoA-II with f_{ctd}	1.03	0.30	0.29	0.47	2.13	0.163	0.210	159
CSA A23.3-14 ²³	34*	No factor	1.06	0.24	0.22	0.54	1.54	0.144	0.187	134
N7 24	40	With f_{ctm}	0.67	0.17	0.26	0.32	1.03	0.444	0.551	395
Yang ²⁴	41	$\text{with} f_{ctd}$	1.11	0.40	0.36	0.48	2.29	0.203	0.179 0.436 0.341 0.162 0.498 0.210 0.187 0.551 0.257 0.231	175
Brunesi and	42	EC2+RF (C_s) with f_{ctm}	0.96	0.25	0.26	0.55	1.54	0.190	0.231	209
Nascimbene ¹⁸	43	EC2+RF (C_s) with f_{ctd}	1.33	0.35	0.26	0.76	2.18	0.195	0.234	127
Park et al. ¹³	44	ACI 318+RF = η refer to Table 1	1.44	0.39	0.27	0.75	2.43	0.255	0.308	151
El Sayed et al. ¹¹	45	ACI+RF = k refer to Table 1	1.19	0.27	0.23	0.65	1.83	0.177	0.216	155

^{*}Analysis repeated for comparison reasons.

The effective crack spacing S_{ze} is calculated as follows

$$S_{ze} = \frac{35 \, d_v}{15 + d_{ag}} \tag{23}$$

with $d_v = \max(0.9d_p, 0.72h)$; and d_{ag} is the maximum aggregate size, taken not greater than 20 mm. The web shear stress v_{cw} is determined using Eq. (10). Finally, the web-shear strength is estimated using Eq. (24)

$$V_{cw} = d_v v_{cw} \sum_{i=1}^{n} \varphi_{w,i} b_{w,i}$$
 (24)

It is worth noting that, as the effect of the axial load is not explicitly considered in this approach, the simplified method should be regarded as a conservative approach.

Limit condition for assessing strength decay of deep PHCS

In this study, deep PHCS were defined as members with $h \ge 315$ mm, as recommended by the ACI 318 Code. ¹⁶ However, as shown in Fig. 10, the V_{test}/V_{pred} did not exhibit a strong correlation respect to the member thickness. In other words, in many cases, unmodified provisions were able to predict the web-shear strength of deep members. For instance, the application of the ACI 318-19 method in members with thicknesses within the range of 350 to 450 mm resulted in V_{test}/V_{pred} ranging from 0.57 to 1.52. However, for members with h > 450 mm, V_{test}/V_{pred} ranged from 0.91 to 1.21.

In response, this study proposes a new parameter based on the effective depth and the ratio of outer-to-inner web thickness $d_p(b_{w,ext}/b_{w,int})$ as the limiting condition for using the proposed modified design provisions. Figures 10(d) to (f) show the measured-to-predicted ratios versus the proposed parameter for the current design provision. As can be seen, for values

of the proposed parameter less than 400 mm, current design provisions predict the web-shear capacity of the members satisfactorily. Nonetheless, for greater values, significant decreases in web-shear strength are observed. Moreover, the correlation between the proposed parameter and V_{test}/V_{pred} was indicated by the relatively high coefficient of determination R.

Example of application of modified ACI 318-19 approach

This example considers observation 39 of the compiled data set, reported in Palmer and Schultz.⁶ The PHCS was reported to fail in web-shear at an applied shear of 277.36 kN.

First, the suitability of the modified ACI 318-19 provisions needs to be checked. Because the parameter $d_p(b_{w,ext}/b_{w,int}) = 365 \text{ mm} \times (72.5 \text{ mm} / 48.4 \text{ mm}) = 542 \text{ mm} > 400 \text{ mm}$, the modified ACI 318-19 provision is used.

The cross section of the unit comprised six inner webs (48.8 mm wide) and two outer webs (72.5 mm wide). However, following the proposed design procedure in Fig. 7, two inner webs shall be neglected in the calculations due to their lack of prestressing strands. Therefore, $N_{ext} = 2$ and $N_{int} = 4$. The shear stress distribution factors are estimated as $\varphi_{w,int} = (48.8/72.5) = 0.67$ and $\varphi_{w,ext} = (72.5/72.5) = 1$, then the web shear stress, according to the modified ACI 318-19 approach (Eq. (15)), is calculated as follows

$$\begin{bmatrix} v'_{cw,ext} \\ v'_{cw,int} \end{bmatrix} = 0.29 \sqrt{55.1} + 0.3 \times 0.5 \times 0.48 \times \begin{bmatrix} 1.86 \\ 2.75 \end{bmatrix}$$
$$= \begin{bmatrix} 2.43 \\ 2.57 \end{bmatrix} MPa$$

with the effective shear stress computed as

$$v_{cw} = \min\left(\frac{2.43}{1}, \frac{2.57}{0.67}\right) = 2.43 \text{ MPa}$$

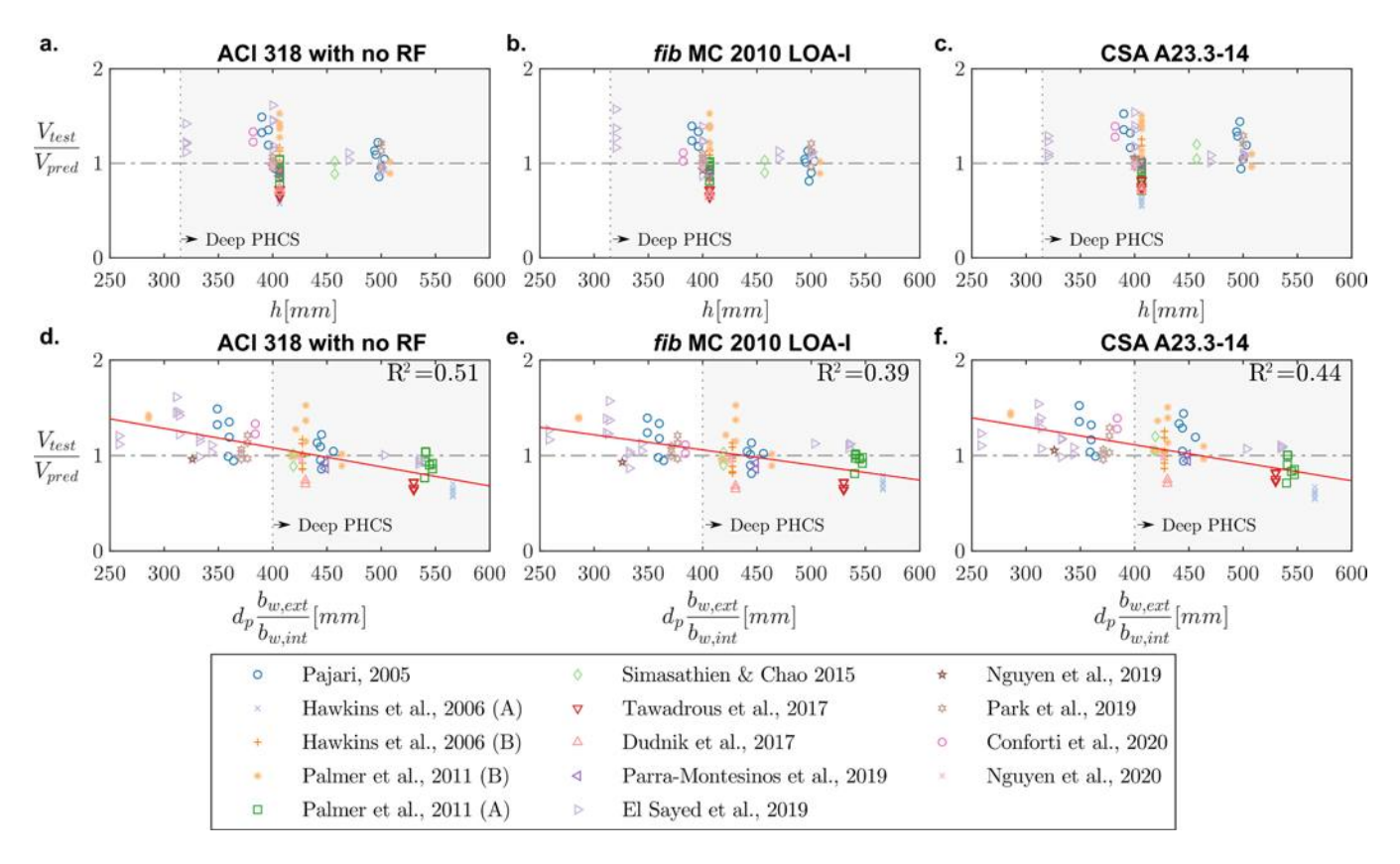


Fig. 10—Measured-to-predicted ratios versus height and limiting parameter d_p(b_{w,ext}/b_{w,int}).

Finally, for typical cases, the web-shear strength is given by Eq. (25)

$$V_{cw} = v_{cw}(\varphi_{w,ext}b_{w,ext}N_{ext} + \varphi_{w,int}b_{w,int}N_{int})d_p$$
 (25)

Therefore, $V_{cw} = 2.43 \times (1 \times 72.5 \times 2 + 0.67 \times 48.8 \times 4) \times (363.5/1000) = 244 \text{ kN}.$

Using the simplified approach—that is, assuming φ_{pc} = 0—the web-shear strength is computed as

$$V_{cw} = 0.29\sqrt{55.1}(1 \times 72.5 \times 2 + 0.67 \times 48.8 \times 4) \times (363.5/1000) = 216 \text{ kN}$$

Thus, $V_{test}/V_{pred} = 277.36 \text{ kN/244 kN} = 1.14 \text{ is calculated}$ for the modified ACI 318 expression. For the simplified expression, the ratio is $V_{test}/V_{pred} = 277.36 \text{ kN/216 kN} = 1.28$. For comparison purposes, the ACI 318-19 web-shear expression ratio is 1.47 (with RF = 0.5) and 0.73 (no RF), respectively. Similar procedures are used for the modified fib MC 2010 and CSA A23.3 design procedures.

COMPARATIVE ACCURACY AND SAFETY OF MODIFIED EXPRESSIONS

Comparison against current design provisions

Figure 11 shows measured-to-predicted ratios versus the $d_p(b_{w,ext}/b_{w,int})$ parameter for current design provisions, the previous proposal, and modified provisions. The measured-to-predicted ratios for the current design provisions (Fig. 11(a) to (c)) indicated that proposed modifications (Fig. 11(g) to (i)) offer safer predictions without compromising accuracy. For instance, proposed modifications lead

to an increase in minimum V_{test}/V_{pred} values compared to current design provisions, with improvements ranging from 0.57 to 0.86 (ACI 318-19), 0.64 to 0.86 (*fib* MC 2010), and 0.54 to 0.80 (CSA A23.3). Mean values of modified design expressions are less than 1.25, with COV ranging from 0.17 to 0.18, indicating a "very good" score based on the system presented by Frosch and Wolf.³⁷

Modifications to the ACI 318-19 provisions led to notable improvements, including a 20% reduction in total PEN (from 114 to 90) and decreased COV by 22% (from 0.23 to 0.18).

The current design approach of ACI 318, which involves an RF of 0.5, prioritizes safety over accuracy, as evidenced by the V_{test}/V_{pred} ranging from 1.14 to 3.23, with a mean of 2.05 and COV of 0.23. However, this degree of conservatism may be unnecessary given that the simplified ACI-modified expression ($\varphi_{pc} = 0$) proposed in this study displayed significantly superior statistical parameters. The proposed simplified approach yielded V_{test}/V_{pred} ranging from 0.92 to 1.96, a mean of 1.36, and a COV of 0.18, and resulted in improvements in the total PEN by 21%, the NMAE by 47%, and the NRSME by 42%.

The proposed modifications to the *fib* MC 2010 expression showed significant improvements in safety. Despite using the design tensile strength f_{ctd} , unsafe V_{test}/V_{pred} values were still calculated. The statistical parameters also showed enhancements, including an increase in the minimum value of V_{test}/V_{pred} from 0.64 to 0.86 and a decrease in both COV from 0.21 to 0.17 and total PEN by 27% compared to the code provision.

For the CSA A23.3 provision, significant decreases in the COV of 18% (0.22 to 0.18) and total PEN of 27% (134 to

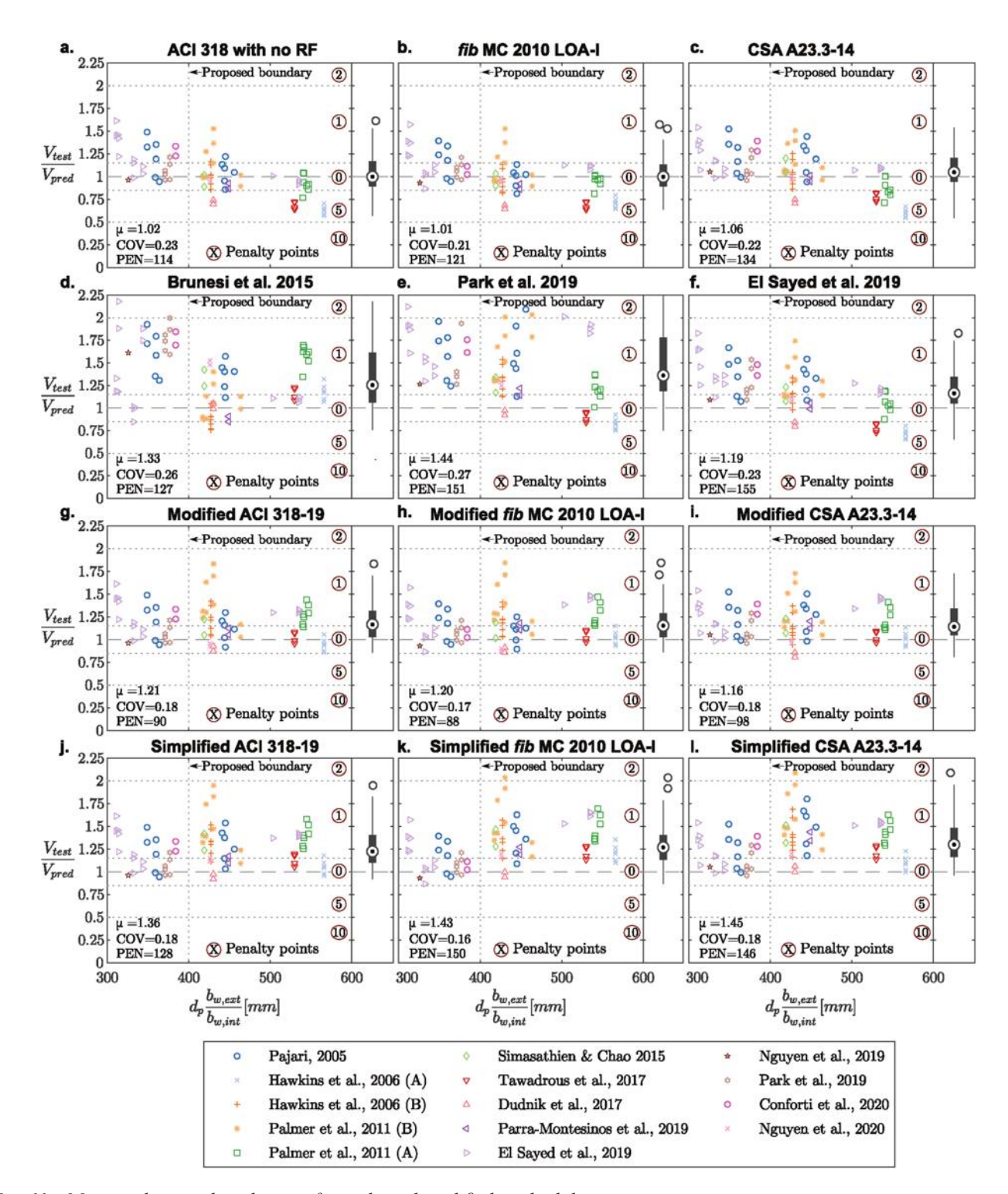


Fig. 11—Measured-to-predicted ratios for code and modified methodologies.

98) were computed. Meanwhile, minimal reductions were measured in the NMAE (6%) and the NRSME (4%).

Comparison against previous proposals in literature

Figures 11(d) to (f) display measured-to-predicted ratios for previous proposals in the literature. Similar to current design provisions, the modified design expressions outperformed the statistical parameters of previous proposals. For example, modifying the ACI 318 web-shear strength provision resulted in reductions of 31%, 33%, and 20% in COV

compared to the formulations by Brunesi and Nascimbene, ¹⁸ Park et al., ¹³ and El Sayed et al., ¹¹ respectively. The total PEN also decreased by 29%, 40%, and 41%, respectively. Moreover, the simplified ACI 318 approach proposed in this work also exhibited superior performance compared to previous proposals in terms of statistical parameters (refer to Tables 3 and 4). Likewise, a safer minimum value of V_{test}/V_{pred} of 0.96 was measured, in comparison with the minimum V_{test}/V_{pred} for the previous proposals of 0.76 (Brunesi and Nascimbene¹⁸), 0.75 (Park et al. ¹³), and 0.65 (El Sayed et al. ¹¹).

CONCLUSIONS

This study evaluated the main factors affecting the shear strength of deep prestressed hollow core slabs (PHCS). To this end, the accuracy and safety of three main design methods used to estimate deep PHCS's web-shear strength were first assessed, confirming unsatisfactory demand-to-capacity ratios.

The effect of three factors on the web-shear strength—that is, effective compressive stress, biaxial tensile strength, and shear stress distribution across the section width—was identified and quantified.

A tensile strength reduction factor of 0.60 was found to be required due to the biaxial stress state at the critical point and the typical use of high-strength concrete in the manufacturing of PHCS.

In addition, a new approach was introduced for incorporating the shear stress distribution into design provisions. The proposals account for the typical differences in the width and prestressing level in outer and inner webs.

Furthermore, the study proved that reducing the effective compressive stress in concrete at the critical point to 50% improved web-shear strength predictions. This reduction factor was supported by previous research attributing changes in the effective compressive stress to factors such as void shape, shear lag, and greater initial end slip, which are expected to be more critical in deep PHCS.

Although additional parameters such as size-effect factor and parabolic stress ratio were evaluated, they had minimal impact on the predictions and were excluded from the final expression for simplicity.

The proposed modifications to current design provisions improved safety and accuracy, increasing the minimum testto-predicted strength ratio, and decreasing the coefficient of variation (COV). Moreover, a simplified design procedure was presented, which neglects the beneficial effect of the prestressing force on the shear capacity. The simplified approach showed significant improvements in safety and accuracy compared to current design provisions and previous proposals in the literature.

The study recommended a new parameter to limit the application of current design provisions based on the effective depth and the ratio of outer-to-inner web thickness. It was shown that for values greater than 400 mm, proposed modifications in design provisions are necessary to avoid overestimating web-shear strength. This parameter can also be a limiting condition for cross-section geometry, but further research is needed to validate its applicability.

Finally, although the proposed modifications can be easily integrated into design standards, experimental investigations and validations are recommended to refine the proposed methodologies.

AUTHOR BIOS

Ernesto Hernández is a PhD Candidate in earthquake engineering at the University of Canterbury, Christchurch, New Zealand. His research interests include the shear behavior, seismic performance, modeling, and sustainability of concrete structures.

Alessandro Palermo is a Professor of Structural Engineering in the Department of Civil and Natural Resources Engineering at the University of Canterbury. His research interests include structural engineering,

140

with a special emphasis on developing and implementing innovative and sustainable technologies that minimize post-earthquake damage to the built

Ali Amin is a Senior Lecturer in the School of Civil Engineering at the University of Sydney, Sydney, NSW, Australia. He received his BE and PhD from the University of New South Wales, Sydney, NSW, Australia, in 2011 and 2015, respectively. His research interests include the structural design and analysis of fiber-reinforced and high-performance concretes.

NOTATION

area of PHCS section A_c

a, b,

c, dparameters in Hampel et al.'s failure envelope

shear span

web width at neutral axis

outer web width at neutral axis $b_{w,ext}$

width at web type i

inner web width at neutral axis width of unreinforced webs

 C_s strength modification factor taking into account void's shape in

Brunesi and Nascimbene's method

 $C_1, C_2,$

constants for determining C_s in Brunesi and Nascimbene's

method

effective depth prestressing force

concrete compressive strength

effective compressive stress in concrete

effective compressive stress in concrete at web i

tensile strength

design tensile strength

effective stress in prestressing steel after allowances for all

prestress losses

biaxial tensile strength

overall thickness or depth of member

second moment of area

transmission length of prestressing strands according to fib MC $l_{bpt,95\%} =$

transfer of transmission length of prestressing strands

 l_x distance from edge of member to critical point

number of entries in data set

 $Q \atop R_{2ct}$ first moment of area above and about centroidal axis

reduction factor for tensile strength

first moment of area above and about centroidal axis in fib MC

2010 design provision

cracking shear strength

cracking shear strength of outer webs

 $V_{\mathit{cr},int}$ cracking shear strength of inner webs

web-shear strength

predicted web-shear strength

measured shear strength

maximum web-shear strength per web type

shear stress

 v_{cw} effective web-shear stress considering shear distribution

 $v_{cw,i}'$ web-shear stress from design standards

height of neutral axis

 y_i actual value

 \hat{y}_i predicted value

 φ_{cp} reduction factor to effective compressive stress in concrete

shear stress factor at web i principal stress in tension

principal stress in compression

REFERENCES

- 1. Anderson, A. R., "Shear Strength of Hollow Core Members," Technical Bulletin 78-B1, Concrete Technology Associates, Tacoma, WA, 1978.
- 2. Becker, R. J., and Buettner, D. R., "Shear Tests of Extruded Hollow-Core Slabs," PCI Journal, V. 30, No. 2, 1985, pp. 40-54. doi: 10.15554/ pcij.03011985.40.54
- 3. Walraven, J. C., and Mercx, W. M., "The Bearing Capacity for Prestressed Hollow Core Slabs," Heron, V. 28, No. 3, 1983, pp. 1-46.
- 4. Pajari, M., "Resistance of Prestressed Hollow Core Slabs against Web Shear Failure," VTT Research Notes 2292, Technical Research Centre of Finland, Espoo, Finland, 2005.
- 5. Hawkins, N. M., and Ghosh, S. K., "Shear Strength of Hollow-Core Slabs," PCI Journal, V. 51, No. 1, 2006, pp. 110-114.

- 6. Palmer, K. D., and Schultz, A. E., "Experimental Investigation of the Web-Shear Strength of Deep Hollow-Core Units," *PCI Journal*, V. 56, No. 4, 2011, pp. 83-104. doi: 10.15554/pcij.09012011.83.104
- 7. Simasathien, S., and Chao, S.-H., "Shear Strength of Steel-Fiber-Reinforced Deep Hollow-Core Slabs," *PCI Journal*, V. 60, No. 4, 2015, pp. 85-101. doi: 10.15554/pcij.07012015.85.101
- 8. Tawadrous, R., and Morcous, G., "Shear Strength of Deep Hollow-core Slabs," *ACI Structural Journal*, V. 115, No. 3, May 2018, pp. 699-709. doi: 10.14359/51701298
- 9. Dudnik, V. S.; Milliman, L. R.; and Parra-Montesinos, G. J., "Shear Behavior of Prestressed Steel-Fiber-Reinforced Concrete Hollow-Core Slabs," *PCI Journal*, V. 62, No. 4, 2017, pp. 58-72.
- 10. Parra-Montesinos, G. J.; Fargier-Gabaldón, L. B.; and Al-Tameemi, M., "Shear Strength of Precast, Prestressed Steel Fiber Reinforced Concrete Hollow-Core Slabs," Department of Civil and Environmental Engineering, University of Wisconsin-Madison, Madison, WI, 2019.
- 11. El-Sayed, A. K.; Al-Negheimish, A. I.; and Alhozaimy, A. M., "Web Shear Resistance of Prestressed Precast Deep Hollow Core Slabs," *ACI Structural Journal*, V. 116, No. 1, Jan. 2019, pp. 139-150.
- 12. Nguyen, T. N. H.; Tan, K.-H.; and Kanda, T., "Investigations on Web-Shear Behavior of Deep Precast, Prestressed Concrete Hollow Core Slabs," *Engineering Structures*, V. 183, 2019, pp. 579-593. doi: 10.1016/j. engstruct.2018.12.052
- 13. Park, M.-K.; Lee, D. H.; Han, S.-J.; and Kim, K. S., "Web-Shear Capacity of Thick Precast Prestressed Hollow-Core Slab Units Produced by Extrusion Method," *International Journal of Concrete Structures and Materials*, V. 13, No. 1, 2019, p. 7. doi: 10.1186/s40069-018-0288-x
- 14. Conforti, A.; Ortiz-Navas, F.; Piemonti, A.; and Plizzari, G. A., "Enhancing the Shear Strength of Hollow-Core Slabs by Using Polypropylene Fibres," *Engineering Structures*, V. 207, 2020, p. 110172. doi: 10.1016/j.engstruct.2020.110172
- 15. Nguyen, H. T. N.; Tan, K. H.; and Kanda, T., "Effect of Polypropylene and Steel Fibers on Web-Shear Resistance of Deep Concrete Hollow-Core Slabs," *Engineering Structures*, V. 210, 2020, p. 110273. doi: 10.1016/j.engstruct.2020.110273
- 16. ACI Committee 318, "Building Code Requirements for Structural Concrete (ACI 318-19) and Commentary (ACI 318R-19) (Reapproved 2022)," American Concrete Institute, Farmington Hills, MI, 2019, 624 pp.
- 17. Palmer, K. D., and Schultz, A. E., "Factors Affecting Web-Shear Capacity of Deep Hollow-Core Units," *PCI Journal*, V. 55, No. 2, 2010, pp. 123-146. doi: 10.15554/pcij.03012010.123.146
- 18. Brunesi, E., and Nascimbene, R., "Numerical Web-Shear Strength Assessment of Precast Prestressed Hollow Core Slab Units," *Engineering Structures*, V. 102, 2015, pp. 13-30. doi: 10.1016/j.engstruct.2015.08.013
- 19. EN 1992-1-1, "Eurocode 2: Design of Concrete Structures Part 1-1: General Rules and Rules for Buildings," European Committee for Standardization, Brussels, Belgium, 2005.
- 20. Fan, S.; Zhang, Y.; Nguyen, T. N. H.; and Tan, K. H., "Toward Consistent Prediction of Web-Shear Capacity for Hollow-Core Slabs Using Strut-and-Tie Models," *Journal of Structural Engineering*, ASCE, V. 148, No. 7, 2022, p. 04022081 doi: 10.1061/(ASCE)ST.1943-541X.0003346

- 21. Jonsson, E., "Shear Capacity of Prestressed Extruded Hollow-Core Slabs," *Nordic Concrete Research*, V. 7, 1988, pp. 167-187.
- 22. fib, "fib Model Code for Concrete Structures 2010," Fédération Internationale du Béton, Lausanne, Switzerland, 2013.
- 23. CSA A23.3-14, "Design of Concrete Structures," CSA Group, Toronto, ON, Canada, 2014.
- 24. Yang, L., "Design of Prestressed Hollow Core Slabs with Reference to Web Shear Failure," *Journal of Structural Engineering*, ASCE, V. 120, No. 9, 1994, pp. 2675-2696. doi: 10.1061/(ASCE)0733-9445(1994)120:9(2675)
- 25. Pajari, M., "Web Shear Failure in Prestressed Hollow Core Slabs," *Journal of Structural Mechanics*, V. 42, No. 4, 2009, pp. 83-104.
- 26. Brooks, M. D., and Gerstle, K. H., "Effect of Initial Strand Slip on the Strength of Hollow-Core Slabs," *PCI Journal*, V. 33, No. 1, 1988, pp. 90-111. doi: 10.15554/pcij.01011988.90.111
- 27. Hampel, T.; Speck, K.; Scheerer, S.; Ritter, R.; and Curbach, M., "High-Performance Concrete under Biaxial and Triaxial Loads," *Journal of Engineering Mechanics*, ASCE, V. 135, No. 11, 2009, pp. 1274-1280. doi: 10.1061/(ASCE)0733-9399(2009)135:11(1274)
- 28. Kupfer, H.; Hilsdorf, H. K.; and Rusch, H., "Behavior of Concrete Under Biaxial Stresses," *ACI Journal Proceedings*, V. 66, No. 8, Aug. 1969, pp. 656-666.
- 29. Hussein, A., and Marzouk, H., "Behavior of High-Strength Concrete under Biaxial Loading," *ACI Structural Journal*, V. 97, No. 1, Jan.-Feb. 2000, pp. 27-36.
- 30. Kupfer, H. B., and Gerstle, K. H., "Behavior of Concrete under Biaxial Stresses," *Journal of the Engineering Mechanics Division*, ASCE, V. 99, No. 4, 1973, pp. 853-866. doi: 10.1061/JMCEA3.0001789
- 31. Marí, A.; Bairán, J. M.; Cladera, A.; and Oller, E., "Shear Design and Assessment of Reinforced and Prestressed Concrete Beams Based on a Mechanical Model," *Journal of Structural Engineering*, ASCE, V. 142, No. 10, 2016, p. 04016064. doi: 10.1061/(ASCE)ST.1943-541X.0001539
- 32. Traina, L. A., and Mansour, S. A., "Biaxial Strength and Deformational Behavior of Plain and Steel Fiber Concrete," *ACI Materials Journal*, V. 88, No. 4, July-Aug. 1991, pp. 353-362.
- 33. Task Group 8.2, "Constitutive Modelling of High Strength / High Performance Concrete," *fib* Bulletin 42, Fédération Internationale du Béton, Lausanne, Switzerland, 2008.
- 34. Plemenos, D., and Miaoulis, G., eds., *Intelligent Computer Graphics* 2010, Springer, 2010, 256 pp.
- 35. Collins, M. P., "Evaluation of Shear Design Procedures for Concrete Structures," report prepared for the CSA Technical Committee on Reinforced Concrete Design, 2001.
- 36. Moraes Neto, B. N.; Barros, J. A. O.; and Melo, G. S. S. A., "Model to Simulate the Contribution of Fiber Reinforcement for the Punching Resistance of RC Slabs," *Journal of Materials in Civil Engineering*, ASCE, V. 26, No. 7, 2014, p. 04014020. doi: 10.1061/(ASCE)MT.1943-5533.0000913
- 37. Frosch, R., and Wolf, T., "Simplified Shear Design of Prestressed Concrete Members," Purdue University, West Lafayette, IN, 2003.

Ciassoom

Integrate (aci) into your classroom!

To support future leaders, ACI has launched several initiatives to engage students in the Institute's activities and programs – select programs that may be of interest to Educators are:

- Free student membership encourage students to sign up
- Special student discounts on ACI 318
 Building Code Requirements for Structural
 Concrete, ACI 530 Building Code Requirements and Specification for Masonry
 Structure, & Formwork for Concrete manual.
- Access to Concrete International free to all ACI student members
- Access to ACI Structural Journal and ACI Materials Journal – free to all ACI student members
- Free sustainability resources free copies of Sustainable Concrete Guides provided to universities for use in the classroom
- Student competitions participate in ACI's written and/or team-based competitions

- Scholarships and fellowships students who win awards are provided up to \$15,000 and may be offered internships and paid travel to attend ACI's conventions
- ACI Award for University Student Activities receive local and international recognition for your University's participation in concreterelated activities
- Free access to the ACI Collection of Concrete Codes, Specifications, and Practices – in conjunction with ACI's chapters, students are provided free access to the online ACI Collection
- ACI online recorded web sessions and continuing education programs – online learning tools ideal for use as quizzes or in-class study material

Title No. 121-S24

Outrigger Action in Tall Core-Wall Buildings with Flat-Plate Framing

by Connie I. Chen and Jack P. Moehle

In tall core-wall buildings with concrete unbonded post-tensioned flat-plate gravity framing, modeling the behavior of the slab-wall-column framing under earthquake loading can be crucial to determining structural response quantities for the design of the flat-plate framing. The outrigger action of the gravity system also affects the overall dynamic properties of the building and may affect wall moment and shear demands. The outrigger effect can be modeled using a slab-beam model, which uses linear-elastic frame elements with concentrated nonlinear hinges at each end. In this study, the slab-beam model is calibrated using results from a slab-wall-column laboratory test. Recommendations suitable for design-office practice are presented.

Keywords: earthquake engineering; flat plate; gravity framing; nonlinear modeling; outrigger action; plastic hinge; post-tensioned slab; slab-column joint; slab-wall connection.

INTRODUCTION

Reinforced concrete core walls are a prevalent seismicforce-resisting system in tall buildings. The typical layout is a centrally located core wall surrounded by gravity framing, which often consists of concrete unbonded posttensioned slab-column framing. The slab-column framing acts as an outrigger for the overall building and thereby contributes to the overall overturning resistance. The resulting accumulation of axial forces on the perimeter columns can potentially be large enough to control the column design. For these reasons, guidelines for tall building design (PEER TBI 2017; LATBSDC 2020) recommend that gravity framing be included in the dynamic analysis model to obtain the best estimate of the expected response.

ASCE/SEI 7-16 (2017) and ACI 318-19 (ACI Committee 318 2019) require gravity systems to be designed for gravity loads, including vertical seismic load effects. ASCE/SEI 7 also requires the gravity system under risk-targeted maximum considered earthquake (*MCE_R*) loading to satisfy deformation compatibility using the mean building displacements from the suite of nonlinear response-history analyses. The current prescriptive provisions of the building code are based on a traditional approach that requires that the prescribed lateral forces be resisted by vertical elements of the seismic-force-resisting system that have been detailed to be capable of lateral force resistance without critical strength decay. For reinforced concrete, only special moment frames and special structural walls (and not flat-plate frames) are permitted to resist prescribed lateral earthquake forces.

The coupling between a core wall and slab-column framing can be modeled by including equivalent slab-beams connecting the core walls to the perimeter columns. The slab-beam model can be an assembly of a linear-elastic frame element, representing the effective stiffness of the slab, and nonlinear moment-rotation hinges at both ends, representing the post-yield response of the slab-wall and slab-column connections. In this study, the stiffness and strength of the slab-beams are calibrated using test results reported by Klemencic et al. (2006). An example calculation using a typical story of a tall core-wall building with flatplate gravity framing shows the importance of considering the "outrigger effect" when determining column axial forces for design.

RESEARCH SIGNIFICANCE

This study proposes a model for the stiffness and strength of slab-wall-column outrigger framing systems calibrated by laboratory test data. An example calculation of the outrigger effect on column axial force in a typical story of a tall corewall building shows the potential importance of including the slab outrigger effect in design.

STRUCTURAL SYSTEM DESCRIPTION

This study is developed considering a 40-story-tall archetypal building with the floor plan shown in Fig. 1. The structural system includes a centrally located core wall, which supports gravity loads and is the primary lateral-forceresisting system, and slab-column framing, which is intended primarily to support gravity loads. For tall buildings on the West Coast of the United States, wall thicknesses typically range from 24 to 42 in. (610 to 1070 mm), and column cross-sectional dimensions typically range from 24 to 48 in. (610 to 1220 mm). Typical unbonded post-tensioned flat-plate floors have thicknesses of approximately 8 in. (203 mm) with spans of approximately 25 to 35 ft (7.6 to 10.7 m), although shorter spans sometimes occur to accommodate architectural requirements.

The two options for construction are either to cast the wall ahead of the slab-column framing and then cast the slab-column framing with connections to the previously cast wall, or to cast each level and its components sequentially along the height of the building. The first option creates a vertical cold joint between the flat plate and the core wall. The cold joint needs to be capable of resisting out-of-plane

ACI Structural Journal, V. 121, No. 2, March 2024.

MS No. S-2023-062.R l, doi: 10.14359/51740250, received September 20, 2023, and reviewed under Institute publication policies. Copyright © 2024, American Concrete Institute. All rights reserved, including the making of copies unless permission is obtained from the copyright proprietors. Pertinent discussion including author's closure, if any, will be published ten months from this journal's date if the discussion is received within four months of the paper's print publication.

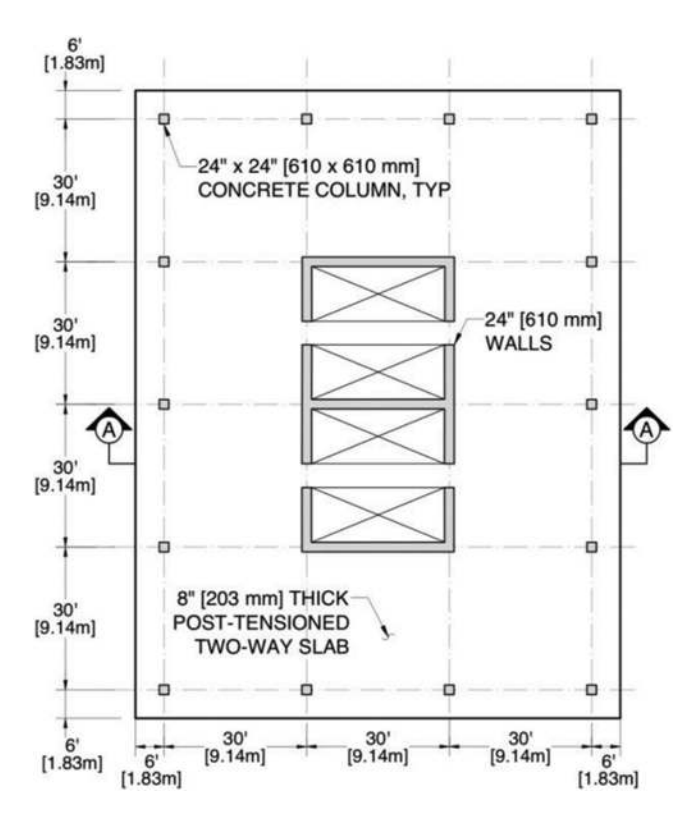


Fig. 1—Plan view of mid-level floor of archetypal tall corewall building with flat-plate gravity framing.

shear and moment due to gravity and other loads as well as in-plane diaphragm forces, all while sustaining rotations as the building sways under earthquake shaking. A common approach is to anchor the slab post-tensioning just short of the wall and lap-splice it with mild reinforcement that connects across the vertical joint at the wall interface using form-saver mechanical splices. Questions about the performance capability of this connection detail led to the development of a laboratory testing program.

LABORATORY TESTS

Laboratory tests were conducted to study the behavior of the slab-wall-column framing described in the previous section (Klemencic et al. 2006). The present study focuses on Specimen 2 of that test program. The test specimen dimensions are shown in Fig. 2. The 10 ft (3.05 m) width of the specimen represents approximately one-third of a typical span in the transverse direction. The slab had six ASTM A416 Grade 270, 1/2 in. (13 mm) diameter unbonded post-tensioning tendons spaced at 18 in. (457 mm) on center, draped in the longitudinal direction to be 6.5 in. (165 mm) above the bottom of the slab at the column and 1 in. (25 mm) above the bottom of the slab at midspan, with anchors placed one slab thickness (8 in. [203 mm]) from the face of the wall. Figure 3 identifies additional details at the slab-wall connection. The slab-column connection was reinforced with 10 No. 5 (No. 16) top bars centered on the column in each direction and three No. 5 (No. 16) bottom bars through the column cage. All nonprestressed reinforcement was ASTM A615 Grade 60 (Grade 420). The slab-column connection had three stud rails extending from each face, each with nine 1/2 in. (13 mm) diameter studs at 3-3/4 in.

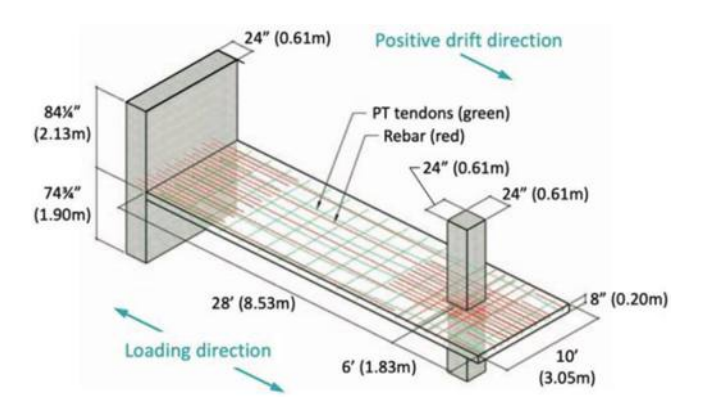


Fig. 2—Isometric view of test specimen (adapted from Klemencic et al. [2006]). (Full-color PDF can be accessed at www.concrete.org.)

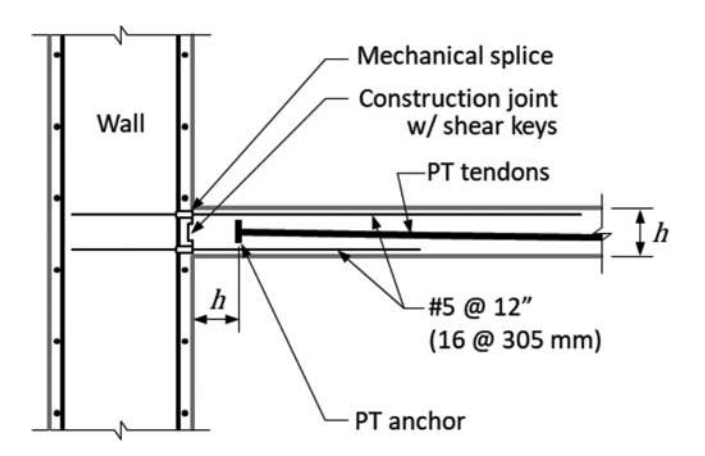


Fig. 3—Test specimen detailing at slab-wall connection for Specimen 2.

(95 mm) spacing made from low-carbon steel C1015 in accordance with ASTM A108 ($f_y = 50 \text{ ksi } [345 \text{ MPa}]$). The mean concrete compressive strength of the slab concrete was 6.1 ksi (42 MPa).

In the test setup, lead weights were distributed over the plan area of the slab to simulate expected superimposed gravity loads of approximately 30.5 lb/ft² (1.46 kPa). The wall and column were pinned at the base, and reversed cyclic lateral forces were applied simultaneously at the top of the wall and column in the loading direction, as shown in Fig. 2. The lateral forces resulted in reversed cyclic lateral displacements with progressively increasing amplitudes corresponding to drift ratios. Positive drift ratio was defined as the direction from the wall toward the column. In a real building, loading in the negative direction would subject the wall segment (representing the wall flange) to flexural tension, resulting in wall flange uplift in upper stories that would increase the rotational demands on the slab. To approximate this effect, the testing protocol doubled the imposed displacements for loading in the negative direction (Klemencic et al. 2006).

Figure 4 presents the measured relationship between total lateral force and lateral drift ratio. (The building equivalent drift ratio is defined as the test specimen drift ratio for positive drifts and half those values for negative drifts to approximate the uplift effect described in the previous paragraph.)

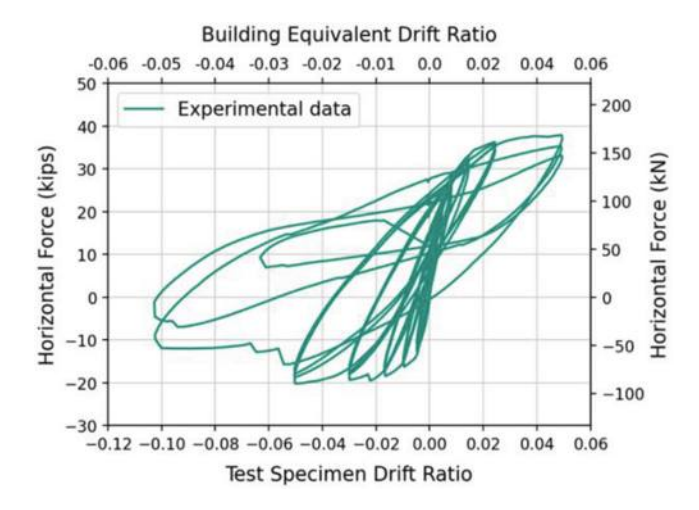


Fig. 4—Measured relationship between total horizontal force and drift ratio.

The relationship shows nearly linear behavior for small drift ratios with progressively softer, nonlinear behavior as drift amplitudes increased. Strength degradation resulting from the fracture of slab top dowel bars is apparent for building equivalent drift ratios beyond -0.025.

The calculation of slab moment strength requires an estimate of the post-tensioning force in the slab. Figure 5 shows the measured force in a single strand as a function of the test specimen drift ratio. This study is mainly interested in positive drift ratios, as these correspond to hogging rotation in the slab (that is, tension near the top surface) near the slab-column connection. The strand force increases with both increasing lateral drift and repeated cycles at the same drift level.

The increase in post-tensioning force with increasing drift can be explained in terms of the idealized connection deformations shown in Fig. 6, which is adopted from ACI 550.3-13 (Joint ACI-ASCE Committee 550 2013). The interface of the slab and column is assumed to develop a single crack that rotates about the neutral axis. The opening of the crack at the level of the strand is $\delta_{prs} = \theta(d_p - c)$, where θ is the crack opening angle, d_p is the depth from the extreme compression fiber to the centroid of the strand, and c is the flexural compression depth at the probable moment strength. As a simplification, the opening angle θ is approximated as being equal to the drift ratio. If the crack opening produces strand elongation that is spread uniformly along the unbonded strand length L_{ups} , then the change in strain is $\Delta \varepsilon_{prs} = \delta_{prs}/L_{ups}$. Note that a significant change in stress would only occur under positive drift (hogging rotation at the column) because of the 6.5 in. (165 mm) elevation of the strand above the bottom of the slab at the column. A crack opening at the slab-wall connection does not produce strand elongation because the strand stops one slab thickness from the face of the wall. From this model, the change in strand force is $\Delta F_{ps} = A_{ps}E_{ps}\Delta \varepsilon_{ps}$, where the area of a single tendon $A_{ps} = 0.153 \text{ in.}^2 \text{ (98.7 mm}^2\text{)}$ and the modulus of elasticity $E_{ps} = 27,000$ ksi (197,000 MPa). Combining terms, the change in strand force ΔF_{ps} in terms of drift ratio (δ_x/h_{sx}) is

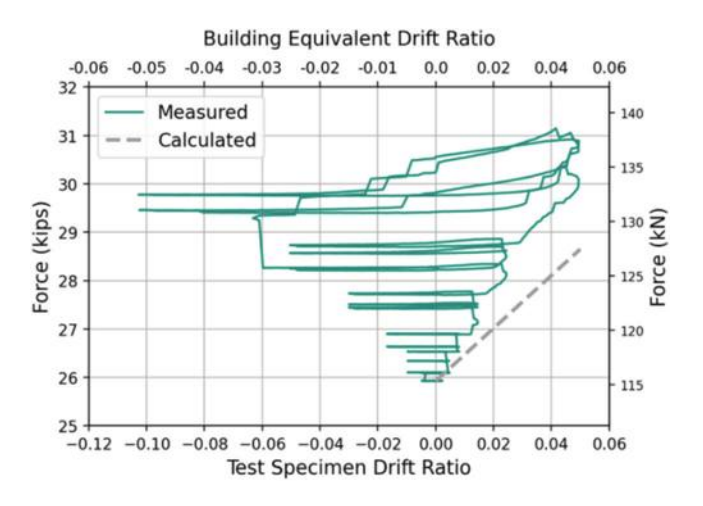


Fig. 5—Measured and calculated strand prestress force versus drift ratio.

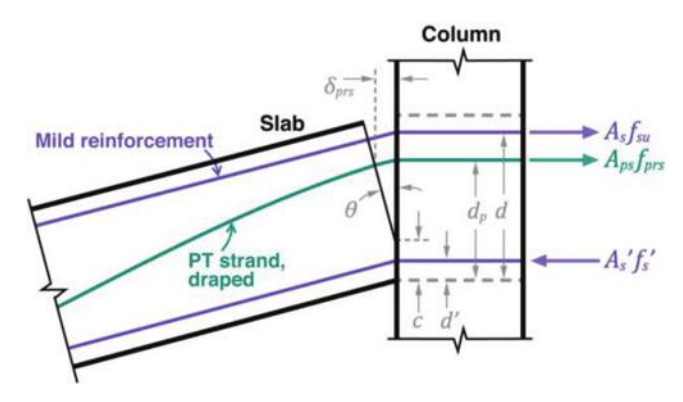


Fig. 6—Rotation of slab-column joint elongates prestressing strand.

$$\Delta F_{ps} = A_{ps} E_{ps} \frac{d_p - c}{L_{ups}} \left(\frac{\delta_x}{h_{sx}} \right)$$
 (1)

Figure 5 shows the calculated variation of strand tensile force with increasing drift ratio. The slope of the calculated relationship is close to the slope measured during loading cycles of increasing lateral drift. The calculated relationship falls short of the measured relationship overall, however, because the analytical model does not include the progressive increase in tendon force for repeated load cycles at constant amplitude.

EQUIVALENT FRAME MODELING

Modeling a slab-wall-column framing system using plate-bending elements is usually impractical for nonlinear response-history analysis of a tall building. A more common approach is to subdivide the flat plate into a series of equivalent frames spanning between the wall(s) and columns. Each equivalent frame consists of a slab-beam strip centered on a column representing the mechanical properties of the slab bounded by panel centerlines between columns (Fig. 7). Slab-column connections and slab-wall connections may have different mechanical properties because of their different support conditions. To represent this behavior, the approach adopted (Hwang and Moehle 2000) divides the slab-beam at the midpoint of the span, with different beam effective widths in the two beam halves (Fig. 7).

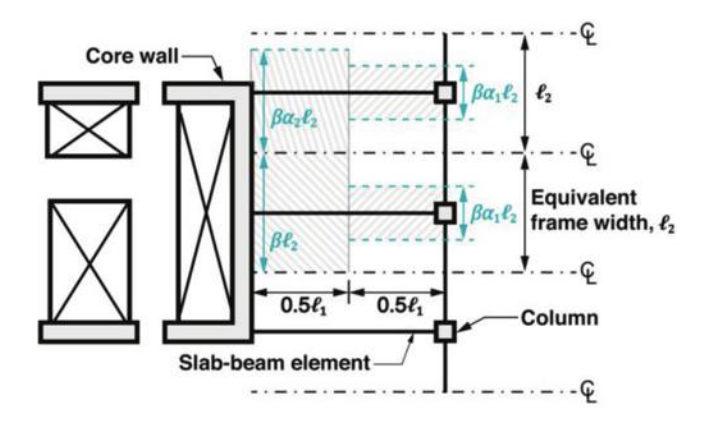


Fig. 7—Framing system is modeled using series of equivalent beam-column-wall frames.

In a complete building model, nonlinear behavior may occur in the slab, columns, and walls. A nonlinear response can be represented using a variety of nonlinear modeling approaches (for example, PEER TBI [2017]). To model the laboratory test specimen (Fig. 2), the model shown in Fig. 8 is adopted. The slab-beam model consists of three linear-elastic beam elements: one for the half span nearer the column, one for the half span nearer the wall, and another for the slab cantilever. A bilinear hysteretic moment-rotation hinge was placed at each end of the beam to represent the nonlinear slab-wall or slab-column response, which corresponds to a lateral side-sway mechanism that was confirmed by structural analysis. (Hinges distributed along the span should also be considered in cases where hinging could occur along the slab span.) The column and wall were significantly stronger than the slab connections and, consequently, were modeled using linear-elastic line elements.

Slab effective lateral stiffness

When a slab-column connection is subjected to lateral loading, the slab experiences moments and rotations that are largest near the column and decrease with increasing transverse distance from the column. Vanderbilt and Corley (1983) describe an equivalent or effective beam-width model in which the slab is replaced by a prismatic beam of width $b_e = \alpha \ell_2$ having equivalent rotational stiffness, where the coefficient α accounts for the nonuniform rotation of the slab across its width, and ℓ_2 is the width of the slab panel perpendicular to the direction that slab moments are being determined (Fig. 7). Flexural stiffness is calculated from the gross section of the slab considering the slab-beam effective width and total thickness h. Vanderbilt and Corley (1983) proposed an additional reduction factor β to account for the effect of slab cracking on effective stiffness.

Hwang and Moehle (2000) proposed that the coefficient b_e for interior slab-column connections be determined as

$$b_e = 2c_1 + \ell_1/3 \tag{2}$$

where c_1 is the dimension of the rectangular or equivalent rectangular column measured in the direction of the span ℓ_1 , where ℓ_1 is the span length in the direction that moments are being determined, measured center-to-center of supports.

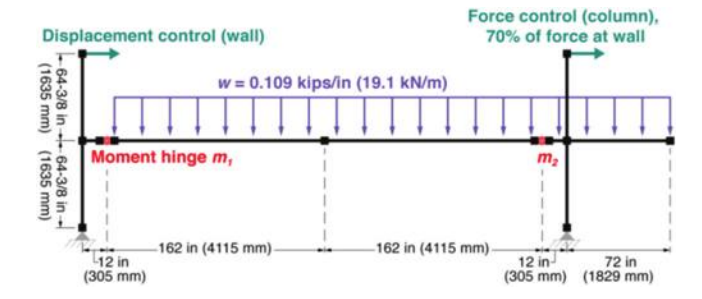


Fig. 8—Analytical model of specimen from laboratory test.

The equation was derived from the results of elastic-plate theory and finite element analyses for slab panels having $2/3 \le \ell_2/\ell_1 \le 3/2$. It is intended to be used in an analytical model that represents the slab-column joints as rigid. For a slab-wall connection in which the slab frames into the wall flange along its entire width, $b_e = \ell_2$ should be used. Based on a study summarized in Appendix A, for a slab-wall connection in which the slab frames into the wall flange along only a portion of its width, the value of b_e can be taken equal to the contact width plus 0.7 times the width of the equivalent frame extending beyond the flange.

For nonprestressed slabs, Hwang and Moehle (2000) proposed

$$\beta = \frac{4c_1}{\ell_1} \ge \frac{1}{3} \tag{3}$$

The lower limit of $\beta = 1/3$ is consistent with the proposal by Vanderbilt and Corley (1983). For post-tensioned slabs, Kang and Wallace (2005) proposed a lower limit of $\beta = 1/2$, considering reduced cracking due to the compression effects of prestressing. This approach to stiffness modeling using an effective beam width is recognized in ASCE/SEI 41-17 (2017).

In a building model where column and wall yielding might occur, the adopted analytical models should adequately represent the effects of axial-flexural interaction. For walls, it is also important to model flange uplift associated with axial elongation and neutral axis migration. For modeling this test specimen, however, inelastic response and uplift are not expected, so linear-elastic line elements are adopted for columns and walls.

The effective width represented by Eq. (2) is not directly applicable to the slab-column connection of the laboratory test structure because the transverse dimension of the test slab (Fig. 2) is only approximately one-third of the transverse span in a typical building (Fig. 1), and the slab aspect ratio falls outside the range for which Eq. (2) was derived. If this limitation is ignored, then the calculated effective width at the slab-column connection is equal to $b_e = 2 \cdot 24$ in. + 348 in./3 = 164 in. (2 · 0.61 m + 8.84 m/3 = 4.27 m), which exceeds the provided width of 120 in. (3.05 m). Here, $b_e = 120$ in. (3.05 m) is taken at both the column and wall connections, which is the correct value at the slab-wall connection but slightly overestimates the effective width at the slab-column connection. To account for slab cracking, the additional stiffness reduction factor $\beta = 1/2$ is applied.

Table 1—Summary of strength limits at slab-column connection

Strength limit		Expected strength at critical section	Moment strength at column face, kip·in. (kN·m)			
(a) One-way shear strength of	full slab	$V_n = 162 \text{ kip } (719 \text{ kN})^*$	23,000 (2600)			
(b) Elayanal atnonath of full clab	Hogging	$M_{pr} = 3150 \text{ kip} \cdot \text{in.} (360 \text{ kN} \cdot \text{m})$	3150 (360)			
(b) Flexural strength of full slab	Sagging	$M_{pr} = 1260 \text{ kip·in.} (143 \text{ kN·m})$	1260 (143)			
(c) Flexural strength of effective	Hogging	$M_{pr} = 1810 \text{ kip} \cdot \text{in.} (205 \text{ kN} \cdot \text{m})$	3020 (342)			
transfer width	Sagging	$M_{pr} = 764 \text{ kip in. } (86.3 \text{ kN m})$	1270 (144)			
(d) Two-way shear transferred acro	ss connection	$M_{sc} = 8490 \text{ kip·in. } (960 \text{ kN·m})^{\dagger}$	8030 (908)			

^{*}Located at h/2 from the face of the column.

[†]Located at the center of the critical section.

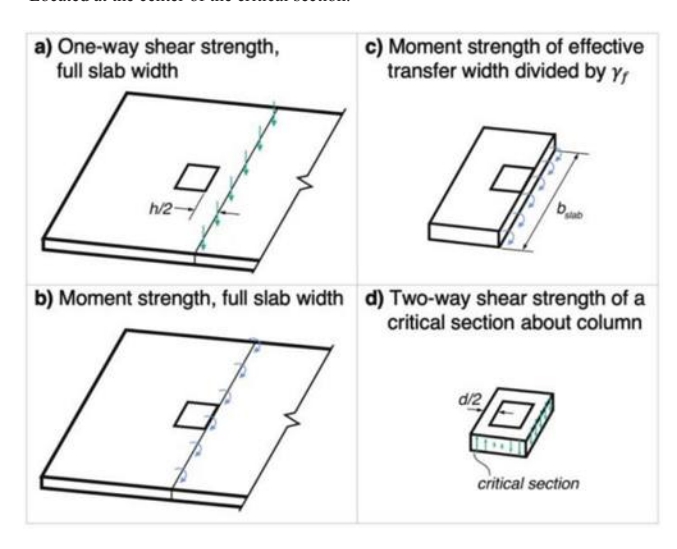


Fig. 9—Four limits on strength at slab-column connection.

Slab-wall and slab-column connection strengths

In the general case, connection strength can be limited by either the strength of the slab or the strength of the supporting column or wall. In the test structure (Fig. 2), as in most tall buildings, connection strength is limited by the slab.

The slab-wall connection strength is taken as the probable moment strength M_{pr} following the method in ACI 318. Zero axial force in the slab is assumed because the prestressing stops short of the wall (Fig. 3) and the externally applied forces in the test setup produce negligible slab axial force. (In a real building, however, there may be some in-plane inertial forces and precompression from the post-tensioned slab extending around the core wall.) Considering top and bottom Grade 60 No. 5 at 12 in. (Grade 420 No. 16 at 305 mm), the probable moment strength based on a maximum bar stress capacity of $1.25f_y$ is calculated as 1640 kip·in. (185 kN·m). One-way shear strength at the connection with the wall does not limit connection moment transfer strength.

At a slab-column connection, strength can be limited by four different strength quantities (Fig. 9): 1) one-way shear strength of the full transverse width of the slab; 2) moment strength of the full transverse width of the slab; 3) moment transfer strength as limited by slab moment capacity near the column; and 4) two-way shear strength of a critical section about the column.

The one-way nominal shear strength of the full transverse width of the slab is the sum of shear strength contributions from concrete and shear reinforcement, $V_n = V_c + V_s$, taken at

the critical section for prestressed slabs located at a distance h/2 from the face of the column. V_c is calculated following ACI 318 for concrete shear strength in prestressed flexural members, where V_c is the lesser of the flexure-shear strength and web-shear strength. The shear capacity provided by shear reinforcement in the form of three stud rails is $V_s =$ $3A_{v}f_{vt}d/s$, where A_{v} is the area of a single stud, f_{vt} is the stud yield strength, d is the effective depth of the slab (taken as at least 0.8h for prestressed two-way slabs), and s is the spacing of the studs measured perpendicular to the assumed one-way shear failure line. The moment at the face of the column corresponding to the development of V_n at h/2 from the face was estimated using a linear-elastic analytical model with geometry similar to the one shown in Fig. 8. The resulting moment greatly exceeded moments corresponding to other failure modes (Table 1), such that the details of the calculation were not critical.

The moment strength of the full transverse width of the slab is adapted from the ACI 318 method for the probable moment strength M_{pr} . The strain of the concrete section and bonded reinforcement is assumed to vary linearly through depth, with a peak compressive strain equal to 0.003. Stress in the bonded reinforcement is proportional to strain, up to a limiting stress of $1.25f_v$. Force in the unbonded prestressing strands is assumed to vary with lateral drift ratio, as described previously in relation to Fig. 6 and Eq. (1). The depth to the neutral axis c is obtained from iteration, assuming the axial force in the post-tensioned section is equal to the number of post-tensioning tendons multiplied by the calculated final prestress force per tendon, F_{ps} . Given the specified effective prestress force $F_{pe} = 26.8 \text{ kip/strand}$ (119 kN) before testing and the drift ratio at MCE_R demand levels is assumed equal to 1.5 times the design limit of 0.02, the calculated final prestress force F_{ps} for hogging rotation is

$$\Delta F_{ps} = A_{ps} E_{ps} \frac{d_p - c}{L_{ups}} \left(\frac{\Delta_x}{h_{sx}} \right) =$$

$$(0.153 \text{ in.}^2)(27,000 \text{ ksi}) \left(\frac{6.5 \text{ in.} - 1.22 \text{ in.}}{400 \text{ in.}} \right) (0.03) = 1.64 \text{ kip}$$

$$\left[(9.871 \times 10^{-5} \text{ m}^2)(186,200 \text{ MPa}) \left(\frac{0.1651 \text{ m} - 0.0310 \text{ m}}{10.16 \text{ m}} \right) \right]$$

$$= 7.28 \text{ kN}$$

$$F_{ps} = F_{pe} + \Delta F_{ps} = 28.4 \text{ kip } (126 \text{ kN})$$

The resulting probable moment strength is M_{pr} = 3150 kip·in. (360 kN·m) for the top of the slab in tension and M_{pr} = 1260 kip·in. (143 kN·m) for the bottom of the slab in tension.

The slab-column connection moment transfer strength should also be checked using the two-way shear strength design model of ACI 318 and ACI 352.1R-11 (Joint ACI-ASCE Committee 352 2012). This requires checking both a bending moment strength limit and a two-way shear stress limit. According to the model, a fraction γ_f of the total connection transfer moment M_{sc} is resisted by slab flexure across a width b_{slab} centered on the column and extending 1.5 slab thicknesses on both sides of the column. $\gamma_f = 0.6$ for columns with a square cross section (ACI 318). Following procedures for calculating probable moment strength outlined previously, $M_{pr} = 1810$ kip·in. (205 kN·m) for a width b_{slab} when the top of the slab is in tension. The moment transfer strength limited by slab flexure when loading in the positive direction is $M_{sc} = M_{pr}/\gamma_f = 3020 \text{ kip·in.}$ (342 kN·m). Using the same procedure for the bottom of the slab in tension, a moment transfer strength limited by slab flexure is calculated as $M_{sc} = 1270 \text{ kip·in.} (144 \text{ kN·m}).$

The moment transfer strength can also be limited by the two-way shear strength of a critical section about the column. According to the model in ACI 318, the combination of direct shear V_u and moment transfer M_{sc} produces shear stress v_u that varies linearly along a critical section located d/2 from the column face, as defined by Eq. (4)

$$v_u = \frac{V_u}{b_o d} \pm \frac{\gamma_v M_{sc} c'}{J_c} \tag{4}$$

where b_o is the perimeter of the critical section for two-way shear, $\gamma_v = 1 - \gamma_f$; c' is the distance from the centroid of the critical section to the location of the shear stresses v_u ; and J_c is the equivalent of the polar moment of inertia for the slab critical section. Details for the calculation of v_u in Eq. (4) are provided in ACI 318 and standard texts (for example, Wight [2016]). For design, the ultimate shear stress v_u is compared with a design shear-stress capacity ϕv_n , and from Eq. (4), M_{sc} can be solved as limited by nominal two-way slab shear capacity stress. For test specimens and checks at MCE_R loading, $\phi = 1.0$. The resulting moment capacity is $M_{sc} = 8490 \text{ kip in.}$ (960 kN·m). M_{sc} is defined at the center of the critical section and is transferred to the column face using the linear-elastic model, as described previously for one-way shear, resulting in a moment capacity of 8030 kip·in. (908 kN·m) at the face of the column.

Comparison of measured and calculated forcedisplacement relationships

The analytical model of Fig. 8 was implemented in the finite element software OpenSees (McKenna et al. 2010). The nonlinear moment hinges representing the slab-wall (m_1) and slab-column (m_2) connections were modeled with zero-length plastic hinges using a uniaxial bilinear hysteretic material ("Hysteretic"), with strengths limited by the smallest values calculated in the preceding section considering various possible limiting strengths. The deformation

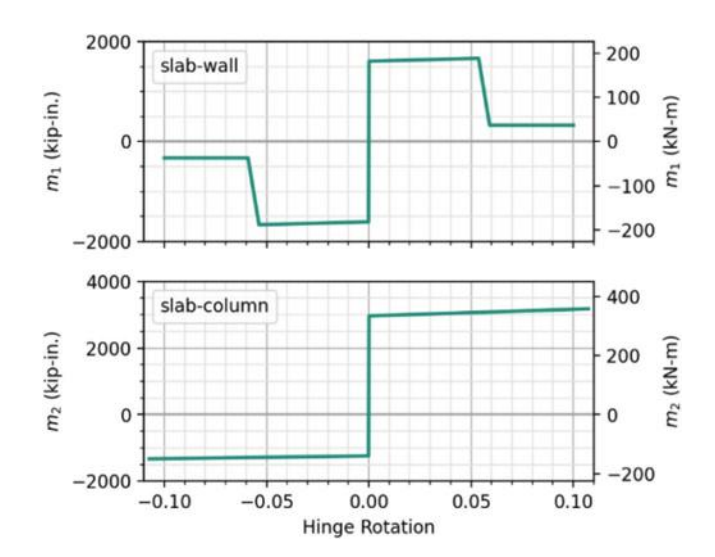


Fig. 10—Moment-rotation hinge properties at slab-wall (m_1) and slab-column (m_2) connections.

capacities of the moment hinges were calibrated based on the observations from the laboratory experiment, with the limiting envelope relationships shown in Fig. 10. Both hinges are bilinear with infinite initial stiffness and reach their calculated moment strength at a rotation of 0.032, corresponding to a drift ratio of 0.03 at MCE_R demand levels. A nominal amount of strain hardening (2%) was incorporated to reflect material strain hardening at both connections. The slab-wall hinge has a strength drop at a rotation of ± 0.054 , corresponding to a drift ratio of 0.05, which is when, during the experiment, several top bars at the slab-wall connection fractured. The residual strength of the slab-wall hinge is approximated as one-fifth of the calculated hinge strength. The slab-column connection performed well until the end of the test, so a rotation capacity of ± 0.10 was somewhat arbitrarily assigned for the connection. Data reported in ACI 352.1R-11 suggest a median rotation capacity of approximately 0.05 for nonprestressed slabs with shear reinforcement, and a larger capacity would generally be expected for post-tensioned slabs. The hysteretic response of the model was calibrated using the hysteretic material parameters for pinching, damage, and unloading stiffness to achieve strength degradation similar to the experimental data. The OpenSees result was checked using an elastic-perfectly plastic limit analysis with good results.

Figure 11 compares the measured and calculated force-displacement relationships. The figure inset shows the first load cycles up to a drift ratio of 0.005, showing that the initial stiffness of the analytical model is in agreement with that of the test results. The upper limit of force measured during the experiment closely matches the upper limit of the force in the OpenSees analytical model for loading in the positive direction. In the negative direction of loading, the model overestimates strength. A plausible reason for the overestimation is that the effective slab width for moment transfer, b_{slab} , is not applicable when the bottom of the slab is in tension. However, even when reducing the effective slab width to the width of the column, 24 in. (610 mm), the model still overestimates strength in the negative direction by approximately 20%. It is possible that the hogging

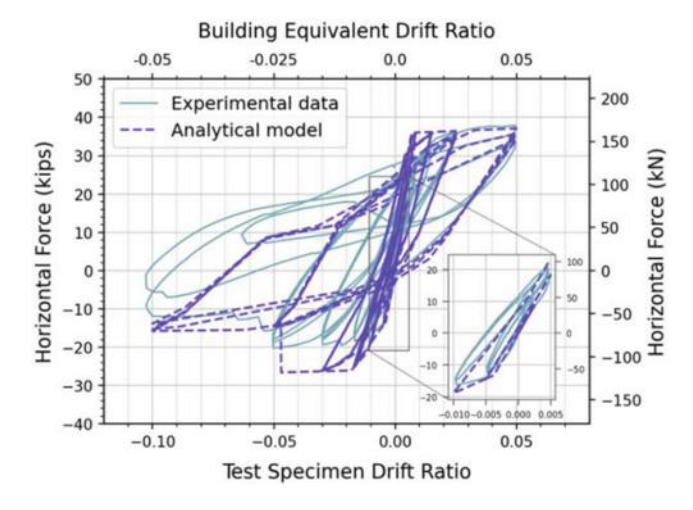


Fig. 11—Comparison of calculated plastic capacity from analytical model to experimental results from test specimen.

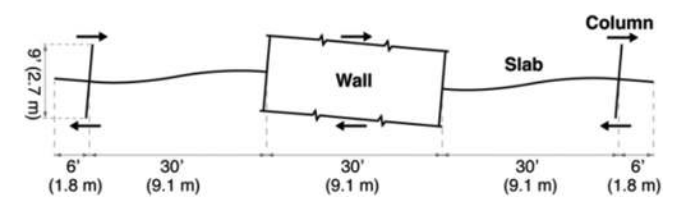


Fig. 12—Elevation view of example structure through section A-A (Fig. 1) under rotation from lateral earthquake forces.

moment from the gravity load applied to the slab was not overcome by the lateral load in the negative direction at the drift ratios from the laboratory test, leading to the slab not fully developing its strength with the bottom of the slab-column joint in tension.

EXAMPLE CALCULATION: OUTRIGGER EFFECT ON COLUMN AXIAL FORCES

This section presents an example calculation to illustrate the effect of slab-column outrigger framing on column axial forces for an archetypical tall core-wall building with 40 stories. The building is assumed to be located in San Francisco, CA, assigned to Risk Category II, at a site with Site Class C, Seismic Design Category D, and $S_{DS} = 1.2g$ (ASCE/SEI 7). The building has a regular floor plan, as shown in Fig. 1, and a typical story height of 9 ft (2.7 m). Table 2 lists the design dead and live loads.

Forces in this example are calculated for a typical edge column in a single story using the ASCE/SEI 7 load combinations, assuming the slab-column frame is not a part of the lateral-force-resisting system and considering lateral loading in one horizontal direction only. The axial force is calculated for a single story at the column shown on the right in Fig. 12. The forces would sum over the height of the building for the total column axial force, although it is plausible that not all the axial forces are at their peak value at the same time. The dead and live loads on the column are found using the tributary area method. The live loads are reduced by a factor of 0.4. By ASCE/SEI 7, columns should be designed for four load combinations: 1.4D, 1.2D + 1.6L, 1.2D + 0.5L + E, and 0.9D - E, where E does not include the horizontal earthquake

Table 2—Assumed dead and live loads

	Load source	Distributed load				
	Slab self-weight	100 lb/ft² (4.79 kPa)				
Dead	Additional per floor	25 lb/ft² (1.20 kPa)				
Dead	Cladding (perimeter)	15 lb/ft² (0.72 kPa)				
	Column self-weight	600 lb/ft (8.76 kN/m)				
Live	Offices	50 lb/ft ² (2.39 kPa)				

Table 3—Resulting column axial force for each load combination

		Column axial force, kip (kN)							
Case No.	Load combination	Without E_h	With E_h						
1	1.4D	123 (549)							
2	1.2D + 1.6L	126 (560)						
3	$1.2D + 0.5L + E_v + E_h$	133 (593)	153 (681)						
4	$0.9D - E_v - E_h$	58.2 (259)	37.3 (166)						

force E_h because the slab-column framing is assumed not to contribute to the lateral resistance of the building. Horizontal earthquake forces cause the "outrigger effect" on the slab-column gravity framing and increase the axial forces on the columns. This example compares the effect of including the horizontal earthquake load on the column axial force.

The horizontal earthquake force E_h is taken as the lateral capacity of the slab-wall-column subsystem. The value of the axial force on the column for each of the four load cases is calculated with and without the inclusion of the horizontal earthquake force E_h .

The moment strength of the slab-wall connection is calculated according to the method for M_{pr} from ACI 318 for the slab section at the wall, using Grade 60 No. 5 at 12 in. (No. 16 at 305 mm) top and bottom, similar to the test specimen configuration. The section analysis of the full slab cross section with a width of 30 ft (9.14 m) results in a probable moment strength of 4920 kip·in. (556 kN·m) at the slab-wall connection. The slab-column connection in this example is identical to that of the test specimen, except the transverse dimension of the slab is 30 ft (9.14 m). Of the four checks for limiting moment strength, the moment strength, when limited by one-way shear, greatly exceeds moments corresponding to other failure modes. The one-way moment strength of the slab is $M_{pr} = 3450 \text{ kip} \cdot \text{in}$. (390 kN·m) at the column face. The moment transfer strength in flexure is the same as that of the test specimen when using an effective transfer width of $b_{slab} = c_2 + 3h$, while the moment transfer strength in two-way shear is $M_{sc} = 6690 \text{ kip} \cdot \text{in.}$ (756 kN·m), which translates to 6810 kip·in. (770 kN·m) at the column face. The limiting moment strength at the slab-column connection is controlled by the moment transfer strength in flexure, M_{sc} = 3040 kip·in. (344 kN·m).

The resulting column axial forces calculated for the right-hand column are shown in Table 3. The column axial force increases by 15% for load combination 3 (1.2D + 0.5L + E) when including the effect of the horizontal earthquake load. The substantial increase in axial force when accounting for the outrigger action of gravity framing under earthquake

loading indicates that earthquake loads may be significant enough to control the axial design of gravity columns in tall buildings with flat-plate gravity framing. This example demonstrates that for a structure with the given dimensions, which are typical among tall core-wall buildings, neglecting the behavior of the slab outriggers may result in underdesigned gravity columns. The outrigger effect on column axial force would tend to increase for columns located closer to the core wall than is assumed in this example.

SUMMARY AND CONCLUSIONS

Many tall core-wall buildings use unbonded posttensioned flat-plate gravity framing with perimeter columns. This framing participates in resisting lateral forces as a building sways under earthquake shaking and produces outrigger action that affects column axial forces. The outrigger effect can also modify the overall building dynamic properties and dynamic response, as well as modify the wall shears due to the frame-wall interaction between the wall and the outrigger slab-column frame. However, these additional effects are beyond the scope of this paper, which focuses instead on the outrigger modeling problem. An analytical model using outrigger slab-beams was developed to demonstrate an effective method for modeling the stiffness, strength, and nonlinear force-deformation relationship of a slab-wall-column frame. The outrigger beams had stiffness based on the effective beam-width model and strengths based on expected strengths calculated in accordance with ACI 318. The analytical model was calibrated to previous laboratory testing by Klemencic et al. (2006). Results of the analytical model were used to study the likely effects of outrigger action on the design axial forces for columns in an archetypal tall building.

The output load-deformation response from the analytical simulation showed that the effective beam-width model estimated the lateral stiffness of a slab-wall-column framing very well compared with test data. As part of the calculation for probable moment strength in a post-tensioned slab, a linear relationship was defined for the change in force due to the elongation of the post-tensioning tendons with an increasing drift ratio. The strength estimates for the slabwall and slab-column connections gave a good estimate of peak lateral force in the positive direction (slab top in tension at the slab-column connection) and an overestimate in the negative direction compared with test data.

For the given example story of a tall building, accounting for the outrigger effect by including horizontal earthquake loads in design load combinations for the gravity framing system resulted in a 15% increase in column axial force in a single story. The effect of this discrepancy may also be amplified over many stories in a tall building. It is recommended to include the outrigger effect in typical tall buildings to obtain a better estimate of column design axial force.

AUTHOR BIOS

Connie I. Chen received her BS, MS, and PhD from the University of California, Berkeley, Berkeley, CA. She received the 2019 National Science Foundation (NSF) Graduate Research Fellowship and the 2022-2023 Earthquake Engineering Research Institute (EERI)/Federal Emergency Management Agency (FEMA) National Earthquake Hazards Reduction

Program (NEHRP) Graduate Fellowship. Her research interests include $tall\ buildings,\ reinforced\ concrete\ structures,\ and\ earth quake\ engineering.$

ACI Honorary Member Jack P. Moehle is a Professor at the Graduate School in Civil and Environmental Engineering at the University of California, Berkeley. He is past Chair of ACI Committee 318, Structural Concrete Building Code. His research interests include the design and analysis of structural systems, with an emphasis on earthquake engineering, reinforced concrete construction, and the development of professional design guidance.

ACKNOWLEDGMENTS

This material is based upon work supported by the National Science Foundation Graduate Research Fellowship under Grant No. DGE 1752814. Any opinions, findings, and conclusions or recommendations expressed in this material are those of the authors and do not necessarily reflect the views of the National Science Foundation.

NOTATION

area of single post-tensioned tendon

 $\dot{A_v}$ area of single shear stud

effective beam width

perimeter of critical section for two-way shear at slab-column

effective slab width for moment transfer in flexure at column

flexural compression depth at probable moment strength c'

distance from centroid of column critical section to location of eccentric shear stresses

dimension of rectangular column parallel to direction of loading c_1

dimension of rectangular column perpendicular to c_1

slab effective depth

depth from extreme compression fiber to centroid of post-

tensioned reinforcement

modulus of elasticity of prestressing steel

specified effective prestress force final force in prestressing steel yield stress of nonprestressed steel

yield stress of shear reinforcing steel

slab thickness height at story x

equivalent of polar moment of inertia for slab critical section in two-way shear

 L_{ups} ℓ_1 ℓ_2 M_{pr} M_{sc} s V_c length of unbonded post-tensioning steel length of span parallel to direction of loading length of span perpendicular to direction of loading

probable moment strength

moment transfer strength about slab-column connection

spacing of shear studs measured parallel to rail shear strength contribution from concrete

one-way nominal shear strength

shear strength contribution from shear reinforcement

factored shear demand

shear stress along column critical section in two-way shear

w distributed load

factor of stiffness reduction due to rotation across transverse width of slab

factor of stiffness reduction due to concrete cracking

width of crack opening at height of post-tensioning steel at slabcolumn connection

 δ_x lateral drift at story x strain in prestressing steel

fraction of transfer moment M_{sc} transferred by slab flexure γ_f

fraction of transfer moment M_{sc} transferred by slab shear stress

opening angle of crack at slab-column connection

REFERENCES

ACI Committee 318, 2019, "Building Code Requirements for Structural Concrete (ACI 318-19) and Commentary (ACI 318R-19) (Reapproved 2022)," American Concrete Institute, Farmington Hills, MI, 624 pp.

ASCE/SEI 7-16, 2017, "Minimum Design Loads and Associated Criteria for Buildings and Other Structures," American Society of Civil Engineers, Reston, VA, 800 pp.

ASCE/SEI 41-17, 2017, "Seismic Evaluation and Retrofit of Existing Buildings," American Society of Civil Engineers, Reston, VA, 576 pp.

CSI, 2021, "SAP2000 Integrated Software for Structural Analysis and Design, v23.3.0" Computers and Structures, Inc., Walnut Creek, CA.

Hwang, S.-J., and Moehle, J. P., 2000, "Models for Laterally Loaded Slab-Column Frames," *ACI Structural Journal*, V. 97, No. 2, Mar.-Apr., pp. 345-352.

Joint ACI-ASCE Committee 352, 2012, "Guide for Design of Slab-Column Connections in Monolithic Concrete Structures (ACI 352.1R-11)," American Concrete Institute, Farmington Hills, MI, 28 pp.

Joint ACI-ASCE Committee 550, 2013, "Design Specification for Unbonded Post-Tensioned Precast Concrete Special Moment Frames Satisfying ACI 374.1 (ACI 550.3-13) and Commentary (Reapproved 2022)," American Concrete Institute, Farmington Hills, MI, 28 pp.

Kang, T. H.-K., and Wallace, J. W., 2005, "Dynamic Responses of Flat Plate Systems with Shear Reinforcement," *ACI Structural Journal*, V. 102, No. 5, Sept.-Oct., pp. 763-773.

Klemencic, R.; Fry, J. A.; Hurtado, G.; and Moehle, J. P., 2006, "Performance of Post-Tensioned Slab-Core Wall Connections," *PTI Journal*, V. 4, No. 2, Dec., pp. 7-23.

LATBSDC, 2020, "An Alternative Procedure for Seismic Analysis and Design of Tall Buildings Located in the Los Angeles Region," Los Angeles Tall Buildings Structural Design Council, Los Angeles, CA, 92 pp.

McKenna, F.; Scott, M. H.; and Fenves, G. L., 2010, "Nonlinear Finite-Element Analysis Software Architecture Using Object Composition," *Journal of Computing in Civil Engineering*, ASCE, V. 24, No. 1, Jan., pp. 95-107.

PEER TBI, 2017, "Guidelines for Performance-Based Seismic Design of Tall Buildings," PEER Report No. 2017/06, Version 2.03, Tall Buildings Initiative, Pacific Earthquake Engineering Research Center, University of California, Berkeley, Berkeley, CA, 143 pp.

Vanderbilt, M. D., and Corley, W. G., 1983, "Frame Analysis of Concrete Buildings," *Concrete International*, V. 5, No. 12, Dec., pp. 33-43.

Wight, J. K., 2016, *Reinforced Concrete: Mechanics and Design*, seventh edition, Pearson Education, Hoboken, NJ, 1168 pp.

APPENDIX A: EFFECTIVE BEAM WIDTH FOR SLAB WITH PARTIAL CONNECTIVITY TO WALL

A study was done to calculate the moment-rotation stiffness of a slab-wall connection in which the slab connects directly to a flanged wall along half of the slab equivalent frame width. An alternative approach would be required for a slab framing into the edge of a blade wall. Figure A1 shows the overall geometry of the assumed floor system with the equivalent frame under consideration shown shaded.

A linear-elastic model of the equivalent frame was implemented using the software SAP2000 (CSI 2021). The slab was modeled using thin shell elements with infinite in-plane rigidity. Slab free edges were unrestrained, while the edges parallel to the equivalent frame (dashed lines in Fig. A1) were restrained to have zero rotation about the dashed lines. The wall and columns, including the regions common to the slab, wall, and columns, were modeled as rigid. Shear deformations were neglected, and a Poisson's ratio of 0.2 was assumed.

Two different imposed deformation patterns were considered. In the first, the core wall was assumed to rotate about gridline D in Fig. A1. This deformation pattern is considered to be representative of deformations occurring in the lower stories of a tall core-wall building and is referred to as the lower-story condition. In the second pattern, the core wall was assumed to rotate about gridline E. This deformation pattern is considered to be more representative of deformations occurring in the upper stories of a tall core-wall building, where accumulation of flexural tension strain in the tension flange has resulted in wall uplift and is referred to as the upper-story condition. In both cases, the columns were assumed to rotate about their centroid at the base of

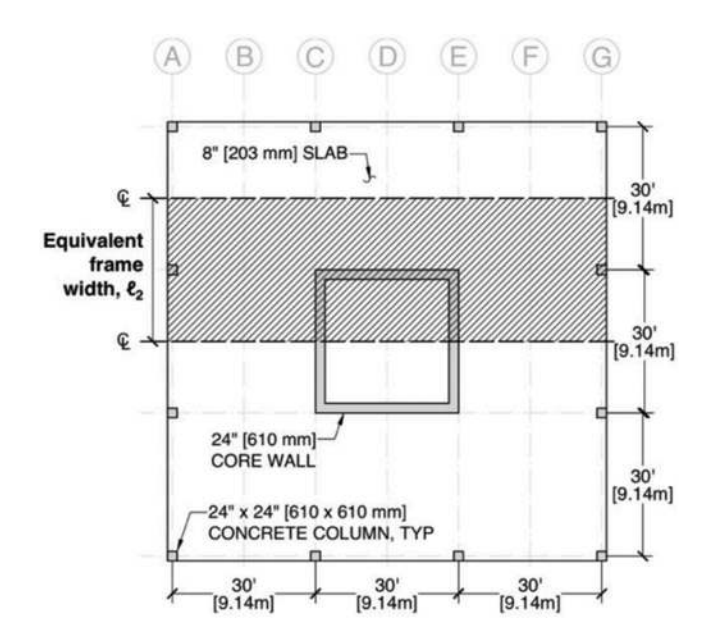


Fig. A1—Floor plan used for finite element model.

Table A1—Effective beam width coefficients

		Span AC	Span EG		
Lower-story	b/ℓ_2 at column*	0.40	0.40		
boundary condition	b/ℓ_2 at wall	0.88	0.88		
Upper-story	b/ℓ_2 at column*	0.39	0.42		
boundary condition	b/ℓ_2 at wall	0.90	0.83		

^{*}Compare with Hwang and Moehle (2000); $b_e/\ell_2 = 168 \text{ in./}360 \text{ in.} = 0.47.$

the column. A unit rotation was imposed on the wall and columns in both deformation patterns.

The effective beam width coefficient was found by first determining the stiffness of the model with the full slab modeled using shell elements. The slabs in each equivalent frame are divided at the midpoint of the span and replaced with beams of effective widths, calibrated such that the beam end moment matches the total moment in the slab across the equivalent frame width at the wall and the column. Table A1 lists the resulting effective beam widths.

Note that the calibrated effective beam widths on the column side are smaller than the values calculated from Hwang and Moehle (2000). The difference may relate to the different geometries of the framing spans, different modeling assumptions, and approximations in deriving the factors in Hwang and Moehle (2000).

The effective beam width coefficients ranged from 0.83 to 0.90 and were not strongly affected by the two different rotation axes considered. The effective beam width in this study comprised half the width of the equivalent frame that was rigidly connected to the wall, plus an additional effective width for the other half of the equivalent frame extending beyond the wall. In the interest of simplicity and applicability to a wider range of geometries, it is recommended to use an effective width equal to the width of contact between the slab and wall plus 0.7 times the width of the equivalent frame extending beyond the wall.

ARE YOU A RESEARCHER?

SIGN UP FOR ORCID TODAY!

1 Register

2 Use your ORCID ID

3 Share

ORCID provides a digital identifier that distinguishes you from every other researcher and, through integration in key research workflows such as manuscript and grant submission, supports automated linkages between you and your professional activities, ensuring that your work is recognized.

ORCID services are FREE and it's as easy as 1-2-3.

WWW.ORCID.ORG

Title No. 121-S25

Effect of Bond Condition on Cyclic Behavior of Post-Tensioned Concrete Beams with Carbon Fiber-Reinforced Polymer Tendons

by Fei Peng, Weichen Xue, and Shulu Zhang

The lack of ductility is the main concern in the use of carbon fiber-reinforced polymer (CFRP) reinforcement as prestressing tendon in concrete members. To address this concern, a partially bonded concept has been proposed. In this approach, CFRP tendons are intentionally debonded from the concrete in the middle region of the prestressed concrete beam, while remaining bonded at each end. In this study, eight post-tensioned beams, including five beams with CFRP tendons and three beams with steel tendons, are tested under cyclic loading. Three bond conditions, including fully bonded, partially bonded, and fully unbonded, are considered. The results indicate that increasing the unbonded length of the tendon changed the failure mode from CFRP rupture to concrete crushing. There is a trend that the flexural capacity decreased with the increase of the unbonded length. The displacement ductility (μ) of partially bonded CFRP prestressed beams ranged from 5.38 to 5.70, which is significantly higher than that of the fully bonded beam ($\mu = 2.83$) and slightly lower than that of the fully unbonded beam ($\mu = 6.10$). Finally, by introducing a relative bond length coefficient into the ultimate tensile stress equation for internally unbonded tendons, a modified design approach for estimating flexural capacities of the partially bonded beams is proposed. The experimental flexural capacities are in close agreement with the values predicted using the modified design approach.

Keywords: carbon fiber-reinforced polymer (CFRP); cyclic behavior; ductility; partially bonded; prestressed concrete beam.

INTRODUCTION

Corrosion-induced deterioration of steel strands is one of the major reasons that the structural integrity of prestressed concrete structures is compromised before the structures reach their expected lifespan (Grace et al. 2013). Substituting steel strands with fiber-reinforced polymer (FRP), particularly carbon FRP (CFRP), offers a viable solution due to its exceptional properties such as corrosion resistance, high strength-to-weight ratio, fatigue resistance, and low relaxation (Grace et al. 2013; Peng and Xue 2018a). However, the inherent brittleness of FRP limits the ductility of structural members.

Enhancing the ductile behavior of the structural concrete members reinforced with FRP reinforcements has remained the focus of research in recent years. Various concepts have been investigated to achieve this objective, including promoting ductile compression failure through the use of fiber-reinforced concrete (FRC) (Fischer and Li 2003; Peng et al. 2023) and employing hybrid reinforcing schemes (Safan 2013; Peng and Xue 2018b). It is generally recommended to design the flexural reinforcement ratio to exceed

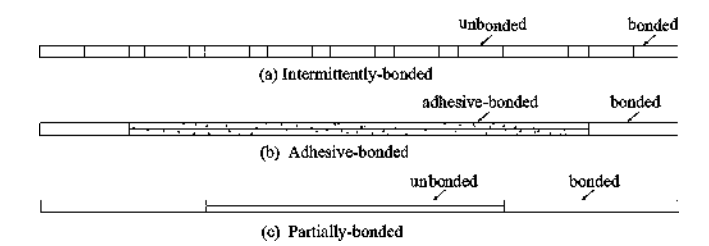


Fig. 1—Types of partial bonding of FRP tendons.

the balanced ratio (Peng and Xue 2019a; Poudel et al. 2022; Peng et al. 2023), at which the rupture of FRP tendons and concrete crushing occur simultaneously. However, employing a high FRP reinforcement ratio can be uneconomical. An alternative approach to prevent tendon rupture and improve beam ductility is the use of unbonded FRP tendons. Unbonded tendons are allowed to slip, relieving strains from critical sections and distributing them along the beam length, thereby delaying or preventing FRP tendon rupture (Grace and Abdel-Saved 1998; Heo et al. 2013; Sun et al. 2022; Au and Du 2008). This implies that even if a prestressed concrete beam with unbonded FRP tendons has a significantly lower flexural reinforcement ratio compared to the balanced reinforcement ratio in the bonded case, concrete crushing may occur prior to FRP tendon rupture (Au and Du 2008; Lee et al. 2017). Nevertheless, the anchorage of fully unbonded FRP prestressed concrete members remains a critical challenge. Despite efforts made over the past two decades, efficient and competitive prestressing anchor systems for FRP tendons are still limited (Jeong et al. 2019).

To address these issues, the concept of partially bonded FRP systems was introduced. Lees and Burgoyne (1999) first proposed partial bonding as a means to improve the ductility of concrete beams prestressed with FRP tendons. In their proposal, partial bonding was achieved in two ways, either by intermittently bonding sections of tendons, or by coating the tendon with a resin, as shown in Fig. 1(a) and (b), respectively. The flexural behavior of fully bonded, fully unbonded, and partially bonded pretensioned concrete beams was compared by Lees and Burgoyne (1999). The study concluded that partially bonded beams exhibited an ultimate

ACI Structural Journal, V. 121, No. 2, March 2024.

MS No. S-2023-065.R1, doi: 10.14359/51740251, received July, 17, 2023, and reviewed under Institute publication policies. Copyright © 2024, American Concrete Institute. All rights reserved, including the making of copies unless permission is obtained from the copyright proprietors. Pertinent discussion including author's closure, if any, will be published ten months from this journal's date if the discussion is received within four months of the paper's print publication.

load capacity equivalent to fully bonded beams and a rotation capacity comparable to fully unbonded beams. However, the construction complexity associated with these partial bonding patterns may limit their practical application. Latterly, several researchers (Rizkalla 2000; Dorian 2002) proposed an alternative partial bonding pattern, wherein the tendons were debonded from the concrete in the middle region of the beam and bonded to the concrete at each end, as shown in Fig. 1(c). This partial bonding pattern has been introduced to strengthen existing structural members using FRP strips (Choi et al. 2011a; Sharaky et al. 2015; Chen et al. 2021).

Several studies have investigated the mechanical behavior of partially bonded CFRP prestressed concrete beams. Rizkalla (2000) and Dorian (2002) conducted flexural tests on pretensioned concrete beams containing a hybrid arrangement of partially bonded CFRP tendon and nonprestressed stainless steel bars under static loading. The results indicated that an increase in the unbonded length led to a decrease in ultimate capacity while promoting improved deformability. Jeong et al. (2019) evaluated the fatigue performance of post-tensioned concrete beams with partially bonded CFRP tendons. It was found that the partially bonded CFRP prestressed beams exhibited satisfactory fatigue performance, with no signs of cracks or stiffness degradation during fatigue loading. Furthermore, the ductility index of the partially bonded CFRP prestressed beams was comparable to that of beams prestressed with steel tendons.

In summary, the partially bonded FRP reinforcing scheme offers a competitive technique in terms of ductility, end-anchored ability, and cost-effectiveness. Furthermore, the addition of fibers in concrete can further enhance the ductility of FRP prestressed concrete beams. However, there is limited research conducted on the mechanical behavior of partially bonded CFRP prestressed concrete beams. This paper, therefore, presents a detailed experimental study on FRC beams with partially bonded CFRP tendons. Eight post-tensioned beams are tested under low reversed cyclic loading. The test results are presented in terms of failure modes, hysteresis curves, skeleton curves, load capacity, displacement ductility, and energy dissipation capacity.

RESEARCH SIGNIFICANCE

Despite the competitiveness of the partial bonding concept in terms of ductility and end-anchoring ability, there is a lack of comprehensive research on the cyclic behavior of partially bonded CFRP prestressed concrete beams. The main objective of this research is to investigate the cyclic behavior the polypropylene FRC beams with partially bonded CFRP tendons. In addition, a design approach will be proposed for predicting the flexural capacity of these beams. The findings from this study will contribute to a better understanding of the cyclic performance of partially bonded CFRP prestressed concrete beams and provide a practical design tool for their structural application.

EXPERIMENTAL PROGRAM

Test specimens

In engineering practice, few concrete beams are prestressed exclusively with CFRP reinforcements due

to their lack of ductility and control of crack distribution. To enhance ductile behavior and provide crack control, an alternative approach is to incorporate nonprestressed bars such as galvanized, epoxy-coated, or stainless steel (Peng and Xue 2018b). This study adopts a partially prestressed scheme where CFRP strands serve as prestressing tendons, and epoxy-coated steel bars are used as nonprestressed bars.

A total of eight post-tensioned concrete beam specimens, including five beams prestressed with CFRP strands and three beams prestressed with steel strands, were designed, constructed, and tested. Among the CFRP prestressed beams, one was fully bonded, one was fully unbonded, and the remaining beams were partially bonded. The fully bonded beam was designed to fail due to CFRP rupture, while the partially bonded beam, with the central portion of the tendon debonded from the concrete, was expected to fail through concrete crushing. All specimens were doubly reinforced, with the top flexural reinforcements chosen to produce negative flexural strength similar to positive loading cases. Each beam had a rectangular cross section of 150 x 250 mm (5.9 x 9.9 in.) and a span of 3500 mm (13.8 in.). Details of the tested beams are provided in Table 1 and Fig. 2. The test parameters included the unbonded length of prestressing tendon and the type of tendon used. In this study, all specimens were designed with a consistent partial prestressing ratio (PPR) of 0.55, which is defined as

$$PPR = \frac{A_p f_{pu}}{A_p f_{pu} + A_s f_v} \tag{1}$$

where A_s is the area of steel bars in tension; A_p is the area of prestressing tendons; f_y is the yield strength of steel bar in tension; and f_{pu} is the ultimate tensile strength of prestressing tendon

It should be noted that the effective cross-sectional area of CFRP strands differs from that of steel strands, making it challenging to maintain the same reinforcement ratio in beams with different prestressing tendon types. To investigate the influence of prestressing tendon type, the CFRP prestressed beams were designed to have the same PPR and jacking stress as the steel prestressed beams. To ensure a flexural failure mode, all specimens within the shear span were equipped with 8 mm (0.3 in.) diameter steel stirrups spaced at intervals of 100 mm (3.9 in.).

The specimens are referred to using acronyms that indicate their various characteristics. The first part of the acronym indicates the bond condition ("FB" for fully bonded, "PB" for partially bonded, and "UB" for unbonded). The second part of the acronym represents the type of prestressed tendon ("S" for steel strand and "C" for CFCC). The last part of the acronym indicates the unbonded length of the tendon, which can be 0, 1100, 1900, 2700, or 3500 mm (43.3, 74.8, 106.3, or 137.8 in.). Following this notation, Specimen PB-C-11 is a beam prestressed with partially bonded CFCC tendons, with an unbonded length of 1100 mm (43.3 in.).

Material properties

All specimens were designed with concrete with a target compressive strength of 50 MPa (7.3 ksi). The concrete used

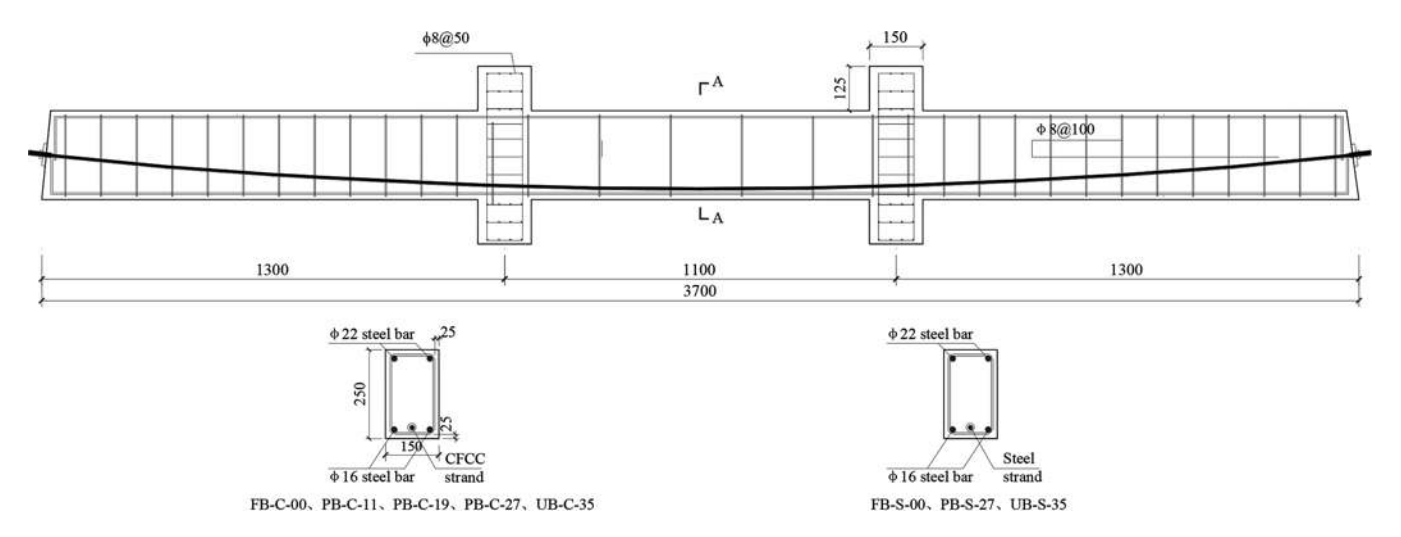


Fig. 2—Dimensions and reinforcement details of test specimens. (Note: Units in mm; 1 mm = 0.0394 in.)

Table 1—Details of specimens

Specimens	Unbonded length, mm	Tendons	Effective prestress, MPa	Top longitudinal reinforcements	Bottom longitudinal reinforcements
FB-C-00	0	1φ ^{cfrp} 12.5	829	2F22	2F16
PB-C-11	1100	1φ ^{cfrp} 12.5	927	2F22	2F16
PB-C-19	1900	1φ ^{cfrp} 12.5	914	2F22	2F16
PB-C-27	2700	1φ ^{cfrp} 12.5	894	2F22	2F16
UB-C-35	3500	1φ ^{cfrp} 12.5	890	2F22	2F16
FB-S-00	0	1φ ^s 12.7	838	2F22	2F16
PB-S-27	2700	1φ ^s 12.7	880	2F22	2F16
UB-S-35	3500	1φ ^s 12.7	880	2F22	2F16

Note: 1 MPa = 0.145 ksi.

Table 2—Material properties of concrete

Specimens	Modulus of elasticity E_c , MPa	Cube compressive strength f_{cu} , MPa	Splitting strength f_{st} , MPa
FB-C-00	3.62 × 10 ⁴	65.20	4.62
PB-C-11	3.54×10^{4}	65.88	4.36
PB-C-19	3.68×10^{4}	61.75	4.64
PB-C-27	3.61 × 10 ⁴	55.48	4.17
UB-C-35	3.79×10^{4}	57.76	4.64
FB-S-00	3.53×10^{4}	57.80	4.45
PB-S-27	3.48×10^{4}	58.83	4.17
UB-S-35	4.12 × 10 ⁴	60.23	4.64

Note: 1 MPa = 0.145 ksi.

in this study was a FRC previously developed by the authors previously (Xue et al. 2011). The mixture design consisted of 260 kg/m³ (16.22 lb/yd³) of cement, 260 kg/m³ (16.22 lb/yd³) of grinded blast-furnace slags, 188 kg/m³ (11.74 lb/yd³) of water, 684 kg/m³ (42.70 lb/yd³) of middle grit, 1024 kg/m³ (63.93 lb/yd³) of gravels, and 1.8 kg/m³ (0.11 lb/yd³) of polypropylene fibers. The inclusion of ground blast-furnace slags in concrete with a fineness of 5×10^3 cm²/g attempted to enhance the activity of admixtures. Additionally, the addition of polypropylene fibers (15 mm [0.6 in.] in length) with 2.3% volume fraction of cement attempted to increase

the anti-dry-shrinkage cracking property of cement mortar in the hardening stage. On the day of testing, the concrete compressive strength, splitting strength, and modulus of elasticity for each beam were determined in accordance with the Chinese standard GB/T 50081 (2019). Table 2 lists the measured mechanical properties of the concrete for each beam.

The 12.5 mm (0.5 in.) diameter, seven-wire CFCC strand and 12.7 mm (0.5 in.) diameter, seven-wire steel strand were used as the prestressing tendons. The CFCC strand possessed an effective cross-sectional area of 75.6 mm² (0.117 in.²) and a guaranteed ultimate tensile strength of 1860 MPa (270 ksi). The tensile properties of CFCC strands were determined as per ASTM D7205 (2021) with a measured tensile strength of 2400 MPa (348 ksi). The steel strand had an effective cross-sectional area of 98.7 mm² (0.153 in.²) and an ultimate tensile strength of 1860 MPa (270 ksi). Mild steel bars were used as nonprestressed reinforcements and stirrups. Table 3 lists the mechanical properties of the steel reinforcements used in this study.

Fabrication and prestressing

A partially bonded reinforcing scheme has a portion of the reinforcement intentionally unbonded. In this study, the unbonded length of the prestressing tendon was situated within the middle portion of the simply supported beam,

Table 3—Mechanical properties of steel bars and prestressing tendons

Bar type	Designation	Yield strength, MPa	Ultimate tensile strength, MPa	Modulus of elasticity, MPa	Elongation ratio	
	Ф8	313	425	200	27.7%	
Steel bar	Ф16	385	550	200	29.1%	
	Ф22	371	556	200	30.4%	
Steel strand	φ ^s 12.7	_	1861	195	5.5%	
CFCC strand	ф ^{сfrр} 12.5	_	2400	150	1.6%	

Note: 1 MPa = 0.145 ksi.

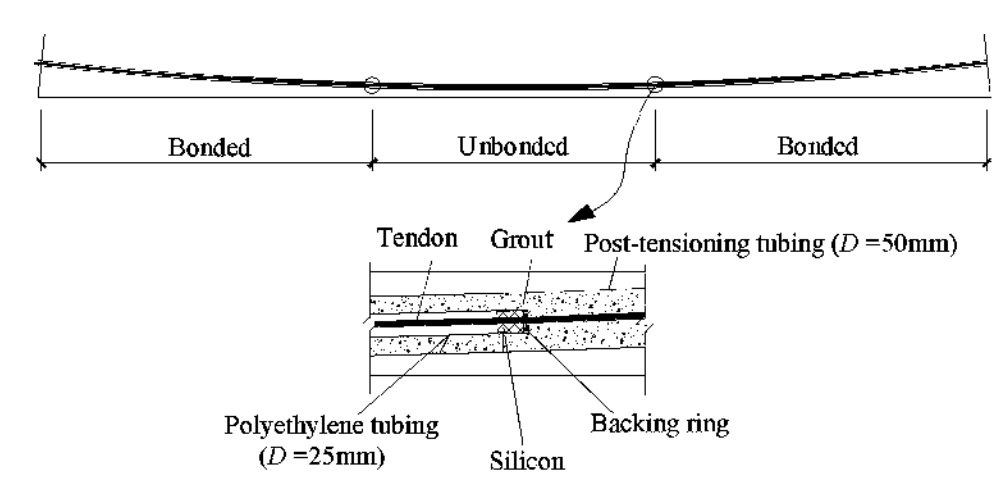


Fig. 3—Preparation of partially bonded tendon. (Note: 1 mm = 0.039 in.)

while the end portions were bonded, as shown in Fig. 3. Special preparation of the partially bonded tendons was necessary. A 25 mm (1 in.) diameter polyethylene duct was threaded over the tendon to achieve the desired unbonded length. Silicon was used to seal both ends of the duct, and electrical tape was wrapped around the silicon at both ends of the tendon to prevent concrete penetration into the duct.

The post-tensioning for CFRP was achieved using a bonded anchorage system and a hydraulic jack. The maximum permissible stress in CFRP at jacking specified in ACI 440.4R (2004) is 65% of its specified tensile strength. In this study, jacking stress of $0.55f_{pk}$, where f_{pk} represents the manufacturer provided guaranteed CFRP tensile strength, was selected. The compressive concrete strength on the day of prestressing was at least 80% of its target compressive strength. The CFRP strand was post-tensioned at one end of the beams to a target prestressing force. After prestressing, post-tensioning plastic ducts were filled with grout. On the day of testing, the effective prestress for each specimen was measured, as listed in Table 1. It was observed that the prestress losses for CFRP tendons ranged from 10 to 19%.

Test setup and instrumentation

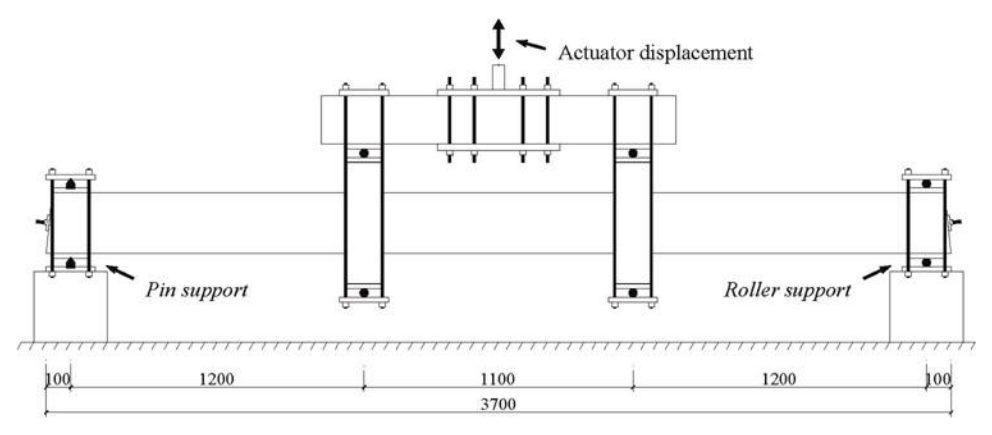
As shown in Fig. 4, all beams were tested under four-point loading which was cyclically applied by using a hydraulic testing machine. The loading protocol, which consists of two phases in conformance with Chinese standard GB/T 50152 (2012), is presented in Fig. 5. The first phase is a load-controlled cycle, where the specimens are loaded downwardly and upwardly, respectively, until cracks formed. The second phase is a displacement-controlled cycle at a rate of 1 mm/min, in which three cycles are repeated at each step.

In this phase, the specimens are loaded to multiples of Δ_y , where Δ_y is the displacement corresponding to the yielding of the tensile steel bars at bottom of the beams. During testing, the applied loads were monitored through load cells. Three linear variable differential transformers (LVDTs) with an accuracy of 0.001 mm were mounted along the beams to measure vertical deflection at the support and midspan. Electrical resistance strain gauges were mounted on the longitudinal steel bars and prestressing tendons to measure their strains.

TEST RESULTS AND DISCUSSIONS Cracking behavior and failure modes

During the testing process, flexural cracks were initiated in the pure bending region of the tested beams. Table 4 lists the flexural cracking load for each beam. As the applied load increased, the existing flexural cracks extended in length and width along with occurrence of a few new flexural cracks. During upward loading, the cracks at the bottom closed and flexural cracks were observed at the top of the concrete at the pure bending sections. Following the yielding of mild steel reinforcements, flexure-shear cracks could be observed, and the flexural cracks continued to propagate. Subsequently, the length and width of the existing cracks continued to increase, with no new cracks forming. Eventually, a large number of vertical cracks and a few horizontal cracks could be observed around midspan sections of beams. Typical ultimate deformation of the tested beams is depicted in Fig. 6.

As expected, all beams exhibited flexural failure. With the exception of the fully bonded beam (FB-C-00), the final failure of all specimens was caused by crushing and spalling of concrete at pure bending sections, accompanied by



(a) Scheme proposal



(b) Final test setup

Fig. 4—Test setup. (Note: Units in mm; 1 mm = 0.0394 in.)

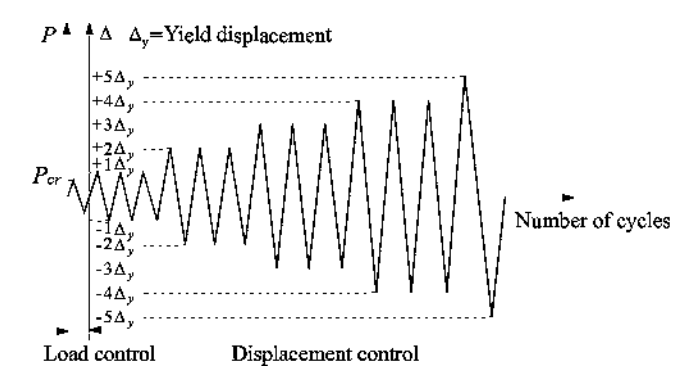


Fig. 5—Loading protocol.

buckling of longitudinal steel bars, referred to as a compression failure. The failure of Specimen FB-C-00, on the other hand, was controlled by rupture of the CFRP tendon accompanied by insignificant crushing of concrete, referred to as a tension failure. This is because the unbonded portion is free to slip, resulting in more or less equalized strain along the unbonded length of the tendon and reduced strain at the critical section. These two types of failure modes are depicted in Fig. 7. At the onset of failure, the strain of CFRP tendon in FB-C-00 was observed to approach its ultimate tensile strain. For partially bonded and fully unbonded beams, however, the maximum strain in the CFRP tendons did not exceed their ultimate tensile strain, ranging between 0.011 and 0.013.

Hysteresis curves

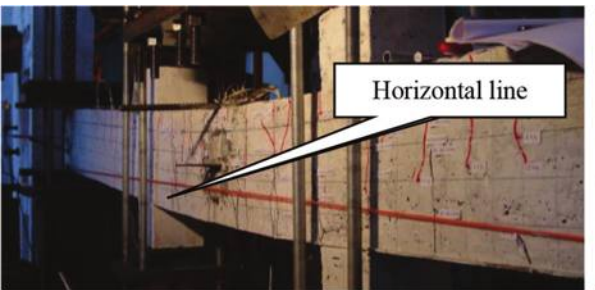
The load-midspan displacement hysteresis curves of all the tested beams are shown in Fig. 8. Prior to concrete cracking, the hysteresis curves were basically linear, with relatively small areas of hysteretic loops. No obvious degradation in flexural stiffness could be observed and the residual deformation was negligible. After flexural cracking of the specimens, the load-midspan displacement hysteresis curve became nonlinear. The areas of hysteretic loops became larger, indicating that energy dissipation increased. When the midspan displacement was below $3\Delta_{\nu}$, the maximum load obtained in the next two cycles was nearly the same as that in the first cycle at the same level of displacement. This indicates that the strength degradation of the beams under reverse cyclic loading was negligible. When the midspan displacement exceeded $3\Delta_{\nu}$, however, a strength reduction was observed, which can be attributed to cumulative damage resulting from the load repetition. For instance, at a displacement level of $4\Delta_v$, a strength reduction of 5.2 and 14.3% was observed in Specimens PB-C-11 and PB-C-19 under downward loading, respectively.

As observed in Fig. 8, all hysteresis curves exhibited noticeable pinching, which can be attributed to the influence of prestressing. It was found that the beams prestressed with steel strands underwent more loading cycles than those prestressed with CFRP strands. This is expected because the CFRP is an elastic and brittle material that does not exhibit yielding behavior. With the exception of the fully bonded CFRP prestressed concrete beam (Specimen

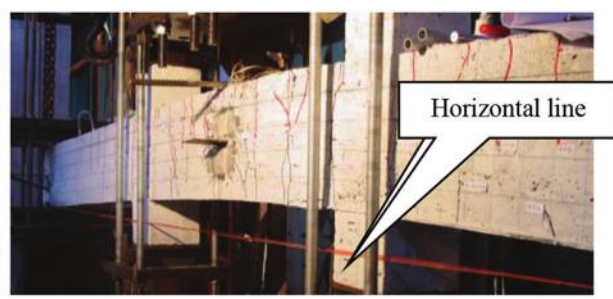
Table 4—Test results

Specimens	Loading direction P_{cr} , ki		P_y , kN	P_{max} , kN	Δ_{cr} , mm	Δ_y , mm	Δ_u , mm	Δ_u/Δ_y	P _{max,exp} /P _{max,pre}
FD C 00	↓	25.3	82.7	93.7	2.70	23.70	65.95	2.83	_
FB-C-00	1	-20.0	-86.8	-100.8	-2.45	-23.35	-60.57	_	_
DD C 11	↓	25.5	70.3	101.8	3.06	20.31	115.81	5.70	1.09
PB-C-11	1	-15.0	-88.9	-93.4	-1.01	-21.82	-95.47	_	_
PB-C-19	↓	30.0	79.6	98.8	3.47	21.76	117.1	5.38	1.07
PB-C-19	1	-10.5	-87.9	-88.6	-0.21	-22.99	-55.62	_	_
DD C 27	↓	26.5	64.0	87.2	2.42	21.79	119.50	5.48	0.97
PB-C-27	1	-20.0	-93.5	-94.5	-1.44	-21.82	-71.50	_	_
UB-C-35	↓	25.0	66.6	87.3	2.85	20.66	126.3	6.10	0.95
OB-C-33	1	-18.0	-85.4	-86.4	-1.85	-23.54	-76.75	_	_
FB-S-00	↓	23.0	82.9	110.9	3.12	23.80	133.67	5.62	_
FB-S-00	↑	-18.0	-87.0	-99.1	-1.98	-21.16	-134.16	_	_
PB-S-27	↓	29.8	62.5	86.0	1.71	20.19	133.08	6.59	0.93
rD-3-4/	1	-23.0	-96.6	-101.0	-1.64	-21.14	-74.30	_	_
UB-S-35		25.0	61.0	93.3	-3.59	19.29	135.24	7.01	0.98
UD-3-33	1	-20.0	-90.3	-94.3	-1.91	-21.73	-75.92	_	_

Note: 1 mm = 0.0394 in.; 1 kN = 0.2248 kip; 1 MPa = 0.145 ksi.

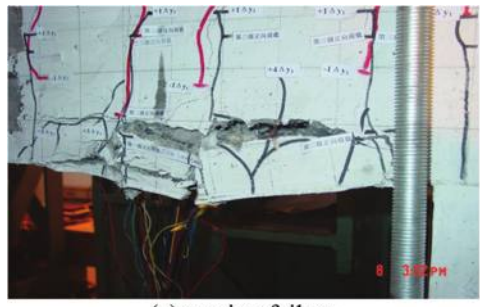


(a) downward ultimate deformation



(b) upward ultimate deformation

Fig. 6—Ultimate deformation of typical test beams.



(a) tension failure

at high of the constraint of t

(b) compression failure

Fig. 7—Typical failure modes of test beams.

FB-C-00), which failed after only three load cycles, all the CFRP prestressed concrete beams sustained no fewer than five loading cycles. This is because the fully bonded CFRP prestressed concrete beam exhibited a premature failure due to rupture of CFRP before concrete crushing.

Skeleton curves

Skeleton curves are envelopes of hysteresis curves. Generally, the skeleton curves of structural members under cyclic loading are close to those under monotonic loading in both shape and values. Figure 9 shows the skeleton curves for each specimen. Prior to cracking, the skeleton curves are approximately linear and the effects of bond are negligible because of insignificant change in tendon stress in this elastic stage.

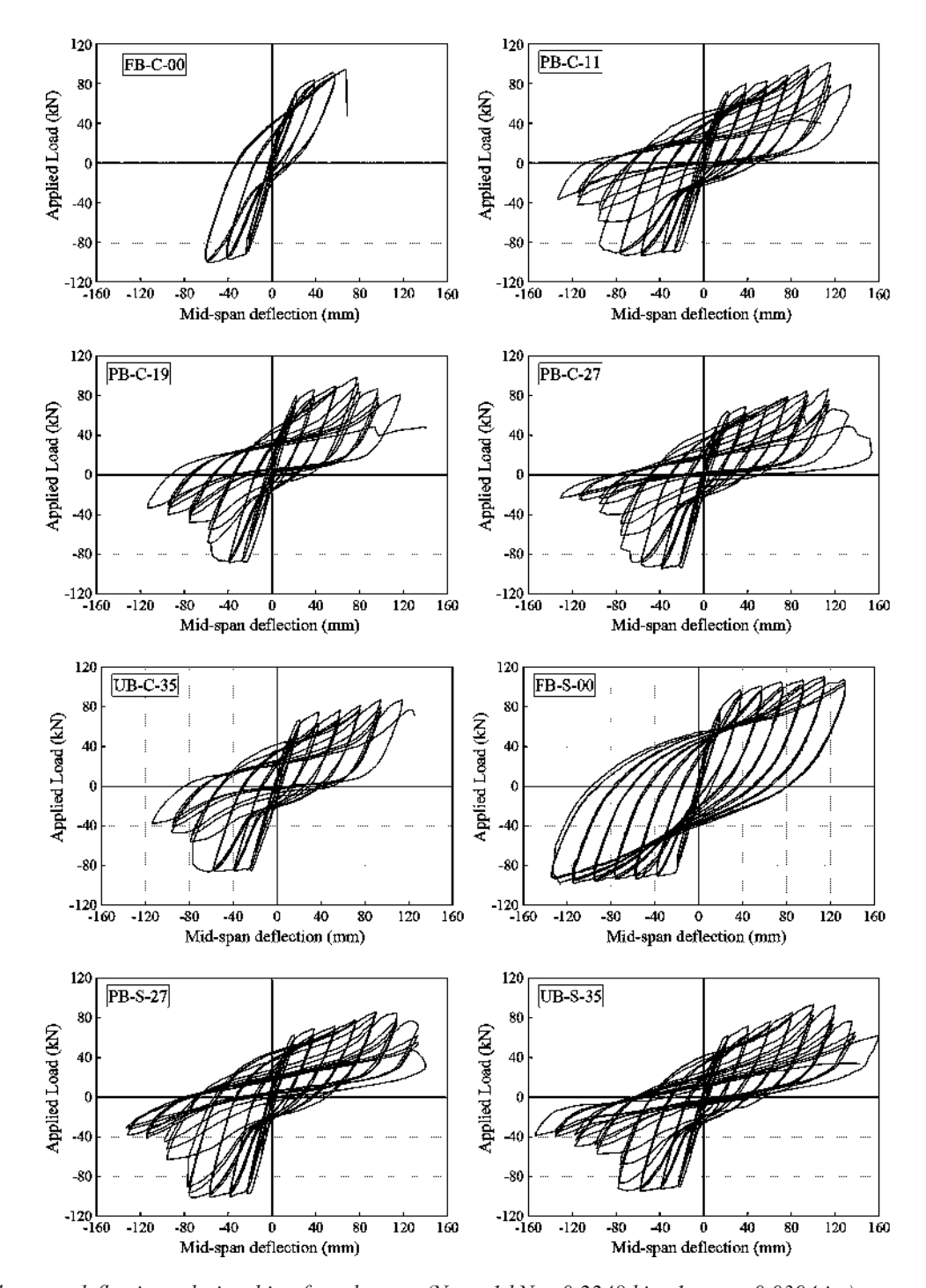


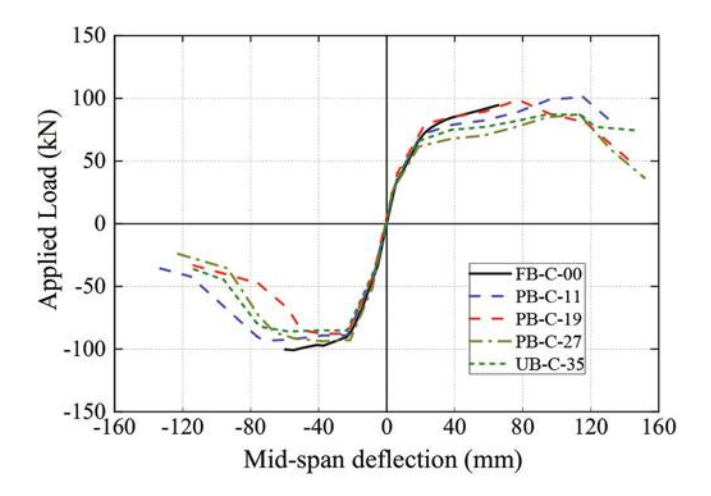
Fig. 8—Load versus deflection relationship of test beams. (Note: 1 kN = 0.2248 kip; 1 mm = 0.0394 in.)

After cracking, the loading increment lagged behind the deformation increment and stiffness degraded apparently. In the post-cracking stage, the fully bonded CFRP prestressed beams are shown to be stiffer than unbonded and partially bonded ones. This is because tendon stress increases faster in fully bonded prestressed beams than in partially bonded and unbonded prestressed beams. After yielding of the tensile steel bar, obvious inflection points could be observed in the skeleton curves. Thereafter, stiffness continued to degrade until the maximum load point. When the midspan displacement exceeded $4\Delta_y$, obvious overall strength degradation could be observed in the partially bonded and fully unbonded beams under downward loading, which was

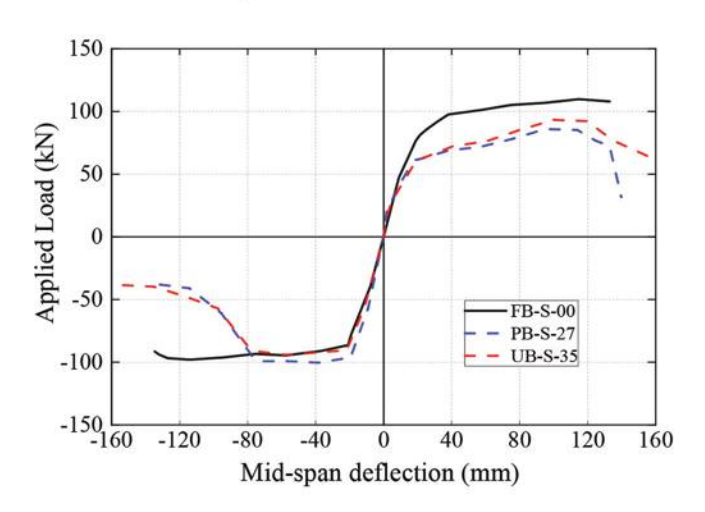
significantly different from the downward behavior. This is attributed to the fact that the prestressing tendon is placed at the bottom of the beams.

Load-carrying capacity

Table 4 lists the cracking loads, yielding loads (corresponding to the yielding of the nonprestressed steel bars), and maximum loads of the specimens. It was observed that the cracking loads under downward loading were influenced little by the unbonded length of CFRP tendons. However, a trend was observed where the maximum loads (P_{max}) decreased as the unbonded length of the CFRP tendons increased. Specifically, as the unbonded length increased



(a) CFRP prestressed concrete beams



(b) steel prestressed concrete beams

Fig. 9—Skeleton curve. (Note: 1 kN = 0.2248 kip; 1 mm = 0.039 in.)

from 1100 to 2700 mm (43.3 to 106.3 in.), the P_{max} under downward loading decreased by 14.3%. This trend is expected as the unbonded portion allows for slippage, and the tendon strain at the peak load generally decreases as the unbonded length increases. Similar findings have also been reported in reinforced concrete beams strengthened with partially bonded near-surface-mounted FRP bars/strips (Sharaky et al. 2015; Choi et al. 2011b). When the unbonded length was beyond 2700 mm (106.3 in.), however, further increases in unbonded length had a negligible effect on P_{max} . It is important to note that the fully bonded CFRP prestressed beam (FB-C-00) exhibited a flexural capacity 8.0% lower than that of Specimen PB-C-11. This is because Specimen FB-C-00 experienced a premature failure due to rupture of CFRP before concrete crushing occurred. In contrast, an opposite trend was noticed in the prestressed beams with steel strands, where the maximum load capacity of the fully bonded prestressed beam (FB-S-00) was 29.0% higher than that of the partially bonded prestressed beam (PB-S-27).

This is because both beams failed due to concrete crushing, and the stress in the fully bonded prestressed beam was higher than that in the partially bonded prestressed beam.

Displacement ductility

Ductility is a measure of the ability of a structural member to sustain large inelastic deformation without substantial decrease in load-carrying capacity. It serves as a warning sign before the occurrence of structural collapse. The ductility of a structural concrete beam can be expressed using the displacement ductility coefficient as follows

$$\mu = \frac{\Delta_u}{\Delta_v} \tag{2}$$

where Δ_y is the displacement corresponding to the yielding of the beam specimens; and Δ_u is the displacement at failure or the displacement corresponding to 80% maximum load in descending part of the skeleton curves, whichever is smaller (Park 1989). The measured Δ_u for each beam is provided in Table 4. When subjected to downward loading, the beams with the partially bonded CFRP tendon exhibited significantly higher deformability compared to the fully bonded CFRP prestressed concrete beam. This is due to the fact that the fully bonded beam exhibited a premature failure of CFRP rupture. Because the strains in the partially bonded tendon are relieved from critical sections and averaged out along the unbonded length, there was a trend that the deformability slightly increased as the unbonded length of the CFRP tendon increased.

The measured ductility coefficients of each beam are provided in Table 4, where only the ductility under downward loading was considered. The displacement ductility coefficients of partially bonded CFRP prestressed concrete specimens were in the range of 5.38 to 5.70, indicating that the specimens behaved in a relatively ductile manner. As observed in Table 4, the beams prestressed with steel strands displayed a more ductile behavior than those prestressed with CFRP strands. This can be attributed to the fact that CFRP possesses a linear elastic stress-strain relation and is inherently brittle in nature.

The bond condition had a significant effect on the displacement ductility of CFRP prestressed concrete beams under downward loading, as evident in Table 4. The displacement ductility of the partially bonded prestressed beams (PB-C-11, PB-C-19, and PB-C-27) was significantly higher than that of the fully bonded prestressed beam ($\mu = 2.83$) and slightly lower than that of the fully unbonded prestressed beam ($\mu =$ 6.10). This is expected because the fully bonded prestressed beam failed due to rupture of the CFRP tendon, whereas the partially bonded and fully unbonded prestressed beams failed due to concrete crushing. Among the partially bonded prestressed beams tested, varying the unbonded length from 1100 to 2700 mm (43.3 to 106.3 in.) had an insignificant effect on the ductility, although the displacement ductility appeared to increase slightly increased with increasing the unbonded length.

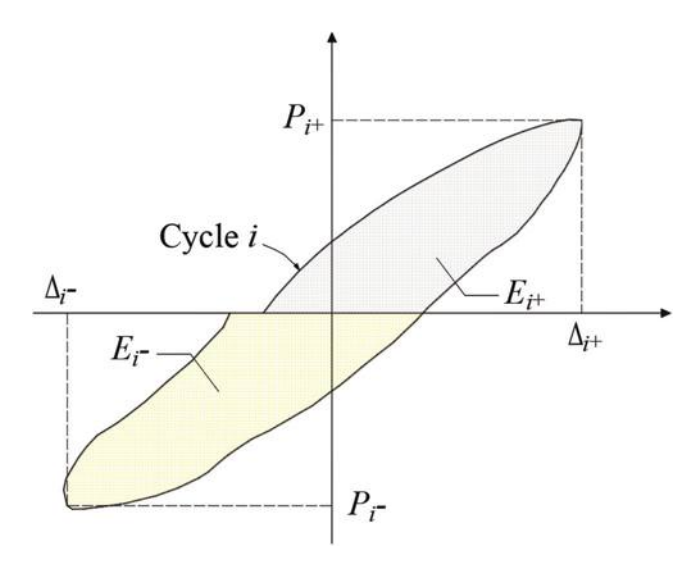
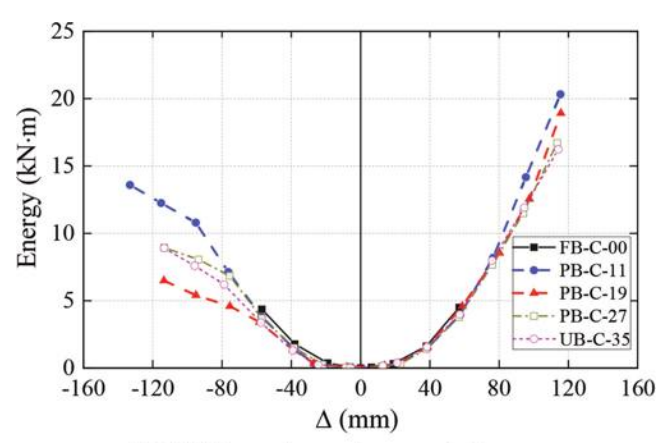


Fig. 10—Definition of energy dissipation.

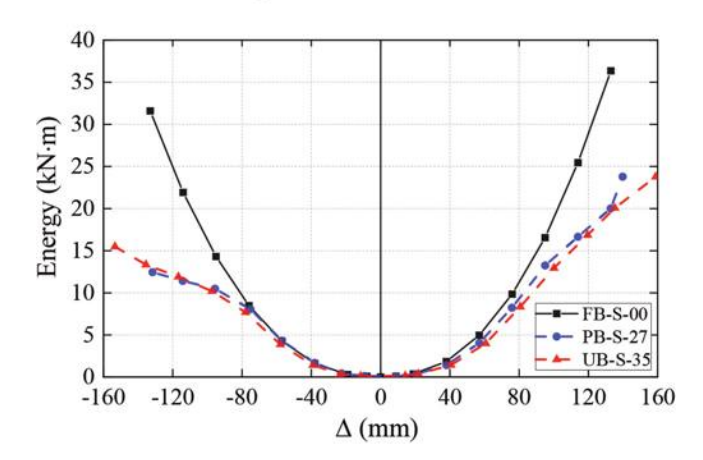
Energy dissipation capacity

The energy dissipation capacity of a structural member is a valuable indicator for evaluating the seismic performance of the member. To quantify the energy dissipated during a single load cycle, the Trapezoid Rule was employed to calculate the area enclosed by the applied load versus midspan deflection curve. In Fig. 10, the shaded area represents the energy dissipation corresponding to the *i*-th loading cycle during downward or upward loading. It should be noted that the energy calculation for each step is the average of every three load cycles. The accumulated dissipated energy is obtained by summing up the shaded areas over the entire loading process.

Figure 11 shows the cumulative energy dissipated in each cycle for the tested beams. Initially, the accumulated energy dissipation remained relatively small until the midspan displacement reached Δ_{v} . As the applied displacement increased, the cumulative energy dissipation also increased. Up to a midspan displacement of $2\Delta_v$, the energy dissipated during upward loading was nearly equivalent to that during downward loading. Nevertheless, when the midspan displacement exceeded $3\Delta_{\nu}$, less energy was dissipated during upward loading compared to downward loading. This discrepancy can be attributed to the placement of the prestressing tendon at the bottom of the beam, resulting in significant overall strength degradation in the hysteresis loops during upward loading. Specimen FB-C-00, which experienced premature CFRP rupture, exhibited the lowest energy dissipation upon failure, accounting for approximately 25% of the energy dissipated in the partially bonded specimens. As depicted in Fig. 11(a) and (b), increasing the unbonded length of the prestressing tendons slightly reduced the cumulative energy dissipation. This can be attributed to the fact that prestressed beams with longer unbonded lengths exhibited lower load-carrying capacities. Figure 12 compares the cumulative energy dissipation in Specimen PB-C-27 (partially bonded CFRP tendon) with that in Specimen PB-S-27 (partially bonded steel tendon). Under identical loading cycles with the same downward displacements, the beam with the partially bonded CFRP



(a) CFRP prestressed concrete beams



(b) Steel prestressed concrete beams

Fig. 11—Cumulative energy dissipation. (Note: 1 kN·m = 8.86 kip·in.; 1 mm = 0.0394 in.)

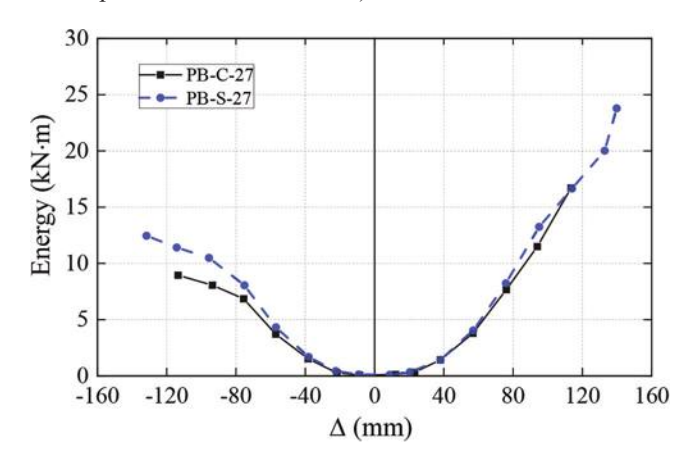


Fig. 12—Comparison of cumulative energy dissipation. (Note: 1 kN·m = 8.86 kip·in.; 1 mm = 0.039 in.)

tendon demonstrated a similar energy dissipation capacity to the beam with the partially bonded steel tendon, indicating that the fully bonded CFRP tendon beam exhibits a favorable energy dissipation capacity.

DESIGN APPROACH FOR FLEXURAL CAPACITY

Currently, there is a lack of design guidelines for prestressed concrete beams with partially bonded CFRP tendons. In this study, the flexural design method previously

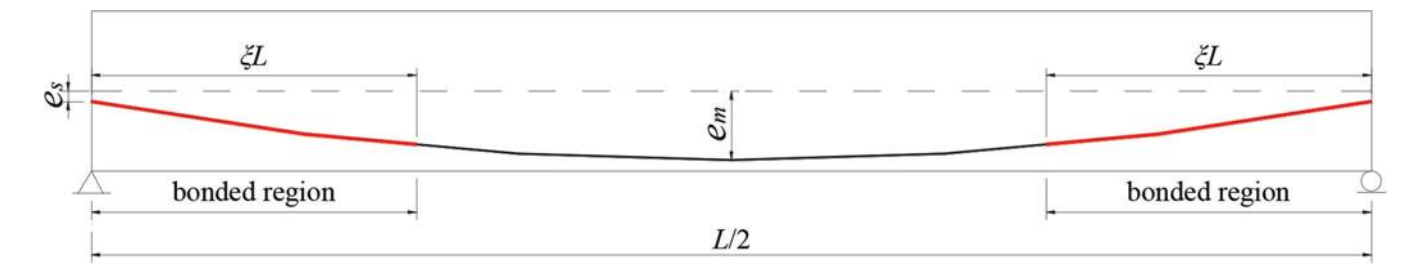


Fig. 13—Schematic diagram of partially bonded prestressed concrete beam.

developed by the authors (Peng and Xue 2019b) for fully unbonded post-tensioned concrete members was modified for predicting the flexural capacity of the partially bonded beams. This modified design method was used to predict the flexural capacity of the partially bonded beams. For partially prestressed beams with partially bonded CFRP tendons and nonprestressed steel bars, the flexural capacity can be determined by

$$M_{u} = A_{s}'f_{y}'\left(\frac{\beta_{1}c}{2} - d_{s}'\right) + A_{s}f_{y}\left(d - \frac{\beta_{1}c}{2}\right) + A_{p}f_{p}\left(d_{p} - \frac{\beta_{1}c}{2}\right)$$
(3)

where A_s' is the area of steel bars in compression; b is the width of member; f_c' is the cylinder compressive strength of concrete; f_y' is the yield strength of steel bar in compression; f_p is the ultimate tensile stress in partially bonded or fully unbonded tendon; d_s' is the distance from the extreme compression fiber to the centroid of compression reinforcing bars; c is the distance from extreme compression fiber to the neutral axis at ultimate limit state; and β_1 is the ratio of depth of equivalent rectangular stress block to depth of neutral axis.

Because the ultimate stress in partially bonded tendons is member-dependent rather than section-dependent, an accurate prediction for the ultimate stress of the tendons is more difficult than that of bonded ones. The authors (Peng and Xue 2019b) have proposed an ultimate tensile stress equation for the unbonded tendon. For simplification, this equation was modified for the partially bonded tendon by introducing a relative bond length coefficient ξ (Fig. 13)

$$f_p = f_{pe} + \frac{E_p \varepsilon_{cu} e_m}{c} \frac{\chi}{(1 - \xi)} \left(\frac{1}{f} + \frac{d_p}{L} + \frac{0.1Z}{L} \right) \left(1 + \frac{e_s}{e_m} \zeta \right)$$
(4)

where f_p is the ultimate tensile stress in the partially bonded tendon; f_{pe} is the effective prestressed stress; E_p is the elastic modulus of the tendon; e_m is the tendon eccentricity at beam midspan; e_s is the eccentricity at the support; L is the span length; Z is the shear span; χ is the normalized tendon elongation parameter, $\chi = 1 + 0.15(e_s/e_m - 1)^2 \le 1.6$; ε_{cu} is the ultimate compressive strain of concrete; and f = 10 for a single concentrated load, 3 for two-third-point loads, and 6 for a uniform load application, respectively.

It should be mentioned that if the CFRP stress obtained from Eq. (4) is equal to or larger than the ultimate tensile strength f_{pu} , the expected failure mode is rupture of CFRP. Otherwise, concrete crushing will govern the failure. To

compute f_p from Eq. (4), the value of depth of the neutral axis at ultimate limit state c should be computed. By considering the equilibrium of internal forces, the depth of neutral axis c can be solved by

$$A_s'f_{v}' + 0.85\beta_1 f_c'bc = A_s f_v + A_p f_p$$
 (5)

Simultaneously solving Eq. (4) and (5) results in a quadratic equation in c with the following root

$$c = \frac{-B_1 + \sqrt{B_1^2 - 4A_1C_1}}{2A_1} \tag{6}$$

where
$$A_1 = 0.85 \beta_1 f_c' b$$
; $B_1 = A_s' f_y' - A_s f_y - A_p f_{pe}$; and $C_1 = -A_p E_p \varepsilon_{cu} e_m \frac{\chi}{1 - \xi} \left(\frac{1}{f} + \frac{d_p}{L} + \frac{0.1Z}{L} \right) \left(1 + \frac{e_s}{2 e_m} \right)$

For partially bonded or fully unbonded prestressed concrete beams, Table 4 compares the predictions according to the presented design approach against the experimental maximum loads. In general, the predictions are in good agreement with the experimental results. The experimental load-carrying capacity is on average 1.00 of the predicted value, with a standard deviation of 6.6%.

SUMMARY AND CONCLUSIONS

In this study, eight post-tensioned concrete beams were tested to investigate the cyclic behavior of prestressed concrete beams with partially bonded carbon fiber-reinforced polymer (CFRP) tendons. Furthermore, a modified design approach for determining the flexural capacity of the beams was proposed. Based on the analysis of the experimental results, the following conclusions can be drawn:

- 1. Increasing the unbonded length of the CFRP tendons shifted the failure mode from CFRP tendon rupture to concrete crushing. The post-tensioned concrete beam with fully bonded CFRP tendons failed due to tendon rupture, while the post-tensioned beams with partially bonded or fully unbonded tendons failed due to concrete crushing.
- 2. There was a trend that the maximum loads decreased with increasing unbonded length of CFRP tendons.
- 3. The displacement ductility of partially bonded prestressed beams ranged from 5.38 to 5.70, which was significantly higher than that of the fully bonded prestressed beam ($\mu = 2.83$) and slightly lower than that of the fully unbonded prestressed beam ($\mu = 6.10$).
- 4. The partially bonded CFRP prestressed concrete beams exhibited acceptable energy dissipation capacity, and

increasing unbonded length of prestressing tendons would slightly decrease the accumulated energy dissipation.

5. The experimental flexural capacities were in close agreement with the values estimated using the proposed design approach for partially bonded prestressed concrete beams. The experimental flexural capacity was on average 1.00 of the predicted value, with a standard deviation of 6.6%.

AUTHOR BIOS

Fei Peng is an Associate Professor in the College of Civil Engineering at Hunan University, Changsha, China, where he received his BS in 2013. He received his PhD from Tongji University, Shanghai, China, in 2019. His research interests include reinforced concrete structures with fiber-reinforced polymers and ultra-high-performance concrete structures.

Weichen Xue is the corresponding author and a Professor in the Department of Structural Engineering at Tongji University. He received his BS from Harbin Engineering University, Harbin, Heilongjiang, China, in 1990; his MS from Harbin Institute of Technology, Harbin, Heilongjiang, China, in 1992; and his PhD from Southeast University, Nanjing, Jiangsu, China, in 1995. His research interests include precast, prestressed concrete structures, and fiber-reinforced polymer composites.

Shulu Zhang is a Master's Student in the Department of Structural Engineering at Tongji University. He received his BS from East China Jiaotong University, Nanchang, Jiangxi, China, in 2004. His research interests include reinforced concrete structures.

ACKNOWLEDGMENTS

The authors gratefully acknowledge the financial support of the Fund of the National Natural Science Foundation of China (No. 52130806 and No. 52008165).

REFERENCES

ACI Committee 440, 2004, "Prestressing Concrete Structures with FRP Tendons (ACI 440.4R-04)," American Concrete Institute, Farmington Hills, MI, 35 pp.

ASTM D7205-21, 2021, "Standard Test Method for Tensile Properties of Fiber Reinforced Polymer Matrix Composite Bars," ASTM International, West Conshohocken, PA, 13 pp.

Au, F. T. K., and Du, J. S., 2008, "Deformability of Concrete Beams with Unbonded FRP Tendons," *Engineering Structures*, V. 30, No. 12, pp. 3764-3770. doi: 10.1016/j.engstruct.2008.07.003

Chen, C.; Chen, J.; Zhou, Y.; Sui, L.; and Hu, B., 2021, "Design of Ductile H-Anchorage for Strengthening Reinforced Concrete Beams with Prestressed FRP," *Construction and Building Materials*, V. 307, Nov., p. 124883. doi: 10.1016/j.conbuildmat.2021.124883

Choi, H. T.; West, J. S.; and Soudki, K. A., 2011a, "Effect of Partial Unbonding on Prestressed Near-Surface-Mounted CFRP-Strengthened Concrete T-Beams," *Journal of Composites for Construction*, ASCE, V. 15, No. 1, Feb., pp. 93-102. doi: 10.1061/(ASCE)CC.1943-5614.0000149

Choi, H. T.; West, J. S.; and Soudki, K. A., 2011b, "Partially Bonded Near-Surface-Mounted CFRP Bars for Strengthened Concrete T-Beams," *Construction and Building Materials*, V. 25, No. 5, May, pp. 2441-2449. doi: 10.1016/j.conbuildmat.2010.11.056

Dorian, P. T., 2002, "Deformability and Ductility of Partially-Prestressed Concrete Beams Containing CFRP/Stainless Steel Reinforcements," master's dissertation, Queen's University, Kingston, ON, Canada, 255 pp.

Fischer, G., and Li, V. C., 2003, "Deformation Behavior of Fiber-Reinforced Polymer Reinforced Engineered Cementitious Composite (ECC) Flexural Members under Reversed Cyclic Loading Conditions," *ACI Structural Journal*, V. 100, No. 1, Jan.-Feb., pp. 25-35.

GB/T 50081, 2019, "Standard for Test Methods of Concrete Physical and Mechanical Properties (GB/T 50081-2019)," China Architecture & Building Press, Beijing, China, 103 pp.

GB/T 50152, 2012, "Standard for Test Method of Concrete Structures (GB/T 50152-2012)," China Architecture & Building Press, Beijing, China, 119 pp.

Grace, N. F., and Abdel-Sayed, G., 1998, "Ductility of Prestressed Concrete Bridges Using CFRP Strands," *Concrete International*, V. 20, No. 6, June, pp. 25-30.

Grace, N. F.; Ushijima, K.; Matsagar, V.; and Wu, C., 2013, "Performance of AASHTO-Type Bridge Model Prestressed with Carbon Fiber-Reinforced Polymer Reinforcement," *ACI Structural Journal*, V. 110, No. 3, May-June, pp. 491-501.

Heo, S.; Shin, S.; and Lee, C., 2013, "Flexural Behavior of Concrete Beams Internally Prestressed with Unbonded Carbon-Fiber-Reinforced Polymer Tendons," *Journal of Composites for Construction*, ASCE, V. 17, No. 2, Apr., pp. 167-175. doi: 10.1061/(ASCE)CC.1943-5614.0000306

Jeong, Y.; Kim, W. S.; Gribniak, V.; and Hui, D., 2019, "Fatigue Behavior of Concrete Beams Prestressed with Partially Bonded CFRP Bars Subjected to Cyclic Loads," *Materials (Basel)*, V. 12, No. 20, Oct., p. 3352. doi: 10.3390/ma12203352

Lee, C.; Shin, S.; and Lee, H., 2017, "Balanced Ratio of Concrete Beams Internally Prestressed with Unbonded CFRP Tendons," *International Journal of Concrete Structures and Materials*, V. 11, No. 1, pp. 1-16. doi: 10.1007/s40069-016-0171-6

Lees, J. M., and Burgoyne, C. J., 1999, "Experimental Study of Influence of Bond on Flexural Behavior of Concrete Beams Pretensioned with Aramid Fiber Reinforced Plastics," *ACI Structural Journal*, V. 96, No. 3, May-June, pp. 377-385.

Park, R., 1989, "Evaluation of Ductility of Structures and Structural Assemblages from Laboratory Testing," *Bulletin of the New Zealand National Society for Earthquake Engineering*, V. 22, No. 3, pp. 155-166. doi: 10.5459/bnzsee.22.3.155-166

Peng, F., and Xue, W., 2018a, "Design Approach for Flexural Capacity of Concrete T-Beams with Bonded Prestressed and Nonprestressed FRP Reinforcements," *Composite Structures*, V. 204, pp. 333-341. doi: 10.1016/j.compstruct.2018.07.091

Peng, F., and Xue, W., 2018b, "Analytical Approach for Flexural Capacity of FRP Prestressed Concrete T-Beams with Non-Prestressed Steel Bars," *Journal of Composites for Construction*, ASCE, V. 22, No. 6, p. 04018063. doi: 10.1061/(ASCE)CC.1943-5614.0000903

Peng, F., and Xue, W., 2019a, "Reliability-Based Design Provisions for Flexural Strength of Fiber-Reinforced Polymer Prestressed Concrete Bridge Girders," *ACI Structural Journal*, V. 116, No. 1, Jan., pp. 251-260. doi: 10.14359/51710876

Peng, F., and Xue, W., 2019b, "Calculating Method for Ultimate Tendon Stress in Internally Unbonded Prestressed Concrete Members," *ACI Structural Journal*, V. 116, No. 5, Sept., pp. 225-234. doi: 10.14359/51716764

Peng, F.; Xue, W.; and Yu, T., 2023, "Cyclic Behavior of Polypropylene Fiber Reinforced Concrete Beams with Prestressed CFRP Tendons and Nonprestressed Steel Bars," *Engineering Structures*, V. 275, Jan., p. 115201. doi: 10.1016/j.engstruct.2022.115201

Poudel, P.; Belarbi, A.; Gencturk, B.; and Dawood, M., 2022, "Flexural Behavior of Full-Scale, Carbon-Fiber-Reinforced Polymer Prestressed Concrete Beams," *PCI Journal*, V. 67, No. 5, Sept.-Oct., pp. 22-39. doi: 10.15554/pcij67.5-01

Rizkalla, N. S., 2000, "Partial Bonding and Partial Prestressing Using Stainless Steel Reinforcement for Members Prestressed with FRP," master's dissertation, Queen's University, Kingston, ON, Canada, 212 pp.

Safan, M. A., 2013, "Flexural Behavior and Design of Steel-GFRP Reinforced Concrete Beams," *ACI Materials Journal*, V. 110, No. 6, Nov.-Dec., pp. 677-685.

Sharaky, I. A.; Torres, L.; and Sallam, H. E. M., 2015, "Experimental and Analytical Investigation into the Flexural Performance of RC Beams with Partially and Fully Bonded NSM FRP Bars/Strips," *Composite Structures*, V. 122, pp. 113-126. doi: 10.1016/j.compstruct.2014.11.057

Sun, Y.; Wu, T.; Liu, X.; and Zhang, B., 2022, "Failure Mode and Flexural Capacity of Concrete Beams Prestressed with Unbonded FRP Tendons," *Composite Structures*, V. 283, p. 114956. doi: 10.1016/j. compstruct.2021.114956

Xue, W.; Cheng, B.; Zheng, R.; Li, L.; and Li, J., 2011, "Seismic Performance of Nonprestressed and Prestressed HPC Frames under Low Reversed Cyclic Loading," *Journal of Structural Engineering*, ASCE, V. 137, No. 11, pp. 1254-1262. doi: 10.1061/(ASCE)ST.1943-541X.0000367

CALL FOR ACTION

ACI Invites You To...

Share your expertise

Do you have EXPERTISE in any of these areas?

- BIM
- Chimneys
- Circular Concrete Structures Prestressed by Wrapping with Wire and Strand
- Circular Concrete Structures Prestressed with Circumferential Tendons
- Concrete Properties
- Demolition
- Deterioration of Concrete in Hydraulic Structures
- Electronic Data Exchange
- Insulating Concrete Forms, Design, and Construction
- · Nuclear Reactors, Concrete Components
- Pedestal Water Towers
- Pipe, Cast-in-Place
- Strengthening of Concrete Members
- Sustainability

Then become a REVIEWER for the ACI Structural Journal or the ACI Materials Journal.

Become a
Reviewer for the
ACI Journals

How to become a Reviewer:

- 1. Go to: http://mc.manuscriptcentral.com/aci;
- 2. Click on "Create Account" in the upper right-hand corner; and
- 3. Enter your E-mail/Name, Address, User ID and Password, and Area(s) of Expertise.

Update your Manuscript Central user account information

Did you know that the database for MANUSCRIPT CENTRAL, our manuscript submission program, is separate from the ACI membership database?

How to update your user account:

- 1. Go to http://mc.manuscriptcentral.com/aci;
- 2. Log in with your current User ID & Password; and
- 3. Update your E-mail/Name, Address, User ID and Password, and Area(s) of Expertise.

QUESTIONS?

E-mail any questions to Journals.Manuscripts@concrete.org.



Title No. 121-S26

Response of Reinforced Concrete Shell Elements Subjected to In-Plane and Out-of-Plane Shear

by Giorgio T. Proestos, Evan C. Bentz, and Michael P. Collins

This paper investigates the response of reinforced concrete shell elements subjected to all eight stress resultants (in-plane shear, two out-of-plane shears, torsion, two axial loads, and two moments). Twelve new experiments subjected to different combinations of in-plane and out-of-plane loads are presented. The experiments examine the influence of varying quantities of transverse shear reinforcement and concrete strengths. The paper also presents a new nonlinear, high-powered, macro finite element model called Shell II. The Shell II method is a three-layered model based on the equations of the Modified Compression Field Theory and is capable of predicting the full three-dimensional load-deformation response of shell elements subjected to combined loads. Shell II is also used to examine the experimental results in the context of in-plane versus out-of-plane shear-stress interaction diagrams. The results highlight the importance of considering combined loading in predicting the response of shells in three dimensions.

Keywords: axial stress; experiments; interaction diagrams; moments; shear; shells; three-dimensional; torsion.

INTRODUCTION

Complex reinforced and prestressed concrete structures often consist of members subjected to combinations of all eight stress resultants that can act on shell elements. These sectional resultants are one in-plane shear, V_{xy} ; two out-ofplane shears, V_{xz} and V_{yz} ; two axial loads, N_x and N_y ; two moments M_x and M_y ; and one torsion, M_{xy} (refer to Fig. 1). Some examples of structures that can be modeled as an assemblage of shell elements include walls, slabs, foundations, nuclear containment structures, offshore oil-platforms, grain silos, hydroelectric facilities, and dams. For example, in nuclear containment structures, a loss of coolant accident may result in axial tensions in the containment walls. If the incident was caused by an earthquake, aftershocks can induce additional in-plane and out-of-plane forces to the structure. Out-of-plane shears can also arise in locations where out-of-plane deformations are restrained by foundations or other rigid elements such as ring beams.

Figure 1 shows representations of a nuclear containment structure (bottom-left), walls subjected to combined loading (bottom-middle), and a bridge deck (bottom-right), where individual shell elements are highlighted. Figure 1 also shows the eight shell stress resultants (top-left) and the University of Toronto Shell Element Tester (SET) used to perform the experiments discussed in this paper (top-right).

The purpose of this paper is to summarize an investigation on the influence of combined loads on the response of reinforced concrete shell elements and to present an analytical model capable of predicting the full load-deformation

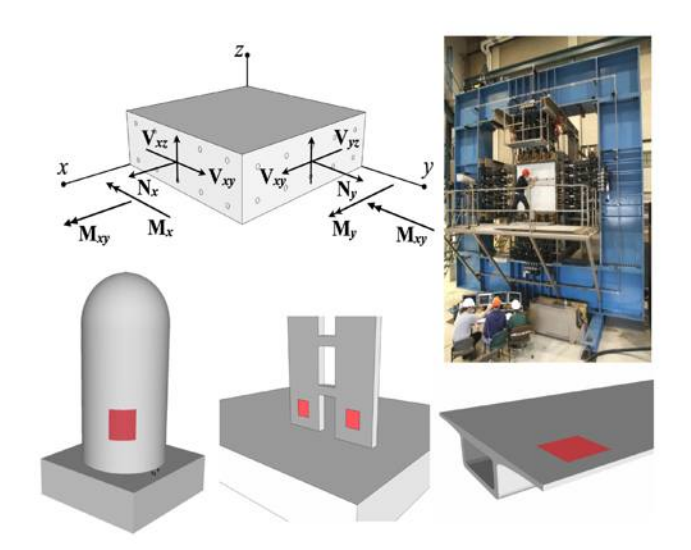


Fig. 1—Members subjected to eight shell element stress resultants.

response of these members. While the response of elements subjected to in-plane shear, biaxial stresses, and flexure have been studied previously, much less research has been conducted on the response of elements subjected to combined in-plane and out-of-plane shear. 1-4 To address this research gap, this paper first presents 12 experiments conducted on the SET. The experiments explore the influence of different loading ratios, reinforcement ratios, and concrete strengths on the member response. For members subjected to three-dimensional loads, the number of different combinations of loading ratios, concrete properties, and reinforcement properties is large. Provided there are eight stress resultants and approximately 10 design variables, conducting only three tests for each design variable would give 387 million experiments needed to explore all the interactions. Given the relatively small number of experiments available to examine these phenomena a model, based on a rational framework of equilibrium, compatibility, and stress-strain relationships is needed to predict the response of members and better interpret the experimental results. Thus, this paper presents a high-powered, macro finite element model capable

ACI Structural Journal, V. 121, No. 2, March 2024.

MS No. S-2023-133.R l, doi: 10.14359/51740252, received September 21, 2023, and reviewed under Institute publication policies. Copyright © 2024, American Concrete Institute. All rights reserved, including the making of copies unless permission is obtained from the copyright proprietors. Pertinent discussion including author's closure, if any, will be published ten months from this journal's date if the discussion is received within four months of the paper's print publication.

of predicting the full load deformation response of shell elements in three-dimensions. The method, called Shell II, is a three-layered model based on the Modified Compression Field Theory (MCFT). The results from Shell II are compared to the experiments presented in this paper. The model is used to predict the experimental response and is also used to show the interactions of members subjected to combinations of in-plane versus of out-of-plane-shear.

RESEARCH SIGNIFICANCE

Complex reinforced concrete structures are often modeled with three-dimensional shell elements representing slabs and walls or other structural components which can resist eight stress resultants. The interaction between these stress resultants is poorly understood with relatively few experiments and models available to quantify the safety of structures. This paper presents a new series of 12 experiments and model results to improve understanding of the response of shell elements subjected to combined loads.

EXPERIMENTAL PROGRAM

To investigate the response of shell elements subjected to combined loads, 12 shell elements, PS1 to PS12, were tested to failure with the SET. The SET consists of 60 servo-controlled hydraulic actuators: 40, 100 ton in-plane actuators and 20, 50 ton out-of-plane actuators. All actuators have a displacement potentiometer to monitor their position and a load cell to monitor their force. Simultaneously, all actuators are individually controlled in either force or displacement. Together, these actuators are capable of applying all eight stress resultants on test specimens measuring 1626 x 1626 mm (64 x 64 in.).

As a part of the PS series of tests, 10 specimens, PS1 to PS6 and PS9 to PS12, were subjected to combined in-plane and out-of-plane shear stresses, while PS7 and PS8 were only subjected to in-plane stresses. For the out-of-plane tests, the specimens measured 285 mm (11.2 in.) thick and contained 2.93% reinforcement in two layers along the xdirection and 1.95% reinforcement in two layers along the y-direction. For PS7 and PS8, measuring 278 mm (10.9 in.) thick, 3.00% reinforcement was provided in two layers along the x-direction and 0.67% reinforcement was provided along the y-direction. To induce in-plane shear stresses and torsions, the x-direction and y-direction reinforcement was oriented at 45 degrees to the actuators of the SET. PS5, PS6, and PS12 contained 0.197% transverse shear reinforcement corresponding to a quantity of shear reinforcement, $\rho_z f_v$, of 0.934 MPa (135 psi), while PS9 included 0.350% transverse shear reinforcement ($\rho_z f_v = 1.66$ MPa [241 psi]). This transverse shear reinforcement was provided in the form of headed bars placed through the thickness of the specimens in a grid of 6 x 6 bars for PS5, PS6, and PS12 and a grid of 8 x 8 for PS9 along the horizontal and vertical directions of the specimen. These headed bars had a bearing area of four times the bar area and extended beyond the in-plane reinforcement (refer to Fig. 2 inset photographs). The clear cover for all specimens was 53 mm (2.09 in.), except PS7 and PS8, which had a clear cover of 50 mm (1.97 in.). Among other structures, these reinforcement quantities and details are representative of portions of nuclear containment structure walls, grain silos, and off-offshore structures.⁵⁻⁷ Figure 2 provides a summary of the specimen geometry and reinforcement arrangement. Refer to Proestos⁸ for further details.

Table 1 provides a summary of the reinforcement steel properties associated with the stress-strain responses shown in Fig. 2 and the values used in this paper. The specimen concrete strengths were measured by testing $300 \times 150 \text{ mm}$ ($12 \times 6 \text{ in.}$) cylinders. The concrete strengths ranged from 28.5 to 100 MPa (4130 to 14,500 psi) and are summarized in Table 2.

To transfer loads into the specimens, the longitudinal bars were welded to plates and the plates were welded to steel blocks. These blocks were cast into the concrete. Loading yokes were bolted to the blocks and the loading yokes were connected to the actuators through pins. Additional information on the SET and experimental setup can be found elsewhere.^{8,9}

For PS1 and PS2, the in-plane actuators on the left and right side of the specimen and the in-plane actuators on the top and bottom of the specimen were used to apply out-ofplane moments, out-of-plane shears, and in-plane stresses. These forces were applied such that along the x-direction, the shell element was subjected to double curvature. The vertical in-plane actuators applied a net compression force and the horizontal actuators applied a net tension force. Therefore, because the reinforcement was oriented at 45 degrees to the applied axial forces, along the direction of the reinforcement, the element was subjected to shear stresses. There were no axial stresses along the x- or y-directions, nor was any out-of-plane shear along the y-direction on average. PS1 and PS2 are essentially beams in double curvature along the diagonal x-direction with in-plane shear stresses on their top and bottom surfaces. Figure 3 shows a diagram of the out-of-plane shear force and bending moment diagrams on the horizontal and vertical edges of the shell elements. The SET coordinate systems (horizontal and vertical) were at an angle of 45 degrees to the reinforcement (the X-Y coordinates). Figure 3 shows the Mohr circle transformations that relate the applied stresses (SET coordinates) to the stresses along the reinforcement directions (X-Y coordinates).

For PS1 and PS2, all horizontal in-plane and out-of-plane actuators were connected to the specimen. However, for PS3 to PS6 and PS9 to PS12, only the vertical in-plane and out-of-plane actuators were used (in addition to one horizontal actuator to maintain specimen stability). For these specimens, the shell elements were subjected to double curvature and out-of-plane shear along with an axial force in the vertical direction. These applied forces resulted in out-of-plane shear stresses and axial stresses in the x- and y-directions, as well as in-plane shear stresses and torsions. Figure 3 shows the applied vertical shear force and bending moment diagrams; however, for PS3 to PS6 and PS9 to PS12, the horizontal shear force and bending moment diagrams are zero.

PS7 was tested to investigate the shear response of conventionally reinforced elements with high concrete cylinder strengths. Prior to investigating the combined effects of in-plane and out-of-plane shear, PS7 was tested in pure shear. PS8, which was also cast from high-strength concrete, was subjected to pure in-plane shear and biaxial compression.

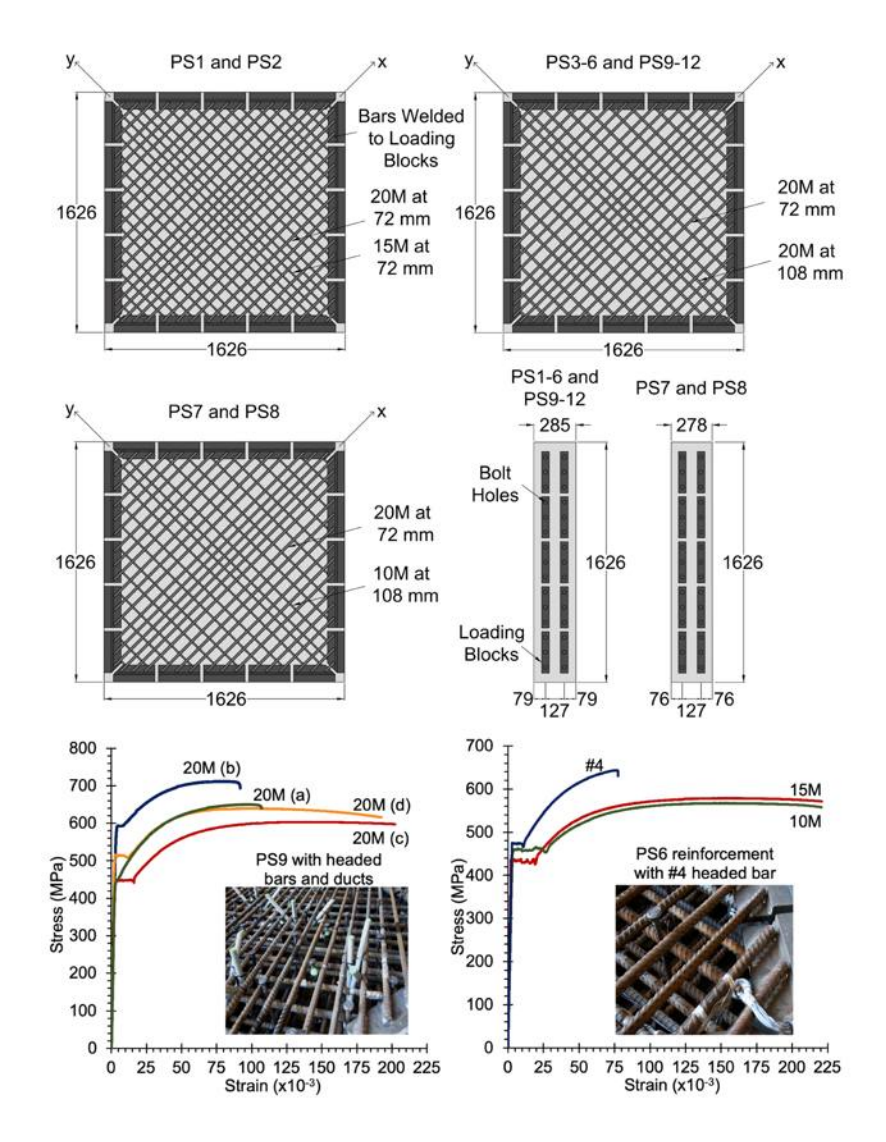


Fig. 2—Reinforcement details and measured steel properties. (Note: 1 MPa = 145 psi; 1 mm = 0.0394 in.; $1 \text{ mm}^2 = 0.00155 \text{ in.}^2$)

Table 1—Summary of reinforcement properties

Bar	Application	A_s , mm ²	f _{yield} , MPa	f _u , MPa	$\varepsilon_{sh}, \times 10^{-3}$	$\varepsilon_u, \times 10^{-3}$
20M (a)	x-direction, PS1 and PS2	300	448	655	5.70	111.6
20M (b)	x- and y-direction, PS3 to PS6, PS9 and PS10	300	593	712	8.86	88.6
20M (c)	x-direction, PS7 and PS8	300	445	604	11.21	140.6
20M (d)	x- and y-direction, PS11 and PS12	300	515	640	11.50	94.1
15M	y-direction, PS1 and PS2	200	433	579	19.10	153.3
10M	y-direction, PS7 and PS8	100	461	564	29.84	143.8
No. 4	z-direction, PS5, PS6, PS9, and PS12	127	474	644	10.72	76.3

Note: All bars are Canadian bar designations except No. 4 bar, which is U.S. bar designation.

Note: 1 MPa = 145 psi; 1 mm² = 0.00155 in.²

All tests were loaded monotonically until failure. For PS1 to PS10, the tests were loaded with the applied forces increasing proportionally to failure. For PS11 and PS12, however, the in-plane axial compression and in-plane shear was applied as a constant load of –3.50 MPa and the out-of-plane shears and moments were increased to failure. All specimens except PS7 and PS8 were pre-cracked to avoid first cracking governing failure. PS1 and PS2 were pre-cracked

by applying forces along the x-direction, whereas PS3 to PS6 and PS9 to PS12 were pre-cracked by applying vertical tension until a well-distributed crack pattern was observed.

Table 2 provides a summary of the specimen properties and loading ratios applied to the specimens. For convenience, the shear stresses at failure are also included in the table.

One important aspect of the PS experimental series was to instrument the test specimens so that both detailed in-plane

Table 2—Summary of specimen properties and applied loading

		x-d	lirection	reinforce	ment	y-direction reinforcement				z-direc	tion reinfo	rcement*			
Test	f _c ', MPa	x-bar	ρ _x , %	f_{yx} , MPa	f _u , MPa	y-bar	ρ _y , %	f _{yy} , MPa	f_u , MPa	ρ_z , %	f_{yz} , MPa	f _u , MPa	v _{xy} :v _{xz} ratio [†]	v _{xy} , MPa	v _{xz} , MPa
PS1	41.8	20M	2.93	448	655	15M	1.95	433	579	_	_	_	1.20:1	2.42	2.02
PS2	45.4	20M	2.93	448	655	15M	1.95	433	579	_	_	_	5.18:1	7.46	1.44
PS3	28.5	20M	2.93	593	712	20M	1.95	593	712	_	_	_	0.72:1	0.60	0.83
PS4	30.6	20M	2.93	593	712	20M	1.95	593	712	_	_	_	8.46:1	3.57	0.42
PS5	43.2	20M	2.93	593	712	20M	1.95	593	712	0.197	474	644	0.72:1	0.92	1.28
PS6	49.9	20M	2.93	593	712	20M	1.95	593	712	0.197	474	644	3.61:1	3.41	0.94
PS7	98.7	20M	3.00	445	604	10M	0.67	461	564	_	_	_	pure v_{xy}	5.39	_
PS8	100.0	20M	3.00	445	604	10M	0.67	461	564	_	_	_	$-0.40:1 f_n: v_{xy}$	9.11	_
PS9	38.2	20M	2.93	593	712	20M	1.95	593	712	0.350	474	644	3.29:1	3.61	1.10
PS10	39.8	20M	2.93	593	712	20M	1.95	593	712	_	_	_	-2.07:1	-3.14	1.52
PS11	98.3	20M	2.93	515	640	20M	1.95	515	640	_	_	_	0:1‡	-3.50	1.93
PS12	98.3	20M	2.93	515	640	20M	1.95	515	640	0.197	474	644	0:1 ‡	-3.50	2.33

^{*}z-direction reinforcement are U.S. No. 4 bars in all cases used.

Note: 1 MPa = 145 psi.

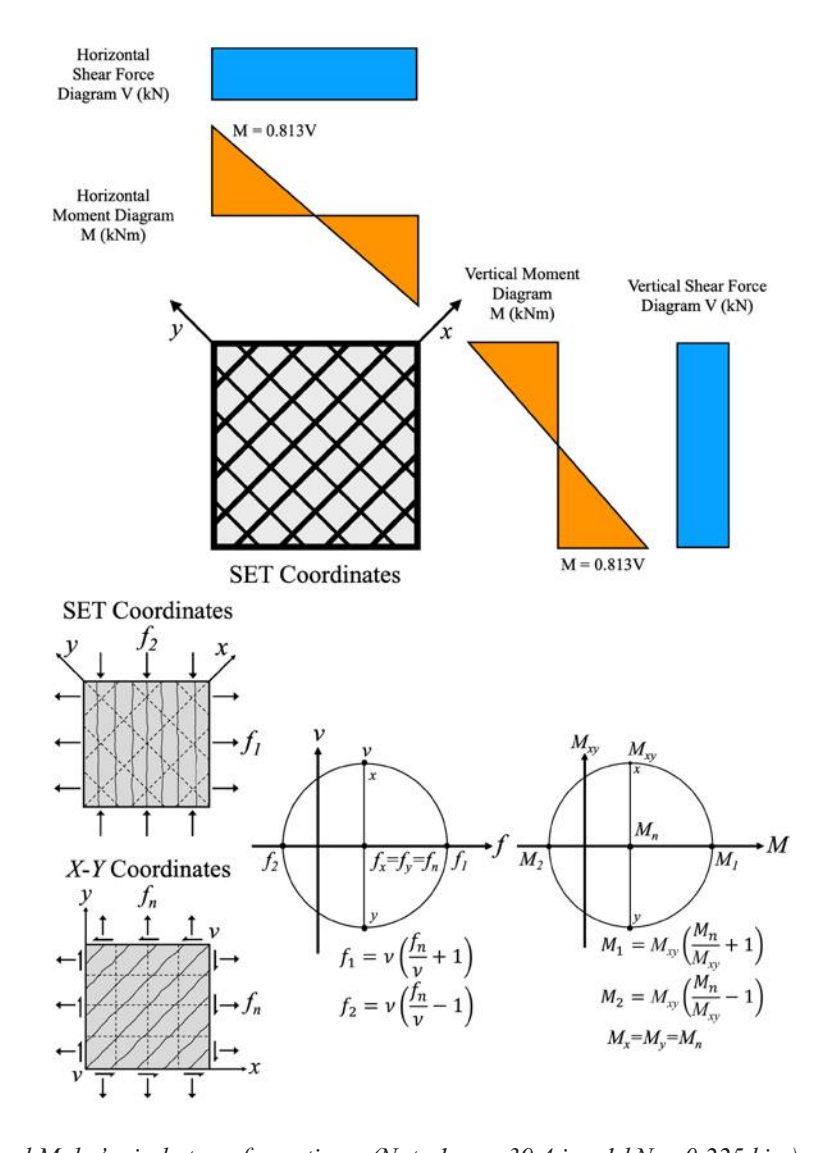


Fig. 3—Applied loads and Mohr's circle transformations. (Note 1 m=39.4 in.; 1 kN=0.225 kip.)

[†]Specimens PS3, PS4, PS5, PS6, PS9, PS10, PS11, and PS12 also have: $v_{xz} = v_{yz}$ and $f_x = f_y = v_{xy}$.

[‡]PS11 and PS12 have constant applied $f_x = f_y = v_{xy}$ of -3.50 MPa.

and out-of-plane displacements and strains could be monitored throughout loading. On each of the two in-plane surfaces, six linear variable differential transformers (LVDTs) were used to monitor the average strains over the specimen. On each face, two LVDTs monitored the horizontal strains, two LVDTs measured the vertical strains, one LVDT monitored the x-direction strain, and one LVDT the y-direction strain. In addition to these 12 LVDTs, 36 infrared light-emitting diodes (LEDs) were placed in a 6 x 6 grid spaced approximately 225 mm (8.86 in.) apart on the back surface. The LED data was used to monitor how the in-plane strain field varied over the specimen surface. In addition to these in-plane measurements, out-of-plane measurements were monitored using linear potentiometers. A total of 15 potentiometers were used in an arrangement of five sets of three potentiometers. As shown in Fig. 4, each set of three potentiometers consisted of two potentiometers placed through the thickness of the shell, oriented approximately 45 degrees to the out-of-plane axis and one potentiometer placed directly through the thickness of the shell. Prior to casting, ducts were placed through the shell thickness. After casting, each linear potentiometer was mounted on a bracket that was connected to a dowel. The end of the dowel was affixed to the opposite face of the shell element. For the diagonal ducts, the reinforcement arrangement often did not allow for the ducts to be inclined at exactly 45 degrees; therefore, they were placed at angles as close to 45 degrees as possible, shown as θ_1 and θ_3 in Fig. 4. These actual angles were measured and accounted for in the calculations of the strains.

For PS1 and PS2, all five sets of three potentiometers were arranged to align with the x-direction longitudinal steel. Thus, they were used to obtain a Mohr circle of strain on the x-z plane. For PS3 to PS6 and PS9 to PS12, three of these linear potentiometer rosettes were used to measure strains in the y-z plane and two were used to monitor strains on the x-z plane. These out-of-plane rosette measurements were used to determine the average strain response of the specimens and were combined with in-plane displacement measurements from the LVDTs and LEDs to determine the three-dimensional response of the members. This displacement field data was used in conjunction with measurements from the 60 load cells to determine the entire three-dimensional load-deformation response of the test specimens.

EXPERIMENTAL OBSERVATIONS

This section provides a summary of the experimental observations made for the PS series of experiments. Specimen PS1 was subjected to in-plane shear and out-of-plane shear along the x-direction. The companion specimen, PS2, was also subjected to these stress resultants. PS1 had an in-plane shear stress to out-of-plane shear stress ratio of 1.20, whereas PS2 had an in-plane to out-of-plane shear stress ratio of 5.18. Both members failed by out-of-plane shear. PS1 and PS2 did not contain any out-of-plane shear reinforcement and were governed by the amount of shear that could be transmitted by aggregate interlock stresses on the out-of-plane shear cracks that formed. PS1 reached a peak in-plane shear strength of 2.42 MPa (351 psi) and an out-of-plane

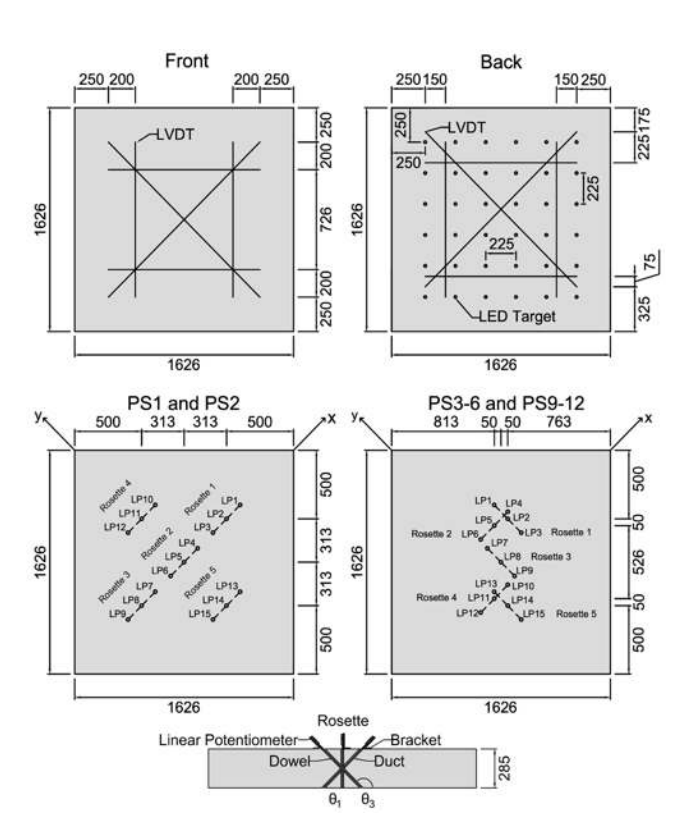


Fig. 4—In-plane LVDT and LED instrumentation (top) and out-of-plane linear potentiometers (bottom). (Note: 1 mm = 0.0394 in.)

shear strength of 2.02 MPa (293 psi), whereas PS2 reached an in-plane shear strength of 7.46 MPa (1082 psi) and an out-of-plane shear strength of 1.44 MPa (209 psi). Therefore, PS2 failed at an out-of-plane shear stress 29% lower than PS1 as a result of the additional 5.04 MPa (783 psi) of in-plane shear stress. This relative reduction in out-of-plane shear strength, because of the additional in-plane shear, demonstrates the strong interaction between in-plane versus out-of-plane shear stresses.

Unlike PS1 and PS2, PS3 to PS6 and PS9 to PS12 were subjected to in-plane biaxial stresses equal to the in-plane shear stress. They were also subjected to out-of-plane shear stresses along the y-direction equal to the out-of-plane shear stresses along the x-direction. PS3 was subjected to an in-plane shear to out-of-plane shear stress ratio of 0.72, while PS4 was subjected to an in-plane to out-of-plane shear stress ratio of 8.46. PS3 reached an in-plane shear strength of 0.60 MPa (87 psi) and an out-of-plane shear strength of 0.83 MPa (120 psi). PS4 reached a peak out-of-plane shear strength of 0.42 MPa (61 psi) and an in-plane shear strength of 3.57 MPa (518 psi). Therefore, PS4, which failed in out-of-plane shear, failed at an out-of-plane shear stress 51% of PS3.

PS5 and PS6 were companion specimens to PS3 and PS4 but included out-of-plane shear reinforcement. A quantity of 0.934 MPa (135 psi) was provided in a square grid of 6 x 6 of No. 4 headed bars. Similar to PS3, PS5 was loaded with an in-plane to out-of-plane shear stress ratio of 0.72. PS5 failed an out-of-plane shear stress 1.54 times greater than PS3. PS6 failed at an in-plane shear stress of 3.41 MPa (494 psi), similar to that of PS4, which failed at 3.57 MPa

(518 psi). However, PS6 failed at an out-of-plane shear stress 2.24 times larger than PS4. Thus, the inclusion of out-of-plane transverse reinforcement made the shell elements significantly stronger.

To investigate the influence of high-strength concrete on shear performance, PS7 and PS8 were first tested without the out-of-plane shear stresses or moments. PS7 was tested in pure in-plane shear, while PS8 was tested in pure in-plane shear and biaxial compression. PS7 and PS8 were heavily reinforced in the x-direction but lightly reinforced in the ydirection; this was selected to represent webs of members such as bridge girders or containment structures in their transverse direction. PS7 failed in a brittle manner at an in-plane shear strength of 5.39 MPa (782 psi). PS8 was subjected to in-plane shear and biaxial compression equal to -0.4v. This quantity of biaxial compression resulted the member reaching a higher ultimate in-plane shear strength, 9.11 MPa (1321 psi). Up to the final load stage, PS8 exhibited a well-distributed crack pattern. However, once the load reached the peak and the shear strains increased beyond 5.93×10^{-3} , a single crack dominated the response. That is, a crack near the top quarter of the shell element began to widen and failed by slipping across the crack interface. This slip was visually observable and was measured in the LED data. This type of shear failure, dominated by a single crack, was typical of the PC series of tests conducted by Calvi et al. 10,11

PS10, PS11, and PS12 were tested in combined biaxial compression and in-plane shear along with out-of-plane shear. The sign of the in-plane shear applied to PS3 to PS6 and PS9 resulted in tensile strains aligning with the tensile strains from the out-of-plane shear stresses. In contrast, the sign of the in-plane shear for PS10, PS11, and PS12 is such that the compression field from the in-plane shear stress has the tendency to reduce tensile strains arising from the out-of-plane shear stresses. These loading conditions result in significantly larger out-of-plane shear failure stresses for PS10 in comparison to companion specimens PS3 and PS4. PS10 did not include any transverse shear reinforcement and failed at a peak out-of-plane shear strength of 1.52 MPa (220 psi). This is 3.62 times higher than the failure stress of PS4, and is a result of the biaxial compressive stresses and sign of the in-plane shear stresses.

PS11 and PS12 were loaded with a constant -3.50 MPa (-508 psi) of in-plane shear stress and biaxial compression. The out-of-plane shear and moments were then increased proportionally to failure. PS11 did not contain any transverse shear reinforcement and is a high-strength companion to specimen PS10. Once reaching the peak load, PS11 suffered an abrupt out-of-plane shear failure. The particularly brittle failure can be attributed to the lack of transverse reinforcement, the high concrete strength, the biaxial compressive stresses, and the sign of the in-plane shear stresses. While the concrete cylinder strength was 2.5 times higher than PS10, PS11 failed at an out-of-plane shear stress of 1.93 MPa (280 psi), only 1.27 times higher than that of PS10.

PS12 was a companion specimen to PS11 but included transverse shear reinforcement. The transverse reinforcement greatly assisted in reducing the brittle nature of the failure. PS12 failed at an out-of-plane shear stress of 2.33 MPa

(338 psi). The beneficial effects of the transverse reinforcement were limited because flexural stresses combined with in-plane shear stresses near the corner of the element likely governed the ultimate load.

Figure 5 shows photographs of the shell elements after failure and includes the marked cracks. The load deformation response of the members is discussed in subsequent sections.

HIGH-STRENGTH REINFORCED CONCRETE SUBJECTED TO IN-PLANE SHEAR

PS7 and PS8 were cast from high-strength concrete. As a result of these high concrete strengths, the cracks were observed to cleave the aggregate rather than go around them and the cracks were seen to be straighter than similar members cast from lower-strength concrete. PS7 and PS8 had similar quantities of x-direction reinforcement to other experiments in the series, but relatively small amounts of y-direction reinforcement. Typically, under these reinforcement conditions, the shear cracks tend to rotate as stresses increases. This manifested itself as secondary cracks that form at smaller angles with respect to the x-reinforcement. This has been documented elsewhere in members subjected to in-plane shear and biaxial stresses. 1,5,12 While this mechanism of crack rotation occurs for members cast from normal-strength concretes, at very high concrete strengths, it is difficult for new cracks to form. Rather than new cracks forming, shear stresses cause slip along existing cracks. This was observed in PS7 and PS8. The slip of the critical crack for PS8 can be visually observed in Fig. 5.

The MCFT is capable of predicting the full load deformation response of PS7 and PS8. Previous studies have demonstrated that the MCFT can predict the response of membranes and shells in two dimensions well.^{1,5} When the same constitutive models as used by Proestos et al.5 are used to predict the response of PS7 and PS8, the MCFT overpredicts the peak load with test-to-predicted ratios of 0.81 and 0.75, respectively. The overpredictions may be a result of the overestimation of the amount of crack rotation that is capable for such high-strength concrete. To assess the ability for these constitutive models to capture the member response, the model was executed but prohibited the crack rotation after its initial formation. Using this limited crack rotation implementation of the MCFT, the test-to-predicted ratio for PS7 and PS8 was 1.01 and 0.90, respectively. The experimental and predicted shear stress-shear strain response is shown in Fig. 6. While for Fig. 6, the crack was limited to rotating 0 degrees, other assumptions can also be used. These comparisons are described elsewhere.8

In conducting these analyses, the constitutive laws were not altered; therefore, while limiting the crack rotations accounts, in part, for the effects of using high-strength concrete, additional modifications may also be warranted. Additionally, PS7 and PS8 contained 4.48 times more x-direction reinforcement than y-direction reinforcement. Under different loading conditions or reinforcement quantities, these considerations may require modification or be less important in predicting the member response. For example, for PS11, which has no transverse reinforcement, once the first major out-of-plane cracks form, the load-carrying

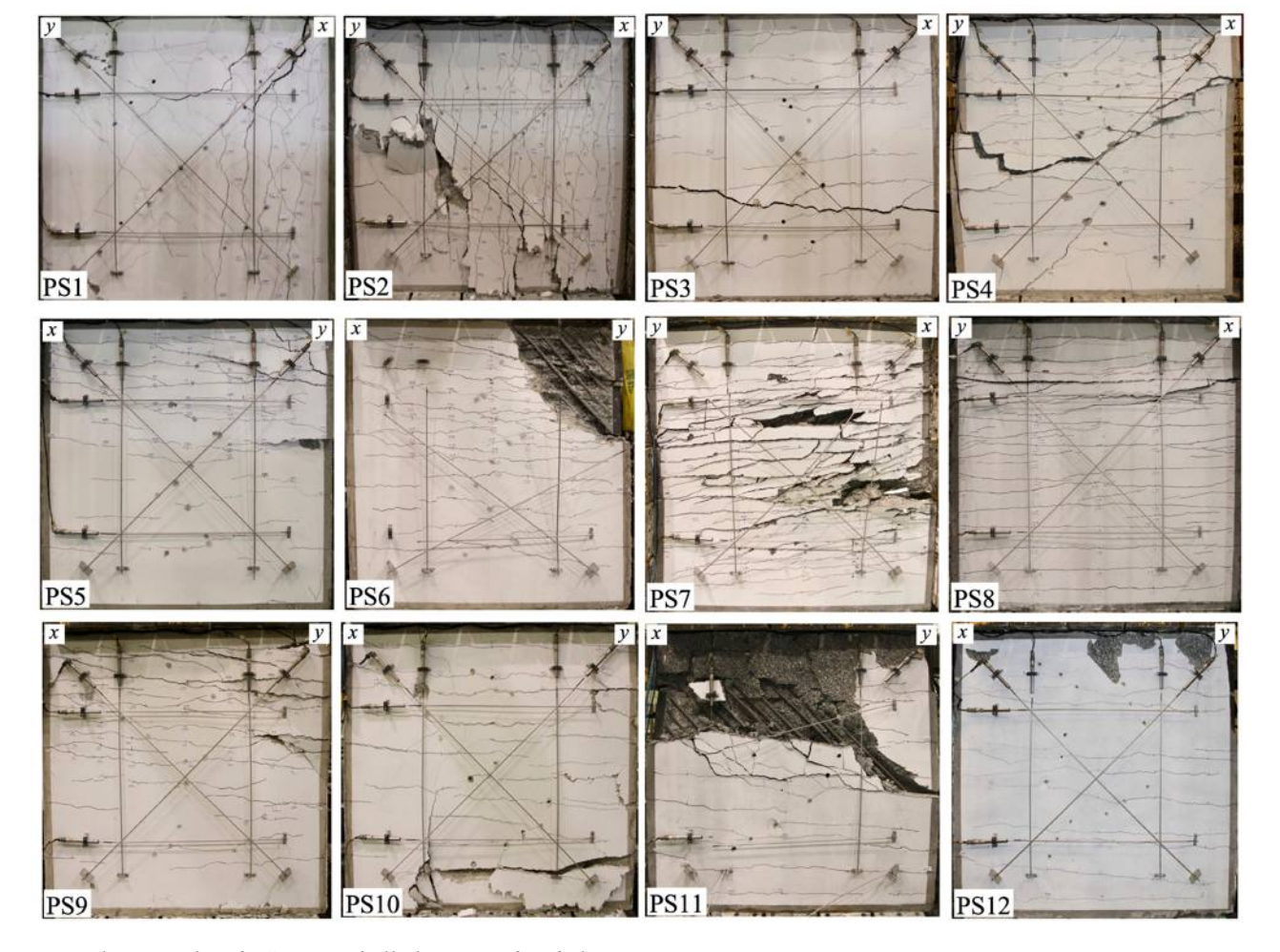


Fig. 5—Photographs of PS series shell elements after failure.

capacity reduced rapidly before any significant rotation could occur. For PS12, the ultimate load became governed not by out-of-plane shear cracks but by in-plane shear cracks and moments in the member. Therefore, while limiting the rotation of the crack is appropriate for PS7 and PS8, it is not needed for PS11 or PS12.

SHELL II—HIGH-POWERED, MACRO ELEMENT FINITE ELEMENT MODEL FOR REINFORCED CONCRETE SHELL ELEMENTS

To better understand the results of the 12 experiments presented, they will be compared to predictions from a new numerical model, Shell II. There exist several nonlinear finite element tools capable of modeling shell structures, including VecTor4, specifically formulated for shells. 13-15 These models, based on the Disturbed Stress Field Theory 16 and MCFT, 1 were developed at the University of Toronto and have shown to provide good results for a wide range of structures and loading conditions. In an effort to reduce the complexity of multilayer or multi-element models, a new, macro finite element model for reinforced concrete shells called Shell II has been developed. The purpose of developing this model was specifically to assess the shear and torsion response of shell elements subjected to combined in-plane and out-of-plane loads.

The model is a simplified three-layered model comprised of two, two-dimensional membrane elements and a threedimensional core. One membrane on top and one membrane on the bottom carry the axial loads, in-plane shears, and moments, while the triaxial core carries the out-ofplane shear stresses. This three-layered model is a threedimensional version of the traditional truss model for shear two chords connected by a thin web. Part of the reason for developing this Shell II method was to evaluate the predicted shear strength of shells in a manner that is consistent with design code approaches that rely on the two-dimensional truss model for shear, such as those in CSA A23.3-19,17 AASHTO LRFD 9th Edition, 18 and AS 3600-2018, 19 among others. The motivation for implementing this model in a finite element framework is to capture the effects of full member response that arise. A more detailed description of the Shell II model can be found in the appendix to this paper and in Proestos.8

The Shell II method was used to model the PS series of tests. Each shell was modeled with a grid of 16 by 16 elements. To simulate the effects of transverse clamping that would occur around the boundary of the shell from the loading yokes, one line of the edge elements (approximately 6% into the specimen) included additional transverse reinforcement such that these boundary elements did not fail in out-of-plane shear. Two nodes were restrained from

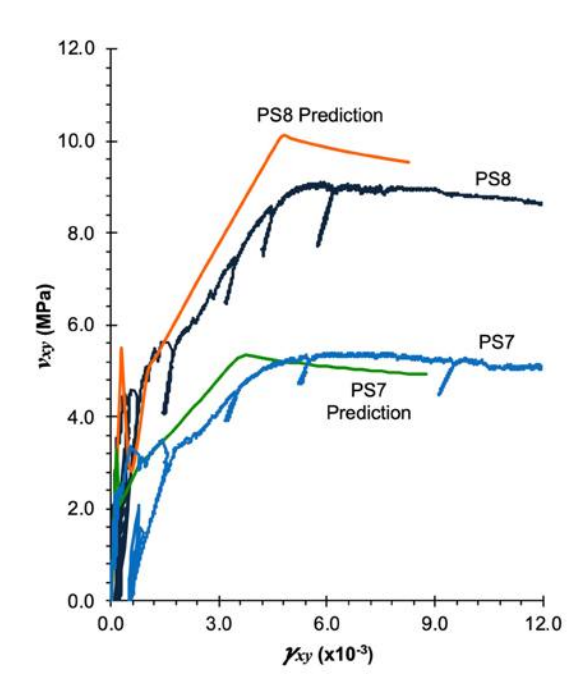


Fig. 6—Experimental and predicted shear stress versus shear strain response for PS7 and PS8. (Note: 1 MPa = 145 psi.)

vertical translation, one from horizontal translation and three from out-of-plane translations. These six translational fixities provide the minimum needed to satisfy static equilibrium. The forces were applied to the shell boundary to replicate uniform in-plane shear and biaxial stress as well as the out-of-plane shears and the corresponding moments. The models were constructed in SET coordinates with an example shown in Fig. 7.

Figure 7 shows the experimental and predicted in-plane shear stress versus in-plane shear strain. The experimental plots have numbered dots indicating the load stages. Load stage zero corresponds to the pre-cracking procedure described previously. A significant residual strain caused by this pre-cracking process can be observed in the responses of PS3, PS5, and PS10. This implementation of the Shell II method does not account for this plastic offset, therefore the predictions from Shell II for these specimens is manually shifted so that the strain response begins at the same value for zero shear stress. For completeness, the unshifted prediction passing through the origin is also plotted with a dotted line.

The in-plane shear stress versus shear strain response is reasonably predicted by Shell II. Generally, the cracked elastic response of the experiments is well predicted except for PS10, which exhibits more positive in-plane shear strain than predicted. A similar discrepancy is seen in PS11 and PS12. First, it should be noted that the magnitude of the strains is relatively small for these specimens. Additionally, this discrepancy can be partly attributed to the selection of the specific location of the elements used for comparison. For consistency, the elements corresponding to where the experimental instrumentation were located used for comparison to the model and were not changed across all the specimens examined.

Figure 8 shows the experimental and predicted out-ofplane response for the PS series. In Fig. 8, the experimental values can be identified as they have numbered points indicating the load stages. The experimental responses are labeled to distinguish the x-z and y-z directions. The Shell II predictions for the x-z direction are shown as a solid line, and as a dotted line in the y-z direction.

PS4, PS6, and PS9 are predicted to have softer responses than exhibited in the experiments. This discrepancy is likely a result of comparing smeared crack predictions with the out-of-plane measurements taken at discrete locations. If the out-of-plane shear cracks do not cross the through the thickness potentiometers located at discrete locations, it is possible to overestimate the predicted strains. For all other specimens, the overall specimen response is reasonably predicted by Shell II.

A summary of the 10 Shell II predictions for the tests subjected to out-of-plane shear are shown in Table 3. The test-to-predicted ratio of the peak load is 1.05 with a coefficient of variation of 8.9%. The most conservative result is 1.17 (PS5) and the least conservative result is 0.88 (PS4).

IN-PLANE SHEAR VERSUS OUT-OF-PLANE SHEAR INTERACTION DIAGRAMS

In the design and analysis of shell elements subjected to combined loads, it is often valuable to examine interaction diagrams. Of particular interest in this experimental series is the interaction of in-plane and out-of-plane shear stresses. First, Shell II is used to predict an interaction diagram for the PS1 and PS2 specimens. This interaction diagram, shown in Fig. 9, compares the influence of in-plane shear, v_{xy} , with out-of-plane shear in the v_{xz} direction. On the x-axis, an additional point, KS, is included (details on the KS series of tests can be found elsewhere⁵). For members subjected to pure in-plane shear, the test-to-predicted ratio for the MCFT against similar elements is plotted. This is also shown in Fig. 10. The verification and reliability of the in-plane response is described elsewhere.⁵ It should be noted that for the interaction shown in Fig. 9, Shell II predicts a symmetrical interaction about the vertical axis. That is, the same interaction is predicted for positive and negative shear stresses.

To examine PS3 to PS6 and PS9 to PS12, the interaction predicted by Shell II is shown in Fig. 10. Each line segment uses the specific reinforcement properties and concrete cylinder strengths associated with each specimen or companion specimens.

Unlike with PS1 and PS2, this interaction is not symmetrical about the vertical axis. This asymmetry results from the orientation of the in-plane and out-of-plane compression fields. For the positive in-plane shear stresses, the compression fields align and the cracks from the in-plane shear stress add to the tensile straining caused from the out-of-plane shear stresses. Conversely, for negative in-plane shear stresses, the compression field from the in-plane shear closes the out-of-plane shear cracks. This clamping of the out-of-plane shear cracks increases the strength of the members. For PS3 to PS6 and PS9 to PS12, this asymmetry is further emphasized by the biaxial tension and biaxial compression that is applied in proportion to the in-plane shear stress.

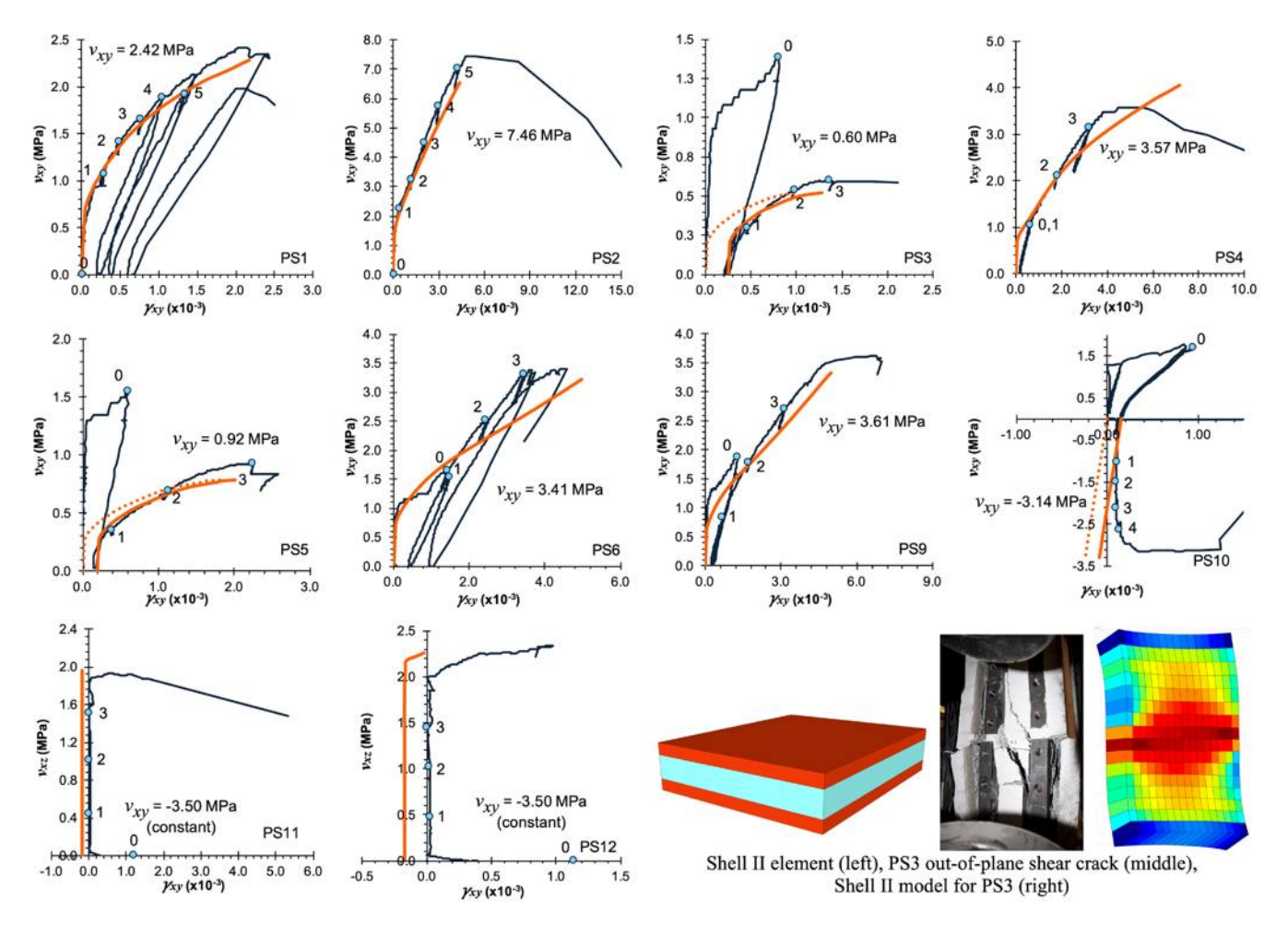


Fig. 7—Shell II predictions for in-plane shear stress versus in-plane shear strain. (Note: 1 MPa = 145 psi.)

The SP series of shell tests conducted by Adebar and Collins⁷ also demonstrated this phenomenon. The SP series of tests, however, did not include biaxial tension or biaxial compression and therefore demonstrates the asymmetry also occurs solely as a result of the sign of the in-plane shear. Figure 11 shows the SP series of tests on an interaction diagram along with the corresponding Shell II predictions. The average properties of the specimens are also shown in Fig. 11. Additional information can be found elsewhere.⁷

It can be seen that Shell II predicts the shear stress resulting in transverse yielding for the SP series well. The peak load is somewhat underpredicted. However, as other researchers have noted, the ultimate loads were high as a result of boundary effects. Therefore, the out-of-plane shear stress to cause first transverse reinforcement yielding is used for comparison to model predictions. 7,13,20 It is important to note the asymmetry in this diagram and the peak that forms for in-plane shear stresses that close the out-of-plane diagonal cracks. For SP4 and members with such large compressive stresses, the out-of-plane response becomes brittle without substantial strength beyond cracking. For these reasons, it is important to consider the sign of the in-plane shear stress when examining the out-of-plane shear behavior. In situations where shells are subjected to reverse cyclic loading or other scenarios that may result in pre-cracking, caution should be used to ensure that post-cracking strength is sufficient.

CONCLUSIONS

The paper presents the results from the PS series of reinforced concrete shell element tests conducted to investigate the response of members subjected to all eight stress resultants. The experimental series investigates the influence of reinforcement quantity, concrete strength, and loading ratio on the combined in-plane and out-of-plane shear response of shells. The results indicated that there is a significant interaction between the in-plane and out-of-plane shear response.

PS1 and PS2 were tested with combinations of in-plane shear v_{xz} , out-of-plane shear, and the corresponding moments. PS2 failed at an out-of-plane shear stress 29% lower than PS1 as a result of the additional 5.04 MPa (731 psi) of in-plane shear stress. PS3 to PS6 and PS9 were tested with in-plane shear and biaxial tension along with v_{xz} and v_{yz} out-of-plane shear stresses, and their corresponding out-ofplane moments. As a result of the additional 5.95 times larger biaxial tension and in-plane shear, PS4 reached a peak out-of-plane shear of only approximately half that of PS3. The influence of the in-plane shear and biaxial tension was also observed in PS5 and PS6; however, the use of transverse shear reinforcement improved their out-of-plane shear response in comparison to their PS3 and PS4 companion specimens. PS9, with larger quantities of transverse reinforcement, failed at higher out-of-plane shear stresses than the PS6 companion specimen.

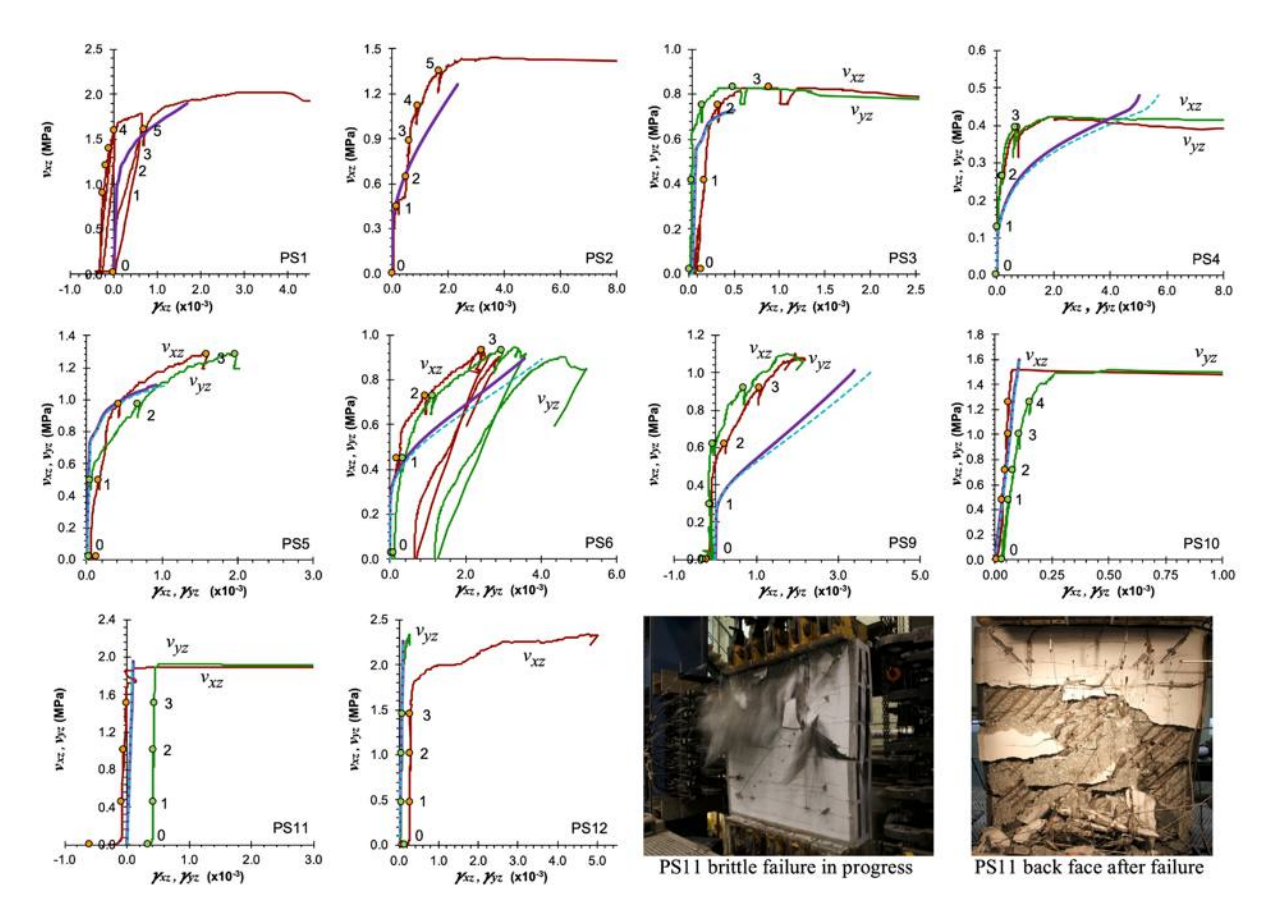


Fig. 8—Shell II predictions for out-of-plane shear stress versus out-of-plane shear strain. (Note: 1 MPa = 145 psi.)

Table 3—Shell II peak stress predictions

				Expe	riment		Shell II predictions	
Test	f _c ', MPa	ρ _z f _{yield} , MPa	v_{xy} : v_{xz} ratio	v _{xy} , MPa	v_{xz} , MPa	v _{xy} , MPa	v_{xz} , MPa	Test/Pred
PS1	41.8	_	1.20:1	2.42	2.02	2.28	1.90	1.06
PS2	45.4	_	5.18:1	7.46	1.44	6.53	1.26	1.14
PS3	28.5	_	0.72:1	0.60	0.83	0.52	0 .73	1.14
PS4	30.6	_	8.46:1	3.57	0.42	4.06	0.48	0.88
PS5	43.2	0.934	0.72:1	0.92	1.28	0.79	1.09	1.17
PS6	49.9	0.934	3.61:1	3.41	0.94	3.22	0.89	1.06
PS9	38.2	1.659	3.29:1	3.61	1.10	3.33	1.01	1.09
PS10	39.8	_	-2.07:1	-3.14	1.52	-3.31	1.60	0.95
PS11	98.3	_	0:1	-3.50	1.93	_	1.95	0.99
PS12	98.3	0.934	0:1	-3.50	2.33	_	2.26	1.03
							Mean	1.05
							COV, %	8.9

Note: 1 MPa = 145 psi.

PS7 and PS8, cast from 98.7 and 100.0 MPa (14,300 and 14,500 psi) concrete, respectively, were in-plane tested used to examine the shear response of high-strength reinforced concrete. PS7 was tested in pure in-plane shear, while PS8 was tested with in-plane shear and biaxial compression. As a result of the high-strength concrete, the aggregate cleaved, resulting in smooth shear cracks. Additionally, the high-strength concrete made it difficult for secondary cracks to form as shear stresses increased. This caused slipping along

shear cracks as stresses increased. When the amount of crack rotation in the Modified Compression Field Theory (MCFT) was limited to capture these phenomenon, the test-to-predicted ratios for PS7 and PS8 were 1.01 and 0.90, respectively.

PS10, PS11, and PS12 were tested with combinations of in-plane shear and biaxial compression combined with v_{xz} and v_{yz} out-of-plane shear stresses, and their corresponding out-of-plane moments and torsions. In addition to demonstrating the influence of biaxial compression, these tests demonstrate

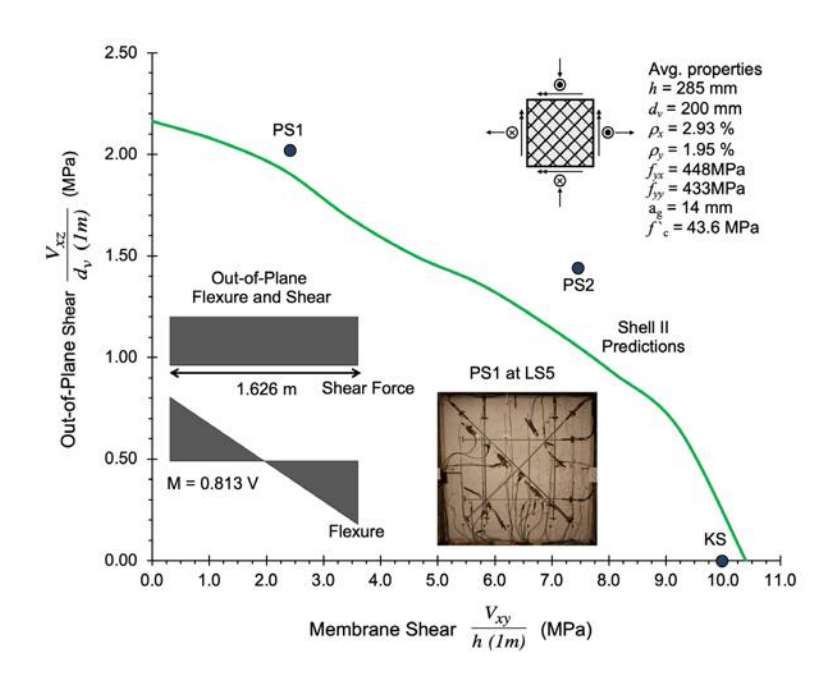


Fig. 9—Shell II predictions for PS1 and PS2, in-plane versus out-of-plane shear interaction. (Note: 1 MPa = 145 psi; 1 mm = 0.0394 in.)

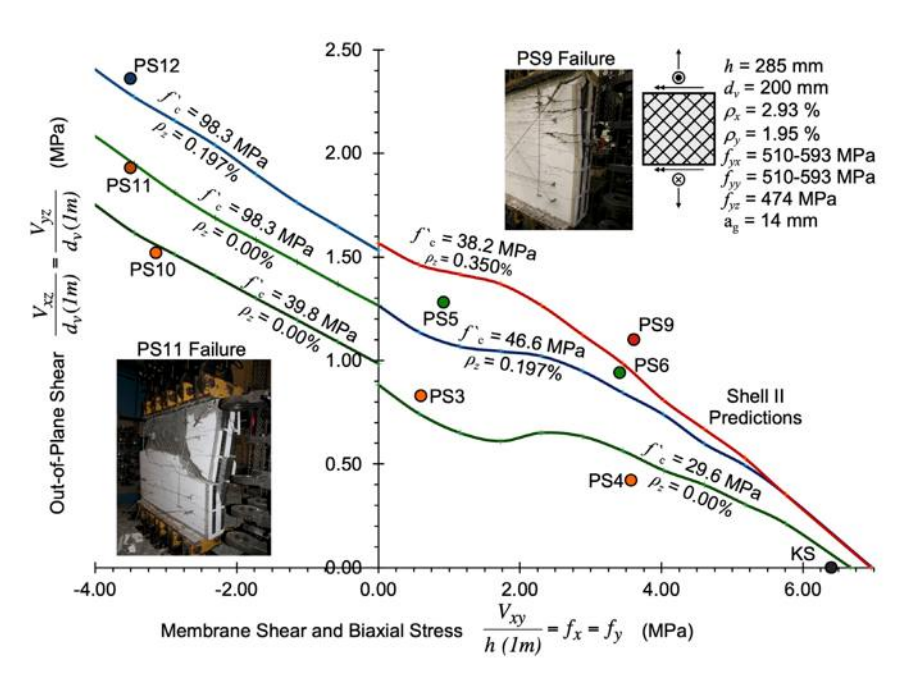


Fig. 10—Shell II predictions for PS3 to PS6 and PS9 to PS12, in-plane versus out-of-plane shear interaction. (Note: 1 MPa = 145 psi; 1 mm = 0.0394 in.)

the influence of the sign of the in-plane shear stress. PS10 failed at higher out-of-plane shear stresses compared to PS3 and PS4.

PS11 demonstrated the increase in strength as a result of high-strength concrete without any transverse reinforcement. However, the failure of PS11 was extremely brittle and without warning. PS12, which contained modest quantities of transverse reinforcement, controlled the transverse cracks.

Shell II, a new high-powered macro finite element method, based on the MCFT, is presented. This three-layer model capable of predicting the entire load deformation response of shells, showed to provide good results for the PS series of tests with an average test-to-predicted ratio for the peak load

of 1.05 and a coefficient of variation of 8.9%. Shell II was also used to develop interaction diagrams corresponding to the PS series of tests presented in this paper and the SP series of tests conducted by Adebar and Collins. The results indicate that Shell II is capable of predicting the response of shells for a variety of loading conditions including combinations of in-plane and out-of-plane shear stresses.

Caution should be used when making generalizations of in-plane versus out-of-plane shear interaction diagrams. As is demonstrated, the interaction diagrams are neither linear, circular, nor elliptical, and can change based on the specific member properties and loading ratios. Additionally, engineers should use caution as the interaction diagrams can be

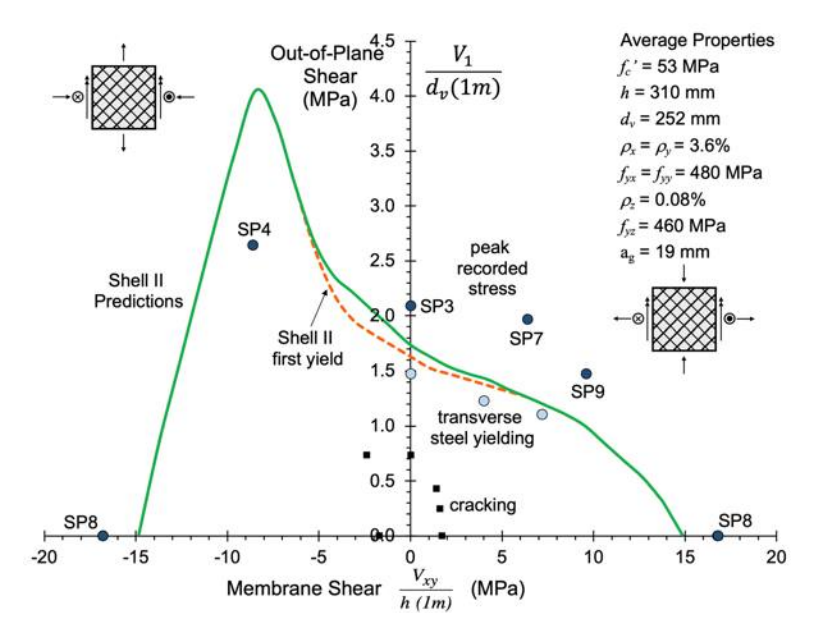


Fig. 11—Shell II predictions for Adebar and Collins' SP series. (Note: 1 MPa = 145 psi; 1 mm = 0.0394 in.)

asymmetrical with respect to the in-plane shear stress. This emphasizes the importance of having tools such as Shell II capable of capturing the complex interactions observed. In situations where significant combined in-plane shear and out-of-plane stress occur, engineers should consider the effects these combined loads will have on member response. Some scenarios may warrant the use of transverse shear reinforcement to control cracking or improve the resilience of these structures when subjected to an extreme event.

AUTHOR BIOS

ACI member Giorgio T. Proestos is an Assistant Professor at North Carolina State University, Raleigh, NC. He received his BASc in Engineering Science, his MASc, and his PhD from the University of Toronto, Toronto, ON, Canada, in 2012, 2014, and 2018, respectively. He is the Secretary of Joint ACI-ASCE Committee 445, Shear and Torsion, and a member of Joint ACI-ASCE Subcommittee 445-E, SOA Torsion. He received the ACI Chester Paul Seiss Award in 2018 and the ACI Design Award in 2017.

Evan C. Bentz, FACI, is Professor and Associate Chair (undergrad) of civil engineering at the University of Toronto. He received his BASc from the University of Waterloo, Waterloo, ON, Canada, in 1994 and his PhD from the University of Toronto in 2000. He is a member of Joint ACI-ASCE Committee 445, Shear and Torsion, and is past Chair of ACI Committee 365, Service Life Modeling. He received the ACI Chester Paul Seiss Award in 2018 and the ACI Design Award twice.

ACI Honorary Member Michael P. Collins is a University Professor Emeritus of structural engineering at the University of Toronto, where he has led a long-term research project aimed at developing rational but simple shear and torsion design procedures for both reinforced and prestressed concrete members. The results of this work have influenced design provisions for buildings, bridges, nuclear containment structures, and offshore concrete platforms. He has six awards from ACI.

ACKNOWLEDGMENTS

The Natural Sciences and Engineering Research Council of Canada's long-term support of the shear and torsion research program at the University of Toronto is greatly appreciated. The authors would also like to thank Headed Reinforcement Corporation who provided the headed bars used for the transverse shear reinforcement.

NOTATION

area of the steel A_{\cdot} maximum coarse aggregate size material stiffness matrix

effective depth effective shear depth d_v F_g
f_c
f_c
f_c
f_n
f_u
f_x
f_y
fyield
f_{yx}
f_{yy}
f_z
f_z
f₁
f₂ global forces compressive strength of concrete concrete cracking stress axial stress when $f_x = f_y = f_n$ ultimate stress of reinforcement axial stress in x-direction axial stress in y-direction yield stress of reinforcement yield stress of x-direction reinforcement yield stress of y-direction reinforcement yield stress of z-direction reinforcement axial stress in z-direction major (most tensile) principal stress minor principal stress in two dimensions and intermediate principal stress in three dimensions $\begin{array}{c}
f_3\\[f]\\h\\K_g\end{array}$ minor principal stress in three dimensions stress tensor total member height

global stiffness matrix

torsional moment

stiffness matrix in local coordinates

moment in direction of maximum moment

moment in direction of minimum moment

transverse shear force in direction of maximum out-of-plane

minor principal strain in two dimensions and intermediate prin-

moment when $M_{\rm r} = M_{\rm v} = M_{\rm n}$

bending moment on x-face

bending moment on y-face

axial force in x-direction

axial force in y-direction rotational transformation matrix

in-plane shear force in x-y plane

transverse shear force in x-z plane

transverse shear force in y-z plane

in-plane shear stress in x-y plane

global displacement field

axial strain in x-direction axial strain in y-direction

axial strain in z-direction

strain tensor

strain-hardening strain strain at ultimate stress

out-of-plane shear stress in x-z plane

out-of-plane shear stress in y-z plane

major (most tensile) principal strain

minor principal strain in three dimensions

in-plane engineering shear strain in x-y plane

cipal strain in three dimensions

 K_{loc}

 M_n

 M_{x}

 M_{xy}

 M_v

 $\dot{M_1}$

 M_2

 N_x

 N_y

 v_{xy}

 v_{xz}

 v_{yz}

 δ_g

 ε_{sh}

 ε_u

εχ

 ε_{y}

 ε_z ϵ_1

63

E3

[3]

 γ_{xz} = transverse engineering shear strain in x-z plane

 γ_{yz} = transverse engineering shear strain in y-z plane

 ρ_x = amount of reinforcement in the x-direction

 ρ_y = amount of reinforcement in the y-direction

 ρ_z = amount of reinforcement in the z-direction

REFERENCES

- 1. Vecchio, F. J., and Collins, M. P., "The Modified Compression Field Theory for Reinforced Concrete Elements Subjected to Shear," *ACI Journal Proceedings*, V. 83, No. 2, Mar.-Apr. 1986, pp. 219-231.
- 2. Kaufmann, W., Strength and Deformations of Structural Concrete Subjected to In-Plane Shear and Normal Forces, Birkhäuser Basel, 1998, 149 pp.
- 3. Kirschner, U., "Investigating the Behaviour of Reinforced Concrete Shell Elements," PhD thesis, Department of Civil Engineering, University of Toronto, Toronto, ON, Canada, 1986, 208 pp.
- 4. Polak, M. A., and Vecchio, F. J., "Nonlinear Analysis of Reinforced-Concrete Shells," *Journal of Structural Engineering*, ASCE, V. 119, No. 12, 1993, pp. 3439-3462. doi: 10.1061/(ASCE)0733-9445(1993)119:12(3439)
- 5. Proestos, G. T.; Bae, G. M.; Cho, J. Y.; Bentz, E. C.; and Collins, M. P., "Influence of High-Strength Bars on Shear Response of Containment Walls," *ACI Structural Journal*, V. 113, No. 5, Sept.-Oct. 2016, pp. 917-927. doi: 10.14359/51688750
- 6. Proestos, G. T., "Influence of High-Strength Reinforcing Bars on the Behaviour of Reinforced Concrete Nuclear Containment Structures Subjected to Shear," MASc thesis, Department of Civil Engineering, University of Toronto, Toronto, ON, Canada, 2014, 155 pp.
- 7. Adebar, P., and Collins, M. P., "Shear Design of Offshore Structures," ACI Structural Journal, V. 91, No. 3, May-June 1994, pp. 324-335.
- 8. Proestos, G. T., "Modelling Reinforced and Prestressed Concrete Structures Subjected to Shear and Torsion," PhD thesis, University of Toronto, Toronto, ON, Canada, 2018, 332 pp.
- 9. Ruggiero, D. M., "The Behaviour of Reinforced Concrete Subjected to Reversed Cyclic Shear," PhD thesis, Department of Civil Engineering, University of Toronto, Toronto, ON, Canada, 2015, 433 pp.
- 10. Calvi, P. M.; Bentz, E. C.; and Collins, M. P., "Model for Assessment of Cracked Reinforced Concrete Membrane Elements Subjected to Shear and Axial Loads," *ACI Structural Journal*, V. 115, No. 2, Mar. 2018, pp. 501-509. doi: 10.14359/51701093
- 11. Calvi, P. M.; Bentz, E. C.; and Collins, M. P., "Pure Mechanics Crack Model for Shear Stress Transfer in Cracked Reinforced Concrete," *ACI Structural Journal*, V. 114, No. 2, Mar.-Apr. 2017, pp. 545-554. doi: 10.14359/51689460
- 12. Bhide, S. B., and Collins, M. P., "Influence of Axial Tension on the Shear Capacity of Reinforced Concrete Members," *ACI Structural Journal*, V. 86, No. 5, Sept.-Oct. 1989, pp. 570-581.
- 13. Hrynyk, T. D., and Vecchio, F. J., "Capturing Out-of-Plane Shear Failures in the Analysis of Reinforced Concrete Shells," *Journal of Structural Engineering*, ASCE, V. 141, No. 12, 2015, p. 04015058.. doi: 10.1061/(ASCE)ST.1943-541X.0001311
- 14. Hrynyk, T. D., "Behaviour and Modelling of Reinforced Concrete Slabs and Shells Under Static and Dynamic Loads," PhD thesis, Department of Civil Engineering, University of Toronto, Toronto, ON, Canada, 2013, 436 pp.
- 15. Vecchio, F. J., "VecTor Suite of Programs," VecTor Analysis Group, http://www.vectoranalysisgroup.com/. (last accessed Jan. 18, 2024)
- 16. Vecchio, F. J., "Disturbed Stress Field Model for Reinforced Concrete: Formulation," *Journal of Structural Engineering*, ASCE, V. 126, No. 9, 2000, pp. 1070-1077. doi: 10.1061/(ASCE)0733-9445(2000)126:9(1070)
- 17. CSA A23.3-19, "Design of Concrete Structures," CSA Group, Toronto, ON, Canada, 2019, 301 pp.
- 18. AASHTO, "LRFD Bridge Design Specifications and Commentary," ninth edition, American Association of State Highway Transportation Officials, Washington, DC, 2020, 1914 pp.
- 19. AS 3600-2018, "Concrete Structures," Standards Australia, Sydney, NSW, Australia, 2018, 256 pp.
- 20. Bentz, E. C., "Sectional Analysis of Reinforced Concrete," PhD thesis, University of Toronto, Department of Civil Engineering, Toronto, ON, Canada, 2000, 316 pp.
- 21. Vecchio, F. J., "Reinforced Concrete Membrane Element Formulations," *Journal of Structural Engineering*, ASCE, V. 116, No. 3, 1990, pp. 730-750. doi: 10.1061/(ASCE)0733-9445(1990)116:3(730)
- 22. Selby, R. G., "Nonlinear Finite Element Analysis of Reinforced Concrete Solids," master's thesis, University of Toronto, Toronto, ON, Canada, 1990, 144 pp.
- 23. Adebar, P., "Shear Design of Concrete Offshore Structures," PhD thesis, Department of Civil Engineering, University of Toronto, Toronto, ON, Canada, 1989.

24. Collins, M. P., and Mitchell, D., *Prestressed Concrete Structures*, Prentice Hall, Englewood Cliffs, NJ, 1991, 766 pp.

APPENDIX A

For completeness, this appendix serves to provide additional information, including supplemental experimental information and a supplemental explanation of the nonlinear finite element model Shell II.

ADDITIONAL DETAILED EXPERIMENTAL DATA FOR THE PS SERIES

Table A1 provides a summary of the peak stresses, loading ratios and strains at peak stress for each of the 12 test specimens is the PS series. The values presented correspond to when the peak out-of-plane shear stress is reached. In some cases, at an instant after this loading is reached, the strains grow quickly.

The variables ϵ_{xy-1} and ϵ_{xy-2} are the in-plane principal tensile strains on the surface of the shell element as determined from the LVDT and LED data. The variables ϵ_1 , ϵ_2 , and ϵ_3 are the principal strains in three dimensions, as determined from the in-plane and out-of-plane instrumentation. The variable ϵ_1 is the most tensile principal strain and ϵ_3 is the most compressive principal strain.

Figure A1 shows the crack patterns at the last load stage as seen from the front face of the specimens. The widths of the lines are scaled such that the thinnest line represents a crack width of 0.05 mm (0.00197 in.) and the largest width is scaled to the largest crack measuring 3.50 mm (0.1378 in.) shown on PS7.

SHELL II—HIGH-POWERED, MACRO ELEMENT FINITE ELEMENT MODEL FOR REINFORCED CONCRETE SHELL ELEMENTS

Shell II is a high-powered, non-linear, macro finite element model based on the Modified Compression Field Theory (MCFT). The method uses a three-layered model comprised of two, two-dimensional membrane elements and a three-dimensional core. One membrane on top and one membrane on the bottom carry the axial loads, in-plane shears, moments, and torsions, while the triaxial core carries the out-of-plane shear stresses.

The Shell II macro element has 24 degrees of freedom, comprised of three orthogonal translational degrees of freedom at each of the eight nodes; refer to Fig. A2.

The bottom two-dimensional membrane element is connected at nodes 1, 2, 3, and 4 and the top membrane element is connected to nodes 5, 6, 7, and 8. Both membrane elements use rectangular iso-parametric bi-linear shape functions and implement the equations of MCFT in two dimensions. The core element shares nodes 1 through 8 and is connected at the eight corners. This element is a rectangular iso-parametric element that uses trilinear shape functions and implements the MCFT in three dimensions. The development of stiffness matrices for the two dimensional and three-dimensional elements use classical finite element approaches; their implementation and compatibility with the MCFT are detailed elsewhere. 8,14,20-23

The membrane elements are each taken to have a thickness of half the shell height, while the triaxial core is taken

to have a thickness equal to the shear depth $d_v = 0.9d$. It should be noted that while these are the default settings of the model, other assumptions can also be used. To ensure that the axial stiffnesses and in-plane shear stiffnesses of the core are not double counted, these stiffnesses are excluded from addition to the local stiffness matrix of the three-dimensional element. The material axial stiffness in the x-and y-directions, along with the in-plane shear stiffness from the three-dimensional MCFT, are neglected in the stiffness of the triaxial core. Specifically, for the material stiffness matrix, D, shown in Eq. (1), the D_{11} , D_{22} , D_{44} , D_{12} , D_{21} , D_{14} , D_{41} , D_{24} , and D_{42} terms in Eq. (2) are neglected.

$$[f] = [D][\varepsilon] \tag{1}$$

$$\begin{pmatrix}
f_x \\
f_y \\
f_z \\
v_{xy} \\
v_{yz} \\
v_{yz} \\
v_{yz}
\end{pmatrix} = \begin{pmatrix}
D_{11} & D_{12} & D_{13} \\
D_{21} & D_{22} & D_{23} \\
D_{31} & D_{32} & D_{33}
\end{pmatrix} \begin{pmatrix}
\varepsilon_x \\
\varepsilon_y \\
\varepsilon_z \\
\gamma_{xy} \\
\gamma_{yz} \\
\gamma_{xz}
\end{pmatrix} (2)$$

This stiffness decoupling approach ensures that the axial stiffnesses, and in-plane shear stiffness are not double counted while also ensuring that when these actions are combined with out-of-plane stresses, the correct interactions are captured. Specifically, the off-diagonal stiffness components of the triaxial core are included in the stiffness matrix. These off diagonal terms are critical in correctly capturing the effect of out-of-plane stresses on the in-plane response. For example, the MCFT predicts that a pure out-of-plane shear, v_{xz} , causes substantial demand on the x-direction reinforcement. The strains caused in the x-direction as a result of v_{xz} shear stresses arise mathematically from the off-diagonal terms.

In addition to these model assumptions, the element formulation assumes the z-direction clamping stress (f_z) in

the triaxial core element is equal to 0. In the model, the x-direction, y-direction, and in-plane shear strain distributions through the depth of the member remain linear. Because only one element is used, the out-of-plane shear strain distributions are constant through the depth.

The solution algorithm for the shell finite element method begins by defining the geometry of the structure, nodes, elements, boundary, and load conditions. The properties of each element are then defined. In addition to the input of the geometric parameters, the following material properties are also input: the maximum compressive concrete cylinder stress, maximum coarse aggregate size, reinforcement in up to three directions, the reinforcement Young's modulus, the reinforcement yield stress, and average crack spacing in the x-, y-, and z-directions. For each load level, multiple iterations are carried out until convergence is achieved. From the global displacement field, δ_g , predicted by the finite element process, the element strains are calculated.

These strains are then used to determine the secant stiffnesses in the principal directions for the membrane and triaxial elements using the equations of the MCFT in two and three dimensions, respectively. A detailed summary of three-dimensional equations of the MCFT can be found elsewhere and a brief summary of the key constitutive relationships is provided as follows. 8,20,23

Shell II uses the Modified Popovics relationship described by Collins and Mitchell for the concrete compressive response.²⁴ Additionally, if one principal strain is positive (tensile), Eq. (3) is used for the compression softening relationship. If two principal strains are positive, Eq. (4) is used.

$$f_{2,3 \text{ max}} = \frac{f_c'}{0.8 + 170 \,\varepsilon_1} \tag{3}$$

$$f_{3 max} = \frac{f_c'}{0.8 + 170\sqrt{(\epsilon_1)^2 + (\epsilon_2)^2}}$$
 (4)

Table A1—Stresses and strains at peak load for PS series of experiments

Test	f_c' , MPa	ρ _z f _{yield} MPa	v_{xy} : v_{xz} ratio*	v _{xy} , MPa	ν _{xz} , MPa	γ_{xy} , $\times 10^{-3}$	γ_{xz} , $\times 10^{-3}$	$\begin{array}{c} \gamma_{yz}, \\ \times 10^{-3} \end{array}$	ϵ_x , $\times 10^{-3}$	ϵ_y , $\times 10^{-3}$	ϵ_z , $\times 10^{-3}$	$\begin{array}{ c c c c c c c c c c c c c c c c c c c$	ϵ_2 , $\times 10^{-3}$	ϵ_3 , $\times 10^{-3}$	$\epsilon_{xy-1}, \times 10^{-3}$	$\epsilon_{xy-2}, \times 10^{-3}$
PS1	41.8	_	1.20:1	2.42	2.02	2.14	2.81	_	0.87	0.96	3.85	4.45	0.86	0.53	1.99	-0.15
PS2	45.4	_	5.18:1	7.46	1.44	5.04	3.66	_	1.51	2.64	4.83	5.19	2.82	-0.76	4.65	-0.52
PS3	28.5	_	0.72:1	0.60	0.83	1.25	0.81	0.43	0.20	0.75	0.64	0.95	0.16	-0.05	1.17	-0.19
PS4	30.6	_	8.46:1	3.57	0.42	4.48	2.05	1.97	1.19	1.70	1.61	4.05	0.76	-2.42	3.70	-0.81
PS5	43.2	0.934	0.72:1	0.92	1.28	2.15	1.55	1.88	0.58	2.16	0.88	2.39	0.40	-0.19	2.53	-0.14
PS6	49.9	0.934	3.61:1	3.41	0.94	4.57	2.45	3.32	0.82	4.21	1.48	5.11	0.31	-0.19	5.11	-0.57
PS7	98.7	_	pure v_{xy}	5.39	_	6.23	_	_	1.41	4.42	_	_	_	_	6.39	-0.54
PS8	100.0	_	$-0.40:1$ $f_n: v_{xy}$	9.11	_	5.93	_	_	1.38	3.58	_	_	_	_	5.66	-0.67
PS9	38.2	1.659	3.29:1	3.61	1.10	6.70	1.95	1.74	1.05	2.08	1.24	4.45	0.88	-2.34	4.98	-1.80
PS10	39.8	_	-2.07:1	-3.14	1.52	0.32	0.11	0.53	0.04	0.27	0.45	0.56	-0.08	-0.22	0.37	-0.02
PS11	98.3	_	0:1 [†]	-3.50	1.93	1.58	6.33	0.82	0.88	1.65	3.43	6.98	0.90	0.29	2.06	0.30
PS12	98.3	0.934	0:1†	-3.50	2.33	-0.10	4.80	0.27	-0.04	-0.01	2.23	5.67	0.65	0.06	-0.04	-0.01

^{*}Specimens PS3, PS4, PS5, PS6, PS9, PS10, PS11, and PS12 also have: $v_{xz} = v_{yz}$ and $f_x = f_y = v_{xy}$.

Note: 1 MPa = 145 psi.

[†]PS11 and PS12 have a constant applied $f_x = f_y = v_{xy}$ of -3.50 MPa.

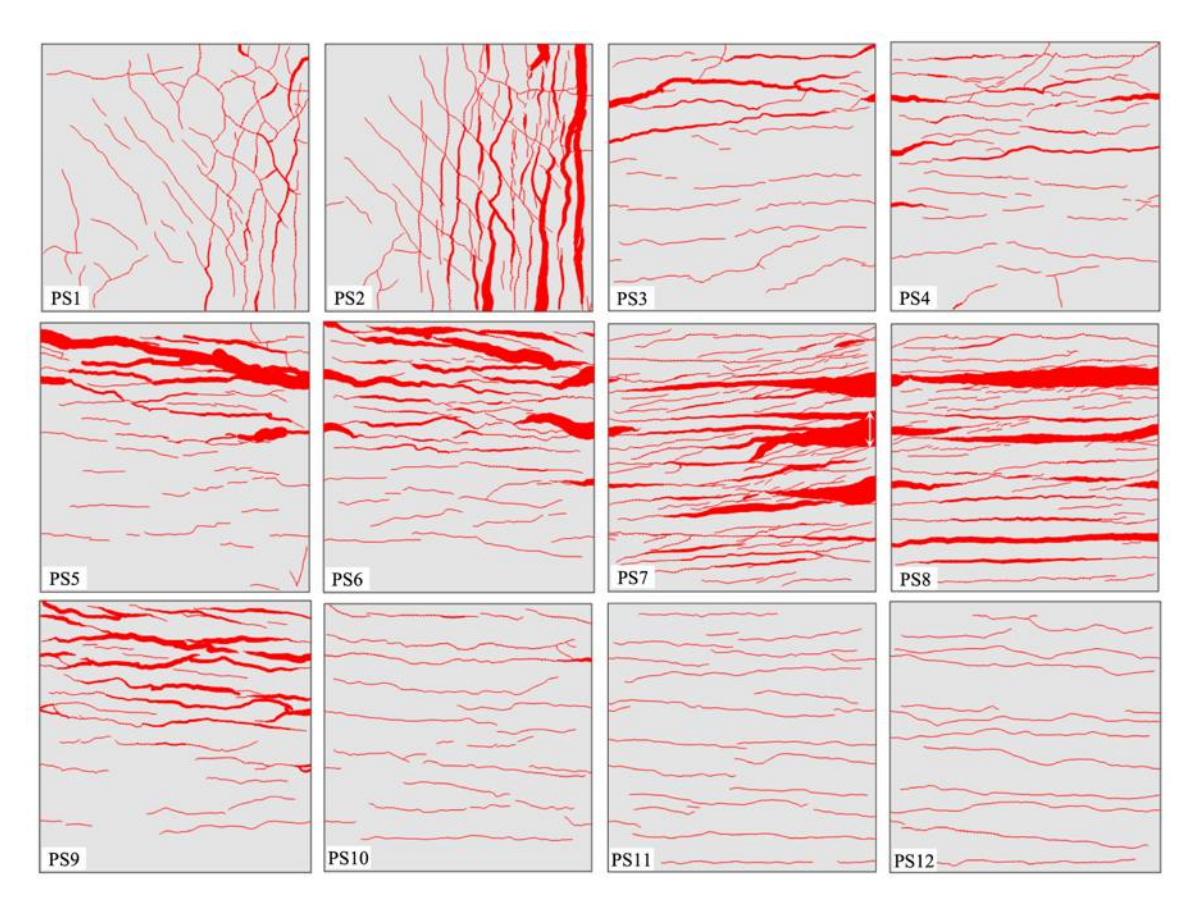


Fig. A1—Front-face crack width diagrams at last load stage (line widths scaled with smallest crack 0.05 mm and largest crack width of 3.50 mm crack shown in PS7). (Note: 1 mm = 0.0394 in.)

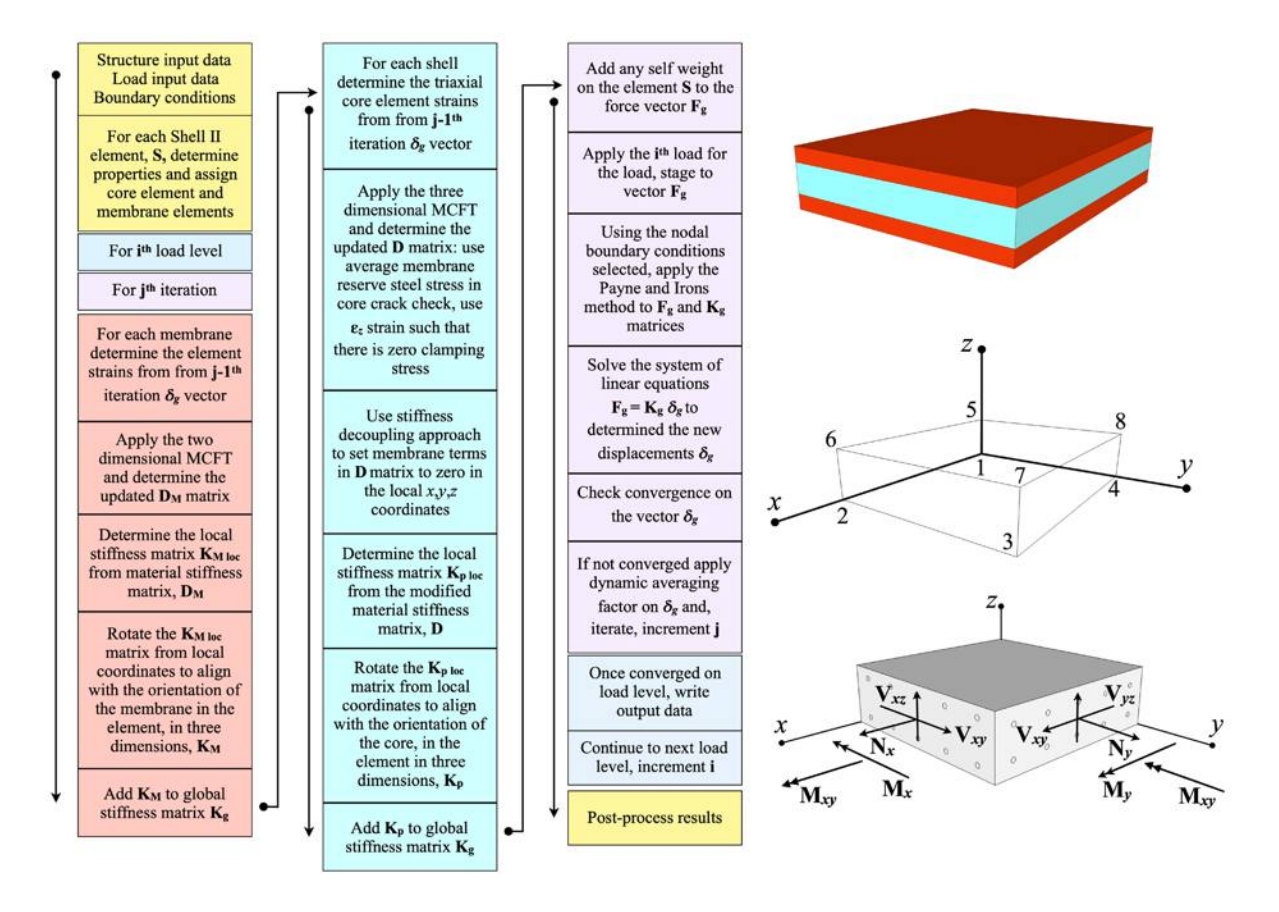


Fig. A2—Shell II method and algorithm (left); element representation, node location, and sign convention (right).

Shell II uses the tension stiffening relationship shown in Eq. (5), where f_{cr} is the cracking stress for concrete.

$$f_1 = \frac{f_{cr}}{1 + \sqrt{500\,\varepsilon_1}}\tag{5}$$

Once these principal concrete stresses are determined, the secant stiffnesses are calculated. The stiffnesses in the principal directions are used to build material stiffness matrixes, D, that are transformed into the local x-y-z coordinate system. These concrete stiffnesses are then added to the steel stiffness in the local x-, y-, and z-directions. The material stiffness matrixes D are then used to build stiffness matrices in local coordinates (K_{loc}). As previously described, these matrices are either associated with 12-degrees-of-freedom elements (for the two, two-dimensional membrane elements) or 24-degrees-of-freedom elements (for the three-dimensional rectangular prism elements). This integration is carried out with the shape functions B for the elements as shown in Eq. (6)

$$K_{loc} = \int B^T DB \ dvol \tag{6}$$

These local K_{loc} matrixes relate forces to translational displacements that are then rotated into global coordinate

matrixes, K, and compiled to build a global stiffness matrix K_g (refer to Eq. (7) and (8)).

$$K = T^T K_{loc} T (7)$$

$$F_g = K_g \delta_g \tag{8}$$

Once these stiffness matrixes are built, the boundary conditions and applied loads are imposed. The matrix is inverted, and a new estimate of the displacements is obtained. The new displacement field provides new estimates of strains in the elements and therefore, new stiffnesses. Iterations are conducted until convergence on the nodal displacements is achieved. This is repeated for each load level. For each converged load level, displacement fields, shell element data, and sub-element (membrane and triaxial core) data are written to file. Post-processing and visualization of the data can then occur. Figure A2 provides a summary of the Shell II method solution algorithm, sign convention, and a representation of the Shell II elements. The subscripts M and P denote two-dimensional membrane elements or three-dimensional solid elements (prisms). The variable F_g denotes the global force vector. Additional details regarding the model assumptions and its implementation can be found elsewhere.8

Title No. 121-S27

Behavior of Shear-Critical Concrete Deep Beams Monitored with Digital Image Correlation Equipment

by Dhanushka K. Palipana and Giorgio T. Proestos

This paper discusses the behavior of large-scale reinforced concrete deep beams that failed in shear and were monitored with full field-of-view, digital image correlation (DIC) equipment. Six shear-critical deep beams, measuring 4.88 x 1.11 m, were tested to failure. The specimens were point-loaded and simply supported, with three members examining the influence of asymmetrical loading conditions. The members were tested with various loading plate sizes and shear span-depth ratios. High-resolution displacement and strain field data obtained throughout loading are used to examine the member response. Principal compressive strain field diagrams of the deep beams at peak load are discussed. The paper presents crack patterns and crack kinematics, including crack widths and crack slips along critical shear cracks, determined from the DIC data throughout loading. The paper discusses crack dilatancy—that is, crack slips versus crack widths—along critical shear cracks, throughout loading, and at multiple locations. The results improve understanding of the detailed displacement field response of large shear-critical reinforced concrete deep beams, which can be used to improve kinematic and constitutive models, such as aggregate interlock models, for large-scale members.

Keywords: asymmetrical loading; deep beams; digital image correlation (DIC); disturbed regions; experiments; reinforced concrete; shear.

INTRODUCTION

Reinforced concrete deep beams such as transfer girders in high-rise buildings, corbels, and bent caps in bridges are used to transfer large loads (refer to Fig. 1). These "disturbed regions" have small shear span-depth ratios, typically less than 2.5, and the strain distributions through their depth are nonlinear. Therefore, beam theory becomes insufficient to predict response, and more refined methods are needed to describe the behavior. In practice, these reinforced concrete structural elements can be subjected to symmetrical as well as asymmetrical loading. That is, some members may be point-loaded in the center of their spans; in other cases, the loading elements may be offset from the center of the spans, or lateral loads can give stress resultants from supported members acting away from the midspan of the deep beams (refer to Fig. 1).

Often, as a part of maintenance programs and evaluating the degradation of aging concrete infrastructure, these structural elements can require inspections or monitoring to ensure their suitability for continued use. Cracking is an important indicator of distress and the level of safety in concrete members. Often, visual inspections are carried out, and the crack widths are compared with the allowable limits in codes and guidelines. ^{4,5} The recommended limits on crack widths are often not structure-specific and may only give general categorizations.

Additionally, some of the guidance documents do not distinguish between shear cracks and flexural cracks. This makes it difficult for engineers to interpret crack information. The literature has also explored various approaches for the assessment of structures from the perspective of damage indexes.⁶ In scenarios where more complex analyses are conducted, engineers can compare observed crack widths, crack slips, and crack shapes with predictions from nonlinear models and finite element tools. While these approaches can provide important information when conducting assessments, there are often issues reconciling the crack shapes observed with crack shapes in models, as well as reconciling observed crack widths and slips with model predictions. Thus, a better understanding of the detailed response of deep beams, including how the crack widths and slips vary along the critical cracks and throughout loading, particularly for large-scale members, is important.

Shear failures in concrete deep beams are brittle compared to flexural failure modes; therefore, when assessing such members, it is important to correctly interpret crack information that may be observed. Shear cracks in reinforced concrete deep beams develop at approximately two-thirds of their ultimate strength and often develop under service conditions. Thus, it is common to observe fully developed shear cracks in deep concrete beams during inspections.⁷ This often raises questions as to the safety of the members. To improve the methods by which concrete deep beams that exhibit shear cracking are assessed, methods that directly input the crack information, including the crack shape, width, and slip, are needed to determine structural safety. Additionally, as field inspection technologies and measurement techniques improve, interpreting detailed crack data, including the crack shape, widths, and slips, becomes more important.⁸ Some researchers report crack widths at a single location or the maximum crack width; however, the literature contains very limited, if any, data for large-scale shear-critical deep beam experiments that present the detailed kinematics of the cracks at multiple locations throughout loading. 9-11

To help improve assessment methods for shear-critical reinforced concrete deep beams and to better understand the behavior of cracks in deep members throughout loading, this paper presents a series of six large-scale, monotonically

ACI Structural Journal, V. 121, No. 2, March 2024.

MS No. S-2023-134.R l, doi: 10.14359/51740253, received September 19, 2023, and reviewed under Institute publication policies. Copyright © 2024, American Concrete Institute. All rights reserved, including the making of copies unless permission is obtained from the copyright proprietors. Pertinent discussion including author's closure, if any, will be published ten months from this journal's date if the discussion is received within four months of the paper's print publication.

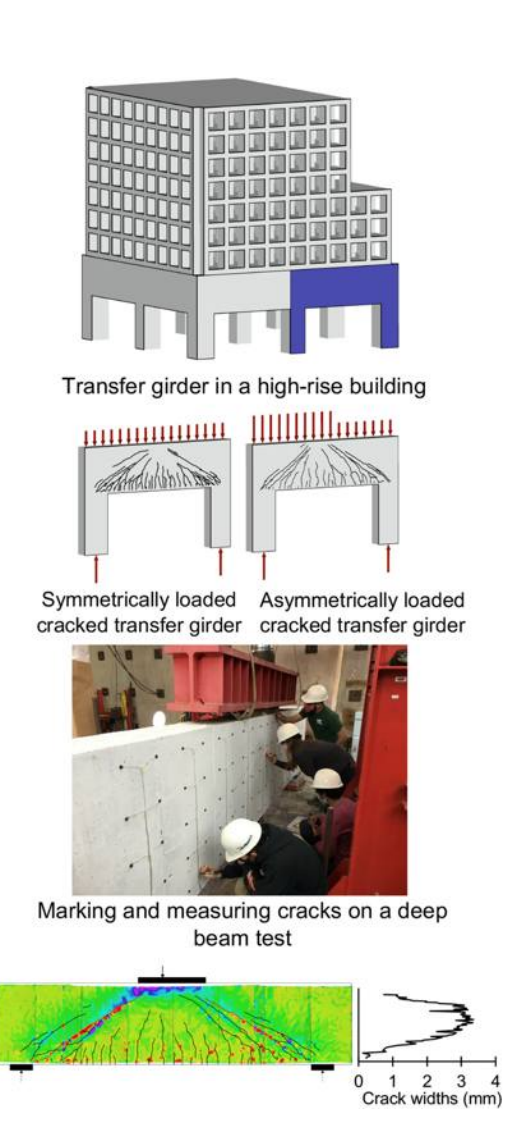


Fig. 1—Transfer girder in high-rise building; symmetrically and asymmetrically loaded cracked transfer girders; marking and measuring cracks on deep beam test; and compressive strain fields obtained using DIC, and crack pattern and widths obtained using DIC data.

loaded deep beams monitored using a full field-of-view three-dimensional (3-D) digital image correlation (DIC) system. Given the importance of testing large-scale members, as a result of the size effect in shear, the experimental program and measurements presented are important to improve the understanding of shear-critical deep beams and inform models appropriate for large-scale members. 12-14 DIC techniques can be used to obtain high-resolution displacement field data over the entire specimen, throughout loading, in laboratory settings. DIC is a noncontact, optical data acquisition method that can be used to measure the two-dimensional (2-D) and 3-D displacement fields on the specimen surface subjected to loads (refer to Fig. 1). A speckle pattern is applied on the surface of the object, and cameras record the characteristics of the surface in image pixels. DIC analysis software tracks the subsets of pixels based on their unique gray value information using an image correlation algorithm. The quality of DIC data depends on the hardware configuration, test setup, quality of calibration, and user care. The image contrast, size and randomness of the speckle pattern, and lighting conditions can also affect the quality of data obtained. DIC techniques provide more refined (higher-resolution) data than other displacement measurement techniques, such as infrared light-emitting diodes (LEDs), strain gauges, linear variable differential transformers (LVDTs), or other discrete displacement measurement approaches. ^{15,16}

For the experiments presented in this paper, six highresolution cameras (three sensor pairs) were used in tandem to capture the detailed displacement field of the entire surface of the large-scale deep beams. The paper first presents high-resolution displacement and strain field data obtained throughout loading and discusses member response in the context of the detailed measurements observed. The displacement and strain field data are then used to obtain crack patterns and crack kinematics for the critical shear cracks. The paper also discusses how the crack widths vary along the height of the specimens and the observed crack dilatancy throughout loading. The results of the data and experimental program can be used to inform codes and standards, such as ACI 318-19,17 AASHTO LRFD,18 CSA A23.3:19,19 ACI 224R-01,4 and the AASHTO Manual for Bridge Element Inspection.⁵ An analytical evaluation of the specimens can be found elsewhere. 2,3,20

RESEARCH SIGNIFICANCE

This paper presents a series of six large-scale shear-critical deep beam experiments monitored with high-resolution, full field-of-view, 3-D DIC equipment. The displacement fields and strain fields over the entire surface of the specimens were obtained throughout loading. Detailed displacement and strain field data are used to obtain crack patterns and crack kinematics up to failure. The results provide new insight into the complex behavior of shear-critical reinforced concrete deep beams.

EXPERIMENTAL PROGRAM

A series of six shear-critical deep beam tests, the CCR series, conducted at the Constructed Facilities Laboratory at North Carolina State University, Raleigh, NC, is examined in this paper. The beams measured 4877 mm long, 305 mm wide, 1105 mm deep, and had an effective depth of 909 mm. The longitudinal reinforcement consisted of No. 9 headed bars. Nine bars were used to reinforce the bottom of the beams, giving a longitudinal reinforcement ratio of 2.09%. Two bars were used to reinforce the top of the members in the compression region. Stirrups bent from No. 3 bars were placed at 330 mm along the span, giving a transverse reinforcement ratio of 0.141%. The specimen details for the CCR series of tests are shown in Fig. 2. The steel coupon test data, Young's modulus (E), yield stress (f_v), strainhardening strain (ε_{sh}) , ultimate strength (f_u) , and strain at ultimate strength (ε_u) are shown in Fig. 3. These steel reinforcement ratios and steel material properties used are typical of a variety of structures, including bridge substructure components and transfer girders in buildings. The concrete cylinder strengths for the specimens (f_c) are given in Table 1. It should be noted that a maximum coarse aggregate size (a_g) of 19 mm was used.

Table 1—Summary of CCR test specimen properties

Specimen	f_c' , MPa	a/d (north)	a/d (south)	l_{b1} , mm	Loading configuration		
CCR1	34.5	2.25	2.25	610	Symmetrical loading		
CCR2	35.8	2.00	2.00	610	Symmetrical loading		
CCR3	39.5	1.80	1.80	610	Symmetrical loading		
CCR4	37.8	1.80	2.25	914	Asymmetrical loading on symmetrical loading plate		
CCR5	41.5	1.80	2.50	610	Symmetrical loading on asymmetrical loading plate		
CCR6	39.3	2.11	2.39	914	Asymmetrical loading on symmetrical loading plate		

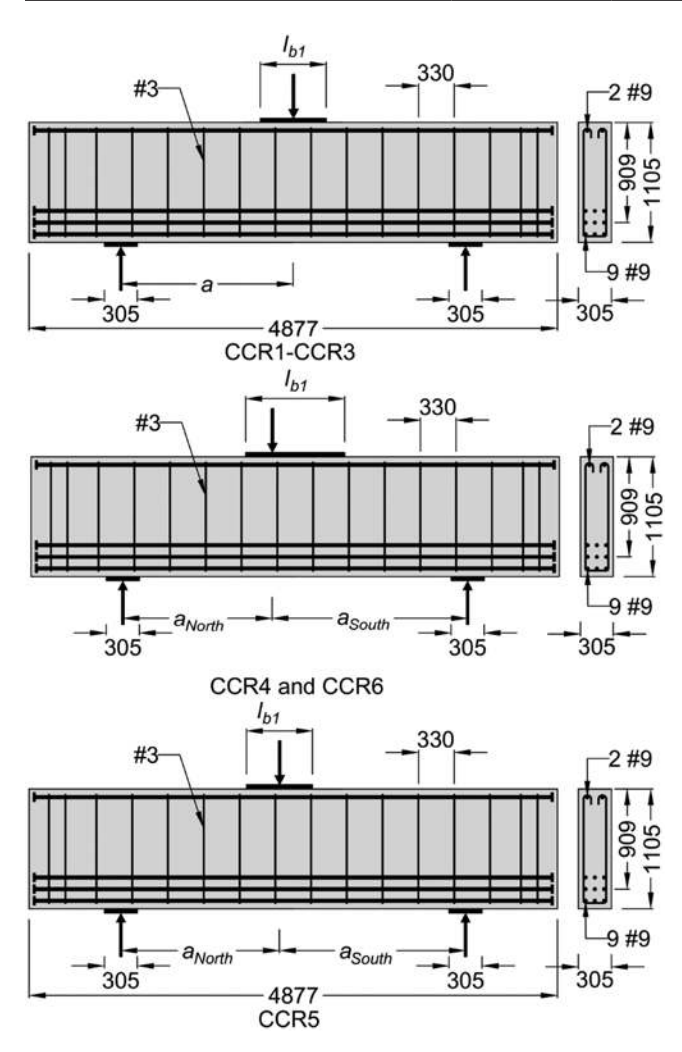


Fig. 2—Geometric and reinforcement details for CCR1 to CCR6. (Note: All dimensions are in mm.)

Deep beams often exhibit a critical shear crack that extends from the inner edge of the support plate to near the edge of the loading plate. This critical crack often has the largest crack widths on a given shear span and governs the response of the member. The critical loading zone is the highly compressed region under the loading plate that carries a substantial amount of shear.²¹ Varying the global critical crack angle and the size of the critical loading zone assists in investigating the behavior of deep beams by changing the key variables that influence related load-carrying mechanisms.^{9,22} Thus, the shear span-depth ratios (a/d) and the loading plate sizes (l_{b1}) were varied to observe the influence of the global critical crack angles and the size of the critical

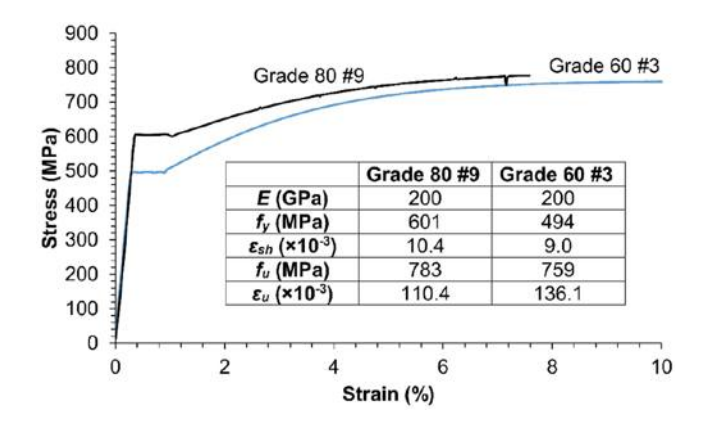


Fig. 3—Stress versus strain response of steel coupons and reinforcement properties.

loading zone on member response (refer to Table 1). These loading and supporting plate sizes are representative of a variety of structures and conditions, including conditions that may arise from columns supporting bridge substructure components and transfer girders supporting columns or walls in high-rise structures.

In addition to these variables, three loading configurations were explored. Specimens CCR1 to CCR3 were symmetrically loaded, where the load was centered on the loading plate and the loading plate was centered on the specimen. These specimens had the same l_{b1} (measuring 610 mm) and a/d ranging from 1.80 to 2.25. Specimens CCR4 to CCR6 were asymmetrically loaded. For CCR4 and CCR6, the load was applied 203 mm and 127 mm offset from the center of the symmetrically arranged loading plates, respectively. For CCR5, the loading plate was offset 318 mm from the center of the beam, and a load centered on the plate was applied. Specimens CCR4 to CCR6 were tested to examine the influence of asymmetrical conditions on the member response. Therefore, these loading arrangements represent symmetrical loading as well as asymmetrical loading conditions that can be the result of architectural requirements, geometrical constraints, or lateral loads that may act on structures.

To obtain high-resolution, full field-of-view deformation data, the entire surface of the west face of the beam was monitored with a full field-of-view 3-D DIC system. A resolution of approximately 2 pixels/mm was maintained using three stereo systems with two 12.3 megapixel cameras in each system (shown in Fig. 4 [top]). The data from the three systems was combined using a multi-view registration algorithm. A speckle pattern with speckles measuring approximately 2.5 mm in diameter was applied to the specimens.



Collecting deformation data using DIC on the west face



229 mm x 229 mm LED grid used on the east face

Fig. 4—DIC and LED instrumentation on test specimens.

This arrangement resulted in 3 to 5 pixels per speckle. The speckle pattern was applied so that the beam had approximately 50% black-white contrast. This setup resulted in virtual strain gauge lengths of approximately 19 mm; however, this varied somewhat between experiments to accommodate the different clear span lengths. The DIC setup provided the equivalent of approximately 0.5 to 2.0 million strain gauges on the specimen surface. More importantly, the 3-D displacement field was captured for the entire specimen surface throughout loading.

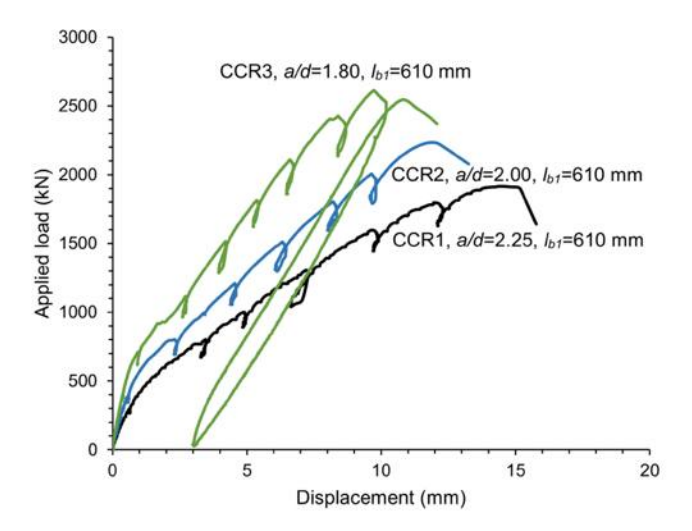
The east face of the beam was instrumented with a 229 x 229 mm grid of 95 infrared LED targets arranged in five rows and 19 columns (shown in Fig. 4 [bottom]). These targets were tracked using a 3-D position tracking camera to capture the deformation response. This data was used to verify and validate the DIC deformation field data obtained.

All six specimens were simply supported. The support plates measured 305 x 305 x 51 mm and rested on roller supports. The loading plate measured l_{b1} x 305 mm x 76 mm, where l_{b1} is given in Table 1. A soft fiberboard sheathing was used between the loading plate and the beam to ensure the load was evenly distributed on the top surface of the beam. A spreader beam was used to distribute the load from the actuator to the loading plate. A spherical bearing was used between the actuator head and the spreader beam to ensure that moments were not transmitted through the actuator.

The specimens were loaded monotonically to failure. Load stages were periodically conducted, and crack comparator gauges were used to manually mark and measure the cracks on the east face of the specimens. In addition to the DIC photos, during the experiments, high-resolution photos were taken locally on the specimens.

GLOBAL RESPONSE OF CCR SPECIMENS

Initial loading resulted in flexural cracks on the tension side of the beam under the loading plate. As the load increased, flexural cracks extended toward the compression region. Shear cracks formed in the clear span. Increased load resulted in stable shear cracks that widened until failure. All



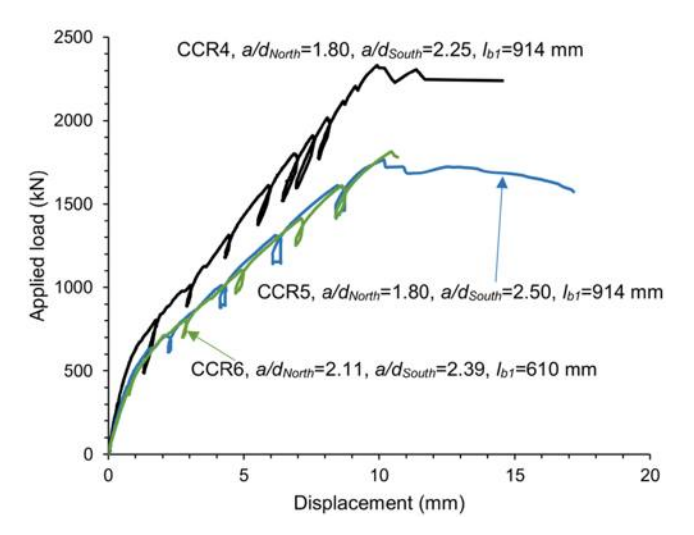


Fig. 5—Load versus beam displacement on flexural tension side at section under applied load for: (top) CCR1 to CCR3; and (bottom) CCR4 to CCR6.

specimens failed in shear. Specimens CCR1 to CCR3 and CCR6 exhibited an abrupt brittle failure, marked by shear crack widening and crushing near the critical loading zone. While CCR4 and CCR5 were also relatively brittle, they failed in a somewhat less abrupt manner. At the peak loads, the longitudinal bars of the specimen had not yielded. No splitting cracks were observed along the bottom of the beam.

The load versus displacement responses for all six specimens are shown in Fig. 5. The displacement on the flexural tension side of the beam at a section under the load was obtained from the DIC displacement field and accounts only for the relative displacement of the beam with respect to the supports. The top portion of Fig. 5 compares the response of CCR1 to CCR3, which are grouped as members with the same l_{b1} . The figure demonstrates that for specimens with the same l_{b1} , the strength of the specimen increases with decreasing a/d. The displacement at the peak load decreases with decreasing a/d. All specimens except CCR3 failed catastrophically and could not be reloaded. CCR3 was reloaded after reaching the peak load to determine the residual capacity. After unloading and reloading, the load does not exceed the first peak. This shows that the monotonic peak load of CCR3 was reached in the initial loading

Table 2—Summary of experimental results observed for CCR series

Specimen	Applied load at first flexural cracking, kN	Applied load at first shear cracking, kN	First cracking shear span	Peak load, kN	Peak shear force on failure span, kN	Displacement at peak load, mm	Failure span	Maximum crack width at peak load, mm	Maximum crack slip at peak load, mm
CCR1	238	768	North	1916	958	14.6	South	3.65	2.61
CCR2	226	752	North	2235	1118	11.9	North	4.70	4.33
CCR3	380	969	North	2614	1307	9.7	South	2.82	1.55
CCR4	293	973	South	2333	1296	9.9	North	2.29	1.97
CCR5	360	711	North	1765	739	10.2	South	2.33	1.14
CCR6	259	793	North	1816	964	10.4	North	2.82	1.87

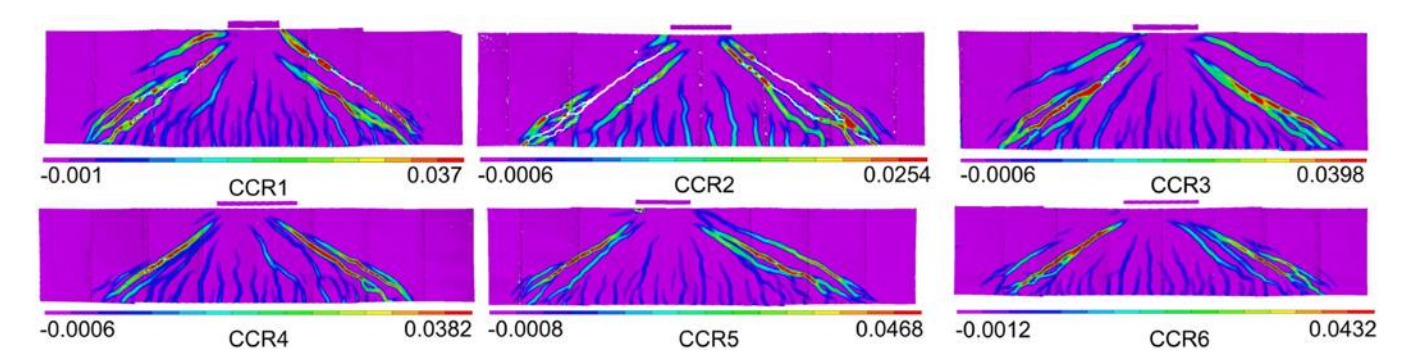


Fig. 6—Principal tensile strain fields (ε_1) at peak load for CCR1 to CCR6. (Note: Full-color PDF of this paper can be accessed at www.concrete.org.)

and is equal to the maximum applied load of 2614 kN. Figure 5 also examines the response of CCR4 to CCR6 and compares asymmetrically loaded members. Although CCR4 and CCR5 had the same a/d_{North} value and l_{b1} , the smaller a/d_{South} value for CCR4 resulted in a response with a higher peak load than CCR5. CCR5 and CCR6, which had different a/d and l_{b1} values, showed a similar response. This is likely from the combined effect of specimens with different a/d, l_{b1} , and specific crack geometries, resulting in different shear responses. 9,22 That is, the combination of a/d, effective l_{b1} , specific crack geometry, crack widths, and crack slips contributed to the specific member response. The detailed response, including crack widths and slips, will be described in subsequent sections.

Table 2 provides a summary of the response of CCR1 to CCR6, including the values for first cracking, peak load, peak shear force on the failure span, displacement at the peak load, maximum observed crack width, and maximum observed crack slip. Typically, when two shear spans with different a/d and the same l_{b1} are considered, the shorter shear span has the higher strength. 23,24 This was observed in CCR5, where the effective l_{b1} remained the same in both shear spans. The shear span of CCR5, which had a larger a/d, failed. However, for the CCR4 and CCR6 beams, the shorter shear span failed. For these members, although the a/d is smaller, the asymmetrical loading arrangement changes the effective l_{b1} and specific crack geometry, which results in a varied contribution of shear-transfer mechanisms. 9,22 Therefore, although the shorter shear spans are typically expected to have higher strengths, when the loading is asymmetrical, the shorter shear span can be critical.

PRINCIPAL TENSILE AND COMPRESSIVE STRAIN FIELDS

Figure 6 shows a map of the principal tensile strain fields at the peak load for CCR1 to CCR6. The high-strain regions indicate the cracked regions. These tensile strain fields are used to develop crack diagrams, discussed in the next section. Figure 7 shows a map of the principal compressive strain fields at the peak load for CCR1 to CCR6. The strain fields show high compressive strains beneath and near the edges of the loading plates. The strains below the plate are not uniform and increase near the edges of the plate. This results from the compatibility of the rigid plate and the beam bending beneath it. These results are consistent with prior studies and are discussed elsewhere. 25,26 For CCR6, the distribution under the plate is also influenced by the asymmetrical loading conditions. The diagrams also show the load arching from the loading plate to the support plates along compression struts. This behavior is typical of deep beams and demonstrates that the members are indeed disturbed regions. Additionally, the strain fields indicate that near the loading plates, the strains in the concrete exceed the strains at peak cylinder concrete stress. This is a result of the biaxial compression conditions that occur near the plates. For example, near the loading plate of CCR1, the largest principal compressive strain observed was -14.3×10^{-3} . It can also be observed that the strains along the compression struts that arch from the load are typically less than the strains at peak concrete cylinder stress. For instance, in specimen CCR6, the principal compressive strains observed along the struts were less than -2.1×10^{-3} .

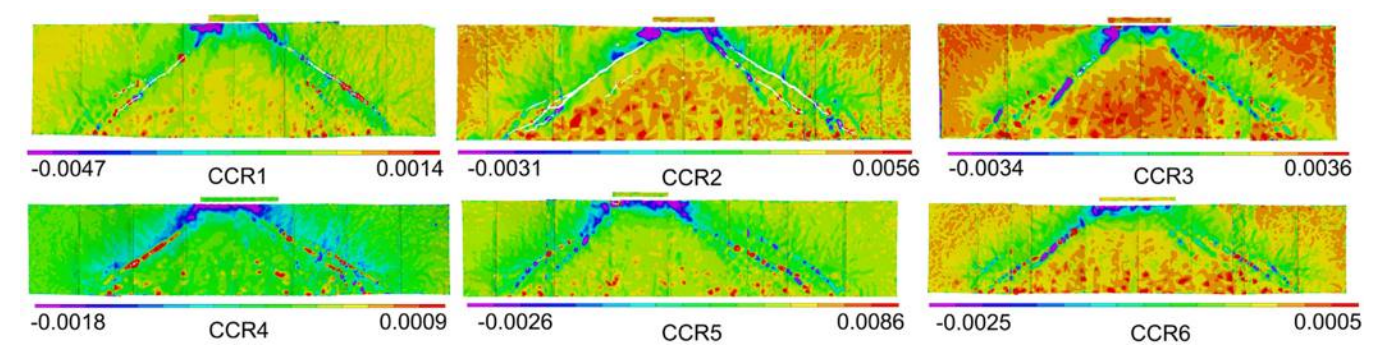


Fig. 7—Principal compressive strain fields (ε_2) at peak load for CCR1 to CCR6. (Note: Full-color PDF of this paper can be accessed at www.concrete.org.)

CRITICAL SHEAR CRACK KINEMATICS FROM DIC DATA

In this research, an open-source tool called the automated crack detection and measurement (ACDM) tool, developed by Gehri et al.,²⁷ was used to generate crack patterns from the DIC data. The principal tensile strains from the DIC data are input into the ACDM tool, which uses regions of high strains along with a mapping algorithm to detect and map the crack regions. Figure 8 (right) shows a summary of the crack patterns that were generated using the ACDM tool at the peak load for CCR1 to CCR6. These crack patterns are compared with the perspective-corrected photographs of crack patterns on the east face of the specimens in Fig. 8 (left), and they agree reasonably well. In some places, manual corrections were needed to correct minor discrepancies between the visually observed crack patterns and the outputs from the ACDM tool. The critical crack in reinforced concrete deep beams is typically the crack that extends from the inner edge of the support plate to near the edge of the loading plate. This crack typically has the largest crack width. The location and magnitude of crack widths were used to manually identify the critical cracks. The critical cracks were verified by comparing them with the visually observed crack patterns and crack widths on both faces of the specimen. In Fig. 8, the critical crack for CCR1 to CCR6 is shown in red for each shear span.

To obtain the local crack kinematics, namely the widths and slips, the critical crack was discretized into small crack segments. The critical crack was discretized using the intersection points of the crack on a grid equal to the maximum coarse aggregate size (19 mm). This crack discretization grid size was recommended by Trandafir et al.22 Then, for each crack segment (approximately 22 mm long), the crack kinematics were determined by considering the relative displacements of each of the two sides of the crack (refer to Fig. 9). A detailed discussion of how the crack kinematics were calculated for each crack segment is described in Langer²⁸ and Palipana et al.9 The reference points on either side of the crack were approximately 5 to 40 mm apart. Data points were selected so that they do not cross adjacent cracks or encroach on the boundary of cracks, where the DIC data can give spurious results. It should be noted that this discretization process and the determination of the crack kinematics is algorithmic and eliminates the need for manual interpretation of the crack data, thereby improving consistency.

First flexural and shear cracking

The crack patterns and the crack kinematics were used to determine the cracking response of the member, namely, identifying when the first flexural cracking and first shear cracking occurred. In the global response of the member, when the first flexural cracking occurs, the stiffness of the member gradually decreases from the elastic stiffness and tends toward the cracked elastic stiffness. This can be observed in the load versus displacement plots in Fig. 5. Table 2 summarizes the loads at which the first flexural cracking occurs for each specimen. A crack width of 0.05 mm was used as a minimum threshold to determine the first cracking because this can be visually verified during the experiment. CCR3 had the smallest a/d and the largest first flexural cracking load of 380 kN. CCR2, which had an a/d of 2.0, had the smallest first flexural cracking load of 226 kN.

A significant decrease in stiffness is observed when shear cracking occurs (refer to Fig. 5). Typically, shear cracks in deep beams are angled cracks that occur in the clear shear span. For consistent comparisons across the specimens, the load at which the first shear cracking occurs is taken as the load at which the critical shear crack reaches the midheight of the beam. A crack width of 0.05 mm was used as a minimum threshold to determine the first cracking because this can be visually verified during the experiment. The load at first shear cracking and the first shear span to exhibit shear cracking are given in Table 2. The principal tensile strain field diagrams for CCR1 to CCR6 at the first shear cracking load are shown in Fig. 10. The yellow ovals in Fig. 10 indicate the first critical shear crack identified.

The north shear span of CCR1 and the south shear span of CCR4 had an a/d of 2.25; the shear forces at which the first shear cracking occurs are 384 and 432 kN, respectively. CCR4 has a 13% higher shear cracking shear force than CCR1; this is likely attributed to the large effective l_{b1} . The north shear span of CCR3 and the north shear span of CCR5 had an a/d of 1.80. The shear forces at which the first shear cracking occurs are 485 and 413 kN, respectively. Thus, although CCR5 and CCR3 have the same a/d_{North} and l_{b1} value, CCR5 has a 15% lower shear cracking resistance than CCR3.

Crack widths and slips at peak load

For CCR1 to CCR6, the crack widths calculated from the displacement field for each crack segment are shown in Fig. 11 over the member height at the peak load. To verify

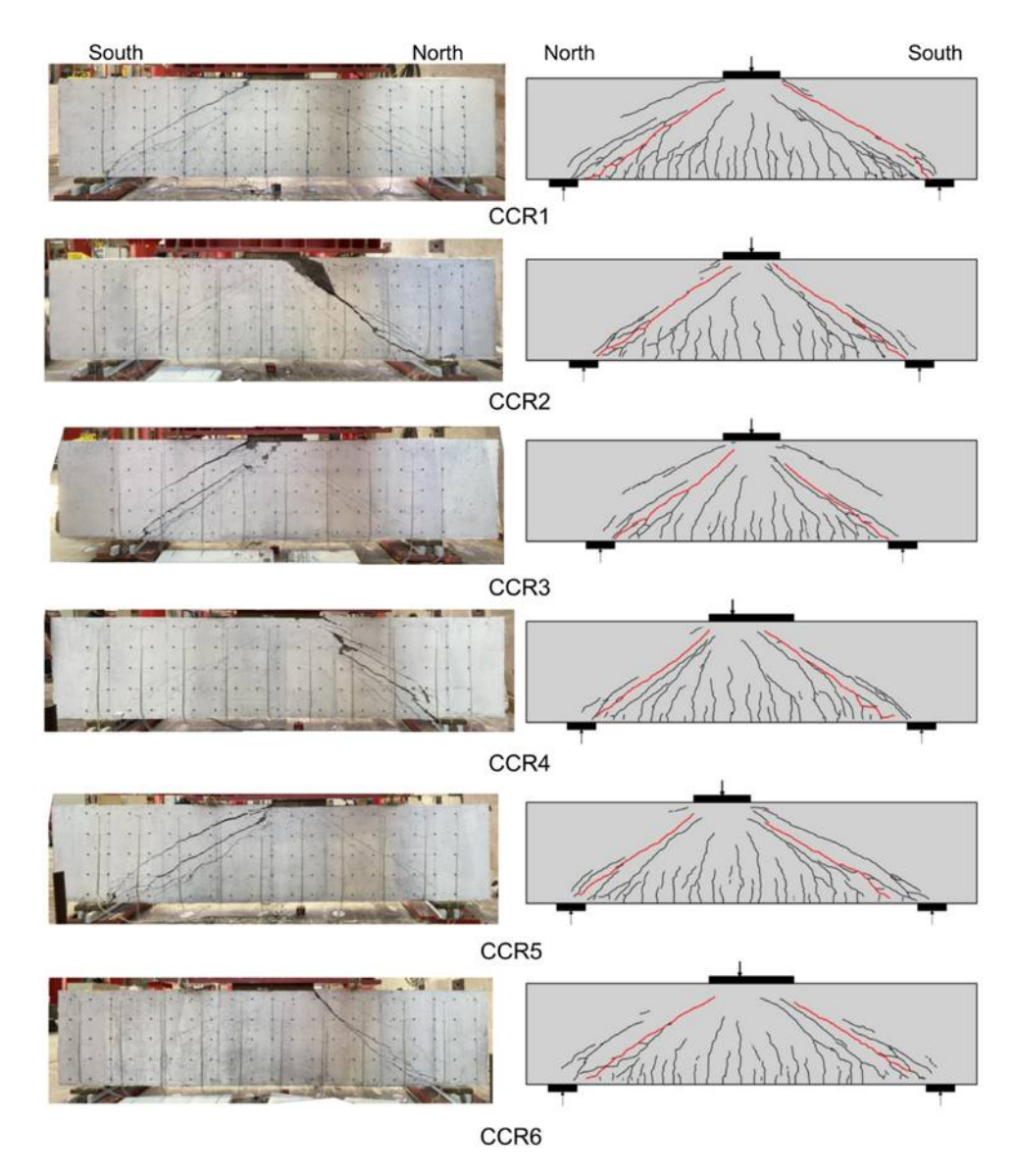


Fig. 8—(Left) Crack patterns on east face of specimens at failure; and (right) crack patterns obtained from DIC with critical crack highlighted in red for CCR1 to CCR6 at peak load. (Note: Full-color PDF of this paper can be accessed at www.concrete.org.)

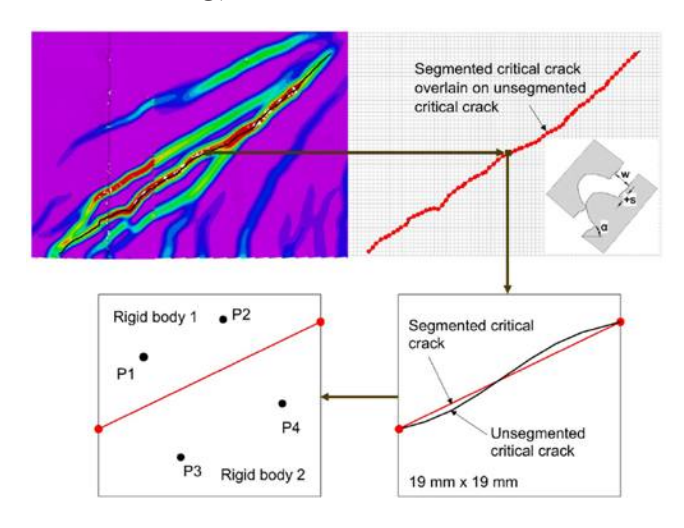


Fig. 9—Determining crack widths and slips on uniform grid (north shear span of CCR3).

and validate these results, Fig. 11 also shows the crack widths from the DIC data compared with the manually measured crack widths at the last load stage prior to failure. The differences between the manual measurements and crack widths from the displacement field data likely arise from subjective interpretations of crack widths and the local crack angles measured using crack comparators. Discrepancies may also arise from differences between the two surfaces measured, where nearby different secondary cracks may have influenced the crack widths of the critical crack.

Understanding the variation in the crack kinematics along the height of the beam is important to assist in conducting a detailed assessment of cracks. Specifically, being able to understand the variation in crack widths along member depth can help inform the relationship between maximum crack width and ultimate conditions, where the maximum crack width is expected to occur, and how the maximum crack width compares to cracks near the tension or compression region. As seen in Fig. 11, the crack widths are a maximum

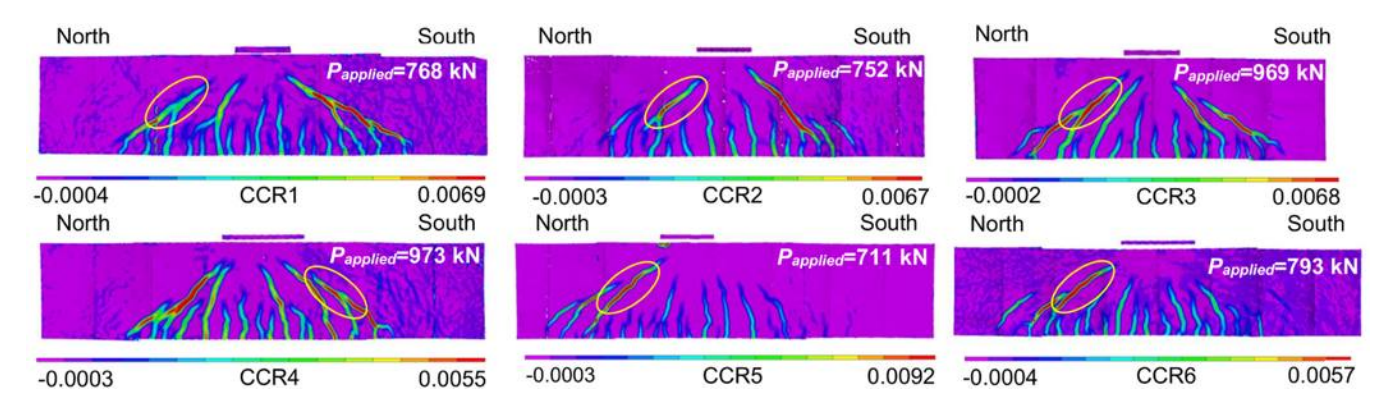


Fig. 10—Principal tensile strain fields (ε_1) at first shear cracking for CCR1 to CCR6. (Note: Full-color PDF of this paper can be accessed at www.concrete.org.)

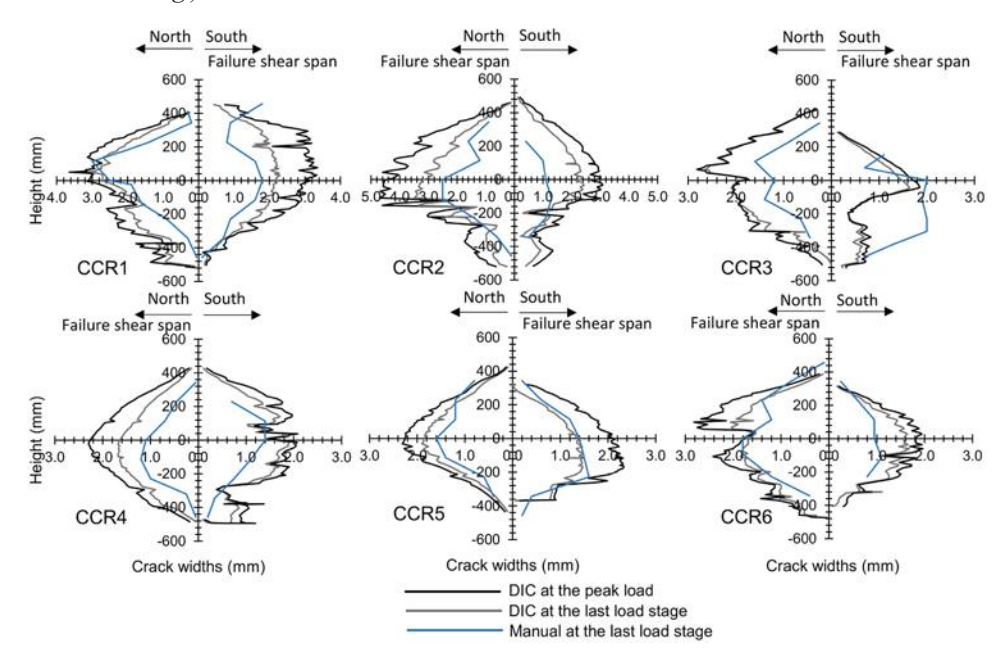


Fig. 11—Variation in crack widths with height along critical crack for CCR1 to CCR6 at last load stage and at peak load.

in the middle third of the section and decrease to a minimum near the top and bottom of the beam. This is consistent with the variation in crack widths along the height observed in previous studies. For the CCR series of tests, the maximum crack width is approximately 3.5 times the crack width at the height of the longitudinal reinforcement. The maximum crack widths observed for CCR1 to CCR6 at the peak load are given in Table 2.

The variation in crack slips is complex and depends on the local crack shape and the global kinematics of the beam projected onto the local crack. The maximum crack slips observed for CCR1 to CCR6 at the peak load are given in Table 2. The sign convention of crack slips is such that when the top face of the crack moves upwards, it is considered a positive slip (refer to Fig. 12). Here, w is the crack width, s is the crack slip, and α is the angle of the crack segment considered. Figure 12 shows the variation in crack slips of the south critical crack for specimen CCR2 at load stages 4 to 6 and at the peak load. As can be seen, the overall pattern of crack slips remains the same, but the magnitude of the slips increases with the load. The rapid variation in slips is not noise in the data and is consistent for increasing loads.

This rapid variation is due to the rapid variation in the local crack angle along the height of the member for the small crack segments used. To illustrate this, Fig. 12 also shows the crack angle of each crack segment for which the crack slip is plotted. The inset photo in Fig. 12 also shows that along a crack, the local angle can vary rapidly. Therefore, when the deformation field is projected onto these local axes, the values for slip can change rapidly from one crack segment to the next. The crack angle also has an influence on the variation in the crack widths, as seen in Fig. 11.

Figure 13 shows how the largest cracks vary with load for various crack segments. The solid lines correspond to the failure shear span for each specimen, and the dashed lines correspond to the non-failure shear span. The label for each curve indicates the specimen, the north or south shear span, and the a/d of the shear span. The crack widths are measured at the maximum crack width location of the critical crack on each shear span. For all the beams, this location is in the middle third of the height of the member. Once cracking occurs, the crack widths increase approximately linearly with the load. The rate at which the crack width increases varies for each shear span examined. For CCR1 and CCR3

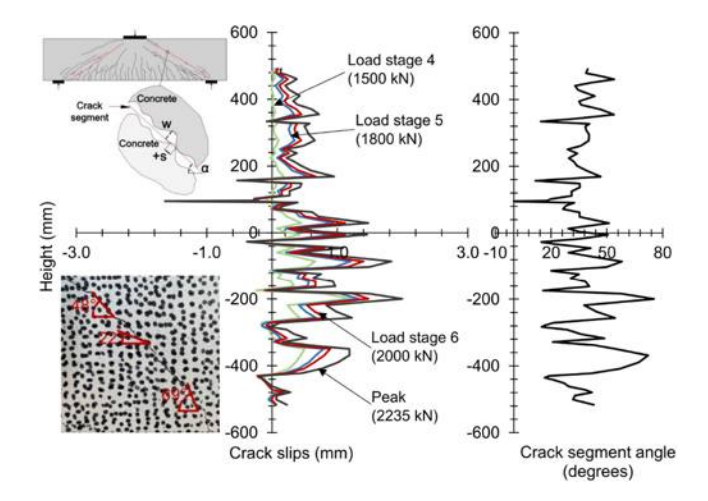


Fig. 12—Variation in crack slips and crack angle along height of CCR2 for south critical crack at load stages 4 to 6 and peak load.

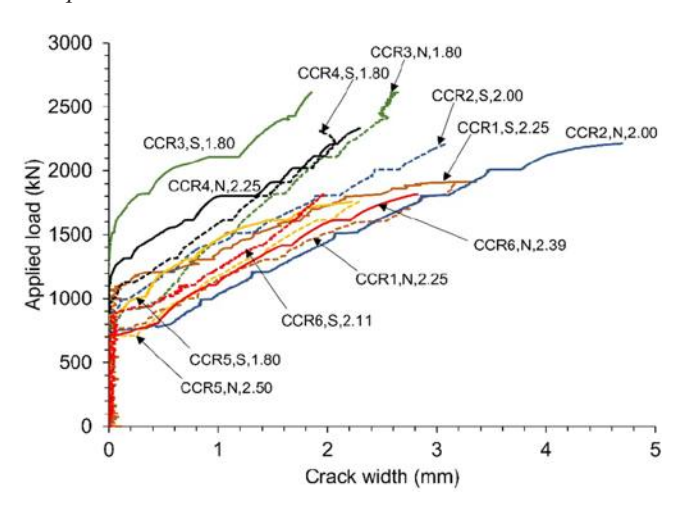
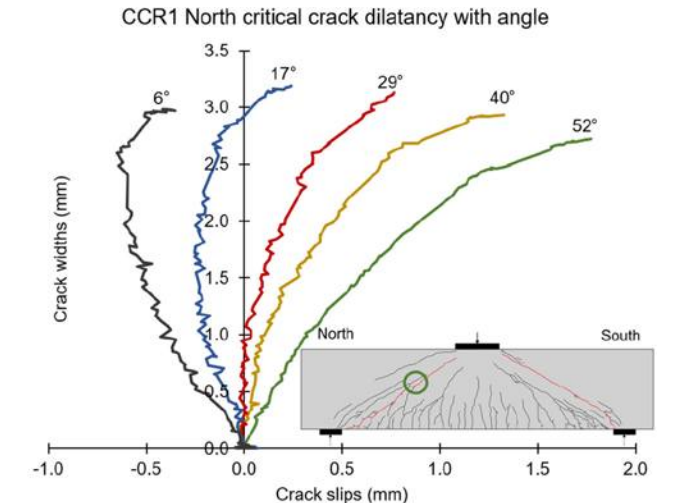


Fig. 13—Variation in crack widths with load for varying a/d. Label for each curve indicates specimen, north or south shear span, and a/d of shear span.

to CCR5, the non-failure shear span showed larger crack widths than the failure shear span at the maximum crack width location. For CCR2 and CCR6, the failure shear span showed larger crack widths than the non-failure shear span at the maximum crack width location. This observation demonstrates that determining the critical shear span solely based on the magnitude of the crack widths or using only limited measuring locations can yield insufficient structural assessments. Additionally, the maximum crack widths for the 12 shear spans vary from 1.85 to 4.70 mm at the peak load. Thus, interpreting the behavior of deep beams from crack information is complex, and the heuristic methods found in codes and guidance documents may not be sufficient to prioritize structural performance from crack information alone.

Figure 14 shows the variation in crack widths with crack slips throughout loading for nine crack segments in CCR1. The figure compares the response of crack segments at approximately the same location: near the midheight of the beam on the north shear span or the bottom of the critical crack in the south shear span (indicated by the green circles



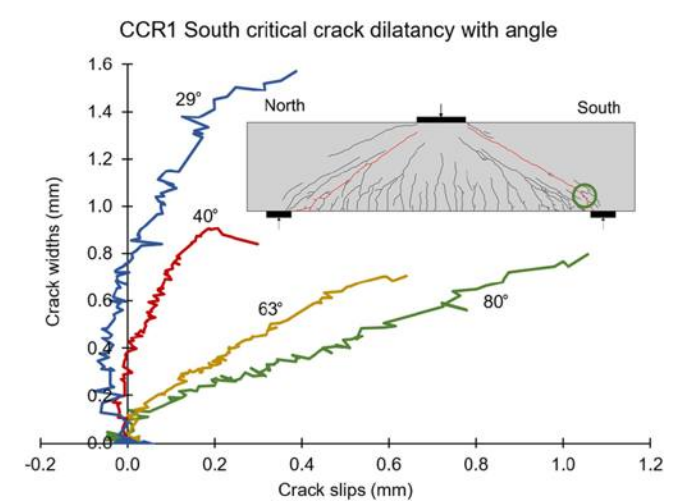


Fig. 14—Crack dilatancy throughout loading for CCR1 north critical crack and south critical crack.

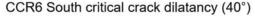
in Fig. 14). By examining cracks near the same location in the member, the influence of the crack segment angle (α) on the variation in the crack width with crack slip throughout loading can be examined in isolation from the global kinematics of the beam. In Fig. 14, the number label for each curve indicates the angle of the crack segment with the horizontal axis (refer to α in Fig. 12). This variation in crack width with the crack slips, as the crack width grows, is called crack dilatancy and is important for formulating aggregate interlock models. ²⁹⁻³¹

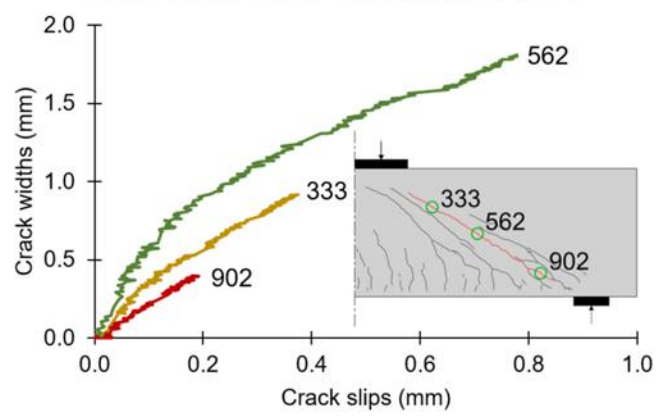
The crack dilatancy varies with the local crack angle, α, in a complex manner. First, for small angles, the crack slips increase in the negative direction with increasing crack widths. Then, the slips reach a maximum, and the cracks begin to slip in the opposite direction. Refer to the crack segments labeled 6 and 17 degrees for the north shear span of CCR1 and 29 degrees for the south shear span of CCR1 (Fig. 14). Second, for medium crack segment angles, the crack widths increase while the crack slips remain approximately zero. Then, the crack widths increase simultaneously with the crack slips. Refer to the crack segments labeled 29 degrees in the north shear span of CCR1 and 40 degrees in the south shear span of CCR1 (Fig. 14). For these crack

segments, the crack width versus crack slip behavior is similar to the crack kinematics proposed in the Guidotti aggregate interlock model.31,32 Specifically, the crack kinematics described in the Guidotti aggregate interlock model involve an initial pure crack opening, followed by a proportional increment of opening and sliding of the crack. The kinematic path described by Guidotti³¹ is consistent with observations shown for the cracks labeled 29 degrees in the north shear span of CCR1 and 40 degrees in the south shear span of CCR1 (Fig. 14). Third, as the crack segment angle increases, the crack slips increase positively with the crack widths. Refer to the lines labeled 40 and 52 degrees in the north shear span of CCR1 and the lines labeled 63 and 80 degrees in the south shear span of CCR1 in Fig. 14. This behavior of crack slips increasing positively with crack width is similar to the crack kinematic response in the aggregate interlock model proposed by Ulaga. 32,33 Specifically, the crack kinematics described in the Ulaga aggregate interlock model involve a proportional increment of crack opening and sliding throughout loading. The kinematic path described by Ulaga³³ can be observed in the cracks labeled 40 and 52 degrees in the north shear span of CCR1 and the lines labeled 63 and 80 degrees in the south shear span of CCR1 (Fig. 14). For all the crack segments shown in Fig. 14, the slope of the curve decreases with increasing slips. These observations on crack dilatancy indicate that the local crack angle has a significant influence on the crack kinematic path and dilatancy. This suggests more advanced crack kinematic models accounting for these variations, including aggregate interlock models, could be developed for large-scale members to capture these differences in member response.

Figure 15 shows how the global kinematics of the member can influence the crack dilatancy for crack segments with the same local crack angle. In Fig. 15, the number label indicates the vertical distance from the top of the beam to the center of the crack segment; the locations of the segments are also shown on the inset diagram and circled in green. As can be seen from Fig. 15, when the crack segments are closer to the midheight of the specimen, where the crack widths are larger, they tend to show larger slopes in the crack dilatancy response. Away from the midheight of the specimens, either near the flexural compression or flexural tension region, the crack dilatancy slope decreases. Thus, in addition to observing differences in crack dilatancy for different local crack angles, the global kinematics of the members also influence the crack dilatancy of crack segments along the height of the specimens.

The nonlinear crack dilatancy response throughout loading has been explored by others, including Calvi et al.³⁴ and Ruggiero.³⁵ According to these authors, the nonlinear response of the crack dilatancy results from how the aggregate particles interact along the crack. Specifically, Calvi et al.³⁴ proposed that the crack evolves in a manner consistent with the shape of the steepest face of the aggregate particle. This shape of the steepest face of the aggregate particle is referred to as the local crack shape in this paper. Even for crack segments close to one another and with the same crack angle, it is possible that the local crack shape





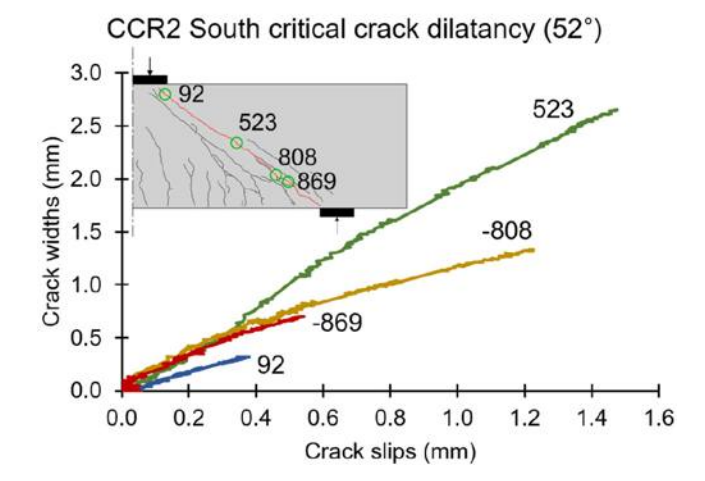


Fig. 15—Crack dilatancy for crack segments with same crack angle at different locations along critical crack for CCR2 and CCR6.

might differ. This can result in different crack dilatancies for cracks with the same approximate locations and the same crack angle. Calvi et al.³⁴ observed that initially, the increase in crack width and the crack slip are quite stiff due to compression at the contact points. Local crushing then occurs, changing the original crack surface. Calvi et al.³⁴ proposed that with further loading, as the local crack surface degrades, crack dilatancy softens. Therefore, degradation of the crack surface results in a nonlinear crack dilatancy response, where the crack width-crack slip ratio decreases as loading progresses. Calvi et al.34 and Ruggiero35 both tested panel elements subjected to uniform distributions of shear stress without the complexities of the moment. The results presented in Fig. 14 and 15 corroborate this explanation for crack dilatancy but for large-scale deep beam experiments. Therefore, other than the crack segment angle and the crack segment location along the crack, crack dilatancy likely depends on the shape of the aggregate at the contact points, local aggregate deformation due to crushing at the contact points, or a combination of both. The complex dilatancy responses observed indicate that more complex aggregate interlock models may be needed to capture the crack kinematic behavior of crack segments along the critical shear cracks in large-scale beam members.

CONCLUSIONS

This paper presents experimental results from a series of six large-scale shear-critical deep beam experiments monitored with full field-of-view digital image correlation (DIC) equipment throughout loading. The variables explored were shear span-depth ratio (a/d), loading plate size (l_{b1}) , and loading configuration. All the specimens were monotonically loaded. With initial loading, flexural cracks occurred on the tension side of the beam under the loading plate. Further increase in the load resulted in shear cracks. Ultimately, all the specimens failed in shear. Typically, for beams with similar sections, as the shear spans get shorter, the strength of the member increases. However, it was observed that when a beam is asymmetrically loaded, the shorter shear span can be critical. The results also showed that as the a/ddecreased, the ultimate strength of the specimens increased, and the displacement at the ultimate load decreased. The asymmetrically loaded specimens showed that the strength of the specimens and the failure span depend on the effective a/d and effective l_{b1} .

The paper presents high-resolution, full field-of-view displacement field data for all six deep beams, obtained from DIC measurements. Specifically, the paper presents the principal tensile and principal compressive strain fields obtained at the peak load. The tensile strain fields showed the flexural and shear cracked regions. The compressive strain fields showed highly compressed load-transfer paths and the compression struts that arch from the load to the supports. The compressive strains also showed the complex distribution of strains beneath the loading plates and the high strains located near the edge of the plates.

The DIC data and principal tensile strains were also used to generate crack patterns using the automated crack detection and measurement (ACDM) tool. The critical cracks were discretized, and the crack displacements, crack widths, and crack slips were calculated using the DIC displacement fields. The loads at which the first flexural cracking and shear cracking of the specimens occur were determined using the DIC data. The results showed that for shear spans with the same a/d, shear cracking forces can differ depending on the effective l_{b1} . The results also showed that even for shear spans with the same a/d and effective l_{b1} , shear cracking forces differed. The variation in crack widths along the height of the critical crack showed that the crack widths are largest near the middle of the section, away from the crack control provided by the longitudinal reinforcement or flexural compression region. It was shown that the crack slips vary rapidly along the height due to the rapid variation in the local crack angle along the critical crack. Results showed that the shear span with larger crack widths may not indicate the failure shear span.

The crack information obtained was then used to investigate crack dilatancy, the variation in crack widths with crack slips throughout loading. This paper presents, for the first time, crack dilatancy data for large-scale shear-critical deep beams. It was observed that the crack dilatancy varied depending on the crack angle and location of the crack segment in the member. For small crack angles, the crack slips increase in the negative direction with increasing

crack widths. They then reach a maximum crack slip, and then the crack slips increase in the positive direction. As the crack angle increases, the initial crack slips are close to zero, followed by an increase in crack slips positively with the crack widths. As the crack angles further increase, the crack slips and widths increase proportionally with loading. The crack segments closer to the midheight of the specimen, where the crack widths are larger, tend to show larger slopes in the crack dilatancy response. The crack dilatancy observations were consistent with previous research on panel tests subjected to pure shear and biaxial stresses. Specifically, the slope of the crack dilatancy curve changes continuously throughout loading, likely because of the degradation of the crack surfaces as the crack deforms.

The results in this paper show that the crack behavior of large-scale reinforced concrete deep beams is complex. Simply comparing crack widths with limits in codes and guidance documents or comparing limited measurement data to models can lead to inaccurate structural assessments. Therefore, a thorough understanding of crack kinematics is required when assessing large-scale structures based on cracks. While these complexities may not need to be considered in every analysis, understanding them may be needed to fully understand the shear behavior of deep concrete beams.

AUTHOR BIOS

ACI member **Dhanushka K. Palipana** is a Postdoctoral Researcher at the University of Kansas, Lawrence, KS. She is a member of Joint ACI-ASCE Subcommittees 445-E, Shear & Torsion-SOA Torsion, and 445-F, Interface Shear. She received her BSc Eng from the University of Peradeniya, Peradeniya, Sri Lanka, in 2017, and her PhD from North Carolina State University, Raleigh, NC, in 2023.

ACI member Giorgio T. Proestos is an Assistant Professor at North Carolina State University. He received his BASc in Engineering Science, MASc, and PhD from the University of Toronto, Toronto, ON, Canada, in 2012, 2014, and 2018, respectively. He is Secretary of Joint ACI-ASCE Committee 445, Shear and Torsion, and a member of Joint ACI-ASCE Subcommittee 445-E, Shear & Torsion-Torsion. He received the ACI Design Award in 2017 and the ACI Chester Paul Siess Award in 2018.

ACKNOWLEDGMENTS

The authors would like to thank Headed Reinforcement Corp. for their donation of headed reinforcing bars used in this experimental series.

REFERENCES

- 1. Mihaylov, B. I.; Bentz, E. C.; and Collins, M. P., "Behavior of Large Deep Beams Subjected to Monotonic and Reversed Cyclic Shear," *ACI Structural Journal*, V. 107, No. 6, Nov.-Dec. 2010, pp. 726-734.
- 2. Palipana, D. K., and Proestos, G. T., "Large-Scale Shear Critical Reinforced Concrete Deep Beam Experiments Monitored with Full Field of View Digital Image Correlation Equipment," *26th International Conference on Structural Mechanics in Reactor Technology (SMiRT-26)*, Division V, Berlin/Potsdam, Germany, July 2022, 10 pp..
- 3. Palipana, D. K., and Proestos, G. T., "Asymmetrical Loading of Reinforced Concrete Deep Beams Monitored with Full Field-of-View Digital Image Correlation," *Proceedings of the 14th* fib *PhD Symposium in Civil Engineering*, M. di Prisco, A. Meda, and G. L. Balázs, eds., Rome, Italy, Sept. 2022, pp. 105-112.
- 4. ACI Committee 224, "Control of Cracking in Concrete Structures (ACI 224R-01) (Reapproved 2008)," American Concrete Institute, Farmington Hills, MI, 2001, 46 pp.
- 5. AASHTO, "Manual for Bridge Element Inspection," second edition, American Association of State Highway and Transportation Officials, Washington, DC, 2019, 126 pp.
- 6. Woods, J. E.; Yang, Y.-S.; Chen, P.-C.; Lau, D. T.; and Erochko, J., "Automated Crack Detection and Damage Index Calculation for RC Structures Using Image Analysis and Fractal Dimension," *Journal of Structural*

- Engineering, ASCE, V. 147, No. 4, Apr. 2021, p. 04021019. doi: 10.1061/(ASCE)ST.1943-541X.0002970
- 7. Zaborac, J.; Athanasiou, A.; Salamone, S.; Bayrak, O.; and Hrynyk, T. D., "Crack-Based Shear Strength Assessment of Reinforced Concrete Members Using a Fixed-Crack Continuum Modeling Approach," *Journal of Structural Engineering*, ASCE, V. 146, No. 4, Apr. 2020, p. 04020024. doi: 10.1061/(ASCE)ST.1943-541X.0002564
- 8. Spencer, B. F. Jr.; Hoskere, V.; and Narazaki, Y., "Advances in Computer Vision-Based Civil Infrastructure Inspection and Monitoring," *Engineering*, V. 5, No. 2, Apr. 2019, pp. 199-222. doi: 10.1016/j. eng.2018.11.030
- 9. Palipana, D. K.; Trandafir, A. N.; Mihaylov, B. I.; and Proestos, G. T., "Framework for Quantification of Shear-Transfer Mechanisms from Deep Beam Experiments," *ACI Structural Journal*, V. 119, No. 3, May 2022, pp. 53-65. doi: 10.14359/51734485
- 10. Peng, F.; Cai, Y.; Yi, W.; and Xue, W., "Shear Behavior of Two-Span Continuous Concrete Deep Beams Reinforced with GFRP Bars," *Engineering Structures*, V. 290, Sept. 2023, Article No. 116367. doi: 10.1016/j. engstruct.2023.116367
- 11. Silveira, M. V. G.; Paini, B.; Bitencourt, L. A. G. Jr.; and Das, S., "Design and Experimental Investigation of Deep Beams Based on the Generative Tie Method," *Engineering Structures*, V. 255, Mar. 2022, Article No. 113913. doi: 10.1016/j.engstruct.2022.113913
- 12. Bažant, Z. P., "Size Effect on Structural Strength: A Review," *Archive of Applied Mechanics*, V. 69, No. 9-10, Nov. 1999, pp. 703-725. doi: 10.1007/s004190050252
- 13. Collins, M. P.; Quach, P. T.; and Bentz, E. C., "Shear Behavior of Thick Slabs," *ACI Structural Journal*, V. 117, No. 4, July 2020, pp. 115-126. doi: 10.14359/51724666
- 14. Trandafir, A. N.; Proestos, G. T.; and Mihaylov, B. I., "Detailed Crack-Based Assessment of a 4-m Deep Beam Test Specimen," *Structural Concrete*, V. 24, No. 1, Feb. 2023, pp. 756-770. doi: 10.1002/suco.202200149
- 15. Ulzurrun, G. S. D., and Zanuy, C., "Time-Variation of Shear Forces Affecting the Impact Resistance of Reinforced Concrete Beams," *Hormigón y Acero*, 2022, prepublished. doi: 10.33586/hya.2022.3088
- 16. Siebert, T.; Becker, T.; Spiltthof, K.; Neumann, I.; and Krupka, R., "High-Speed Digital Image Correlation: Error Estimations and Applications," *Optical Engineering*, V. 46, No. 5, May 2007, Article No. 051004. doi: 10.1117/1.2741217
- 17. ACI Committee 318, "Building Code Requirements for Structural Concrete (ACI 318-19) and Commentary (ACI 318R-19) (Reapproved 2022)," American Concrete Institute, Farmington Hills, MI, 2019, 624 pp.
- 18. AASHTO, "AASHTO LRFD Bridge Design Specifications and Commentary," ninth edition, American Association of State Highway and Transportation Officials, Washington, DC, 2020, 1912 pp.
- Transportation Officials, Washington, DC, 2020, 1912 pp.
 19. CSA A23.3:19, "Design of Concrete Structures," CSA Group, Toronto, ON, Canada, 2019, 301 pp.
- 20. Palipana, D. K., "Assessment of Shear Transfer Mechanisms in Reinforced Concrete Deep Beams from Experiments with Full Field-of-View Displacement Field Data," PhD thesis, North Carolina State University, Raleigh, NC, 2023, 440 pp.
- 21. Mihaylov, B. I.; Bentz, E. C.; and Collins, M. P., "Two-Parameter Kinematic Theory for Shear Behavior of Deep Beams," *ACI Structural Journal*, V. 110, No. 3, May-June 2013, pp. 447-456.

- 22. Trandafir, A. N.; Palipana, D. K.; Proestos, G. T.; and Mihaylov, B. I., "Framework for Crack-Based Assessment of Existing Lightly Reinforced Concrete Deep Members," *ACI Structural Journal*, V. 119, No. 1, Jan. 2022, pp. 255-266. doi: 10.14359/51733143
- 23. Ma, C.; Xie, C.; Tuohuti, A.; and Duan, Y., "Analysis of Influencing Factors on Shear Behavior of the Reinforced Concrete Deep Beams," *Journal of Building Engineering*, V. 45, Jan. 2022, Article No. 103383. doi: 10.1016/j.jobe.2021.103383
- 24. Smith, K. N., and Vantsiotis, A. S., "Shear Strength of Deep Beams," *ACI Journal Proceedings*, V. 79, No. 3, May-June 1982, pp. 201-213. doi: 10.14359/10899
- 25. Proestos, G. T.; Palipana, D. K.; and Mihaylov, B. I., "Evaluating the Shear Resistance of Deep Beams Loaded or Supported by Wide Elements," *Engineering Structures*, V. 226, Jan. 2021, Article No. 111368. doi: 10.1016/j.engstruct.2020.111368
- 26. Qambar, M., and Proestos, G. T., "Experimental Investigation of Reinforced Concrete Deep Beams with Wide Loading Elements," *ACI Structural Journal*, V. 119, No. 4, July 2022, pp. 239-250. doi: 10.14359/51734497
- 27. Gehri, N.; Mata-Falcón, J.; and Kaufmann, W., "Automated Crack Detection and Measurement Based on Digital Image Correlation," *Construction and Building Materials*, V. 256, Sept. 2020, Article No. 119383. doi: 10.1016/j.conbuildmat.2020.119383
- 28. Langer, M., "Evaluation of the Load-Bearing Mechanisms in Coupling Beams and Shear Walls based on DIC Measurements," MSc thesis, University of Liège, Liège, Belgium, 2019, 136 pp.
- 29. Calvi, P. M.; Bentz, E. C.; and Collins, M. P., "Model for Assessment of Cracked Reinforced Concrete Membrane Elements Subjected to Shear and Axial Loads," *ACI Structural Journal*, V. 115, No. 2, Mar. 2018, pp. 501-509. doi: 10.14359/51701093
- 30. Cavagnis, F.; Fernández Ruiz, M.; and Muttoni, A., "An Analysis of the Shear-Transfer Actions in Reinforced Concrete Members without Transverse Reinforcement Based on Refined Experimental Measurements," *Structural Concrete*, V. 19, No. 1, Feb. 2018, pp. 49-64. doi: 10.1002/suco.201700145
- 31. Guidotti, R., "Poinçonnement des Planchers-Dalles avec Colonnes Superposées Fortement Sollicitées," PhD thesis, Thesis No. 4812, École Polytechnique Fédérale de Lausanne, Lausanne, Switzerland, 2010, 446 pp. (in French)
- 32. Campana, S.; Fernández Ruiz, M.; Anastasi, A.; and Muttoni, A., "Analysis of Shear-Transfer Actions on One-Way RC Members Based on Measured Cracking Pattern and Failure Kinematics," *Magazine of Concrete Research*, V. 65, No. 6, Mar. 2013, pp. 386-404. doi: 10.1680/macr.12.00142
- 33. Ulaga, T., "Betonbauteile mit Stab- und Lamellenbewehrung: Verbund- und Zuggliedmodellierung," PhD thesis, Thesis No. 15062, Zurich, Switzerland, ETH Zürich, Zürich, Switzerland, 2003, 167 pp. (in German)
- 34. Calvi, P. M.; Bentz, E. C.; and Collins, M. P., "Pure Mechanics Crack Model for Shear Stress Transfer in Cracked Reinforced Concrete," *ACI Structural Journal*, V. 114, No. 2, Mar.-Apr. 2017, pp. 545-554. doi: 10.14359/51689460
- 35. Ruggiero, D. M. V., "The Behaviour of Reinforced Concrete Subjected to Reversed Cyclic Shear," PhD thesis, University of Toronto, Toronto, ON, Canada, 2015, 455 pp.

In 2023, the individuals listed on these pages served as technical reviewers of papers offered for publication in ACI periodicals. A special "thank you" to them for their voluntary assistance in helping ACI maintain the high quality of its publication program.

A. Abbas, Waleed

University of Technology Iraq *Al-Sinaa Street, Baghdad, Iraq*

Abdeldjalil, Mhammed

University of Science and Technology of Oran Mohamed-Boudiaf

El Mnaouar, Algeria

Abdellatef, Mohammed

The University of New Mexico Albuquerque, NM, United States

Abdulla, Nwzad

Salahaddin University-Erbil *Erbil, Iraq*

Abdullah, Saman

University of California, Los Angeles Los Angeles, CA, United States

Abdul-Razzaq, Khattab

University of Diyala Diyala, Iraq

Abed, Ziyad

University of Technology Iraq Baghdad, Baghdad, Iraq

Abellan-García, Joaquin

Universidad del Norte
Barranquilla, Colombia

Abousnina, Rajab

University of Southern Queensland *Toowoomba*, *QLD*, *Australia*

Abraham, Sarah Mariam

Birla Institute of Technology and Science Pilani *Pilani, Rajasthan, India*

Abu Obeidah, Adi

Rutgers, The State University of New Jersey *Piscataway, NJ, United States*

Abuzeid, Al-Tuhami

Badr for Consulting and Retrofitting Cairo, Nasr City, Egypt

Accornero, Federico

Shantou University Shantou, China

Acun, Bora

UBC Okanagan Kelowna, BC, Canada

Adak, Dibyendu

National Institute of Technology Meghalaya Shillong, Meghalaya, India

Adekunle, Saheed

King Fahd University of Petroleum and Minerals Dhahran, Saudi Arabia

Afif, Rahma

Damascus University Faculty of Civil Engineering Damascus, Syrian Arab Republic

Aghamohammadi, Omid

Isfahan University of Technology Isfahan, Islamic Republic of Iran

Aguayo, Federico

University of Washington Seattle, WA, United States

Agustiningtyas, Rudi

Ministry of Public Works and Public Housing Bandung, Indonesia

Ahani, Elshan

Sahand University of Technology *Tabriz, Islamic Republic of Iran*

Ahmad, Subhan

Aligarh Muslim University Faculty of Engineering and Technology

Aligarh, Uttar Pradesh, India

Ahmadi Nedushan, Behrooz

Yazd University Yazd, Yazd, Islamic Republic of Iran

Ahmed, Afaf

Sohar College of Applied Sciences *Sohar, Oman*

Ahmed, Mohamed

Université de Sherbrooke Sherbrooke, QC, Canada

Ahmed, Mshtaq

King Saud University
Riyadh, Riyadh, Saudi Arabia

Ahmed, Saddam

Anna University

Chennai, Tamil Nadu, India

Ahn, Seong Ryong

Seoul National University Seoul, Seoul, Republic of Korea

Aire, Carlos

National Autonomous University of Mexico Mexico, DF, Mexico

Akakin, Tumer

Aggregate and Ready Mix Association of Minnesota Eagan, MN, United States

Akalin, Ozlem

PLUSTECHNO Ltd Istanbul, Turkey

Akhlaghi, Alireza

Isfahan, Islamic Republic of Iran

Akkaya, Yildir

İstanbul Teknik Üniversitesi Maslak, Sarıyer, Istanbul, Turkey

Al Mansouri, Omar

CSTB

Marne-la-Vallée, France

Alam, A.K.M. Jahangir

Bangladesh University of Engineering and Technology (BUET) Dhaka, Bangladesh

Al-Ani, Moustafa

Auckland, New Zealand

Alcocer, Sergio

Institute of Engineering, UNAM *Mexico City, DF, Mexico*

Aldea, Corina-Maria

St. Catharines, ON, Canada

Aldwaik, Mais

Russeifa, Zarqa, Jordan

Al-Harthy, Ali

Sultan Qaboos University *Al-Khaudh, Oman*

Ali, Elias

Case Western Reserve University Cleveland, OH, United States

Ali, Yahia

Nanjing, Jiangsu, China

Alimrani, Naser

Budapest University of Technology and Economics *Budapest, Budapest, Hungary*

Aljewifi, Hana

Université de Cergy-Pontoise *Elbeida, Libya*

Al-Kamal, Mustafa

Al-Nahrain University Baghdad, Baghdad, Iraq

Alkhairi, Fadi

Magna MEP

Dubai, United Arab Emirates

Alkhrdaji, Tarek

Structural Technologies Columbia, MD, United States

Almasabha, Ghassan

The Hashemite University Sahab, Amman, Jordan

Almbaidheen, Khalil

Mapei SpA

Dubai, United Arab Emirates

Almuhsin, Bayrak

University of Technology Iraq Karrada, Baghdad, Iraq

Al-Najmi, AbdulQader

Amman, Jordan

Al-Nasra, Moayyad

American University of Ras Al Khaimah School of Engineering Ras Al Khaimah, United Arab Emirates

Al-Qaralleh, Mohammad

Mutah University Karak, Jordan

Al-Sadoon, Zaid

University of Sharjah College of Engineering Sharjah, United Arab Emirates

Al-Tameemi, Mohamed

University of Wisconsin–Madison *Madison, WI, United States*

Al-Zuheriy, Ahmed

University of Technology - Iraq Baghdad, Baghdad, Iraq

Amir, Sana

Delft University of Technology

Delft, South Holland, Netherlands

Anaokar, Manoj

NMIMS Deemed to be University - Mumbai Campus *Mumbai, Maharashtra, India*

Antoni, Antoni

Petra Christian University Surabaya, Indonesia

Anwari, Qareeb Ullah

NUST Institute of Civil Engineering Islamabad, Islamabad, Pakistan

Anyaoha, Uchenna

University of British Columbia Okanagan *Kelowna, BC, Canada*

Arabzadeh, Abolfazl

Tarbiat Modares University Tehran, Islamic Republic of Iran

Arafa, Ahmed

Université de Sherbrooke Sherbrooke, QC, Canada

Araghi, Hassan

Islamic Azad University, South Tehran Karaj, Tehran, Islamic Republic of Iran

Aras, Murat

Bilecik Şeyh Edebali University Bilecik, Bilecik, Turkey

Arce, Gabriel

Virginia Transportation Research Council Charlottesville, VA, United States

Arcine, Maicon de Freitas

Universidade Federal de São Carlos São Carlos, São Paulo, Brazil

Aristizabal-Ochoa, Jose

National University of Colombia Medellín, Antioquia, Colombia

Arito, Philemon

University of Namibia
Ongwediva, Oshana, Namibia

Asadian, Alireza

Concordia University Montreal, QC, Canada

Ashish, Deepankar Kumar

Yonsei University Seodaemun-gu, Seoul, Republic of Korea

Ashrafy, Mohammad

Islamic Azad University – Arak Branch Kermanshah, Islamic Republic of Iran

Assaad, Joseph

University of Balamand Balamand, Lebanon

Assi, Lateef

Al-Mustaqbal University College Hillah, Babylon, Iraq

Attia Ahmed, Mohamed

Ain Shams University Faculty of Engineering *Cairo*, *Egypt*

Attiogbe, Emmanuel

Discovery Bay, CA, United States

Attiyah, Ali

University of Kufa Kufa, Iraq

Awida, Tarek

SQC International Consultants *Kuwait, Kuwait, Kuwait, Kuwait*

Avdin, Ertug

Lefke Avrupa Üniversitesi Lefke, Cyprus

Aziminejad, Armin

Islamic Azad University Science and Research Branch Tehran, Tehran, Islamic Republic of Iran

Aziz, Ali

Al-Mustansiriyah University-College of Engineering Baghdad, Baghdad, Iraq

BS, Sindu

CSIR Structural Engineering Research Centre Chennai, India

Babatola, Oluwatosin

Akure, Ondo, Nigeria

Bacinskas, Darius

Vilnius Gediminas Technical University Vilnius, Lithuania

Bahij, Sifatullah

King Fahd University of Petroleum and Minerals Dhahran, Dammam, Saudi Arabia

Bai, Shaoliang

Chongqing University Chongqing, China

Balouch, Sana

University of Dundee

Dundee, United Kingdom of Great Britain and Northern Ireland

Banjara, Nawal

CSIR Structural Engineering Research Centre Chennai, Tamil Nadu, India

Bao, Chao

Ningxia University *Yinchuan, China*

Basereh, Sina

Mar Structural Design Berkeley, CA, United States

Bassuoni, Mohamed T.

University of Manitoba Winnipeg, MB, Canada

Baty, James

Concrete Foundations Association Mount Vernon, IA, United States

Behnoud, Ali

Aurecon Australia Group Ltd Sydney Neutral Bay, NSW, Australia

Bektas, Fatih

Minnesota State University, Mankato *Mankato, MN, United States*

Benaicha, Mouhcine

AMU

Marseille, France

Benítez, Pablo

Universidad Nacional de Itapúa Encarnación, Itapúa, Paraguay

Benliang, Liang

Shanghai, China

Berenguer, Romildo

Universidade Federal de Pernambuco Centro de Ciências Exatas e da Natureza *Recife, Brazil*

Beyene, Mengesha

Turner-Fairbank Highway Research Center McLean, VA, United States

Bharadwaj, Keshav

Indian Institute of Technology Delhi New Delhi, India

Bhojaraju, Chandrasekhar

St Joseph Engineering College Mangalore, Karnataka, India

Bilek, Vlastimil

ŽPSV a.s.

Brno, Czech Republic

Bilisik, Kadir

Erciyes University
Kayseri, Central Anatolia, Turkey

Billah, AHM Muntasir

University of Calgary Calgary, AB, Canada

Blandón Valencia, John

National University of Colombia Medellin *Medellin, Antioquia, Colombia*

Bonacci, John

Karins Engineering Group Sarasota, FL, United States

Borzovič, Viktor

Slovak University of Technology in Bratislava, Faculty of Civil Engineering

Bratislava, Slovakia

Boulifa, Ridha

Mohamed-Cherif Messaadia University-Souk Ahras Souk Ahras, Algeria

Bouzid, Haytham

Université Ibn Khaldoun Tiaret *Tiaret, Algeria*

Braestrup, Mikael

Rambøll Group A/S
Copenhagen, Denmark

Brahma, Abdelmalek

Université Saad Dahlab Blida Blida, Algeria

Brena, Sergio

University of Massachusetts Amherst, MA, United States

Browning, JoAnn

University of Kansas-Civil, Environmental & Architectural Engineering

Lawrence, KS, United States

Buitrago, Manuel

Universitat Politècnica de València *Valencia, Spain*

Bujnak, Jan

Peikko Group Corporation Kráľová nad Váhom, Slovakia

Burak Bakir, Burcu

Orta Doğu Teknik Üniversitesi Ankara, Turkey

Buttignol, Thomaz Eduardo

Universidade Estadual de Campinas - Campus Cidade Universitária Zeferino Vaz Campinas, SP, Brazil

C, Akin

KCG College of Technology Chennai, India

Cafarelli, Renato

Politecnico di Torino *Turin, Italy*

Cai, Jingming

Southeast University Nanjing, Jiangsu, China

Calderon, Victor

North Carolina State University Raleigh, NC, United States

Campos, Claudia

Universidade Federal Fluminense Rio de Janeiro, Rio de Janeiro, Brazil

Cao, Jian

Nanchang Institute of Technology *Nanchang, Jiangxi, China*

Carloni, Christian

Case Western Reserve University Cleveland. OH. United States

Carlton, Aerik

Exponent

Warrenville, IL, United States

Carpio, Víctor

Escuela Politécnica Nacional *Quito, Pichincha, Ecuador*

Carrette, Jordan

Crosier Kilgour and Partners Ltd *Winnipeg, MB, Canada*

Cascudo, Oswaldo

Universidade Federal de Goiás *Goiânia*, *GO*, *Brazil*

Chakkamalayath, Jayasree

Kuwait Institute for Scientific Research Safat, Kuwait

Chakraborty, Arun

Bengal Engineering and Science University Howrah, West Bengal, India

Chang, Jeremy

Holmes Aus & NZ Christchurch, New Zealand

Chang, Wei

Harbin, China

Chao, Shih-Ho

The University of Texas at Arlington *Arlington, TX, United States*

Chapirom, Aphai

Suranaree University of Technology Institute of Science Nakhon Ratchasima, Nakhon Ratchasima, Thailand

Chellappan, C. Selin Ravikumar

Malla Reddy Engineering College Secunderabad, Telangana, India

Chen, Xu

University of Colorado Boulder Boulder, CO, United States

Cheng, Jianwei

China University of Mining and Technology *Xuzhou, Jiangsu, China*

Cheng, Min-Yuan

National Taiwan University of Science and Technology Taipei, Taiwan, China

Chidambaram, R. Siva

CSIR-Central Building Research Institute Roorkee, Uttarakhand, India

Cho, Soon-Ho

Gwangju University Gwangju, Republic of Korea

Choi, Yoon Suk

Korea Conformity Laboratories Seoul, Republic of Korea

Choong, Kokkeong

Universiti Sains Malaysia Penang, Seberang Perai Selatan, Malaysia

Chorzepa, Migeum

Park Ridge, IL, United States

Chowdhury, Sharmin

Boğaziçi University Istanbul, Turkey

Chu, S. H.

Columbia University
New York, NY, United States

Ciggelakis, William

Professional Service Industries San Antonio. TX. United States

Cladera, Antoni

University of the Balearic Islands *Palma, Balearic Islands, Spain*

Clementino, Fabio

IFPI

Teresina, Piauí, Brazil

Climent, Miguel

University of Alicante *Alicante, Spain*

Cuenca, Estefania

Politecnico di Milano *Milan, Italy*

da Silveira, Rodrigo

Universidade Federal de Santa Maria Santa Maria, Rio Grande do Sul, Brazil

Dadvar, Sayyed Ali

University of Sherbrooke Sherbrooke, QC, Canada

Dave, Shemal

Marwadi Education Foundation's Group of Institutions Jamnagar, Gujarat, India

Davila, Jose

University of Huelva, Escuela Técnica Superior de Ingeniría Palos de la Frontera, Huelva, Spain

DC, Mitra

College of Engineering Trivandrum *Thiruvananthapuram, Kerala, India*

De Brito, Jorge

IST / TUL Lisbon, Portugal

de Oliveira, Gabriel

Unicamp

Campinas, São Paulo, Brazil

De Rooij, Mario

TNO

Delft, Netherlands

Degtyarev, Vitaliy

Lexington, SC, United States

del Rey Castillo, Enrique

University of Auckland Auckland, Auckland, New Zealand

Delalibera, Rodrigo

University of São Paulo São Carlos, São Paulo, Brazil

Dhole, Rajaram

Katy, TX, United States

Dhonde, Hemant

University of Houston Houston, TX, United States

Dias, WPS

University of Moratuwa Moratuwa, Sri Lanka

Diniz, Sofia Maria

Federal University of Minas Gerais School of Engineering Belo Horizonte, Minas Gerais, Brazil

Dogan, Unal

Istanbul Technical University Istanbul, Turkey

Dolan, Charles

University of Wyoming Laramie, WY, United States

Dong, Jiangfeng

Sichuan University *Chengdu, China*

Dongell, Jonathan

Pebble Technology International Scottsdale, AZ, United States

Donmez, Abdullah

İstanbul Teknik Üniversitesi Istanbul, Turkey

Du, Lianxiang

The University of Alabama at Birmingham Birmingham, AL, United States

Du, Yingang

Anglia Ruskin University

Chelmsford, United Kingdom of Great Britain and Northern Ireland

Dugvekar, Mitali

MANIT

Bhopal, Madhya Pradesh, India

Dundar, Cengiz

Cukurova University Adana, Turkey

Dwairi, Hazim

The Hashemite University Zarqa, Zarqa, Jordan

Ekenel, Mahmut

International Code Council-Evaluation Service Los Angeles, CA, United States

El-Ariss, Bilal

United Arab Emirates University Al Ain, United Arab Emirates

Elbady, Ahmed

Université de Sherbrooke Sherbrooke, QC, Canada

El-Dash, Karim

College of Technological Studies *Kuwait, Kuwait*

El-Gendy, Mohammed

Winnipeg, MB, Canada

El-Hassan, Hilal

United Arab Emirates University Faculty of Engineering Al Ain, United Arab Emirates

Elkafrawy, Mohamed

American University of Sharjah Sharjah, United Arab Emirates

El-Maaddawy, Tamer

United Arab Emirates University
Al Ain, Abu Dhabi, United Arab Emirates

Elmasry, Mohamed

Arab Academy for Science, Technology and Maritime Transport Alexandria, Egypt

Elmenshawi, Abdelsamie

University of Calgary Calgary, AB, Canada

Elnady, Mohamed

Mansoura University Vancouver, BC, Canada

El-Refaie, Sameh

El-Gama City, Mataria, Cairo, Egypt

El-Salakawy, Ehab

University of Manitoba Winnipeg, MB, Canada

El-Sayed, Ahmed

University of Sherbrooke Sherbrooke, QC, Canada

Elsayed, Tarek

Cairo, Egypt

Eltahawy, Reham

Ain Shams University *Cairo*, *Egypt*

Ercolino, Marianna

University of Greenwich Faculty of Engineering and Science
Chatham Maritime, United Kingdom of Great Britain and
Northern Ireland

Eskandari, Rasoul

Kashmar, Khorasan Razavi, Islamic Republic of Iran

Etman, Emad

El-Mahalla El-Kubra, Egypt

Ewis, Ahmed

Cairo, Egypt

Ezeldin, Samer

The American University in Cairo Cairo, Egypt

Faleschini, Flora

University of Padova *Padua*, *Italy*

Fan, Shengxin

Nanyang Technological University Singapore, Singapore

Fanella, David

Concrete Reinforcing Steel Institute Schaumburg, IL, United States

Fantilli, Alessandro Pasquale

Politecnico di Torino Turin, Italy

Faraone, Gloria

San Diego State University San Diego, CA, United States

Fargier, Luis

Kiewit Infrastructure Engineers Englewood, CO, United States

Faria, Duarte

Faculdade de Ciências e Tecnologia Caparica-Lisbon, Portugal

Farshadfar, Omid

Thornton Tomasetti

Lawrence, KS, United States

Farzadnia, Nima

Missouri University of Science and Technology *Rolla, MO, United States*

Farzam, Masood

Structural Engineering Tabriz, Islamic Republic of Iran

Fatemi, Hassan

Montreal, QC, Canada

Fernandes, Fernando Antonio da Silva

Federal University of Pará - Campus Salinópolis - Faculty of Engineering

Salinópolis, Pará, Brazil

Fernandez Montes, David

Madrid, Madrid, Spain

Fick, Damon

Bozeman, MT, United States

Fikry, Ahmed

Helwan University Cairo, Egypt

Fitik, Birol

Hochschule für Technik Stuttgart Stuttgart, Germany

Folino, Paula

University of Buenos Aires Buenos Aires, Argentina

Franco-Lujan, Victor

Tecnológico Nacional de México Mexico City, Mexico City, Mexico

Fu, Tengfei

Fuzhou, Fujian, China

G D R N, Ransinchung

Roorkee, Uttarakhand, India

Gąćkowski, Roman

Częstochowa University of Technology Częstochowa, Poland

Gadkar, Shubhada

Ontario, CA, United States

Galati, Nestore

Structural Technologies Columbia, MD, United States

Gallandorm, Edith

PCI

Chicago, IL, United States

Gan, Dan

Chongqing, China

Ganesan, N.

National Institute of Technology Calicut Calicut, India

Gao, Peng

Hefei University of Technology Hefei, China

Gao, Xiangling

Tongji University Shanghai, China

Garcia Troncoso, Natividad Leonor

ESPOL

Guayaquil, Ecuador

Gayed, Ramez

University of Calgary Calgary, AB, Canada

Geng, Yan

MCC Central Research Institute of Building and Construction Co. Ltd.

Beijing, Beijing, China

Getaz, James

Shockey Precast Group Winchester, VA, United States

Ghannoum, Wassim

The University of Texas at Austin *Austin, TX, United States*

Gheni, Ahmed

Komar University of Science and Technology Sulaymaniyah, Iraq

Ghiami Azad, Amir Reza

University of Tehran Boston. MA. United States

Ghimire, Krishna

Kansas State University

Manhattan, KS, United States

Ghoddousi, Parviz

Iran University of Science and Technology Tehran, Tehran, Islamic Republic of Iran

Ghugal, Yuwaraj

Government College of Engineering, Karad Karad, Maharashtra, India

Giduquio, Marnie

National Taiwan University of Science and Technology *Taipei, Taiwan, China*

Girgin, Canan

Yıldız Technical University *Istanbul, Turkey*

Glegorio, Marcio

Portland, OR, United States

Goel, Rajeev

CSIR-Central Road Research Institute *Delhi, India*

González, Javier

University of the Basque Country Bilbao, Basque Country, Spain

Govan, G. Elangovan

Civil Engg

Chennai, Tamil Nadu, India

Guades, Ernesto

Technical University of Denmark Lyngby, Denmark

Guan, Bowen

Xi'an, China

Gujar, Abhay

Dr. Babasaheb Ambedkar Technological University Satara, Maharashtra, India

Guo, Honglei

Wuhan Polytechnic University Wuhan, Hubei, China

Guo, Liping

Southeast University Nanjing, Jiangsu, China

Habulat, Afifudin

Universiti Teknologi MARA Permatang Pauh, Penang, Malaysia

Haddadin, Laith

United Nations

New York, NY, United States

Hadje-Ghaffari, Hossain

John A. Martin & Associates, Inc. Los Angeles, CA, United States

Haggag, Hesham

Haggag Consultancy for Construction Cairo, Cairo, Egypt

Hamed, Ehab

The University of New South Wales Sydney, NSW, Australia

Han, Baoguo

Dalian University of Technology Dalian, China

Haneefa Kolakkadan, Mohammed

SSN College of Engineering Kalavakkam, Tamil Nadu, India

Harith, Iman

Babylon, Iraq

Hassan, Mostafa

University of Connecticut Storrs, CT, United States

Hassanpour, Sina

Sharif University of Technology Tehran, Tehran, Islamic Republic of Iran

Henigal, Ashraf

Suez University Suez, Egypt

Hentges, Tatiane

Unisinos

São Leopoldo, Rio Grande do Sul, Brazil

Heras Murcia, Daniel

University of New Mexico
Albuquerque, NM, United States

Himawan, Aris

Singapore, Singapore

Ho, Johnny

The University of Hong Kong Hong Kong, Hong Kong, China

Horowitz, Bernardo

Recife, PE, Brazil

Hosseini, Seyed Mohammad

University of Sherbrooke Sherbrooke, QC, Canada

Hoult, Neil

Toronto, ON, Canada

Hu, Nan

South China University of Technology Guangzhou, Guangdong, China

Hu, Zhong-Wei

Nanjing, China

Huang, Chung-Ho

National Taipei University of Technology Taipei, Taiwan, China

Huang, Jianwei

Southern Illinois University Edwardsville Edwardsville, IL, United States

Huang, Xiaobao

Oakland University
Rochester, MI, United States

Huang, Yuan

Hunan University Changsha, Hunan, China

Huo, Jingsi

Huaqiao University Xiamen, Fujian, China

Hurtado, Pablo E.

Simpson Gumpertz & Heger Inc. *Atlanta, GA, United States*

Hussain, Safdar

MS Ramaiah University of Applied Sciences Bangalore, Karnataka, India

Huts, Andriy

Politechnika Rzeszowska im. Ignacego Łukasiewicza Rzeszów, Poland

Hwang, Hyeon Jong

Seoul National University Seoul, Republic of Korea

Hwang, Shyh-Jiann

National Taiwan University *Taipei, Taiwan, China*

Ibrahim, Ayoob

University of Wollongong Wollongong, NSW, Australia

Ibrahim, Izni

Universiti Teknologi Malaysia Johor Bahru, Johor, Malaysia

Ichinose, Toshikatsu

Meijo University Nagoya, Aichi, Japan

Idrees, Maria

University of Engineering and Technology Lahore Lahore, Punjab, Pakistan

Idrisi, Amir Hussain

Michigan Technological University Houghton, MI, United States

Ilki, Alper

Istanbul Technical University Istanbul, Turkey

Ioannou, Sokrates

Higher Colleges of Technology Abu Dhabi, United Arab Emirates

Irassar, Edgardo

Dep. Ingeniería Civil - UNCPBA Olavarría, Buenos Aires, Argentina

Isik, Ercan

Bitlis Eren Üniversitesi Bitlis, Turkey

Islam, Mohammad Momeen Ul

RMIT University
Melbourne, VIC, Australia

Ismail, Kamaran

The University of Sheffield
Sheffield, United Kingdom of Great Britain and Northern Ireland

Ismail, Mohamed

Memorial University of Newfoundland St. John's, NL, Canada

Jagad, Gaurav

Sardar Vallabhbhai National Institute of Technology Surat, Gujarat, India

Jahami, Ali

University of Balamand Faculty of Engineering *El-Koura, Lebanon*

Jang, Bong

K-water Deajeon, Republic of Korea

Jang, Seung Yup

Korea National University of Transportation *Uiwang, Gyeonggi-do, Republic of Korea*

Jansen, Daniel

California Polytechnic State University San Luis Obispo, CA, United States

Janssen, Donald

Seattle, WA, United States

Januzzi, Rafael

Universidade Federal de Ouro Preto Ouro Preto, Minas Gerais, Brazil

Javed, Ali

Florida International University Miami, FL, United States

Jędrzejewska, Agnieszka

Silesian Technical University *Gliwice, Poland*

Jensen, Elin

Lawrence Technological University Southfield, MI, United States

Jensen, James

San Mateo, CA, United States

Jeyan Sudhakar, Alein

SRM Institute of Science and Technology Kattankulathur, India

Jiang, Hua

McDermott International Inc. *Plainfield, IL, United States*

Jiang, Liying

Jensen Hughes Inc. Lexington, MA, United States

John. V. Thomas

CUSAT Kochi, Kerala, India

Johnston, David

North Carolina State University Raleigh, NC, United States

Jozić, Dražan

Faculty of Chemical Technology Split, Croatia

K, K B Prakash

Government Engineering College, Haveri *Haveri, Karnataka, India*

K, Sargunan

Malla Reddy Engineering College *Secunderabad, India*

Kadima Lukanu Lwa Nzambi, Aaron

Universidade Federal do Pará *Belém, Brazil*

Kaliyavaradhan, Senthil

Hunan University Changsha, Hunan, China

Kalliontzis, Dimitrios

University of California, San Diego San Diego, CA, United States

Kamath, Muralidhar

Manipal Academy of Higher Education Dakshima Kannada, Karnataka, India

Kan, Yu-Cheng

Chaoyang University of Technology *Taichung County, Taiwan, China*

Kanaan, Dima

Concordia University - Sir George Williams Campus Montreal, QC, Canada

Kanagaraj, Ramadevi

Kumaraguru College of Technology *Coimbatore, Tamil Nadu, India*

Kandasami, Siyakumar

Larsen and Toubro Ltd. *Chennai, Tamil Nadu, India*

Kankam, Charles

Kwame Nkrumah University of Science & Technology Kumasi, Ghana

Kanta Rao, Velidandi

Central Road Research Institute New Delhi, Delhi, India

Kar, Arkamitra

Birla Institute of Technology and Science Pilani *Hyderabad, Telangana, India*

Karade, Sukhdeo

CSIR-Central Building Research Institute Roorkee, Uttarakhand, India

Karakale, Vail

Marmara Üniversitesi Istanbul, Turkey

Karayannis, Christos

Democritus University of Thrace *Xanthi, Greece*

Karimi, Hossein

Eindhoven University of Technology Eindhoven, Netherlands

Kaya, Osman

Muğla Sıtkı Koçman Üniversitesi Muğla, Turkey

Kazemi, Mohammad

Sharif University of Technology Tehran, Tehran, Islamic Republic of Iran

Ke, Guo-Ju

Research Institute of Highway Ministry of Transport *Beijing, China*

Keskin, Süleyman

Muğla Sıtkı Koçman Üniversitesi Muğla, Turkey

Khabaz, Amjad

Hasan Kalyoncu University Gaziantep, Turkey

Khajehdehi, Rouzbeh

SJCA P. C. *Indianapolis, IN, United States*

Khaliq, Wasim

National University of Sciences and Technology Islamabad, ICT, Pakistan

Khan, Sadaqat Ullah

NED University of Engineering and Technology *Karachi, Sindh, Pakistan*

Khatib, Jamal

University of Wolverhampton

Wolverhampton, United Kingdom of Great Britain and Northern Ireland

Khennane, Amar

UNSW @ ADFA

Canberra, ACT, Australia

Khorramian, Koosha

Dalhousie University

Halifax, NS, Canada

Kim, Chulgoo

Seoul National University

Seoul, Republic of Korea

Kim, Kil-Hee

Kongju National University

Kongju, Chungnam, Republic of Korea

Kim, Tae-Hoon

Korea Railroad Research Institute

Uiwang, Republic of Korea

Kim, Taehwan

University of New South Wales

Sydney, NSW, Australia

Kisicek, Tomislav

Civil Engineering Faculty

Zagreb, Croatia

Koehler, Eric

Titan America

Norfolk, VA, United States

Kopiika, Nadiia

Lviv Polytechnic National University

Lviv, Ukraine

Kotecha, Payal

The University of Texas at Arlington

Daytona Beach, FL, United States

Kreiger, Eric

U.S. Army Corps of Engineers Construction Engineering

Research Laboratory

Champaign, IL, United States

Krstulovic-Opara, Neven

ExxonMobil Production Co.

Houston, TX, United States

Kumar, Mayank

NIT Kurukshetra

Kurukshetra, Haryana, India

Laco, Jan

D-Phase a.s.

Bratislava, Slovakia

Lai, James

Sacramento, CA, United States

Lai, Jianzhong

Nanjing University of Science and Technology

Nanjing, Jiangsu, China

Lakavath, Chandrashekar

Indian Institute of Technology Hyderabad

Hyderabad, Telangana, India

Lakshmi, R

Kamaraj College of Engineering and Technology

Virudhunagar, Tamil Nadu, India

Lantsoght, Eva

Delft University of Technology

Delft, Netherlands

Lapi, Massimo

Università degli Studi di Firenze

Florence, Italy

Lederle, Rita

University of St. Thomas

Saint Paul, MN, United States

Lee, Chadon

Chung-Ang University

Anseong, Gyeonggi, Republic of Korea

Lee, Chang Hoon

Cornell University

Ithaca, NY, United States

Lee, Deuckhang

Chungbuk National University

Cheongju, Republic of Korea

Lee, Heui Hwang

HNTB Corporation - Oakland

Oakland, CA, United States

Lee, Hung-Jen

National Yunlin University of Science and Technology

Douliou, Taiwan

Lee, Ju Dong

Texas A&M Transportation Institute

Bryan, TX, United States

Lehman, Dawn

University of Washington

Seattle, WA, United States

Lequesne, Rémy D.

University of Kansas Lawrence, KS, United States

Li, Bo

The Hong Kong Polytechnic University Kowloon, Hong Kong, China

Li, Fumin

China University of Mining and Technology *Xuzhou, Jiangsu, China*

Li, Genfeng

Chongqing University of Arts and Sciences *Chongqing, China*

Li, Ning

Tianjin University Tianjin, Tianjin, China

Liao, Wen-Cheng

National Taiwan University *Taipei, Taiwan, China*

Libre, Nicolas Ali

Missouri University of Science and Technology Rolla, MO, United States

Lignola, Gian Piero

Università degli Studi di Napoli Federico II Scuola Politecnica e delle Scienze di Base Naples, Italy

Lin, Wei-Ting

Dept. of Civil Engineering *Yilan, Taiwan, China*

Liu, Chengqing

Southwest Jiaotong University Chengdu, Sichuan, China

Liu, Kai-Wei (Victor)

Prairie View A&M University Prairie View, TX, United States

Liu, Peng

Changsha, China

Liu, Wenguang

Shanghai University Shanghai, Shanghai, China

Liu, Xuejian

The University of Texas at Arlington *Arlington, TX, United States*

Liu, Zhengyu

Iowa State University of Science and Technology Ames, IA, United States

Lizarazo Marriaga, Juan

Universidad Nacional de Colombia - Sede Bogotá Bogotá, Colombia

Looi, Daniel

Swinburne University of Technology - Sarawak Campus Kuching, Malaysia

Lopes, Sergio

University of Coimbra *Coimbra, Portugal*

Lu, Tingting

Xi'an, Shaanxi, China

Luan, Yao

Saitama University Saitama, Japan

Lubell, Adam

Read Jones Christoffersen Ltd. *Vancouver, BC, Canada*

Lutomirska, Marta

Warsaw University of Technology Faculty of Civil Engineering Warsaw, Poland

Lv, Henglin

Xuxhou, Jiangsu, China

Ma, Zhongguo

University of Tennessee Knoxville, TN, United States

Maage, Magne

Skanska Norge AS Trondheim, Norway

MacDougall, Colin

Queen's University Kingston, ON, Canada

Maganti, Ravindra Krishna

Guntur Engineering College Guntur, Andhra Pradesh, India

Mahadik, Vinay

University of Stuttgart Stuttgart, Germany

Maheswaran, Chellapandian

Mepco Schlenk Engineering College Sivakasi, Tamil Nadu, India

Mahfouz, Ibrahim

Cairo, Egypt

Mander, John

Texas A&M University

College Station, TX, United States

Mardi, Sahand

QIAU

Qazvin, Islamic Republic of Iran

Marikunte, Shashi

Southern Illinois University Carbondale, IL, United States

Marques, Marília

Rio Paranaíba, Minas Gerais, Brazil

Martinez Andino, Marcos

DeSimone Consulting Engineers *Atlanta, GA, United States*

Mata, Luis

University of Toledo Toledo, OH, United States

Mata-Falcón, Jaime

ETH Zurich, Institute of Structural Engineering Zurich, Zurich, Switzerland

Matta, Fabio

University of South Carolina Columbia, SC, United States

Mazzotti, Claudio

University of Bologna Bologna, Bologna, Italy

McCall, W

Concrete Engineering Consultants *Charlotte, NC, United States*

Medallah, Khaled

Saudi Aramco IKPMS Al Khobar, Saudi Arabia

Meydanli Atalay, Hilal

Kocaeli University Kocaeli, Turkey

Mirrashid, Masoomeh

Semnan University
Semnan, Islamic Republic of Iran

Mirzaee, Alireza

Shiraz, Islamic Republic of Iran

Mitrofanov, Vitalii

Center for Advanced Design Methods of Concrete Structures *Poltava, Ukraine*

Miura, Taito

Nagoya University Nagoya, Aichi, Japan

Mogili, Srinivas

National Taiwan University *Taipei, Taiwan, China*

Mohamed, Ashraf

Alexandria University Alexandria, Egypt

Mohamed, Nayera

Assiut University Assiut, Egypt

Mohammed, Tarek

Islamic University of Technology Gazipur, Dhaka, Bangladesh

Mohee, Fai

TMBN Extrados Inc. Toronto, ON, Canada

Mondal, Bipul

Chittagong University of Engineering & Technology Chattogram, Bangladesh

Montoya Coronado, Luis Alberto

Palma, Spain

Moradi, Hiresh

Amirkabir University of Technology Tehran, Islamic Republic of Iran

Moreno, Carlos

Instituto Politécnico de Bragança Bragança, Bragança, Portugal

Morgese, Maurizio

University of Illinois Chicago *Chicago, IL, United States*

Mostafa, Ibrahim

University of Sherbrooke Sherbrooke, QC, Canada

Mostafa, Mostafa M. A.

Al-Azhar University - Assiut Branch *Qena, Egypt*

Mostofinejad, Davood

Isfahan University of Technology Isfahan, Islamic Republic of Iran

Motaref, Sarira

University of Connecticut Storrs, CT, United States

MS, Sandeep

Muthoot Institute of Technology and Science *Cochin, Kerala, India*

Mubin, Sajjad

University of Engineering and Technology, Lahore *Lahore, Punjab, Pakistan*

Mukai, David

University of Wyoming Laramie, WY, United States

Musselman, Eric

Villanova University Villanova, PA, United States

Mutsuddy, Rupak

Bangladesh University of Engineering and Technology *Dhaka, Bangladesh*

N, Pannirselvam

SRM Institute of Science and Technology Kanchipuram, Tamil Nadu, India

Nabavi, Seyed Esrafil

Rezvanshahr, Islamic Republic of Iran

Nabil, Mohamed

Heriot-Watt University - Dubai Campus Dubai, United Arab Emirates

Naganathan, Sivakumar

Universiti Tenaga Nasional Kajang, Selangor, Malaysia

Nair, Sooraj

United States Gypsum Corporation Libertyville, IL, United States

Najimi, Meysam

Iowa State University Ames, IA, United States

Namakiaraghi, Parsa

Philadelphia, PA, United States

Narayanan, Subramanian

Gaithersburg, MD, United States

Naser, M. Z.

Clemson University
Clemson, SC, United States

Nazarimofrad, Ebrahim

Bu-Ali Sina University Hamedan, Islamic Republic of Iran

Neithalath, Narayanan

Clarkson University
Potsdam, NY, United States

Nguyen, Hai

Huntington, WV, United States

Nguyen, Tan

Ton Duc Thang University Ho Chi Minh City, Viet Nam

Nguyen, Thi Thu Dung

Shimizu Corporation *Chuo-ku, Tokyo, Japan*

Nili, Mahmoud

Bu-Ali Sina University Hamedan, Islamic Republic of Iran

Nishiwaki, Tomoya

Tohoku University Sendai, Japan

Nishiyama, Minehiro

Kyoto University *Kyoto, Japan*

Noshiravani, Talayeh

EPFL

Lausanne, Switzerland

Obla, Karthik

National Ready Mixed Concrete Association Silver Spring, MD, United States

Okeil, Ayman

Louisiana State University Baton Rouge, LA, United States

Okumus, Pinar

University at Buffalo Buffalo, NY, United States

Ombres, Luciano

University of Calabria *Cosenza, Italy*

Oritola, Sikiru

Universiti Teknologi Malaysia Skudai, Malaysia

Orta, Luis

ITESM

Zapopan, Jalisco, Mexico

Ortiz-Lozano, Jose

Autonomous University of Aguascalientes Aguascalientes, Aguascalientes, Mexico

Ou, Yu-Chen

National Taiwan University Taipei, Taiwan, China

Oukaili, Nazar

University of Baghdad Baghdad, Iraq

Oz, Hatice Oznur

Niğde Ömer Halisdemir University Niğde, Turkey

Ozyildirim, H. Celik

Virginia Transportation Research Council Charlottesville, VA, United States

P, Mary

Indian Institute of Technology Madras Chennai, Tamil Nadu, India

Pacheco, Alexandre

Universidade Federal do Rio Grande do Sul (UFRGS) *Porto Alegre, RS, Brazil*

Pacheco, Jose

MJ2 Consulting, PLLC Chicago, IL, United States

Palazzo, Gustavo

National Technological University Ciudad Mendoza, Mendoza, Argentina

Palieraki, Vasiliki

National Technical University of Athens *Zografou, Athens, Greece*

Pan, Wang Fook

SEGi University Petaling Jaya, Selangor, Malaysia

Panchmatia, Parth

Kansas State University

Manhattan, KS, United States

Pandit, Poornachandra

Manipal Institute of Technology *Manipal, India*

Pantazopoulou, Stavroula

York University - Keele Campus *Toronto, ON, Canada*

Parastesh, Hossein

University of Science and Culture Tehran, Tehran, Islamic Republic of Iran

Park, Min-Kook

Delft University of Technology Delft, Netherlands

Parsekian, Guilherme

UFSCar São Carlos, Brazil

Parthasarathy, Pavithra

Hong Kong University of Science and Technology Kowloon, Hong Kong, China

Patil, Sagar

Tatyasaheb Kore Institute of Engineering & Technology Warananagar, Maharashtra, India

Paul, Alvaro

Universidad de los Andes Santiago, Las Condes, Chile

Paulson, Conrad

Wiss, Janney, Elstner Associates, Inc. *Pasadena, CA, United States*

Peng, Fei

Hunan University Changsha, China

Perceka, Wisena

Parahyangan Catholic University Faculty of Engineering Bandung, West Java, Indonesia

Persson, Bertil

Bara, Sweden

Piccinin, Roberto

Hilti, Inc.

Tulsa, OK, United States

Pierott, Rodrigo

Universidade Estadual do Norte Fluminense Darcy Ribeiro Campos dos Goytacazes, RJ, Brazil

Pincheira, Jose

University of Wisconsin–Madison Madison, WI, United States

Pocesta, Ylli

Debar, North Macedonia

Pourazin, Khashaiar

Pars AB Tadbir Consulting Engineering Company *Tehran, Islamic Republic of Iran*

Pourbaba, Masoud

Islamic Azad University, Maragheh Maragheh, East Azerbaijan, Islamic Republic of Iran

Prakash, M N

J.N.N. College of Engineering Shimoga, Karnataka, India

Praul, Michael

FHWA

Augusta, ME, United States

Presuel-Moreno, Francisco

Florida Atlantic University

Dania Beach, FL. United States

Princigallo, Antonio

Heidelberg Materials Italia Cementi S.p.A Peschiera Borromeo, Milan, Italy

Pugliaro, Andrea

Senior Materials and Laboratory Engineer (Civil and Geotechnical)
Savona, Italy

Putra Jaya, Ramadhansyah

Universiti Teknologi Malaysia Gambang, Pahang, Malaysia

Pv, Premalatha

CARE School of Engineering *Tiruchirappalli, India*

Qian, Chen-Hui

Shanghai Jiao Tong University Shanghai, China

Qian, Kai

NTU

Singapore, Singapore

Qissab, Musab

Al-Nahrain University Baghdad, Iraq

Quach, Phillip

RJC Engineers
Toronto, ON. Canada

Quintana Gallo, Patricio

Czech Technical University in Prague Prague, Czech Republic

Quiroga, Pedro

Escuela Colombiana de Ingeniería Julio Garavito Bogotá, Colombia

Rafi, Muhammad

NED University of Engineering and Technology Karachi, Sindh, Pakistan

Raghavendra, T.

R.V. College of Engineering, Visvesvaraya Technological University

Bangalore, Karnataka, India

Ragheb, Wael

Alexandria University Windsor, ON, Canada

Rahal, Khaldoun

Kuwait University Safat, Kuwait

Ramaswamy, Ananth

Indian Institute of Science Bangalore, Karnataka, India

Ramirez, Julio

Purdue University
West Lafayette, IN, United States

Rasul, Mehboob

Sumitomo Mitsui Construction Co Ltd *Chuo, Japan*

Razaqpur, A. Ghani

McMaster University Hamilton, ON, Canada

Rezaifar, Omid

Semnan, Semnan, Islamic Republic of Iran

Ridha, Maha (Lianne)

Melbourne, VIC, Australia

Rizwan, Syed Ali

National University of Computer and Emerging Sciences -Lahore Campus Lahore, Punjab, Pakistan

Rodrigues, Publio

LPE Engenharia e Consultoria São Paulo, Brazil

Rodriguez, Mario

National Autonomous University of Mexico Mexico City, Mexico

Rojas Aguero, Rosangel

Universidade Federal do Rio Grande Rio Grande, Rio Grande do Sul, Brazil

Roy, Arunabha Mohan

University of Michigan Ann Arbor, MI, United States

Rughooputh, Reshma

University of Mauritius *Moka, Mauritius*

S, Kumaravel

Annamalai University
Cuddalore, Tamil Nadu, India

S A, Jaffer Sathik

CSIR-SERC

Chennai, Tamil Nadu, India

Saedi, Houman

Tarbiat Modares & Tabriz University and TSML Co. *Tehran, Islamic Republic of Iran*

Saeed, Yasir

Portland State University Portland, OR, United States

Saeki, Tatsuhiko

Niigata University Niiagta, Japan

Safiuddin, Md.

George Brown College Toronto, ON, Canada

Sahoo, Kirtikanta

Rourkela, India

Said, Shwan

Erbil, Iraq

Sakban, Haider

Piscataway, NJ, United States

Saleh Ahari, Reza

Ege University İzmir, Turkey

Salib, Sameh

Markham, ON, Canada

Sánchez, Isidro

University of Alicante Alicante, Alicante, Spain

Santos, Daniel

Polytechnic School of the University of São Paulo São Paulo, São Paulo, Brazil

Santos, Jose

University of Madeira Funchal, Portugal

Santos, Sérgio

SBS Engineering Consultancy Goiânia, Goiás, Brazil

Sapp, James

ATMI Precast Aurora, IL, United States

Sartaji, Parisa

Ardabil, Islamic Republic of Iran

Sato, Yuichi

Kyoto University Kyoto, Kyoto, Japan

Sayed Ahmed, Mahmoud

Toronto Metropolitan University *Toronto, ON, Canada*

Sayın, Barış

Engineering Faculty Istanbul, Turkey

Schlicke, Dirk

Graz University of Technology Graz, Austria

Seco, Laura

Coimbra, Portugal

Semelawy, Mohamed

Western University London, ON, Canada

Sengupta, Amlan

Indian Institute of Technology Madras Chennai, Tamil Nadu, India

Serry, Mohamed

The Arab Contractors *Cairo, Egypt*

Sezen, Halil

Ohio State University

Columbus, OH, United States

Sha, Fei

Shandong University Jinan, Shandong, China

Shabana, Islam

University of Sherbrooke Sherbrooke, QC, Canada

Shafigh, Payam

Kuala Lumpur, Malaysia

Shafiq, Nasir

Universiti Teknologi PETRONAS Tronoh, Perak, Malaysia

Shaik, Madeena Imam Shah

Advanced Construction Technology Services SAL Riyadh, Saudi Arabia

Sharifzad, Shayan

The University of Texas at Arlington College of Engineering *Arlington, TX, United States*

Sharma, Akanshu

Institute of Construction Materials Stuttgart, Germany

Shehata, Medhat

Toronto Metropolitan University *Toronto, ON, Canada*

Shekarchi, William

Austin, TX, United States

Shen, Yin

Tongji University Shanghai, China

Shete, Vivek

TKIET Warananagar Panhala, Maharashtra, India

Shetty, Kiran

Manipal Institute of Technology Manipal, Karnataka, India

Shi, Caijun

Hunan University Changsha, Hunan, China

Shi, Xianming

Washington State University Pullman, WA, United States

Shin, Hyeongyeop

Seoul National University

Gwanak-gu, Seoul, Republic of Korea

Shumuye, Eskinder Desta

Shenzhen University College of Civil and Transportation Engineering Shenzhen, GD, China

Shuraim, Ahmed

King Saud University Riyadh, Saudi Arabia

Siddique, Mohammad

Bangladesh University of Engineering and Technology Dhaka, Bangladesh

Silfwerbrand, Johan

KTH Royal Institute of Technology *Stockholm, Sweden*

Silva, Marcos

Campinas, Brazil

Simplício, Marcos

Universidade Federal de Sergipe *Aracaju, Sergipe, Brazil*

Singh, Brijesh

Faridabad, Haryana, India

Singh, Harvinder

Guru Nanak Dev Engineering College Ludhiana, Punjab, India

Singh, Navdeep

Jalandhar, Punjab, India

Singh, Surender

Indian Institute of Technology Madras Chennai, Tamil Nadu, India

Sivey, Paul

Sivey Enterprises
Hilliard, OH, United States

Smadi, Mohammad

Jordan University of Science and Technology *Irbid*, *Jordan*

Soares, Renan

Universidade Federal de Pernambuco *Recife, Pernambuco, Brazil*

Soliman, Ahmed

Western University London, ON, Canada

Solnosky, Ryan

Penn State University Park University Park, PA, United States

Soltani, Mahmoodreza

Bradley University Caterpillar College of Engineering and Technology

Peoria, IL, United States

Sonkusare, Hemantkumar G H Raisoni College of Engineering Nagpur, Maharashtra, India

Sonyal, Muhammad

University of Engineering and Technology, Lahore Lahore, Punjab, Pakistan

Sorensen, Taylor

Brigham Young University Provo, UT, United States

Spinella, Nino

University of Catania Faculty of Engineering Catania, Italy

Spyridis, Panagiotis

Institute for Structural Engineering Vienna, Austria

Sreekala, R

Structural Engineering Research Centre Chennai, Tamil Nadu, India

Sreenivasappa, Nandeesh

Ramaiah Institute of Technology Bangalore, Karnataka, India

Stalin Anto, Karthiga

Bannari Amman Institute of Technology Sathyamangalam, Tamil Nadu, India

Stojadinovic, Bozidar

Swiss Federal Institute of Technology Zurich. Switzerland

Stucchi, Fernando

Polytechnic School of the University of São Paulo *Adamantina, SP, Brazil*

Su, Yu-Min

National Kaohsiung University of Science and Technology Kaohsiung, Taiwan, China

Suda, Vijaya

Vardhaman College of Engineering Shamshabad, Telangana, India

Sultan, Mohamed

Al-Azhar University Cairo, Egypt

Sun, Jing

Beijing, China

Sun, Qiaorong

Hohai University
Nanjing, Jiangsu, China

Suryawanshi, Yogesh

JSPM's Imperial College of Engineering and Research, Wagholi *Pune, Maharashtra, India*

Swamy, H C

Bangalore, Karnataka, India

Tabkhi Wayghan, Amir Reza

Carleton University Faculty of Engineering and Design Ottawa, ON, Canada

Tabsh, Sami

American University of Sharjah Sharjah, United Arab Emirates

Tadros, Maher

e.construct.USA, LLC Omaha, NE, United States

Tajaddini, Abbas

University of Bath Faculty of Engineering and Design Bath, United Kingdom of Great Britain and Northern Ireland

Tan, Kiang Hwee

National University of Singapore Singapore, Singapore

Tang, Chao-Wei

Cheng Shiu University
Niaosong District, Kaohsiung City, Taiwan, China

Tang, Fujian

Dalian University of Technology Dalian, Liaoning, China

Tang, Xiusheng

Nanjing Hydraulic Research Institute *Nanjing, China*

Tawfic, Yasser

Minia University
Minia, Minia, Egypt

Teodoro, Rodrigo

Goiânia, Goiás, Brazil

Thokchom, Suresh

Manipur Institute of Technology Imphal, Manipur, India

Tian, Ying

University of Nevada, Las Vegas Las Vegas, NV, United States

Tiznobaik, Mohammad

The University of British Columbia | Okanagan Campus Kelowna, BC, Canada

Tkach, James

Largo Concrete, Inc. San Diego, CA, United States

Tognonvi, Tohoue Monique

Université de Sherbrooke Sherbrooke, QC, Canada

Tomas, Antonio

Technical University of Cartagena Cartagena, Spain

Topuzi, Dritan

Schöck Bauteile GmbH Toronto, ON, Canada

Torabian, Ala

Isfahan, Islamic Republic of Iran

Tore, Erkan

Balıkesir University
Balıkesir, Balıkesir, Turkey

Tosun, Kamile

Dokuz Eylül University İzmir, Turkey

Tran, Mien

Ho Chi Minh City University of Technology Ho Chi Minh City, Viet Nam

Trejo, David

Oregon State University Corvallis, OR, United States

Tripathi, Deep

University of Sherbrooke Faculty of Engineering Sherbrooke, QC, Canada

Tuchscherer, Robin

Northern Arizona University Flagstaff, AZ, United States

Ueda, Naoshi

Kansai University Suita, Osaka, Japan

Umipig, Jorge

Vista Land & Lifescapes, Inc.

Mandaluyong City, Metro Manila, Philippines

Ungermann, Jan

RWTH Aachen University Aachen, Germany

Uzel, Almıla

Yeditepe University Istanbul, Turkey

Vaz Rodrigues, Rui

Universidade de Lisboa Instituto Superior Técnico Lisbon, Portugal

Venkataraman, Jayakumar

IFET College of Engineering Viluppuram, Tamil Nadu, India

Vollum, Robert

Department of Civil and Environmental Engineering London, United Kingdom of Great Britain and Northern Ireland

Vosahlik, Jan

ICON

Austin, TX, United States

Vosoughi, Payam

Caltrans

Rancho Cordova, CA, United States

Vu, Ngoc Son

Hanoi University of Civil Engineering *Hanoi, Viet Nam*

Wally, Gustavo

Universidade Federal do Rio Grande do Sul *Porto Alegre, Brazil*

Wang, Ben

University of Houston Houston, TX, United States

Wang, Dun

Research Institute of Structural Engineering & Disaster Reduction, Tongji University Shanghai, China

Wang, Hongze

Inner Mongolia University of Technology Hohhot, Inner Mongolia, China

Wang, Kejin

Iowa State University Ames, IA, United States

Wang, Xiao-Yong

Kangwon National University Chuncheon, Republic of Korea

Wardhono, Arie

The State University of Surabaya Surabaya, East Java, Indonesia

Wei-Jian, Yi

Changsha, China

Werner, Anne

SILIE

Edwardsville, IL, United States

Windisch, Andor

Karlsfeld, Germany

Witwit, Jaafar

Baghdad, Iraq

Won, Moon

Texas Tech University

Lubbock, TX, United States

Wong, Sook Fun

Nanyang Technological University Singapore, Singapore

Wu, Chao

Wuhan University of Technology Wuhan, Hubei, China

Wu, Kai

Nanjing, Jiangsu, China

Wu, Ruoyang

University of Utah Herriman, UT, United States

Wu, Yu-You

Foshan University Foshan, Guangdong, China

Wu, Zhimin

Dalian University of Technology Dalian, Liaoning, China

Xi, Xun

University of Strathclyde

Glasgow, United Kingdom of Great Britain and Northern Ireland

Xia, Jin

Zhejiang University

Hangzhou, Zhejiang, China

Xie, Guoshuai

Wuhan University

Wuhan, Hubei, China

Xie, Jun

Ministry of Transport Research Institute of Highways

Beijing, China

Xie, Tianyu

RMIT University

Melbourne, VIC, Australia

Xu, Aimin

ARRB Group

Melbourne, VIC, Australia

Yan, Peiyu

Tsinghua University

Beijing, China

Yang, Junlong

Dalian University of Technology

Dalian, China

Yang, Keun-Hyeok

Kyonggi University

Suwon, Gyeonggi-do, Republic of Korea

Yang, Rick

SNC-Lavalin Engineers and Constructors Inc

Houston, TX, United States

Yang, Shuyan

Yinchuan City, China

Yang, Sung Chul

Hongik University

Mapo-gu, Republic of Korea

Yang, Yunyun

Guanghan, China

Yankelevsky, David

National Building Research Institute

Haifa, Israel

Yapa, Hiran

University of Peradeniya Faculty of Engineering

Peradeniya, Sri Lanka

Yaqub, Muhammad

University of Engineering and Technology, Taxila

Taxila, Punjab, Pakistan

Yassein, Mohamed

Abu Dhabi, Abu Dhabi, United Arab Emirates

Yasso, Samir

University of Mosul

Mosul, Nineveh, Iraq

Yazbeck, Fouad

360 TANGENT Engineering Consultancy

Abu Dhabi, United Arab Emirates

Yazdani, Nur

The University of Texas at Arlington

Arlington, TX, United States

Yekrangnia, Mohammad

Shahid Rajaee Teacher Training University

Tehran, Islamic Republic of Iran

Yerramala, Amarnath

University of Dundee

Dundee, United Kingdom of Great Britain and Northern Ireland

Yi, Yousun

The University of Texas at Austin

Austin, TX, United States

Yildirim, Salih

Columbia University

New York, New York, United States

Yindeesuk, Sukit

University of Illinois Urbana-Champaign

Urbana, IL, United States

Yingjie, Shan

Central South University

Changsha, Hunan, China

Youdong, Xing

Guilin, China

Yousefpour, Hossein

The University of Texas at Austin

Austin, TX, United States

Youssef, Ahmed

Giza, Giza, Egypt

Youzhi, Liu

China Institute of Water Resources and Hydropower Research

Beijing, China

Yuan, Qiang

Central South University

Changsha, China

Yüksel, Isa

Bursa Technical University Bursa, Turkey

Yuniarsyah, Eko

Institut Teknologi Bandung Bandung, Indonesia

Zaki, Adel

SNC-Lavalin

Montreal, QC, Canada

Zandparsa, Kumars

California State University, Long Beach Long Beach, CA, United States

Zanuy, Carlos

Universidad Politécnica de Madrid *Madrid, Madrid, Spain*

Zapata, Luis

Universidad Industrial de Santander Bucaramanga, Santander, Colombia

Zega, Claudio

CONICET

La Plata, Argentina

Zeidan, Mohamed

Southeastern Louisiana University College of Science and Technology

Hammond. LA. United States

Zeris, Christos

National Technical University of Athens *Zografou, Greece*

Zhang, Changhui

Zhengzhou University Zhengzhou, Henan, China

Zhang, Feng

Nanjing Hydraulic Research Institute *Nanjing, China*

Zhang, Hongen

Tongji University Shanghai, China

Zhang, Peng

Karlsruhe Institute of Technology (KIT) Karlsruhe, Germany

Zhang, Qian

Nanjing, China

Zhang, Qin

Dalian University of Technology Dalian, Liaoning, China

Zhang, Wei

University of Tsukuba Tsukuba, Japan

Zhao, Tiejun

Qingdao, China

Zhao, Xingzhuang

University of Maryland College Park College Park, MD, United States

Zhao, Xin-Yu

South China University of Technology Guangzhou, China

Zheng, Dafeng

Guangzhou, Guangdong, China

Zheng, Herbert

Gammon Construction Limited Hong Kong, Hong Kong, China

Zheng, Yu

Dongguan University of Technology Dongguan, Guangdong, China

Zheng, Yulong

Jiangsu University Zhenjiang, China

Zhenhong, Wang

China Institute of Water Resources and Hydropower Research *Beijing, China*

Zhong, Rui

Southeast University Nanjing, China

Zhu, Hai

Charlotte, NC, United States

Zhu, Wenjun

L'Institut National des Sciences Appliquées de Toulouse Toulouse, Toulouse, France

Zhu, Yanping

Missouri University of Science and Technology Rolla, MO, United States

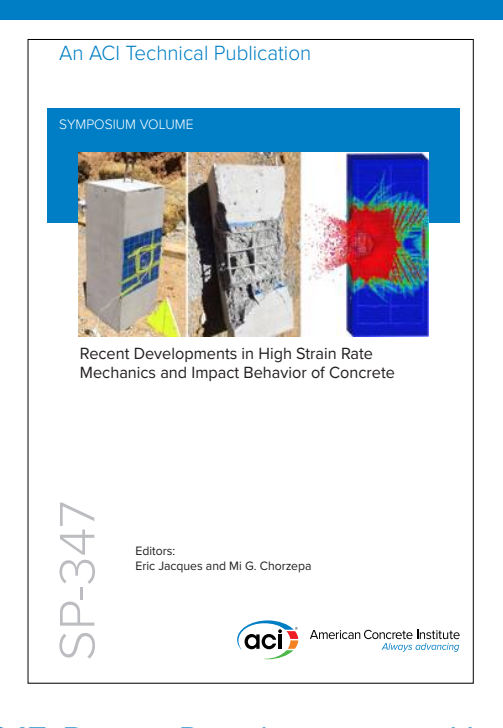
Zornoza, Emilio

University of Alicante Alicante, Alicante, Spain

Zych, Mariusz

Politechnika Krakowska im. Tadeusza Kościuszki Krakow, Poland

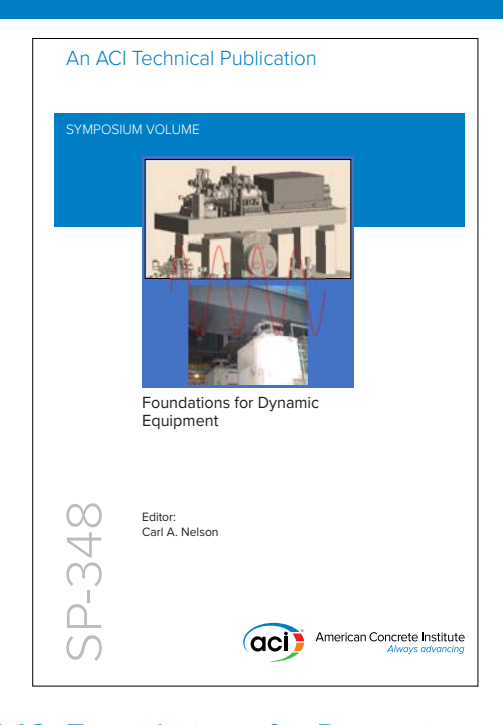
Symposium Publications from ACI



SP-347: Recent Developments in High Strain Rate Mechanics and Impact Behavior of Concrete

This Symposium Volume reports on the latest developments in the field of high-strain-rate mechanics and behavior of concrete subject to impact loads. This effort supports the mission of ACI Committee 370, Blast and Impact Load Effects, to develop and disseminate information on the design of concrete structures subjected to impact, as well as blast and other short-duration dynamic loads.

Available in PDF format: \$69.50 (ACI members: \$39.00) (\$30.50 savings)



SP-348: Foundations for Dynamic Equipment

This special publication grew out of the Technical Session titled "Application of ACI 351-C Report on Dynamic Foundations," held at the ACI Spring 2019 Convention in Québec City, Québec. Following this event, ACI Committee 351 decided to undertake a special publication with contributions from those session participants willing to develop their presentations into full-length papers. Three papers included in the current publication were contributed by these presenters and their coauthors, with six additional papers provided by others.

Available in PDF format: \$69.50 (ACI members: \$39.00) (\$30.50 savings)















American Concrete Institute

This joint special issue of the ACI Structural Journal and ACI Materials Journal contains nine manuscripts focused on construction aspects of additive construction using cement-based materials; these papers cover structural topics on testing reinforced beams and modeling the construction process, and materials topics on the characterizing extrusion, enhancing, and testing mechanical properties; shoreline resiliency; fracture behavior; and quality control methods.

The American Concrete Institute (ACI) is a leading authority and resource worldwide for the development and distribution of consensus-based standards and technical resources, educational programs, and certifications for individuals and organizations involved in concrete design, construction, and materials, who share a commitment to pursuing the best use of concrete.

Individuals interested in the activities of ACI are encouraged to explore the ACI website for membership opportunities, committee activities, and a wide variety of concrete resources. As a volunteer member-driven organization, ACI invites partnerships and welcomes all concrete professionals who wish to be part of a respected, connected, social group that provides an opportunity for professional growth, networking, and enjoyment.

